ISSN 0858-2114

International Agricultural Engineering Journal

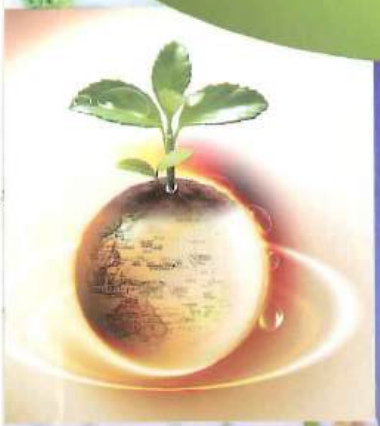

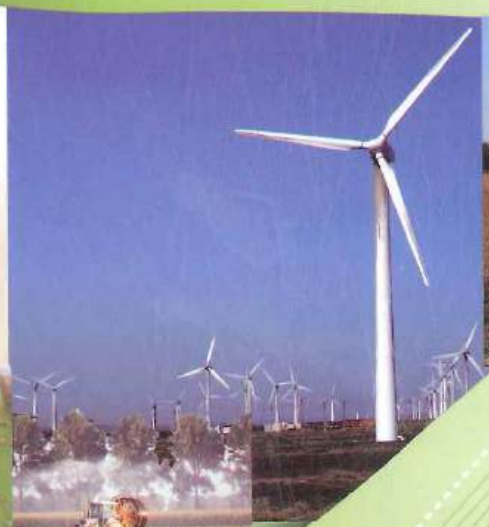

Published by Asian Association for Agricultural Engineering (AAAE)

Vol.26, No.4, 2017

AAAE Secretariat

AAAE was formed for the general advancement of the agricultural engineering profession and its practice in all aspects, especially in Asia and the Pacific region. Since its establishment in 1990, AAAE has played an important role in promoting agricultural engineering worldwide by means of publishing the International Agricultural Engineering Journal (IAEJ), holding biannual academic conferences, exchanging visits among its members, etc. At present, AAAE has more than 260 members in the field of agricultural engineering from 30 countries and regions all over the world.

AAAE has kept developing since its headquarters were shifted to China in April 2010. During the previous seven years, the Secretariat was located in Chinese Academy of Agricultural Mechanization Sciences (2010). Led by AAAE former President Prof. Li Shujun and Secretary General Prof. Zhang Lanfang, the Association has expanded its impacts through holding academic events and working on IAEJ. In March, 2017, due to retirement of Prof. Zhang Lanfang, Prof. Cheng Yongqiang from China Agricultural University was nominated as the Secretary General of AAAE and Executive Editor-in-Chief of IAEJ. Thanks to the solid foundation the former Secretariat has laid, AAAE has grown to an influential platform to enhance communication, motivate knowledge sharing among experts in agricultural engineering all over the world.

The Secretariat is now located in College of Food Science and Nutritional Engineering, China Agricultural University with several staff members working for AAAE routine work. The AAAE Secretary General Prof. Cheng Yongqiang is an expert in food science and head of Department of Food Science and Engineering, and has been an active participant in international academic activities in agricultural engineering. He undertakes the administrative duties associated with AAAE in liaison with the President and the Executive Council. According to the AAAE Statutes, the Secretary General makes appropriate decisions in absence of the President in consultation with the Executive Council members.

College of Food Science and Nutritional Engineering of China Agricultural University will offer a good platform for future growth of the association, for its strength in academic researches and its intensive cooperation with universities, institutes and enterprises in China and abroad. Moreover, China Agricultural University as the origin of modern higher education of agriculture in China that integrates agronomy, life sciences, agricultural engineering and food sciences will provide strong support to the Association.

The Treasurer of AAAE is Ms. Zhou Rong. She is responsible for maintaining records of the income and expenditures of the Association, and providing an annual accounts statement during the General Body meeting of AAAE.

AAAE is one of the world's leading international academic societies in the agricultural engineering field. The AAAE Secretariat will continue to do a better job according to the working plan made by the AAAE President and approved by the AAAE Executive Council meeting. The AAAE Secretariat would like to work together and collaborate with all its members worldwide for the purpose of promoting the advancement of agricultural engineering to upgrade the quality of life of people.

Contact Information:
Secretariat of Asian Association for Agricultural Engineering (AAAE)
Mail Box No. 40, East campus of China Agricultural University, No. 17 Qinghua East Road, Haidian District, 100083 Beijing, China
Tel: +86-10-62737401 Fax:+86-10-62737401
Email: aaaese@aliyun.com iaejeditor@aliyun.com

International Agricultural Engineering Journal

An International Journal on Research and Development in Agricultural Engineering
Published by the Asian Association for Agricultural Engineering (AAAE)

Any statements or views expressed in the papers published in this journal are those of authors, and the Editor or Association will not be responsible for the accuracy of such statements or views.

Aims and Scope: The aim of this journal is to communicate advances in Agricultural Engineering, with particular reference to Asia, to practicing professionals in the field. The scope will include soil and water engineering, farm machinery, farm structures, post-harvest technology, biotechnology food processing and emerging technologies. Subjects of general interest to agricultural engineers such as ergonomics, energy, systems engineering, precision agriculture, protected cultivation, terramechanics, instrumentation, environment in agriculture and new materials are also included.

Publication Schedule: International Agricultural Engineering Journal is published in four issues per year.

Subscriptions: For academic institutions, the annual subscription is US$ 280 per calendar year. The journal copies will be mailed by sea mail.

Correspondence: All manuscripts and other correspondence should be directed to the Executive Editor-in-Chief, Department of Food Science and Engineering, College of Food Science and Nutritional Engineering, China Agricultural University. E-mail: iaejeditor@aliyun.com

---

Any statements or views expressed in the papers published in this journal are those of author/s, and the Chief Editor, Assistant/Associate Editors or AAAE will not be responsible for the accuracy of such statements or views expressed in the published manuscripts.

INTERNATIONAL AGRICULTURAL ENGINEERING JOURNAL

Published by

ASIAN ASSOCIATION FOR AGRICULTURAL ENGINEERING (AAAE)

Vol. 26, No. 4, 2017

TABLE OF CONTENTS

Small tractor navigation system based on tandem PD control law

Tian Guangzhao, Gu Baoxing*, Xu Weiyue, Zhou Jun

(*Engineering College, Nanjing Agricultural University, Nanjing 210031, China*)

Abstract: In order to determine a useful and applicable navigation control system for autonomous agricultural vehicles, a Dongfanghong SG250 tractor was modified to use as an experimental platform. The original manual steering hydraulic system was changed into an autonomous one that could be controlled by an MCU. Several sensors (speed, vision, steering angle sensor and RTK GPS) were then fixed to the tractor to detect external environmental parameters and its current state. Then, a steering model was constructed and an adaptive PD controller was used to direct the tractor's steering precisely. Next, another tandem PD controller, which consisted of the steering controller and a lateral motion controller, was used as the navigation controller, again without using a kinematic model of the tractor. Finally, the performance of the navigation control system was evaluated for three kinds of navigation tasks: line tracking, obstacle avoidance and turning. Experimental results showed that without a kinematic model, the tractor could be controlled precisely only with the tandem PD controller, which only used the lateral deviation as the system input without course deviation. This research provided an effective solution to the agricultural vehicle navigation issue.

Keywords: agricultural vehicle, lateral deviation, navigation, tandem PD controller, sensor

Citation: Tian, G. Z., B. X. Gu, W. Y. Xu, and J. Zhou. 2017. Small tractor navigation system based on tandem PD control law. International Agricultural Engineering Journal, 26(4): 1–9.

1 Introduction

The rapid development of computer and electronic technology has an impressive impact on agricultural machinery in recent years. Autonomous tractors can help farmers in improving work efficiency and reducing production costs. It is currently being researched by engineers and researchers in the world.

During the past decade, enormous progresses in tractor navigation technique have been made. Barawid et al. (2006) developed an automatic guidance system which was capable in navigating an autonomous vehicle between trees' rows in real-time. Gan-Mor et al. (2007) recorded the deviations from a predetermined route of a three-point hitch implement mounted on a RTK-DGPS-based automatically guided tractor and concluded that the implement deviation was strongly dependent on the distance from the tractor rear axle. Subsequently, Kise et al. (2008) developed a stereovision sensing system for 3D crop row structure mapping and tractor guidance. Luo et al. (2009) developed a navigation control system based on RTK-DGPS for the Dongfanghong X-804 tractor by using the vehicle's kinematic and steering model. Zhu et al. (2010) carried out a research that focused only on PWM based controlled spraying in an unmanned aerial vehicle. Two helicopters were used in this work by inertial measurement unit, magnetometer and GPS. Gomez-Gil et al. (2011) developed two new control laws for navigation control of tractors, one for following straight lines and another for tracking circular arcs. Xiang et al. (2011) designed and constructed an agricultural remote sensing system based on an autonomous helicopter for field image capturing. The main purposes were: developing a ground base station for mission planning, flight command activation and flight monitoring, developing a navigation system and flight path planning method to determine the necessary overlaps of images. Ismail et al. (2012) designed a computer-controlled system to be mounted on an autonomous tractor after electromechanical

Received date: 2017-02-11 **Accepted date:** 2017-10-17

* **Corresponding author: Gu Baoxing,** lecture of Engineering College, Nanjing Agricultural University, 210031, P. R. China. Email: gbx@njau.edu.cn, Tel: +8615077889303.

modifications. The system was designed and attached on the tractor to direct it to move toward a desired position automatically through operator-issued commands. Backman et al. (2012) developed a new kind of navigation system for agricultural tractors, whose focus was on trajectory control via Nonlinear Model Predictive tractor path. Besides, Backman et al. (2013) discussed the applicability of the ISO 11783 network protocol in a distributed combined guidance system for tractors. Choi et al. (2014) detected crops height using LRF for autonomous navigation of a combine harvester. A probabilistic model for navigation of the vehicle in maize field using LRF was also developed based on a particle filter.

The researches mentioned above are almost suitable for large tractors, most of which, especially produced by world famous agricultural machinery companies, preserve an electro-hydraulic interface when assembled. In rural areas of south China, small tractors are widely used as the traction machineries to seed, fertilizer and harvest on account of the long and narrow farmland topology. But most of the small tractors have no electro-hydraulic interfaces because of the cost. This research reported the development of an autonomous small tractor which had undergone electro-hydraulic and multisensory modification. Without the use of a kinematic model, the tractor can be controlled precisely only through the tandem PD control method, which, in the absence of course deviation, uses lateral deviation as the system input. This provides us a simple and applicable solution that can be efficiently realized to deal with the small tractor navigation in the long and narrow farmland topology.

2 Structure of navigation system

In order to achieve autonomous navigation, specific sensors need to be mounted on the tractor, while the hydraulic steering system of the tractor also needs to be modified. The main equipment and sensors used to construct the tractor navigation system are introduced below.

2.1 Experimental platform

In this experiment, the Dongfanghong SG250 tractor was used. Figure 1 shows a view of the tractor and Table 1 contains some of the tractor's basic characteristics.

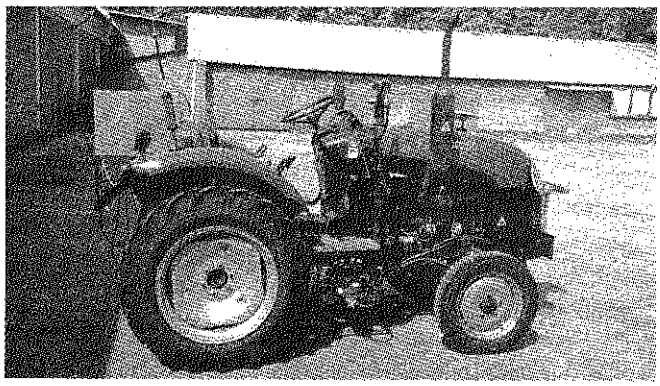

Figure 1 Dongfanghong SG250 tractor

Table 1 Main parameters of Dongfanghong SG250 tractor

Parameter	Value
Engine type	Laidong KM385BT
Rated power, kW	18.4
Drive mode	Two-wheel drive
Dimensions, mm	3490×1450×1550
Wheel base, mm	1690
Minimum turning radius, m	3.5±0.2
Speed range, km h^{-1}	2.07-29.65

2.2 Speed sensor

A DjRVS II Doppler radar was used as the speed sensor. As seen in Figure 2, the radar was mounted at the front of the tractor at an angle of 35°±5°. The measurement range of the radar was 0.53-107 km h^{-1} with an accuracy of ±5%.

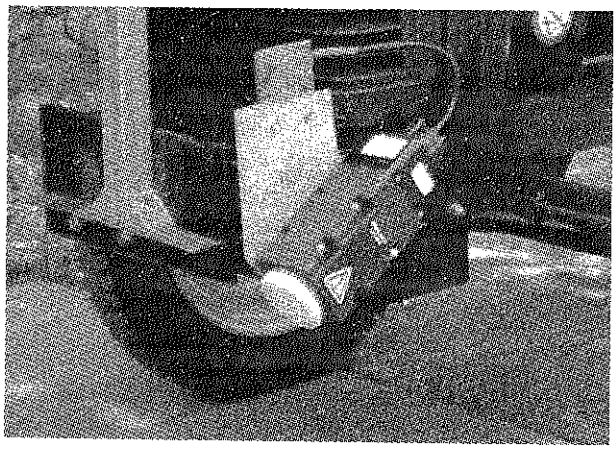

Figure 2 Assembly view of Doppler radar

2.3 Vision sensor

In order to determine the location of obstacles, a Bumblebee XB3 digital camera was fixed on the head of tractor (Figure 3). The main characteristics of the camera are as follows: a 1/3" CCD image sensor, a focal length of 6 mm and 3 micro-lenses.

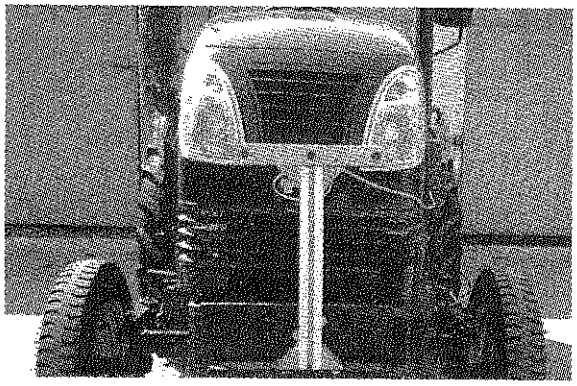

Figure 3 Assembly view of stereo vision camera

2.4 Angle sensor

The accurate determination of the front wheels' steering angle is especially significant to navigation system. In order to measure steering angle accurately, two potentiometers were mounted on the front axle with a belt connecting to a vertical shaft, which was welded to the steering knuckle (Figure 4). The angle sensors were with an accuracy of ±0.5°.

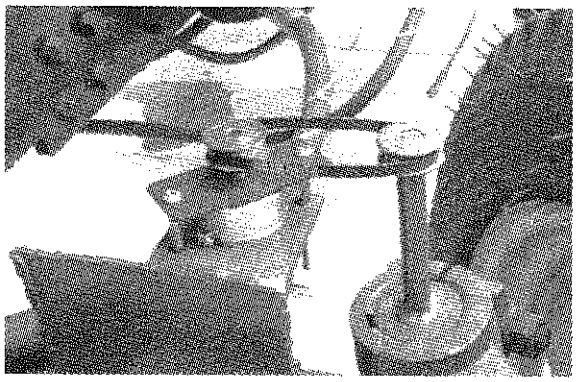

Figure 4 Assembly view of angle sensor

2.5 Satellite position system

As seen in Figure 5, a GPS system was attached to the metal shell of the tractor to obtain coordinate data when the tractor was located in the field. Using two GPS antennas, not only could the position data be retrieved, but course information could be obtained as well. The primary GPS antenna was located at the bonnet and above the front axle of the tractor. The secondary antenna position was 1 m from the primary one at the bonnet of the tractor. The static location error of GPS was less than 2 cm. Angle direction ranged from −180° to 180°. The course angle ranged from 0° to 180° when the direction was changing from True North to True South and from −180° to 0° when the direction was changing from True South to True North, with clockwise turning being considered as an increase in angle value (Figure 6).

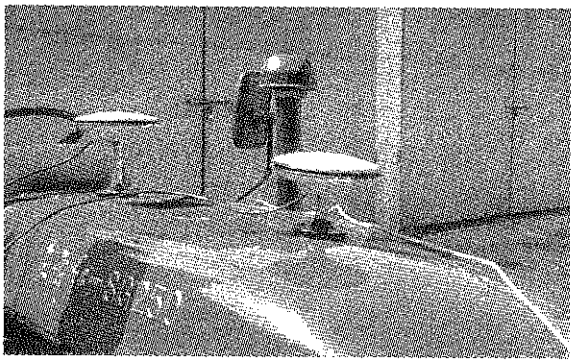

Figure 5 Assembly view of GPS antennas

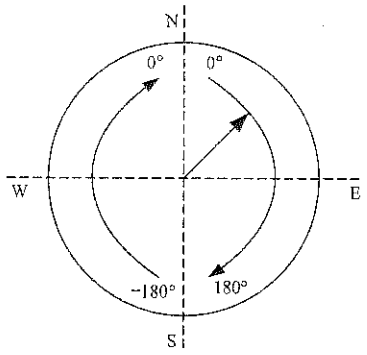

Figure 6 Course range

2.6 Hydraulic steering system

Originally, steering was performed by the driver using the steering wheel. The original hydraulic system was modified, as shown in Figure 7, so, after the modification, the oil flow and the direction in the steering jack could be adjusted using a proportional directional valve. Two-position four-way valve worked at left position, two-position three-way valve worked at right position and proportional directional valve worked at middle position

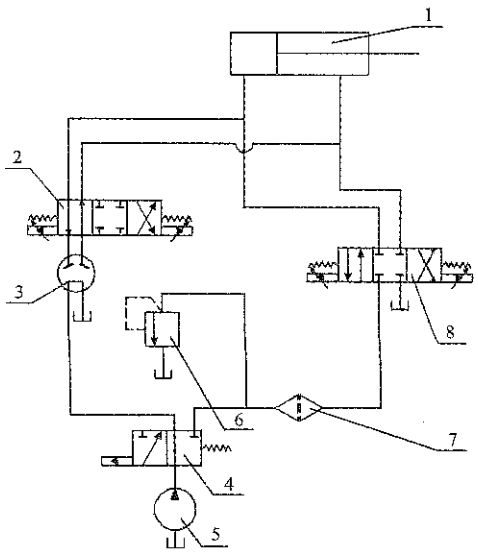

1. Steering jack 2. Two-position four-way valve 3. Hydraulic steering gear 4. Two-position three-way valve 5. Fluid pump 6. Overflow valve 7. Oil filter 8. Proportional directional valve

Figure 7 Schematic view of improved hydraulic steering system

in initial state. After receiving control signals of MCU, two-position four-way valve worked at right position and two-position three-way valve worked at left position. The original oil-way was blocked and the new oil-way was unimpeded. Proportional directional valve would just the oil flow and direction according to the bipolar control signals which were given to the electro-hydraulic proportional controller. In this manner, the wheels could turn left or right.

3 Steering system design

3.1 Steering system modeling

The steering system model could not be formulated with the tractor at rest, as determination of the relevant parameters required a drive signal. Thus, the steering system's Micro Programmed Control Unit (MCU) was programmed so that the proportional directional valve changed the steering angle to the given value at a fastest rate when the real steering angle was not equal to the input signal.

A series of steering step signals with amplitudes g equal to ±10°, ±15° and ±20° were input to the MCU with the tractor moving linearly at a speed of 0.5 m s^{-1} and a direction of 0°. The step responses obtained are shown in Figure 8 and Table 2.

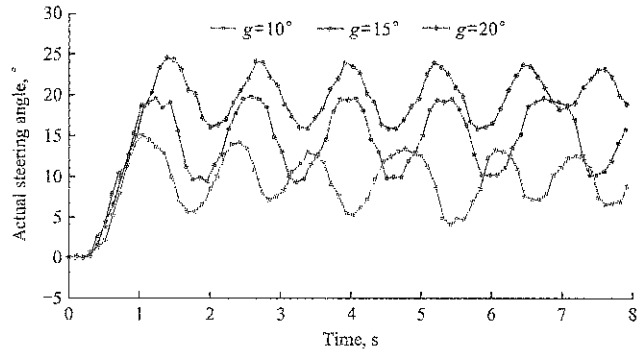

a. g = 10°, 15°, 20°

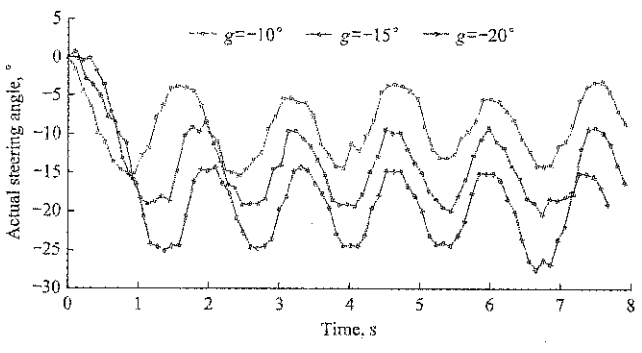

b. g = –10°, –15°, –20°

Figure 8 System step response under different input amplitudes

Table 2 Step response characteristics

Amplitude g,°	Peak time t_p, sec	Overshoot, °	Overshoot percent σ, %
10	1.04	4.97	49.7
15	1.23	4.51	30.1
20	1.39	4.53	22.7
–10	0.95	5.18	51.8
–15	1.13	4.01	26.7
–20	1.28	4.56	22.8
Average	1.17	4.63	34.0

As evident from the corresponding 6 curves above, the steering control system behaved like a second-order system. The system damping factor ζ and natural oscillation frequency ω_n were obtained using experimental data, as shown in Equation (1). Since $0<\zeta<1$, the system was under-damped, and therefore insufficiently attenuated. A PD controller, therefore, was attached to the system to increase damping and improve system's variation prediction. The closed-loop transferred function $\Phi(s)$ of the steering system's model then became as follows:

$$\zeta = \sqrt{\frac{\ln^2 \sigma}{\pi^2 + \ln^2 \sigma}} = 0.325 \quad (1)$$

$$\omega_n = \frac{\pi}{t_p \sqrt{1-\zeta^2}} = 2.84 \text{ rad s}^{-1} \quad (2)$$

$$\Phi(s) = \frac{\omega_n^2}{s^2 + 2\zeta\omega_n + \omega_n^2} = \frac{8.07}{s^2 + 1.85s + 8.07} \quad (3)$$

where, s was the complex variable.

3.2 Steering controller simulation

The PD controller system was simulated using Matlab to determine the most appropriate proportionality coefficient K_p and differential coefficient K_d values using a larger input angle, in this case g=20°. Empirical law, which is commonly used in practical engineering, was used to tune the PD controller parameters. Finally, it was found that the system has a fast settling time and low overshoot when the proportional coefficient K_p=20 and differential coefficient K_d=0.8. Figure 9 showed a portion of the simulation results when K_d=0.8.

3.3 Experiments and analysis steering system

To verify whether the PD controller performed well or not, a series of verification experiments were conducted after the simulation. The amplitudes g of the step response inputs used were again ±10°, ±15° and ±20° respectively in order to facilitate the analysis. As

shown in Figure 10 and Table 3, the step response of the steering system improved considerably compared to the initial behavior shown in Figure 8.

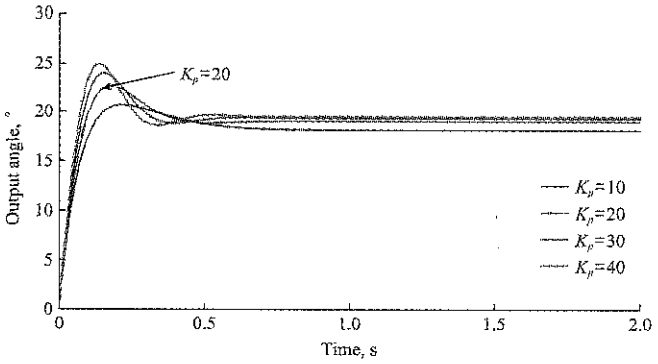

Figure 9 Steering angle output versus time for an input signal of 20° and different values K_p

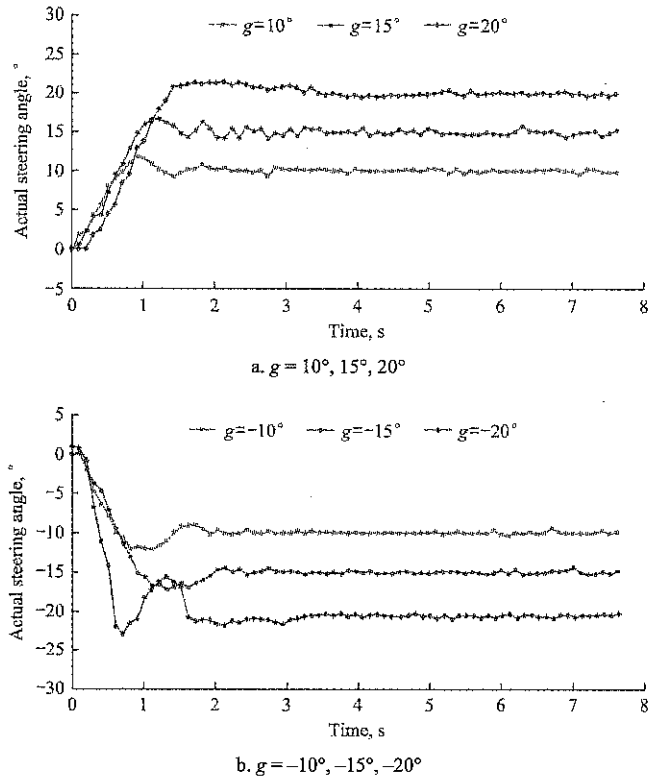

a. g = 10°, 15°, 20°

b. g = –10°, –15°, –20°

Figure 10 System step response with different input amplitudes using the PD controller

Table 3 Step response characteristics using the PD controller

Amplitude g, °	Steady-date error, °	Error, %	Overshoot, %	Overshoot σ, %
10	0.41	4.1	1.82	18.2
15	0.25	1.7	1.63	10.7
20	0.32	1.6	1.53	7.7
–10	0.21	2.1	2.13	21.3
–15	0.28	1.9	2.20	14.7
–20	0.45	2.2	1.87	9.4
Average	0.32	2.3	1.86	13.7

3.4 Design of adaptive PD steering controller

All the experiments above were completed at a tractor speed of 0.5 m s^{-1}. However, this speed may change according to the different working demands, so the relationship between different speeds and PD parameters must be established. Table 4 showed the corresponding optimal K_p and K_d values obtained at four different speed values using the same approach as described above.

Table 4 Optimal PD controller parameters at different speeds

Speed, m s^{-1}	K_p	K_d
0.2	25	1.4
0.5	20	0.8
0.8	18	0.6
1.1	15	0.5

Using the values of Table 4, two models for determining the relationship between PD parameters and speed were established using cubic curve fitting. The results were shown in Figure 11.

$$K_p = -24.69v^3 + 53.7v^2 - 44.63v + 31.98 \quad (4)$$

$$K_d = -1.85v^3 + 5^2 - 4.78v + 2.17 \quad (5)$$

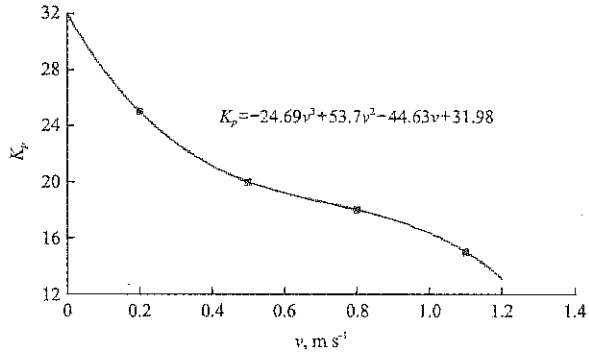

a. Relationship between K_p and speed

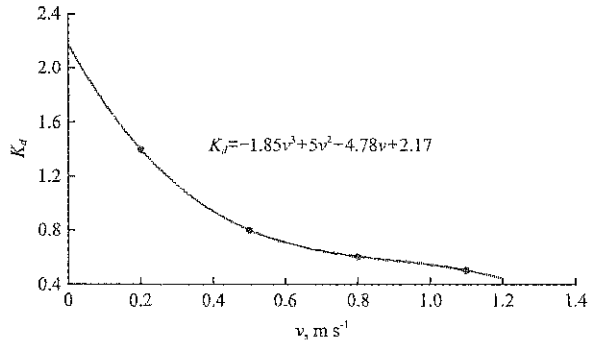

b. Relationship between K_d and speed

Figure 11 Cubic curve fitting

In order to evaluate the accuracy of the models mentioned above, the tractor was given a bipolar sine signal as the drive signal, at two different speeds, 0.3 and 0.7 m s^{-1} respectively. The experimental results were presented in Figure 12. K_p and K_d equaled 22.76 and 1.14

respectively when the speed was 0.3 m/s, and 18.58 and 0.64 at 0.7 m/s. The corresponding average delay times were 0.81 and 0.84 s, while the steady-state errors were 0.25° and 0.41°, respectively.

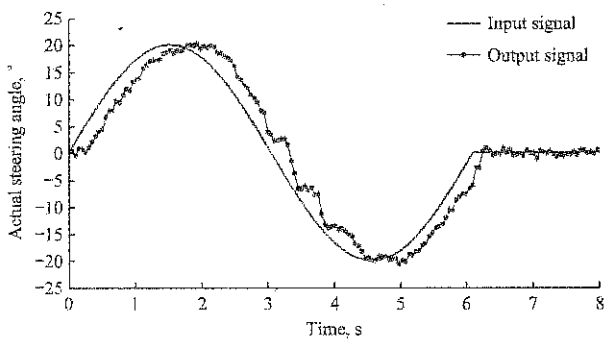

a. v=0.3 m/s

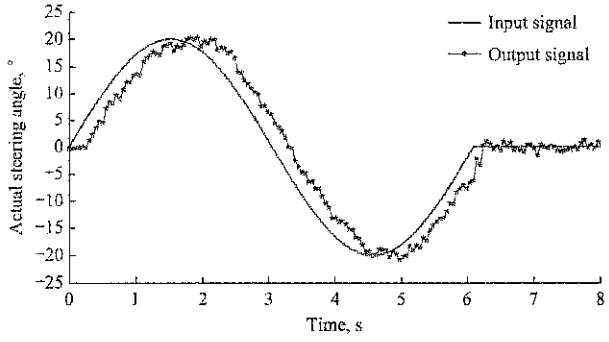

b. v=0.7 m/s

Figure 12 Sine responses at different speeds

4 Navigation system design

4.1 Navigation control system

4.1.1 Structure

The navigation control system comprises the steering and lateral motion control systems (Figure 13). The steering controller was discussed in the previous section, and here the lateral motion controller would be presented.

There were two closed-loop control systems in the navigation control system. The primary loop was used to control the lateral motion of the tractor using real position data measured by GPS and continuously comparing them to the input trajectory. Then, the lateral deviation was calculated and input to the lateral motion controller, whose output was the angle control signal of the steering system. Finally, the angle control signal was input to the lateral motion model. The secondary loop was used to control the steering of the tractor, where the expected movement angle was provided by the lateral motion controller. The real steering angle was measured by angle sensors and compared to the expected movement angle. The deviation between the two values was calculated and input to the steering controller.

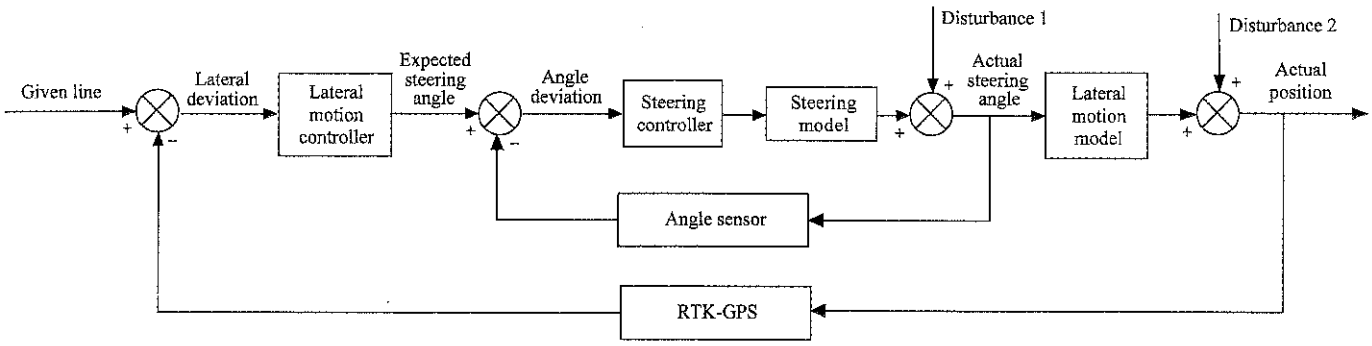

Figure 13 Tandem PD navigation control system

Both the steering and the lateral motion control systems were second-order systems. Therefore, the two systems, connected in series, were analyzed separately in order to avoid producing a higher order system.

4.1.2 Navigation controller

The analysis of the steering controller was presented in the previous section. The lateral motion model, however, was unknown, so the lateral motion controller, which was also a PD controller, could not be simulated. Therefore, the corresponding parameters were again obtained with empirical law which was common used in engineering.

For these experiments, an original position of the tractor was considered at 1.1±0.2 m away from the input position. Then, the tractor was allowed to track the line. Figure 14 showed the experimental results for K_p and K_d when the tractor speed was 0.2 m/s. Using a similar approach as before, the optimal values for K_d and K_p were obtained at speeds of 0.5, 0.8 and 1.1 m/s; the corresponding values were shown in Table 5. Finally, the determined relationship between the lateral motion parameters and speed were shown in Equations (6) and (7).

$$K_p = -12.35v^3 + 35.19v^2 - 36.48v + 27.99 \quad (6)$$

$$K_d = -0.62v^3 + 1.48v^2 - 1.30v + 1.05 \quad (7)$$

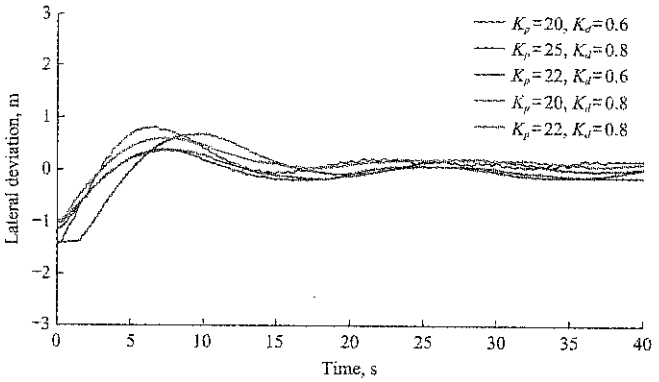

Figure 14 Experimental results of line tracking with different parameters

Table 5 Optimal PD controller parameters at different speeds

Speed v, m s^{-1}	K_p	K_d
0.2	22	0.85
0.5	17	0.70
0.8	15	0.65
1.1	14	0.60

4.2 Navigation experiments

In order to evaluate the performance of the navigation controller, three different kinds of navigation experiments were conducted. They were line tracking, obstacle avoidance and turning.

4.2.1 Line tracking experiments

Before the experiments, the coordinates of two points were selected using RTK-GPS, and the straight line trajectory between the two points was formed. The initial position of the tractor was 1.2±0.1 m away from the target line with a steering angle of 0°±1° and a speed of 0.5 m/s. An analog signal within the range of –10 V to 10 V was provided by the MCU to control the steering wheels.

Figure 15 showed the experimental results. In Figure 15a, the solid line was the actual motion trajectory and the dashed one indicated the target line. Starting from a distance of 1.2 m, the tractor's trajectory clearly converged with the target line. The lateral deviation from the target line was shown in Figure 15b. After the tractor reached a steady state, the maximum lateral deviation was –0.134 m with an average of –0.037 m and a RMSE of 0.0687. Figure 15c showed the expected angle values based on the steering controller's model and the real angle values obtained.

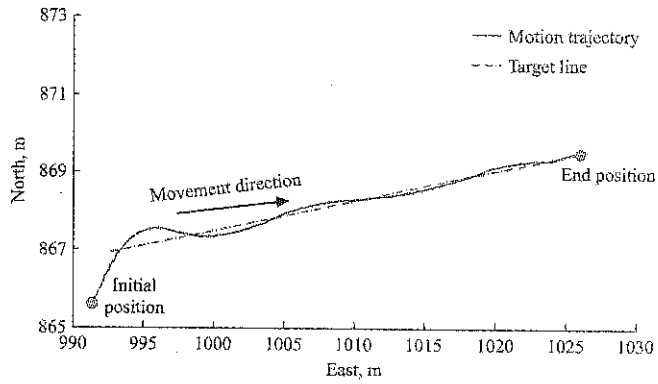

a. Vehicle trajectory

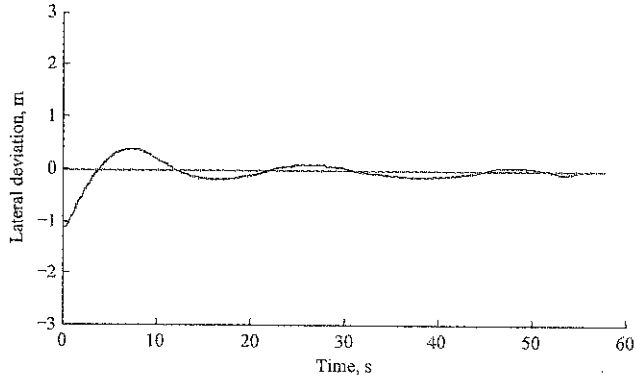

b. Variation of lateral error

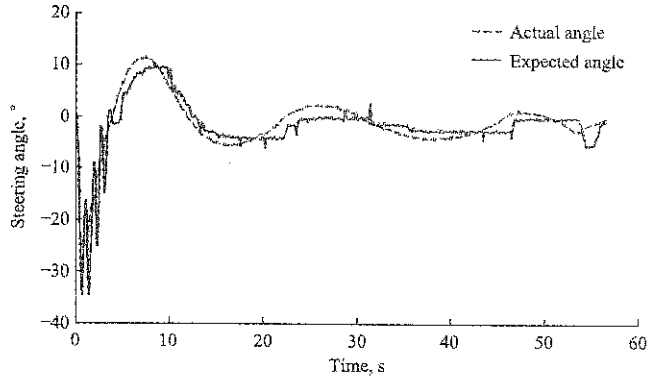

c. Variation of steering angle

Figure 15 Experimental results of line tracking

4.2.2 Obstacle avoidance experiments

As noted above, a Bumblebee XB3 camera was used to detect bulging obstacles in the tractor's trajectory (Figure 16). Massive feature points of the obstacles were collected by the stereovision camera. Then we can get the coordinate data of the points. According to the coordinates of the feature points, dimensions and distance of the obstacles can be calculated easily.

During the experiments, a big stone was put in the middle of the target line. The tractor's initial state was 0.3±0.1 m far away from target line with a steering angle of 0°±1° and a speed of 0.5 m/s. The experimental results obtained were shown in Figure 17, where (a) showed the

expected and actual motion trajectories. First, the tractor tracked its target line and then an obstacle was identified using machine vision, whereupon the expected line was changed to another trajectory according to the obstacle dimensions. Then, the tractor tracked the new target line. Finally, after the obstacle has been cleared, the tractor resumed tracking of the original line. After the tractor returned to its steady status, the maximum lateral deviation from the resumed trajectory line was 0.102 m with an average of –0.012 m and an RMSE of 0.0312.

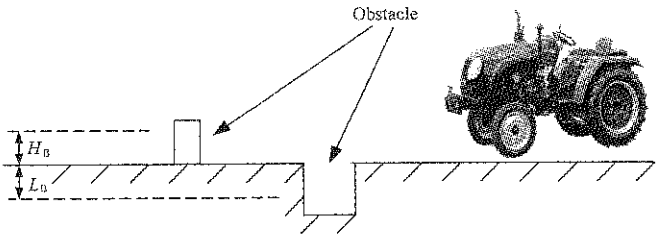

Figure 16 Obstacle patterns

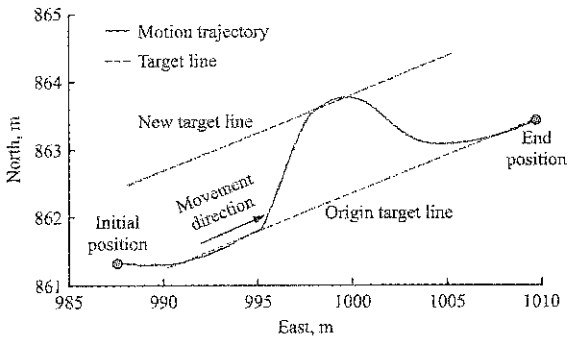

a. Vehicle trajectory

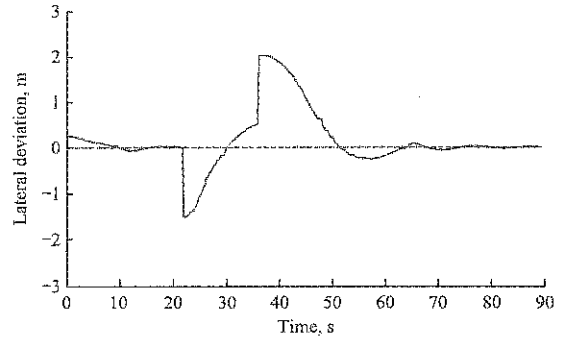

b. Variation of lateral error

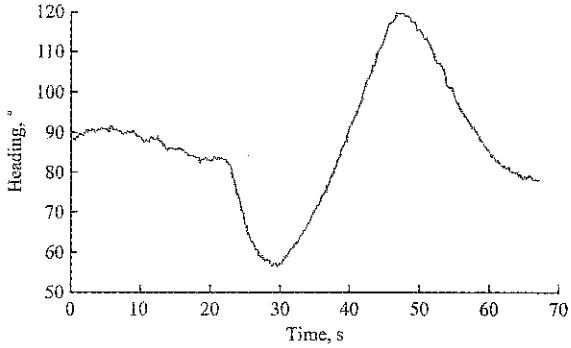

c. Variation of heading

Figure 17 Experimental results of the obstacle avoidance

The lateral deviations were shown in Figure 17b. Once the obstacle has been cleared, the tracked line was changed back to the original target, which was indicated by the two changes in lateral deviation in the figure. Figure 17c showed the variations of the heading during the obstacle avoidance procedure.

4.2.3 Turning experiments

After given two different turning radiuses, the tractor could work with small line spacing. The large and small radii were set to 4 and 3.5 m respectively for the turning experiments. The tractor's initial state was 0.1±0.1 m from the target line with a steering angle of 0°±1° and a speed of 0.5 m/s.

The motion trajectory is shown in Figure 18a. The tractor tracked the first line until the end of the field. Then, it turned around with a radius of 4 m. After that,

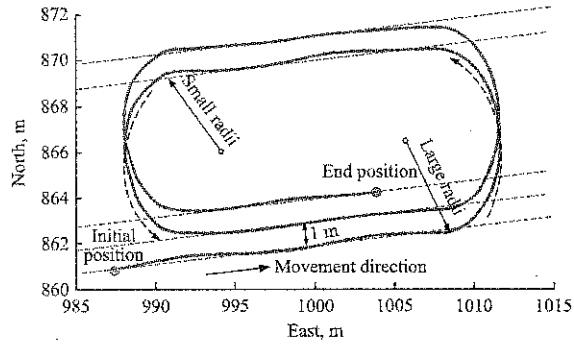

a. Vehicle trajectory

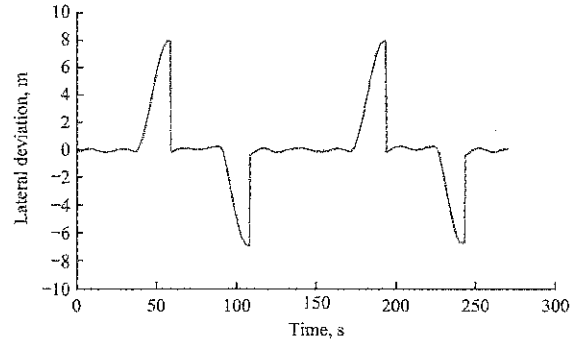

b. Lateral error variation

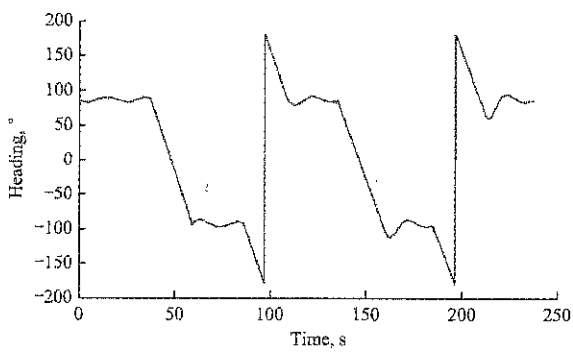

c. Heading variation

Figure 18 Experimental result of turning procedure

the tracking line was moved to new coordinates, and the tractor tracked the new line until the other end of the field. Afterwards, the tractor turned again around, this time with a radius of 3.5 m and the target line was moved again and so on.

The lateral deviation measurements were shown in Figure 18b. The reason for the several big deviations is that the target line was changed back and forth when the tractor was at the end of the field. During the line tracking process, the maximum lateral deviation was 0.082 m with an average of 0.056 m and an RMSE of 0.0975. The average line spacing was 1.03 m with an RMSE of 0.0816.

Variations of the course angle were shown in Figure 18c. In this case, the sharp changes are due to that the +180° and −180° in the angle measurement domain coincide, as shown in Figure 6.

5 Conclusions

The present work investigated an autonomous navigation system of a small tractor with a modified hydraulic steering system. Several sensors were mounted to the tractor to assess ground layout and the tractor's current state. The main conclusions are summarized as follows.

1) The steering controller which was constructed and evaluated using simulations and it performed well in experiments. Its adaptive behavior was calculated that the optimal working parameters for the controller were tested according to the various speeds.

2) The navigation controller, consisting of the steering and lateral motion controllers, could direct the tractor to accomplish three navigation tasks, i.e. linear trajectory tracking, obstacle avoidance and turning around. Without using a specific kinematic model, the tractor could be controlled precisely only via a tandem PD controller, which only used the lateral deviation as the system input without course deviation. This provided us a simple and applicable solution to the agricultural vehicle navigation issue.

Acknowledgments

This work was supported by the National Natural Science Foundation of China (Grant No. 31401291), the Fundamental Research Funds for Central Universities (Grant No. KJQN201556) and the Natural Science Funds of Jiangsu Province (Grant No. BK20140729).

[References]

[1] Backman, J., T. Oksanen, and A. Visala. 2012. Navigation system for agricultural machines: Nonlinear Model Predictive path tracking. *Comput. Electron. Agric.*, 82(3): 32–43.

[2] Backman, J., T. Oksanen, and A. Visala. 2013. Applicability of the ISO 11783 network in a distributed combined guidance system for agricultural machine. *Biosystems Engineering*, 114(3): 306–317.

[3] Barawid, O. C., A. Mizushima, K. Ishii, and N. Noguchi. 2006. Development of an autonomous navigation system using a two-dimensional laser scanner in an orchard application. *Biosystems Engineering*, 96(2): 139–149.

[4] Choi, J., X. Yin, L. Yang, and N. Noguchi. 2014. Development of a laser scanner-based navigation system for a combine harvester. *Engineering in Agriculture Environment and Food*, 7(1): 7–13.

[5] Gan-Mor, S., R. L. Clark, and B. L. Upchurch. 2007. Implement lateral position accuracy under RTK-GPS tractor guidance. *Comput. Electron. Agric.*, 59(1): 31–38.

[6] Gomez-Gil, J., J. C. Ryu, S. Alonso-Garcia, and S. K. Agrawal. 2011. Development and validation of globally asymptotically stable control laws for automatic tractor guidance. *Appl. Eng. Agric.*, 27(6): 1099–1108.

[7] Ismail, W. I. W., R. M. Hudzari, M. K. M. Saufi, and L. T. Fung. 2012. Computer-controlled system for autonomous tractor in agricultural application. *Journal of Food Agricultural Environment*, 10(2): 350–356.

[8] Kise, M., and Q. Zhang. 2008. Development of a stereovision sensing system for 3D crop row structure mapping and tractor guidance. *Biosystems Engineering*, 101(2): 191–198.

[9] Luo, X. W., Z. G. Zhang, Z. X. Zhao, B. Chen, L. Hu, and X. P. Wu. 2009. Design of DGPS navigation control system for Dongfanghong X-804 tractor. *Trans Actions of the Chinese Society of Agricultural Engineering*, 25(11): 139–145. (In Chinese with English abstract)

[10] Xiang, H., and L. Tian. 2011. Development of a low-cost agricultural remote sensing system based on an autonomous unmanned aerial vehicle (UAV). *Biosystems Engineering*, 108(2): 174–90.

[11] Zhu, H., Y. B. Lan, and W. F. Wu. 2010. Development of a PWM precision spraying controller for unmanned aerial vehicles. *Journal of Bionic Engineering*, 7(3): 276–83.

Optimum design and experimental verification of tunnel drying room based on numerical simulation

Dai Jianwu[1], Qin Wen[2], Wu Zhijun[1], Wang Ya[1], Huang Ruqi[1], Zhang Lihua[1*]

(1. *College of Mechanical and Electrical Engineering, Sichuan Agricultural University, 625014, Ya'An, Sichuan Province, China*
2. *College of Food Science, Sichuan Agricultural University, 625014, Ya'An, Sichuan Province, China*)

Abstract: The air flow characteristics of the tunnel drying room were investigated and optimized based on numerical simulation. The original model and four modified models were presented for evaluation. Results indicated that the air flow velocity of the primary model presented downward trend along the height, while the values on both sides of the gaps were much bigger than the other areas. Most volumetric hot air flowed through the gaps between wagon and wall of the tunnel drying room. Closing up the short-cut of air flow had significant effect on the improvement of flow field uniformity in the modified models. And the distribution of air velocity at different heights was homogeneous. The locating position of the first deflector had a decisive influence on the whole flow field distribution along with the radial direction. The optimum solution of modeling was got under the baffle distance with double-dryer wagon width and the first deflector should be flush with the fan. The distribution trend of simulation results showed little difference compared to the experimental data and the maximum relative error under different locations changed from 4.2% to 7.7%. The results provide a reference for the optimization design of structures similar to the drying room.

Keywords: tunnel drying room, numerical simulation, optimum design

Citation: Dai, J. W., W. Qin, Z. J. Wu, Y. Wang, R. Q. Huang, and L. H. Zhang. 2017. Optimum design and experimental verification of tunnel drying room based on numerical simulation. International Agricultural Engineering Journal, 26(4): 10–15.

1 Introduction

Tunnel drying room is one of the most widely used equipment for production of dehydrated fruits, vegetables, noodles and Chinese herbal medicines due to its low equipment and operation cost, simple structure and easily controlled parameters (Mansell et al., 2002; Zhang et al., 2005). Currently, many drying equipment with advanced drying technology, such as freeze drying, microwave drying and far infrared drying, have been developed and more and more applied to the different kinds of materials extensively. But tunnel drying room, which belongs to the type of convective air drying, would still occupy an important position for a long time from the comprehensive considerations of technical and economical respects in China (Wang et al., 2009). And many researches have been carried out to investigate the drying kinetics of carrots (Wu et al., 2006), preserved fruits (Han et al., 2010) and plums (Shen et al., 2010), etc. However, the existing problem of tunnel drying room at present is mainly about the non-uniformity of whole drying process. Non-uniform distribution of airflow field can cause inconsistence of materials quality, prolong the drying time, consume more energy and reduce the efficiency of drying operation (Goyal et al., 2007). The materials of partial region in the drying room may even generate decomposition for lack of the air flow. Therefore, it is essential to optimize the flow field structure of the passageway in the tunnel drying room.

Computational fluid dynamics (CFD) is a common tool for predicting the heat distribution and fluid flow pattern (Sonthawi et al., 2016). It can provide detailed information on airflow patterns and ensure the convenient design of agricultural equipment. So far, many researchers and scientists have applied CFD in designing

Received date: 2017-06-30 **Accepted date:** 2017-09-12

* **Corresponding author: Zhang Lihua,** Ph.D., Professor of College of Mechanical and Electrical Engineering, Sichuan Agricultural University, 625014. Email: 364720874@qq.com. Tel: +86-0835-2882013, Fax: 0835-2882013.

and performance evaluation of drying systems. Xu et al. (2005) studied the optimization design of gas distribution chamber in wall-mounted gas boiler. Zhu et al. (2007) employed CFD to determine the optimal design of inlet conduit for technical innovation of large pumping stations. Tian et al. (2009) accomplished the improved design of airflow distribution chamber in air-impingement oven based on Fluent. Tekasakul et al. (2015) solved the non-uniform flow and large temperature variation in a natural rubber smoking room without air circulation by CFD.

However, there is not significant literature concerning flow field optimization of the passageway in tunnel drying room. In this paper, the CFD was used to simulate the air velocity at various locations of the passageway based on the differential equation and RNG k-ε turbulence model. And the optimal structural model simulation and experimental results were also compared and analyzed.

2 Experimental setup and instruments

A schematic diagram of the tunnel drying room and its accessories is shown in Figure 1. This tunnel dryer consists of an axial flow fan mounted on the top side wall for air circulation, a steam heater located behind the fan for heating the airflow, the arc-shaped wind deflector mainly used for conducting the airflow direction and a proportional–integral–derivative controller (E5CN, Omron, Tokyo, Japan) to control the drying air temperature and absolute humidity. In this system, there were 12 dryer wagons on the track to load the materials and the dimensions of each were measured about 1.4× 0.5×1.3 m. The absolute humidity of the air flow could be regulated by changing the condition of the electromagnetic valves connected to a positive pressure area. Fresh air was heated when it came and contact with outer surface of heat exchanger tubes. The gap between the end face of the wagons and the top surface of the wall was about 10 cm, while the bottom spacing was about 5 cm. And both the distances on the left and right gap were 10 cm, respectively.

The temperature of heat exchanger tubes was kept at 60°C. And air velocity in the drying chamber was measured with Founder Probe Anemometer (Founder, Beijing, China), with the accuracy of ±0.1 m s^{-1}. The data was recorded continuously using a data logger (Wisco, DL2200). The thermocouple signals, collected by an SHT75 sensor (Sensirion, Shenzhen, China), were multiplexed to a data acquisition card and shown in the touch control screen (Weinview, Shenzhen, China). During the experiments, temperature and absolute humidity of the surroundings changed from 18°C to 31°C and from 4.3 to 7.9 g kg^{-1}, respectively. All experiments were performed in triplicate and the average values were used for determining the velocity distribution uniformity.

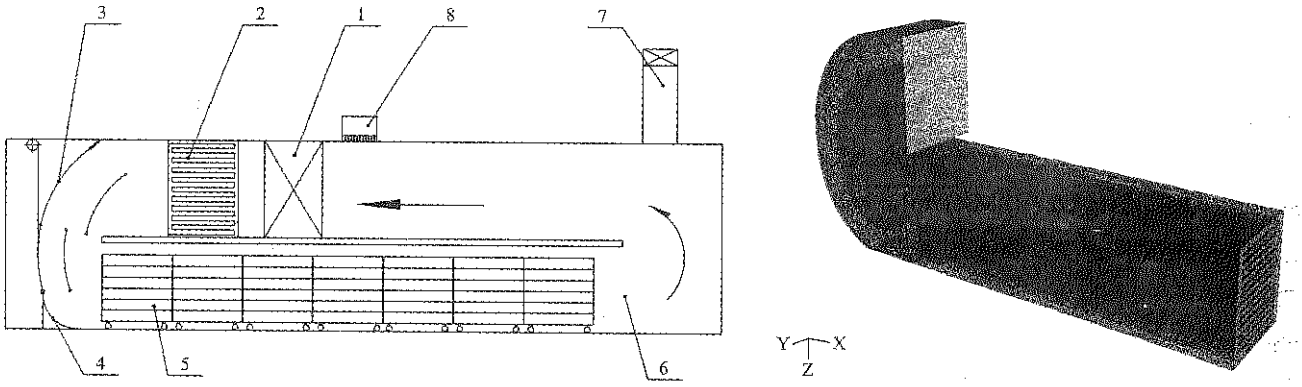

1. Axial flow fan 2. Steam heater 3. Removable guide plate 4. Fixed guide plate 5. Dryer wagon 6. Drying chamber 7. Moisture-removing exit 8. Fresh air inlet

Figure 1 Schematic and grid diagram of tunnel drying room

3 Simulation approach

3.1 Mathematical model

Mathematical model is based on provisions of continuum mechanics and represents a system of balance equations that include mass, momentum, and energy conservation equations. The governing partial differential equations are expressed below (Zhai et al., 2008; Li et al.,

2011):

Continuity equation:

$$\frac{\partial u_i}{\partial x_i}=0 \tag{1}$$

Momentum equation:

$$\rho\frac{\partial(u_iu_j)}{\partial x_j}=\frac{\partial}{\partial x_j}\left[\mu(\frac{\partial u_i}{\partial x_j}+\frac{\partial u_j}{\partial x_i})-\frac{2}{3}\mu\delta_{ij}\frac{\partial u_k}{\partial x_k}\right]-\frac{\partial p}{\partial x_i} \tag{2}$$

where, u_i, u_j represent the velocity component vectors (m s^{-1}); p is the pressure (N m^2); t is time (s); ρ is the density (kg m^{-3}), and μ is the dynamic viscosity (N s m^{-2}).

The RNG k-ε turbulent model was chosen with the constant parameters (C_μ=0.0845, $C_{1\varepsilon}$=1.42, $C_{2\varepsilon}$=1.68, δ_k=δ_ε=1.39) for the curved wall conditions. The equations for the kinetic energy of turbulence (k) and its dissipation rate (ε) are given as the additional parameters (Yuan et al., 2006; Zhu et al., 2007).

$$\frac{\partial k}{\partial t}+u_i\frac{\partial k}{\partial x_i}=\frac{\partial}{\partial x_j}\left[\alpha_k\frac{\mu_{eff}}{\rho}\frac{\partial k}{\partial x_j}\right]+\frac{G_k}{\rho}-\varepsilon \tag{3}$$

$$\frac{\partial(\rho\varepsilon)}{\partial t}+\frac{\partial(\rho\varepsilon u_i)}{\partial x_j}=\frac{\partial}{\partial x_j}\left[\left(\alpha_\varepsilon\mu_{eff}\right)\frac{\partial\varepsilon}{\partial x_j}\right]+C^*_{1\varepsilon}\frac{\varepsilon}{k}G_k-C_{2\varepsilon}\rho\frac{\varepsilon^2}{k} \tag{4}$$

where x_i, x_j are both the coordinate components; G_k is the addition item caused by energy of turbulence.

The total number of element mesh generation of the original physical model with unstructured algorithm was about 760000 using pre-processing software GAMBIT2.2. The meshing grid density was set at low level because of the complexity in the drying chamber and the restricted resources. The standard wall function was used to compute and amend in this simulation.

The segregated solver according to the SIMPLE algorithm was used with the Gauss-Seidel relaxation scheme and the second-order upwind convection scheme. The convergence of the solution was assessed by the residuals as well as by monitoring the air velocity in the drying chamber. Iteration errors should be negligible since all simulations fulfill the convergence criteria of max residuals less than 10^{-4}.

3.2 Initial and boundary conditions

The inlet boundary was defined as velocity inlet with the velocity value of 8 m s^{-1} and the flow direction was normal to the boundary. The inlet turbulence intensity was estimated at about 2.67% according to the hydraulic diameter and empirical equation. Pressure outlet was chosen for the outlet boundary and its turbulence intensity was set to be 5%.

Air properties were assumed to be constant; thermal conductivity of 0.02 W(m $K)^{-1}$, the specific heat of 1.005 kJ (kg $K)^{-1}$ and density of 1.06 kg m^{-3}.

3.3 Numerical computation and evaluation indicators

In order to estimate the distribution uniformity of the air flow in the drying chamber, the speed deviation ratio (E) and the non-uniform coefficient (M) were chosen as the comprehensive evaluation indicators as follows (Lei et al., 2011; Han et al., 2010; Li et al., 2010; Wang et al., 2011; Dai et al., 2015).

The speed deviation ratio (E) is an important parameter in describing the fluctuation degree of air flow velocity along with the height direction of dryer wagons using Equation (5):

$$E=\frac{|\overline{V_L}-\overline{V_a}|}{\overline{V_a}}\times100\% \tag{5}$$

where, $\overline{V_L}$ and $\overline{V_a}$ are the mean of airflow velocity at each layer and the population mean of whole cross section, respectively. The magnitude of the speed deviation ratio represents the wide difference intensity between the above two factors.

The non-uniform coefficient (M) is computed using Equation (6) and expressed as the whole deviation level.

$$M=\frac{\sigma_v}{v_a}\times100\%=\frac{\sqrt{\frac{1}{n-1}\sum_{i=1}^{n}(V_i-\overline{V_a})^2}}{\overline{V_a}}\times100\% \tag{6}$$

where, σ_v is standard deviation, n is the number of layers, and V_i is the airflow velocity at each point. The non-uniform coefficient is mainly used to evaluate the local deviation situation of airflow distribution.

4 Results and discussion

As shown in Figure 2, the simulation results indicated that the air flow velocity of the original model presented downward trend along with the height direction at the middle of trays in the dryer wagon, while the values on both sides of the gaps were much bigger than the other areas. This illustrates that most volumetric hot air flowed through the space between the dryer wagon and the

passageway of the tunnel drying room, and it was also called the air flow short-circuit. The efficiency of heat utilization was low and a great deal of energy has been wasted. The airflow velocity passed through the interval of dryer wagon above the materials ranged from 11.7 to 20.3 m/s under the design condition. The minimum value was got in the tenth row. The M and E values of primary model were calculated to be 0.18 and 0.41, respectively. However, the velocity values through the gaps changed from 24.2 to 28.1 m s^{-1}. This illustrates that the primary model is far from perfect.

Figure 2 Flow characteristics distribution of original structure

The path of air flow short-circuit in the modified models was blocked with silicone rubber (Figure 3). The interval distance was set to be integral multiples of the dryer wagon length according to the flow field characteristics. The results of numerical modeling showed that closing up the short-cut of air flow had significant effect on the improvement of flow field uniformity. The distribution of air velocity at different heights was homogeneous in the modified models. And the locating position of the first deflector had a decisive influence on the whole flow field distribution along with the radial direction. It might be due to the fact that the wind resistance crossing over the trays was significantly greater than that of the gaps. Hence the hot airflow would rather choose the low flow-resistance path in the areas with little flow field influence. And the air velocity would decrease gradually with the increase of blowing distance.

From Figure 4, it can be seen that the velocity vector field of model with baffle distance at one dryer wagon width got great improvement compared to the primary model. The velocity distribution showed a general uniformity and the magnitude of airflow velocity in local area were inconsistent. The value of velocity vector close to the baffle was bigger than the other regions. This might be because baffles blocked the path of short-cut of air flow and hot air had to change the direction of the previous movement. It imposed the effect on the flow field of the passageway in the tunnel drying room. And the average velocity at each layer ranged from 25.4 to 29.1 m/s.

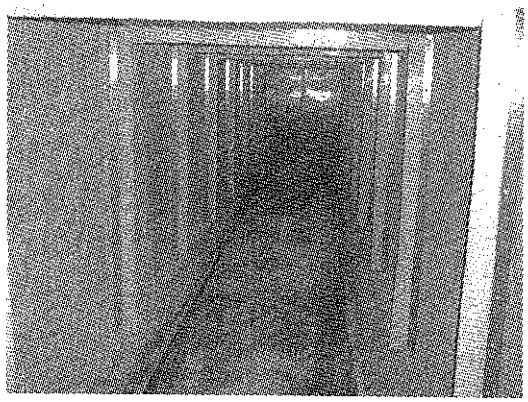

Figure 3 Prototype structure of the optimum design

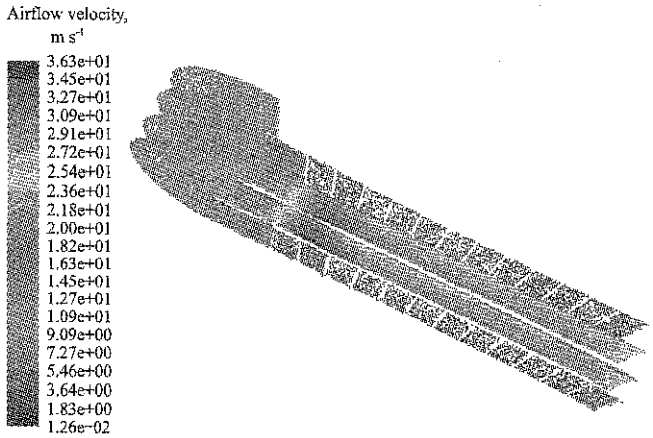

Figure 4 Velocity distribution of modified model with baffle distance at one dryer wagon width

With the increase of baffle distance in different models, the flow distribution of high values backward migrates gradually. This phenomenon might be due to the fact that the locating position of the first deflector was closest to the above axial flow fan. And the magnitude of the pressure vector in the position was greatest at the same time. Thus, the air velocity close to the baffle was significantly bigger than the others. The optimum solution of modeling was got under the baffle distance with double-dryer handcart width and the first deflector should be flush with the fan. As shown in Figure 5, when the velocity passed through the middle dryer wagon, it

was changed from 25 to 26.8 m/s, which showed almost the same state. The M and E values were calculated to be 0.07 and 0.13, respectively.

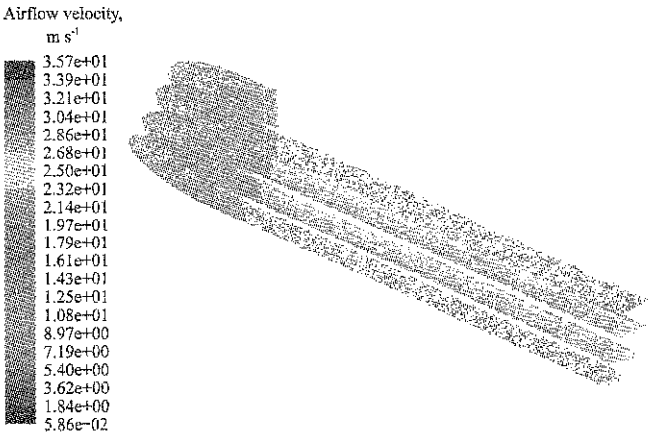

Figure 5 Velocity vector distribution of optimization model

In order to verify the accuracy of the numerical simulation, the verification test was carried out. A Frequency Converter (ACS100) was used to vary the air velocity. From Figure 6, it can be seen that the distribution trend of simulation results showed little difference compared to the experimental data and the maximum relative error under different conditions changed from 4.2% to 7.7%, showing an increasing trend as mass flow increased. The results provide a reference for the uniformity design of structures similar to the tunnel drying room.

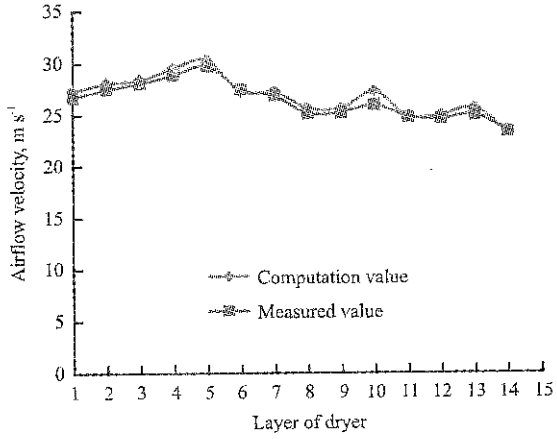

Figure 6 Experimental performance curves of the optimum design

5 Conclusion

The air flow characteristics of the tunnel drying room were investigated and optimized based on numerical simulation in this investigation. The air flow velocity of the original model presented downward trend along with the height direction at the middle of trays in the dryer wagon, while the values on both sides of the gaps were much bigger than the other areas. Most volumetric hot air flowed through the gaps between the wagon and the wall of tunnel drying room. Closing up the short-cut of air flow had significant effect on the improvement of flow field uniformity in the modified models. The locating position of the first deflector had a decisive influence on the whole flow field distribution along with the radial direction. The optimum solution of modeling was got under the baffle distance with double-dryer wagon width and the first deflector should be flush with the fan. The velocity passed through the middle dryer wagon changed from 25 to 26.8 m/s at the design conditions and the M and E values were calculated to be 0.07 and 0.13, respectively. The distribution trend of simulation results showed little difference compared to the experimental data and the maximum relative error under different locations changed from 4.2% to 7.7%.

Acknowledgements

This research has been partially supported by the Natural Science Foundation of Sichuan (Grant No. 035Z1986). Authors are highly grateful for the support.

[References]

[1] Dai, J. W., H. W. Xiao L. Xie, D. Wang, X. M. Li, and Z. J. Gao. 2015. Design and experiment of tilted tray air-impingement dryer. *Transactions of the Chinese Society for Agricultural Machinery*, 46(7): 238–244. (In Chinese with English abstract)

[2] Goyal, R. K., K. Arp, M. R. Manikantan, and S. M. Ilyas. 2007. Mathematical modeling of thin layer drying kinetics of plum in a tunnel dryer. *Journal of Food Engineering*, 79(1): 176–180.

[3] Han, Q. H., H. H. Wu, J. P. Ye, Z. H. Mao, and Z. Kang. 2010. Monitoring and controlling system of temperature and humidity for tunnel-type dryer. *Transactions of the Chinese Society for Agricultural Machinery*, 41(4): 119–123. (In Chinese with English abstract)

[4] Han, W. T., P. T. Wu, Q. Yang, and H. Feng. 2005. Advances and comparisons of uniformity evaluation index of sprinkle irrigation. *Transactions of the Chinese Society of Agricultural Engineering*, 21(9): 172–177. (In Chinese with English abstract)

[5] Lei, X. L., H. X. Li, Q. Zhang, and T. Wang. 2011.

Regulation performance and optimal design of the gas adjust-screen in boiler steering rooms. *Journal of Huazhong University of Science and Technology*, 39(10): 128–132.

[6] Li, G. W., Y. Wang, X. L. Lv, and W. H. Li. 2011. Numerical simulation of three-dimensional flow field in centrifugal pump with deviated short splitter vanes. *Transactions of the Chinese Society of Agricultural Engineering*, 27(7): 151–155. (In Chinese with English abstract)

[7] Li, J. S., J. F. Yin, H. Zhang, and Y. F. Li. 2010. Field evaluation of drip fertigation uniformity effects on distributions of water and nitrate in soil. *Transactions of the Chinese Society for Agricultural Machinery*, 26(12): 27–33. (In Chinese with English abstract)

[8] Mansell, R, B. Suite, and G. A. Roswell. 2002. Engineering a "fish-dry". *Food Engineering*, 29(11): 30–37.

[9] Wang J. H., and Q. J. Liu. 2009. Design and key techniques on U-shaped tunnel-drying room for aquatic products. *Transactions of the Chinese Society of Agricultural Engineering*, 25(10): 296–301. (In Chinese with English abstract)

[10] Shen, X. X., B. S. Li, and W. T. Liu. 2010. Effects of different drying methods on physicochemical properties of salted plum. *Modern Food Science and Technology*, 26(12): 1305–1313.

[11] Sonthikun, S., P. Chairat, and K. Fardsin. 2016. Computational fluid dynamic analysis of innovative design of solar biomass hybrid dryer: An experimental validation. *Renewable Energy*, 92(8): 185–191.

[12] Tian, S.T., Z. J. Gao. 2009. Improved design of airflow distribution chamber in air-impingement oven based on Fluent. *Modern Food Science and Technology*, 25(6): 612–616.

[13] Wang, L.H., Z. J. Gao, and H. Lin. 2011. Pulsed air-impingement dryer. *Transactions of the Chinese Society for Agricultural Machinery*, 42(10): 141–144. (In Chinese with English abstract)

[14] Wu, H. P., H. Z. Fan, B. Dai, and X. Zhang. 2006. Improved design of tunnel dry facilities for dehydrating vegetables for increasing thermal efficiency. *Transactions of the Chinese Society of Agricultural Engineering*, 22(12): 99–102. (In Chinese with English abstract)

[15] Xu, P., Y. Z. Shi, and Z. Fu. 2005. Optimization design of gas distribution chamber in wall-mounted gas boiler. *Gas and Heat*, 25(6): 5–8.

[16] Zhai, Z. P., C. G. Wang. 2008. Numerical simulation and optimization for air flow in an impeller blower. *Transactions of the Chinese Society for Agricultural Machinery*, 39(6): 84–87. (In Chinese with English abstract)

[17] Zhang, W. H., X. L. Zhang, and T. B. Wang. 2005. Multiple enzymatic extraction of active constituents of tea leaves (Natural Science Network Edition). *Science Journal of Northwest University Online*, 3(7): 1–6.

[18] Zhu, H. G., S. Q. Yuan, H. L. Liu, and W. D. Shi. 2007. Numerical simulation of the 3-D flow of a volute-type discharge passage in large pumping stations. *Transactions of the Chinese Society for Agricultural Machinery*, 38(8): 49–53. (In Chinese with English abstract)

[19] Zhu, H. G., and S. Q. Yuan. 2006. Optimal design of inlet conduit for technical innovation of large pumping stations. *Journal of Hydroelectric Engineering*, 25(2): 51–55.

Simulation design and experiment of a directional seed-feeding device

Liu Cailing, Li Yanni, Song Jiannong*, Zhang Fuyin, Wei Dan, Zheng Shengxiang

(*College of Engineering, China Agricultural University, Beijing 100083, China*)

Abstract: A directional seed-feeding device was developed to meet the precision planting requirement of low sowing quantity for non-circular seed. The kinematics analysis was carried out. The key parameters of the directional seed-feeding device were designed and the structure of v-groove was optimized using EDEM. Rice seeds of "Chang Lixiang" were taken as research object. The Quadratic Orthogonal Rotation Combination tests and verification tests under the conditions of optimization parameters were performed. The results showed that the factors and interaction between the factors affected directional transportation of seeds. The reasonable matching of seed-feeding frequency and seed-filling frequency was the key to ensure the qualified index. The theoretical analysis was consistent with the experimental results. The qualified index of 2±1 grains in per hole was greater than 90% and the index of single grain in per hole reached up to 85.05% when installation angle, vibration direction angle, vibration frequency, amplitude and rotational speed of seeding wheel were 3.5°31.5°, 34.76 Hz, 3.7 Vp and 7 r min^{-1}, respectively. The working performance of the device can meet the precision planting requirement of low sowing quantity for non-circular seed.

Keywords: simulation, optimization, directional seed-feeding device, EDEM, design, test

Citation: Liu, C. L., Y. N. Li, J. N. Song, F. Y. Zhang, D. Wei, and S. X. Zheng. 2017. Simulation design and experiment of a directional seed-feeding device. International Agricultural Engineering Journal, 26(4): 16–24.

1 Introduction

Precision seed-metering technology can save cost and raise income, which is popular in modern agricultural production (Yang et al., 2016). Especially with the rapid development of breeding, seed processing and agronomic cultivation technology in recent years, precision sowing of a single grain has become the main feature and development direction of modern sowing technology (Peng et al., 2017; Zhao et al., 2015).

Currently, for round or nearly round seeds with regular shape such as corn and soybean, precision sowing of a single grain has been realized (Yao et al., 2016; Su et al., 2014; Singh et al., 2005). The research and application of seeding a single grain are also increasing for non-circular seeds such as rice, peanut, wheat (Liang et al., 2001; Ma et al., 2010; Yang et al., 2014). At present wheat sowing of a single grain has not yet been achieved. The planting method of close row spacing and uniform sowing was studied in sowing of a single wheat seeds in Hebei Agricultural University and some progress has been obtained (Ma et al., 2010; Hou et al., 2014). Precision sowing of rice stresses the thin planting and sowing of a single grain has been required, which can promote tillering and increase the yield. But considering the germination rate of seeds, missing-transplanting rate and seedling injury rate, the seeding index is determined as 1-2 grains in per hole (Li et al., 2014). Therefore, the development trend of precision sowing technology is to reduce the number of seeds in per hole. Increasing the index of single grain in per hole and reducing leakage index are still difficult for non-circular seeds in precision sowing of low sowing quantity because of complex seed-filling process.

There are two main types of precision seed-metering devices: mechanical and pneumatic (Liao et al., 2014; Wang et al., 2010; Wang et al., 2015; Shi et al., 2015). In fact, pneumatic seed-metering device is expensive. Also,

Received date: 2017-08-09 **Acceptedate:** 2017-09-12

* **Corresponding author: Song Jiannong,** Ph.D, Professor, College of Engineering, China Agricultural University, Beijing 100083. China. Email: cailingliu@163.com.

blocking problem of suction needle plug has not been resolved. The mechanical seed-metering devices are more common applied. Especially the hole-type seed-metering device has been widely used in the application of round or near round seeds. But, the filling procession of wheat, rice and other non-circular seeds is extremely complex. To improve the index of single grain in per hole of hole-type seed-metering device, it is an effective way to control motion posture of seeds and make them arrange in an orderly manner (Han et al., 2015; Yang et al., 2013; Qi et al., 2014). In order to meet the requirements of the precision seed-metering of the non-circular seed and improve the index of 1-2 grains in per hole, a directional seed-feeding device was designed by the method of controlling the motion posture of seeds. The working mechanism of the directional seed-feeding device by vibration was analyzed theoretically, the key parameters were optimized by the bench test to provide reference for the machine design.

2 Structure and working mechanism of the directional seed-feeding device

The directional seed-feeding device is the key to achieve precision seeding, whose structure was shown in Figure 1. It is composed of electromagnetic exciter and the directional seed-feeding mechanism which consists of seed box, high edge v-groove, low edge v-groove and outlet (Figure 2).

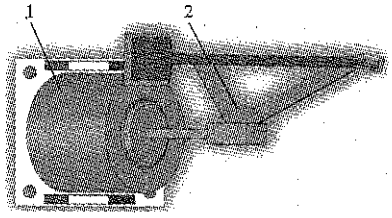

1. Electromagnetic exciter 2 Directional seed-feeding mechanism

Figure 1 Structure of the directional seed-feeding device

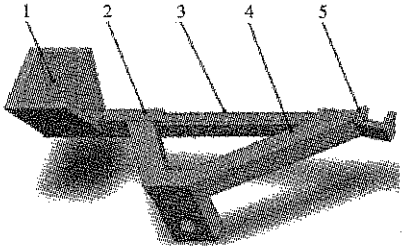

1. Seed box 2. High edge v-groove 3. Low edge v-groove 4. Frame 5. Outlet

Figure 2 The directional seed-feeding mechanism

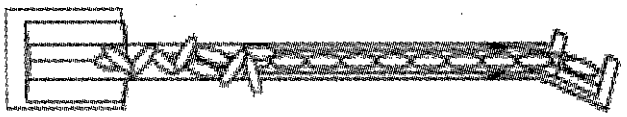

Figure 3 Sorting effect of v-groove

The directional seed-feeding mechanism is connected with the electromagnetic exciter. Seeds in the v-groove shows slightly boiling state, and the small beating reduces its internal friction. The design of v-groove structure makes the seed to continuously adjust itself for "flat" and "lateral" state of the minimum potential energy and change the motion posture, which ensures that all of the seeds in the v-groove are continuously, directionally, uniformly conveyed in the long axis direction of the seeds. When the seeds arrive at the end of the v-groove, they are in parallel to the horizontal axis of the hole wheel under the action of the outlet 5. The device helps to reduce the number of seeds in per hole and improve the index of single grain in per hole (Figures 6 and 7).

Rice seeds of "Chang Lixiang" were used for designing the v-groove structure. The high edge v-groove plays a transitional effect, whose depth is 5 mm and length is 30 mm, slightly larger than the thickness of a rice seed, in which 2-3 layers of seeds can be stored to ensure uninterrupted flow of rice seeds. The low edge v-groove plays the effect of combing seeds, whose depth is 3 mm and length is 75 mm, in which the layer of uniformly sorted seeds are stored. The sorted effect of rice seeds was shown in Figure 3. The width of the outlet opening is 1.2 times length of the seed long axis, the bottom is inclined downwards, and the thickness is slightly shorter than that of the seed short axis to restrict seed posture so that the long axis of a seed is parallel to the hole wheel axle. The outlet tail of v-groove is designed into a round shape, which matches with the round wall of the hole wheel to ensure that the seed posture does not be changed. The gap between the outlet and the hole wheel can ensure that the seed does not leak out.

3 Kinematic analysis of a seed in the directional seed-feeding mechanism

3.1 Motion condition analysis of a seed

The force of a seed in the v-groove was shown in Figure 4. The positive direction of axis X is parallel to the working surface, the positive direction of axis Y is

perpendicular to the v-groove. According to vibration theory, (Wen ET AL., 2001), forward sliding index D_k, reverse glide index D_q, and throwing index D were shown in Equation (1), Equation (2), and Equation (3), respectively.

$$D_k = \frac{\omega^2 \lambda \cos(\varphi_e - \beta)}{g \sin(\varphi_e - \alpha)} \quad (1)$$

$$D_q = \frac{\omega^2 \lambda \cos(\varphi_e + \beta)}{\sin(\varphi_e + \alpha)} \quad (2)$$

$$D = \frac{\omega \lambda^2 \sin\beta}{g \cos\alpha} \quad (3)$$

where, ω is vibration frequency, rad/s; λ is amplitude in the vibration direction, m; φ_e is equivalent static friction angle, φ_e=arctan (tanφ/sinθ), φ is static friction angle; 2θ is the included angle of the v-groove, 70°, the rest variables were explained in Figure 4. The forward sliding condition is $D_k \geq 1$, the reverse glide condition is $D_q \geq 1$, the condition of not being thrown is $D<1$. To improve the conveying efficiency and reduce friction, sliding up along v-groove is hoped. Therefore, the limitation condition without reverse glide is determined that D_k is two-three, D_q is one. In order to ensure the stability of conveying seeds, the throwing index is less than one.

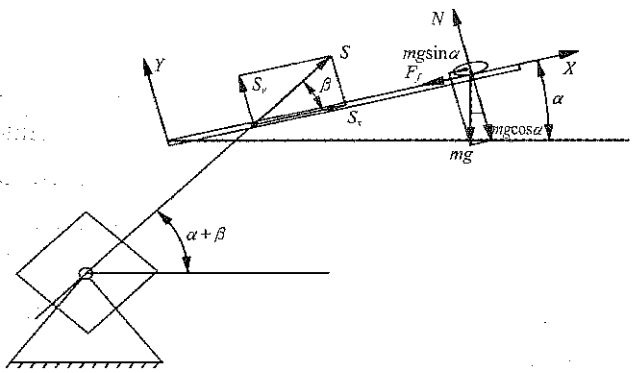

Note: m is the quality of a seed, kg; g is gravitational acceleration, m/s^2; α is installation angle of v-groove,(°); β is vibrator direction angle, (°); N is positive pressure force on the seed, N; F_f is the friction, force,N; S is amplitude, mm.

Figure 4 Motion of v-groove and force of a seed

3.2 Parameters selection and calculation

3.2.1 Installation angle α and vibration direction angle β

The vibration conveying requires that the maximum lift angle is not more than 15° when the conveyor is inclined upward. The installation angle is designed to be 4°. The material of the v-groove is nylon. The measured friction coefficient between rice seed and v-groove is 0.47. 2θ of included angle of the v-groove is 70°. φ_e of equivalent static friction angle is 39.33° by calculating. D_k is two-three and D_q is one. β is from 26.5° to 34.5° according to Equation (1) and Equation (2). The vibration direction angle β is designed to be 31°.

3.2.2 Amplitude λ and vibration frequency f

Electromagnetic vibration machine usually is applied for high frequency and small amplitude. The larger amplitude of the v-groove can cause the deviation between the outlet and the hole so as to affect seed-filling. According to the sizes of the outlet, hole and length of the seed, 2λ should be less than 1 mm. λ is designed to be 0.35 mm. The vibration frequency is from 32.8 Hz to 37.8 Hz according to Equation (1). The vibration frequency f is designed to be 35 Hz.

The forward sliding index D_k, reverse glide index D_q, throwing index D are 2.49, 1 and 0.892 respectively, accurately calculated by Equation (1), Equation (2) and Equation (3) based on above design parameters. The theoretical calculation results showed that the device could stably convey seeds up into the v-groove, which didn't slide down and be throwed. The directional seed-feeding device has good working performance of uniform sorting, steady conveying and distribution along the axial of the hole wheel, which helps to improve the index of single grain in per hole

4 Simulation optimization of the structure of v-groove by EDEM

With the development of computer simulation technology, the discrete element method has been widely used in the field of agricultural engineering research. In order to verify the influence of design parameters of v-groove on uniform sorting, steady conveying and seed-filling effects, the vibration process of the v-groove was simulated by EDEM. The structure of the v-groove was optimized.

4.1 Creation of simulation model

One hundred rice seeds of "Chang Lixiang" with uniform sizes and without awns were used, whose sizes of length, width and thickness were measured. The average value of length, width and thickness were 9.09, 2.92 and 2.09 mm, respectively. The modeling method of multi-balls element aggregate was adopted for creating the discrete element model of an ellipsoid rice seed. An

ellipse formed by the outsourcing line of 5 ball elements was used, whose length of elliptical long axis and short axis were 9.09 and 2.47 mm, respectively. The size of elliptical short axis is average of width and thickness. The radiuses of ball elements were 0.84, 1.125, 1.235, 1.125, and 0.84 mm, respectively from left to right. The ball elements were exactly symmetrical. The distance between the sphere centre of left two ball elements and that of middle ball element were 1.80 and 3.20 mm, respectively. The model of multi-balls element aggregate was very similar to the real contour of the rice seed (Figure5).

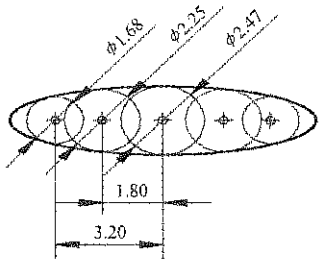

a. 2-D model with mult-balls

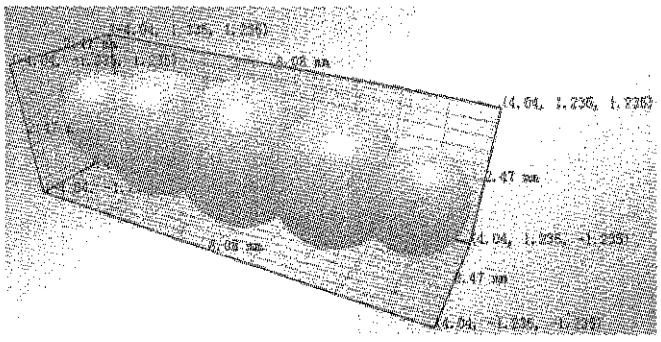

b. 3-D model of EDEM

Figure 5 Model with mult-balls

Based on parameter design of the directional seed-feeding device and study on the existing seeding wheel, the geometric assembly model of v-groove and seeding wheel was built using solidworks (Figure 6). The modeling parameters of the directional seed-feeding mechanism were referenced in section 3.2. The parameters of length, width and depth of an asymmetric hole with inclined angle 45° are 11, 6.75 and 3.5 mm, respectively. The diameter of seeding wheel is 220 mm.

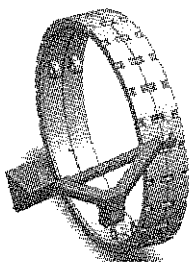

Figure 6 Geometry model of hole wheel with v-groove

4.2 Setting of simulation parameters

According to the physical characteristics of seeds, non-sliding contact model of Hertz-Mindlin was selected. The physical and mechanical parameters were self-tested except the recovery coefficient and the static friction coefficient between seeds and contact material (Lu et al., 2016; Qiu et al., 2012; Jia et al., 2014; Hu et al., 2014). The density, poisson's ratio, shear modulus of seeds are 1239 kg m^{-3}, 0.25, 181.5 MPa, respectively. The recovery coefficient, the static friction coefficient and rolling friction coefficient between seeds are 0.3, 0.56, 0.15, respectively. The density, poisson's ratio, shear modulus of contact material (ABS) are 1080 kg/m^3, 0.39, 318.9 MPa, respectively. The recovery coefficient, static friction coefficient and rolling friction coefficient between seeds and v-groove are 0.48, 0.55, 0.1, respectively. The seed production rate was set to 7 particles/s. The determined time step is 25% using rayleigh wave method and the total simulation time is set to 15 s.

4.3 Analysis of simulation results

Three-dimensional geometric model was loaded into EDEM. The process of conveying seeds of the v-groove of directional seed-feeding mechanism was simulated at the rotational speed of seeding wheel of 7 r min^{-1}. Simulation effect was shown in Figure 7a. The long axis of the seeds was parallel to the horizontal axis of the seeding wheel, which were in "flat" and "lateral" states in the v-groove. The continuous rice seeds stream was realized with the end to the end along the long axis direction of the seeds. The good sorting and conveying effect of the v-groove was verified. Parameters design is basically reasonable. However, the array effect of the single layer of seeds was not good to lead to non-uniform seeds-feeding, so the ordered performance of seeds got worse at the location of seed-filling because of multilayer accumulation of seeds. Therefore, the trapezoidal combing needle was installed on the lower edge v-groove to remove accumulated excess seeds, ensure uniform, sorting, steady conveying and improve the index of single grain in per hole. The structure of the needle was shown in Figure 7c. The effect of sorting and conveying of the v-groove was shown in Figure 7b after the combing needle was installed. The results showed that the combing

needle didn't affect the motion of the seeds at the bottom of v-groove and combed away the excess seeds. The design ensured that the seeds were orderly and continuously delivered to the outlet. The problem of multilayer accumulation of seeds was solved.

The combination of multiple groups of directional seed-feeding mechanism can realize precision planting requirements with different row spacing. The simulation results of the combined mechanism (Figure 7d), which consisted of 14 groups of the seed-feeding mechanism and matched with a seedling tray of 14×31 holes, showed that the index of single grain in per hole, the index of multi-grains in per hole and the leakage index in per hole were 93.15%, 2.98% and 3.87%. The preliminary design showed that the device had good effect on precision seeding and improved the index of single grain in per hole.

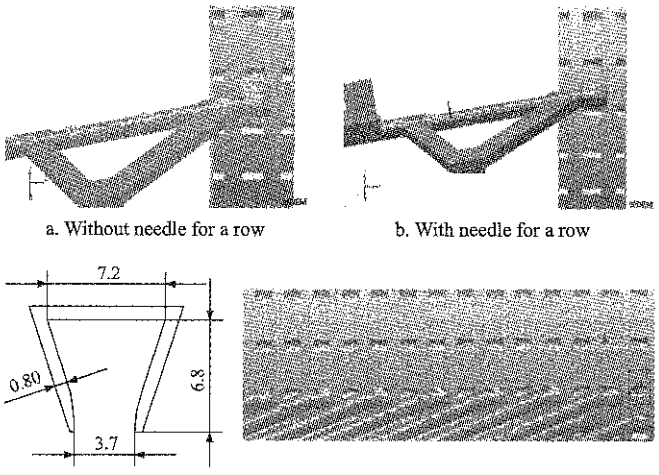

a. Without needle for a row b. With needle for a row

c. Stucture of the needle d. With needle for 14 rows

Figure 7 Simulation results of directional seed-feeding

5 Tests and parameters optimization

In order to study working performance of the directional seed-feeding mechanism and optimize design parameters, a test-bed was built. The tests were finished at the sowing lab of College of Engineering, China Agricultural University.

5.1 Test conditions

Rice seeds of "Chang Lixiang" with uniform grain size and without awns were used, whose three dimensions were shown in 4.1. The average moisture content was measured as 10% by the drying box of "DHG-9140A". The test-bed consists of the directional seed-feeding mechanism, electromagnetic exciter, signal generator and power amplifier of "WD.28-JZQ", the hole-wheel seed-metering device, high-speed photography system (Figure 8, Figure 9). The directional seed-feeding mechanism was processed using the 3D printer of "Dimension Elite" produced by "Stratasys". The high-speed photography system of "PhantomV9.1" produced by "Vision Research" was adopted to capture image and analyze data. The hole-wheel seed-metering device used in the 2ZBL-400P seedling production line from our topic group was applied.

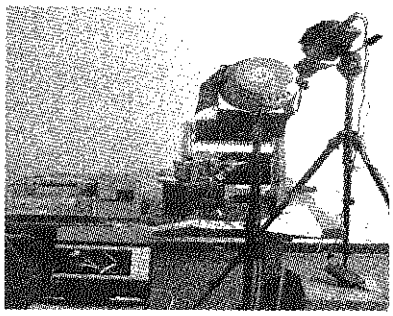

Figure 8 Test bed

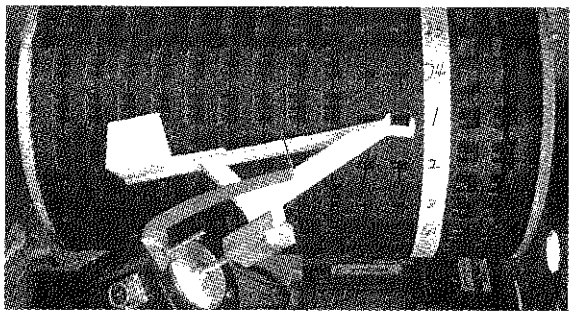

Figure 9 Assembly diagram of the seeding wheel the directional seed-feeding device

5.2 Test indexes and factors

The Quadratic Orthogonal Rotation Combination tests were performed with five factors of installation angle α, vibration direction angle β, vibration frequency f, voltage value V_p (amplitude) and rotational speed of seeding wheel. Corresponding coding factors were Z_1, Z_2, Z_3, Z_4, Z_5, respectively. Factors and codes were shown in Table 1. The ratio of the number of holes with one seed, the number of holes with two-three seeds, the number of holes with zero seed and the total number of holes are marked as the index of single grain in per hole Y_1, the index of multi-grains in per hole Y_2 and leakage index Y_3, respectively.

5.3 Results and discussion

The test results were shown in Table 2. The main factors were screened out and regression equations of Y_1, Y_2 and Y_3 were taken by multiple regression fitting and

variance analysis using Design-Expert 8.0.6 software.

Table 1 Coding table of levels of factors

Code	A, (°)	B, °	F, Hz	V_p, V	N, r/min
–2	2	27	31	3.6	4
–1	3	29	33	3.8	5
0	4	31	35	4.0	6
1	5	33	37	4.2	7
2	6	35	39	4.4	8

Table 2 Experiment design and results

No.	α, °	β, °	f, Hz	V_p, V	n, r/min	Y_1, %	Y_2, %	Y_3, %
1	5	33	37	4.2	7	55.00	39.17	5.83
2	5	33	37	3.8	5	43.33	52.50	4.17
3	5	33	33	4.2	5	50.83	45.83	3.34
4	5	33	33	3.8	7	70.00	10.00	20.00
5	5	29	37	4.2	5	59.17	28.33	12.50
6	5	29	37	3.8	7	69.17	9.17	21.66
7	5	29	33	4.2	7	69.17	12.5	18.33
8	5	29	33	3.8	5	65.00	18.33	16.67
9	3	33	37	4.2	5	49.17	46.67	4.16
10	3	33	37	3.8	7	63.33	30.83	5.84
11	3	33	33	4.2	7	60.83	24.17	15.00
12	3	33	33	3.8	5	40.00	5.83	54.17
13	3	29	37	4.2	7	67.50	28.33	4.17
14	3	29	37	3.8	5	56.67	36.67	6.66
15	3	29	33	4.2	5	52.50	40.00	7.50
16	3	29	33	3.8	7	68.33	21.67	10.00
17	6	31	35	4.0	6	41.67	54.17	4.16
18	2	31	35	4.0	6	55.00	39.17	5.83
19	4	35	35	4.0	6	41.67	55.00	3.33
20	4	27	35	4.0	6	64.17	25.83	10.00
21	4	31	39	4.0	6	50.83	44.17	5.00
22	4	31	31	4.0	6	53.33	10.00	36.67
23	4	31	35	4.4	6	47.50	49.17	3.33
24	4	31	35	3.6	6	60.83	24.17	15.00
25	4	31	35	4.0	8	66.67	22.5	10.83
26	4	31	35	4.0	4	45.83	46.67	7.50
27	4	31	35	4.0	6	52.50	40.83	6.67
28	4	31	35	4.0	6	61.67	33.33	5.00
29	4	31	35	4.0	6	52.50	42.50	5.00
30	4	31	35	4.0	6	56.67	38.33	5.00
31	4	31	35	4.0	6	68.33	27.50	4.17
32	4	31	35	4.0	6	54.17	40.83	5.00
33	4	31	35	4.0	6	58.33	34.17	7.5
34	4	31	35	4.0	6	58.33	37.50	4.17
35	4	31	35	4.0	6	46.67	45.00	8.33
36	4	31	35	4.0	6	46.67	50.83	2.50

$$Y_1=53.72-0.13Z_1-5.00Z_2+0.55Z_3-1.59Z_4+6.19Z_5-2.70Z_1Z_3-1.05Z_1Z_5+1.56Z_2Z_5-1.57Z_4Z_5-0.70Z_1^2+0.76Z_4^2+1.28Z_5^2 \quad (4)$$

$$Y_2=41.33+0.48Z_1+4.93Z_2+6.74Z_3+5.42Z_4-6.11Z_5+6.15Z_1Z_2-3.12Z_1Z_5+4.58Z_2Z_3+2.08Z_2Z_4-3.33Z_3Z_4-1.08Z_2^2-4.41Z_3^2-2.01Z_4^2-2.53Z_5^2 \quad (5)$$

$$Y_3=4.95-0.35Z_1+0.07Z_2-7.29Z_3-3.81Z_4-0.08Z_5-6.15Z_1Z_2+2.70Z_1Z_3+4.17Z_1Z_5-4.58Z_2Z_3-2.08Z_2Z_4-1.56Z_2Z_5+3.33Z_3Z_4+1.57Z_4Z_5+0.70Z_1^2+1.08Z_2^2+4.41Z_3^2+1.25Z_4^2+1.25Z_5^2 \quad (6)$$

F-test results of regression model of Y_1, Y_2 and Y_3 were all highly significant ($P<0.01$). Regression orthogonal design eliminates the correlation between coefficients and the absolute value of regression coefficient indicates the importance of the factors. The results of regression equation and variance analysis showed that the important factors affecting Y_1 were rotational speed of seeding wheel, vibration direction angle, amplitude, vibration frequency and installation angle in turn, and rotational speed of seeding wheel and vibration direction angle presented highly significance; the important factors affecting Y_2 were vibration frequency, rotational speed of seeding wheel, amplitude, vibration direction angle and installation angle in turn, and vibration frequency, rotational speed of seeding wheel, amplitude and vibration direction angle presented highly significance; the important factors affecting Y_3 were vibration frequency, amplitude, installation angle, rotational speed of seeding wheel and vibration direction angle, and vibration frequency and amplitude presented highly significance interaction between the factors had different effects on the evaluating index, which indicates that seeds motion process is complex, and different factors and interaction between the factors affects directional seeds transport.

There were no more than three grains filling in one hole in the experiment, and the filling effect of 1-2 grains in one hole was better, so it was significant to reduce the leakage index. Regression analysis showed that effects of vibration frequency and amplitude on the leakage index was highly significant, the forward sliding index is proportional to the square of the vibration frequency, which is in agreement with the analytical conclusion as described in Equation (1). The effects of vibration frequency on conveying seeds is especially sensitive. Combined with the motion analysis of seeds, vibration frequency, amplitude, installation angle and vibration direction angle affect the forward sliding index of seeds, seed-feeding frequency and conveying effect. The reasonable parameter design is the key to convey seeds uniformly, improve the seed-filling performance. The rotational speed of seeding wheel affects seed-filling frequency, so reasonable matching of seed-feeding

frequency and seed-filling frequency is the key to ensure the qualified index. The theoretical analysis is consistent with the experimental results.

6 Multi objective parameters optimization and experimental verification

In order to further improve the index of single grain in per hole, reduce the index of multi-grains in per hole and leakage index, the mathematical model was established based on the boundary conditions of the factors, as followed in Equation (7).

$$\begin{cases} \max Y_1(\alpha,\beta,f,V_p,n) \\ \min Y_2(\alpha,\beta,f,V_p,n) \\ \min Y_3(\alpha,\beta,f,V_p,n) \\ \text{s.t.} \quad 2° \le \alpha \le 6° \\ \qquad 27° \le \beta \le 35°, \\ \qquad 31 \le f \le 39, \\ \qquad 3.6 \leqslant Vp \le 4.4; \\ \qquad 4 \le n \le 8 \end{cases} \tag{7}$$

Design-Expert 8.0.6 was used to optimize the parameters in the range of test factors by Response Surface Methodology. The index of single grain in per hole, the index of multi-grains in per hole and leakage index were 84.37%, 9.76% and 5.87%, respectively when installation angle, vibration direction angle, vibration frequency, amplitude and rotational speed of seeding wheel were 3.5°, 31.5°, 34.76 Hz, 3.7 V_p and 7 r/min, respectively.

To verify optimization results, optimized parameters were adjusted and the validation test was repeated for 10 times under the conditions of continuous running five cycles. The average values of the index of single grain in per hole, the index of multi-grains in per hole and leakage index were 85.05%, 8.75% and 6.20%, respectively, which was basically consistent with optimization results. The qualified index of 2±1 grains in one hole was 93.8%. The results of high-speed photography (two cycles) are shown in Figure 10.

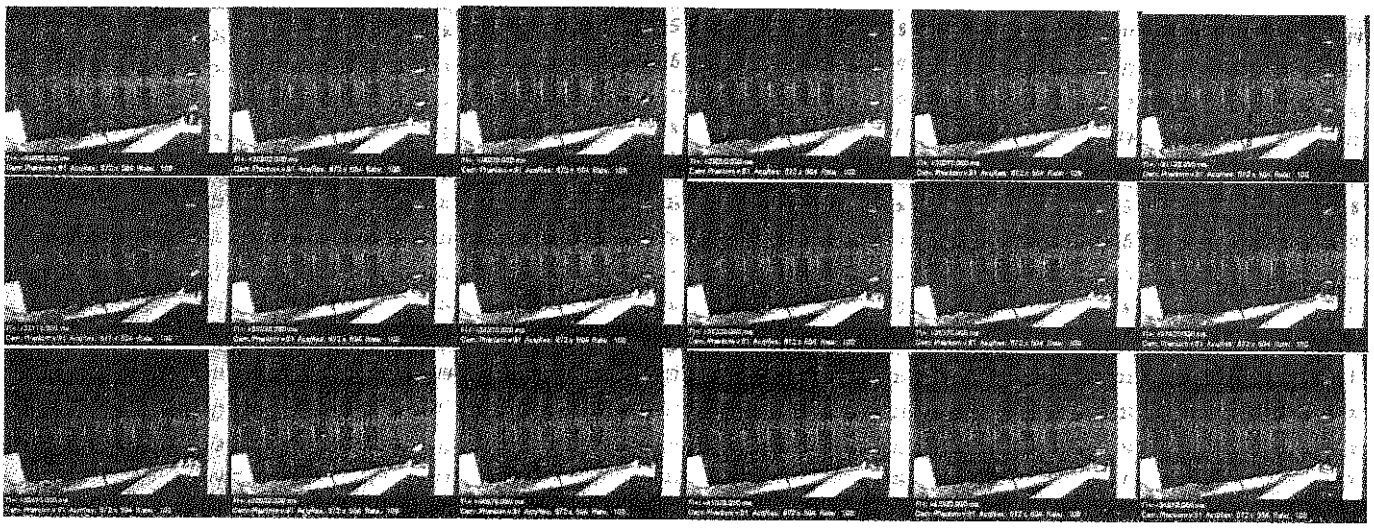

Figure 10 Seed-filling effects diagram taken by high speed photography

7 Conclusions

1) The directional seed-feeding device was designed, the structure of v-groove was optimized and feasibility of structure design was verified using EDEM.

2) Based on kinematic analysis, the Quadratic Orthogonal Rotation Combination test was performed with five factors. The nonlinear regression models of relation between the text indexes and factors were established and the influence of the factors on the test indexes was analyzed.

3) Multi objective parameters optimization was carried out, and the results showed that the index of single grain in per hole, the index of multi-grains in per hole and leakage index were 84.37%, 9.76% and 5.87%, respectively when installation angle, vibration direction angle , vibration frequency, amplitude and rotational speed of seeding wheel were 3.5°, 31.5°, 34.76 Hz, 3.7 V_p and 7 r/min, respectively. The results of experimental verification showed that the qualified index of 2 ± 1 grains in one hole was greater than 90% under the optimized parameters combination, and were basically

consistent with the optimized results.

4) The combination of multi-groups of the seed-feeding mechanism can realize precision planting requirements with different row spacing. The study provides the basis for the optimization design of precision seeding device of low sowing quantity suitable for non-circular ellipsoid seeds.

Acknowledgements

Financial support for this study was provided by the National Keypoint Research and Invention Program of the Thirteenth (2016YFD020060704).

[References]

[1] Han, B., F. C. Meng, L. N. Liang, Y. X. Ge, and H. Y. Xu. 2015. Performance experiment of directional precision seeding device for japonica rice. *Transactions of the Chinese Society of Agricultural Engineering*, 31(16): 8–15. (In Chinese with English abstract)

[2] Hou, L. L. 2014. Development of the 7.5 cm row spacing mechanical seeder for wheat. MS dissertation. agricultural mechanization Hebei Agricultural University. Baoding.

[3] Hu, J. P., C. J. Zhou, C. Hou, and J. Wang. 2014. Simulation Analysis of seed-filling performance of magnetic plate seed-metering device by discrete element method. *Transactions of the Chinese Society for Agricultural Machinery*, 45(2): 94–98. (In Chinese with English abstract)

[4] Jia, F. G., Y. L. Han, Y. Liu, Y. Cao, and Y. Shi. 2014. Simulation prediction method of repose angle for rice particle materials. *Transactions of the Chinese Society of Agricultural Engineering*, 30(11): 254–260. (In Chinese with English abstract)

[5] Li, Z. H., X. Ma, J. F. Xie, G. R. Chen, Z. X. Zhen, X. S Tan, and Y. Q. Huang. 2014. Experiment on precision seedling raising and mechanized transplanting of hybrid rice under low sowing rate in double cropping area. *Transactions of the Chinese Society of Agricultural Engineering*, 30(6):17–27. (In Chinese with English abstract)

[6] Liang, S. Y., J. Feng, A. J. Zeng, W. T. Song, Y. J. Liu, and H. L. Hu. 2001. Performance experiments of the seed meter device with combined sucker. *Transactions of the Chinese Society of Agricultural Engineering* , 17(3): 84–87. (In Chinese with English abstract)

[7] Ma, L. 2010. Study on the new kind tube-slit air-suction wheat seeding machine. MS dissertation. agricultural mechanization Hebei Agricultural University. Baoding

[8] Liao, Q. X., C. X. Shu, and H. W. Gao. 2004. Study on new-type pusher and ejector of horizontal plate precision metering. *Transactions of the Chinese Society for Agricultural Machinery*, 35(1): 60–64. (In Chinese with English abstract)

[9] Lu, F. Y., X. Ma, L. Qi, S. Y. Tan, L. K. Jiang, and G. D. Sun. 2016. Parameter optimization and experiment of vibration seed-uniforming device for hybrid rice based on discrete element method. *Transactions of the Chinese Society of Agricultural Engineering*, 32(10): 17–25. (In Chinese with English abstract)

[10] Peng, Q. J., S. C. Jian, Q. H. He, Q. K. Fu, and H. Yue. 2017. Development of a single grain of wheat precision seeder. *Journal of Agricultural Mechanization Research*, 7: 71–75.

[11] Qi, L., Z. T. Tan, and X. Ma. 2014. Optimization and test of operational parameters of pneumatic vibration uniform-seeds device. *Journal of Jilin University: Engineering and Technology Edition*, 44(6): 1684–1691.

[12] Qiu, B. J., G. W. Jiang, N. Yang, X. P. Guan, J. J. Xie, and Y. M. Li. 2012. Discrete element method analysis of impact action between rice particles and impact-board. *Transactions of the Chinese Society of Agricultural Engineering*, 28(3): 44–49. (In Chinese with English abstract)

[13] Singh, R. C., G. Singh, D. C. Sarawat. 2005. Optimisation of design and operational parameters of a pneumatic seed metering device for planting cotton seeds. *Biosystems Engineering*, 92(4): 429–438.

[14] Shi, S. 2015. Design and experimental research of the pneumatic maize precision seed-metering device with combined holes. MS dissertation, Beijing: China Agricultural University. Beijing.

[15] Su, W., Q. H. Lai, K. Luo, J. Zhao, and H. Zhang. 2014. Design and experiment for soybean high-speed Precision vacuum seed metering. *Soybean Science*, 33(4): 594–598.

[16] Wang, C., J. N. Song, J. C. Wang, C. L. Liu, and J. W. Wu.. 2010. Dropping progress of rice seed metering device with hole. *Transactions of the Chinese Society for Agricultural Machinery*, 41(8): 39–42. (In Chinese with English abstract)

[17] Wang, J. W., H. Tang, W. Q. Zhou, W. P. Yang, and Q. Wang.. 2015. Improved design and experiment on pickup finger precision seed metering device. *Transactions of the Chinese Society for Agricultural Machinery*, 46(9): 68–76. (In Chinese with English abstract)

[18] Wen, B. C., S. Y. Liu, J. He. 2001. Theory and dynamic design method of vibration machine. Beijing: *China Machine Press*. (in Chinese)

[19] Yang, L., B. X. Yan, D. X. Zhang, T. L. Zhang, Y. X Wang, and T. Cui. 2016. Research progress on precision planting technology of maize. *Transactions of the Chinese Society of Agricultural Engineering*, 47(11): 38–48. (In Chinese with English abstract)

[20] Yang, R. B., H. H. Chai, and S. Q. Shang. 2014. Performance

of metering device with declined discon peanut seeder. *Transactions of the Chinese Society for Agricultural Machinery*, 45(6): 79–84. (In Chinese with English abstract)

[21] Yang, Y. L., S. Gu, K. Li, K. Liu, Q. Zhang, L. X. Zhong, D. D. Jia, and X. L. Liu.. 2013. Parameters optimization of directing precision seeder for large cucurbitaceous seeds. *Transactions of the Chinese Society of Agricultural Engineering*, 29(13): 15–22. (In Chinese with English abstract)

[22] Yao, P F. 2016. Research on design and seed spacing uniformity experiment of the variable-volume hole precision seeder. MS dissertation. agricultural engineering Jilin University. Changchun.

[23] Zhang, G. Z., S. S. Zhang, W. P. Yang, K. Lu, Z. Q. Lei, and M. Yang. 2016. Design and experiment of double cavity side-filled precision hole seed metering device for rice. *Transactions of the Chinese Society of Agricultural Engineering*, 32(8): 9–17. (In Chinese with English abstract)

[24] Zhao, X. K. 2015. Development of densely row spacing evenly wheat seeder. MS dissertation. Hebei Agricultural University. Baoding.

Membrane-soil separation for the shovel-screen type residual plastic film collector

Zhang Yaping, Hu Zhichao*, You Zhaoyan, Shen Cheng, Gu Fengwei, Wu Feng

(*Nanjing Research Institute for Agricultural Mechanization, Ministry of Agriculture, Nanjing 210014, China*)

Abstract: The membrane-soil separation technique based on shovel-screen type residual plastic film collector (hereafter referred to as shovel-screen collector) has been studied, a kind of multi-stage membrane- soil separation device was designed to enhance the membrane-soil separation effect from four aspects, including installing the soil-breaking device, increasing the screening distance, installing the soil-guiding device, and adjusting the inclination angle of back-screen. By applying the above devices, the structure of 1MCS-100 type residual plastic film collector (hereafter referred to as 1MCS-100 collector) was optimized. The type of the vibrating screens was sawtooth screen, whose spacing was 15 mm, minimum screening distance was 1300 mm, amplitude was 48 mm and vibration frequency was 3.7 Hz. The width of sawtooth bar was 18 mm, whose tooth height was 5 mm and the thickness was 1.5 mm. The length of the soil-breaking roller was 920 mm, of which the outer diameter was 170 mm, and the inner diameter was 150 mm. The inclination angle of back-screen was 10 degrees, and the minimum distance between soil-guiding device and the back-screen surface was 30 mm. Taking the recovery rate of residual film and film soil ratio as evaluation indexes, a field contrast test of the non-optimized machine and the optimized machine was carried out. Test results showed that the average recovery rate of residual film and average film soil ratio of non-optimized machine were respectively 83.87% and 0.14, the corresponding values of optimized machine were respectively 85.72% and 0.5. The results indicated that the average recovery rate of residual film of optimized machine just had a slight improvement, but the film soil ratio was significantly improved, which demonstrated the structure optimization of 1MCS-100 collector was effective, and the multi-stage membrane- soil separation device is distinctly useful for the enhancement of membrane-soil separation effect. This study can not only provide reference for the research of membrane-soil separation, but also be helpful to reduce the agricultural pollution.

Keywords: shovel-screen, residual plastic film collector, membrane-soil separation, verification test

Citation: Zhang, Y. P., Z. C. Hu, Z. Y. You, C. Shen, F. W. Gu, and F. Wu, 2017. Membrane-soil separation for the shovel-screen type residual plastic film collector. International Agricultural Engineering Journal, 26(4): 25–32.

1 Introduction

Film mulching cultivation in China was an agricultural planting model introduced from Japan in 80 s, and the usage amount of agricultural plastic film in China increased about 4.1 million tons from 2010 to 2014. Film mulching cultivation is increasing production and gaining agricultural economic benefits, but it is also bringing a series of environmental problems at the same time. Nowadays, agricultural plastic film pollution has become one of the main agricultural pollution sources in China (Da, 2015). If the waste agricultural plastic film cannot be recycled with effective treatment, along with the increase of film mulching cultivation year, the amount of residual plastic film in the soil will continue to increase, which will impede the permeation of soil capillary water and natural water, affect the absorption of soil moisture and block the movement of water, thereby destroy the soil structure, lower the fertility levels and impede the growth and development of crops, even lead to secondary salinization of soil and the difficulty of the groundwater to seep, eventually result in a substantial reduction of crop production (Yan et al., 2014; Yan et al., 2014). Therefore, the efficient recovery and reuse of residual plastic film have become a new challenge for researchers

Received date: 2017-07-19 **Accepted date:** 2017-09-20

* **Corresponding author: Hu Zhichao,** Professor of Nanjing Research Institute for Agricultural Mechanization, Ministry of Agriculture of the P.R.C., 210014 China. Email: nfzhongzi@163.com. Tel: +86-025-84346246, Fax: +86-025-84346256.

(Yan et al., 2016).

In order to solve the problem of agricultural plastic film pollution, many kinds of residual plastic film recycling machines have been developed both at home and abroad. The typical residual plastic film collector in foreign country is film winding machine (Zhang, 2015), such as Plastic Mulch Lifter Wrapper-PR2500 produced by Australian CropCare Company, which recycled the residual plastic film with a good operation effect, by way of the combination of the soil loosening shovel, the film lifting wheel and the film winding roller. The harvesting effect of domestic film winding machine is unsatisfactory, because the agricultural plastic film used in China is generally thin and easily broken (You et al., 2016). In view of the above situation, many domestic research institutes have developed a variety of shovel-screen collectors which were simple in structure and reliable in operation, especially suitable for sandy soil or sandy loam soil (Yan et al., 2017). Membrane-soil separation is the key technology of shovel-screen collector, and it's also the difficult point of research and development (Lyu et al., 2015). Both domestic and overseas researchers have done relevant work on membrane-soil separation of residual plastic film collector. Manlio et al. (1978) developed an aculei type film picking device, including an endless belt conveyor which carries on the surface thereof a plurality of aculei that pick out plastic film containing waste material placed on the surface of the conveyor belt. Brooks et al. (1995) developed a mulch film recycling baler, including a grid screen which separated the soil from the mixture, a hydraulic-driven conveyor belt which transported the plastic film to a hopper type film-collecting basket for package processing. Zhang et al. (2013) developed a membrane separation and transportation device, including many discs installed on a support frame with an inclination angle of 40 degrees, which was driven by sprockets. During working, residual plastic film and broken soil were stirred up to the discs by the film- taking mechanism of the collector, then the broken soil fell to the ground under the operation of gravity, and the residual plastic film moved along the outer circle of the discs to the film-collecting box at the back of the device. Wang (2005) conducted a research on separation and dithering transmission system device of the polythene film collector, in which the type of vibrating screen was determined as rod screen, the frequency and amplitude of the vibrating screen and the inclination angle of the screen surface were calculated. In this study, aiming at the problem of low efficiency of membrane-soil separation for shovel-screen collector, the membrane-soil separation technology was studied and analyzed with the research object of 1MCS-100 type residual plastic film collector, which was developed by Nanjing Research Institute for Agricultural Mechanization, Ministry of Agriculture, and then the structure optimization of 1MCS-100 type collector was carried out based on the research findings.

2 Design of multi-stage membrane soil separation device

The operation of shovel-screen collector should undergo three processes: film lifting, film transporting and film collecting. The shovel will dig up many clods in the process of film lifting, and the remaining plastic film in the membrane-soil mixture will be fed into the film-collecting basket after the vibration screening of the film transporting stage. Incomplete separation will lead to the increase of film soil ratio, which will be unfavorable to the recovery and utilization of residual plastic film (Wang, 2005). The main reasons for the difficulty of membrane-soil separation are that the clods cannot be broken sufficiently, the screening time is not long enough, and the resistance of screen surface is too high etc. In view of these reasons, the multi-stage membrane-soil separation device has been designed, which promoted separation of membrane-soil from different aspects at different stages of operation. The specific technical means are as follows: install soil-breaking device, increase screening distance, install the soil-guiding device and adjust the inclination angle of back-screen. According to the above measures, the 1MCS-100 collector (presented in Figure 1) was improved, and the 1MCDS-100B collector (hereafter referred to as 1MCDS-100B collector) (presented in Figure 2) was obtained.

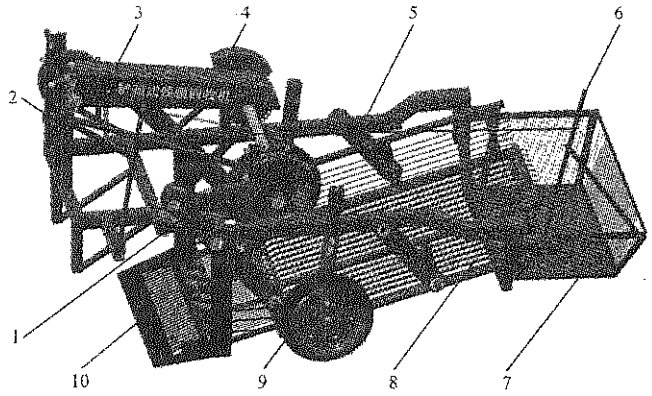

1. Vibration driving device 2. Hitch frame 3. Transmission device 4. Eccentric block 5. Frame 6. Unloading device 7. Film-collecting basket 8. Vibrating screen 9. Depth stop 10. Digging shovel

Figure 1 1MCS-100 type residual plastic film collector

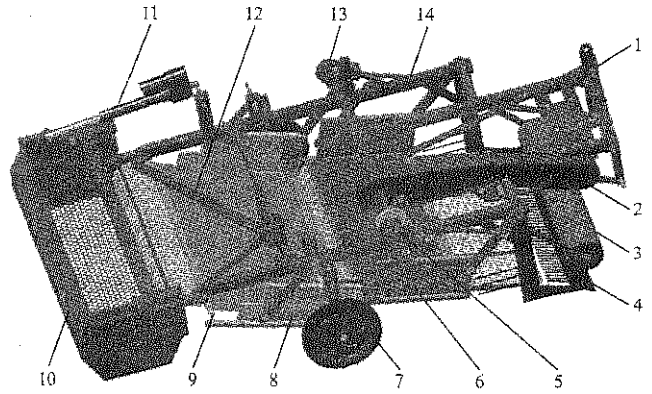

1. Hitch frame 2. Transmission device 3. Soil-breaking roller 4. Digging shovel 5. Vibration driving device 6. Fore-screen 7. Depth stop 8. Back-screen 9. Ball stud 10. Film-collecting basket 11. Unloading device 12. Soil-guiding device

Figure 2 1MCDS-100B type residual plastic film collector

2.1 Installation of the soil-breaking device

The past tests showed that some large clods and residual film were mixed together during the operation, because these clods with large volume were unable to be sifted through the vibrating screen, in contrast, they were transported to the basket with the residual plastic film together. By installing the soil-breaking device, some clods will be broken to a great extent before the end of the film-collecting process, which will contribute to the membrane-soil separation. For the shovel-screen collector, there are two methods for soil breaking in the process of film lifting and film transporting: first, install the soil-breaking roller (presented in Figure 3) at the front and the top of the digging shovel (Wang et al., 2011), which will break the clods before they reach the vibrating screen. For instance, 1MCDS-100B type machine was equipped with a roller in front of the machine, whose length was 920 mm, outer diameter was 170 mm and inner diameter was 150 mm; second, use a vibrating screen with the capacity of soil breaking. Thus, soil breaking and membrane-soil separation can be carried out at the same time. For example, the collectors of type 1MCS-100 and 1MCDS-100B, were all equipped with sawtooth screen (presented in Figure 4) of the same specifications. The width of sawtooth bar was 18 mm, whose tooth height was 5 mm and thickness was 1.5 mm. During operation, the sawtooth crashed clods to break them due to the vibration of screen surface, and small pieces of soil leaked from the screen gap easily.

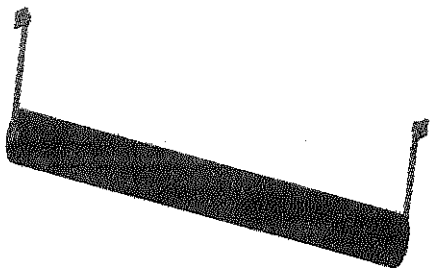

Figure 3 Soil-breaking roller

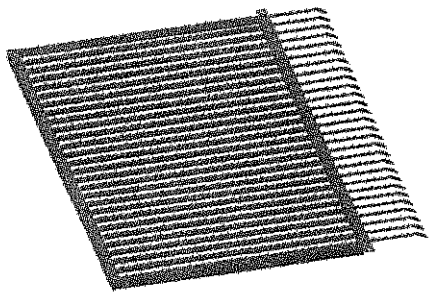

Figure 4 Sawtooth screen

2.2 Increment of the screening distance

Screening distance is the track length that the membrane-soil mixture passed from reaching the screen surface to leaving it. When the moving speed of the mixture on the screen surface is constant, the larger the screening distance is, the longer the effective screening time is, and the more thorough the membrane-soil separation is. By extending the length of the vibrating screen, the screening distance can be increased. 1MCDS-100B collector was equipped with a vibrating screen of double-screen structure, which prolonged the length of the screen surface indirectly, and the screening distance was the sum of the track length of the mixture on the fore-screen and back-screen under this circumstance. In other words, when the length of fore-screen is L_1 and the length of back-screen is L_2, then the minimum

screening distance L equals L_1 plus L_2 ($L = L_1 + L_2$, for the 1MCDS-100B collector, L = 1300 mm). During operation, the residue plastic film was screened through the fore-screen and the back-screen in sequence, and finally collected into the film-collecting basket. The fore-screen and back-screen were both composed of a screen bed and a screen plate, wherein the screen bed was fixed with the vibration driving device, and the screen plate was connected with the screen bed through bolts to facilitate disassembly and replacement. The front screen bed and the back screen bed were arranged in parallel. The front screen bed was on the upper part, and the back part of the fore-screen was overlapped with the front part of the back-screen to prevent falling of the residual plastic film from the junction of fore-screen and back-screen.

2.3 Installation of the soil-guiding device

It was found in the experiments that some big clods had been rolling back and forth on the vibrating screen and couldn't be sifted out. In order to solve this problem, the soil-guiding device was installed above the vibrating screen, and its operation principle diagram is shown in Figure 5 (the arrow indicates the direction of motion). The soil-guiding was mainly accomplished by a baffle shaped like "V", including a left baffle, a right baffle and an arc baffle, which played the role of preventing winding. The thickness of the baffle was 2 mm, the radius of the arc baffle was 50 mm, and the angle of "V" was 90 degrees (the commissioning test showed that when the angle was about 90 degrees, the movement of big clods was smoother and the end of "V" baffle was close to the bilateral openings). During operation, when the machine was moving forward, some big clods directly discharged from both sides of the machine to the ground under the guidance of the V-shaped baffle. The remaining little broken soil and residual plastic film, passing through the gap between the V-shaped baffle and the screen face, were further transported for subsequent screening. The minimum gap between the V-shaped baffle and the screen surface was adjustable between 10-120 mm, and the soil-guiding device and the frame were bonded by a U-shaped bolt.

2.4 Adjustment of the inclination angle of back-screen

For the double-screen type residual plastic film collector with sawtooth screen, most of the soil in the membrane-soil mixture could be sifted out from the gap of sawtooth bar on the screen surface. Some soil slided to the ground from the interface of the fore-screen and the back-screen under the action of gravity, and the movement of this soil was greatly influenced by the inclination angle of back-screen (Zou et al., 2010). If the angle is too small, the soil cannot be slid down to the ground and will be transported to the film-collecting basket with the residual plastic film, which will lead to the increase of film soil ratio. On the contrary, if the angle is too large, the residual plastic film on the back-screen cannot continue conveying back. Therefore, in order to have a better effect of membrane-soil separation, it is necessary to enlarge the inclination angle of back-screen in a reasonable range. The Equation (1) was obtained through the force analysis of the soil which was slipped from the interface between the fore-screen and the back-screen (shown in Figure 6).

$$\begin{aligned} mg \cdot \sin\alpha &> f \\ f &= u_1 N \\ N &= mg\cos\alpha \end{aligned} \tag{1}$$

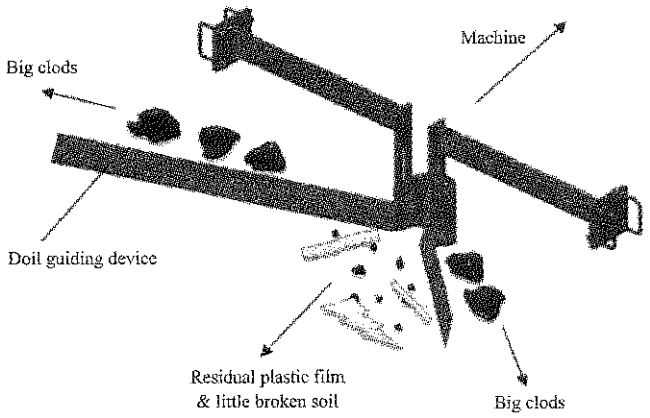

Figure 5 Operation principle diagram of soil-guiding device

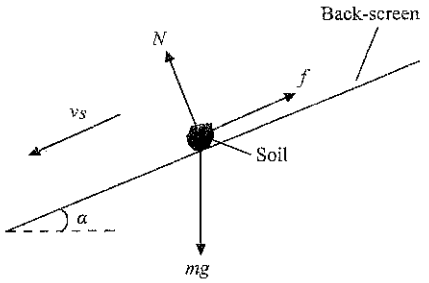

Figure 6 Force analysis of soil on back-screen

From Equation (1), the condition of soil sliding down was obtained:

$$\tan\alpha > u_1 \quad (2)$$

According to the same method above, the residual plastic film on the back-screen was subjected to force analysis, and the condition of the backward transportation of the residual film was obtained:

$$\tan\alpha < u_2 \quad (3)$$

Referring to the Equations (2) and (3), in order to ensure the smooth slide of some soil down to the ground from the junction of fore-screen and back-screen and the smooth delivery of the residual plastic film, the inclination angle of back-screen needs to meet the following condition:

$$\arctan u_1 < \alpha < \arctan u_2 \quad (4)$$

Under the condition of Equation (4), it is beneficial for the soil to slide down from the interface of the two screens under the action of gravity, so as to heighten the effect of membrane-soil separation. The inclination angle of back-screen can be adjusted by the ball stud, as is shown in Figure 7a, and the ball stud was composed of a ball head and a bolt bar. There was a groove of a certain depth at the bottom of the ball head, and the bolt bar could rotate around the center of the ball head, so as to ensure the bolt bar is always perpendicular to the screen bed. Figure 7b is the installation diagram of the ball stud. The ball head of the ball stud was welded with the angle iron at the rear of the back-screen, the ball stud was connected with the screen bed through three nuts. The back-screen bed was clamped by two of the three, which were respectively arranged at the upper and the lower sides of the back-screen bed, and another nut was located at the upper end of the bolt bar to tighten the ball head. When the back-screen plate is not raised, each ball stud only needs one nut to be tightened from the lower side of the screen bed. By adjusting the ball stud, the position of the rear end of the back-screen can be raised or pulled down so as to realize the step-less regulation of the inclination angle of back-screen surface in the range of 0-10 degrees. During the field operation, in order to achieve the best effect of membrane-soil separation, the angle should be adjusted to the appropriate value according to the different operation objects and working environment.

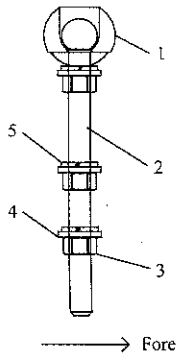

1. Ball head 2. Bolt bar 3. Nut 4. Flat washer 5. Spring washer

a. Ball stud

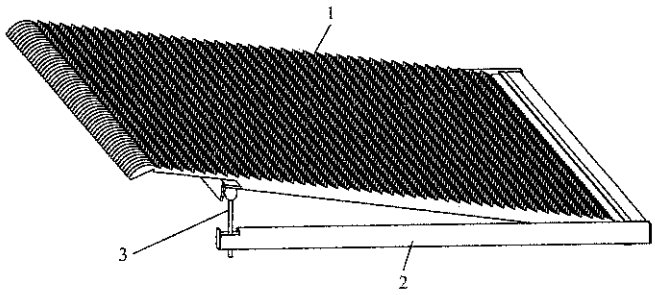

1. Screen plate 2. Screen bed 3. Ball stud

b. Installation diagram of the ball stud

Figure 7 Ball stud and its installation diagram

3 Verification test

According to the above plan, 1MCS-100 collector was optimized, and 1MCDS-100B collector was obtained, as is shown in Figure 2. In order to verify the effectiveness of the optimization scheme, the field contrast test was conducted on the non-optimized machine and optimized machine.

3.1 Test condition

In September 2016, the residual plastic film recycling test was carried out in Liuhe Experimental Base of Jiangsu Academy of Agricultural Sciences (Figure 8). The soil type of experimental field was sandy loam, soil moisture content was 9.6%, and soil hardness was 116 kPa. The preceding peanut was planted with the mode of one ridge two rows film mulching cultivation. The ridge distance was 80 cm, the ridge height was 15 cm, the film thickness was 0.008 mm, and the film width was 700 mm. The parameters of the vibrating screen affect the performance of the two machines directly, for example, if the spacing of sawtooth bar is too large, the film leakage will lead to a low recovery rate of residual film. On the contrary, if the spacing is too small, the film soil ratio will be reduced. In order to select the proper parameters, the commissioning test was carried out before the

verification test. The type of vibrating screens for the two machines were determined as the sawtooth screen, whose spacing was 15 mm, amplitude was 48 mm, and vibration frequency was 3.7 Hz. For 1MCDS-100B collector, the inclination angle of back-screen was adjusted to 10 degrees (the rear end of back-screen was about 50 mm high). The minimum distance between the soil-guiding device and the back-screen surface was adjusted to 30 mm, to ensure the large clods, whose diameter was more than 30 mm, would not be able to convey backwards through the back-screen surface. The power source of the two tested machines was the Huanghai Jinma 304A tractor, which provided power and traction for the two machines. The tractor has four gears, and an H-L gear (switch high speed or low speed). The gear of tractor was set as low 3th, and the machine forward speed was about 0.66 m/s under this condition. The field contrast test was conducted under the above test conditions, and the operation performance of the two machines was relatively stable.

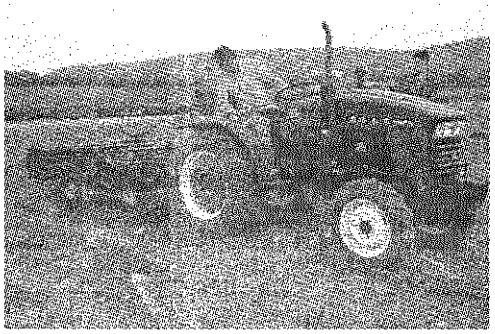

Figure 8 Field test

3.2 Test index

The recovery rate of residual film and the film soil ratio were taken as the test indexes in this experiment. On the premise that the recovery rate of the residual film met the standard requirements, the test was mainly focused on the film soil ratio and compared the effect of membrane-soil separation on the two machines. Referring to the PRC standard (GBT 25412-2010), the recovery rate of residual film and the film soil ratio were calculated according to the Equations (5) and (6).

3.2.1 Recovery rate of residual film

Ten measuring points were took respectively before and after the recycling operation, and each measuring point was 5 m in length, 700 mm in width, and 150 mm in sampling depth. The agricultural plastic films of all measuring points were picked out, then washed, dried and weighed respectively, and the recovery rate of residual film at each measuring point was calculated according to the following Equation (5):

$$\eta = 1 - \frac{X}{X_0} \times 100\% \tag{5}$$

where, η is the recovery rate of residual film, %; X is the weight of the agricultural plastic film in the measuring point area after working, g; X_0 is the weight of the agricultural plastic film in the measuring point area before working, g.

3.2.2 Film soil ratio

In the process of the recovery of the residual plastic film, when the film-collecting basket is filled with materials, it needs to stop film unloading. After unloading the film, the discharged materials were collected and weighed. The films were picked out from the mixture, then washed, dried, and weighed. Materials selected at random for 10 times while unloading were weighed separately. Then, weigh the net weight of the agricultural plastic film according to the above processing method, and calculate the film soil ratio by the following Equation (6):

$$\tau = Y/(Y_0 - Y) \tag{6}$$

where, τ is the film soil ratio; Y is the net weight of the agricultural plastic film, g; Y_0 is the weight of the film and the soil, g.

3.3 Test results and analysis

The test results are shown in Table 1, after processing the experimental data by data analysis software, Figures 9-11 were obtained. Analysis of Table 1, Figures 9-11 showed:

The average recovery rates of residual plastic film of 1MCS-100 collector and 1MCDS-100B collector were 83.87% and 85.72% respectively. The former was slightly lower than the latter, and the overall performance of two machines was of little difference. All of them met the standard requirements (topsoil recovery rate >80%). The average film soil ratios of 1MCS-100 type collector and 1MCDS-100B type collector were 0.14 and 0.50 respectively. The latter was about 3.6 times as much as the former, and its effect of membrane-soil separation was better.

Table 1 Test results

No.	1MCS-100 type residual plastic film collector		1MCDS-100B type residual plastic film collector	
	Recovery rate of residual film, %	Film soil ratio	Recovery rate of residual film, %	Film soil ratio
1	87.22	0.17	84.44	0.36
2	84.16	0.12	80.25	0.47
3	86.25	0.17	84.29	0.62
4	81.66	0.15	87.28	0.58
5	82.25	0.14	85.67	0.44
6	79.57	0.11	88.62	0.51
7	80.58	0.13	83.66	0.46
8	83.64	0.16	86.45	0.45
9	87.76	0.13	87.33	0.61
10	85.59	0.15	89.25	0.49
Average value	83.87	0.14	85.72	0.5
Standard deviation	2.83	0.02	2.67	0.08
Coefficient of variation, %	3.37	14.29	3.11	16

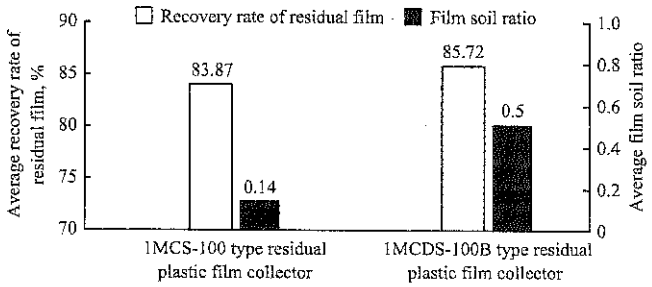

Figure 9 Comparison of average residue plastic film recovery rates and average film soil ratios between 1MCS-100 collector and 1MCDS-100B collector

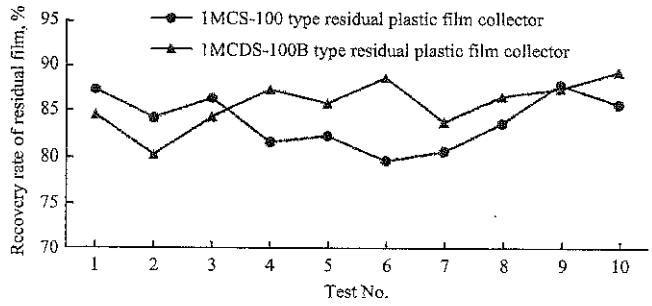

Figure 10 Comparison of residue plastic film recovery rates between 1MCS-100 collector and 1MCDS-100B collector

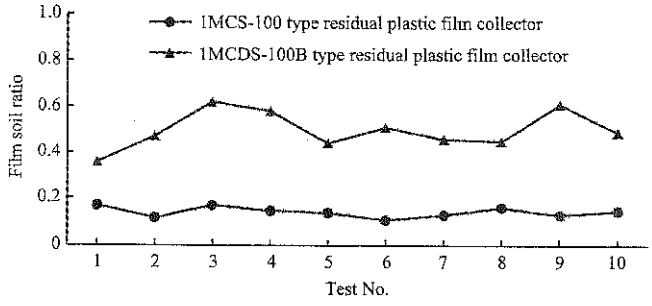

Figure 11 Comparison of film soil ratios between 1MCS-100 collector and 1MCDS-100B collector

The test showed when the two machines both met the requirements of recovery rate of residual film, the membrane-soil separation effect of 1MCDS-100B collector was better than that of 1MCS-100 collector. This proved that the optimized scheme was effective and feasible, and the application of membrane-soil separation technology has a remarkable influence on improving the membrane-soil separation effect of shovel-screen collectors.

4 Conclusions

1) The structure of 1MCS-100 collector was optimized by multi-stage membrane-soil separation device, and 1MCDS-100B collector has been obtained. The contrast test showed that the film soil ratio of the optimized machine was about 3.6 times as much as that of the non-optimized one, and the effect of optimization was remarkable.

2) The multi-stage membrane-soil separation device can heighten the membrane-soil separation effect of the shovel-type collector, which is conducive to the recovery and reuse of the residual plastic film and has a great significance on solving agricultural plastic film pollution.

Acknowledgements

This study was supported by the Special Program for Agro-scientific Research in the Public Interest "Technical Scheme for Comprehensive Treatment of Farmland Residual Film Pollution" (201503105), Innovation Engineering of the Chinese Academy of Agricultural Sciences—Harvest Machinery of Underground Fruits.

[References]

[1] Brooks, T. W. 1995. Apparatus for removing and baling plastic mulch. United States: NO. 5452652[P], 1995-09-26.

[2] Da, J. D. 2015. Studies on reasonable use & residue management by agricultural plastic film mulching- A case study at Yong Feng Town, Liangzhou, Wuwei, Gansu, China. *Lanzhou University*. (In Chinese)

[3] GB/T 25412-2010, Mulch film residue collector[S]. Beijing: *Standards Press of China*.

[4] Lv, Z. Q., L. Zhang, G. L. Zhang, and S. F. Liu. 2015. Design and test of chain guide rail-type plastic film collector. *Transactions of the Chinese Society of Agricultural*

Engineering, 31(18): 48–54. (In Chinese with English abstract)

[5] Manlio, C. 1978. Machine for tearing waste bags and separating out plastic film bag material. United States: NO. 4067506[P], 1978-01-10.

[6] Wang, X. F., X. J. Zhang, S. H. Ma, H. Zhang, W. Wang, and J. L. Liang. 2011. Finite element analysis of clod crushing rake tooth in field cleaning machine. *Transactions of the Chinese Society for Agricultural Machinery*, 42(04): 58–61. (In Chinese with English abstract)

[7] Wang, X. M. 2005. Research and design on separation and dithering transmission system of the polythene film collector. Beijing, *China Agricultural University*. (in Chinese)

[8] Yan, C. R., E. K. Liu, F. Shu, Q. Liu, S. Liu, and W. Q. He. 2014. Review of agricultural plastic mulching and its residual pollution and prevention measures in China. *Journal of Agricultural Resources and Environment*, 31(2): 95–102. (In Chinese)

[9] Yan, C. R., W. Q. He, N. C. Turner, E. K. Liu, Q. Liu, and S. Liu. 2014. Plastic-film mulch in Chinese agriculture: Importance and problems. *World Agriculture*, 4(2): 32–36.

[10] Yan, W., Z. C. Hu, N. Wu, H. B. Xu, Z. Y. You, and X. X. Zhou. 2017. Parameter optimization and experiment for plastic film transport mechanism of shovel screen type plastic film residue collector. *Transactions of the Chinese Society of Agricultural Engineering*, 33(1): 17–24. (In Chinese with English abstract)

[11] Yan, W., Z. C. Hu, X. X. Zhou, H. B. Xu, Z.Y. You, and N. Wu. 2016. Present situation of research and expectation on picking-up mechanism of plastic film collectors. *Journal of Agricultural Mechanization Research*, (10): 258–268. (In Chinese)

[12] You, Z. Y., F. W. Gu, F. Wu, Z. C. Hu, Y. L. Zhang, and L. B. Tu. 2016. Research on ridged peanut residue plastic film recycling technology. *Journal of Agricultural Mechanization Research*, (1): 207–211. (In Chinese)

[13] Zhang, B. F. 2015. Design and study of film recycling machine in Autumn. *Xinjiang Agricultural University*. (In Chinese)

[14] Zhang, J., W. Z. Yang, X. Y. Xie, D. H. Mu, and J. Zhang. 2013. Design and experimental research on separating used plastic film from soil and transporting used plastic film mechanism. *Agricultural Science & Technology and Equipment*, (02): 29–30, 33. (In Chinese with English abstract)

[15] Zou, Z. W., and G. X. Chu. 2010. ZD-type linear thickness of sieve surface segmentation and increase inclination of surface. *Coal Mine Machinery*, 31(08): 125–126. (In Chinese)

Development and evaluation of a pulling-type mechanical weeder for paddy fields

Prathuang Usaborisut*, Watcharachan Sukcharoenvipharat, Pawin Thanpattranon

(Department of Agricultural Engineering, Faculty of Engineering at Kamphaengsaen, Kasetsart University, Kamphaengsaen Campus, Nakhonpathom, Thailand)

Abstract: Weeding is one of the most difficult tasks in rice production. To avoid adverse effects from chemical methods, mechanical weeders have been introduced. To improve worker comfort, a pulling-type mechanical weeder was developed and studied to acquire information for optimal application and also for the design of a tractor-drawn mechanical weeder. The prototype of pulling-type weeder weighed 18.6 kg. Three tests were conducted to study the effects on weeder performance of the number of weeding passes, the equipment's weight and their combination. The weeder needed 136 N draft to pull on the first pass and even more for successive passes. The speed of movement reduced on successive passes. Weeding efficiency increased with an increasing number of passes up to 89.2% after four repetitive passes. On the other hand, weeding efficiency could be increased by adding more weight to the weeder. With a total weight of 30.6 kg, the weeder worked with an efficiency of 88.3%. The combination of four repetitive passes and a weight of 30.6 kg resulted in the highest weeding efficiency of 95.8%. However, weeding with 30.6 kg weight for two passes was not significantly different from four passes.

Keywords: mechanical weeder, pulling-type, paddy field, weeding efficiency

Citation: Prathuang, U., W. Sukcharoenvipharat, and P. Thanpattranon. 2017. Development and evaluation of a pulling-type mechanical weeder for paddy fields. International Agricultural Engineering Journal, 26(4): 33–37.

1 Introduction

Rice is one of the important food crops for the world. Thailand has the sixth-largest amount of land under rice cultivation and is ranked as the second-largest exporter globally (Cai, 2015). Weeding is one of the critical stages in rice cultivation and affects the yield and quality of rice. Weeds decrease crop yields from 15% to 50% depending on the species, density and weeding time through competition with the main crop for light, water and nutrition (Hasanuzzaman et al., 2009). Weeding is labor intensive requiring between 10 to 15 persons per hectare in paddy fields, depending on the weed density and species. Haq and Islam (1985) reported that weeding amounted to 21.6% of rice production costs in Bangladesh. The shortage of labor resulting from migration from rural to urban areas has made it difficult to meet peak demands for paddy production (Abubakar et al., 2011). However, this could be aided by introducing a mechanical weeder. In addition to labor reduction, the use of a mechanical weeder should be accelerated due to the concerns over environmental degradation and the growing demand for non-chemical weed control that ensures food safety.

Many researchers have developed mechanical weeders. The Cono-weeder, a mechanized weeding (manual) method, is capable of weeding about 0.18 ha/day. Parida (2002) modified the IRRI conical weeder and evaluated its performance in paddy fields and reported that under experimental conditions, the field capacity and field efficiency of the weeder were 0.2 ha/h and 80%, respectively. Other relevant studies showed that the application of a weeder would increase the field capacity and decrease the time and cost of the weeding operation (Gite and Yadav, 1990; Kumar et al., 2000). Manuwa et al. (2009) designed and developed a power weeder with a working width of 0.24 m for weeding in

Received date: 2017-07-24 **Accepted date:** 2017-11-03

* **Corresponding author: Prathuang Usaborisut,** Department of Agricultural Engineering, Faculty of Engineering at Kamphaengsaen, Kasetsart University, Thailand. Email: fengptu@ku.ac.th, Tel: +6634351896, Fax: +6634351896.

row-crop planting. The effective field capacity, fuel consumption and field efficiency of the machine were 0.53 ha/h, 0.7 L/h and 95%, respectively. Fazlolallh et al. (2001) conducted the research to compare two mechanical weeders in rice: mechanical weeder with engine power and mechanical weeder without engine power. They reported that both provided effective and economical weed control resulting in good yield. Victor and Verma (2003) designed and developed a power operated rotary weeder for wet land paddy by using a 0.5 hp petrol driven engine with a reduction gear box. They concluded that with 200 mm spacing, the field capacity varied between 0.04-0.06 ha/h and weeding efficiency was 90.5%. Reviews of these reports showed that all mechanical weeders are of the pushing types which are tough work and quickly make the workers exhausted. Operational difficulties and a slow weeding rate may lead to major drawbacks with this kind of weeder, particularly in large-scale cultivation.

Therefore, the main objective of the current study was to develop a pulling-type mechanical weeder and to study the factors affecting its performance and efficiency in weeding in order to serve as the basic information for designing a tractor-drawn mechanical weeder.

2 Materials and methods

A pulling-type mechanical weeder was developed. The main components were similar to those on a conventional mechanical weeder except for the handle attachment and the weight container. The handle of a conventional weeder is attached to the frame on the rear portion. On the other hand, the developed weeder had a fixed joint between the handle rod end and the front part of the frame. A weight container was added to provide vertical load adjustment. The developed weeder itself weighed 18.6 kg. Figure 1 shows the main components of the developed mechanical weeder and Figure 2 shows a rotor with its toothed configuration.

Field experiments were conducted in paddy fields to evaluate the new weeder. The pulling angle was set as low as possible in order to avoid any lifting force acting on the weeder. Figure 3 shows a person pulling the weeder at an angle of the handle of about 20° which was the least angle still comfortable for the worker. The parameters assessed were the draft requirement, equipment weight and the number of passes by the weeder. Draft force was measured by a portable electronic scale (Angyu) with capacity of 50 kg and resolution of 10 g. A square loop (0.25 m^2) was randomly thrown to locate the experimental plots and the number of weeds included in the loop was counted before and after weeding. The weeding efficiency or weeding index was calculated using the following formula (Remesan et. al., 2007):

$$Weeding\ Efficiency = \frac{W_1 - W_2}{W_1} \quad (1)$$

where, W_1 - Number of weeds before weeding; W_2 - Number of weeds after weeding.

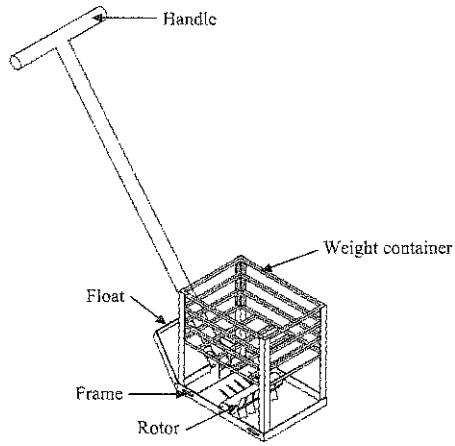

Figure1 Pulling-type mechanical weeder

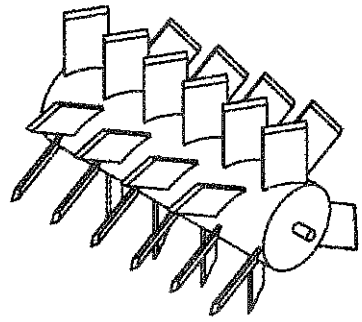

Figure 2 Rotor with fixed teeth

Figure 3 Pulling-type mechanical weeder during testing in paddy field

3 Results

3.1 Weeding with different numbers of passes

Under its own weight of 18.6 kg, the developed weeder was pulled in the paddy field for different numbers of passes over the same area. Four test plots were used that were different in terms of weed size and number. The average numbers of weeds were 10.5, 18.5, 36.5 and 166.0 for plot 1 to plot 4, respectively (Table 1). The average lengths of the weeds in the plots were 34.8, 23.5, 15.8 and 5.3 cm, respectively. Plot characteristics affected the speed and draft of the weeder but not its weeding efficiency. The average speed for all plots was 0.43 m s^{-1} and was the lowest on plot 1 and the highest on plot 2 with a relative difference of 63.64%. The average draft for all plots was 156.8 N. Plot 4 required the least draft of 111.2 N for weeding, with the highest draft in plot 3 of 1.84 times higher.

Table 1 Weeding data of different plots for the test of different numbers of passes

Plot No.	No. of weeds	Speed, m/s	Draft, N	Efficiency, %
1	10.5a	0.33a	134.4b	73.0a
2	18.5a	0.54c	176.5c	65.3a
3	36.5a	0.40b	205.1d	74.8a
4	166.0b	0.43b	111.2a	70.8a

Note: Figures in the same column with the same letter are not significantly different using Duncan's multiple range test (p<0.05).

Pulling the weeder in the paddy field for different numbers of passes affected the working performance (Table 2). The average speeds for one pass and two passes were significantly higher than those for three and four passes, and the highest difference was 36.36%. For all passes, the average speed was 0.38 m/s. The average draft for all passes was 165.1 N, with one pass need the lowest draft of 136.0 N. The average draft increased with the number of passes. The average draft for four repetitive passes was 34.04%, higher than that for one pass. The average weeding efficiency was 71.73%. The highest was 89.2% after four repetitive passes.

3.2 Weeding with different weeder weights

By adding dead weight, it was possible to determine the effect of changes in the weeder weight of 18.6, 26.6 and 30.6 kg. The average numbers of weeds in three tested plots were 18.4, 19.5 and 129.1, respectively (Table 3). The average lengths of the weeds in the three plots were 22.6, 28.3 and 5.1 cm, respectively. Plot characteristics also affected the weeder's speed and draft but not its weeding efficiency. The average speed for all plots was 0.38 m s^{-1} and was the lowest for plot 1. The average draft for all plots was 184.5 N, with plot 3 having the least draft of 169.0 N required for weeding, while the greatest draft found in plot 2, which was 17.04% higher.

Table 2 Performance for different numbers of passes by the weeder

No. of passes	Speed, m s^{-1}	Draft, N	Efficiency, %
1	0.41b	136.0a	59.0a
2	0.45b	164.3b	62.7ab
3	0.34a	177.8bc	76.0bc
4	0.33a	182.3c	89.2c

Note: Figures in the same column with the same letter are not significantly different using Duncan's multiple range test (p<0.05).

Table 3 Weeding data of different plots for different weight tests

Plot No.	No. of weeds	Speed, m/s	Draft, N	Efficiency, %
1	18.4a	0.30a	186.6b	71.8a
2	19.5a	0.42b	197.8c	69.8a
3	129.1b	0.42b	169.0a	76.9a

Note: Figures in the same column with the same letter are not significantly different using Duncan's multiple range test (p<0.05).

The weight of the weeder affected its weeding performance. The speed decreased with increased weeder weight. In contrast, the draft requirement increased with increased weeder weight. The average draft for all weights was 182.8 N. The 30.6 kg weeder needed 63.46%, more draft than the 18.6 kg weeder. The weeding efficiency also increased when the weight increased. The average weeding efficiency was 73.23%, while the maximum efficiency was 88.3% of the 30.6 kg weeder.

Table 4 Performance of different weights weeders

Weight, kg	Speed, m/s	Draft, N	Efficiency, %
18.6	0.44c	136.0a	59.0a
26.6	0.37b	190.0b	72.4b
30.6	0.31a	222.3c	88.3c

Note: Figures in the same column with the same letter are not significantly different using Duncan's multiple range test (p<0.05).

3.3 Weeding under a combination of weeder weights and number of passes

Twelve treatments of weeding were generated by the combination of four passes and three different weights of the equipment. Table 5 shows the treatments and working efficiency arranged in increasing order of working

efficiency values. There were different efficiencies under different combinations. The minimum efficiency occurred with the combination of one pass and the lightest weight (W1P1) while the maximum efficiency was for the combination of four passes and the heaviest weight (W3P4) with an increment of 88.95%.

Table 5 Working efficiency of different weeding treatments

Treatment	Efficiency, %
W1P1	50.7a
W1P2	53.5ab
W2P1	59.9abc
W2P2	66.5bcd
W1P3	72.5cde
W2P3	74.7de
W3P1	81.0e
W3P2	83.6ef
W1P4	84.0ef
W3P3	84.0ef
W2P4	86.1ef
W3P4	95.8f

Note: Figures in the same column with the same letter are not significantly different using Duncan's multiple range test (p<0.05).

W and P stand for equipment weight and number of passes, respectively, and their values increase by the number after each of the letters.

The pulling-type weeder developed in the study seemed to work efficiently under certain situations and had similar performance statistics under different weed situations in the different study plots. One pass of the weeder seemed to destroy less weeds and a greater number of repetitive passes was needed to obtain a higher weeding efficiency. However, the weeder speed reduced with the higher numbers of passes due to the soil being more difficult to walk on in the successive passes. In addition, the average draft increased since the soil may have increased in resistance to the weeder with each successive pass. On the other hand, using the weeder for one pass could produce a higher working efficiency by increasing the weight of the weeder. With a total weight of 30.6 kg, one pass of the weeder seemed to show good weeding efficiency as four passes of the weeder with no weight added. From the tests involving a combination between the number of passes and the equipment weight, there were no significant differences with a total weight of 30.6 kg with either two, three or four repetitive passes and these options should be suitable to use a pulling-type weeder that can obtain a working efficiency higher than 80%.

The average speeds in the tests were in the range of 0.31-0.45 m/s and were considerably higher than the speeds of the TNAU pushing-type Cono-weeder. According to the test results presented by Shakya etal. (2016), the TNAU Cono-weeder developed by Tamil Nadu Agricultural University had a speed of 0.278-0.286 m s^{-1}. It is easier walking in front of the pull-type weeder as the operator is on firmer soil compared to using a pushing-type weeder and this advantage may result in a higher working speed. This effect was confirmed by the fact in the current study that the speed reduced with higher numbers of repetitive passes. Another factor may result from the applied force characteristics. An operator has to apply both horizontal and vertical forces with a pushing-type weeder. The horizontal force moves the weeder forward while the vertical force pushes the weeder's teeth into the weeds in the soil. On the other hand, an operator only has to apply horizontal force when operating the pulling-type weeder. Shakya et al. (2016) reported that the weeding efficiency was 77.41% with the TNAU Cono-weeder. Mohammad (2011) also reported a similar weeding efficiency of 73.2% with a conical weeder while hand weeding resulted in a weeding efficiency of 96.7%. Weeding by the developed pulling-type weeder with one pass had a low weeding efficiency of 59.0%. It needed three repetitive passes or increasing the weight to 26.6 kg to achieve efficiency comparable with earlier research reports. The average drafts for pulling the developed weeder were in the range of 136.0-182.3 N which were lower than the 285.7 N pushing force of the TNAU Cono-weeder reported by Shakya etal. (2016). The TNAU Cono-weeder weighed about 6 kg while the developed pulling-type weeder weighed 18.6 kg. In addition to the horizontal force, an operator of a pushing-type weeder can apply vertical force to push the weeds into the soil. This vertical force also affects the horizontal force. On the other hand, the vertical force for a pulling-type weeder is equal to the weight of the weeder and the operator cannot apply more vertical force to the weeder.

3.4 Design parameters applied to development of a tractor-drawn mechanical weeder

The test result could be applied as basic information for the design of a tractor-drawn mechanical weeder. The parameters taken into consideration should include the weight of weeder and number of passes. From the test result, the best weeding efficiency derived from the weeder weight of 30.6 kg and passage numbers of two or more. Therefore, the weeding unit should provide vertical load more than 300.2 N (30.6×9.81) and compose of twin rotors in tandem. Since rice transplanter is 6-rows working width, the developing weeder should have seven weeding units. The test results recommended that the weeder might need draft force of more than 1556.1 N (7×222.3). Summarily, the developing weeder should have total weight of about 220 kg with seven weeding units. It can also be attached to a small tractor.

4 Conclusion

The developed pulling-type weeder weighed 18.6 kg. It needed 136 N draft for the first pass and more for successive passes. The weeder speed was reduced with successive passes. With its own weight, the weeding efficiency was quite low at 59.0% for one pass and this increased with an increasing number of repetitive passes up to the highest efficiency of 89.2% with four repetitive passes. On the other hand, high weeding efficiency with one weeder pass could be achieved by adding more weight to the weeder. With an increased total weight of 30.6 kg, the weeder could work as efficiently with fewer passes than it did with four repetitive passes and no weight added. The combination test indicated that working with the 30.6 kg weeder for two repetitive passes could achieve a weeding efficiency not significantly different from working with four repetitive passes.

Acknowledgments

The authors gratefully acknowledge the Agricultural Research Development Agency (ARDA) and the National Research Council of Thailand for the financial support under the research project entitled "Research and development of rice weeder attached to narrow steel wheel tractor".

[References]

[1] Abubakar, M. S., D. Ahmad, O. Jamarei, S. Samsuddin and M. Norhisam. 2011. Evaluation of a dual-purpose chemical applicator for paddy fields. *American Journal of Applied Sciences*, 8(4): 1–4. DOI: 10.3844/ajassp.2011.362.367

[2] CAI. 2015. Agricultural Statistics of Thailand, Crop Year 2015. Centre for Agricultural Information, Office of Agricultural Economics, Ministry of Agriculture and Cooperatives, Bangkok, Thailand, pp: 215.http://www.oae.go.th/download/download_journal/2558/yearbook57.pdf (Accessed on October 18, 2016)

[3] Fazlollah, E. C., H. Bahrami, and A. Asakereh. 2001. Evaluation of traditional, mechanical and chemical weed control methods in rice fields. *Australian Journal of Crop Science*, 5(8): 1007–1013.

[4] Gite, L. P., and B. G. Yadav. 1990. Optimum handle height for a push pull type manually operated dry land weeder. *Ergonomics*, 33(33): 1487–1494.

[5] Haq, K. A., M. D. Islam. 1985. Performance of indigenous hand weeders in Bangladesh. *Agricultural Mechanization in Asia, Africa and Latin America*, 16(4): 47–50.

[6] Hasanuzzaman, M., M. Fujita, M. N. Islam, K. U. Ahamed, and K. Nahar, 2009. Performance of four irrigated rice varieties under different levels of salinity stress. *International Journal of Integrative Biology*, 6(2): 85–90.

[7] Kumar, V. J. F., C. D. Durairaj, and V. M. Salokhe. 2000. Ergonomic evaluation of hand weeder operation using simulated actuary motion. *International Agricultural Engineering Journal*, 9(1): 29–39.

[8] Manuwa, S. I., O. O. Odubanjo, B. O. Malumi, and S. G. Olofinkua. 2009. Development and performance evaluation of a row-crop mechanical weeder. *Journal of Engineering & Applied Sciences*, 4(4): 236–239.

[9] Mohammad, R. A. 2011. Field performance evaluation of mechanical weeders in the paddy field. *Scientific Research and Essays*, 6(25): 5427–5434.

[10] Parida, B. C. 2002. Development and evaluation of star-cum conoweeder for rice. *Agricultural Mechanization in Asia, Africa and Latin America*, 33(3): 21–22.

[11] Remesan, R., M. S. Roopesh, N. Remya, and P. S. Preman, 2007. Wet land paddy weeding- A comprehensive comparative study from South India. *Agricultural Engineering International: the CIGR Ejournal*. Manuscript PM 07 011. Vol. IX.

[12] Shakya, H. B., M. R. Parmar, M. T. Kumpava, and. R. Swarnkar. 2016. Development and performance evaluation of manually operated Cono-weeder for paddy crop. *International Refereed Journal of Engineering and Science* (IRJES), 5(7): 6–17.

[13] Victor, V. M., and A. Verma. 2003. Design and development of power operated rotary weeder for wetland paddy. *Agricultural Mechanization in Asia, Africa and Latin America*, 34(4): 27–29.

Comprehensive effect of different subsoilers on fuel consumption, soil condition and yield based on field experiments and linear weighted model

Liu Jun'an, Wang Xiaoyan*, Li Hongwen, He Jin, Wang Qingjie, Niu Qi, Hu Hongnan

(*College of Engineering, China Agricultural University, Beijing 100083, China*)

Abstract: Subsoiling tillage is widely applied in most areas of China because of its soil condition improvement and yield increasing effects. Researches have been conducted on reducing soil resistance and saving energy for subsoiling tillage. Some studies have also been done on soil condition and yield improvement effects of subsoiling treatments. It is necessary to conduct the research considering energy saving, yield increasing and soil condition improvement together to identify relatively better subsoilers for specific soil conditions in terms of reducing energy consumption in the mean time of increasing crop yield and improving soil conditions. A series of subsoilers with different tine shapes and structural parameters were evaluated by field tests in this paper. Commonly used chisel-shape subsoiler (CS), arrowhead-shape subsoiler (AS) and wing-shape subsoiler (WS) were tested, together with the treatment non-subsoiling (NS), in field for 3 years in annual spring maize planting area of Northeast China, where the soil type is brown loam soil. Soil bulk density, moisture content, cone index at 0-40 depth, maize root and yield characteristics were measured for tillage treatments with different subsoilers. In addition, a linear weighted math model was developed based on the indexes of fuel consumption, soil condition improvement and yield increase rate to analyze the comprehensive effect of different subsoilers. The results indicated that: subsoiler tine shape had significant impact on fuel consumption. The fuel consumption for CS was lower than that for AS and WS by 57.29% and 132.96% respectively. All the three subsoilers treatments significantly improved soil condition and maize yield, compared with NS, annual average yields of CS, AS and WS treatments were increased by 24.82%, 20.43% and 19.86%, respectively. While the effect on soil condition improvement of different subsoilers had no obvious difference. The evaluation on the comprehensive effects of the three subsoilers on fuel consumption, soil condition improvement and yield increase showed that CS subsoiler was the relative best subsoiler of the three types in this experimental condition for it was more energy saving than WS and AS subsoiler with similar effect level on soil condition and yield as WS and AS. This research provided some methods to evaluate comprehensive effects of subsoiling and further to select or optimize subsoiler types for specific soil condition.

Keywords: Subsoiler, linear weighted model, soil condition improvement, fuel consumption, energy saving, yield increase, comprehensive effect

Citation: Liu, J. A., X. Y. Wang, H. W. Li, J. He., Q. J. Wang, Q. Niu, and H. N. Hu. 2017. Comprehensive effect of different subsoilers on fuel consumption, soil condition and yield based on field experiments and linear weighted model. International Agricultural Engineering Journal, 26(4): 38–51.

1 Introduction

Subsoiling tillage is widely applied in most area of China because of its soil condition improvement and yield increasing effect (Williams et al. 2006; Jain et al., 2006). Subsoiling tillage has been being actively promoted by government in the form of tillage subsidy in arid and semi-arid regions of North China. As indicated in the available literature and research achievement, the research about subsoiling tillage is mainly in the following two aspects in China: One aspect is about energy saving and traction resistance reduction of

Received date: 2017-09-28 **Accepted date:** 2017-10-26

* **Corresponding author: Wang Xiaoyan**, Ph.D., Professor, Department of Agricultural Engineering, China Agricultural University, 100083, Beijing, China. Email: xywang@cau.edu.cn.

subsoiling. To reduce the traction resistance of subsoiling tillage, the shape and key parameters of subsoilers were designed and optimized based on simulation experiments (Mootaz et al., 2004; Mak et al., 2012), biological profile modeling (Li et al., 2016), mathematical modeling (Yu et al., 2007), vibration subsoiling (Li et al., 2012; Xirui et al., 2016) and regression experiment (Zhu et al. 2009; Abdul et al., 2002). Another aspect is about effect of subsoiling on yield increasing and soil condition improvement compared with tillage method such as rotary tillage, no-till seeding and etc. (Li et al., 2014; Hassan et al., 2007). Nowadays, the types of subsoilers are growing with the development of subsoiling research and application area of subsoiling technology. It appears to be necessary to conduct the research combining energy saving and yield increasing and soil condition improvement together.

He Jin et al. (2006) made a comparative study on the effect of subsoiling and conventional tillage on soil condition improvement and economic effect by continuous experiments in Shouyang and Linfen in Shanxi province and Daxing in Hebei province, respectively. Some studies have also been done on the relationship between the total energy input and total biomass output of different agricultural production practices (Demircan et al. 2006; Yalcin et al., 2006; Hamzei et al., 2016). A series experiments were conducted by Raper et al. (2007) to investigate the yield increasing and fuel consumption in different operation depths. The result showed the yield increase effect of site-specific subsoiling (25, 35, or 45 cm depths subsoiling) was statistically equivalent to that of uniform-depth (45 cm) subsoiling, while it was more energy efficient than uniform-depth subsoiling. However, the research focusing on the comprehensive effects of different types of subsoilers on fuel consumption, soil condition improvement and yield was relatively few.

Chisel-shape subsoiler (CS), arrowhead-shape subsoiler (AS) and wing-shape subsoiler (WS) were the most common subsoilers in Northeastern China (Wang et al., 2011). Research conducted in spring maize producing region in Liaoning province proved that soil disturbance and traction resistance were significantly affected by the change of subsoiler tine shapes (Liu et al., 2017). It was easier for CS to break soil hardpan for its narrower tine shape, WS may cause wider trench cross-sectional area and needed higher fuel consumption for its wider tine shape (Liu et al., 2017). In spring maize producing area in Northeastern China, where the climate is windy and dry in spring, rainy season concentrated from June to September, subsoiling followed by rotary tillage before seeding is the commonly used tillage practice. If the subsoiler tine shape was too narrow, the soil might not be effectively subsoiled and the effects of subsoiling on improving soil conditions, promoting crop growth and increasing yield might not be achieved. WS subsoiler could obtain more soil disturbance but it may not bring significant differences on the further yield increase, while WS subsoiler would cause higher fuel consumption comparing with CS subsoiler for its wider tine shape. Excessive soil disturbance might have negative effect on soil moisture-holding capacity in windy and dry season.

Therefore, to determine the comprehensive effects of different types of subsoilers, the commonly used CS subsoiler, AS subsoiler and WS subsoiler were tested in this paper in brown loam soil condition in Northeastern China. What's more, to evaluate the comprehensive effects of those subsoilers, a linear weighted math model (Zhou, 2010; Elahi et al., 2014) was developed based on 6 indexes concerning fuel consumption, soil condition improvement and yield increasing effect of subsoiling. According to the 6 indexes, a comprehensive coefficient would be obtained for each type of subsoiler by the model to identify which subsoiler is the most suitable one for the specific soil conditions.

The purpose of this paper was to estimate the comprehensive effect of three subsoilers (CS, AS and WS) on fuel consumption, soil condition and yield attribute, to investigate whether the change of subsoiler tine shape has significant effect on yield increase and subsoiling effect, and then to optimize the tine shape of subsoiler in experimental area in Northeast China. This research could provide some methods to evaluate comprehensive effects of subsoiling and further to select or optimize subsoiler types for specific soil condition.

2 Materials and methods

2.1 Experimental treatments design

Three different types of subsoilers (CS, AS and WS) were chosen as subsoiling implements for three subsoiling treatments, respectively, and non-subsoiling was set as NS treatment, and every treatment was replicated three times, therefore with 4 treatments of 3 replications, 12 experimental plots in total were set up with size of each plot 2.4 × 40 m. According to Liu et al. (2017), the optimized structural parameters (Figure 1) of subsoiler were selected as shown in Table 1. Where, α was rake angle, β was wingspan angle for AS and WS, W was width of subsoilers. According to the local tillage practice and subsoiling operation requirements, the subsoiling depth was set as 40 cm with working velocity of 3 km h^{-1} during subsoiling operation. The subsoiling machinery type was 1S−200, and four straight shanks were installed on the subsoiling machinery.

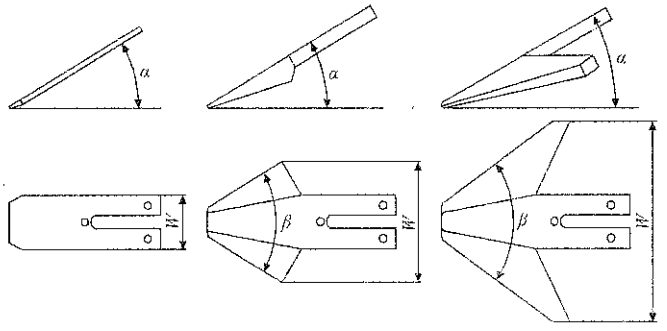

a. CS subsoiler b. AS subsoiler c. WS subsoiler

Figure 1 Structural diagram of three types of subsoilers

Table 1 Structural Parameters of Subsoiler tines

Subsoiler tine shape	Rake angle α, (°)	Wingspan angle β, (°)	Width W, mm
CS subsoiler	21	—	80
AS subsoiler	21	60	120
WS subsoiler	21	60	300

2.2 Site description

In April 2013, the field subsoiling experiment was conducted in Wufeng town of Zhangwu County (122°25'E, 42°15'N) in Liaoning province, China before maize seeding. The soil pH value was 7.9 and the soil type was brown loam soil. The annual average rainfalls from 2013 to 2015 were 788.1, 362.9 and 573.2 mm, respectively. The weather was quite dry from 2014 to 2015, and the rainfall always concentrated in June to September. Natural rainfall was the only moisture source for crop without irrigation. Before field subsoiling experiment, the maize straw cover rate on soil surface was below 10%, and soil bulk densities at 0-20 and 20-40 cm depths were 1.54 g cm^{-3} and 1.69 g cm^{-3}, respectively. Soil gravimetric moisture contents were 19.2% and 20.8%, respectively. Soil cone indexes at 0-10, 10-20, and 20-40 cm depths were 603, 1136 and 1250 kPa, respectively. The amount of fertilizer was same in each experimental plot.

2.3 Measurements indices and methods

The fuel consumption of subsoiling operation of three types of subsoilers was measured during subsoiling operation. According to local farming practices, field subsoiling experiment was followed by shallow rotary cultivation before maize seeding. The soil properties indices and maize growth and yield characteristics were tested during the key growing stage for three years from 2013 to 2015.

2.3.1 Fuel consumption

The measurement of fuel consumption was carried out by using the integrated field testing system (designed by China Agricultural University, Beijing, China) and suspension bracket (Qiaoet al., 2013) (Figure 2). The integrated testing system consisted of test platform (powered by M904 Lovol tractor), sensing system, and data acquisition system. The sensing system included fuel consumption measurement system (measuring fuel consumption), six-component test force device (measuring draft) and the other sensing equipment. The data acquisition system was used to collect and transmit experimental data to PC by wireless transmitting device. During the field experiment, the subsoiling suspension bracket was connected to the test platform by three-point linkage. The experimental subsoilers were mounted on traverse beam of the suspension bracket and could be adjusted up and down according to the subsoiling requirements.

Fuel consumption Q of each subsoiling treatment was measured by the sensing system (Qiao et al. 2013) which consisted of FZ-2100 continuous mass flowmeter and FM-2500 flow readout box. According to the Coriolis principle (O' Banion 2013), the fuel consumption was measured by the mass flowmeter. The fuel consumption

was different between the load test value q_1 and the no-load test value q_0. The measuring area for each set subsoiling experiment plot was 2.4×40 m, i.e. the last read data were (q_1-q_0)g/(2.4×40 m). Since the weight of 1 L diesel was 0.84 kg (GB/T19147-2003), the fuel consumption data could be converted to liters per hectare, based on Equation (1), the fuel consumption was presented by Equation (2).

$$\frac{g}{40\ \text{m}\times 2.4\ \text{m}}=\frac{10^3 g}{10^3\times 40\ \text{m}\times 2.4\ \text{m}}=\frac{1}{4\times 2.4}\cdot\frac{\text{kg}}{\text{hm}^2}=\frac{1}{9.6}\cdot\frac{\text{L}}{0.84}\cdot\frac{1}{\text{hm}^2}=\frac{1}{8.064}\cdot\frac{\text{L}}{\text{hm}^2} \quad (1)$$

$$Q=\frac{(q_1-q_0)\,g}{2.4\ \text{m}\times 40\ \text{m}}=\frac{(q_1-q_0)\text{L}}{8.064\ \text{hm}^2} \quad (2)$$

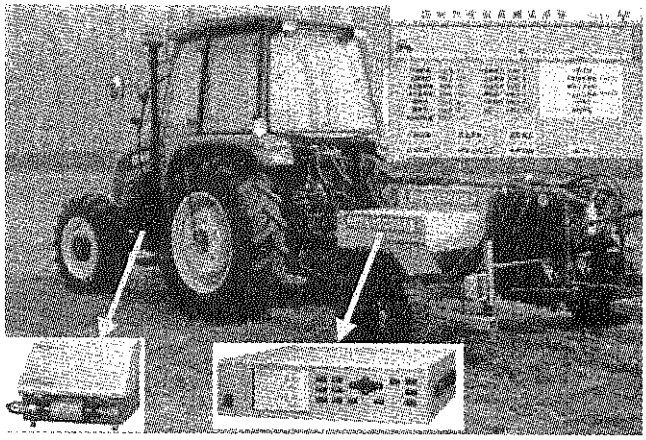

Figure 2 Field integrated test system

2.3.2 Soil condition improvement

To estimate the effect of these subsoilers on the change of soil condition, the indices like soil bulk density, soil volumetric moisture content and cone index were measured in each field plot.

(1) Soil bulk density and volumetric moisture content

According to GB/T50123-1999, the soil bulk density and volumetric moisture content in 0-10, 10-20, 20-30 and 30-40 cm soil layer in each plot was measured in three key growing stages (seeding stage, elongation stage and ripe stage) in 2013-2015, respectively. Since the ridge center was the most densely growing area of maize root, ridge center was chosen as main sampling location of soil cores. Based on bulk density data, the soil moisture was presented by Equation (3) (Yi Yanli 2003).

$$C=\frac{(m_1-m_2)}{\rho V_1}\times 100\% \quad (3)$$

where, C was the soil volumetric water moisture (%); m_1 and m_2 were the weights of wet and dry soil, respectively (g); V_1 and ρ were volumes of soil sampling ring (cm^3) and water density (g/cm^3), respectively.

(2) Soil cone index

Soil cone index was determined by soil compaction meter (Field Scout TM SC-900, Spectrum Technologies, Aurora, USA). The value of cone index was recorded at each 2.5 cm interval of soil depth. Both in subsoiling treatment plot and NS plot, cone index was measured in 0-45 cm soil layer. Due to soil compaction and rainfall penetration, the cone index at crop ripe stage was relatively higher than that at other growing stage (Zhang, 1993; Lin et al., 2009), thus the cone index was measured at ripe stage, and the measuring point was same to the acquisition point of soil sample, which was in between of each two maize plants on the ridges.

2.3.3 Maize root characteristics and yield

(1) Maize root characteristic

The maize root characteristic of each replicated treatment was checked at ripe stage by digging maize root sample. The digging space was a circular area with a radius of 30 cm to the depth of 50 cm and the root center was the center of the circle. In each plot, 3 roots, which were in the same ridge row and close to each other, were randomly chosen as samples. Root samples were cleaned carefully in water and ensured no break as much as possible. The length and dry root weight of each plot was recorded, respectively (Gong et al., 2009).

(2) Maize yield

In ripe stage, maize yield Y and hundred seed weight M were determined by manual harvesting, threshing and air-drying the grain to moisture content of 14% with maize ears taken from 10 m lengths of two rows selected randomly from each of the replicated treatment. Eight maize ears were chosen randomly in same ridge row as samples. The number of seed rows on maize ear A and number of seeds on seed row B were recorded, the yield was presented by Equation (4) (Mahapatra 2010).

$$Y=\frac{N\times A\times B\times M}{a\times b\times 2\times 100}\times 10000 \quad (4)$$

where, Y is maize yield, kg hm^{-2}; N is the number of effective ears in the sampling rows; M is the 100-seed weight, kg; A and B are the number of rows and kernels

long per ear, respectively; a and b are the length and width of each row (m), respectively.

2.4 Evaluation method for comprehensive effect of subsoiler

Linear weighted model is a comprehensive evaluation and analysis method for the evaluation of objectives with multiple different types or different order of magnitude indexes. This method is widely applied in agricultural engineering (Li et al., 2015) and other research fields (Zhou, 2010; Elahiet al., 2014). Based on the data of subsoiling field experiments, the comprehensive effect of CS, AS and WS subsoiler was analyzed and evaluated by using the linear weighted model. According to the analysis results, the influence of parameters of subsoiler tine shapes on the comprehensive effect was discussed and the relative optimum subsoiler shape was identified for the research region.

2.4.1 Evaluation indexes

The comprehensive effect of subsoilers was a comprehensive manifestation of the effect of various aspects of subsoiling operation. In this paper, the comprehensive effect of subsoiling mainly included three aspects: fuel consumption (Zambillo et al., 2010), soil condition improvement, crop growth and yield (Li et al., 2000; Raper et al., 2009). Fuel consumption index was cost-type indicator and the value was expected to be as lower as possible, and soil condition improvement and crop growth and yield effects indicators were effective indicators and the value was expected to be as higher as possible(Jin et al., 2015).

In order to quantitatively analyze the comprehensive effect of the different subsoilers, according to the analysis of the existing literatures (Li et al., 2000; Zhang et al., 2013), the 3-year average values of soil moisture content increase rate (compared with CK), soil bulk density reduction rate at 10-40 cm soil layer (compared with CK) and soil cone index reduction rate at 10-30 cm (compared with CK) were obtained as the evaluation indexes to indicate soil improvement effect. The 3-year average values of yield increase rate and root length increase rate of different subsoiling treatments (compared with CK) were tested as indicators for effect on yield and crop growth. Therefore, six indexes were determined and selected to form the indexing system: fuel consumption, bulk density reduction rate, soil moisture content increase rate, soil cone index reduction rate, root length increase rate and yield increase rate.

2.4.2 Standardization of indicators

1) Uniformization of indicator type

According to the classification criteria of producer expectation, fuel consumption was 'minimum' indicator (the lower the better), while the other five indicators were 'maximum' indicators (the higher the better). Each indicator type should be uniformed before performing the integrated weighting calculation. The reciprocal method was used to convert fuel consumption Q into 'maximum' indicator as shown in Formula (5). After uniformization, the indicators were recorded as x_{i1}, x_{i2}, x_{i3}, x_{i4}, x_{i5}, x_{i6}; i were 1, 2, 3, representing CS subsoiler, AS subsoiler and WS subsoiler, respectively.

$$x_{i1} = \frac{1}{Q_i} \tag{5}$$

2) Standardization of evaluation indicators

Since the unit of fuel consumption Q was different from the other five indicators, in order to avoid the impact of the difference of units of the indicators and the problem of "large number submerge small numbers", the 6 individual indicator needed to be nondimensionalized by the standard deviation method (Martinelli et al, 2012), then be used for comprehensive evaluation. As it was shown in Equations 6-8, the standardization of each indicator was based on average value of each subsoiling treatment, each index value was compared with the average value. If the standardized indicator was negative, it meant the original value was lower than the average level; otherwise, it was higher than the average level.

$$x'_{ij} = \frac{x_{ij} - \overline{x_j}}{S_j} \tag{6}$$

$$\overline{x_j} = \frac{1}{3}\sum_{i=1}^{3} x_{ij} \tag{7}$$

$$S_j = \left[\frac{1}{3}\sum_{i=1}^{3}\left(x_{ij} - \overline{x_j}\right)^2\right]^{1/2} \quad j=1,2,3,4,5,6 \tag{8}$$

where, x_{ij} was the original index value; x_{ij}' was the standardized index value; $\overline{x_j}$ was the average value of the j-th index of the three kinds of subsoilers, and S_j was

the standard deviation of the j-th index.

2.4.3 Weight of evaluation index

To ensure the evaluation results of comprehensive evaluation model could reflect the difference of each evaluation object and to eliminate the impact of difference of dimension of each indicator, the weight of each evaluation index was determined by the variation coefficient of each indicator (Elahi et al., 2014; Jian et al., 2015). The calculation method of weight was presented by Equations (9, 10).

$$\omega_j = C_j \Big/ \sum_{j=1}^{6} C_j \tag{9}$$

$$C_j = \frac{S_j}{x_j} \tag{10}$$

where, C_j was the coefficient of variation of the j-th index; and ω_j was the weight coefficient of the j-th index.

2.4.4 Construction of comprehensive evaluation model

Comprehensive effect evaluation model of subsoilers included 6 indicators in fuel consumption, soil condition improvement and effects of crop growth and yield increase, which belonged to multi factor evaluation system. Therefore, a multi factor linear weighted comprehensive evaluation model was adopted (Elahi et al., 2014; Zhao et al., 2016), LWM_i value Equation (11) was as follows:

$$\begin{aligned} LWM_i &= f(x_{ij}) = \sum_{j=1}^{6} \omega_j x_{ij}' \\ &= \omega_1 x_{i1}' + \omega_2 x_{i2}' + \omega_3 x_{i3}' + \omega_4 x_{i4}' + \omega_5 x_{i5}' + \omega_6 x_{i6}' \end{aligned} \tag{11}$$

where, LWM_i was the comprehensive effect coefficient of subsoilers i, by which the comprehensive effect of various type subsoilers was evaluated. Since individual indicators x_{ij}' was "maximum value", and weights (ω_j) were between 0 and 1, so LWM_i was also expected to be the higher the better. The higher the LWM_i value was, the better the comprehensive effect of the corresponding subsoiler would be. According to LWM_i value and positive and negative of individual standardized indexes, comprehensive effect of each subsoiler could be divided into the following level standard:

First level, $LWM_i > 0$ and standardized values of the 6 indicators were all positive, This meant that fuel consumption of the subsoiler was lower, yield increase and soil improvement indexes were higher, and comprehensive effect of the subsoiler was better than any other subsoilers in this evaluation system;

Second level, $LWM_i > 0$ and some of standardized values were negative. One or several effect indicators of subsoiler were lower than the average value, but comprehensive effect was higher than the average value;

Third level, $LWM_i = 0$. This result meant two possibilities: all effects indicators were equal to average value or effects indicators had both positive and negative values with positive values offset negative values, so LWM_i value was zero. It was indicated the comprehensive effect of the subsoiler were on the average level;

Fourth level, $LWM_i < 0$. All or some of the standardized values of the 6 indicators were negative. It meant several or all effects indicators were below the average level, and comprehensive effect were below the average level.

2.5 Data processing

To analyze the experimental data, Microsoft Office Excel and SPSS 19.0 statistical analysis software (SPSS Inc., Illinois, USA) were used in one-way ANOVA analysis and LSD method was used to perform the significance test (P=0.05).

3 Result and discussion

3.1 Fuel consumption

The fuel consumption value and variance analysis result of each subsoiler were presented in Figure 3 and Table 2. The fuel consumptions of CS, AS and WS subsoilers were 14.89, 23.42 and 34.69 L hm^{-2}, respectively. The fuel consumption of CS was found to be statistically lower than those of AS and WS by 57.29% and 132.96%, respectively, and the fuel consumption of AS was lower than that of WS subsoiler by 48.10% (P<0.05). This result indicated that the change of tine shape had a very significant impact on fuel consumption. The tillage traction resistance was one important determining factor of fuel consumption, higher traction resistance resulted in higher fuel consumption (Jin et al., 2006).

The effects of CS, AS and WS subsoiler on soil disturbance and traction resistance had been investigated at the same experimental field, where the soil condition

was the same to this paper (Jin et al., 2006). The trench cross-sectional area of three subsoilers were shown in Figure 4. The T_{CA} (trench cross-sectional area) for WS was significantly greater than that for CS and AS by 49.8% and 30.0%, respectively, and T_{CA} for AS was greater than that for CS by 15.3% (P<0.05). The widths of CS, AS and WS subsoilers were 80, 120, and 300 mm, respectively, the soil disturbance and fuel consumption were increasing when the subsoiler tine was wider.

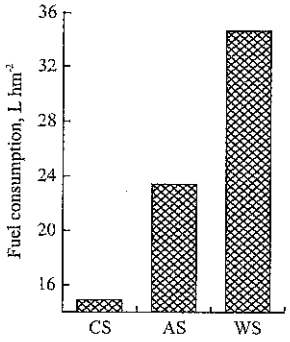

Figure 3 Fuel consumption of different subsoilers

Table 2 Variance analysis of fuel consumption

Sources	Sum of squares	Degree of freedom	Mean square	F value	P-value	F crit
Inter-group	7596.169	2	3798.085	163.2893	5.87E-06	5.143253
Inner group	139.5591	6	23.25984			
Total	7735.728	8				

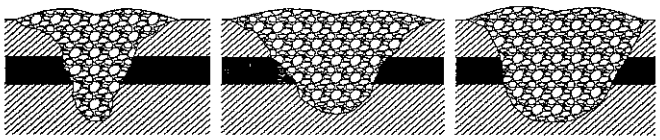

a. CS trench shape b. AS trench shape c. WS trench shape

Note: The black color area in each Figure represent non-subsoiling soil hard pan, diagonal line area in each figure represent non-subsoiling area.

Figure 4 Subsoiling trench shape of different subsoiling tines

Qi et al. (2015) analyzed the effect of tine shape on traction resistance. The result showed that the connect area between subsoiler and soil was different with the varied tine shape, which resulted in the differences of shear force and normal force, the traction resistance increased with the increase of the area of shovel tine. Meanwhile, wider tine shape of subsoiler would have a greater range of disturbance on soil, which would request higher power consumption.

3.2 Soil condition

3.2.1 Soil bulk density

The bulk density in 0-10 cm soil layer and mean bulk density in 10-40 cm soil layer were presented in Table 3. It indicated that, in 2013-2015, the soil bulk density in 0-10 cm soil layer of each treatment was 1.23-1.49 g/cm^3, and no significant difference was found among the four treatments. The main reason might be the rotary cultivation operation conducted before seeding in each treatment plot. However, in seeding stage in 2013, in 10-40 cm soil layer, compared to NS treatment, the soil bulk densities of CS, AS, and WS subsoiling treatment deceased by 9.74%, 9.74% and 10.38%, respectively.

The mean values of decreasing rate of bulk density compared with NS in 10-40 cm soil layer were presented in Figure 5. As it could be seen from Figure 5, in the three years (2013-2015), mean values of reduction rate of bulk density of three subsoiling treatments (CS, AS, WS)compared with NS were 6.19%, 6.53%, and 7.68%, respectively.

Table 3 Soil bulk density of 0-40 cm layers in key growing stages of spring maize under different treatment

g·cm^{-3}

Soil layer, cm	Treatment	2013			2014			2015		
		Seeding stage	Elongation stage	Ripe stage	Seeding stage	Elongation stage	Ripe stage	Seeding stage	Elongation stage	Ripe stage
0-10	NS	1.39^a	1.44^a	1.42^a	1.33^a	1.41^a	1.36^a	1.29^a	1.43^a	1.36^a
	CS	1.23^a	1.41^a	1.36^a	1.21^a	1.37^a	1.34^a	1.24^a	1.38^a	1.46^a
	AS	1.29^a	1.40^a	1.41^a	1.30^a	1.48^a	1.32^a	1.38^a	1.49^a	1.38^a
	WS	1.38^a	1.38^a	1.34^a	1.38^a	1.37^a	1.36^a	1.22^a	1.39^a	1.41^a
10-40	CK	1.54^a	1.64^a	1.67^a	1.55^a	1.67^a	1.67^a	1.59^a	1.66^a	1.68^a
	CS	1.39^b	1.54^b	1.57^b	1.49^b	1.57^b	1.56^b	1.49^b	1.57^b	1.60^b
	AS	1.39^b	1.53^b	1.58^b	1.48^b	1.52^b	1.57^b	1.49^b	1.55^b	1.60^b
	WS	1.38^b	1.51^b	1.54^b	1.45^b	1.54^b	1.55^b	1.50^b	1.52^b	1.56^b

Note: Same superscript letter in same vertical line means no significant difference between treatments for every soil layer (P=0.05). Data comparison was just within the same soil layer.

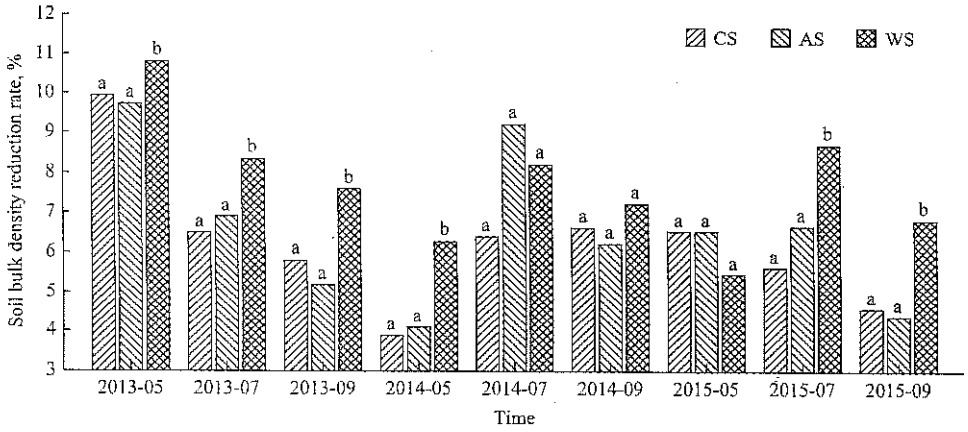

Note: 2013-5, 2013-7, 2013-9 on X-axis mean crop growth stages of seeding, elongation and ripe, respectively. The same in 2014 and 2015.

Figure 5 Reduction rates of soil bulk density in 10-40 cm soil layer in maize growing stage

3.2.2 Soil cone index

As shown in Figure 6, the curve of cone index of each treatment was taken to quantify soil strength. Soil cone index value of every treatment in 2013-2015 varied with depths, increasing from surface to the depth around 15-25 cm then decreasing as depth increases. At 15-25 cm depth, the curve of NS treatment exhibited the maximum values of cone index, mainly resulting from soil compaction in previous years, and the maximum value was up to more than 4000 kPa. Down to the depth of 30 cm, the gap of cone index values between subsoiling treatment and NS treatment were rapidly closing. The decrease rates of soil cone indexes of CS, AS and WS treatment, comparing with NS treatment, were shown in Figure 7. The mean values of cone indexes of CS, AS and WS treatment were statistically lower than that of NS treatment by 41.25%, 39.87% and 32.87%, respectively (P<0.05).

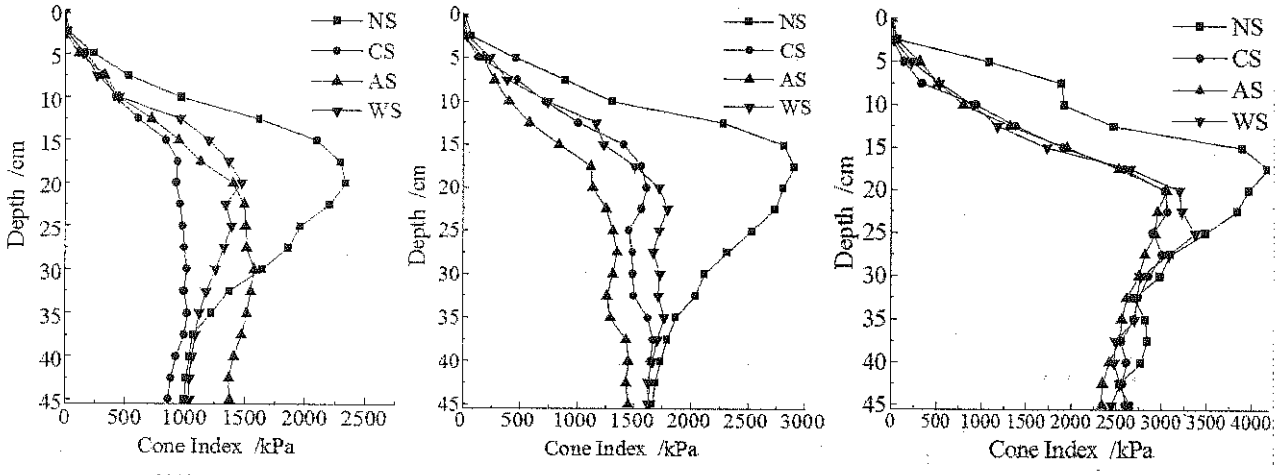

Figure 6 Soil cone indexes of 0-45 cm layers in ripe stage of spring maize under different treatments

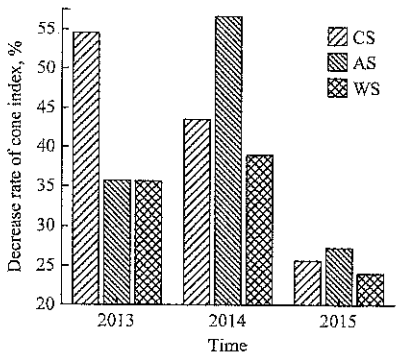

Figure 7 Decreasing rates of soil cone indexes of different subsoiling treatments in 10-30 cm depth

3.2.3 Soil volumetric moisture content

Table 4 showed the soil volumetric moisture content in 0-10 cm soil layer and the mean value of soil moisture content in 10-40 cm soil layer, which was used to evaluate the ability of soil moisture storage of different subsoiling treatments. The increasing rate of volumetric moisture content at the depth of 10-40 cm was shown in Figure 8. The data showed that in 10-40 cm soil layer, the volume moisture contents of subsoiling treatments were higher than that of NS by 0.48%-4.53% in the whole

growing season in 2013 and in the elongation stage in 2014 (Figure 8). From the ripe stage in 2014 to the ripe stage of 2015, the moisture content of subsoiling treatments was higher than that of NS by 2.46%-16.44%. The annual mean values of increase percentage of the moisture content of CS, AS and WS were 6.08%, 6.07% and 7.15% in 2013-2015, compared with NS, respectively.

Table 4 Volumetric soil water moisture in key growing stages of spring maize under different treatments %

Soil layer /cm	Treatment	2013			2014			2015			Average value of every stage		
		Seeding stage	Elongation stage	Ripe stage	Seeding stage	Elongation stage	Ripe stage	Seeding stage	Elongation stage	Ripe stage	Seeding stage	Elongation stage	Ripe stage
0-10	NS	28.89^a	28.82^a	28.64^a	27.04^a	28.93^a	24.74^a	26.19^a	24.66^a	16.10^a	27.37	27.47	23.16
	CS	29.98^a	29.02^a	26.73^a	28.53^a	29.09^a	24.14^a	26.31^a	25.49^a	16.14^a	28.27	27.87	22.34
	AS	29.23^a	29.55^a	28.34^a	28.07^a	29.15^a	24.83^a	27.21^a	25.21^a	14.62^a	28.17	27.97	22.60
	WS	29.95^a	29.72^a	29.34^a	28.17^a	29.84^a	23.37^a	27.81^a	25.41^a	15.99^a	28.64	28.32	22.90
10-40	NS	29.27^a	30.31^a	29.96^a	29.37^a	29.81^a	23.03^a	28.47^a	25.76^a	15.52^a	29.04	28.63	22.84
	CS	30.60^a	30.82^a	30.10^a	30.17^a	30.93^b	26.81^b	29.17^b	27.85^b	17.77^b	29.98	29.87	24.89
	AS	30.56^a	31.10^a	30.51^a	30.08^a	31.49^b	25.60^b	29.91^b	27.58^b	17.75^b	30.18	30.06	24.62
	WS	30.46^a	31.31^a	30.75^a	30.40^a	31.12^b	26.51^b	30.64^b	27.72^b	18.01^b	30.50	30.05	25.09

Note: Same superscript letter in same vertical line means no significant difference between treatments for every soil layer (P=0.05). Data comparison was just within the same soil layer.

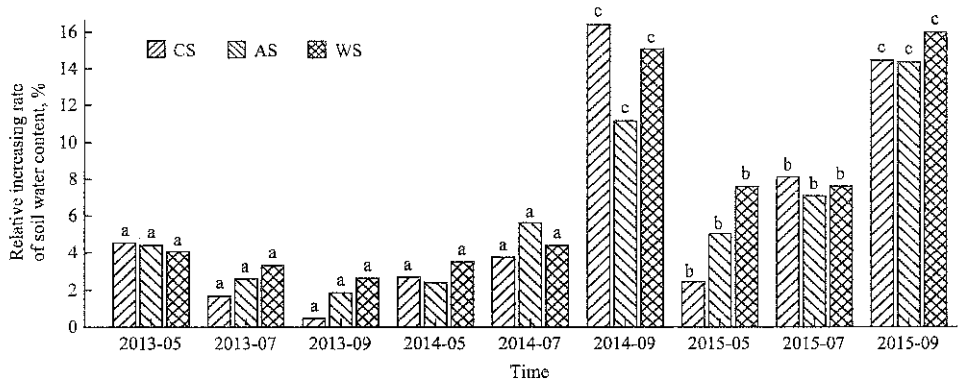

Note: 2013-5, 2013-7, 2013-9 on X-axis mean crop growth stages of seeding, elongation and ripe, respectively. The same in 2014 and 2015.

Figure 8 Increasing rates, compared with NS, of soil moisture content of 10-40 cm soil layer in key growing stages

3.3 Maize root growth and yield

3.3.1 Maize root characteristic

Maize root characteristics of different treatments in the ripe period of 2013-2015 were shown in Table 5 and Figure 9. Significant differences in the root length and root dry weight were found between subsoiling and NS treatment. The root length for subsoiling treatments statistically increased by 8.90%-54.45% compared to those of NS treatment, and the root dry weight of subsoiling treatments was heavier than that of NS treatment by 5.5%-14.7% (P<0.05). An important reason was that the soil condition improved by subsoiling was more conducive to root growth compared to NS treatment. The increase of root length and dry weight indicated that subsoiling could effectively promote root growth by improving soil condition and providing relatively enough moisture and air for maize growth (Mullins et al., 1994; Zhang et al., 2015). According to Table 5, the annual mean values of root length increase rates for CS, AS and WS treatment compared with NS were 17.05%, 16.59% and 26.83%, respectively.

Table 5 Root characteristics under different treatments

Year	Treatment	Root length, cm	Root length increase rate,%	Stem Diameter, mm	Dry root Weight, g	Dry root weight increase rate, %
2013	NS	30.7^a		21^a	34.21^a	
	CS	38.5^b	25.41%^{B}	22^a	37.73^b	4.20%^{A}
	AS	36.3^b	18.24%^{A}	22^a	36.79^b	1.60%^{A}
	WS	38.2^b	24.43%^{B}	23^a	37.95^b	4.81%^{A}
2014	NS	29.2^a		21^a	35.35^a	
	CS	31.8^b	8.90%^{A}	24^a	39.17^b	4.87%^{A}
	AS	33.4^b	14.38%^{B}	23^a	37.28^b	1.15%^{A}
	WS	40.1^c	37.33%^{C}	22^a	38.45^b	2.95%^{A}
2015	NS	31.5^a		19^a	34.77^a	
	CS	36.8^b	16.83%^{A}	22^a	39.89^b	8.49%^{A}
	AS	36.9^b	17.14%^{A}	21^a	38.76^b	5.41%^{A}
	WS	37.4^b	18.73%^{B}	23^a	37.41^b	1.74%^{A}

Note: Same superscript letter in same vertical line means no significant difference between treatments (P<0.05). Data comparison was just within the same year.

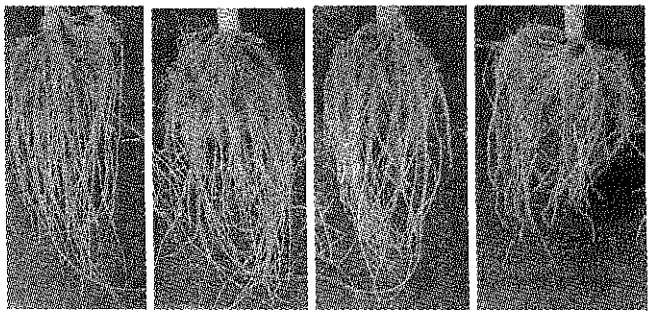

a. CS root b. AS root c.WS root d. NS root

Figure 9 Spring maize root under different treatments in 2014

3.3.2 Maize yield

Maize yield and the characteristics of maize ear in different treatments were shown in Table 6. According to Table 6 and variance analysis, from 2013 to 2015, the average yields of CS, AS and WS treatments were higher than that of NS by 24.82%, 20.43%, and 19.86% (P=0.012533), respectively. It was seen the hundred seeds weight of CS, AS and WS treatment increased by 6.8%, 7.4% and 6.5%, respectively (P<0.05). The increase in the hundred seeds weight was the direct reason for the increase of yield. It has been found that a good soil condition and adequate moisture were important factors for the increase in hundred seeds weight (Li et al., 2013; Tan et al., 2011). This result proved that subsoiling could significantly increase the yield of maize (Li et al., 2000; Jin et al., 2007).

Table 6 Maize ear characteristics and yield of different treatments

Year	Treatment	Number of maize ear in each row	Ear row, line	Seed number per row	Hundred seed weight, g	Yield, kg·hm^{-2}	Average yield kg·hm^{-2}
2013	NS	31^a	16.0^a	34.7^a	30.32^a	10127.1^a	
	CS	32^a	15.5^a	35.1^a	32.06^b	11632.7^b	
	AS	31^a	16.5^a	33.4^a	32.16^b	11451.4^b	
	WS	30^a	16.0^a	33.5^a	32.93^b	11037.6^b	
2014	NS	31^a	17.1^a	29.8^a	29.77^a	9021.6^a	
	CS	31^a	17.5^a	30.4^a	32.72^b	11246.8^b	
	AS	32^a	17.3^a	29.3^a	31.41^b	10619.9^b	
	WS	32^a	17.4^a	30.1^a	31.47^b	10992.4^b	
2015	NS	29^a	18.5^a	27.4^a	29.21^a	8058.2^a	9069.0
	CS	32^a	18.0^a	29.7^a	31.49^b	10872.1^b	11250.5
	AS	31^a	18.7^a	29.6^a	30.42^b	10516.0^b	10862.4
	WS	32^a	18.6^a	28.6^a	31.39^b	10373.5^b	10801.2

Note: Same superscript letter in same vertical line means no significant difference between treatments (P=0.05). Data comparison was just between different treatments in same year.

3.4 Comprehensive effect of different subsoilers

Based on the experimental data above, a linear weighted model with 6 indexes was applied to evaluate the comprehensive effects of subsoilers in terms of soil condition, yield and fuel consumption. The original indexes values of every evaluation object (CS, AS and WS subsoiler) were exhibited in Table 7. According to Equations (5)-(11), the standardized indexes value and the corresponding weight value were calculated and presented in Table 8. The values of comprehensive effect coefficients (LWM) of CS, AS and WS were shown in Figure 10 and the LWM values of CS, AS and WS subsoilers were 0.329, –0.308 and –0.021.

Table 7 Original index value of each evaluation object

Subsoiler type	fuel consume, L/hm^2	Soil Bulk density reduction rate, %	Soil Water content increase rate, %	Soil Cone index decrease rate, %	Root length increase rate, %	Yield increase rate, %
CS	14.9	6.19	6.08	41.25	17.05	24.82
AS	23.4	6.53	6.07	39.87	16.59	20.43
WS	34.7	7.68	7.15	32.87	26.83	19.86

Table 8 Standard value and weight of every evaluation object (subsoiler)

No.	x'_{i1}	x'_{i2}	x'_{i3}	x'_{i4}	x'_{i5}	x'_{i6}
Weight	0.361	0.099	0.083	0.099	0.083	0.108
CS	1.078	–0.781	–0.569	0.724	–0.569	1.148
AS	–0.180	–0.346	–0.585	0.417	–0.585	–0.469
WS	–0.898	1.127	1.155	–1.141	1.155	–0.679

On the basis of comprehensive effect coefficient judgment level standard that constructed in 2.4.4 section, it could be seen from Table 8 and Figure 10 that the LWM_i value of CS was the largest, the comprehensive effect of CS treatment belonged to the second level. This meant comprehensive effect level of CS was higher than the average level of the three types of subsoilers, while soil bulk density reduction rate and the increase rate of water content and root length of CS were lower than those of other two subsoilers. The LWM_i value of WS was close to zero level, which meant the comprehensive effect of WS was close to the average level. The LWM_i value of AS belonged to fourth level, this indicated the comprehensive effect of AS was below the average level and as shown in Table 8, except soil cone index, all the effect indexes of AS were below the average level.

According to the six-individual index and LWM_i value analysis, the results indicated that the comprehensive effect of CS was relatively higher than the other two subsoilers, for its yield increase rate was the highest while

the fuel consumption was the lowest. Though the root length increase rate of WS treatment was highest and the ability of improving maize yield of WS was statistically equivalent to CS subsoiler, the maximum traction resistance of WS resulted in maximum fuel consumption, which leading to the reduction of the comprehensive effect for WS treatment.

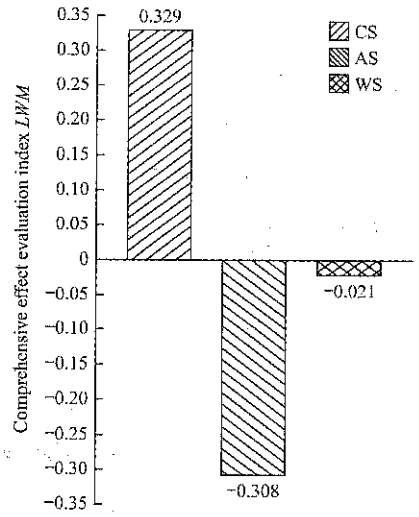

Figure 10 Comprehensive effect evaluation index of every subsoiler

Existing research (Liu et al., 2017; Qi et al., 2015) showed that WS subsoiler produced widest range of disturbance at the depth of 20-40 cm, compared to AS and CS subsoilers. Therefore, WS subsoiler was suitable for inter-row and overall subsoiling, if just to acquire the effect on soil condition improvement without considering about the rest indexes. However, if taking the comprehensive effects, consisting of fuel consumption, soil condition improvement and yield increasing into consideration, the most desired comprehensive effect for subsoiling operation was to obtain relatively highest yield and soil improvement effect with relatively lowest fuel consumption. Analysis results in this paper indicated that the advantage of WS subsoiler in soil condition improvement and crop growth promotion could only last until the next year of subsoiling. What's more, the fuel consumption of WS was significantly higher than that of AS and CS, and its yield increasing effect was just statistically equivalent to that of CS subsoiler. The fuel consumption of AS was also higher than that of CS subsoiler, though its effect on soil condition improvement and yield increase was equivalent to CS subsoiler.

The negative effect of soil compaction on crop growth could often be alleviated by subsoiling. However, the subsoiling operation was often conducted at unnecessarily soil depths or width, wasted energy and excessively disturbed surface soil (Raper et al., 2006). Raper et al. (2007) found that site-specific subsoiling in 25-45 cm depth had same level of yield increasing effect compared to the traditional deep uniform subsoiling to 45 cm, while its fuel consumption was significantly lower than that of uniform deep subsoiling conducted at 45 cm depth. The reduction of fuel consumption for site-specific subsoiling was because its total soil disturbance was less than that of uniform deep subsoiling, which, therefore, led to the reduction of traction resistance. Similarly, in this paper, the lowest fuel consumption of CS subsoiling was mainly due to its minimum soil disturbance. Ibrahim Akinci et al.(2004) also found two-pass subsoiling had more significant effect on the improvement of soil condition, while its effect on yield increase was equivalent to one-pass subsoiling and statistically insignificant.

Summarily, according to the above analysis, it was indicated that, fuel consumption was significantly affected by the change of subsoiler tine shape, and the difference of subsoilers on soil condition improvement could last to the next one or two years after subsoiling operation, but the change of tine shape had little effect on the yield increase. Taking the comprehensive effect on fuel consumption, soil condition improvement and yield increase into consideration, CS subsoiler was proved to be the relatively best subsoiler type compared to WS and AS subsoilers for the experimental region of this paper.

4 Conclusion

(1) The effect of subsoiler tine shape on fuel consumption was evaluated in experimental field at 40 cm depth and 3 km h^{-1} speed. Result indicated the change of subsoiler tine shape had significant impact on fuel consumption. Fuel consumption increased with wider tine, and the fuel consumption of CS was 57.29% and 132.96% (P<0.05), lower than that of AS and WS, respectively.

(2) From the field test in 2013-2015 and exist research, it was found that subsoiling significantly

improved soil condition in terms of soil bulk density, soil moisture and cone index at 10-40 depth. Compared to NS treatment, soil bulk density statistically decreased by 4.97%-16.1% (P<0.05) after subsoiling. Cone index was statistically lower than that of NS treatment by 32.87%-41.25% (P<0.05) at 10-30 cm depth. Soil moisture content, especially when it was dry (2014 and 2015), was statistically improved by 2.46% –16.44% through subsoiling.

(3) Based on the analysis of the effects on fuel consumption, soil condition improvement and yield increase, the comprehensive effect of three subsoilers was evaluated by linear weighted math model. The LWM_i values of CS, AS and WS were 0.329, –0.308 and 0.021, respectively. CS subsoiler was proved to be the relative best subsoiler type in this experimental soil condition for it was more energy saving and had statistically similar soil condition improvement and yield increase effect as WS and AS subsoiler.

Acknowledgement

This work was supported by the Program for Innovative Research Team in Ministry of Education of China (Grant No. IRT13039) and National Natural Science Foundation of China (Grants No. 51205398). We thank all the members working at the Conservation Tillage Research Center (CTRC), Ministry of Agriculture, China Agricultural University for proving their inputs to this work.

[References]

[1] Abo-Elnor, M., R. Hamilton, and J. T. Boyle. 2004. Simulation of soil-blade interaction for sandy soil using advanced 3D finite element analysis. *Soil and Tillage Research*, 75(1): 61–73.

[2] Akinci, I., E. Cakir, M.Topakci, M. Canakci, and O. Inan. 2004. The effect of subsoiling on soil resistance and cotton yield. *Soil & Tillage Research*, 77(2): 203–210.

[3] Antonio, Z. P. M., S. V. C. Eduardo, B. J. Antonio, R. T. Spagnolo, and M. M. D. Barros. 2010. Effects of work operation depth of shanks in a seeder-fertilizer on slip, traction force and fuel consumption of a tractor. *Ciência E Agrotecnologia*, 34(5): 1320–1326.

[4] Demircan, V., K. Ekinci, H. M. Keener, D. Akbolat, and C. Ekinci. 2006. Energy and economic analysis of sweet cherry production in Turkey: A case study from Isparta province. *Energy Conversion & Management*, 47(13): 1761–1769.

[5] Elahi, Y., and M. I. A. Aziz. 2014. Mean-Variance-CvaR model of multiportfolio optimization via linear weighted sum method. *Mathematical Problems in Engineering*, 2014(10): 1–7.

[6] Gong, X. J., C. R. Qian, Y. Yu. 2009. Effects of subsoiling and no-tillage on soil physical characters and corn yield. *Journal of Maize Sciences*, 17(5): 134–137.

[7] Hamzei, J., and M. Seyyedi. 2016. Energy use and input-output costs for sunflower production in sole and intercropping with soybean under different tillage systems. *Soil & Tillage Research*, 157: 73–82.

[8] Hassan, F. U., M. Ahmad, N. Ahmad, and M. K. Abbasi. 2007. Effects of subsoil compaction on yield and yield attributes of wheat in the sub-humid region of Pakistan. *Soil & Tillage Research*, 96(1-2): 361–366.

[9] He, J., H. W. Li, and H. W. Gao. 2006. Subsoiling effect and economic benefit under conservation tillage mode in Northern China. *Transactions of the Chinese Society of Agricultural Engineering*, 22(10): 62–67.

[10] He, J., H. W. Li, X. Y. Wang, A.D. McHugh, W. Y. Li, H. W. Gao, and N. J. Kuhn. 2007. The adoption of annual subsoiling as conservation tillage in dryland maize and wheat cultivation in northern China. *Soil & Tillage Research*, 94 (2): 493–502.

[11] Jain, K. K., V. R. Vagadia, L. P. Singh, and A. H. Memon. 2006. Subsoiling-a strategy to combat water scarcity and enhanced productivity of groundnut crop. *AMA, Agricultural Mechanization in Asia, Africa and Latin America*, 37(3): 68–78.

[12] Jin, T., and B. Z. Moayad. 2006. Effects of rake angle of chisel plough on soil cutting factors and power requirements: a computer simulation. *Soil & Tillage Research*, 88(1-2): 55–64.

[13] Jin, Y., Z. H. Lu, F. F. Tan, M. Zhang, and H. Y. Zhang. 2015. Assessment of ecological carrying capacity on the typical resources-based cities: a case study of Tangshan City. *Acta Ecologica Sinica*, 35(14): 4852–4859

[14] Li, H., H. C. Pang, T. Z. Ren, Y. B. Li, R. Wang, S. W. Niu, and J. W. An. 2013. Effects of deep rotary-subsoiling tillage method on brown physical properties and maize growth in Northeast of China. *Scientia Agricultura Sinica*, 46(3): 647–656.

[15] Li, B., Y. Chen, and J. Chen. 2016. Modeling of soil–claw interaction using the discrete element method (DEM). *Soil & Tillage Research*, 158(1): 177–185.

[16] Li, H. W., J. D. Chen, and W. Y. Li. 2000. Study on

subsoiling technique for conservation tillage field. *Transactions of the Chinese Society of Agricultural Machinery*, 31(6): 42–45.

[17] Li, X., J. F. Fu, D. X. Zhang, T. Cui, and R. Zhang. 2012. Experiment analysis on traction resistance of vibration subsoiler. *Transactions of the Chinese Society of Agricultural Engineering*, 28(1): 32–36.

[18] Li, X., M. J. Tang, D. X. Zhang, W. Wang, and T. Cui. 2014. Effects of sub-soiling on soil physical quality and corn yield. *Transactions of the Chinese Society of Agricultural Engineering*, 30(23): 65–69.

[19] Lin, J. H., Y. R. Sun, Q. M. Zeng, and P. S. Lammers. 2009. Experimental comparison of various models related soil water content and bulk density to cone index—II. Components effect of water content and depth. *Journal of Basic Science & Engineering*, 17(1): 62–68.

[20] Liu, J. A., X. Y. Wang, H. W. Li, J. He, Q. J. Wang, and W. Y. Li. 2017. Optimization of structural parameters of subsoiler based on soil disturbance and traction resistance. *Transactions of the Chinese Society for Agricultural Machinery*, 48(2): 60–67.

[21] Mahapatra, A. K., D. L. Harris, D. L. Durham, S. Lucas, T. H. Terrill, B. Kouakou, and G. Kannan. 2010. Effects of moisture change on the physical and thermal properties of sericea lespedeza pellets. *International Agricultural Engineering Journal*, 19(3): 23–29.

[22] Mak, J., Y. Chen, M. A. Sadek. 2012. Determining parameters of a discrete element model for soil–tool interaction. *Soil & Tillage Research*, 118 (5): 117–122.

[23] Martinelli, E., Q. H. Nguyen, and M. Hjiaj. 2012. Dimensionless formulation and comparative study of analytical models for composite beams in partial interaction. *Journal of Constructional Steel Research*, 75(10): 21–31.

[24] Mouazen, A. M, and H Ramon. 2002. A numerical-statistical hybrid modelling scheme for evaluation of draught requirements of a subsoiler cutting a sandy loam soil, as affected by moisture content, bulk density and depth. *Soil & Tillage Research*, 63(3-4): 155–165.

[25] Mullins, G. L., D. W. Reeves, C. H. Burmester, and H. H. Bryant. 1994. In-row subsoiling and potassium placement effects on root growth and potassium content of cotton. Agronomy Journal, 86 (1): 136–139.

[26] O' Banion, T. 2013. The Direct approach to mass flow measurement. *Chemical Engineering Process*, 109(3): 41–46.

[27] Raper, R. L., and E. B. Schwab. 2009. Development of an in-row subsoiler attachment to reduce smearing. *Applied Engineering in Agriculture*, 7(4): 495–503.

[28] Raper, R. L., D. W. Reeves, J. N. Shaw, E. V. Santen, and P. L. Mask.. 2007. Benefits of site-specific subsoiling for cotton production in Coastal Plain soils, *Soil & Tillage Research*, 96(1-2): 174–181.

[29] Raper, R. L., and J. S. Bergtold. 2006. Using in-row subsoiling and cover crops to increase use of conservation agriculture in the Southern U.S. *ASABE Annual International Meeting*, Paper Number: 061039.

[30] Qi, G. Y., L. Liu, Y. Z. Zhao, Z. P. Gong, Y. Q. Yang, Y. Yang. 2015. Effects of subsoiler's penetrating depth and spade shape on traction resistance. *Journal of Agricultural Mechanization Research*, 11(1): 161–165.

[31] Qiao, X. D., X. Y. Wang, H. Yan, H. W. Li, J. He, and Q. Wang. 2013. Field experiment platform for rear suspension. *Transactions of the Chinese Society for Agricultural Machinery*, 44(8): 63–68.

[32] Qiao, X. D., X. Y. Wang, H. Yan, H. W. Li, J. M. Wu, and X. Sun. 2013. Field test system of rear suspension tools based on virtual instrument. *Transactions of the Chinese Society for Agricultural Machinery*, 44(10): 98–103.

[33] Tan, W. W., Y. Wang, Y. X. Li, C. Liu, Z. Z. Liu, B. Peng, D. Wang, Y. Zhang, B. C. Sun, Y. S. Shi, Y. C. Song, D. G. Yang, T. Y. Wang, and Y. Li.. 2011. QTL mapping of ear traits of maize under different water regimes. *Acta Agronomica Sinica*, 37(2): 235–248.

[34] Wang, W., and L. C. Qiu. 2011. Effect analysis of three kind of subsoiler carry on the deep tillage. *Journal of Agricultural Mechanization Research*, 33(1): 179–182.

[35] Williams, J. D., S. B. Wuest, W. F. Schillinger, and H. T. Gollany. 2006. Rotary subsoiling newly planted winter wheat fields to improve infiltration in frozen soil. *Soil & Tillage Research*, 86 (2): 141–151.

[36] Wu, J., Y. Zhang, and L. G. Hou. 2015. Landscape ecological quality change of Anhui Province in 2000-2010. *Journal of Nanjing Forestry University (Natural Science Edition)*, (2): 84–90.

[37] Yalcin, H., and C. Engin. 2006. Tillage effects and energy efficiencies of subsoiling and direct seeding in light soil on yield of second crop corn for silage in Western Turkey. *Soil & Tillage Research*, 90(1-2): 250–255.

[38] Yi, Y. L. 2009. Soil physics research methods. *Beijing: Publishing House of Peking University.*

[39] Yu, Y. C., W. Y. Liu, Y. F. Zhao, and J. Sun. 2007. Force mathematical model and examination analysis of the column subsoiler. *Transactions of the Chinese Society of Agricultural Engineering*, 23(6): 109–113.

[40] Zhang, X. C., H. W. Li, J. He, Q. J. Wang, Z. Q. Zheng, and P. Jing. 2013. Effects of different tillage managements on characteristics of soil and crop in annual double cropping areas in Northern China. *Transactions of the Chinese Society for Agricultural Machinery*, 44(z1): 77–82, 71.

[41] Zhang, X. R., C. Wang, Z. H. Chen, and Z. W. Zeng. 2016. Design and experiment of a bionic vibratory subsoiler for banana fields in southern China. *Int J Agric & Biol Eng*, 9(6): 75.

[42] Zhang, R. F. H. S. Yang, J. L. Gao, Y. Zhang, Z. J. Wang, and X. Fan. 2015. Effect of subsoiling on root morphological and physiological characteristics of spring maize. T*ransactions of the Chinese Society of Agricultural Engineering*, 31(5): 78–84.

[43] Zhang, L. B. 1993. Test on effect of soil moisture and density on soil cone indexes. *Transactions of the Chinese Society of Agricultural Engineering*, 9(2): 41–44.

[44] Zhao, D. L., M. Du, J. Y. Yang, P. Li, S. He, and D. Zhu. 2016. Simulation and forecast study of land use change based on CA-Markov model. *Transactions of the Chinese Society for Agricultural Machinery*, 47(3): 278–285.

[45] Zhou, T. Y. 2010. Weighting method for a linear mixed model. *Communications in Statistics - Theory and Methods*, 39(2): 214–227.

[46] Zhu, R. X., J. C. Zhang, S. P. Xue, W.S. Yao, and J. Y. Li. 2009. Experimentation about subsoiling technique for conservation tillage. *Transactions of the Chinese Society of Agricultural Engineering*, 25(6): 145–147.

Mechanism analysis and performance experiment of rotating and burying weeding device for paddy field

Wang Jinwu[1*], Tang Han[1], Jiang Dongxuan[1], Tao Guixiang[2], Zhao Jiale[3]

(1. *College of Engineering, Northeast Agricultural University, Harbin* 150030, *China*;
2. *College of Engineering, Heilongjiang Bayi Agricultural University, Daqing* 163319, *China*;
3. *College of Biological and Agricultural Engineering, Jilin University, Changchun* 130025, *China*)

Abstract: The mechanical weeding technology is important in reducing the usage of herbicide and ensuring organic rice production in paddy field. It is an effective approach to replace chemical and manual weeding. The main objective of this research was to solve the problem of mechanical weeding device for paddy field injuring rice seedlings and to study the changing regulation of force which can remove weeds without injuring rice seedlings. The main structure and working principle of a rotating and burying weeding device for paddy field were stated in detail. The burying mechanism of weeding device was analyzed and the comprehensive dynamic model about that machinery and weeds affected mutually was developed. Refer to actual environmental characteristics of paddy field, a real-time test measurement system was designed and built using sensor testing technology for studying rice seedlings injured force. On this basis, single factor tests were conducted to analyze the influences of these factors on rice seedlings injured rate and rice seedlings injured force. The machine forward velocity, cutter-disc rotational speed and distance from soil surface to spring-tooth end were selected as the experimental factors. And then the corresponding regression equations were obtained by analysis. The results showed that, under the condition that the machine forward velocity was 0.14-0.56 m/s, cutter-disc rotational speed was 95-135 r/min and distance from soil surface to spring-tooth end was 6-36 mm, the cutter-disc rotational speed had a significant influence on two experimental indexes. The rice seedlings injured force had a linear increasing trend with the increase of three experimental factors. And the rice seedlings injured rate decreased with the increase of machine forward velocity while increased with the increase of another two factors. This paper could provide an important theoretical basis for improvement and optimization of mechanical weeding device.

Keywords: paddy field, mechanical weeding, burying mechanism, rice seedlings injured force, measurement system, experiment

Citation: Wang, J. W., H. Tang, D. X. Jiang, G. X. Tao, and J. L. Zhao. 2017. Mechanism analysis and performance experiment of rotating and burying weeding device for paddy field. International Agricultural Engineering Journal, 26(4): 52–64.

1 Introduction

Mechanical weeding in paddy field is the advanced technology that kills weeds by burying, cutting or uprooting during suitable growth period of rice seedlings (Ma et al., 2011; Zhang et al., 2015). It can loosen soil around seedling roots, improve the physical properties of soil and reduce environmental pollution compared to the chemical weeding and manual weeding. According to its working status, it can be divided into inter-row weeding and intra-row weeding (Gobora et al., 2013). The intra-row weeding system in paddy field relates to paddy soil, plants, operating machinery and other units which interact with each other and change dynamically. And the plants have characteristics of slim stems, entangling roots, irregular geometric shapes. All of these can result in low operation efficiency and high injure in weeding process. The field applications on the previous weeding equipment showed that inter-row weeding rate can reach 70%, but intra-row weeding rate is very low (less than 60%) and rice injured rate is high (higher than 10%) in Northeast

Received date: 2017-09-16 **Accepted date:** 2017-11-04
* **Corresponding author: Wang Jinwu**, PhD, Professor, Engineering College, Northeast Agricultural University, Harbin, Heilongjiang 150030, China. Tel: +86-451-55191188, Email: jinwuw@163.com.

China (Tao G X et al., 2015; Yang S M et al., 2014). Intra-row weeding is the way of controlling mechanical parts to kill weeds without injuring rice seedlings according to the different depths of root between rice seedlings and weeds. In recent years, many scholars around the world have conducted researches on intra-row mechanical weeding technology (Ishii et al., 2006; Lamm et al., 2002; Zhang et al., 2012). And then the key parts were developed and optimized, such as duckfoot, rotary bladed harrow, powered rotary hoe, staggered comb and control arc, etc. (Zhang et al., 2017; Astrand et al., 2002; Slaughter et al., 2008). At present, the studies of weeding machines are mostly focused on its structure, but the studies of its weeding mechanism, influencing factors and mechanical properties are inadequate relatively.

The research on the mechanical properties of rice seedlings or weeds is an important foundation for the design of agricultural machinery. It also provides basic data for the improvement and optimization of key parts. Researchers have also reported their work on mechanical properties of rice seedlings. Ma et al. (2005) measured rice seedlings' fracture force and pulling force sprouted in plastic cell-trays using self-regulating measurement system. Wang et al. (2014) studied tensile strength of rice seedling and barnyard grass from trays during weeding period using universal testing machine. In the process of mechanical weeding, hardware parts of weeding device are directly contacted with rice seedlings or weeds. And mechanical injury of rice seedlings is one of key factors that restrict the development of weeding technology that requires attention during weeding. Therefore, this work aimed to seek the optimal force range for removing weeds without injuring rice seedlings.

In this case, this paper took a rotating and burying weeding device for paddy field as the research object, and its burying mechanism was analyzed. The comprehensive dynamic model about that machinery and weeds affected mutually was established. On this basis, a real-time test measurement system was designed and built using sensor testing technology for studying rice seedlings injured rate and rice seedlings injured force to estimate the effects of some factors on the experimental indexes, so as to provide an important theoretical basis for designing and controlling mechanical weeding device.

2 Agronomic characteristics and methods of weeding

2.1 Agronomic characteristics

Weeding environment in paddy field is a hybrid system which includes rice seedlings, weeds (barnyard grass as main type), soil and water, etc. The paddy field soil that consists of mud layer and soil layer is very complex. Depths of mud and soil layers are 30-50 and 160-180 mm, respectively. Sow spacing and row spacing of rice seedlings are 100-120 and 300 mm, respectively, as shown in Figure 1.

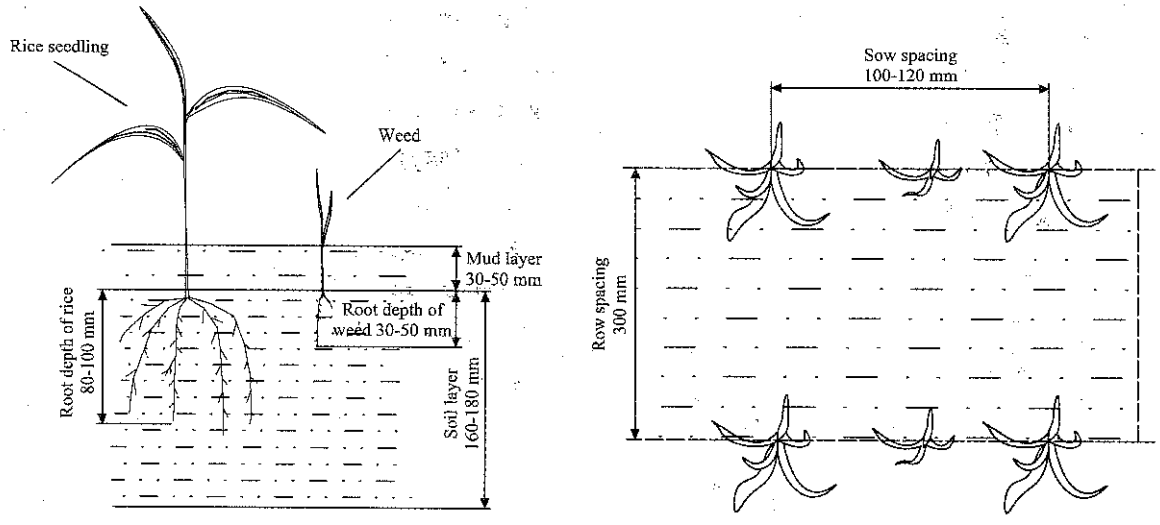

Figure 1 Weeding environmental system in paddy field

The temperature gradually increases from early June in Northeast China. Weeds grow quickly along with the growth of rice seedlings. The vertical root depths of rice seedlings and weeds are 80-100 and 30-50 mm in the

weeding period, respectively. As reported in previous literature and actual field operation, the optimum weeding time are the 7th day and 14th day after transplanting or sowing. (Liu et al., 2012; Dirk A G Kurstjens, 2007; Guo et al., 2016).

2.2 Mechanical methods

Based on the working principles of various mechanical weeding devices, there are three kinds of controlling methods, burying, uprooting, and cutting (Van Der Weide et al., 2008; Johnson III et al., 2012). Burying refers to putting soil layer upon weeds to restrict their photosynthesis. Uprooting is breaking the contact between soil and weed roots. Cutting involves physically shearing off part of weed plants. Burying typically occurs during seedbed preparation, cultivation or after crop emergence. Uprooting and cutting only occur during cultivation or after crop emergence. This paper mainly studied the burying mechanism of weeding device in paddy field, which established theoretical foundation for the ensuing chapters.

3 Structure and principle of weeding device

3.1 Main structure

As shown in Figure 2, the rotating and burying weeding device for paddy field mainly consists of cutter-disc and weeding spring-tooth (Wang et al., 2016). Some screw holes are designed on the cutter-disc with different installation diameters and angles (its diameter range is R_1=50-100 mm and angle range is σ=30-90°). A number of spring-tooth are bolted directly to the cutter-disc (its range is 4-12). The weeding spring-tooth is made of No.45 steel with high elasticity and toughness (its diameter is 5 mm). And the length of weeding spring-tooth is L = 300 mm according to actual requirements of penetrated depth. The end of spring-tooth is designed by using arc-shaped segment to improve the weeding performance. Respectively, the length l, wrap angle α and radius r of arc-shaped segment are 40 mm, 43° and 72 mm.

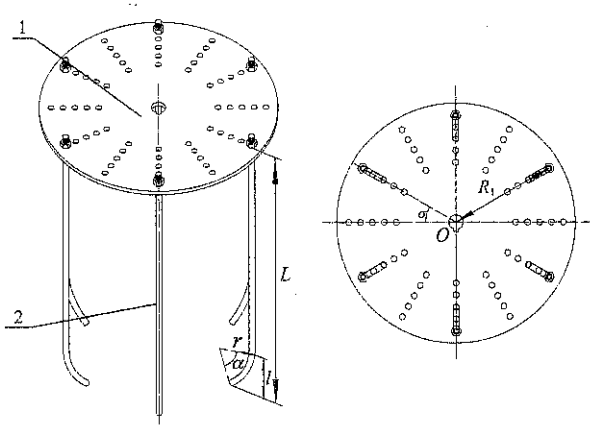

1. Cutter-disc 2. Weeding spring-tooth

Figure 2 Rotating and burying weeding device for paddy field

3.2 Working principle

According to the soft degree of paddy soil and other environmental characteristics in different fields, adjust the initial depth of the whole weeding spring-tooth system before weeding. In the weeding process, single spring-tooth contacts with crops directly in point to reduce the contact area with rice seedlings and increase the contact slip area with soil (Wang et al., 2017). By adjusting the numbers and installation angles of spring-tooth, it can adapt to various operating conditions. The whole weeding spring-tooth system mounted on the cutter-disc with the following compound motion: the circular motion of the cutter-disc, which is known as the relative motion (its relative rotational speed ω also known as the peripheral speed), the other is the convected motion in which the cutter-disc travels along with driving machine (its convected speed v). Each weeding spring-tooth would contact with crop row twice during one rotational period, which can effectively prevent unilateral lodging after weeding. The effective working part of spring-tooth is the arc-shaped segment in soil. The operation areas and trajectories of two endpoints could be obtained by analyzing, as shown in Figure 3.

In order to analyze the influences of different factors on operation areas and trajectories, the ratio λ of the relative cutter-disc rotational speed to the convected machine forward velocity was given (Wang et al., 2016; Wang et al., 2017). By adjusting the ratio λ, it can increase the area of weeding operation and improve the burying performance to meet agronomic requirements of weeding. When the ratio λ is less than 1, the horizontal velocity of spring-tooth is greater than zero, that is, the direction of horizontal velocity is consistent with that of driving machine, and the trajectory of spring-tooth is short amplitude outer cycloid (trajectory III in Figure 3). Under this condition, the spring-tooth has larger effects

on soil and the operation area is relatively dispersed. When the ratio λ is greater than 1, the horizontal velocity of spring-tooth is less than zero, that is, the direction of horizontal velocity is opposite to that of driving machine, and the trajectory of spring-tooth is trochoid (trajectory I in Figure 3). Under this condition, the operation area is relatively distributed and the weeding performance is better.

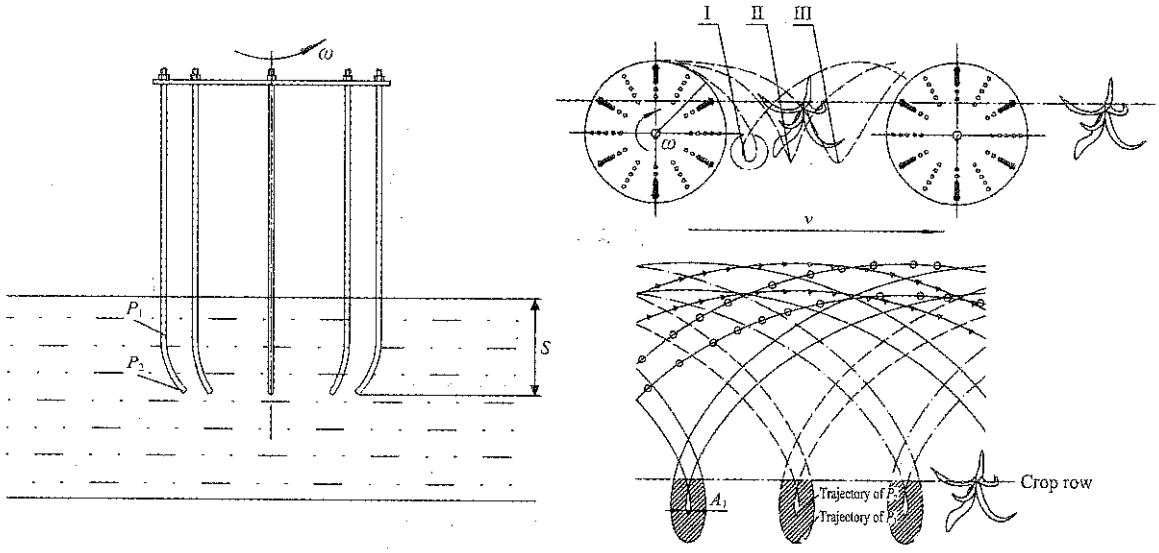

Note: P_1 and P_2 represent the two endpoints of arc-shaped segment of spring-tooth. I, II and III regions represent the weeding control areas of spring-tooth in different conditions, respectively. The circles and triangle represent the weeding control trajectories of spring-tooth in different conditions, respectively. A_1 is the minimum range of trajectories caused by two endpoints of spring-tooth. S is the distance from soil surface to spring-tooth end. v is the machine forward velocity. ω is the cutter-disc rotational speed.

Figure 3 Operation area and trajectory of weeding device

4 Materials and methods

4.1 Analysis of burying weeding mechanism

In order to analyze the burying mechanism of weeding device and research the effects of some factors on weeding performance, the comprehensive dynamic model about that machinery and weeds affected mutually was established. And then the deflection bending parametric equation of weeds was expressed based on the material mechanics. According to the simplified model of actual weeding process, as shown in Figure 4, the weed can be simplified as a homogeneous cantilever beam with free end at top and fixed at base. Taking the center point O of the weed root as the origin of rectangular coordinate system, the positive direction of axis x is along the horizontal soil interface and the positive direction of axis y is along the weed stalk before bending.

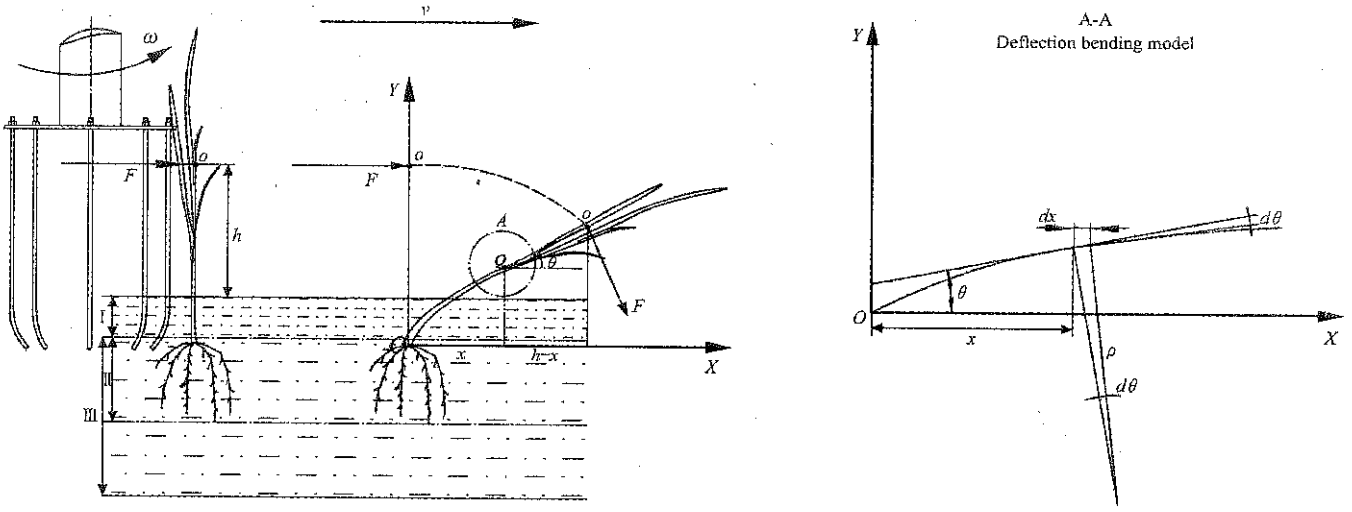

Note: I, II and III regions represent the mud layer, the root dense layer and the soil layer, respectively.

Figure 4 Comprehensive dynamic model of weeding device

Based on material mechanics, the bending weed stalk is simplified as deflection curve, the coordinate of arbitrary point on the curve is $Q(x, y)$ and the parametric equation of curve was given by:

$$y=f(x) \tag{1}$$

According to plane assumption of bending deformation (Wang et al., 2015), the cross section of beam always remains perpendicular to the axis of beam before or after bending deformation, and the angle θ between the axis x and the deflection curve could be expressed:

$$\theta=\arctan(\frac{dy}{dx}) \tag{2}$$

Under the pure bending condition, the relation between bending moment and curvature should meet:

$$\frac{1}{\rho}=\frac{M}{EI} \tag{3}$$

where, M is the bending moment acting in cross section of weed, N·m; E is the elastic modulus of weed, MPa; I is the section inertia of weed, mm^4.

The Equation (2) was transformed as follows:

$$\frac{d\theta}{ds}=\frac{d\theta}{dx}\frac{dx}{ds}=\frac{d}{dx}\left[\arctan\left(\frac{dy}{dx}\right)\right]\frac{dx}{ds} \tag{4}$$

$$ds=\left[1+\left(\frac{dy}{dx}\right)^2\right]^{1/2}dx \tag{5}$$

where, ds is the intersection of two orthogonal tangents, that is the center of curvature, and the radius of curvature ρ could be obtained.

Combining Equations (4) and (5), the nonlinear deflection equation of weed stalk after bending deformation could be derived the following formula:

$$\frac{\frac{d^2y}{dx^2}}{\left[1+\left(\frac{dy}{dx}\right)^2\right]^{3/2}}=\frac{M}{EI} \tag{6}$$

It performed pseudo-linear transform of Equation (6) to simplify solution process. When the weed is buried into the soil layer, the angle θ could be approximated to:

$$\theta\approx\tan\theta=\frac{dy}{dx}=f'(x) \tag{7}$$

From Equations (6) and (7), the approximately differential equation of deflection curve after weeding is buried into the soil layer could be transformed into Equation (8):

$$\frac{d^2y}{dx^2}=\frac{M}{EI} \tag{8}$$

On this basis, the dynamic characteristic of weeding spring-tooth was researched to analyze the effects of some factors on weeding performance. When a single spring-tooth contacts with weed stalk in point directly, the moment on arbitrary cross section could be expressed:

$$M=-[Fg\cos\theta(h-x)+Fg\sin\theta(h-x)\tan\theta]=-\frac{F(h-x)}{\cos\theta} \tag{9}$$

where, F is the resultant weeding force, N; h is the distance from force point to soil surface, mm.

Combining Equations (8) and (9) derived the following formula:

$$EIy''=M=-\frac{F(h-x)}{\cos\theta} \tag{10}$$

And then Equation (10) which is carried out two integrals could be transformed into:

$$EIy=\frac{1}{\cos\theta}(\frac{F}{6}x^3-\frac{Fh}{2}x^2+Cx+D) \tag{11}$$

where, C and D are constant terms. When the force point is the origin of coordinate, that is x=y=0, the constant terms are C=D=0.

The approximately differential equation of deflection curve after weeding is buried into the soil layer could be expressed:

$$EIy=\frac{1}{\cos\theta}(\frac{F}{6}x^3-\frac{Fh}{2}x^2)\quad(0\le x\le H) \tag{12}$$

For one particular crop, the values of elastic modulus and section inertia remain constant. From Equation (12), the value of angle θ decreased with the weeding force by spring-tooth increasing under the condition that the distance h remained constant. That is, the bigger the weeding force is, and it shows that the weeding performance is better. The value of angle θ increased with the distance h increasing under the condition that the weeding force F remained constant. That is, the higher the distance is, and it shows that the weeding performance is worse.

Based on above analysis, the weeding force by spring-tooth is one of the most important factors for

weeding performance, and it also has significant influence on rice seedlings injured problem. When the weeding force is too large, the working efficiency of weeding device will reduce, and the rice seedlings injured rate will increase. When the weeding force is too small, the weeding performance will degrade. The value of weeding force is related to the machine forward velocity, cutter-disc rotational speed, distance from soil surface to spring-tooth end and so on. In this follow-up experiment, in order to seek the optimal force range for removing weeds without injuring rice seedlings, a real-time test measurement system was designed and built using sensor testing technology for studying rice seedlings injured force to estimate the effects of some factors on experimental indexes.

4.2 Test measurement system

Refer to the actual environmental characteristics of paddy field and feasibility of measuring rice seedlings injured force (Qi et al., 2015; Zheng et al., 2017), a real-time test measurement system was designed and built using sensor testing technology for studying rice seedlings injured force. The overall configuration of test bench was shown in Figure 5. The test measurement system consisted of JC-4B type dynamic strain gauge (China Academy of Building Research, its range of input signal was ±10000$\mu\varepsilon$, sampling frequency was greater than or equal to 2kHz and the testing accuracy was 0.1%F.S.), signal acquisition system(two groups of BX120-0.5AA type foils strain gauge sensors connected fully-bridged connection, which was attached to the end of spring-tooth), collector ring, computer, rotating and burying weeding device for paddy field, main frame, transmission system, traction motor, drive motor and soil bin, etc..

In the test, the main frame (1) was driven by traction motor (2) along soil bin, and then the rotating and burying weeding device for paddy field (3) was driven for weeding by the drive motor (6). The forward velocity and rotational speed of weeding device could be adjusted by frequency converting system. The strain gauge sensor was attached to the end of spring-tooth for signal acquisition. Tiny deformation appeared in the local of the spring-tooth in the burying process. The deformation signals were transmitted to dynamic strain gauge (7) by collector ring (5) which could prevent the cable wrapping problem of weeding device during rotational motion. The dynamic stress-strain recorded real-time dynamic strain curve by using computer software to analyze the changing regulation of rice seedlings injured force. The measuring principle of system was shown in Figure 6.

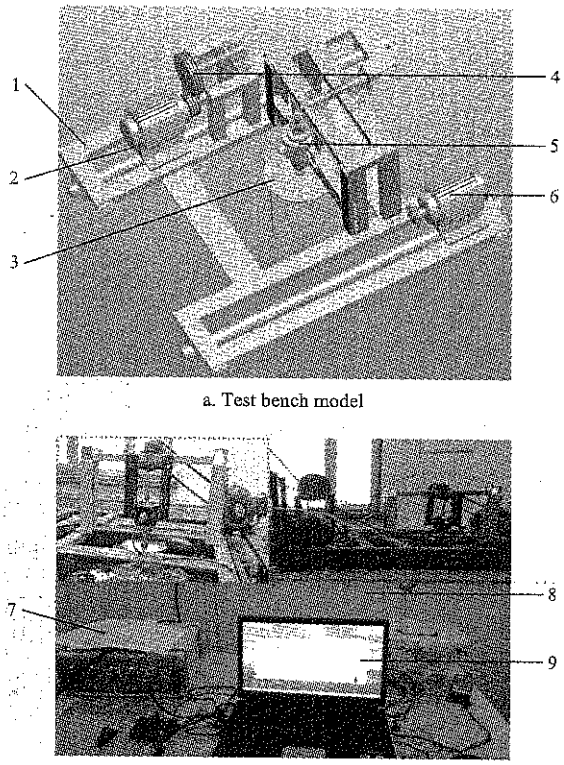

a. Test bench model

b. Actual configuration

1. Main frame 2. Traction motor 3. Rotating and burying weeding device for paddy field 4. Transmission system 5. Collector ring 6. Drive motor 7. Dynamic strain gauge 8. Soil bin 9. Computer

Figure 5 Test measurement system

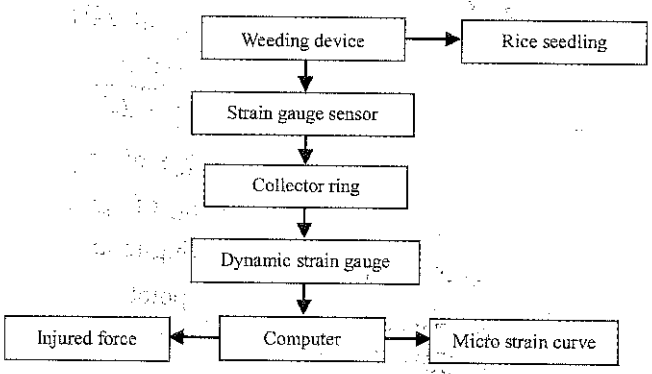

Figure 6 Flow chart of measurement system

In order to ensure the measuring accuracy, the signal acquisition system was composed of two groups of BX120-0.5AA type foils strain gauge sensors connected fully-bridged connection, as shown in Figure 7. The parameters of BX120-0.5AA type foils strain gauge sensor were shown in Table 1.

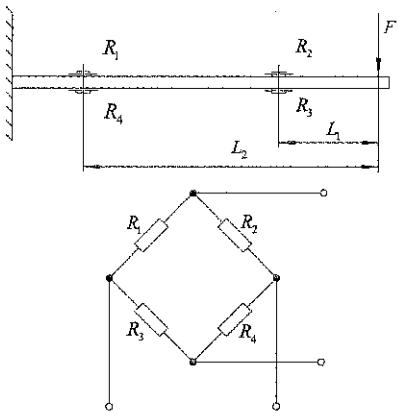

a. Fully-bridged connection mode

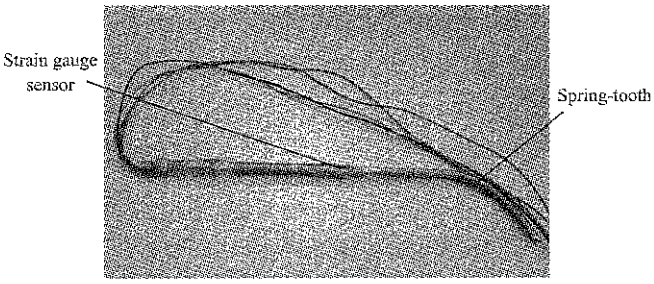

b. Physical diagram

Figure 7 Signal acquisition system

Table 1 Parameters of strain gauge sensor

Type	Resistance, Ω	Sensitive grating ruler, mm	Sensitivity coefficient, %
BX120-0.5AA	119.9±0.1	0.5×0.5	2.08±1

Figure 7a showed that the tension signal could be filtered and received by the strain gauges R_1 and R_2, and the pressure signal could be filtered and received by the strain gauges R_3 and R_4. The strain gauges R_1 and R_4, R_2 and R_3 all showed symmetrical distribution along the center of elastic components. According to the arrayed rule of strain gauges and Hooke's law, the measured strain data could be translated into the values of rice seedlings injured force (Wang et al., 2017; Jin et al., 2015). The transforming relation was as follows:

$$F = \frac{E'W\varepsilon}{2(L_2 - L_2)} \tag{13}$$

where, ε is the strain value of spring-tooth; W is the section modulus in bending of spring-tooth, mm^3; E' is the elastic modulus of spring-tooth, MPa; L_1 and L_2 are the distances from force point to two groups of strain gauges, respectively.

For eliminating the system error, the test measurement system was calibrated. The calibration data and curve were shown in Table 2 and Figure 8. The regression equation of the calibration curve was:

$$\begin{aligned} \mu\varepsilon &= 144.93F - 39.814 \\ R^2 &= 0.9999 \end{aligned} \tag{14}$$

where, $\mu\varepsilon$ is the micro strain of calibrated spring-tooth; T is the loading force, N.

Table 2 Calibration results

Loading force T, N	Micro strain $\mu\varepsilon$
1.46	168
3.29	442
5.54	764
6.92	965
7.99	1124
9.31	1299
11.61	1641
15.37	2191

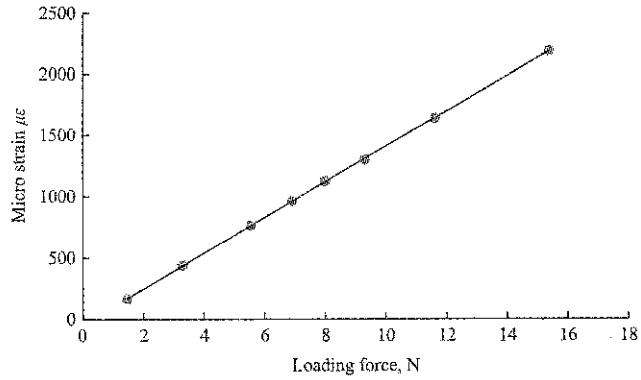

Figure 8 Calibration curve

The determination coefficient R^2 of regression equation that micro strain changed with loading force was 0.9999. After the value was displayed by computer, the rice seedlings injured forces were obtained using Equation (14).

4.3 Test materials

Rice variety "Longyang 12", widely planted in Northeast China, was chosen as the test material. Heights and diameters of 100 rice seedlings were measured on the 7th day after transplantation (the first weeding period). The average height of rice seedlings was 226.5 mm, and the average diameter was 2.1 mm. Experimental field was in Houzhangjia Village, Xingfu Town, Harbin City of China. Rice transplantation was performed manually. Before rice transplantation, the field was not treated with fertilizers nor chemical herbicides. Other paddy fields were managed in accordance with the agricultural production of local actual condition. In order to make the test more convenient, the test seedlings were transplanted to soil bin in Northeast Agriculture University before test. In the process of transplantation, enough soil was put

around roots of rice seedlings from beginning to end, ensuring growth environment of roots consistent with that in the field. The rice seedlings situations in paddy field and soil bin were shown in Figure 9.

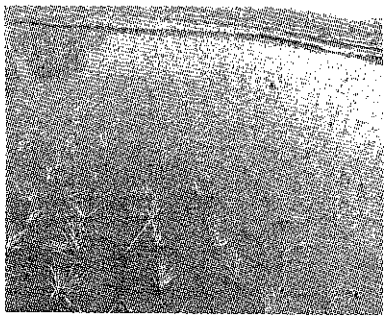

a. Paddy field

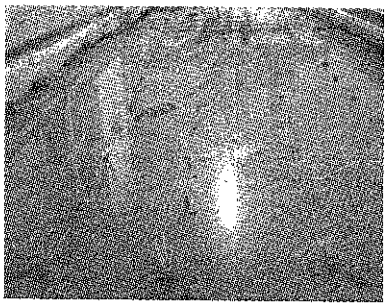

b. Soil bin

Figure 9 Rice seedlings situations in paddy field and soil bin

4.4 Test factors and indexes

Based on the above-mentioned theoretical analysis and actual agronomic requirements of weeding, the machine forward velocity, cutter-disc rotational speed and distance from soil surface to spring-tooth end were selected as the experimental factors on condition that the structure parameters of weeding device were given.

According to the different depths of root between rice seedlings and weeds, when rice seedlings got injured by a certain force, weeds must be buried into the soil. Aiming for estimating the effects of factors on rice seedlings injured rate and rice seedlings injured force, this study analyzed and tested emphatically the critical injured conditions of rice seedlings. Combined with pre-experimental study, this paper defined three kinds of mechanical injured states:

1) The stems and leaves of rice seedlings were buried into soil after weeding, and no photosynthesis could take place in soil.

2) The position of rice seedlings moved more than 20 mm after weeding.

3) The position of rice seedlings moved less than 20 mm after weeding, but the stems of rice seedlings were buried into soil.

On this basis, the rice seedlings injured rate and rice seedlings injured force were selected as the evaluation indexes. The rice seedlings injured force could be obtained by test measurement system. And the calculation equation was as follows:

$$y_1 = \frac{K_2}{K_1} \times 100\% \tag{15}$$

where, y_1 is the rice seedlings injured rate, %; K_1 is the number of rice seedlings before weeding; K_2 is the number of rice seedlings injured after weeding.

4.5 Test methods

Aimed for analyzing the effects of factors on the experimental indexes and studying the changing regulation of force, the single factor tests were carried out and the corresponding regression equations were obtained (Zhang et al., 2015; Lan et al., 2017). Combined with above theoretical analysis, pre-experimental study and the requirements of actual weeding operation, this paper determined the variation ranges of three factors. The factors and levels were shown in Table 3. In single factor tests, ensuring the machine forward velocity was 0.38 m/s, cutter-disc rotational speed was 120 r/min and distance from soil surface to spring-tooth end was 24 mm. In the tests, the soil bin was divided into 3 zones, adjusting zone, testing zone and buffering zone. The whole length of testing zone was 50 m, and the lengths of adjusting and buffering zone were 5 m. The tests for each condition were repeated three times, the averages of data were processed as the final results. The results of pre-experiment showed that, there was the phenomenon which couldn't bury rice seedlings, and it was not effective weeding. Thus, this paper defined it as invalid.

Table 3 Factors and levels of tests

Levels	Factors		
	Machine forward velocity, m s^{-1}	Cutter-disc rotational speed, r min^{-1}	Distance from soil surface to spring-tooth end, mm
1	0.14	95	6
2	0.20	105	12
3	0.26	110	18
4	0.32	115	24
5	0.38	120	30
6	0.44	125	36
7	0.50	130	
8	0.56	135	

4.6 Analysis of strain curve

In the process of test, the real-time data recorded were stored in computer and processed by using the analysis software Excel, and then the varying tendency of micro strain with time could be obtained. A test case was conduct to analyze the mechanical property of rice seedlings. Under the condition that the machine forward velocity was 0.32 m s^{-1}, cutter-disc rotational speed was 120 r min^{-1} and distance from soil surface to spring-tooth end was 20 mm, the micro strain-time curve of rice seedlings was analyzed, as shown in Figure 10. Due to the compound motion of weeding device was composed of the forward motion along with driving machine and the rotational motion about central axis, and the speed varied as the cosine with time, all these reasons resulted in the value of micro strain fluctuate between the maximum and minimum. (Jam, 2013)

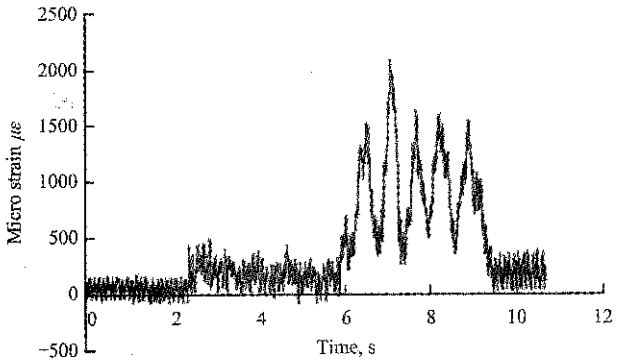

Figure 10 Micro strain-time curve of rice seedlings

Figure 10 showed that the micro strain of rice seedlings increased to the maximum and then rapidly decreased, finally came to the steady state. The actual significance and changing cause of curve in each stage were analyzed. In 0-2 s, the weeding spring-tooth remained still, and the value of micro strain fluctuated around 0$\mu\varepsilon$. In 2-6 s, the weeding spring-tooth started to rotate, its end had no direct contact with soil, and the micro deformation of weeding spring-tooth generated by the influences of frame vibration and air medium. In 6-10 s, the value of micro strain rapidly increased with the spring-tooth gradually contacting with soil. When the spring-tooth contacted with the hybrid system and buried the rice seedlings into soil, the micro strain and force reached the maximum. Thus, the maximum micro strain and force were the critical values which could remove weeds without injuring rice seedlings.

5 Results and analysis

Based on the single factor tests results, the corresponding regression equations were obtained by analysis, and the effects of each factor on rice seedlings injured rate and rice seedlings injured force were analyzed according to the phenomena and results of tests. The schemes and results of single factor tests were shown in Tables 4-6. The tendencies and corresponding regression equations of experimental indexes were shown in Figures 11-13.

5.1 Machine forward velocity

The effects of different machine forward velocities on the experimental indexes were shown in Figure 11. The results of single factor tests showed that, the rice seedlings injured force increased and the rice seedlings injured rate decreased with machine forward velocity increasing as machine forward velocity was 0.14-0.56 m s^{-1}. As machine forward velocity was 0.14-0.38 m s^{-1}, the rice seedlings injured force had an increasing trend with the increase of machine forward velocity. And machine forward velocity had no significant influence on rice seedlings injured force as machine forward velocity was more than 0.38 m s^{-1}. Under the condition that the cutter-disc rotational speed was 120 r/min and distance from soil surface to spring-tooth end was 24 mm, the determination coefficients R^2 of regression equations that rice seedlings injured force and the rice seedlings injured rate changed with machine forward velocity were 0.9658 and 0.9844, respectively.

Table 4 Results of single factor tests of machine forward velocity

Machine forward velocity, m s^{-1}	Rice seedlings injured force, N				Rice seedlings injured rate, %			
	1	2	3	Average	1	2	3	Average
0.14	7.91	8.02	8.13	8.02	6.92	6.87	6.65	6.81
0.20	8.67	9.01	8.81	8.83	5.62	5.89	5.76	5.76
0.26	9.87	9.95	10.02	9.95	5.04	5.11	4.81	4.99
0.32	13.67	13.51	13.9	13.69	4.39	4.52	4.24	4.38
0.38	14.45	14.97	14.78	14.73	3.92	4.00	3.85	3.92
0.44	15.32	15.48	15.79	15.53	3.40	3.72	3.60	3.57
0.50	15.76	15.87	15.92	15.85	3.08	2.91	3.20	3.06
0.56	16.56	16.99	16.73	16.76	2.68	2.34	2.48	2.50

Note: The cutter-disc rotational speed was 120 r min^{-1} and the distance from soil surface to spring-tooth end was 24 mm.

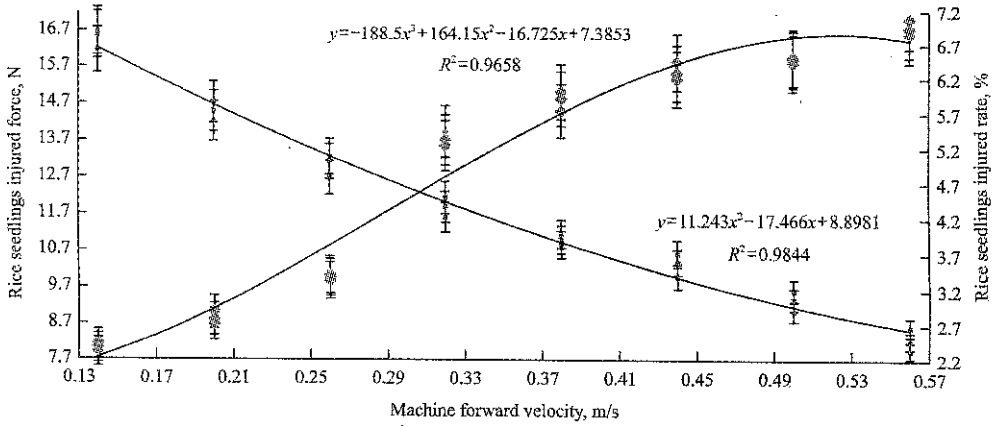

Figure 11 Effects of machine forward velocity

According to the corresponding phenomena and results, the ratio λ of the relative speed to the convected speed decreased with machine forward velocity increasing. The agitation of spring-tooth on paddy soil was more significant and the interaction with spring-tooth and hybrid system was stronger. Statistical analysis showed that, the weeding rate increased first and then decreased with the increase of machine forward velocity. The weeding rate was the minimum as machine forward velocity was 0.38 m/s. The contact time of spring-tooth and rice-seedling root reduced and the weeding control area of single spring-tooth decreased resulted in no effective completion of burying operation.

5.2 Cutter-disc rotational speed

The effects of different cutter-disc rotational speeds on the experimental indexes were shown in Figure 12. The results of single factor tests showed that, the rice seedlings injured force and the rice seedlings injured rate had a linear increasing trend with the increase of cutter-disc rotational speed. Under the condition that the machine forward velocity was 0.38 m/s and distance from soil surface to spring-tooth end was 24 mm, the determination coefficients R^2 of regression equations that the rice seedlings injured force and the rice seedlings injured rate changed with cutter-disc rotational speed were 0.9883 and 0.9995, respectively.

Table 5 Results of single factor tests of cutter-disc rotational speed

Cutter-disc rotational speed, r min^{-1}	Rice seedlings injured force, N				Rice seedlings injured rate, %			
	1	2	3	Average	1	2	3	Average
95	8.76	8.90	8.99	8.88	5.22	5.54	5.76	5.51
100	9.88	9.71	10.03	9.87	6.71	6.63	6.87	6.74
105	11.09	10.98	11.32	11.13	7.51	7.68	7.92	7.70
110	12.22	12.31	12.13	12.22	8.40	8.24	8.04	8.23
115	13.07	13.21	13.13	13.14	9.30	9.70	9.69	9.56
120	13.97	13.93	14.18	14.03	10.35	10.02	10.40	10.26
125	14.87	15.03	14.75	14.88	11.07	11.60	11.24	11.30
130	15.93	16.02	15.95	15.97	11.97	12.34	12.01	12.11

Note: The machine forward velocity was 0.38 m s^{-1} and the distance from soil surface to spring-tooth end was 24 mm.

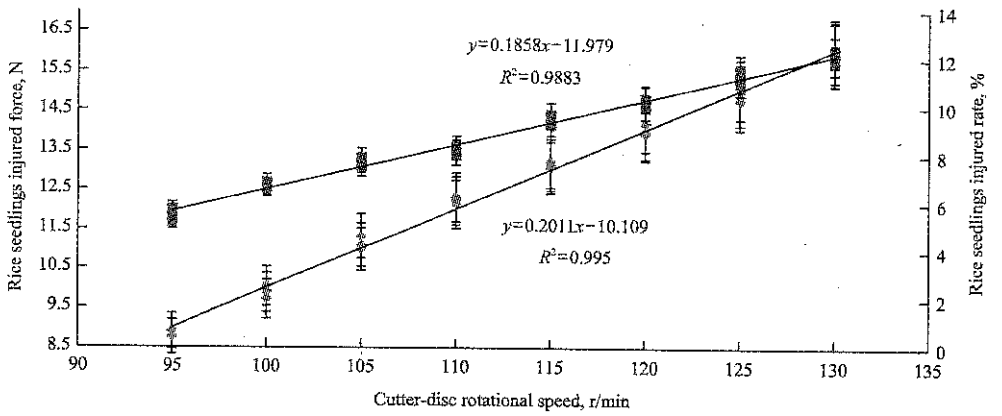

Figure 12 Effects of cutter-disc rotational speed

According to the corresponding phenomena and results, the ratio λ of the relative speed to the convected speed and the weeding control area of single spring-tooth all increased with cutter-disc rotational speed increasing,

and the contact time of spring-tooth and rice-seedling root reduced. Statistical analysis showed that, the weeding rate increased with the increase of cutter-disc rotational speed, but the rice seedlings injured rate also increased correspondingly. In the actual field operations, the reasonable cutter-disc rotational speed should be adjusted to improve the weeding performance.

5.3 Distance from soil surface to spring-tooth end

The effects of different distances from soil surface to spring-tooth end on the experimental indexes were shown in Figure 13. The results of single factor tests showed that, the distance from soil surface to spring-tooth end had significant influence on rice seedlings injured force, but lower significant influence on rice seedlings injured rate. Under the condition that the machine forward velocity of driving machine was 0.38 m/s and cutter-disc rotational speed was 120 r/min, the determination coefficients R^2 of regression equations that rice seedlings injured force and the rice seedlings injured rate changed with distance from soil surface to spring-tooth end were 0.9850 and 0.9837, respectively.

Table 6 Results of single factor tests of distance from soil surface to spring-tooth end

Distance from soil surface to spring-tooth end, mm	Rice seedlings injured force, N				Rice seedlings injured rate, %			
	1	2	3	Average	1	2	3	Average
6	10.18	10.01	10.32	10.17	1.47	1.11	1.30	1.29
12	11.93	11.88	12.01	11.94	1.91	1.80	2.21	1.97
18	12.95	12.86	13.01	12.94	2.71	2.93	3.11	2.92
24	14.11	14.05	14.18	14.11	3.60	3.46	3.78	3.61
30	17.03	17.02	16.98	17.01	4.39	4.80	4.57	4.59
36	17.89	18.01	18.34	18.08	5.21	5.64	5.40	5.42

Note: The machine forward velocity was 0.38 m/s and the cutter-disc rotational speed was 120 r/min.

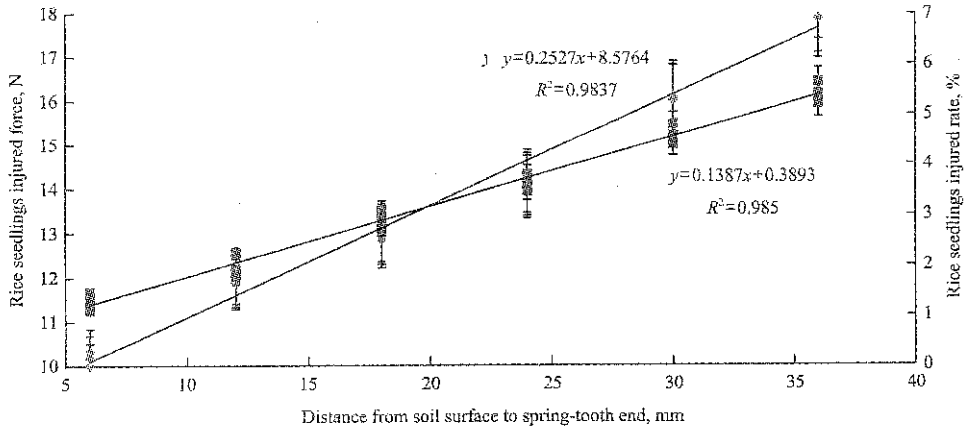

Figure 13 Effects of distance from soil surface to spring-tooth end

According to the corresponding phenomena and results, the contact area between spring-tooth and soil increased with the distance from soil surface to spring-tooth end increasing, and the friction in the operation increased. These reasons increased micro strain of spring-tooth. Statistical analysis showed that, the weeding rate increased first and then was relatively stable with the increase of distance from soil surface to spring-tooth end. The effects of distance from soil surface to spring-tooth end had practical guiding significance for production designers to select working parameters.

6 Discussion and conclusions

6.1 Discussion

In this paper, the changing regulation of force which can remove weeds without injuring rice seedlings was studied based on a kind of designed real-time test measurement system, so as to provide a method for the research on mechanical properties of crop. Due to the operational characteristics of rotating and burying weeding device for paddy field, this study simplified the injured force as the horizontal force for establishing the comprehensive dynamic model. This simplification had some effects on the results of tests. And there was systematic error due to the artificial definition to the several mechanical injured states. This is the inadequacy of this study, and it has yet to be further improved in subsequent research work.

6.2 Conclusions

A rotating and burying weeding device for paddy field was selected as the research object, and a real-time test measurement system was designed and built using

sensor testing technology for studying rice seedlings injured force refer to the actual environmental characteristics of paddy fields. Single factor tests were conducted using the factors of machine forward velocity (0.14-0.56 m/s), cutter-disc rotational speed (95-135 r/min) and distance from soil surface to spring-tooth end (6-36 mm), which significantly affect rice seedlings injured force and rice seedlings injured rate. The cutter-disc rotational speed had a significant influence on two experimental indexes. The rice seedlings injured force had a linear increasing trend with the increase of the three experimental factors. And the rice seedlings injured rate decreased with the increase of machine forward velocity while increased with the increase of another two factors. This paper could provide an important theoretical basis for the improvement and optimization of mechanical weeding device.

Acknowledgements

The authors acknowledge that this research was financially supported by the National Industry System of Rice Technology of P. R. China (CARS-01-44) and the Modern Industrial Technology Collaborative Innovation System in Heilongjiang Province.

[References]

[1] Astrand, B., and A. J. Baerveldt. 2002. An agricultural mobile robot with vision-based perception for mechanical weed control. *Autonomous Robots*, 13(1): 21–35.

[2] Dirk, A. G K. 2007. Precise tillage systems for enhanced non-chemical weed management. *Soil and Tillage Research*, 97(2): 293–305.

[3] Gobora, Z., P. S. Lammers, and M. Martinov. 2013. Development of a mechatronic intra-row weeding system with rotational hoeing tools: Theoretical approach and simulation. *Computers and Electronics in Agriculture*, 98(98): 166–174.

[4] Guo, C. X., Z. B. Li, C. Li, Z. D. Duan, and J. Yue. 2016. Design and implementation of monitoring system of agricultural prices based on ice middleware. *International Agricultural Engineering Journal*, 25(2): 159–170.

[5] Ishii, H., and M. Satho. 2006. Performance of paddy weeding machine and improvements in the performance. *The Crop Science Society of Japan*, 21(7): 22–23. (in Japanese)

[6] Jam, T. 2013. Effect of loading rate on mechanical characteristics of wheat and rice stalk. *Bulgarian Journal of Agricultural Science*, 19(6): 1452–1458.

[7] Jin, X., X. W. Du, J. T. Ji, S. G. Wang, X. Dong, and M. M. Du. 2015. Physical characteristics of plug seedling transplanted by the return-blank type transplanter. *International Agricultural Engineering Journal*, 24(4): 1–10.

[8] Johnson, W. C., M. A. Boudreau, and J. W. Davis. 2012. Implements and cultivation frequency to improve in-row weed control in organic peanut production. *Weed Technology*, 26(2): 334–340.

[9] Lamm, R. D., D. C. Slaugther, and D. K. Giles. 2002. Precision weed control system for cotton. *Transactions of the ASAE*, 45(1): 231–238.

[10] Lan, Y. B., S. D. Chen, and B. K. Fritz. 2017. Current status and future trends of precision agricultural aviation technologies. *International Journal of Agricultural & Biological Engineering*, 10(3): 1–17.

[11] Liu, Y. P., X. Lin, T. H. He, C. Q. Kong, G. H. Li, L. Q. Tang, K. Tian, X. H. Zhong, and N. R. Huang. 2012. Mechanical properties measurement and statistical analysis of paddy stem based on image analysis method. *Journal of Experimental Mechanics*, 27(4): 424–427.

[12] Ma, R. J., Y. G. Qu, Z. X. Zhao, and Z. Y. Mao. 2005. Experimental study on the force of pulling up the rice seedlings sprouted in the plastic cell-tray. *Transactions of the Chinese Society for Agricultural Machinery*, 36(9): 32–36. (In Chinese with English abstract)

[13] Ma, X., L. Qi, B. Liang, Z. T. Tan, and Y. J. Zuo. 2011. Present status and prospects of mechanical weeding equipment and technology in paddy field. *Transactions of the Chinese Society of Agricultural Engineering*, 27(6): 162–168. (In Chinese with English abstract)

[14] Qi, L., Z. W. Liang, X. Ma, Y. X. Tan, and K. T. Jiang. 2015. Validation and analysis of fluid-structure interaction between rotary harrow weeding roll and paddy soil. *Transactions of the Chinese Society of Agricultural Engineering*, 31(5): 29–37. (In Chinese with English abstract)

[15] Slaughter, D., D. Giles, and D. Downey. 2008. Autonomous robotic weed control systems: a review. *Computers and Electronics in Agriculture*, 61(1): 63–78.

[16] Tao, G. X., J. W. Wang, W. Q. Zhou, C. L. Niu, and J. K. Zhao. 2015. Herbicidal mechanism and key components design for paddy weeding device. Transactions of the *Chinese Society for Agricultural Machinery*, 46(11): 57–63. (In Chinese with English abstract)

[17] Van Der Weide, R, Y,, P, O, Bleeker, V. T. J. M. Achten, L. A. P. Lotz, F. Fogelberg, and B. Melander. 2008. Innovation in mechanical weed control in crop rows. *Weed Research*, 48(3): 215–224.

[18] Wang, J. F., J. W. Wang, D. W. Yan, H. Tang, and W. Q. Zhou. 2017. Design and experiment of 3SCJ-2Type row weeding

machine for paddy field. *Transactions of the Chinese Society for Agricultural Machinery*, 48(6): 71–78, 202. (In Chinese with English abstract)

[19] Wang, J. W., G. X. Tao, Y. J. Liu, Z .W. Pan, and C. F. Zhang. 2014. Field experimental study on pullout forces of rice seedlings and barnyard grasses for mechanical weed control in paddy field. *International Journal of Agricultural & Biological Engineering*, 7(6): 1–7.

[20] Wang, J. W., H. Tang, J. F. Wang, D. X. Jiang, and X. Li. 2017. Measurement and analysis of restitution coefficient between maize seed and soil based on high-speed photography. *International Journal of Agricultural & Biological Engineering*, 10(3): 102–114.

[21] Wang, J. W., T. Y. Duo, H. Tang, G. X. Tao, S. M. Yang, and Y. J. Liu. 2016. Weed mechanism and mechanics experiment of vertical weed control device between seedlings in paddy field. *Journal of Northeast Agricultural University*, 47(4): 86–94. (in Chinese)

[22] Wang, J. W., H. Tang, J. F. Wang, H. N. Huang, and N. N. Lin. 2017. Numerical analysis and performance optimization experiment on hanging unilateral ridger for paddy field. *Transactions of the Chinese Society for Agricultural Machinery*, 48(8): 72–80. (In Chinese with English abstract)

[23] Wang, J. W., H. Tang, J. F. Wang, X. Li, and H. N. Huang. 2017. Optimization design and experiment on ripple surface type pickup finger of precision maize seed metering device. *International Journal of Agricultural & Biological Engineering*, 10(1): 61–71.

[24] Wang, Z. M., B. L. Wang, M. H. Zhang, Y. Z. Dai, Z. W. Mo, and X. W. Luo. 2016. Synchronous spraying technology with weeding and dynamic rule of herbicide degradation. *Transactions of the Chinese Society of Agricultural Engineering*, 32(16): 59–64. (In Chinese with English abstract)

[25] Yang, S. M., J. W. Wang, Y. J. Liu, J. F. Wang, and J. K. Zhao. 2014. Design and simulation analysis of vertical weed control device between seedlings in paddy field. *Journal of Agricultural Mechanization Research*, 30(12): 154–157. (In Chinese with English abstract)

[26] Zhang, C. J., J. W. Wang, J. L. Zhao, Y. J. Kong, and C. L. Zhang. 2012. Design and experimental research on device of weeding between seedlings from paddy fields. *Journal of Northeast Agricultural University*, 43(2): 49–53. (in Chinese)

[27] Zhang, H. L., Y. M. Guo, and J. H. Zhang. 2015. Moisture content monitoring system based on relative dielectric constant during vacuum freeze-drying of fruit and vegetable. *International Agricultural Engineering Journal*, 24(2): 104–111.

[28] Zhang, M., M. Xiang, S. Wei, Y. H. Ji, R. C. Qiu, and Q. K. Meng. 2015. Design and implementation of a corn weeding-cultivating integrated navigation system based on GNSS and MV. *Transactions of the Chinese Society for Agricultural Machinery*, 46(S1): 8–14. (In Chinese with English abstract)

[29] Zhang, X. R., and Y. Chen. 2017. Soil disturbance and cutting forces of four different sweeps for mechanical weeding. *Soil and Tillage Research*, 168(1): 167–175.

[30] Zheng, W. X., J. N. Song, C. L. Liu, X. Q. Dong, D. H. Zhang, and H. J. Shi. 2017. Cutting force of dry-wet tobacco stalks after leaf harvest. *International Agricultural Engineering Journal*, 26(1): 143–149.

Design and test of a new reinforced plastic film collector

Hu Can[1,2], Wang Xufeng[1,2], Li Hong[1,2], Wang Long[1,2], Li Junbao[1,2], Yang Ying[1,2*]

(1. *College of Mechanical and Electrical Engineering, Tarim University, Alar Xinjiang 843300, China*;
2. *Key Laboratory of Colleges & Universities under the Department of Education of Xinjiang Uygur Autonomous Region, Alar Xinjiang 843300, China*)

Abstract: The pollution of residual plastic film has now been a difficult problem for farmlands in Xinjiang and mechanical collection is still the main solution by far. In order to raise the collection rate and efficiency, a new kind of plastic filmwas developed by reinforcing mechanical properties of the side and middle parts of the film. To collect the film mechanically, a new collector that can recycle the reinforced film entirely has been researched. The function of film rolling was applied to the collector. The results of our field experiment showed that the mean rate of collecting residual reinforced films is 98.57%, while the mean working efficiency is 0.22 $hm^2 h^{-1}$; both the traveling speed and the rolling speed have significant effect on the collection rate, which, however, was slightly affected by the digging depth. The results suggested that the film is of tensile strength after its mechanical properties have been reinforced, which greatly improved the collection of the side and middle parts of the film that were difficult to be collected and, as a result, increased the collection rate. The experiment also showed that such reinforcement could raise the collection efficiency and has contributedtobetter collection performance, with achieving function of preserving moisture and increasing temperature of the soil.

Keywords: pollution of residual plastic film, field experiment

Citation: Hu, C.,X. F. Wang, H. Li,L.Wang, J. B. Li, and Y. Yang. 2017. Design and test of a new reinforced plastic film collector. International Agricultural Engineering Journal, 26(4): 65–73.

1 Introduction

The south Xinjiang is the most important production base of high quality cotton in China, owing to the long sunshine duration and large difference in temperatures between day and night in this region (Hu et al., 2017). With the pollution of residual plastic film becoming increasingly serious, however, planting environment and sustainable development of cotton production have been severely affected due to the residual film pieces accumulated in the fields over the years. According to the research statistics, the yield of cotton decreases by 10.8% on average when the density of the residues is 400 kg/hm^2 (Liu et al., 2016; He et al., 2009; Dong et al., 2013). In recent years, comprehensive treatment of the pollution which caused by residual plastic films in Xinjiang has become a key subject that needs to be solved immediately (Hou et al., 2002).

At present, there are two technical solutions on the comprehensive treatment: biodegradation and mechanical collection (Kyrikou et al., 2011; Dai et al., 2016). The former is still under research, it is also hard to give solutions to the problems of filming mulching cycle and under film temperature. The latter becomes one of the applicable technical solutions so far. In the developed countries, thick films produced in Europe are usually used to improve the mechanical collection (He et al., 2009; Yan et al., 2006; Liu et al., 2015). This gives us an inspiration to improve the effect of the mechanical collection by reinforcing the mechanical properties of the film itself, which, after being recycled, is more complete, cleaner and can be reused (Yin et al., 2014). Hou developed a spring-tooth film collector, and their field experiment showed that the collection rate was 72%-82% (Hou et al., 2012). Agricultural Mechanization Research Institution of Xinjiang Academy of Agricultural Sciences

Received date: 2017-10-08 **Accepted date:** 2017-11-03

* **Corresponding author: Yang Ying,** Associate Professor, College of Mechanical and Electrical Engineering, Tarim University, Alar Xinjiang 843300, China. Email: 591908603@qq.com.

designed a machine (4JSM-1800) that combined cotton stalk pulverizer and residual film collector. The machine can realize the pulverization of cotton stalks and the collection of residual films at the same time, with the collection rate reaching 85% (Polat et al., 2011; Zhao et al., 2017).

Research results proved that reinforcing mechanical properties of the film itself is an effective way to raise the collection rate. For this issue, a new try of reinforcing the mechanical properties of the side and the middle parts of the film to facilitate the collection was done. To perform the mechanical collection, a machine that was applicable to collect the reinforced films was investigated. The machine can collect a complete piece of the film, therefore, it gave a solution to get rid of the pollution of the residual films.

2 Idea of designing the reinforced film

Film reinforcement is a new concept. It is to reinforce mechanical properties of an ordinary film, which enhances the strength of the film so as to facilitate the collection. In this paper, a reinforcement rib was studied. It is a transparent and plastic tape, made by coating a layer of pressure-sensitive adhesive emulsion on the substrate of BOPE (biaxially oriented polyethylene) (Meng et al., 2013). The reinforcement rib, with the thickness of 0.012 mm and the width of 10 mm, is of strong adhesive property, which made it quickly bonded with apiece of ordinary film. The rib should be adhesive on the one hand, and high strength and ductility on the other hand.

For cotton plantation in Xinjiang, there are three spacing modes: 760 mm, (680+80)×100 mm and (660+100)×100 mm. The reinforcement ribs were distributed on the sides of the spacing to avoid cotton seeds being sowed on the ribs. Figure 1 showed the schematic plot of the reinforced plastic film that is suitable for the (660+100)×100 mm spacing mode. Before film mulching, the mechanical properties of the reinforced plastic film were measured. The average value of the failure load was 19.4 N, and the tensile strength was 44.42 MPa, which was much higher than that of the ordinary plastic film.

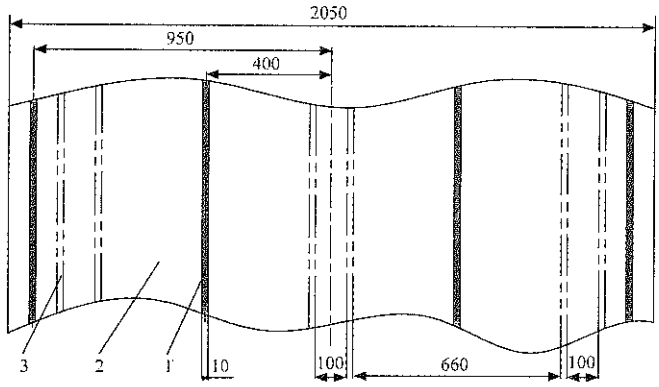

1. Reinforcement rib 2. Ordinaryplastic film 3.Row spacing

Figure 1 Schematic diagram of reinforced film

3 Overall structure and working principle

3.1 Overall structure

Figure 2 showed the design of the reinforced plastic film collector, which consisted of a frame, a power transmission system, a suspension unit, a loosening shovel unit, a film slitting unit, film unfolding unit, a supporting unit, a film rolling unit and a film unloading unit, among which the loosening shovel unit was made of shovels, handles and a plate which was used to adjust the depth. The film rolling unit was made of a frame, supporting rollers, a spindle and a film roller. The film slitting unit was made of a slitting disk, an adjustment lever and a junction plate.

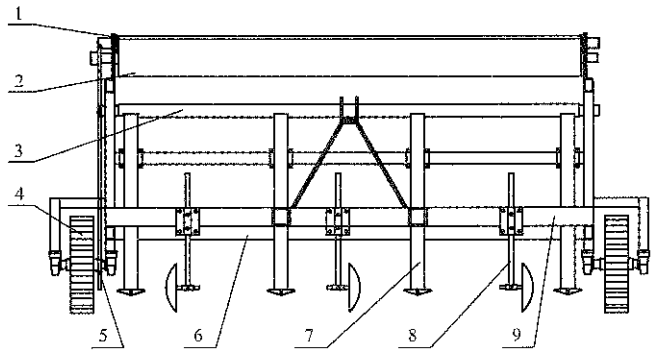

1. Film rolling unit and a film unloading unit 2. Supporting unit 3. Film unfolding unit 4. Ground wheels 5. Frame 6. Power transmission system 7. Loosening shovel unit 8. Film slitting unit 9. Suspension unit

Figure 2 Reinforced plastic film collector

3.2 Working principle of the collector

Figure 3 showed the working principle of the reinforced film collector which was connected to a tractor through a suspension unit. When the tractor moved forward, the ground wheels transferred the power to the supporting roller through a chain wheel. The film rolling unit was placed on and was tangent to the supporting

rollers, and was driven by the friction between them. When start working, the residual film was manually picked up and put on the rolling unit. During the work, the film was cut by the slitting unit and shoveled up from the middle as well as from both sides. Then, the film was unfolded by the unfolding unit and twined on the rolling rod. After the diameter of the reel of the film reached a certain value, the spindle was removed from the film roller to take off the reel of the film to finish the collection. When the film was cut by the slitting unit, the soil and other matters on the film can effectively fall from the cutter. So, they would not be carried to the roller, which increased the efficiency of the collection. The film roller rotated along the direction that was opposite to the rotation of the ground wheels.

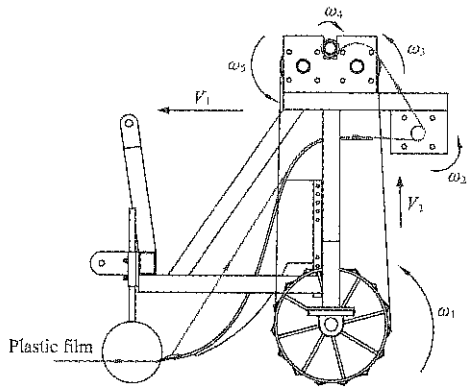

Figure 3 Working principle of the reinforced film collector

When the suspension unit moved forward at the velocity of V1, the ground wheels rotated at the angular velocity of ω_1 and, through the driving chain, the supporting roller 1 and 2 rotated at the angular velocity of ω3 and ω5, respectively. The film rolling unit was placed on and was closely tangent to the supporting rollers, and was driven by the friction between them to collect the residual film.

$$V_2 = \cos\beta * R_1 * \omega_1 \quad (1)$$

where, R_1 is the diameter of the chain wheel which is connected to the ground wheel; β is the angle between the chain and the velocity of the chain wheel; and V_2 is the linear velocity of the chain. The values of ω_3 and ω_5 can be determined from V_2 and the diameters of supporting roller 1 and 2. Our design supporting roller 1 and 2 have the same diameter and are both driven by the chain that moves at the velocity of V_2. Therefore, they also have the same angular velocity, which is:

$$\omega_3 = \omega_5 = \frac{V_2}{\cos\beta * R_2} \quad (2)$$

where, R_2 is the diameter of supporting roller 1 or 2; and ω_4 is the angular velocity of film roller 3, which is driven by the friction between them. The effect of the slide between the film roller and the supporting rollers can be ignored, so we have:

$$\omega_4 = \frac{V_2}{\cos\beta * R_3} \quad (3)$$

where, R_3 is the diameter of the excircle of film roller 3, supporting roller 1 and supporting roller 2. The value of R_3 keeps changing as the film roller is collecting the reinforced film and, as a result, the value of ω_4 is also changing.

4 Design of major units

4.1 Loosening shovel unit

The loosening shovel unit, a key component of the collector, is used to loosen the soil hardened on the film, so as to pick up the film and ensure a smooth collection. It consisted of shovels, handles and depth adjustment plate, as shown in Figure 4 (Ghasem et al., 2013).

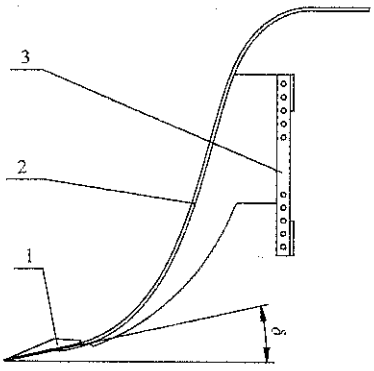

1. Loosening shovel 2. Handles 3. Depth adjustment plate 4. Rakeangle

Figure 4 Loosening shovel unit

This unit was connected to an appropriate position of the frame through bolts (Manoj et al., 2016). The triangular shovels were welded with the handles, and the connection part of the shovel and handle was a circular arc.. The depth of the shovel in soil can be adjusted by controlling the handle and the depth-adjustment plate, and the range of the adjustment along the vertical direction was 20-110 mm.

4.2 Film rolling unit

The film rolling unit, mainly being used to roll the residual film, consisted of a frame, supporting rollers, a

spindle and a film roller. The two supporting rollers were placed in the same horizontal plane. The film roller, which contained a spindle was put on the supporting rollers and was driven by the friction between them. The reel of the film will become larger and larger with the rotation, but the linear velocities of these rollers are always the same. Figure 5 showed the structure of the film rolling unit.

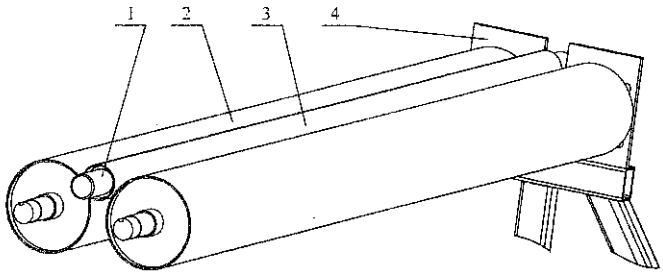

1. Spindle 2. Supporting rollers 3. Film roller 4. Frame

Figure 5 Film rolling unit

The design of the film roller has a direct effect on the collection of the machine. In our design, therefore, the film roller was conveniently retractable, which achieved a function of removing the film collected on the roller quickly and avoided a secondary pollution caused by improper operation. The design principle was: cut the roller into two parts along the axial direction, and one of them was cut at the quantity of 20 mm, also along the axial direction, then the two parts were connected together by using hinges, as shown in Figure 6.

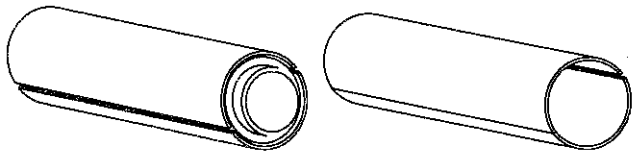

a. Scalable b. Compressible

Figure 6 Film roller conveniently retractable

Before the collection, the spindle is inserted into the film roller. Supported by the spindle, the diameter of the film roller reaches its maximum. At first, the residual film is manually twined on the film roller. To take off the film after the collection is finished, the supporting spindle is pulled out from the film roller, and the diameter of the film roller becomes smaller under compression, which makes it convenient to take off the film from the roller.

4.3 Film slitting unit

As proved in our experiment, the machine cannot work continuously and normally if there was soil hardened on the reinforced film. For this reason, the film slitting unit was designed to solve this problem.

The main function of this unit is to cut the reinforced film to allow the soil and other matters to fall off the film, so as to ensure a regular and continuous collection. The unit was made of a slitting disk, an adjustment lever and a junction plate. The bolted connection between the lever and the disk allowed the adjustment of the horizontal position of the disk, while the bolted connection between the lever and the plate allowed the adjustment of the vertical position of the disk. Figure7 showed the structure of the film slitting unit.

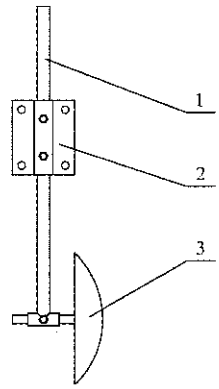

1. Adjustment lever 2. Junction plate 3. Slitting disk

Figure 7 Film slitting unit

5 Field experiment of the prototype

5.1 Experiment materials

A prototype of the reinforced film collector was fabricated according to our design. During the early stage of the experiment, the prototype was tested in a soil-bin lab in Tarim University. Before the test, the reinforced film was paved in the lab by using a film layering sower, as shown in Figure 8. After finishing the prototyping testing, we started the field experiment of the collection, which was conducted in 2# filed in Tarim University. The soil in the experimental field was clay, and the moisture content was 68%. The film mulching condition was consistent with that of the ordinary plastic film. The reinforced film used for the experiment had been treated in insolation weathering for 6 months. The field, with the length of 20 m, was paved with the reinforced films. Figure 9 showed the experiment of collecting the reinforced films. In the field, lines were marked out for every 5 m, and the data for the first 5 m were not recorded. All data of the film were measured and

collected when the machine came to a steady state during the running process.

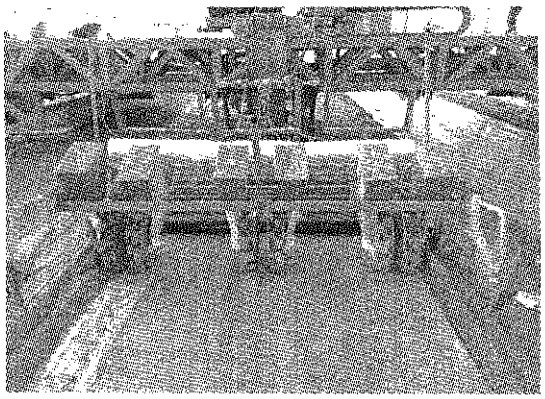

Figure 8 Reinforced film paved by a layering sower

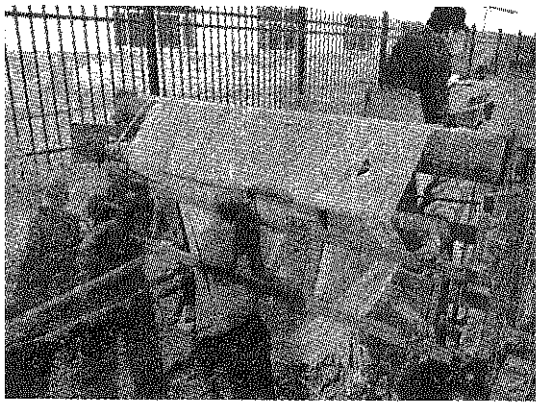

Figure 9 Field experiment of the reinforced film collection

5.2 Experimental method

5.2.1 Experimental factors

The prototype was firstly tested before the field experiment. According to the features of the prototype, we took the forward velocity of the collector, the rotational velocity of the film roller and the in-soil depth of the shovel as the influencing factors.

5.2.2 Experimental level

Single-factor tests were performed before the field experiment. The measurement of the specific indexes conformed to NY/T1227-2006. The Operating Quality of Retrieving Machines for Film Residue, a standard of the Ministry of Agriculture, China. The mechanical properties of the reinforced plastic film were increased, so the recovery rate was greatly improved. The field experiment was carried out to verify the increase of mechanical properties and the increase of recovery rate of mulch film. Based on the single-factor tests, the operating speed of the collector was set at 2, 4 and 6 km/h, respectively; the rotational velocity of the film roller was set at 60, 75 and 90 r min^{-1}, respectively, andthe in-soil depth of the shovel was set at 40, 60 and 80 mm, respectively (Wang et al., 2017).

5.2.3 Orthogonal experimental scheme

The experiment is orthogonal. According to the factor levels, an orthogonal table was designed to contain 3 factors and 3 levels. In consideration of the interactions of the factors, the orthogonal table we usedwas $L_{27}(3^{13})$. Table 1 showedthe orthogonal experiment.

Table 1 Factor level code table

Level	Factor level		
	A Advance speed, km/h	B Rotational speed, r/min	C Working depth, mm
1	2	90	50
2	4	120	100
3	6	150	150

5.3 Experimental indexes

Film collection rate and film collection efficiency were taken as the indexes for the field experiment in accordance with the state standard of GB/T 25412-2010 Mulch Film Residue Collector, with consideration of practical conditions.

(1) Film collection rate:

$$\varphi = \frac{m_1}{m_1 + m_2} \times 100\% \quad (4)$$

where, φ is collection rate; m_1 is weight of the collected films, g; m_2 is weight of the uncollected films, g.

(2) Film collection efficiency

Theoretically, the efficiency of collecting film residues after autumn was:

$$\eta = 0.0001va \quad (5)$$

where, η is collection efficiency, hm^2/h; v is mean velocity of the collector, km/h, and; a is the working width of the collector, mm, B=2200 mm.

6 Experimental results and analysis

6.1 Range analysis

The experimental results shown in table 2 suggested that the reinforcement of the mechanical properties of the film can achieve a high collection rate, with the maximum reaching 99.07%, which, basically, realized the collection of the entire film. Judge from the results of the range R, the sequence of factors that had effect on the collection rate is $(A\times B)_1$>A>$(A\times B)_2$>B>$(B\times C)_1$>

$(B\times C)_2>C>(A\times C)_2>(A\times C)_1$. Both the interaction between the forward velocity and the rolling velocity (i.e. A×B) and the interaction between the forward velocity and the in-soil depth (i.e. A×C) had an effect on the collection rate. $(A\times B)_1$ showedits maximum effect at the second level, with the mean collection rate reaching 93.48%, while factor A showed its maximum effect at the third level, with the mean collection rate reaching 92.81%. For (A×C) at the second and the third levels, the collection rateswere 90.74% and 90.61%, respectively. The range of $(A\times B)_1$ was 5.47, which is larger than those of A, $(A\times B)_2$ and (A×C), so the optimal level was the second level of factor A (when the forward velocity is 4 km/h). Similarly, the optimal level combination is A2B2C3 (when the rolling velocity is 120 r/min and the in-soil depth is 50 mm).

Table 2 Results of orthogonal test

Number Test number	1 A	2 B	3 (A×B)	4 $(A\times B)_2$	5 C	6 $(A\times C)_1$	7 $(A\times C)_2$	8 $(B\times C)_1$	11 $(B\times C)_2$	φ, %	H, $hm^2\ h^{-1}$
1	1	1	1	1	1	1	1	1	1	84.67	0.1825
2	1	1	1	1	2	2	2	2	2	85.96	0.1689
3	1	1	1	1	3	3	3	3	3	86.07	0.1737
4	1	2	2	2	1	1	1	2	3	93.81	0.2045
5	1	2	2	2	2	2	2	3	1	91.77	0.1875
6	1	2	2	2	3	3	3	1	2	92.99	0.1685
7	1	3	3	3	1	1	1	3	2	85.76	0.1292
8	1	3	3	3	2	2	2	1	3	84.57	0.121
9	1	3	3	3	3	3	3	2	1	83.87	0.222
10	2	1	2	3	1	2	3	1	1	93.83	0.2025
11	2	1	2	3	2	3	1	2	2	94.30	0.1834
12	2	1	2	3	3	1	2	3	3	95.94	0.1686
13	2	2	3	1	1	2	3	2	3	89.85	0.2578
14	2	2	3	1	2	3	1	3	1	86.72	0.2284
15	2	2	3	1	3	1	2	1	2	87.93	0.2372
16	2	3	1	2	1	2	3	3	2	89.03	0.185
17	2	3	1	2	2	3	1	1	3	88.60	0.1645
18	2	3	1	2	3	1	2	2	1	87.62	0.2014
19	3	1	3	2	1	3	2	1	1	95.71	0.1769
20	3	1	3	2	2	1	3	2	2	94.69	0.2016
21	3	1	3	2	3	2	1	3	3	96.03	0.1825
22	3	2	2	3	1	3	2	2	3	87.64	0.2264
23	3	2	2	3	2	1	3	3	1	96.02	0.2367
24	3	2	2	3	3	2	1	1	2	95.05	0.2046
25	3	3	1	1	1	3	2	3	2	94.92	0.2113
26	3	3	1	1	2	1	3	1	3	84.70	0.1863
27	3	3	1	1	3	2	1	2	1	90.54	0.1724
K_1	789.47	827.20	792.11	791.36	815.22	811.14	815.48	808.48	810.75		
K_2	813.82	817.82	841.35	830.25	807.33	816.63	812.06	808.28	820.63		
K_3	835.30	789.61	805.13	816.25	816.04	810.82	811.05	822.26	807.21		
k_1	87.72	91.91	88.01	88.01	90.58	90.13	90.61	89.78	90.08		
k_2	90.42	90.87	93.48	92.25	89.70	90.74	90.23	89.81	91.18		
k_3	92.81	87.73	8946	90.78	90.67	90.09	90.12	91.36	89.69		
Range R	5.09	4.18	5.47	4.32	0.97	0.65	0.49	1.58	1.49		
K_1	1.3358	1.6406	1.646	1.8185	1.7761	1.748	1.652	1.6440	1.8103		
K_2	1.8288	1.9516	1.7827	1.4899	1.6783	1.6822	1.6992	1.8384	1.6897		
K_3	1.7987	1.5931	1.7566	1.6944	1.7309	1.7551	1.8341	1.7029	1.6853		
k_1	0.1484	0.1823	0.1829	0.2021	0.1973	0.1942	0.1836	0.1827	0.2011		
k_2	0.2032	0.2168	0.1981	0.1655	0.1865	0.1869	0.1888	0.2043	0.1877		
k_3	0.1999	0.177	0.1952	0.1883	0.1923	0.195	0.2038	0.1892	0.1873		
Range R	0.0548	0.0398	0.0152	0.0365	0.0034	0.0081	0.0023	0.0216	0.0139		

The sequence of factors that have an effect on the collection efficiency is A>B>$(A\times B)_2$>$(B\times C)_1$>$(A\times B)_1$>$(B\times C)_2$>$(A\times C)_1$>C>$(A\times C)_2$. The results of the range R showed that both the interaction between the forward velocity and the rolling velocity (i.e. A×B) and the interaction between the forward velocity and the in-soil depth (i.e. A×C) had an effect on the collection rate. The forward velocity A showed its maximum effect at the second level (when the forward velocity is 4 km/h), with the mean collection efficiency reaching 0.2032 hm^2/h. For (A×B) at the second and the third levels, the mean collection efficiencies were 0.1981 and 0.2021 hm^2/h, respectively; while for (A×C) at the third level, the mean collection efficiencies were 0.195 and 0.2045 hm^2/h, respectively. The range of the forward velocity was larger than those of (A×B) and (A×C), so the optimal level was the second level of the forward velocity A (when the forward velocity is 4 km/h). Similarly, the optimal level of the combination was A2B2C2 (when the rolling velocity is 120 r/min and the in-soil depth is 100 mm).

6.2 Variance analysis

To check the significance of the factors on the collection rate, we performed variance analysis on the indexes, as is shown in Table 3. The analysis results suggested that all factors had effects on the collection rate. Factor A and $(A\times B)_1$ had the maximum effect, of which, the F values were 6.229 and 3.591, respectively, with the significance of $P<0.01$, which indicated that the interaction of the forward velocity and the rolling velocity has significant effect on the collection rate. Factor C has little effect on the collection rate, which indicated that the film is of tensile strength after its mechanical properties have been reinforced. That is to say, the collection can be achieved in a range of the in-soil depth. Therefore, the collection rate can be raised by setting a proper forward velocity.

To check the significance of the factors on the collection efficiency, we also performed the variance analysis on the indexes, as shown in Table 4. The analysis results suggested that the interaction of the factors have little effect on the collection efficiency. Factor A and B have significant effect on the collection efficiency, of which, the F values were4.668 and 3.315, respectively, with the significance of $P<0.01$. Both the forward velocity and the rolling velocity have significant effect on the collection efficiency. The forward velocity was decided by the ground wheels of the prototype, while the film rolling unit was driven by the chain wheel connected to the ground wheels. The rolling velocity was proportional to the forward velocity. Therefore, the collection will be more efficient if the forward velocity is higher.

Table 3 Variance analysis of percent recovery

Source of variance	Sum of squares of deviations	Freedom	mean square	F-measure	Sig.	Significant
A	0.012	2	0.006	6.229	0.023	***
B	0.002	2	0.001	1.276	0.33	*
C	0.001	2	0.001	0.274	0.767	*
$(A\times B)_1$	0.007	2	0.003	3.591	0.077	***
$(A\times B)_2$	0.001	2	0.001	0.691	0.529	*
$(A\times C)_1$	0.001	2	0.001	0.126	0.883	*
$(A\times C)_2$	0.001	2	5.989E-005	0.064	0.939	*
$(B\times C)_1$	0.001	2	0.001	0.785	0.488	*
$(B\times C)_2$	0.001	2	0.001	0.573	0.585	*
error	0.008					
The sum	26.279	38				

Table 4 Variance analysis of recovery efficiency

Source of variance	Sum of squares of deviations	Freedom	mean square	F-measure	Sig.	Significant
A	0.005	2	0.02	4.668	0.055	***
B	0.003	2	0.002	3.315	0.039	***
C	0.001	2	0.000	0.507	0.62	*
$(A\times B)_1$	0.00	2	0.000	0.308	0.743	*
$(A\times B)_2$	0.001	2	0.000	0.509	0.619	*
$(A\times C)_1$	0.000	2	0.000	0.342	0.72	*
$(A\times C)_2$	0.002	2	0.001	1.89	0.213	*
$(B\times C)_1$	0.002	2	0.001	2.102	0.185	*
$(B\times C)_2$	0.001	2	0.001	1.065	0.389	*
error	0.004					
The sum	0.025	38				

7 Conclusions

It can be known from the experiment of the reinforced film collection, improving mechanical properties of the film itself is a feasible way to collect film residues.

(1) The collection of film residues can be improved by reinforcing mechanical properties of the film

Reinforcement ribs are adhered to side and middle parts to enhance mechanical properties of the film, so as to collect the film entirely, with the mean collection rate above 98.57%. The experiment has proved that the

reinforcement of the mechanical properties can raise the collection efficiency and contribute to better collection performance, with achieving function of preserving moisture and increasing temperature of the soil.

(2) The prototype was well designed with a simple structure. It is stable and showed good collection performance. The variance analysis of the prototype suggested that the interaction of the forward velocity and the rolling velocity have significant effect on the collection rate, while the in-soil depth of the shovel has little effect on the collection rate, proving that the film is of tensile strength after its mechanical properties have been reinforced, which greatly improved the collection of the side and middle parts of the film that are difficult to be collected.

(3) Continuous improvement to the reinforced film collector and the film itself

By far, mechanical collection is still the main method to collect film residues. After the mechanical properties of the film being reinforced, the collection rate can be remarkably raised. For the reinforced film collector, the average collection efficiency is 0.22 hm^2/h. With ensuring the collection rate, the efficiency can be further raised by properly increasing the forward velocity of the collector, which can also cut the cost of the collection.

Acknowledgments

The work was supported by the Public Welfare Industry (Agriculture) special researchNo.201503105; National Natural Science Foundation of China No.11562019; National Key Research and Development Plan of the 13th Five-year Plan No.2017YFD0701102-1; Group innovation project of Tarim University No.TDZKCX201501.

[References]

[1] Dong, H.G., T. Liu, Y. G. Li, H. F. Liu, and D. Wang. 2013. Effects of plastic film residue on cotton yield and soil physical and chemical properties in Xinjiang. *Transactions of the Chinese Society of Agricultural Engineering*, 29(8): 91–99. (In Chinese with English abstract)

[2] Dai, F., W. Y. Zhao, F. W. Zhang, Z. Wu, X. Song, and Y. Wu. 2016. Optimization and experiment of operating performance of collector for corn whole plastic film mulching on double ridges. *Transactions of the Chinese Society of Agricultural Engineering*, 32(18): 50–60. (In Chinese with English abstract)

[3] Ghasem, A., and A. Ebrahim. 2013. Design and evaluation a pendulum device to study postharvest mechanical damage in fruits: bruise modeling of red delicious apple. *Australian Journal of Crop Science*, 07(07): 962–968.

[4] He, W. Q., C. R. Yan, C. X. Zhao, R. Q. Chang, Q. Liu, and S. Liu. 2009. Study on the pollution by plastic mulch film and its countermeasures in China. *Journal of Agro-Environment Science*, 28(3): 533–538. (In Chinese with English abstract)

[5] He, W. Q., C. R. Yan,S. Liu, R. Q. Chang, X. J. Wang, S. L. Cao, and Q. Liu. 2009. The Use of Plastic Mulch Film in Typical Cotton Planting Regions and the Associated Environmental Pollution. *Journal of Agro-Environment Science*, 28(8): 1618–1622. (In Chinese with English abstract)

[6] Hou, S. L., S. Y. Hu, J. M. Kong, H. Y. Zhang, M. J. Na, and X. Dong. 2002. Present situation of Research on plastic film residue collector in China. *Transactions of the Chinese Society of Agricultural Engineering*, 18(3): 186–190. (In Chinese with English abstract)

[7] Hu, C., Y. S. Hu, X. F. Wang, and W. Wang. 2017. Effect of residual plastic films on survival rate of cotton seeds in South Xinjiang. *International Agricultural Engineering Journal*, 26(2): 19–25.

[8] Kyrikou, I., D. Briassoulis, M. Hiskakis, and E. Babou. 2011. Analysis of photo-chemical degradation behavior of polyethylene mulching film with pro-oxidants. *Polymer Degradation and Stability*, 96(12): 2237–2252.

[9] Liu, J. D., W. B. Cao, D. Y. Tian, H. Y. Tang, and H. Z. Zhao. 2016. Kinematic analysis and experiment of planetary five-bar planting mechanism for zero-speed transplanting on mulch film. *International Journal of Agricultural and Biological Engineering*, 9(4): 84–91.

[10] Liu, E. K., J. B. Wang, Y. Q. Zhang, D. A. Angers, C. R. Yan, T. Oweis, and B. Q. Chen. 2015. Priming effect of 13C-labelled wheat straw in no-tillage soil under drying and wetting cycles in the Loess Plateau of China. *Scientific Reports*, 05(13826): 13826–13842.

[11] Manoj, K. P., H. K. Sahoo, M. K. Nayak, and C. Ghanshyam. 2016. Plausibility of variable coverage high range spraying: Experimental studies of an externally air-assisted electrostatic nozzle. *Computers and Electronics in Agriculture*, 127: 641–651.

[12] Meng, X. Y., X. F. Wang, C. Hu, J. Y. Jiang, and F. Han. 2013. The Design and test of a new film processing machinery. *Information Technology Journal*, 12(22): 6998–7003.

[13] Polat, R., T. Aktas, and A. Ikinci. 2011. Selected mechanical properties and bruise susceptibility of nectarine fruit. International Journal of Food Properties, 15(6): 1369–1380.

[14] Wang, X. F., C. Hu, B. Lu, and J. Y. Jiang. 2017. Wind tunnel test on damages of plastic film under the wind-sand effect in south Xinjiang of China. *International Agricultural Engineering Journal*, 26(1): 16–23.

[15] Xie, J. H., S. L. Hou, Y. Fu, M. Na, and H. Zhang. 2013. Motion analysis and experiment on spring-tooth mulching plastic film collector. *Transactions of the Chinese Society for Agricultural Machinery*, S1: 94–99. (In Chinese with English abstract)

[16] Yan, C. R., X. R. Mei, W. Q. He, and S. Zheng. 2006. Present situation of residue pollution of mulching plastic film and controlling measures. *Transactions of the Chinese Society of Agricultural Engineering*, 22(11): 269–272. (In Chinese with English abstract)

[17] Yin, T., W. Q. He, C. R. Yan, S. A. Liu, and E. K. Liu. 2014. Effects of plastic mulching on surface of no-till straw mulching on soil water and temperature. *Transactions of the Chinese Society of Agricultural Engineering*, 30(19): 78–87. (In Chinese with English abstract)

[18] Zhao, Y., X. Zheng, X. G. Chen, Q. Niu, C. Ji, and D. X. Zhou. 2017. Design and test of CMJY-1500 type plastic film residue collecting and balling machine. *Transactions of the Chinese Society of Agricultural Engineering*, 33(5): 1–9. (In Chinese with English abstract)

CFD numerical simulation and optimization of the flow fields in the chopping chamber of flail chopper

Zhang Zhiqiang[1], Allen D. McHugh[2], Li Hongwen[1], Chen Liqing[3], He Jin[1], Lu Caiyun[1], Zheng Zhiqi[1], Wang Qingjie[1*]

(1. *College of Engineering, China Agricultural University, Beijing 230036, China*;
2. *International Maize and Wheat Improvement Center, Dhaka 1213, Bangladesh*;
3. *College of Engineering, Anhui Agricultural University, Hefei 230036, China*)

Abstract: The flail chopper is a common agricultural machine used widely to manage in-field crop residues and for mowing cover crops. Straw chopping quality and spreading uniformity have direct impact on seeding quality of no-till seeders, seed germination and crop growth. To understand chopping and spreading performance, three-dimensional flow fields under the hood of a flail chopper were simulated by the computational fluid dynamics (CFD), in which FLUENT software was used and the RNG k-ε turbulence model and multiple reference frame (MRF) method were adopted. Streamlines and core region vortices within the chopping chamber, as well as pressure on targeted sampling planes, rotor and inlet were also analyzed. The simulation results showed that flow at the chopping chamber inlet to the rotor was smooth at relative low velocity. The rotor generated negative pressure at the inlet and increased fluid flow velocity. However, in the chamber, velocity increased and it generated numerous vortices. Consequently, some flow was discharged non-uniformly and at low velocity, while the remaining flow continually rotated with the rotor and with partial lateral transfer. Pressure on the rotor was symmetrically distributed in the axial direction. Regions of high-pressure occurred at chopping blade and fan blade tips. Fan blades increased negative pressure zones at either end of the chopping chamber inlet. However, pressure at outlet was symmetrically distributed horizontally. Mounting guide vanes at the chopping chamber outlet reduced vortices and redirected flows toward the outlet which could improve straw flow-ability and spreading performance. CFD analysis provided the significant information on the influence of flail chopper's design parameters under steady state conditions. To further optimize fluid flow characteristics and performance of the chopper, continued studies under variable conditions are required.

Keywords: flail chopper, chopping chamber, guide vane, fan blades, fluid flow

Citation: Zhang, Z. Q., A. D. McHugh, H. W. Li, L. Q. Chen, H. Jin, C. Y. Lu, Z. Q. Zheng, and Q. J. Wang. 2017. CFD numerical simulation and optimization of the flow fields in the chopping chamber of flail chopper. International Agricultural Engineering Journal, 26(4): 74–84.

1 Introduction

Crop straw field retention has been considered as an important technology to improve soil fertility, increase soil organic matter, improve soil texture, accelerate the activation of microorganism and promote crop growth (Peng et al., 2014; Li et al., 2015). It has also been considered as an environmental-friendly technology by reducing residue burning and fertilizer application (Balwinder-Singh et al., 2011; Bao et al., 2016). Although residue can be retained as standing stubble, it is often chopped and spread by combine harvesters or tractors powered flail choppers. Under the conventional farming, the chopped and mulching straw is often tilled into soil with high soil disturbance tillage machinery before seeding or just left on the soil surface in no-till farming systems (He et al., 2013).

Straw chopping quality and spreading uniformity are key performance parameters on flail choppers (Siemens, 2006), which have direct impact on seeding quality of

Received date: 2017-08-14 **Accepted date:** 2017-11-10
* **Corresponding author: Wang Qingjie,** Ph.D., Associate Professor of College of Engineering, China Agricultural University, Beijing 230036, China. Email: wangqingjie@cau.edu.cn.

no-till seeders, seed germination and crop growth. Straw chopping quality of flail choppers have been studied from numerous aspects of; structural parameters (blade shape, arrangement), operating parameters (rotor speed, forward velocity), and crop straw characteristics (type and moisture content) (Wu et al., 2001; Tavakoli et al., 2009; Jia et al., 2015; Singh et al., 2011).

Once the standing straw is cut by the chopping blades, it is drawn into chopping chamber, the motion of the cut straw is mainly affected by chopping blades and airflow. The influence of chopping blades exists during blade contact the straw, while the airflow influence lasts throughout chopping and spreading processes and affected by the hood shape and design. Air flow acts as the straw carrier, and its distribution has significant effect on straw feeding, chopped quality and spreading uniformity. Therefore, fluid flow dynamics is an important characteristic of flail choppers in determining the mechanisms of straw chopping and spreading. However, few studies have been conducted to determine the impact of chopper parameters on fluid flow characteristics of the straw within the hood of a flail chopper and its discharge.

The flow of straw under field conditions in flail chopper is complex, which makes it difficult to acquire three-dimensional flow characteristics in the chopping chamber in an operational setting. Thus, it is necessary to simulate straw fluidity via Computer Fluid Dynamic (CFD) methods. CFD technology has been widely applied to agricultural equipment design and operational analysis. Tong et al. (2016) simulated the mixed flow fields produced by fans and threshing rollers in an axial flow cleaning device with CFD software. Endalew et al. (2010) simulated air flow and droplet movements for an air-assisted orchard sprayer to improve spray deposition on leaves. Ponpesh et al. (2008) applied CFD modelling to reduce particulate matter emissions of a nut harvester. Wang et al. (2007) constructed a three-dimensional model of a flail chopper to simulate the influences of chopper structural parameters on the wind field. In this paper, the re-normalization group (RNG) k–ε turbulence model and multiple reference frame (MRF) method in FLUENT software were used to simulate three-dimensional fluid flow fields under a common rounded hood flail mower/chopper. Utilizing the above methods, it was hypothesized that the fluid flow performance could be improved by the inclusion of guide vanes mounted at the outlet of a flail chopper.

2 Numerical calculation model

The simulated chopping chamber (Figure 1) consisted of a hood and a flail rotor. The hood consisted of left, and right end plates, front case and backboard. The flail rotor included rotor, chopping blades and fan blades. The fan blades were mounted on the left and right ends of the rotor, while the chopping blades were helical mounted along the rotor. In operation, standing residue is pulled down by the frame of the chopper, and then cut off and gripped by the high-speed chopping blades or flails which are mounted on the rotor in the chopping chamber under the hood. The size reduction of crop residue is conducted by cutting, tearing, rubbing, and striking action of chopping blades in the chamber; the chopped residue is expelled to the ground from the rear of chopping chamber.

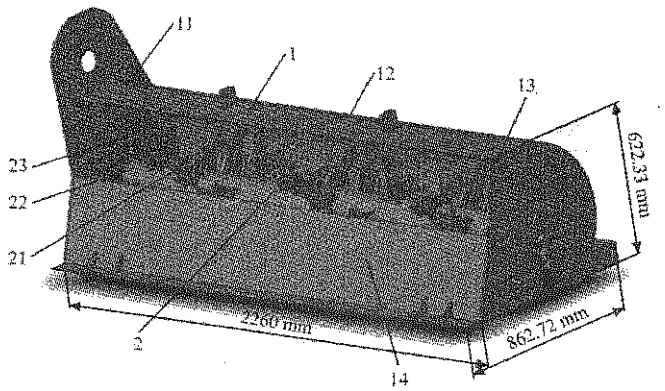

1. Hood 2. Flail rotor 11. Left end plate 12. Front case 13. Right end plate 14. Backboard 21. Chopping blade 22. Rotor 23. Fan blade

Figure 1 Structure diagram of chopping chamber

Hood parameters have a significant influence on fluid flow, which can affect the motion of straw in the chopping chamber (Zheng, 2017). There are generally two types of front case: broken-line type and curved type. The curved type front case (Figure 2) was chosen for the simulation, considering the airflow direction in the chopping chamber is similar to that of a cross-flow fan (Zhang et al., 2017). The equation for the front case profile in the simulation can be written as follows:

$$R=281\cdot e^{\frac{(\theta-30°)}{359°}} \quad (1)$$

where, θ and R are the angle and radius that define a generic point of this profile.

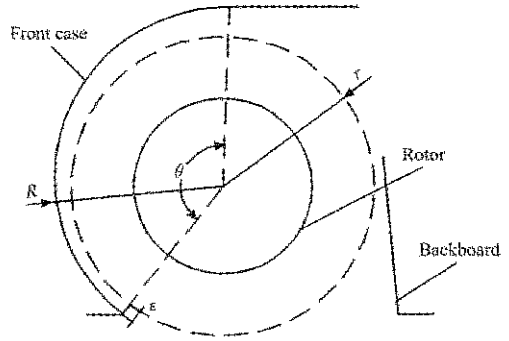

Figure 2 Structural parameters of the curved front case

The main design parameters of the flail chopper, including the chamber used for the simulation, are presented in Table 1.

Table 1 Parameters of chopping chamber

Technical parameters	Design values
Chopping chamber dimensions L×W×H, mm	2260×862.72×622.33
Rotor speed, r/min	2100
Rotor diameter, mm	170
Rotating flail rotor radius, mm	276
Hood clearance, mm	140
Number of chopping blades	42
Chopping blade arrangement	helical
Number of fan blades	12

3 Numerical simulation methods

3.1 Governing equations

To simulate fluid flow characteristics in a chopping chamber, the flow was assumed to be steady, viscous, incompressible, turbulent, and adiabatic. The basic equations of fluid flow, conservation of mass (the continuity equation) and conservation of momentum (the Cauchy). governed the simulation of the fluid flow characteristics.

The equation for the conservation of mass for steady and incompressible flows, in Cartesian tensor form, can be written as follows (Sahili et al., 2013):

$$\frac{\partial}{\partial x_i}(\rho u_i)=0 \quad (2)$$

where, u_i is the velocity component in the i direction; ρ is the fluid density.

The equation for the conservation of momentum for steady flows, in Cartesian tensor form, can be written as follows (Brown et al., 2001):

$$\frac{\partial}{\partial x_j}(\rho u_i u_j)=-\frac{\partial p}{\partial x_i}+\frac{\partial \tau_{ij}}{\partial x_j}+F_i \quad (3)$$

where, p is the static pressure; τ_{ij} is the stress tensor; F_i is the body force.

The continuously rotating of the flail rotor and geometric changes in the circumferential direction generates swirling and rotating flow. A three-dimensional rotating model was built to simulate flow field in the chopping chamber. The RNG k-ε turbulence model as used by Li et al. (2006) was considered more suitable to simulate the turbulent flow in this study than the standard k-ε turbulence model (Tutar and Oguz, 2002).

The equations of RNG k-ε model are as follows:

$$\frac{\partial(\rho k)}{\partial t}+\frac{\partial(\rho k u_j)}{\partial x_j}=\frac{\partial}{\partial x_j}[\alpha_k \mu_e \frac{\partial k}{\partial x_j}]+\rho(P_k-\varepsilon) \quad (4)$$

$$\frac{\partial(\rho \varepsilon)}{\partial t}+\frac{\partial(\rho \varepsilon u_j)}{\partial x_j}=\frac{\partial}{\partial x_j}[\alpha_\varepsilon \mu_e \frac{\partial \varepsilon}{\partial x_j}]+\rho\frac{\varepsilon}{k}(C_{1\varepsilon}{}^{*}P_k-C_{2\varepsilon}{}^{*}\varepsilon) \quad (5)$$

where

$$C_{1\varepsilon}{}^{*}=C_{1\varepsilon}-\eta(1-\eta/\eta_0)/1+\beta\eta^3 \quad (6)$$

and

$$\eta=(2E_{ij}\cdot E_{ij})^{1/2}\frac{k}{\varepsilon} \quad (7)$$

and

$$E_{ij}=\frac{1}{2}(\frac{\partial u_i}{\partial x_j}+\frac{\partial u_j}{\partial x_i}) \quad (8)$$

The constants in the RNG k-ε model are specified as: C_μ=0.0845, α_k=α_ε=1.39, $C_{1\varepsilon}$=1.42, $C_{2\varepsilon}$=1.68, η_0=4.377, β=0.012.

3.2 Boundary conditions

A set of initial and boundary conditions should be provided to solve the equations of motion for any specific flow problems. As the simulation involved a steady-state solution, an initial condition was not set. Boundary conditions which specify the values of dependent variables at the boundaries of the fluid domain were required for the simulation.

No-slip condition and standard wall functions were

used at the end plates and chopping blades. The pressure inlet boundary condition at the chopper inlet was set with a gauge pressure at 0 Pa. The pressure outlet boundary condition was also set at 0 Pa. An interface between the rotor and hood was formed under rotating conditions.

3.3 Computational domain and mesh generation

Flow characteristics differed along the axial direction of the rotor due to the fan blades and the helical arrangement of the chopping blades. Therefore, a three-dimensional model of the chamber (Figure 3) was built while ignoring some characteristics and components of the common flail chopper, such as bearings, blade holders and bolts. The computational domain of the chopping chamber (Figure 4) was acquired by extracting internal flow fields of the simplified three-dimensional structure.

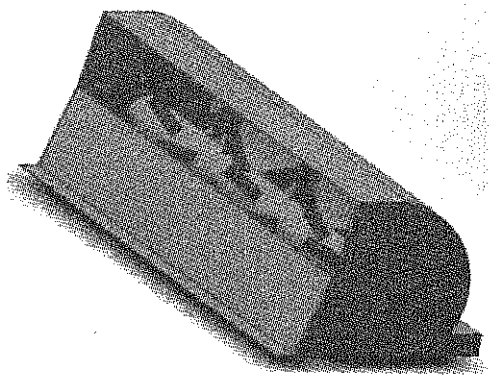

Figure 3 Structure of the simplified 3D chopping chamber

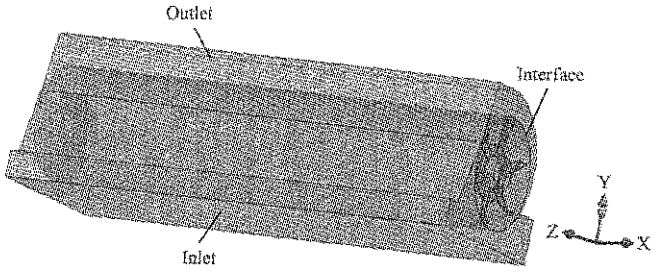

Figure 4 Computational domain of the chamber

The computational domain consisted of a curved hood and rotor domain, while the lower side of the hood was extended to the ground surface (Chon et al., 2005). The hood domain was a stationary region, while the rotor domain was a rotating region. The MRF model was chosen to simulate the rotating region at 2100 r/min.

A tetrahedral mesh (Figure 5a) was generated to account of the complexity of the flail chopper geometry, which was transformed into the polyhedral mesh (Figure 5b). The minimum orthogonal quality, maximum ortho skew and maximum aspect ratio were used to check the mesh quality.

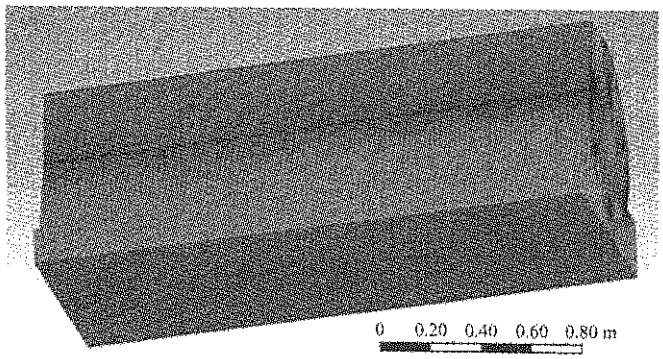

a. Tetrahedral mesh

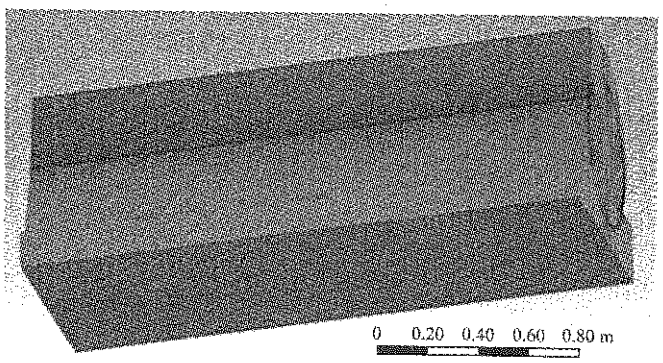

b. Polyhedral mesh

Figure 5 Grid generation for three-dimensional chopping chamber

Comparisons between tetrahedral and polyhedral mesh model were shown in Table 2. The results indicated that the mesh number decreased by 75.5%, when changing from tetrahedral to polyhedral mesh, which was indicative of improved computational speed. Improved mesh quality increased the accuracy of the solution via an increase in minimum orthogonal quality, a decrease in maximum ortho skew and maximum aspect ratio. Therefore, using polyhedral mesh to simulate the flow fields under the hood of a flail chopper ensured computing speed and accuracy.

Table 2 Comparisons between tetrahedral mesh and polyhedral mesh model

Mesh type	Mesh number	Minimum orthogonal quality	Maximum ortho skew	Maximum aspect ratio
Tetrahedral mesh	3568936	0.0995142	0.839327	34.1466
Polyhedral mesh	873186	0.192358	0.807642	19.8306

3.4 Sampling sections

Five sampling sections (planes) P1 to P5 (Figure 6) were selected to analyze fluid flow characteristics in the chopping chamber. Section P1 paralleled the Y-Z plane and passed through the left-side fan blades; section P2

was the symmetrical plane; section P3 paralleled the Y-Z plane and passed through the right-side chopping blades; section P4 was the top plane of the hood; and section P5 paralleled the X-Y plane which passed through the centreline of the rotor.

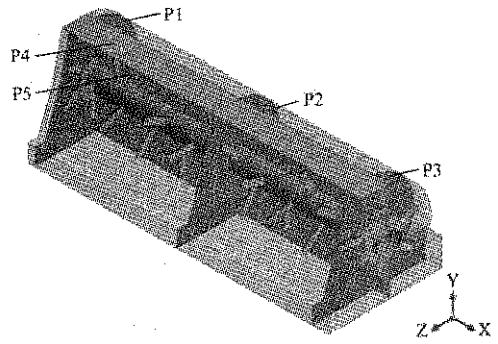

Figure 6 Sampling planes P1-P5 and their locations of sampling sections in the chopping chamber

4 Results and discussions

4.1 Velocity field in the chopping chamber

Streamlines inside the chopping chamber were shown in Figure 7. Flow was turbulent, especially in the flail rotor areas. Rotor rotation forced part of the fluid flowing out at the hood outlet, while part continually rotated with the rotor. Under field condition's chopped straw would have followed the same path (Zhai et al., 2013). A reduction of continually rotating straw by optimizing some design parameters would improve the performance of the flail chopper.

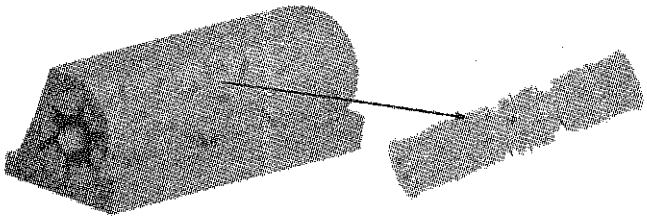

Figure 7 Streamlines in chopping chamber

Numerous vortices were generated on the entire surface of the rotor flails in the core regions of the chopping chamber as shown in Figure 8. The vortices on the chopping blade surfaces were concentrated on the leeward and windward sides of the chopping blade, with larger vortices on the windward side. The formation of the vortices was closely related to the special shape of the hood (curved), therefore straw flow-ability and chopping quality in the chopping chamber could be improved by optimizing the hood structure parameters. Chen et al. (2007) found that by increasing hood angle improved straw chopping quality but increased power consumption.

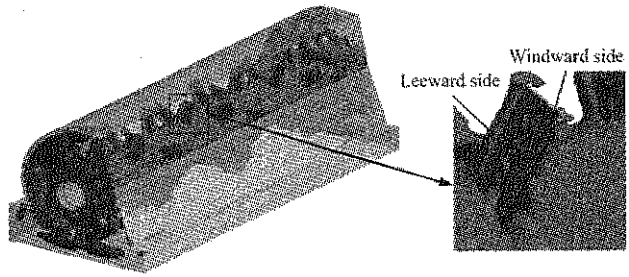

Figure 8 Core vortex regions in the chopping chamber

Streamlines and velocity contours at sampling plans were shown in Figure 9 and Figure 10, respectively. Two disruptive vortex regions appeared at P1 near the lower back and inlet of the chopping chamber (Figure 9a) while at P2 several vortex regions were developed near chopping chamber outlet (Figure 9b). At P3 vortices were generated at the front case (Figure 9c) but generally uniform in the chopping chamber. Results shown in Figure 9d indicated that flow velocity at P5 was layered about the core with the velocity decreasing from the center. Velocity was symmetrically distributed in a horizontal direction with considerable vortices about each chopping blade. Reducing of these vortices and uniform distribution of outlet velocities in the horizontal direction could improve straw spreading uniformity.

Fluid velocity uniformly increased from the rotor surface to the tip of the chopping blades, while it increased unevenly from the rotor surface to the tip of the fan blades (Figure 10a and 10b). The different velocity distributions on the fan blade may be influenced by fan shape which is irregular with some bend and curved surfaces. According to Li et al. (2008) high blade tip velocity (minimum of 48 m s^{-1}) ensures good straw chopping and spreading uniformity.

Fluid flow from the inlet rotor was smooth (Figure 9d and 10c). However, on entering the rotor domain it began to rotate with increasing velocity. On reaching the top of the hood, flow velocity decreased and became less disordered. Under field conditions straw would initially accelerate and then decelerate once in the chamber. Continuous rotation of the rotor converted mechanical energy to fluid kinetic energy, thus increased fluid velocity. Some similar results from fan, pump and other rotating machines, indicated that fluid velocity at inlets

was low and gradually increased with flow direction (Shuai et al., 2015; Wang et al., 2010). In this current study vortices were generated in the rotary sampling plane, especially around the chopping blades and fan blades. The existence of these vortices would decrease straw flow-ability in the chopping chamber.

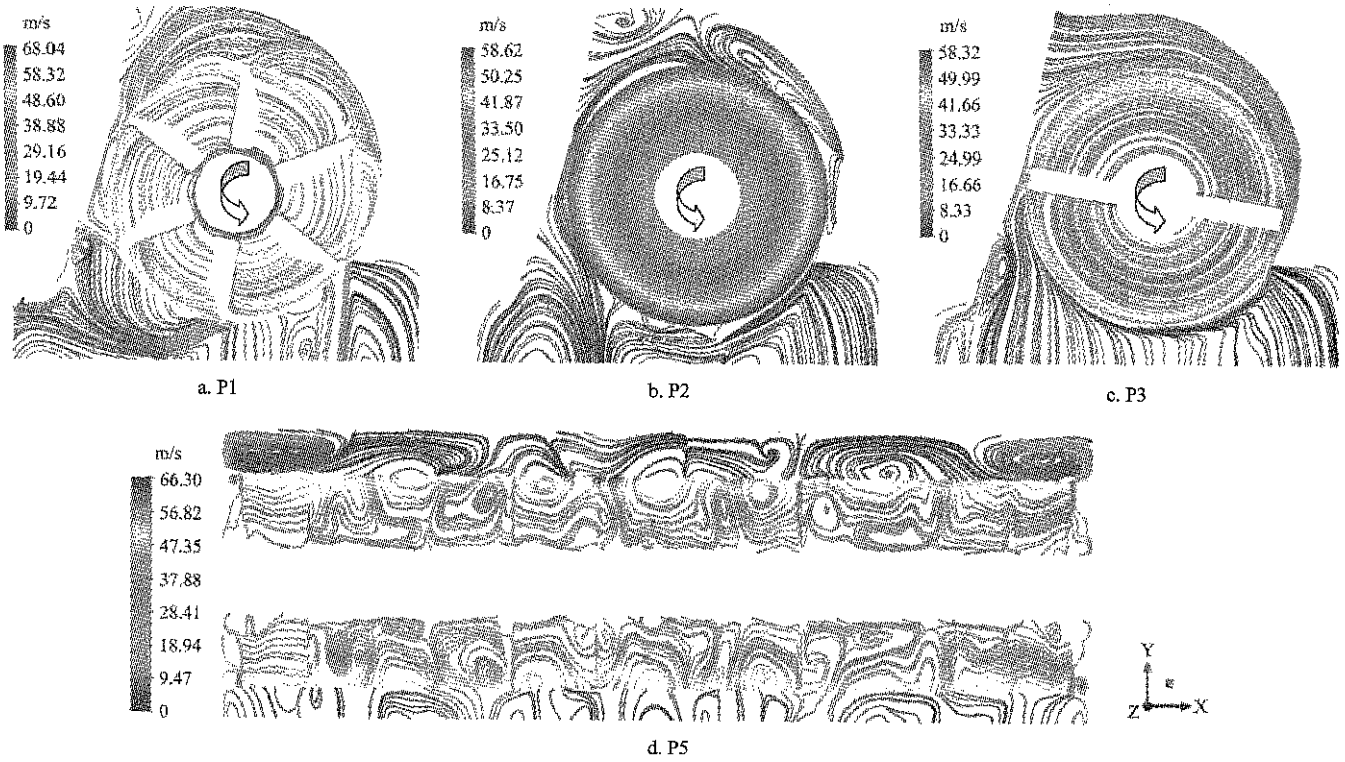

a. P1 b. P2 c. P3

d. P5

Figure 9 Streamlines at sampling plans, P1, P3 and P5 in the chopping chamber and along the rotor core

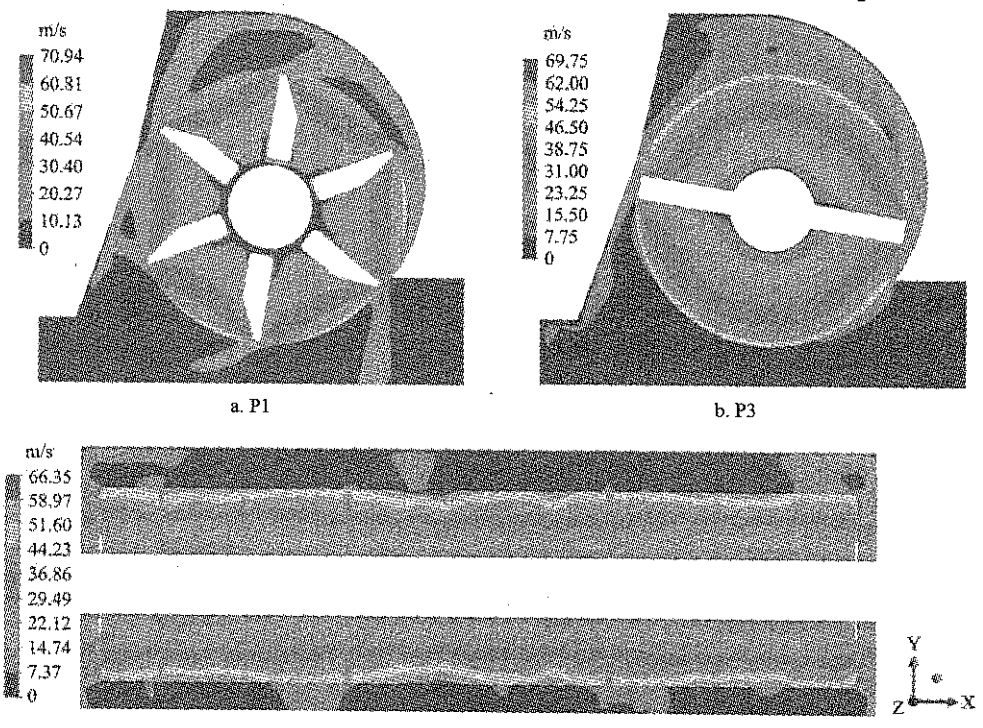

a. P1 b. P3

c. P5

Figure 10 Velocity contours at the P1, P3 and P5 sampling plan

The distribution of velocity vectors in the upper section (P4) was show in Figure 11 and divided into five activity zones. Fluid flow in the zones of P4 was complex, in that flows were expelled, some were transferred from side to side, and other flows re-entered, which were attributed to the helical positioning of the chopping blades. Flow velocities in zone 1 and zone 5 (Figure 12a and 12b) were higher than those in the other three zones.

Although some flows were expelled the majority of flows re-entered P4 via these outer zones. Flows in zone 2 and zone 4 (Figures 12d and 12e) were transverse and exchanging between adjacent zones. The expulsion flow in zone 3 (Figure 12c) was generally concentrated on the right side, but was also expelled from the left side of the zone. Reducing outlet restrictions, reducing flow concentration and transverse flow between chopping blades at P4 with guide vanes would redirect flow through the outlet and improve straw spreading performance.

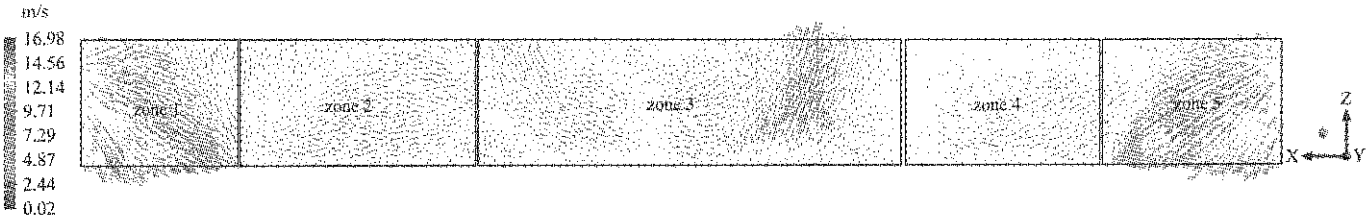

Figure 11 Distribution of velocity vectors in zone 1-5 of section P4

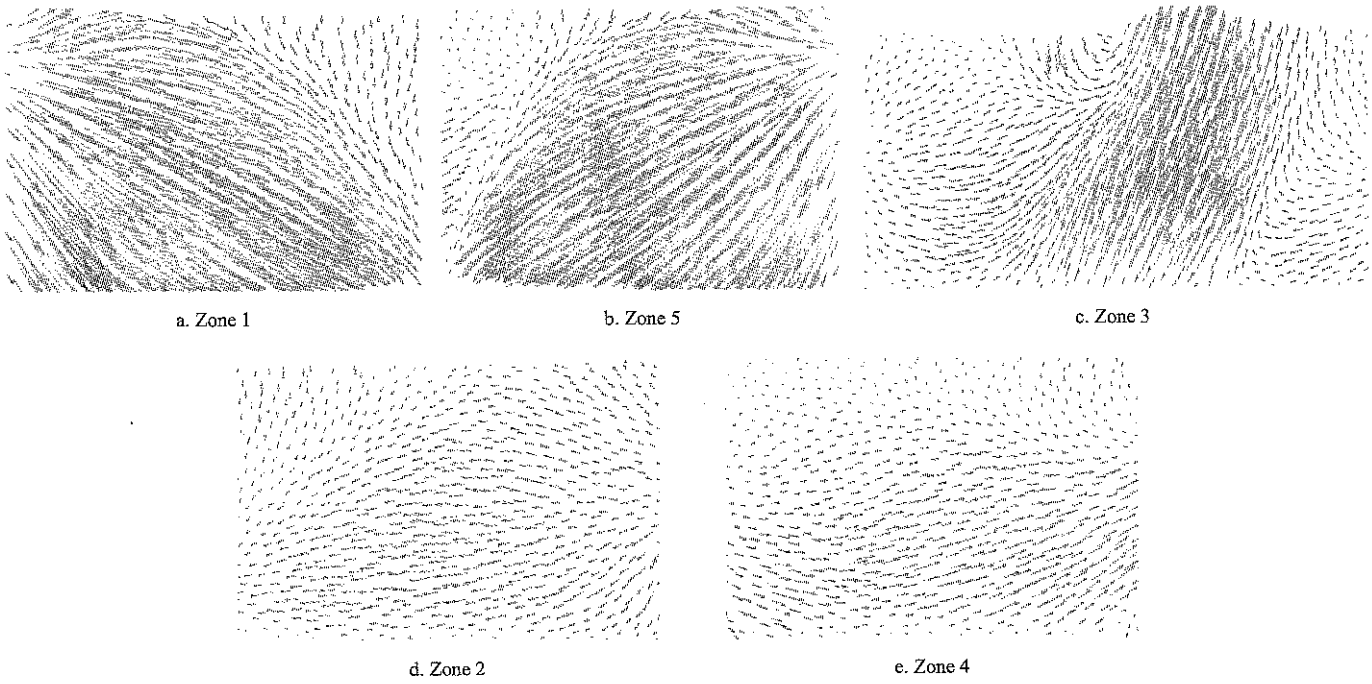

a. Zone 1 b. Zone 5 c. Zone 3

d. Zone 2 e. Zone 4

Figure 12 Magnified distribution of velocity vectors on zones of section P4 of the chopping chamber

4.2 Pressure field in the chopping chamber

Pressure field contours around the rotor and sampling planes were shown in Figure 13 and Figure 14, respectively. Pressure around the rotor was symmetrically distributed in the axial direction, with high-pressure zones occurring at the tip of the chopping blades and fan blades (Figure 13). Yang et al. (2016) also found high pressure regions at the tip of fan blades. In the current study, the pressure on the windward side of the chopping blade and fan blade was higher than that in the surrounding areas, while the opposite was true for the leeward side (Figures 14a and 14c). High pressure on the windward side was expected, as it impacted directly on the fluid flow. Chon et al. (2005) also found that the highest-pressure occurred at the front of rotating blades, and the pressure was generally lower near the rotating centers. Figure 14b was indicative of that pressure increased from surface of the rotor to the windward tips of the flail and increased pressure in hood beyond the blades.

Pressure contours at the chopping chamber inlet as shown in Figure15 indicated the negative pressure generated by the rotor's high-speed revolution, especially around the fan blade areas. The pressure at the outlet was symmetrically distributed in a horizontal direction. According to Sun et al. (2016) negative pressure at the chopping chamber inlet is conducive to straw feeding.

4.3 Flow characteristics in the chopping chamber with guide vanes

In order to improve the spreading uniformity of the chopped straw, several guide vanes were symmetrically

mounted at outlet of the chopping chamber (Zhang et al., 2017). The guide vanes are usually curved plates, which generally influence the motion of straw discharge. The computational domain of the chopping chamber with eight guide vanes for numerical simulation is shown in Figure 16. Plane P4 was divided into nine zones according to the guide vane positions, and nine sampling points were selected on the edge of plane P4 in each zone.

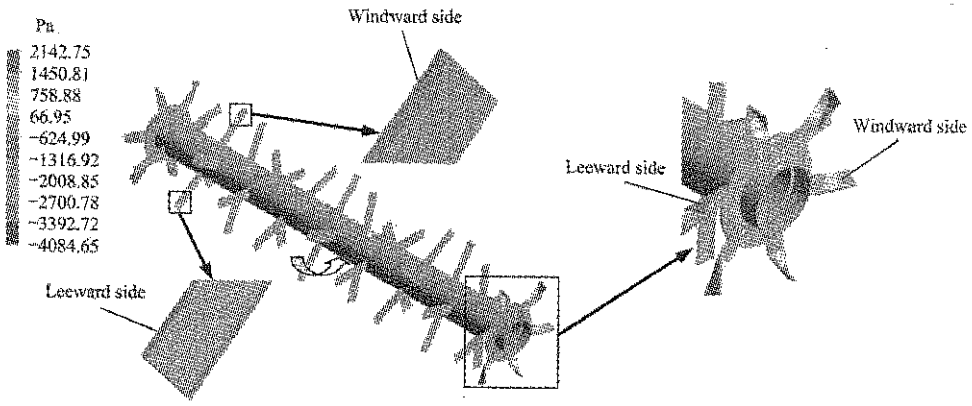

Figure 13 Pressure contours around the rotor and blades

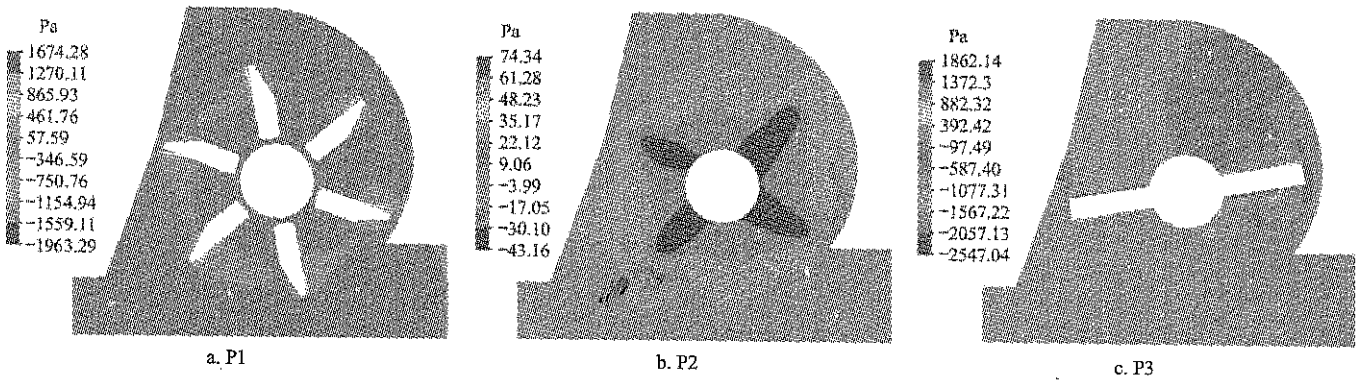

a. P1 b. P2 c. P3

Figure 14 Pressure contour at the sampling planes of P1(a), P2(b) and P3(c) in the chopping chamber

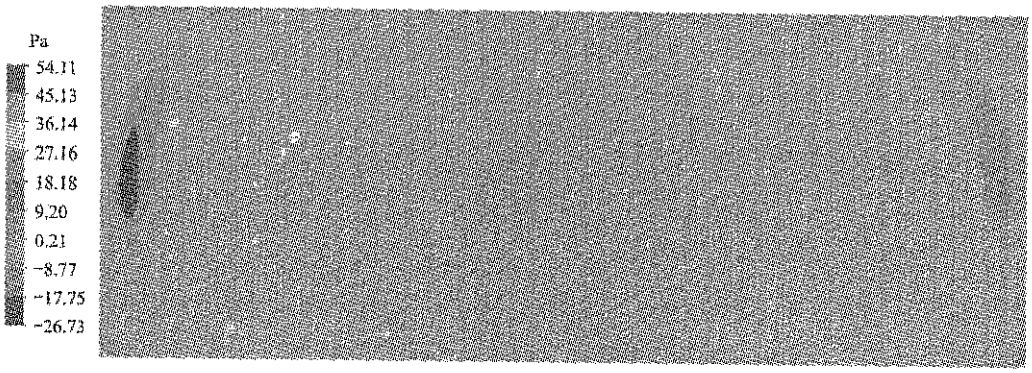

Figure 15 Contours of pressure field at inlet of chopping chamber

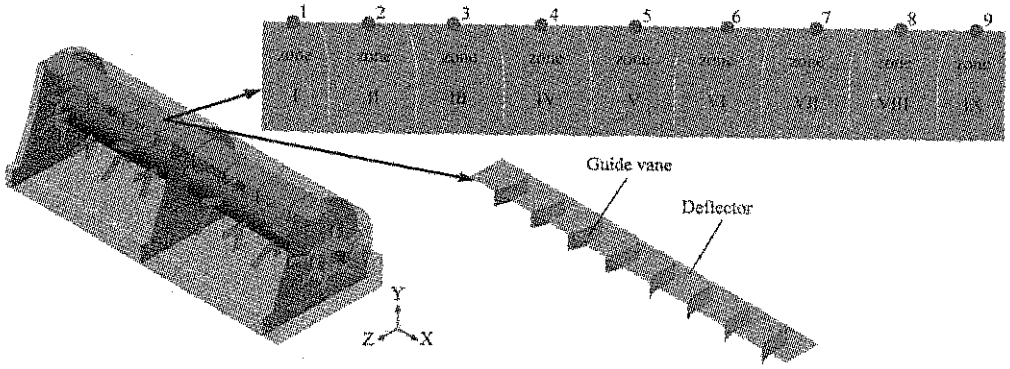

Figure 16 Computational domain of 9 zones (I-IX) and sampling points 1-9 of a chopping chamber fitted 8 with guide vanes

The distribution of velocity vectors on plane P4 using guide vanes demonstrated a significant effect on the fluid flow redirections at the outlet. The fluid velocity in zone I and zone IX (Figures 17a and 17b) was higher than that in other zones due to the fan blades, and most of the flow in these two zones was directed toward the guide vanes with marginal change in direction. Flow in zone V (Figure 17d) was homogeneous and all flow was expelled through the chopping chamber outlet. Flow in zones II and VIII (Figures 17e and 17f) was strongly deflected off the inner vanes. Flow direction in zone III and VII (Figure 17g and 17h) was similar to each other, where central flow was redirected from two adjacent guide vanes to the outlet. Flow vector distribution in zone IV and VI (Figures 17i and 17j) was similar to each other, where fluid flow was deflected off adjacent vanes and discharged centrally. It can be concluded that adding guide vanes at the chopping chamber outlet improved velocity distribution uniformity and increased the amount of discharge flow at outlet by reducing transverse flow and random flow.

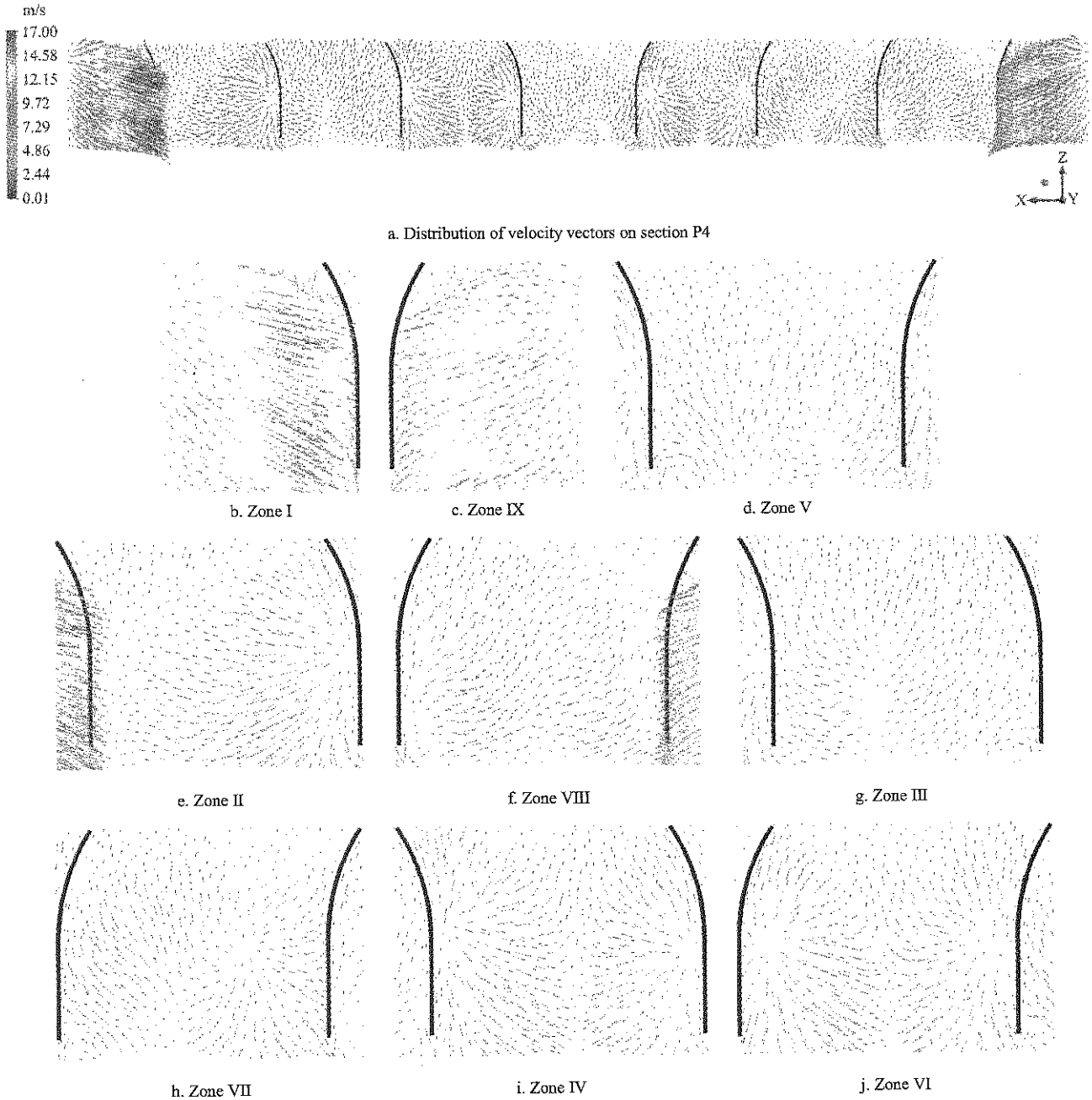

a. Distribution of velocity vectors on section P4

b. Zone I c. Zone IX d. Zone V

e. Zone II f. Zone VIII g. Zone III

h. Zone VII i. Zone IV j. Zone VI

Figure 17 Distribution of velocity vectors on section P4 in the chopping chamber with guide vanes

Streamlines on P1, P2 and P3 shown in Figure 18a, b and c demonstrated that flow in the chopping chamber with guide vanes was relatively smooth, especially at P3. Complex vortices in the regions of P1, P2 and P3 were

reduced after addition of guide vanes, however there were still some recirculation zones on P2. The use of guide vanes appeared to improve flow-ability in chopping chamber compared to chambers without guide vanes (Figure 9).

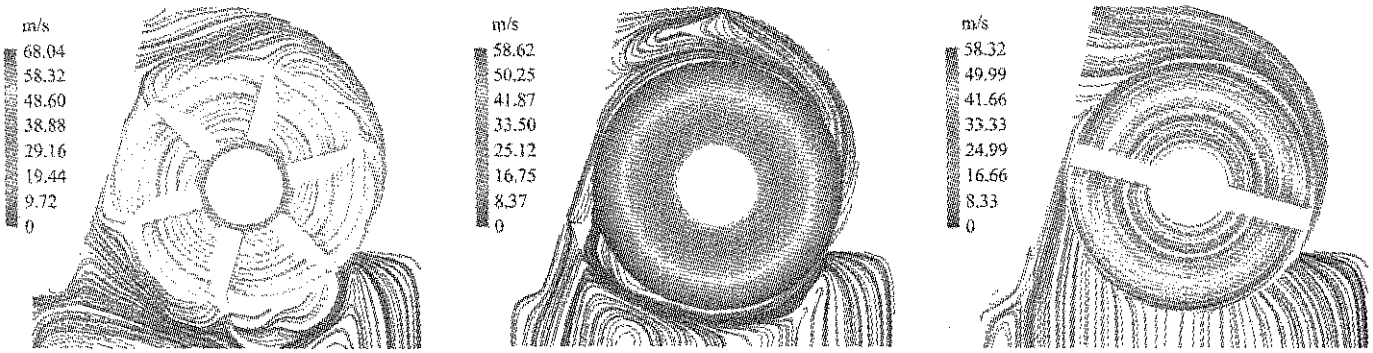

a. P1 b. P2 c. P3

Figure 18 Streamlines on sampling plans in the chopping chamber with guide vanes

Velocities at nine sampling points on P4 shown in Figure 19 were indicative of the non-uniformity in velocity distribution without guide vanes in chopping chambers, especially at points 1, 4 and 9. Whereas with guide vanes at sampling points 2 to 8 along the P4 plane velocity was uniform. Velocity at points 1 and 9 was considerably larger under both simulated conditions, when vanes were included, velocity increased at these two points.

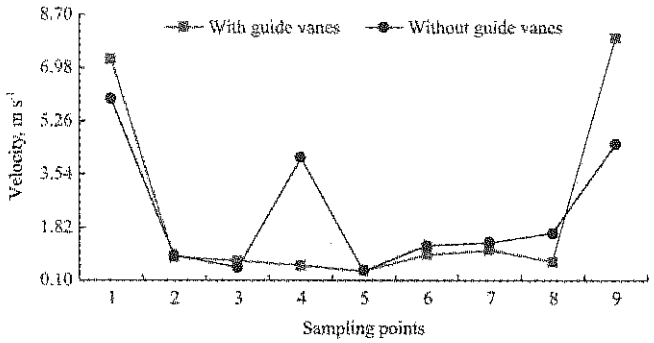

Figure 19 Velocity at sampling points on P4

5 Conclusions

The internal flow field in the chopping chamber of flail chopper, and performance of the flail chopper with and without guide vanes was successfully simulated and analyzed by CFD. The analysis demonstrated:

(1) Flow from the inlet to rotor was initially smooth with relative low velocity, however in the chamber, velocity increased, it generated numerous vortices. Consequently, some flow was discharged non-uniformly and at low velocity, while the remaining flow continually rotated with the rotor and with partial lateral transfer.

(2) Fan blades increased negative pressure zones at either end of the chopping chamber inlet. Pressure on the rotor was symmetrically distributed in the axial direction with highest pressure at blade tips. The pressure and velocity were larger on the windward side of all blades than those in the surrounding areas, while the opposite was true on the leeward side.

(3) Mounting guide vanes at the chopping chamber outlet reduced vortices and redirected flows toward the outlet which could improve straw flow-ability and spreading performance.

Acknowledgments

This work was supported by the Special Fund for Agro-scientific Research in the Public Interest from the Ministry of Agriculture, China (Grant No. 201503136) and the Program for Changjiang Scholars and Innovative Research Team in University of China (Grant No. IRT13039).

[References]

[1] Balwinder-Singh, E. Humphreys, P. L. Eberbach, A. Katupitiya, Yadvinder-Singh, and S. S. Kukal. 2011. Growth, yield and water productivity of zero till wheat as affected by rice straw mulch and irrigation schedule. *Field Crops Research*, 121(2): 209–225.

[2] Bao, H. M., and J. Lin. 2016. The design and simulation analysis of maize field straw chopper. *Journal of Agricultural Mechanization Research*, 11: 99–103. (in Chinese)

[3] Brown, M. 2001. Velocity measurements near an automotive cooling fan. M.S. thesis. Windsor: University of Windsor.

[4] Chen, S. T., X. J. Zhou, Q. X. Shi, S. D. Liu, J. Pang, and G. W. Han. 2007. Experiment and optimization on factors affecting the performance of wheat stalk macerator smashing devices. *Transactions of the Chinese Society for Agricultural*

Machinery, 38(9): 67–70, 62. (In Chinese with English abstract)

[5] Chon, W., and R. S. Amano. 2005. Investigation of flow behavior around corotating blades in a double-spindle lawn mower deck. *International Journal of Rotating Machinery*, 1: 77–89.

[6] Endalew, A. M., C. Debaer, N. Rutten, J. Vercammen, M. A. Delele, H. Ramon, B. M. Nicolaï, and P. Verboven. 2010. A new integrated CFD modelling approach towards air-assisted orchard spraying. Part I. Model development and effect of wind speed and direction on sprayer airflow. *Computers & Electronics in Agriculture*, 71(2): 128–136.

[7] He, Y. C., X. J. Wang, S. L. Cao, J. L. Wang, and M. Wang. 2013. Design of 1JH-3.0 wide field straw chopper. *Journal of China Agricultural University*, 18(6): 180–185. (in Chinese)

[8] Jia, H. L., X. M. Jiang, M. Z. Guo, X. L. Liu, and L. C. Wang. 2015. Design and experiment of V-L shaped smashed straw blade. *Transactions of the Chinese Society of Agricultural Engineering*, 1(1): 28–33. (In Chinese with English abstract)

[9] Li, M., J. L. Wang, Y. G. Deng, H. Huang, J. Zhang, D. Q. Song, and W. W. Lian. 2008. Structural design and experiments on sugarcane leaf shattering and returning machine. *Transactions of the Chinese Society of Agricultural Engineering*, 24(2): 121–126. (In Chinese with English abstract)

[10] Li, X. H., S. J. Zhang, B. L. Zhu, and Q. B. Hu. 2006. The study of the k-ε turbulence model for numerical simulation of centrifugal pump. *7th International Conference on Computer-Aided Industrial Design and Conceptual Design*, Hangzhou.

[11] Li, Y. P., H. W. Meng, J. Jia, K. C. Zhang, J. T. Qi, and X. Zheng. 2015. Development of 4JH -220 shattering and returning machine. *Journal of Agricultural Mechanization Research*, 7: 143–146. (in Chinese)

[12] Peng, C. Y., H. L. Luo, and J. Kong. 2014. Advance in estimation and utilization of crop residues. *Chinese Journal of Agricultural Resources and Regional Planning*, 35(3): 14–20. (in Chinese)

[13] Ponpesh, P., D. K. Giles, and D. Downey. 2011. Modeling turbulent multiphase flow in design of nut harvesters with reduce dust emission and low power demand. *Transactions of the ASABE*, 54(4): 1199–1211.

[14] Sahili, A., B. Zogheib, and M. R. Barron. 2013. 3-D Modeling of axial fans. *Applied Mathematics*, 4: 632–651.

[15] Shuai, Z. J., C. X. Jiang, D. H. Wang, Z. H. Zhou, and F. C. Li. 2015. Numerical simulation of dynamic flow characteristics in centrifugal water pump with three-vaned diffuser. *Advances in Mechanical Engineering*, 7(8): 1–12.

[16] Siemens, M. C., and D. E. Wilins. 2006. Effect of residue management methods on no-till drill performance. *Applied Engineering in Agriculture*, 22(1): 51–60.

[17] Singh, A., L. S. Dhaliwal, and A. Dixit. 2011. Performance evaluation of tractor mounted straw chopper cum spreader for paddy straw management. *Indian Journal of Agricultural Research*, 45(1): 21–29.

[18] Sun, L. J., and J. Feng. 2016. Research on the test method of straw scattering inhomogeneity for smashed straw machine. *Journal of Chinese Agricultural Mechanization*, 37(6): 35–38. (in Chinese)

[19] Tavakoli, H., S. S. Mohtasebi, and A. Jafari. 2009. Physical and mechanical properties of wheat straw as influenced by moisture content. *International Agrophysics*, 23(2): 175–181.

[20] Tong, S. G., Q. Shen, N. Tang, Y. P. Jia, F. Y. Cong, and W. Gu. 2016. Numerical simulation and optimization experiment of mixed flow field on longitudinal axial flow cleaning device. *Transactions of the Chinese Society of Agricultural Machinery*, 47(7): 135–142. (In Chinese with English abstract)

[21] Tutar, M., and G. Oguz. 2002. Large eddy simulation of wind flow around parallel buildings with varying configurations. *Fluid Dynamics Research*, 31(5-6): 289–315.

[22] Wang, J., C. G. Wang, and F. Wang. 2010. Numerical simulation on three-dimensional turbulence air flow of 9R-40 rubbing and breaking machine based on Fluent software. *Transactions of the Chinese Society of Agricultural Engineering*, 26(2): 165–169. (In Chinese with English abstract)

[23] Wang, X. N., C. Q. Li, J. X. Shi, F. Chen, and Y. D. Dong. 2007. Research on simulating the wind field of the field straw chopper with throwing cotton stalk. *Transactions of the Chinese Society of Agricultural Machinery*, 38 (8): 67–69. (In Chinese with English abstract)

[24] Wu, Z. Y., H. W. Gao, and J. G. Zhang. 2001. Study on cutting velocity and power requirement in a maize stalk chopping process. *Transactions of the Chinese Society of Agricultural Machinery*, 32(2): 38–41. (In Chinese with English abstract)

[25] Yang, H. Y. 2016. Inside flow field analysis for counter-rotation axial flow fan based on FLUENT. *Safety in Coal Mines*, 7(6): 170–177. (in Chinese)

[26] Zheng, Z. Q. 2017. Study on corn straw pickup-chopping and ditch-burying returning field machine. Ph.D. diss. Beijing: China Agricultural University. (in Chinese)

[27] Zhang, Z. Q., A. D. McHugh, H. W. Li, J. He, Q. J. Wang, and K. Zhen. 2017. Global overview of research and development of crop residue management machinery. *Applied Engineering in Agriculture*, 33(3): 329–344.

[28] Zhang, Z. Q., J. He, H. W. Li, Q. J. Wang, J. W. Ju, X. L. Yan. 2017. Design and experiment on straw chopper cum spreader with adjustable spreading device. *Transactions of the Chinese Society of Agricultural Machinery*, 48(8): 1–15. In Chinese with English abstract

[29] Zhai, Z. P., Z. Y. Yang, B. Gao, and J. X. Li. 2013. Simulation of solid-gas two-phase flow in an impeller blower based on Mixture model. *Transactions of the Chinese Society of Agricultural Engineering*, 29(22): 50–58. (In Chinese with English abstract)

Influence of straw incorporation and tillage practices on sustainable wheat (*Triticum aestivum L.*) yield and soil organic carbon dynamics in rice-wheat rotation system

Muhammad Sohail Memon[1,2], Ahmed Ali Tagar[2], Jiang Chunxia[1,3], Jiang Sijie[1], Shakeel Ahmed Soomro[1,2], Punhoon Khan Korai[4], Noreena Memon[2], Muhammad Ameen[1], Ji Changying[1*]

(1. *College of Engineering, Nanjing Agricultural University, Nanjing 210031, China*;
2. *Faculty of Agricultural Engineering, Sindh Agriculture University Tandojam 70060, Pakistan*;
3. *Department of Biological and Agricultural Engineering, University of California Davis, CA 95616, USA*;
4. *Institute of Recourses, Ecosystem and Environment of Agriculture, Nanjing Agriculture University, Nanjing 210095, China*)

Abstract: The results of conservation tillage systems are relatively diverse throughout the world owing to the less information on the proper amount/percentages of straw incorporation. It is generally believed that at least 30% of the soil surface should be covered with straw, which is not accurately implemented in the field conditions. Accordingly the present study investigated the effect of different percentages of straw incorporation under reduce tillage method on soil physico-chemical properties, changes in soil organic carbon (SOC), soil carbon storage (SCS) and wheat crop yields in rice-wheat cropping system during 2015-16 to 2016-17 at Nanjing, China, under four different treatments, i) 30% straw incorporation (S_{30}) ii) 60% straw incorporation (S_{60}) iii) 100% straw incorporation (S_{100}) and iv) without straw incorporation used as control (CK). All these treatments were arranged in a randomized complete block design (RCBD) with three replications. The application of straw incorporation showed a positive impact on crop yield and soil fertility. Whereas, after two cropping cycles of wheat crop, S_{60} treatment had the highest effect as compared to other treatments. Soil dry bulk density (0-30 cm) reduced significantly, *i.e.* 1.29, 1.28, 1.27 and 1.30 g/cm^3 under S_{30}, S_{60}, S_{100} and CK respectively, as compared to the pre-treatment value 1.32 g/cm^3, while the soil porosity increased in all treatments in the range of 2.20%-5.50%. Maximum SOC content was remarkably the highest 19.05% under S_{60}, whereas the SCS determined 6,911.48, 7,605.86, 7,192.10 kg/ha in S_{30}, S_{60} and S_{100} respectively, as compared to CK (6,476.01). Furthermore, from the experimental results shown that the straw incorporation treatments represented the highest wheat crop production during the year 2015 to 2017 and were ranked in order S_{60}>S_{30}> S_{100}>CK. Therefore, it is suggested that 60% crop straw incorporation under reduce tillage practice is the best option decrease soil dry bulk density, increase porosity, SOC and SCS as well as achieve optimum yield under the wheat-rice cropping system for agricultural sustainability.

Keywords: Physico-chemical properties, soil organic carbon, percentages of straw incorporation, sustainability, tillage practice, yield

Citation: Memon, M. S., A. A. Tagar, C. X. Jiang, S. J. Jiang, S. A. Soomro, P. K. Korai, N. Memon, M. Ameen, and C. Y. Ji. 2017. Influence of straw incorporation and tillage practices on sustainable wheat (*Triticum aestivum L.*) yield and soil organic carbon dynamics in rice-wheat rotation system. International Agricultural Engineering Journal, 26(4): 85–95.

1 Introduction

Globally agriculture food security has been reduced and is expected to be double by 2050 (Tilman et al., 2011). This is driven by the growing human population and increasing need for animal feed, for these challenges to meeting the high grain demand and securing food supply have been increasingly recognized by various levels of policymakers and scientific communities including high-profile features in Science and Nature

Received date: 2017-09-29 **Accepted date:** 2017-11-10
* **Corresponding Author: Ji Changying, Professor, Ph.D.** College of Engineering, Nanjing Agricultural University, Nanjing 210031, China. Email: chyji@njau.edu.cn.

(Memon et al., 2017; Godfray et al., 2010). Whereas, this depends on agricultural sustainability, which hinges on the efficient and sensible use of water, and agricultural soil resources in a proper manner. Moreover, agricultural land is a natural resource and its quality is mainly based on soil physico-chemical properties that determines the sustainability and crop yield (Anikwe and Ubochi, 2007).

The modern agriculture technologies and conservation agricultural (CA) practices have been successful producing more food whereas, it would be seen that this achievement came at a considerable cost. Beside this tillage method, intensely disturb physical and chemical properties of soil, whereas it is essential to select a proper tillage method that improves the quality of soil and the rate of crop growth (Jabro et al., 2009). However, the variations in soil properties different among the field management methods. Conventional tillage (CT) method is being performed from hundreds of years in China, while it causes a maximum reduction in soil organic carbon, increasing soil disturbance and causing soil erosion. Numerous research experiments have indicated that straw is rich in organic minerals and is considered as an imperative organic natural fertilizer (Tan et al., 2007; Saroa and Lal, 2003), also another research study by Álvaro-Fuentes et al (2009) and Jin et al (2009) was indicated that straw incorporation was beneficial for improving soil fertility and soil structural stability. Furthermore, according to Choudhury et al (2014), residue retaining practice was an important factor for ecological and economic perspective because it saved labor, energy and provided proper soil conditions for crop growth.

There are many tillage practices used worldwide according to the requirements of crop, soil type and environmental conditions, while tillage method under crop residue condition provides desired outcomes. The crop residue or straw is defined as the parts of the harvested crop left in the field, whereas the recycling of crop straw has the benefit of changing the surplus farm waste into a useful product for the nutrient requirement of crops. It has also become a key factor for providing a barrier against soil erosion, improving soil organic carbon (SOC) content, temperature, soil structure, and evaporation (Lal, 2003). Thus, the management of residues/straw is an integral part of tillage method. Traditionally, rice and wheat residues are removed from the agricultural lands to use them for feeding cattle and for some another purposes in Southern Asia. Nowadays, after mechanized harvesting of the crops, the farmers are burning the large quantities of crop straw and then leaving it in the agricultural field (Agarwal et al., 2008) as crop residues interfere with tillage in regards for seeding operations and improving the soil quality. Therefore, the environmental protection agency in China and in other developed countries, governments have banned the burning process of straw in the field and amended laws, framed policies to incorporate straw into the soil. Crop residues/straw may be incorporated partially or fully in soil depending upon cultivation method (Dormaar and Carefoot, 1996).

Tilling is the most effective straw incorporation practice, several researchers have conducted studies to investigate the effect of crop straw distribution, incorporation and displacement (Zhang et al., 2007; M'hedhbi and Gregory, 1989; Anderson, 1967) with different tillage implements presenting that primary tillage equipment such as moldboard plough suppressed the majority of stubbles in the furrow bottom, whereas secondary tillage equipment incorporated minimum straw in profile of soil and accumulated the majority of straw in the upper surface of soil. Moreover, Rice residue incorporation in soil with tillage gave significantly higher wheat production (3.50 ton/ha) as compared to without straw (2.91 ton/ha), besides this cropping system has an immense influence on soil physicochemical properties and thereby on crop production (Rahman, 2003). While soil fertility frequently changes on the response of cropping systems and land use management practices (BARC, 2010; Sidhu and Beri, 1989).

Previous studies mainly focused on SOC and crop yield under different tillage practices on plowing depth and straw retaining. Therefore, the specific objective of this study was to investigate the appropriate percentage of straw used for incorporation under reduce tillage method for improving SOC dynamics, suitable for the soil health, fertility and obtaining higher crop production under

rice-wheat rotation system. The general objectives of the study were (i) to assess the effects of tillage practices under different straw percentages on soil physicochemical properties and (ii) to study the effect of straw incorporation under tillage methods on yield and growth performances of wheat crop and changes in the soil organic matter (SOM).

2 Materials and methods

2.1 Study site description

The field experiments were conducted at Jiangpu experimental farm of Nanjing Agricultural University (32°0′39.21″N, 118°36′46.43″E: 26 m MSL) Pukou district, Nanjing, China (Figure 1) during 2015 to 2017 in a rice-wheat cropping system. The study region is situated in a humid climatic zone with annual average rainfall of 1,062 mm, which is influenced by East Asia Monsoon. However, the annual temperature is 15.9°C and the average annual sunshine time is 2104.0 hours with the forest free period of 220 days.

The soil type at the study site was a waterloggogenic paddy soil and classified as Typic Hapludoll according to the USDA Soil Taxonomy (Soil Survey Staff, 2014) with clay loam texture. The selected physiochemical properties in the soil layer of (0-30 cm depth) are presented in Table 1a and 1b. Prior to the experiment, the study site was planted with rice crop and categorized as rice-wheat rotation system from several decades.

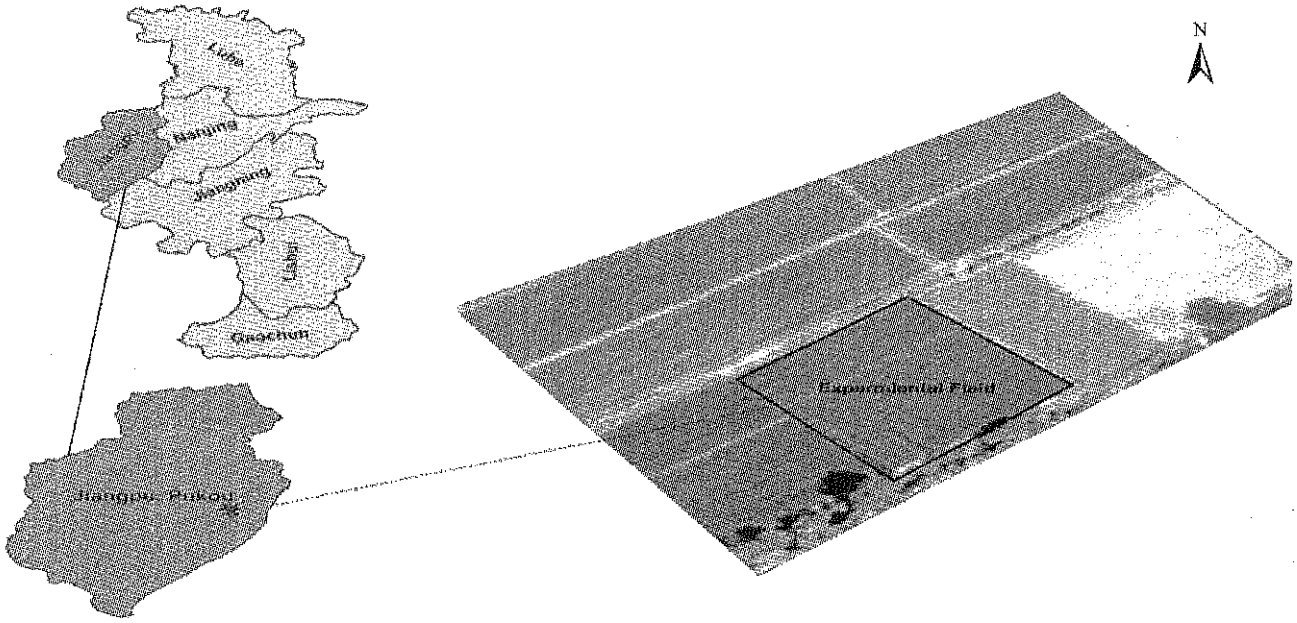

Figure 1 Location of the experimental site

Table 1(a) Analysis for selected soil physical properties before experiment

Depth, cm	pH	Dry Bulk density (Bd), g/cm^3	Particle size distribution,%			Porosity, %	M.C, %
			Clay	Sand	Silt		
0-10	7.47±0.372	1.33±0.013	38.48±0.104	24.72±0.166	36.80±0.088	38.09±0.089	25.66±0.109
10-20	7.60±0.020	1.30±0.020	38.40±0.200	25.20±0.100	36.41±0.100	39.12±0.092	27.54±0.068
20-30	7.84±0.026	1.32±0.030	39.18±0.860	23.85±0.323	37.05±0.304	37.92±0.132	28.08±0.354

Table 1(b) Analysis for selected chemical properties of soil before experiment

Depth, cm	Soil Organic C, g/kg	Available Nitrogen, mg/kg	Available Phosphorous, mg/kg	Available Potassium, mg/kg
0-10	11.59±0.119	83.61±0.387	33.20±0.557	74.64±0.264
10-20	11.58±0.146	82.94±0.280	32.28±0.437	74.77±0.377
20-30	10.99±0.179	82.12±0.569	31.94±0.260	73.76±0.202

Note: ± denoted by Standard Derivation.

2.2 Field management and experimental design

The experiment was started in November 2015 under two growing seasons for the wheat crop. Four treatments were designed on different straw incorporation percent under reduce tillage practice with a ploughing depth of 15 cm was performed with Mould Board Plow in all treatment plots while the straw incorporation was performed on the basis of different percentages *i.e.* i) 30% straw incorporation (S_{30}) ii) 60% straw incorporation (S_{60}) iii) 100% straw incorporation (S_{100}) and iv) without straw incorporation used as control (CK). The average straw yield was 12,100 kg/ha, so that 30% and 60% straw coverage represented 3,630 and 7,260 kg/ha, respectively. These treatments were arranged in Randomized Complete Block Design (RCBD) with three replications. The area for each plot was 4×8 m=24 m^2 and the space between adjacent plot was kept 0.6 m. Chemical fertilizers NPK were added at the following annual rates, N fertilizer as urea at rate of 220 kg/ha, P fertilizer as P_2O_5, 100 kg/ha, and K_2O as K Fertilizer, 85 kg/ha, while phosphorous and potassium fertilizers were applied once before sowing on basal dressing and nitrogen fertilizer was applied at two stages top dressing and basal period, whereas other weed and pest management control were performed by local practices.

2.3 Crop and straw management:

Wheat (cv. Ningmai 8) was planted at a seed rate of 110 kg/ha on 15th December 2015 and 11th December 2016, by using chisel type seed drill at a row spacing of 23 cm. For each growing season, manual weeding was done throughout the experiment. While crop was harvested on 16th June 2016, and 7th June 2017. The rice straw (C/N=51) in our study was collected from preceding harvested crop and applied in treatments on a percentage basis. Moreover, straw was retained manually with topsoil by using hand spade up to 15 cm depth and incorporation into the soil with ploughing. The study site was planted with rice crop prior to the experiment, whereas rice straw contained 22.5%, 18.3% lignin and hemicellulose 36.90% cellulose.

2.4 Sampling collection and measurements

The climatic data for rainfall, maximum & minimum temperatures during study period regarding experiment site were collected from Nanjing weather station, while the monthly distribution of precipitation and temperature during experimental period were shown in Figure 2. After wheat harvesting in each growing season (2015-2017), the soil samples were collected with the help of hand auger (2.64 cm diameter) from five points in each replicated plot, which was mixed together to produce a soil composite sample at depth *viz* 0-10, 10-20, and 20-30 cm layers to determine the physicochemical properties of soil. The soil samples were immediately transported to laboratory, removed stones, plants and organic debris with forceps before use (Lu, 2000), then air dried, and weighed, while the soil samples were dried at 105°C, for determining the soil moisture content. The soil dry bulk density (BD) of samples was measured with core sampler, and soil porosity was computed using relationship between particle density (PD) and BD using Equation (1).

$$\text{Prosity}\ (\%) = \left(1 - \frac{BD}{PD}\right) \times 100 \quad (1)$$

where, *BD*: Soil bulk density (g cm^{-3}) and PD is particle density (g/cm^3).

Afterward, soil samples were passed through a 0.25 mm sieve used for determination of soil chemical properties *i.e.* pH, EC_e, N, P, K and SOC under following standard procedures in the experimental soil. Soil pH was calculated through a digital glass electrode pH meter (WTW pH 522) at a soil-water ratio of 1:2.5 by Alam et al (2014), and soil organic carbon (g/kg) was determined by potassium dichromate oxidation titration method (Lal, 2003), however soil carbon storage (SCS) in soil horizons at thicknesses (0 to 30 cm) was calculated from Equation (2) (Zhang et al., 2013). Moreover; N was measured by the Kjeldahl method (Mehdi et al., 2009) and available K was determined using NH4OAC extraction method (Aramrak et al., 2007) and available P was determined following the Olsen method (Iatrou et al., 2014). The crop growth parameters *i.e.* thousand grain weight (TGW), panicle number, and yield were determined at the different stages of the crop cycle. Threshing was done manually from the one-square-meter area from each plot and then converted into yield per hectare, while data were recorded at 12% water contents after harvesting.

$$SCS = T \times BD \times SOC \times 10000 \quad (2)$$

where, *BD* is the mean Dry Bulk Density at depth of 30 cm; 10000 is the conversion coefficient; *T* is the thickness of soil layer (meter) and the unit of SCS is kg/ha.

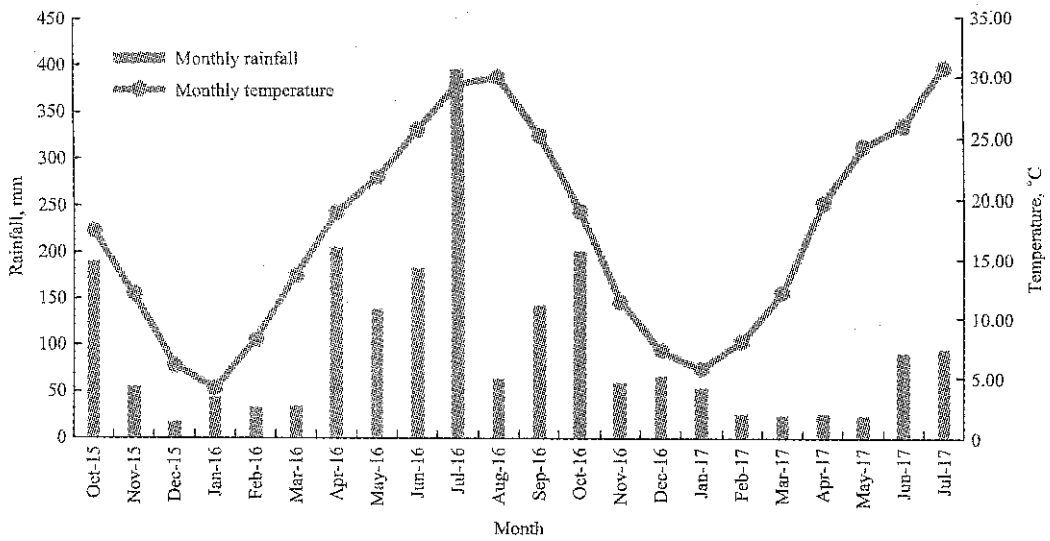

Figure 2 Distribution of mean monthly temperature and rainfall during 2015–2017 at the experimental site

2.5 Statistical analysis

The analysis of variance (ANOVA) for various soil chemical and physical properties, cropping yields and growth parameters were performed using SPSS (version 22). Mean values were compared by Duncan's test (DMRT) method (Jaffer et al, 2010; Steel and Thorii, 1960) and preparation of graphs were done using and Origin Pro 8.

3 Results

3.1 Soil dry bulk density (BD) and porosity

The soil BD and porosity were used as considerable factors regarding changes in the soil quality and structure with different straw percent incorporation under reduce tillage practices. The soil BD (Figure 3A) varied significantly (P<0.05) in different treatments among straw percentages during two-year field experiments. Compared with the mean value before the research experiment (1.32 g/cm^3), the mean BD in the depth of (0-30 cm) under the straw incorporation treatments decreased significantly in the range of 1.20% to 4.27%, while the highest soil BD reduction was found in S_{100} (13.37%), while CK showed lowest BD reduction (8.6%). Moreover, the depthwise soil bulk density changes under S_{100}, S_{60} and S_{30} were showed significantly decrease as compared with CK *i.e* by 2.95%, 2.46% & 1.98% at soil depth of 0-10 cm; 4.27%, 3.56% and 1.73% at the 10-20 cm depth; and 4.53%, 3.92% (P<0.05) and 1.88% at depth of 20-30 cm in the soil profile respectively.

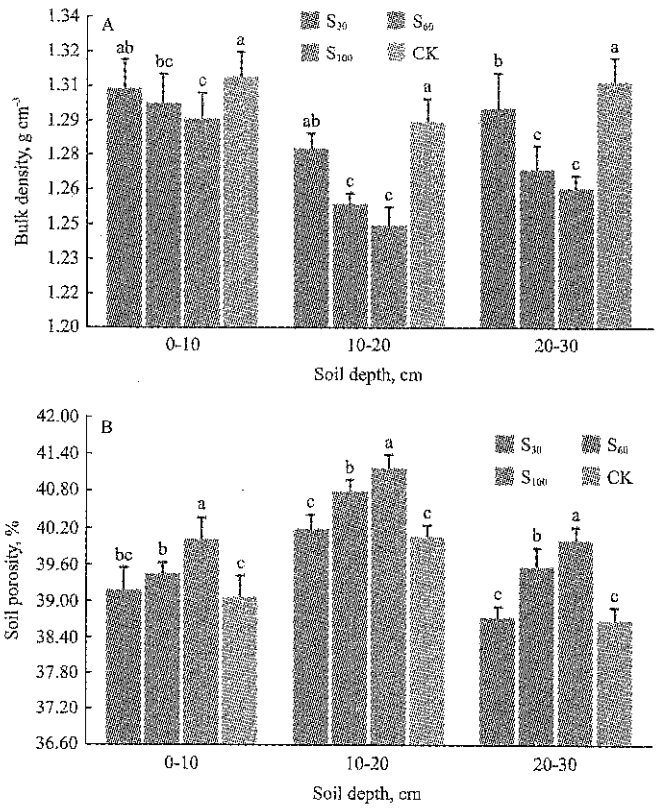

Note: S_{30}, 30% straw; S_{60}, 60% straw; S_{100}, 100% straw incorporation and CK, without straw incorporation. Bars denoted the standard derivation and different lower case letters indicated significant and homogeneity differences at (P<0.05).

Figure 3A and 3B showing changes in soil dry bulk density and porosity at depth 0-30 cm soil profile under different percent of straw incorporation treatments

It was from results that the straw incorporation treatments with different percentages of residue amount significantly increased the soil porosity during the

experimental period, while the T_1 and CK treatments were associated with a non-significant change in the soil profile (Figure 3B). After two years of cropping cycles, the porosity increased by 2.20%-5.50% at the depth of 0-30 cm, while as compared with CK, the S_{100}, S_{60} and S_{30} treatments found positive trend of increasing in the porosity by 5.10% (P<0.05), 3.61% and 2.89% at the depth of 0-10 cm; 5.23%, 4.25% and 2.75% at the 10-20 cm depth; and 5.50%, 4.33% and 2.16% at 20-30 cm depth in the soil profile respectively.

3.2 Soil organic carbon and storage

The impact of crop residue incorporation on SOM was presented in Table 2. The average SOM content in 0-30 cm soil profile under S_{60}, S_{100} and S_{30}, treatments in 2015-2017 were 18.85%, 13.38% and 7.58%, respectively, which were higher than CK treatments, whereas these results were compared with the pretreatment values, the soil organic carbon observed a significant increase (P<0.05) in all experimental treatments. While the mean SOC storage in (0-30 cm) soil depth increased under four different straw percent treatments where were ranked in order as S_{60}>S_{100}> S_{30}>CK. However, in the topsoil layer (0-10 cm) the mean SOC during the study period (2015-17) were significantly (P<0.05) high at 40.35%, 33.34%, 23.91%, and 17.31% under S_{60}, S_{100}, S_{30} and CK respectively as compared before the experiment. Moreover, there was an increasing tendency of (SCS in all experimental treatments during study period from 2015 to 2017 (Table 3). The SCS under S_{60}, S_{100}, S_{30} and CK were 7,566.46, 7,167.36, 6,889.48 and 6,476.01 kg/ha respectively. The highest soil carbon storage rate was observed under S_{60} among other treatments.

Table 2 Influence of straw incorporation and tillage method on soil organic carbon during study period

Crop season	Treatments	Soil organic carbon, SOC, g/kg			Average
		0-10 cm	10-20 cm	20-30 cm	
2015-2016	S_{30}	13.84±0.144^{c}	13.48±0.127^{b}	12.68±0.147^{b}	13.33
	S_{60}	15.97±0.163^{a}	14.70±0.151^{a}	13.35±0.254^{a}	14.67
	S_{100}	14.81±0.207^{b}	14.44±0.178^{a}	13.07±0.137^{ab}	14.10
	CK	13.39±0.177^{d}	12.63±0.244^{c}	12.03±0.141^{c}	12.68
2016-2017	S_{30}	14.87±0.210^{c}	14.60±0.179^{c}	13.82±0.139^{b}	14.43
	S_{60}	16.55±0.191^{a}	16.31±0.122^{a}	15.13±0.140^{a}	16.00
	S_{100}	16.09±0.212^{ab}	15.36±0.154^{b}	14.01±0.144^{b}	15.15
	CK	13.80±0.178^{d}	13.34±0.210^{d}	12.24±0.07^{c}	13.12

Table 3 Soil organic carbon storage under each treatment during study period

Crop season	Treatments	Soil organic carbon, SCS, kg/ha
		Soil depth, 0-30 cm
2015-2017	S_{30}	6,889.48 ±18.42^{c}
	S_{60}	7,566.46 ±15.87^{a}
	S_{100}	7,167.36 ±14.17^{b}
	CK	6,476.01 ±19.01^{d}

Note: ±denoted by Standard Derivation.

3.3 Crop yield

According to the crop production obtained during two years cropping seasons (Figure 4), the results revealed that the straw incorporation treatments were significantly (P<0.05) high as compared to no straw retaining treatment (CK) and ranked as follows: S_{60} (29.84%) > S_{30} (22.61%) > S_{100} (12.54%) > CK, whereas the mean wheat grain yield in 2015-2016 under S_{30}, S_{60}, S_{100} and CK were 3,730.45, 3,887.64 (P<0.05), 3,549.82 (P<0.05) and 3,060.71 kg/ha respectively, while an increasing trend of crop yield was shown among all treatments, *i.e.* 4,120.51, 4,426.30, 3,746 and 3342.30 kg/ha under S_{30}, S_{60} S_{100} and CK respectively in cropping season for 2016-2017.

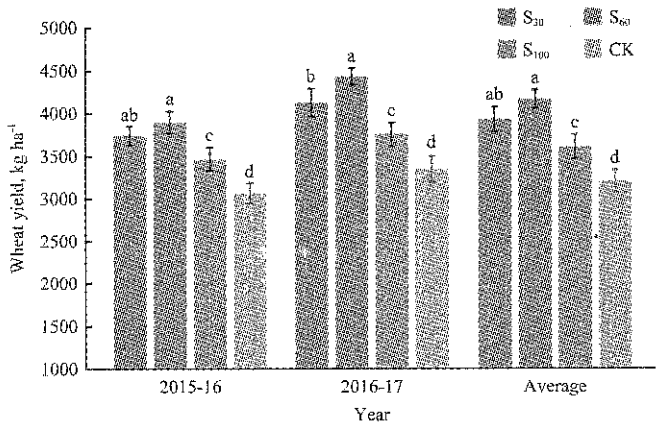

Note: S_{30}, 30% straw; S_{60}, 60% straw; S_{100}, 100% straw incorporation and CK, without straw incorporation.

Figure 4 Wheat crop yields under different straw incorporation treatments

3.4 Crop growth parameters

The crop growth components in 2015-16 (Table 4) indicated that the highest effective spike number was determined in S_{30} (373.47 10^4 kg/ha) treatment and lowest in CK (335.25 10^4 kg/ha) treatments, whereas 1000 grain weight was found significantly (P<0.05) higher under S_{60} (34.50 g) as compared to CK (29.62 g). Statistically ANOVA revealed that the average effective spike numbers were high of 385.69, 384.36, 377.37 and 361.84

10^4 kg/ha, while the 1000 grain weights were 35.35, 33.87, 33.99 and 31.40 g under S_{60}, S_{30}, S_{100} and CK respectively during study period from 2015-2017. These results showed that 60% straw incorporation under reduce tillage practice could increase the 1000 grain weight and effective spike number in the wheat crop during the two-year experiment, which was the important factor to prominent an increment in wheat production.

Table 4 Influence of straw incorporation and tillage on performance of wheat growth

Sampling year	Treatments	Effective spike number, 10^4. Kg/ha	Grains per spike, Number	1000-grain weight, gram
2015-2016	S_{30}	373.47±2.871^a	36.23±1.055^b	32.29±0.375^c
	S_{60}	367.62±1.192^b	37.60±0.447^a	34.50±0.562^a
	S_{100}	344.52±2.043^c	37.32±0.633^a	33.42±0.767^b
	CK	335.25±3.054^d	30.65±0.779^c	29.62±0.318^d
2016-2017	S_{30}	395.24±1.817^c	38.12±0.235^b	35.45±0.304^b
	S_{60}	403.75±1.749^b	39.43±0.517^a	36.20±0.323^a
	S_{100}	410.21±3.675^a	39.96±0.400^a	34.55±0.262^c
	CK	388.42±2.738^d	31.78±0.219^c	33.18±0.175^d

4 Discussion

4.1 Impact of straw incorporation on dry bulk density and porosity of soil

The previous studies (Zhang et al., 2015; Pagliai et al., 2004; Girma and Endale, 1995) stated that the crop residue incorporation into the soil was one of the most significant methods that affected soil dry bulk density and porosity. Wei et al. (2006) compared the application of straw with control treatment (NA) and concluded that BD decreased after the application of crop straw, while lower bulk density observed with apply higher percent of the organic material. However, in this study, BD was significantly decreased in all straw incorporation treatments as compared to CK treatment, whereas this might be due to plowing and incorporation of the aboveground crop straw in the soil. These results are supported by Zhang et al.(2015); Mulumba and Lal, (2008); and Lu (2004), who indicated that the residue incorporation effectively improved soil organic matter and improved the structure of soil and helped to reducing soil dry bulk density, another study conducted by Zhang et al. (2003) and Dam et al (2005). They revealed that tillage method and crop straw management method *i.e* straw incorporation can be potentially led to major changes in physical properties of soil, if both the methods were implemented on continuous cropping for a longer period. While Mulumba and Lal (2008) mentioned that long-term crop residue incorporation method had progressive impacts on soil porosity. In our study, reduce tillage with different percent of straw incorporation on soil porosity were significant high and consistently positive over years, whereas the results (Figure 3b) shown that overall mean soil porosity was increased in 0-30 cm soil depth under straw incorporation treatments as compared to CK treatment, therefore this positive progress was due to the loessal soil particles stick together and form aggregates, so the resultant soil BD was reduced and soil total porosity increased in depth of 0-30 cm soil profile. The impact of crop-residue incorporation was reported to be lower in the deep soil layer as compared to the surface layers of soil (Tripathy and Singh, 2004), additionally our results are in agreement with the finding of He et al.(2009) who concluded that the soil porosity in 0-15 cm layer was higher under the experimental treatments and other numerous studies by Tejada et al. (2008). Zhu et al (2010) also reported that rice straw incorporation in soil increased the SOC concentration and minimize bulk density, thereby improving total porosity, aeration and water-holding capacity during 8 years of experiments in China.

4.2 Impact of straw incorporation on soil organic matter and storage

The soil organic carbon is the main factor that influences physico-chemical and biological properties of soil (Zhang et al., 2014; Haynes and Beare, 1997). The present results of SOC in our study demonstrated that after two years of experiments under rice straw incorporation was significantly increased, and SOC dynamics & storage levels were in the range of 7.07% to 19.05% for straw incorporation treatments in 0-30 cm depth of soil profile as compared to CK treatment, whereas the increasing trend of SOC was probably associated with the percent of straw incorporated to apply the soil under tillage method, as recommended earlier by Zhang et al. (2016); Malhi et al.(2011); Campbell et al. (1998) and Rasmussen and Collins (1991). Moreover, this

may because of the tillage stimulated the oxidation in SOC, with increasing rate of crop straw incorporation in soil to decompose the organic matter, which improved the quality of soil in respect of chemical properties (Zhang et al., 2014; Coppens et al., 2007; Fontaine et al., 2007; Aulakh et al. 1991). Consequently, in this study, the interannual differences in SOC matter presented a relatively stable increasing trend, probably because the changes in soil organic content rates were usually insensitive to current management methods, while, these variations happened slowly and they were comparatively smaller as compared with the appropriate previous soil carbon rate, it particularly occurred when the short quantities of crop residues were incorporated into soil (Zhang et al. 2016; Gong et al. 2009). These experimental results agreed with the previous studies by Bakht et al. (2009) and Surekha et al. (2003) who concluded that the SOC was increased with the application of straw incorporation under silty clay soil and sandy clay loam soil. Furthermore, many factors affected SOC concentration and storage *i.e.* crop residue incorporation, retention, cropping rotation, application of fertilizer, and tillage method (Zhang et al., 2013). The current study revealed that SCS shown an increasing tendency in 0-30 cm soil profile under reduce tillage method with different percent of straw incorporation from 2015-2017 (Table 3), the SCS was almost lowest in CK treatment in each growing season as compared to the straw incorporation treatments due to the relatively lower organic matter values in deep soil layers (20-30 cm). These results are closely similar in SCS studies by Zhang et al. (2013) who indicated that the carbon storage rate was high of 25.94% and 26.98% under CT and RT respectively with residue retention in soil for seven years' experiments.

4.3 Effect of straw incorporation on crop yield

The production of crops is affected considerably by soil fertility and availability of moisture (Zhang et al., 2014b), thus well-managed soils can support sustainable production and enhance soil microbial biomass, growth stage of the crop roots and the crop yields. In our research study, the wheat yield was significantly influenced ($P<$ 0.05) by the straw incorporation for two years with reduce tillage method, according to the results the highest yields (3,887.64 and 4,426.30 kg/ha) were found under S_{60} followed by S_{30} straw incorporation treatment at the rate of 3,730.45 and 4,120.51 kg/ha respectively, while the lowest grain yields (3,060.71 and 3,342.30 kg/ha) were recorded under CK during 2015-16 and 2016-17 respectively. The effective spike number and average thousand grain weight were observed high under S_{60} and S_{30} as compared to S_{100} and CK treatment, it was happen because of due to the excess amount of incorporated crop straw cannot be easily mineralized as well as decomposed (Hejazi et al., 2010). However, incorporation of straw under S_{100} treatment was difficult to incorporation and affcted the emergence rate of wheat crop and growth quality at the seedling stage (Song et al., 2016). These results are in agreement with those reported by Karami et al. (2012); Tripathy and Singh (2004). They reported that the positive effects on the crop yield and soil productivity after crop straw application were attributed mainly to the improved soil quality.

5 Conclusions

After two years' field experiment on rice-wheat rotation system in humid climatic region of China, under reduce tillage method with appropriate percent of crop straw incorporation into soil was effective practice to improve the soil physicochemical and biological properties, soil water storage level, increase the soil organic carbon dynamics, soil carbon storage levels, wheat crop performance and grain yield. The application of straw incorporation significantly reduced the bulk density and increased porosity, whereas an increasing trend was observed in soil organic carbon and carbon storage rate in regarding depth of 0-30 cm under soil profile in all residue incorporation treatments as compared with CK. It is mainly associated with the improvement in soil structure and quality in helping to get higher crop production. However, according to the experiment results of 2015-16-2016-17, the high soil organic carbon and yield obtained were 15.34 g/kg and 4,156.97 kg ha^{-1} under S_{60} as compared to CK treatments, which were 12.90 g kg^{-1} and 3201.50 kg/ha respectively. Therefore, S_{60} (60% of straw incorporation) under reduce

tillage method can be suggested under rice-wheat cropping system in clay loam soil to enhance both agricultural sustainability and crop production with improving soil quality and fertility.

Acknowledgments

This study was sponsored by the National Natural Science Foundation, Grant # 51275250. The first author is thankful to the Chinese Scholarship Council (CSC) for providing the scholarship to pursue Ph.D. we are also grateful to Mr. Zhang Bo and Mr. Fahim Ullah for their help during field experiments.

[References]

[1] Agarwal, S., R. C. Trivedi, and B. Sengupta. 2008. Air pollution due to burning of agricultural residue. *Indian Journal of Air Pollution Control*, 8(1): 51–59.

[2] Alam, M. K., M. M. Islam, N. Salahin, and M. Hasanuzzaman. 2014. Effect of tillage practices on soil properties and crop productivity in wheat-mungbean-rice cropping system under subtropical climatic conditions. *The Scientific World Journal*, 2014(1): 1–15.

[3] Álvaro-Fuentes, J., M. V. López, J. L. Arrúe, D. Moret, and K. Paustian. 2009. Tillage and cropping effects on soil organic carbon in Mediterranean semiarid agroecosystems: testing the century model. *Agriculture, Ecosystems & Environment,* 134(1): 211–217.

[4] Anderson, D. T. 1967. Factors affecting trash conservation with the wide-blade cultivator. *Canadian Agricultural Engineering*, 9(1): 98–127.

[5] Anikwe, M. A. N., and J. N. Ubochi. 2007. Short-term changes in soil properties under tillage systems and their effect on sweet potato (Ipomea batatas L.) growth and yield in an Ultisol in south-eastern Nigeria. *Australian Journal of Soil Research*, 45(5): 351–358.

[6] Aramrak, S., J. Chanchareonsook, C. Suwannarat, and E. Sarobol. 2007. Assessment of multielement extractants for prediction of available potassium in Thai soils. *Kasetsart Journal - Natural Science*, 41(3): 461–466.

[7] Aulakh, M., D. Walters, J. Doran, D. Francis, and A. Mosier. 1991. Crop residue type and placement effects on denitrification and mineralization. *Soil Science Society of America Journal*, 55(4): 1020–1025.

[8] Bakht, J., M. Shafi, M. T. Jan, Z. Shah. 2009. Influence of crop residue management: cropping system and N fertilizer on soil N and C dynamics and sustainable wheat (*Triticum aestivum* L.) production. *Soil Tillage Research*, 104(2): 233–240.

[9] BARC (Bangladesh Agricultural Research Council). 2010. Agricultural Research Priority: Vision 2030 and beyond-a final Report by M. Jahiruddin (Professor, Department of Soil Science, Bangladesh Agricultural University) and M. A. Satter (Chief Scientific Officer, Land and Soil Resource Management, BARC, Bangladesh). Sub sector: Land and Soil Resource Management Bangladesh. *Agricultural Research Council, Farmgate, Dhaka.*

[10] Campbell, C., F. Selles, G. Lafond, B. McConkey, and D. Hahn.1998. Effect of crop management on C and N in long-term crop rotations after adopting no-tillage management: comparison of soil sampling strategies. *Canadian Journal of Soil Science,* 78(1): 155–162.

[11] Choudhury, S.G., S. Srivastava, R. Singh, S.K. Chaudhari, D.K. Sharma, S.K. Singh, and D. Sarkar. 2014. Tillage and residue management effects on soil aggregation, organic carbon dynamics and yield attribute in rice–wheat cropping system under reclaimed sodic soil. *Soil and Tillage Research,* 136(1): 76–83.

[12] Coppens, F., P. Garnier, A. Findeling, R. Merckx, S. Recous. 2007. Decomposition of mulched versus incorporated crop residues: modelling with PASTIS clarifies interactions between residue quality and location. *Soil Biology and Biochemistry,* 39(9): 2339–2350.

[13] Dam, R. F., B. B. Mehdi, M. S. E. Burgess, C. A. Madramootoo, G. R. Mehuys, and I. R. Callum. 2005. Soil bulk density and crop yield under eleven consecutive years of corn with different tillage and residue practices in a sandy loam soil in central. *Canada. Soil Tillage Research,* 84(1): 41–53.

[14] Dormaar, J. F., and J. M. Carefoot.1996. Implication of crop residue and conservation tillage on soil organic matter. *Canadian Journal of Plant Science*, 76(4): 627–634.

[15] Fontaine, S., S. Barot, P. Barré, N. Bdioui, B. Mary, and C. Rumpel. 2007. Stability of organic carbon in deep soil layers controlled by fresh carbon supply. *Nature*, 450(7167): 277–280.

[16] Girma, T., and B. Endale. 1995. Influence of manuring on certain soil physical properties in the Middle Awash area of Ethiopia. *Journal Communications in Soil Science and Plant Analysis*, 26(9-10): 1565–1570.

[17] Godfray, H.C.J., J. R. Beddington, I. R. Crute, L. Haddad, D. Lawrence, and J. F. Muir. 2010. Food security: the challenge of feeding 9 billion people. *Science*, 327(5967): 812–818.

[18] Gong, W., X. Yan, J. Wang, T. Hu, and Y. Gong. 2009. Long-term manure and fertilizer effects on soil organic matter fractions and microbes under a wheat–maize cropping system in northern China. *Geoderma*, 149(3-4): 318–324.

[19] Haynes, R., and M. Beare. 1997. Influence of six crop species on aggregate stability and some labile organic matter

fractions. *Soil Biology Biochemistry*, 29(11): 1647–1653.

[20] He, J., Q. Wang, H. Li, J. N. Tullberg, A. D. McHugh, Y. Bai, X. Zhang, N. McLaughlin, and H. Gao. 2009. Soil physical properties and infiltration after long-term no-tillage and ploughing on the Chinese Loess Plateau. *New Zealand Journal of Crop and Horticultural Science*, 37(3): 157–166.

[21] Hejazi, A., M. J. Bahrani, and S. A. Kazemeini. 2010. Yield and yield components of irrigated rapeseed-wheat rotation as influenced by crop residues and nitrogen levels in a reduced tillage method. *American-Eurasian Journal of Agricultural & Environmental Sciences,* 8(5): 502–507.

[22] Iatrou, M., A. Papadopoulos, F. Papadopoulos, O. Dichala, P. Psoma, and A. Bountla. 2014. Determination of soil available phosphorus using the Olsen and Mehlich 3 methods for Greek soils having variable amounts of calcium carbonate. *Communications in Soil Science and Plant Analysis*, 45(16): 2207–2214.

[23] Jabro, J. D., W. B. Stevens, R. G. Evans, and W. M. Iversen. 2009. Tillage effects on physical properties in two soils of the Northern Great Plains. *Applied Engineering in Agriculture,* 25(3): 377–382.

[24] Jaffer, M. G., M. Srinivasulu, M. Madakka, and V. Rangaswamy. 2010. Influence of insecticides on the activity of amylase and celluase in groundnut (*Arachis hypogea* L.). *Soil Ecology Environment and Conservation*, 16(3): 383–388.

[25] Jin, H., W. Qingjie, H. Li, L. Liu, and H. Gao. 2009. Effect of alternative tillage and residue cover on yield and water use efficiency in annual double cropping system in North China Plain. *Soil and Tillage Research*, 104(1): 198–205.

[26] Karami, A., M. Homaee, S. Afzalinia, H. Ruhipour, and S. Basirat. 2012. Organic resource management: impacts on soil aggregate stability and other soil physicochemical properties. *Agriculture, Ecosystems & Environment,* 148(4): 22–28.

[27] Lal, R. 2003. Carbon sequestration in dryland ecosystems. *Environmental Management.* 33(4): 528–544.

[28] Lu, B. 2004. Improvement of saline fluvo-aquic soil by different agricultural methods. *Chinese Journal of Soil Science* (in Chinese) 35: 166–168.

[29] Lu, R. K. 2000. Agronomical and chemical analysis of soil in *Agriculture Press*, (in Chinese).

[30] Malhi, S., M. Nyborg, T. Goddard, and D. Puurveen. 2011. Long-term tillage: straw management and N fertilization effects on quantity and quality of organic C and N in a Black Chernozem soil. *Nutrient Cycling in Agroecosystems*, 90(2): 227–241.

[31] Mehdi, S., J. Bernie, L. D. Burton, C. A. Grant, M. A. Hajabbasi, and G. A. Kalo. 2009. Sodium hydroxide direct distillation: A Method for estimating total nitrogen in soil. *Communications in Soil Science and Plant Analysis*, 40(15-16): 2505–2520.

[32] Memon, M. S., J. Zhou, J. Guo, F. Ullah, M. Hassan, S. Ara, and C. Y. Ji. 2017. Comprehensive review for the effects of ridge furrow plastic mulching on crop yield and water use efficiency under different crops. *International Agricultural Engineering Journal*, 26(2): 58–67.

[33] M'hedhbi, K., and J. M. Gregory. 1989. Tillage effects on residue cover. ASAE Paper No. 891539. St. Joseph, MI: ASABE.

[34] Mulumba, L. N., and R. Lal. 2008. Mulching effects on selected soil physical properties. *Soil Tillage Research*, 98(1): 106–111.

[35] Pagliai, M., N. Vignozzi, and S. Pellegrini. 2004. Soil structure and the effect of management practices. *Soil Tillage Research*, 79(2): 131–143.

[36] Rahman, M. M., and S. L. Ranamukhaarachchi. 2003. Fertility status and possible environmental consequences of Tista Floodplain soils in Bangladesh. *Thammasaltn International Journal of Science and Technology*, 8(3): 11–19.

[37] Rasmussen, P. E., and H. P. Collins. 1991. Long-term impacts of tillage fertilizer, and crop residue on soil organic matter in temperate semiarid regions. *Advances in Agronomy,* 45(45): 93–134.

[38] Saroa, G. S., and R. Lal. 2003. Soil restorative effects of mulching on aggregation and carbon sequestration in a Miamian soil in central Ohio. *Land Degradation Development*, 14(5): 481–493.

[39] Sidhu, B. S., and V. Beri. 1989. Effect of crop residue management on yields of different crops and soil properties. *Biological Wastes*, 27(1): 15–27.

[40] Soil Survey Staff. 2014. Keys to Soil Taxonomy, 12th ed. USDA-Natural Resources Conservation Service, Washington, DC.

[41] Song, K., J. Yang, Y. Xue, W. Lv, X. Zheng, and J. Pan. 2016. Influence of tillage practices and straw incorporation on soil aggregates, organic carbon, and crop yields in a rice-wheat rotation system. *Scientific Reports*, 6(1): 1–12.

[42] Steel, R. C. B., and J. H. Torii.1960. Principles and Procedures of Statistics, Mc Graw Hall, New York, NY, USA.

[43] Surekha, K., A. P. Kumari, M. N. Reddy, K. Satyanarayana, and P. S. Cruz. 2003. Crop residue management to sustain soil fertility and irrigated rice yields. *Nutrient Cycling in Agroecosystems*. 67(2): 145–154.

[44] Tan, Z., R. Lal, L. Owens, and R. C. Izaurralde. 2007. Distribution of light and heavy fractions of soil organic carbon as related to land use and tillage practice. *Soil Tillage Research*, 92(1-2): 53–59.

[45] Tejada, M., J. L. Gonzalez, A. M. García-Martínez, and J.

Parrado. 2008. Effects of different green manures on soil biological properties and maize yield. *Bioresource Technology*, 99(6): 1758–1767.

[46] Tilman, D., C. Balzer, J. Hill, and B. L. Befort. 2011. Global food demand and the sustainable intensification of agriculture. *Proceedings of the National Academy of Sciences*, 108(50): 20260–20264.

[47] Tripathy, R., and A.K. Singh. 2004. Effect of water and nitrogen management on aggregate size and carbon enrichment of soil in rice–wheat cropping system. *Journal of Plant Nutrition and Soil Science*, 167(2): 216–228.

[48] Wei, C., M. Gao, J. Shao, D. Xie, and G. Pan. 2006. Soil aggregate and its response to land management practices. *China Particuology*, 4(5): 211–219.

[49] Zhang, H. L., Y. D. Qin, and W. S. Zhu. 2003. Effects of tillage of soil physical properties. *Soils* (in Chinese), 35(2): 140–144.

[50] Zhang, J., J. Sun, A. Duan, J. Wang, X. Shen, and X. Liu. 2007. Effects of different planting patterns on water productivity and yield performance of winter wheat in the Huang-Huai-Hai plain of China. *Agricultural Water Management*, 92(1): 41–47.

[51] Zhang, M. Y., F. J. W. Fu-Jun, F. Chen, P. Maphorogetja, and H. Zhang. 2013. Comparison of three tillage systems in the wheat-maize system on carbon sequestration in the North China Plain. *Journal of Cleaner Production*, 54(54): 101–107.

[52] Zhang, P., T. Wei, Y. Li, K. Wang, Z. Jia, Q. Han, and X. Ren. 2015. Effects of straw incorporation on the stratification of the soil organic C, total N and C: N ratio in a semiarid region of China. *Soil and Tillage Research,* 153(1): 28–35.

[53] Zhang, P., T. Wei, Z. Jia, Q. Han, X. Ren, and Y. Li. 2014. Effects of straw incorporation on soil organic matter and soil water-stable aggregates content in semiarid Regions of Northwest China. *PloS one*, 9(3): 1–11.

[54] Zhang, P., T. Wei, Z. Jia, Q. Han, and X. Ren. 2014b. Soil aggregate and crop yield changes with different rates of straw incorporation in semiarid areas of northwest China. Geoderma, 230-231(7): 41–49.

[55] Zhang, P., X. Chen, T. Wei, Z. Yang, Z. Jia, B. Yang, Q. Han, and X. Ren. 2016. Effects of straw incorporation on the soil nutrient contents, enzyme activities, and crop yield in a semiarid region of China. *Soil and Tillage Research*, 160: 65–72.

[56] Zhu, H., J. Wu, D. Huang, Q. Zhu, S. Liu, Y. Su, W. Wei, J. K. Syers, and Y. Li. 2010. Improving fertility and productivity of a highly-weathered upland soil in subtropical China by incorporating rice straw. *Plant and Soil*, 331(1–2): 427–437.

Design and test of rotary tillage nail tooth residual film recycling machine

Zhang Panfeng[1,2], Hu Can[1,2], Wang Xufeng[1,2*], Lu Bing[1,2], Liu Chaoji[1,2]

(1. *College of Mechanical and Electrical Engineering, Tarim University, Alar Xinjiang 843300, China*;
2. *Key Laboratory of Colleges & Universities under the Department of Education of Xinjiang Uygur Autonomous Region, Alar Xinjiang 843300, China*)

Abstract: At present, the problem of pollution from plastic film in farmland in Xinjiang is becoming more and more serious. Due to the plastic film mixing with soil, it is difficult to realize its mechanical collection. In order to solve the problem of mechanical collection of plastic film residue in topsoil, a kind of rotary recovery machine with spike tooth was designed. It can collect the plastic film in topsoil of 0-300 mm aiming at distribution features of plastic film residue in topsoil. The machine works in mode of rotary tillage and sets a certain number of spike teeth in spike tooth cylinder which is driven by rotary tillage. The rotation leads the spike tooth to hook the plastic film in topsoil to separate it from the soil and collect it, which meets the operational requirements. Through the field trial, the results showed that the machine has higher reliability, it collected plastic film in topsoil and worked well in unloading the film; when the cylinder rotates at 120 r/min, moves forward at 4 km/h and operates in depth at 50 mm, it attains the best working performance, and the recovery rate and the recovery efficiency are 74.12% and 0.0758 hm^2/h, respectively. The recovery machine can be applied in the plain cultivation areas after spring plowing and before sowing with an average recovery rate of 69.74%, which can effectively reduce the film residue in soil after plastic film collection.

Keywords: topsoil, rotary tillage nail tooth, residual film recycling, field trial

Citation: Zhang, P. F., C. Hu, X. F. Wang, B. Lu, and C. J. Liu. 2017. Design and test of rotary tillage nail tooth residual film recycling machine. International Agricultural Engineering Journal, 26(4): 96–105.

1 Introduction

The problem of pollution from plastic film in Xinjiang farmland is becoming more and more serious, and it affected the cultivation of farmland and the sustainable development of agriculture (Hu et al., 2017). The residual film of tillage layer has obvious effect on soil structure, water and fertilizer migration and crop yield (Hu et al., 2017). According to the relevant literature, when the residual film density was up to 1000 kg/hm^2, the average cotton yield decreased by 15.8% (Dong et al., 2013). In recent years, the comprehensive management of residual film pollution in Xinjiang has become one of the key issues to be solved urgently. And in the comprehensive management of residual film, there are two kinds of technical solutions: biodegradable membrane technology and residual film recycling machinery. Biodegradable membrane technology is still in the research stage (Ma et al., 2012; Li et al., 2015; Dai et al., 2016), because the film cycle and under film temperature are difficult to be solved; the technology of mechanical film collecting has become one of the main applicable technologies at present.

In the research of mechanical film collecting technology, Hou et al. (2002) studied the elastic tooth residual film reclaiming machine. Through field test, the recovery rate of the residual film of the year's surface was between 72% and 82% (Xie et al., 2013). Agricultural Mechanization Institute of Xinjiang

Received date: 2017-08-12 **Accepted date:** 2017-10-31

* **Corresponding author: Wang Xufeng,** Professor, College of Mechanical and Electrical Engineering, Tarim University, Alar, Xinjiang 843300, China; Key Laboratory of Colleges & Universities under the Department of Education of Xinjiang Uygur Autonomous Region, Alar Xinjiang 843300, China. Email: wxfwyq@126.com.

Academy of Agricultural Sciences developed 4JSM-1800 cotton stalks returning to field and residual film recycling joint operation machine, the machine consists of stem crushing device and plastic film recovery device, and can complete two operations of stalk crushing and residual film recovery. The recovery rate of residual film reached 85%. Wang (2008) combined cotton stalks crushing with residual film recovery characteristics, based on the principle of raking machine, to research and design a kind of suspension type cotton stalks chopping returning to field raking machine. The existing residual film recovery machine is mainly for recovering the surface of the membrane for a year. After the recovery of the topsoil, there are still a lot of residual film residues. As the residual layer was close adhesion with soil, and due to the longer residual time, the mechanical properties of the residual film in soil are low, and difficult to achieve the unloading of film. It increased the difficult of recovering the residual layer of plowing soil (Lou et al., 2002; Lv et al., 2015; Li et al., 2012). However, the residual layer of tillage affected greatly on soil and crop growth, and it is necessary to clean up the residual film of multi-year residue in order to reduce the residue of the tillage layer (Li et al., 2012; Zhang et al., 2015; Zhu et al., 2015).

Therefore, according to the pollution situation in Xinjiang caused by film, and in order to solve the problem of recovering small residual film from years of broken film mulching for agricultural crops, a rotary nail tooth residual film recycling machine was designed, and the recovery of residual film in topsoil was realized.

2 Overall design idea of the residual film recovery

2.1 Overall design of the residual film recycling machine

The depth of Xinjiang cotton field is between 0 and 300 mm (Niu et al., 2016). Before spring sowing, the tillage and soil preparation treatments for 0-300 mm were carried out by tillage machine. The residual films and soil were mixed after the autumn harvest, and it is difficult to realize the separation of the smaller residual films from the soil. According to the preliminary investigation (Niu et al., 2016), the residual films morphology of the soil is mainly between 4 and 25 cm^2, and the residual films are distributed evenly in the soil. The soil agglomeration volume of the cotton field after the rotation is small, and the length of the stubble and straw stubble is in the range of 50-150 mm, and is in the range of 0-2 per square meter. According to the distribution of residual films in soil, the designers used the rotary tillage blade to replace the nail teeth on the operation principle of rotary tillage, making residual film in the topsoil accept force of film device through the rotation of the nail drum, and finally realized film-soil separation of the residual film in the plow layer. At the same time, the weeds, straw, stubble and other debris existed in cotton field must be considered. Therefore, firstly, the rotary tiller nail residue film recycling machine worked in cotton field where there is less soil, weeds, straw, stubble and so on. Secondly, when a small amount of weeds, straw, stubble and other residues were provoked, due to the quality of weeds, straw, root stubble, etc. was far bigger than the quality of residual film, in the rotation of the nail drum, the centrifugal force would throw weeds, straw and stubble out of the nail teeth. Besides, when weeds, straw, and stubble with the residue were provoked together, part of the weeds, straw, root stubble would be brushed under the function of brush. High soil moisture and serious soil agglomeration made the residual films and soil closely sticky together, resulted in difficulties in film collection, so, the adhesion of residual films, weeds, roots, straw and other debris has negative effect on film-collecting. In view of this phenomenon, firstly, the soil moisture in 0-200 mm depth of cotton field in Xinjiang was 10%-16% and the soil solidity was 0-20 kPa in 0-300 mm depth. Most of the soil was sandy and light medium soil, the texture was looser and the soil resistance became smaller after the rotation. Besides, the peeling teeth also have certain detritus function when working with the soil, which can promote recycling of the residual film. When the residual films and weeds, roots, straw and other debris were adhered together, the nail teeth picked up the residual films along with weeds, roots, straw and other debris together, making them separate from the soil. And when the residual films and weeds, roots, straw and other debris were adhered together, it is possible to increase the

rotation speed of the nail drum and reduce the advancing speed of the retractor, so, the contact frequency between the nail teeth and the residual films increased and the effect of residual films recovery was improved. Therefore, according to the design ideas, rotary tillage nail tooth residual film recycling machine overall design was shown in Figure 1.

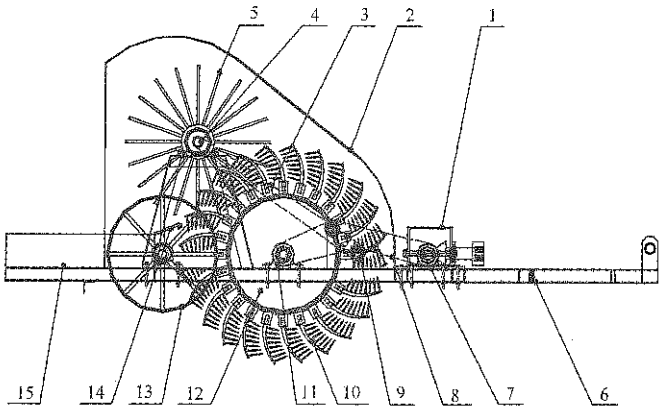

1. Transmission case 2. Shield 3. Chain I 4. Film unloading mechanism sprocket 5. Film releasing mechanism 6. Frame 7. Main sprocket 8. Chain II 9. Reverse sprocket 10. Toothed bar 11. Film lifting device sprocket 12. Nail tooth roller 13. Walking wheel 14. Guide plate 15. Residual film recovery box

Figure 1 Rotary tillage nail tooth plastic film recycling machine

The machine consists of rack, shroud, nail drum, nail, brush roller, guide plate, recycling box, ground wheel and transmission system. On one hand, the nail drum, the nail teeth and the corresponding sprocket constitute the film forming device. On the other hand, the brush roller, the rotating shaft and the corresponding sprocket constitute the unloading device.

Rotating the staple-type residual films recycling machine, the active sprocket drives the reverse sprocket and nail wheel rotation, so that the nail teeth and the soil rolling contact. Due to the nail teeth are connected to the rod teeth, and hang residual films during the process of rotating with the nail teeth drum, the film was completed when the residual layer of soil was separated from the soil. The reverse sprocket is mounted on the back of the active sprocket and is driven by the reverse sprocket on the outside of the chain II, driving the sprocket of the unloading mechanism. And the direction of rotation of the brush roller and the pinch roller is reversed. Brush roll speed is greater than the rotation speed of the nail drum to ensure the brush is on the brush and the nail teeth are on the teeth when the contact frequency is high, so as to achieve residual films unloading process. The residual film is discharged through a guide plate with a certain inclination angle into the residual film recovery box to realize better recovering of the residual films.

2.2 Analysis of film formation process

The rotation of the nail wheel drives the rotation of the nail teeth, and the movement principle process is shown in Figure 2. When the nail teeth move at a certain speed, the nail teeth on the nail teeth have a certain amount of momentum, when the nail teeth and soil residual film contact, the soil residual film with the nail movement complete the film process, the physical meaning of the momentum obtained by the rotation of each pin in the process of rotation, which can be converted into the force of the nail and the residual film, namely:

$$\begin{cases} p_x^i = \sum (mv_x^i) \\ p_y^i = \sum (mv_y^i) \end{cases} \tag{1}$$

$$\begin{cases} \dfrac{dp_x^i}{dt} = \sum F_x^i \\ \dfrac{dp_y^i}{dt} = \sum F_y^i \end{cases} \tag{2}$$

$$F_0^i = \sqrt{\left(\sum F_x^i + \sum F_y^i\right)} \tag{3}$$

In Equations (1)-(3), v_x^i is the speed at the horizontal direction of the first i nail, m s^{-1}; v_y^i is the speed at the vertical direction of the first i nail teeth, m s^{-1}; p_x^i is the momentum in the horizontal direction of the first i nail, kg·m/s; p_y^i is the vertical momentum in the vertical direction of the first i nail, kg·m/s; F_x^i is the forces at the horizontal direction of the first i nail, N; F_y^i is the force in the vertical direction for the first i nail teeth, N; F_0^i is the resultant forces for the first i nails, N; m is the quality of each nail and rod, kg.

So the nail teeth hook the residual film when the nail on the residual force is greater than the residual stress contact force, resulting in residual film in the role of nail from the film, namely:

$$F_0^i > [\sigma] S_0 \tag{4}$$

In Equation (4), $[\sigma]$ is allowable stress for maximum contact of residual film, pa; S_0 is action area, m^2. The physical meaning of the equation is that when the force of

the nail on the residual film is greater than the allowable stress of the residual film and the product of the area of the nail, the nail can puncture the residual membrane and finally achieve the function of hooking membrane.

As the nail tooth roller continues to move, the residual film rotates with the nail until the residual film rotates away from the plowing soil with the nail drum on the spike to complete the filming process.

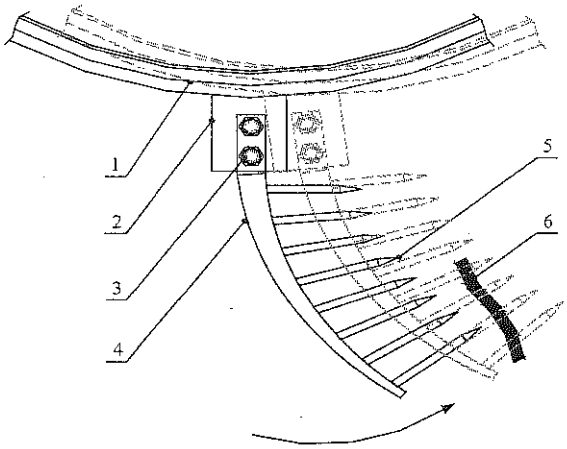

1. Nail tooth roller 2. Nail seat 3. Connecting piece 4. Main nail teeth 5. Small nail teeth 6. Plastic film

Figure 2 Film drawing principle diagram

2.3 Analysis of nail movement track

According to the working principle of the machine, the nail drum on the one hand by the tractor traction forward movement, on the other hand by the tractor power output shaft driven nail tooth drum rotation movement. Therefore, the movement of the nail drum is the vector of the two movements. In order to achieve the best film recovery effect, the nail drum rotation speed should be reasonable, and if the speed is too high, it will cause the pinion load too large, and easily lead to deformation or even broken teeth, while if the speed is too low, it will cause the hook membrane difficult to reduce the residual film recovery (Lou et al., 2002). Set the end of any rod tooth is A, the movement trajectory was shown in Figure 3, and the motion equation of A point is as follows:

$$\begin{cases} x = vt + R\sin\omega t \\ y = R\cos\omega t \end{cases} \tag{5}$$

where, v is the forward speed of a toothed roller, m s^{-1}; ω is rotating angular speed for a toothed roller, rad s-1; R is the radius from the A point to the center of rotation of the rod tooth, mm; t is the working time for the toothed roller, s.

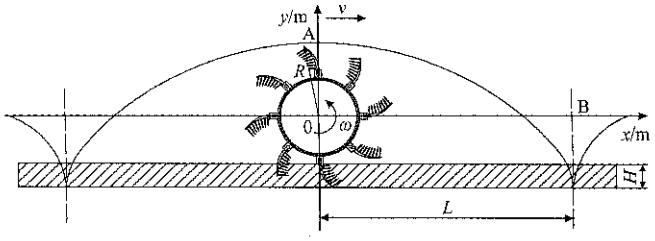

Figure 3 A motion law of spike tooth apex

The horizontal and vertical velocities are:

$$\begin{cases} v_x = \dfrac{dx}{dt} = v + R\omega\cos\omega t \\ v_y = \dfrac{dy}{dt} = -R\omega\sin\omega t \end{cases} \tag{6}$$

The relative rate of change is:

$$\frac{dy}{dx} = \frac{-\sin\omega t}{k + \cos\omega t} \tag{7}$$

In Equations (6)-(7), v_x is horizontal direction speed for nail roller, m s^{-1}; v_y is the vertical speed of the cylinder for the nail tooth, m s-1; v is forward speed for a toothed roller, m s^{-1}; ω is rotating angular speed for a toothed roller, rad s^{-1}; R is nail point A to center of rotation radius, mm; t is working time for nail roller, s; k is for the machine forward speed and drum rotation speed ratio.

3 Design of core components

3.1 Design of film forming parts

As the cotton root growth area is mainly between 0-150 mm below the surface, so the design of the maximum working depth is 150 mm, the maximum diameter is 12 mm, the smallest diameter is 4 mm, and use 45 steel cone rod bending. The area of the residual layer of the tillage layer is between 4 and 25 cm^2, so that the teeth are evenly distributed on the side of the rod teeth to ensure that the spacing is about 18 mm, which can prevent the residual film from causing it be smaller. The length of the small nail is 40 mm, and the diameter is 5 mm with 45 steel. It can prevent the nail from being too long to be easily bend, and also prevent the nail from being too short to accumulate the residual film in the nail. Figure 4 showed the nail teeth and the main parameters of the nail structure were shown in Table 1.

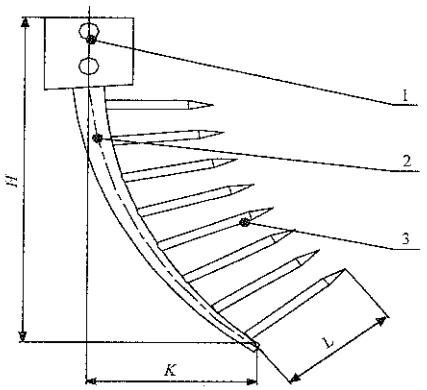

1. Mounting plate 2. Main nail teeth 3. Small nail teeth

Figure 4 Sketch of nail teeth

Table 1 List of nail structure parameter

Project	Length of Main nail teeth H, mm	Deviation displacement L, mm	Length of small nail tooth K, mm
	150	30	40

The nail roller is welded with a rod seat, and the rod base and the rod teeth are connected by bolts, so that the utility model is convenient to disassemble and adjust. A nail tooth is welded on the rod tooth and is used for hooking the residual film to achieve the effect of film opening. A three-dimensional drawing of the film lifting device was shown in Figure 5.

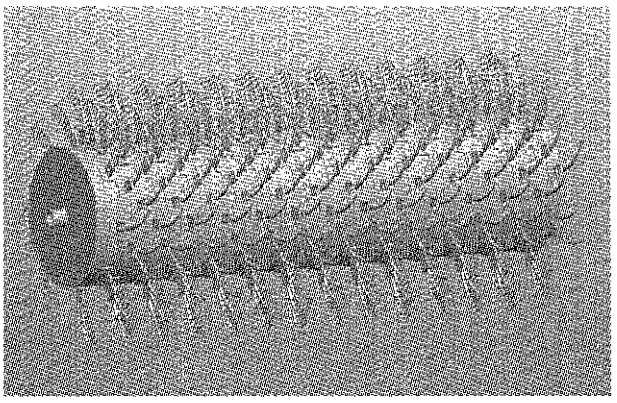

Figure 5 Three dimensional screw tooth roller

The length of the nail roller is 2000 mm, and the diameter is 500 mm. Eight teeth are evenly distributed in a week, and the surface of the roller is 15^0 angles to the teeth of the next week. The teeth between the two adjacent weeks are 50 mm apart, with a total of 12 weeks, and the total number of teeth is 288. Each rod tooth is welded with 8 nail teeth.

3.2 Unloading principle

From the principle of film-unloading, we can be seen that when the residual film is in the nail and do the rotary movement into the working range of the unloading device with the nail, the brush on the brush roller contact, and the residual film on the teeth. And residual film is pegged off into the recovery box because the force of brush on film overcomes the friction between the teeth and film. When the residual film and soil, weeds, roots, straw and other adhesion together, it can increase the rotation speed of the nail drum firstly, and increase the centrifugal force so that the soil, weeds, roots, straw was thrown off. Second, use hard materials such as brush, wire brush and so on to increase the brush speed in order to brush under the residual film, weeds, roots, straw and so on.

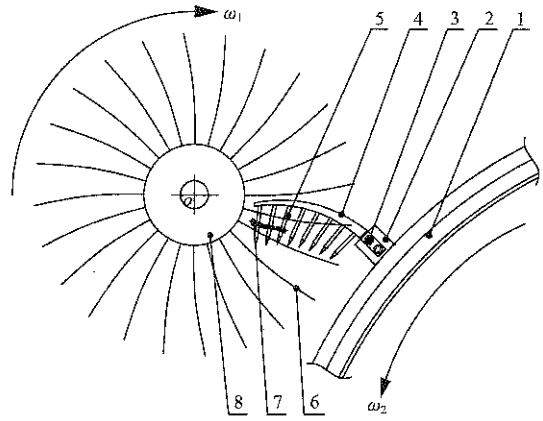

1. Nail tooth roller 2. Nail seat 3. Connecting piece 4. Main nail teeth 5. Small nail teeth 6. Brush 7. Plastic film 8. Brush roller

Figure 6 Film unloading principle diagram

In order to make the brush have a better effect of unloading film, you can increase the brush and the teeth on the contact frequency of the residual film. The movement principle was shown in Figure 6. Namely:

$$\omega_1 \geq -\kappa\omega_2 \quad (8)$$

where, ω_1 is the rotate speed for brush roller, rad s^{-1}; ω_2 is the rotational speed for a toothed roller, rad s^{-1}; κ is the speed ratio.

3.3 Design of unloading mechanism

According to the principle of unloading film, the design of the unloading device was done and it consisted of brush roller, spindle, base, brush and the corresponding sprocket, with which the spindle length is 2.2 m, and diameter is 30 mm. The length of the substrate is 2000 mm, and the diameter is 120 mm. On the substrate, there are 8 mm diameter brush mounting holes. The brush mounting holes are equipped with eight brushes with a diameter of 1.8 mm and a length of 250 mm. The size and density of the brush mounting holes directly affect the number of brushes, and the smaller number of brushes affects the effect of unloading the film. Therefore, the

selection of the brush mounting hole 24 times a week evenly distributed in the brush roller of the week, with the adjacent one week spacing of 12 mm.

4 Field orthogonal test

4.1 Test material

Before the experiment, the total amount of residual films in soil can be obtained by measuring the residual number of residual film in soil plow, which using no less than 10 sample points to measure with plum blossom method. And after the operation of the machine, we measured the remaining number in the cultivated area again, and took it as the residual number of residual film after the experiment. In order to ensure effectiveness of the sample data, the measured sample points after every experiment was three, and finally took the average after obtain the data. Field trials were shown in Figure 7.

Figure 7 Test scenario

4.2 Test methods

Orthogonal experimental design

(1) Test factors

Prototype test is to determine the test factors. Among them, the tractor speed has a great influence on the recovery effect of the residual film, and the tractor speed affects the efficiency of the residual film recovery and the working efficiency. The rotation speed of the nail drum determines the contact frequency of the nail and the residual film, and also affects the residual film recovery effect. Due to the difference of residual film distribution in different depths, the depth of nail teeth has a direct effect on the recovery of residual film and the working resistance of the machine. Therefore, nail wheel rotation speed, tractor forward speed, nail operation depth were selected as the test factors.

(2) Test level

Access to relevant literature (Wang et al., 2011; Zhang et al., 2007) and through consultations with the relevant agricultural operators, it is understood to have the spinning tillage machine tractor speed about 4 km/h. Therefore, the speeds of the recovery machine tractor are 2, 4, and 6 km/h, which can prevent the effect residual film recovery efficiency because of slow speed, excessive wear and tear and reducing of the service life because of fast speed. The diameter of the nail drum is 500 mm, the circumference is 1.57 m. When the speed of the tractor is 6 km/h, the distance traveled per second is 1.6 m. Therefore, the rotation speeds of the selected nail drum are 90, 120 and 150 r/min. Diameter distances are 2.23, 3.14, and 3.925 m, which is about 1.5 times, 2 times, 3 times of tractor. The fastest time the tractor walked was 1.6 meters per time. And at that time, it can prevent leakage and reducing of membrane, and so on. Besides, it also can prevent the reducing of service life because of high speed of the nail roller and the drum. It also meets the motion trajectory rod tip A point showed in Figure 3. In summary, the best data we gained from the test are: three levels of the speed of the tractor are 2, 4 and 6 km h^{-1}, the three levels of the rotation speed of the nail drum are 90, 120 and 150 r/min, the three levels of tooth depth are 50, 100 and 150 mm. The horizontal coding table was shown in Table 2.

Table 2 Factor level code table

Level	Factor level		
	A Advance speed, km/h	B Rotational speed, r/min	C Working depth, mm
1	2	90	50
2	4	120	100
3	6	150	150

(3) Orthogonal test scheme

The orthogonal experiment was adopted. According to the level of factors, three factors and three levels of orthogonal test table was designed, and taking into account the interaction of the factors affecting the machine (Wang et al., 2012), orthogonal table for $L_{27}(3^{13})$ was used. The design of the orthogonal test is shown in Table 3.

Table 3 Results of orthogonal test

Test number	1 A	2 B	3 $(A\times B)_1$	4 $(A\times B)_2$	5 C	6 $(A\times C)_1$	7 $(A\times C)_2$	8 $(B\times C)_1$	11 $(B\times C)_2$	δ, %	η, $hm^2\ h^{-1}$
1	1	1	1	1	1	1	1	1	1	57.85	0.0721
2	1	1	1	1	2	2	2	2	2	66.23	0.0698
3	1	1	1	1	3	3	3	3	3	67.41	0.0801
4	1	2	2	2	1	1	1	2	3	73.35	0.0685
5	1	2	2	2	2	2	2	3	1	74.07	0.0632
6	1	2	2	2	3	3	3	1	2	72.38	0.0723
7	1	3	3	3	1	1	1	3	2	74.19	0.0680
8	1	3	3	3	2	2	2	1	3	60.52	0.0714
9	1	3	3	3	3	3	3	2	1	57.6	0.0702
10	2	1	2	3	1	2	3	1	1	62.31	0.0823
11	2	1	2	3	2	3	1	2	2	61.81	0.0678
12	2	1	2	3	3	1	2	3	3	72.41	0.0725
13	2	2	3	1	1	2	3	2	3	74.12	0.0758
14	2	2	3	1	2	3	1	3	1	70.41	0.0687
15	2	2	3	1	3	1	2	1	2	67.32	0.0702
16	2	3	1	2	1	2	3	3	2	65.51	0.0658
17	2	3	1	2	2	3	1	1	3	69.34	0.0652
18	2	3	1	2	3	1	2	2	1	64.69	0.0635
19	3	1	3	2	1	3	2	1	1	63.27	0.0761
20	3	1	3	2	2	1	3	2	2	48.69	0.0682
21	3	1	3	2	3	2	1	3	3	66.29	0.0703
22	3	2	2	3	1	3	2	2	3	70.16	0.0803
23	3	2	2	3	2	1	3	3	1	73.18	0.0728
24	3	2	2	3	3	2	1	1	2	68.92	0.0743
25	3	3	1	1	1	3	2	3	2	69.37	0.0679
26	3	3	1	1	2	1	3	1	3	60.08	0.0691
27	3	3	1	1	3	2	1	2	1	58.59	0.0710
K_1	603.6	576.28	579.07	591.38	610.1	601.76	600.76	581.99	581.97		
K_2	607.93	637.04	628.6	607.59	594.34	596.56	608.04	585.25	604.43		
K_3	588.5	579.89	592.41	601.11	595.6	601.76	591.28	632.84	613.68		
k_1	67.07	64.03	64.34	65.71	67.79	66.86	66.75	64.67	64.66		
k_2	67.55	70.78	69.84	67.51	66.04	66.28	67.56	65.03	67.16		
k_3	65.39	64.43	65.82	66.79	66.18	66.86	65.7	70.32	68.19		
R	2.15	6.75	5.5	1.8	1.75	0.58	1.86	5.65	3.52		
K_1	0.57	0.66	0.62	0.63	0.65	0.62	0.63	0.65	0.64		
K_2	0.62	0.63	0.65	0.54	0.62	0.63	0.63	0.63	0.62		
K_3	0.65	0.61	0.63	0.66	0.64	0.65	0.65	0.634	0.64		
k_1	0.0628	0.0732	0.0694	0.0705	0.0719	0.0694	0.0695	0.0726	0.0711		
k_2	0.0691	0.07	0.0727	0.0603	0.0685	0.0704	0.0705	0.0695	0.0694		
k_3	0.0722	0.068	0.0699	0.0733	0.0716	0.0721	0.0718	0.0699	0.0715		
R	0.0094	0.0052	0.0033	0.013	0.0034	0.0026	0.0023	0.0031	0.0021		

4.3 Test indexes

According to the national standard GB/T25412-2010 "residual film recovery machine", combined with the actual situation to determine the test indicators, the residual film recovery and residual film recovery efficiency were selected as the field test indicators (Chen et al., 2005).

(1) Recovery rate of residual film

The recovery rate of residual film can be obtained by the following formula:

$$\delta = \frac{M_0 - M_1}{M_0} \times 100\% \tag{9}$$

where, δ is the recovery rate of residual film; M_0 is the total residual membrane residue in soil, g; M_1 is the residue of residual film in soil, g.

(2) Recovery efficiency of residual film

The efficiency of residual membrane recovery is an important indicator of how many areas residual membrane recycling machine works in the unit time. The residual membrane recovery efficiency is given by:

$$\eta = \frac{S}{t} \tag{10}$$

where, η is the recovery efficiency of residual film, $hm^2\ h^{-1}$; S is the operating area of residual film recovery machine, hm^2; t is the operation time of residual film recycling machine, h.

5 Test results and analysis

5.1 Range analysis of test results

The test results are shown in Table 4. Through the analysis of the experimental data in Table 4, we can see that the factors that affected the recovery rate of residual film are (B×C)>(A×B)>B>(A×C)>A>C. The difference R value indicated that the interaction between the rotation speed B and the working depth C(B×C), the interaction between the rotation speed B and the forward speed A(A×B) is significant for the test results. The second levels of (B×C) are 70.32% and 68.19% respectively, and the second levels of (A×B) are 69.84% and 67.51% respectively. When the rotation speed is B_2, the recovery rate of residual film is 67.55%, The comprehensive analysis showed that when the rotation speed of the nail drum B_2 is 120 r/min for the optimal level. Similarly, the tractor forward speed A_2 is 4 km/h and the nail working depth C_1 is 50 mm, and for residual film recovery rate, the best combination levels are, $B_2A_2C_1$. (A×C)>B=(B×C)>C, the difference R value indicates the tractor forward speed A and the nail wheel rotation. The interaction of velocity B(A×B) has a significant effect on the test results, and $(A\times B)_2$ achieves the highest residual film recovery efficiency at the third level of 0.0733 hm^2/h. Tractor forward speed A at the third level can obtain the highest residual film recovery, 0.0722 hm^2/h. Through the comparative analysis, the tractor's forward speed A3 of 6 km/h is the optimal level of residual film recovery. When the rotation speed of the nail drum is 0.25 r/min and the working depth C_1 is 50 mm, thé efficiency of residual film recovery is the best level combination of $A_3B_1C_1$.

5.2 Analysis of variance of residual film recover

The variance calculation results of residual film recovery are shown in Table 4 below. The order of effect on the recovery of residual film is B>(B×C)>A>C>(A×B)>(A×C). Considering the degree of influence of each interaction on the experiment and combining with the data analysis, it can be concluded that the main factors of the residual film recovery rate are the order of the rotation speed of the nail drum, the advancing speed of the tractor and the working depth of the nail. And the residual rate of the residual film is consistent with the law of the residual film recovery. The optimal level of the residual film recovery rate is 120 r/min, the tractor forward speed is 4 km/h and the working depth of the nail C_1 is 50 mm, that is $B_2A_2C_1$, and the residual film recovery rate is up to 74.12%.

Table 4 Analysis of variance of residual film recovery

Source of variance	Sum of squares of deviations	Freedom	mean square	F-measure	sig.	Significant
A	22.976	2	11.488	0.601	0.571	
B	221.634	2	110.877	5.8	0.028	***
C	17.115	2	8.558	0.448	0.654	
$(A\times B)_1$	9.725	2	4.863	0.254	0.781	
$(A\times B)_2$	12.652	2	6.326	0.331	0.728	
$(A\times C)_1$	1.999	2	1.000	0.052	0.949	
$(A\times C)_2$	15.693	2	7.847	0.441	0.676	
$(B\times C)_1$	180.076	2	90.038	4.712	0.044	***
$(B\times C)_2$	59.084	2	29.542	1.546	0.271	
error	152.859	8				
The sum	87503.988	26				

5.3 Analysis of variance of residual film recovery efficiency

The variance calculation and analysis results of residual film recovery efficiency are shown in Table 5. The order of effect on the recovery efficiency of residual membrane is C>B>(A×C)>A>(B×C)>(A×B). Considering the different influence of various sources on the experiment, it can be concluded that various sources have significant effects on the main factors of residual film recovery combining combined with data analysis. The sequence is the rotation speed of the nail drum, the advancing speed of the tractor and the working depth of the nail. According to the average residual film recovery efficiency of 0.07 hm^2/h (Deng et al., 2016), the combination of the residual film recovery efficiency and the average residual film recovery efficiency is the best. And combining with Table 3, it can be concluded that the optimal combination of residual membrane recovery rate was 120 r/min for pin cylinder rotation speed B2, 4 km/h for tractor advancing speed A2 and 50 mm for pinion working depth C1. In other words, when the sequence

was B2A2C1, recovery rate of residual membrane was up to 74.12 %.

Table 5 Analysis of variance of residual film recovery efficiency

Source of variance	Sum of squares of deviations	Freedom	mean square	sig	Significant
A	4.419×10^{-5}	2	2.209×10^{-5}	0.247	
B	1.1×10^{-4}	2	5.571×10^{-5}	0.051	***
C	0	2	0	0	***
$(A\times B)_1$	1.274×10^{-5}	2	6.37×10^{-5}	0.641	
$(A\times B)_2$	1.07×10^{-4}	2	5.35×10^{-5}	0.438	
$(A\times C)_1$	0	2	0	0	***
$(A\times C)_2$	2.394×10^{-5}	2	1.197×10^{-5}	0.149	
$(B\times C)_1$	5.029×10^{-5}	2	2.514×10^{-5}	0.268	
$(B\times C)_2$	2.265×10^{-5}	2	1.132×10^{-5}	0.142	
error	1.37×10^{-4}	8			
The sum	0.135	26			

6 Discussion

According to the field test results, we can calculate that the average index of recovery rate of is 69.74% by adjusting the operating parameters of the prototype. Compared with the recovery mechanism of the surface film, the working efficiency and recovery rate of the residual film are lower. Through the test results, the paper further analyzed the recovery of the residual film of the tillage layer, and obtained the solution.

(1) Effect of the adhesion of residual film fragments on the recovery of residual film

In the plow layer, the residual debris is mainly distributed in the form of 4-25 cm^2. When the fragments are in the soil, they are affected by the migration of the soil, soil, water and fertilizer. The residual film was adhered with the soil and formed shrinkage. That caused difficulties for recycling machinery

(2) Effect of soil resistance on residual film recovery

Under different humidity conditions, the adhesion of soil to the residual film has different effects, and the higher the depth of the work, the greater the mechanical resistance of the soil, which affects the separation efficiency of the film and membrane, and the residual film recovery rate.

(3) Effect of residual film on the recovery of residual film

The problem of residual film recovery is a long-term improvement of the research process. In order to study the problem of residual film recovery, it is necessary to understand how the residual film has been differentiated into smaller crust and migrate in the soil. Residual film and soil adhesion also make membrane soil separation become more difficult to deal with. Solving these problems can help to improve the residual film recovery and operating efficiency.

(4) Effect of the difficulty in unloading the film

The main problem of the residual film recovery machine is the difficulty in unloading film. When the continuous operation is carried out, the friction between the residual film and the nail is larger. Therefore, the effect of different modes, different speed and different angle on film-unloading can be studied.

The rotary tillage nail tooth residual film recycling machine is suitable for the residual film in topsoil. And there are large amounts of residual film in cotton soil, and makes other residual film recycling machine difficult to recycle. And a good recycling result can be obtained through the operation of the machine, although the number of film in the plow layer soil is decrease by 69.74%. In practical application, the cost of farmer's equipment and the high efficiency of operation can be used to optimize the operation process of the residual film recycling machine and the land preparation machinery, thus reducing the operating cost.

7 Conclusions

Through the design and experiment of the rotary tillage nail tooth residual film recovery machine, the main conclusions can be drawn:

(1) The rotary-toothed residual film recovery machine could be used for the recovery of the residual film in the plowing area before planting in spring. The recovery rate is 74.12%, working efficiency is 0.0758 hm^2/h, and the residual amount of residual films in topsoil can be reduced

(2) The design of the brush roller unloading film mechanism has a certain effect of unloading film, and the reliability of the operation is better. It can achieve the deformation of the residual film on the teeth, after the recovery of residual, it is easy to clean and use.

(3) Through the field orthogonal test, the optimal working parameters of the rotary nail-type residual film recovery machine are determined as: the rotation speed of

the screwdriver drum is 120 r/min, the tractor speed is 4 km/h, the working depth of the nail is 50 mm. At this time, the membrane recovery reached the best working condition, the maximum recovery rate of residual film is 74.12% and the residual film recovery efficiency is 0.0758 hm^2/h.

Acknowledgments

The work was supported by the Public Welfare Industry (Agriculture) special research No.201503105; National Natural Science Foundation of China No.11562019; National Key Research and Development Plan of the 13th Five-year Plan No.2017YFD0701102-1; Group innovation project of Tarim University No.TDZKCX201501.

[References]

[1] Chen, F., J. X. Shi, and H. J. Zhao. 2005. Optimum design of fixing cam combination mechanism for collecting plastic residue. *Transactions of the Chinese Society for Agricultural Machinery*, 36(12): 43–46. (In Chinese with English abstract)

[2] Dai, F., W. Y. Zhao, F. W. Zhang, Z. Wu, X. Song, and Y. Wu. 2016. Optimization and experiment of operating performance of collector for corn whole plastic film mulching on double ridges. *Transactions of the Chinese Society of Agricultural Engineering*, 32(18): 50–60. (In Chinese with English abstract)

[3] Deng, X. H. 2016. Application and suggestion of residual film recover mechanization technology in YiLi state. *Agricultural Engineering*, 6(1): 24–25.

[4] Dong, H. G., T. Liu, Y. G. Li, H. F. Liu, and D. Wang. 2013. Effects of plastic film residue on cotton yield and soil physical and chemical properties in Xinjiang. *Transactions of the Chinese Society of Agricultural Engineering*, 29(08): 91–92. (In Chinese with English abstract)

[5] Hou, S. L., S. Y. Hu, J. M. Kong, H. Y. Zhang, and M. J. Na. 2002. Present Situation of Research on plastic film residue collector in China. *International Agricultural Engineering Journal*, 18(3): 186–190.

[6] Hu, K., J. Q. Wang, B. Li, B. Jiang, and S. S. Ding. 2013. Development and experiment of combined operation machine for cotton straw chopping and plastic film collecting. *International Agricultural Engineering Journal*, 29(19): 24–32.

[7] Li, Y., W. Y. Zhao, F. Dai, L. R. Shi, and X. H. Guo. 2016. Development and experiment of combined operation machine for potato harvesting and plastic film collecting. *Journal of Hunan Agricultural University (Natural Sciences)*, 42(1): 102–107.

[8] Lou, X. H., D. G. Zhang, D. Y. Geng, and Y. F. Ji. 2002. Research and design on loosening shovel of polythene film collector. *Transactions of the Chinese Society of Agricultural Engineering*, 18(6): 88–90. (In Chinese with English abstract)

[9] Li, B., J. K. Wang, K. Hu, and B. Jiang. 2012. Analysis and text forward film removing mechanism for polythene film collector. *Transactions of the Chinese Society of Agricultural Engineering*, 28(21): 23–28. (In Chinese with English abstract)

[10] Luo, J. J., R. K. Niu, and X. F. Wang. 2016. Analysis of the current situation of plastic films residue pollution of cotton field in Xinjiang Aksu area. *Journal of Yili Normal University*, 53(2): 56–60.

[11] Lv, Z. Q., L. Zhang, G. L. Zhang, and S. F. Liu. 2015. Design and text of the chain guide rail-type plastic film collector. *Transactions of the Chinese Society of Agricultural Engineering*, 31(18): 48–54. (In Chinese with English abstract)

[12] Ma, S. H., and X. J. Zhang. 2012. Design and experiment of side of use plastic film collector machine. *Transactions of the Chinese Society of Agricultural Engineering*, 2(1): 73–75. (In Chinese with English abstract)

[13] Wang, J. K., W. Fu, and W. B. Wang. 2011. Design of SM-1500 type straw chopping and plastic film residual collector machine. *Transactions of the Chinese Society of Agricultural Engineering*, 27(07): 168–172. (In Chinese with English abstract)

[14] Wang, W. M., and C. G. Wang. 2012. Parameter analysis and simulation of spring-finger cylinder pickup collector. *Transactions of the Chinese Society for Agricultural Machinery*, 43(10): 82–89.

[15] Wang, X. N., J. X. Si, J. X. Guo, and F. Chen. 2008. Experimental study and design on film raking mechanism of hanging film raker with cotton-stalk crushing and returning to field. *Transactions of the Chinese Society of Agricultural Engineering*, 24(1): 135–140. (In Chinese with English abstract)

[16] Xie, J. H., S. L. Hou, Y. Fu, M. Na, and H. Zhang. 2013. Motion analysis and Experiment on spring-tooth mulching plastic film collector. *Transactions of the Chinese Society for Agricultural Machinery*, 44(S1): 94–99.

[17] Zhang, B. F., W. Z. Yang. 2015. Design on roll film residual recover machine. *Agricultural Engineering*, 5(1): 79–82.

[18] Zhang, H. Y., S. L. Hou, M. J. Na, X. Dong, Y. Q. Li, X. L. Yang, and S. M. Peng. 2007. Multifunctional machine for retrieving the used plastic film after harvesting and soil preparation. *Transactions of the Chinese Society of Agricultural Engineering*, 23(8): 130–134. (In Chinese with English abstract)

[19] Zhu, H. J., W. Z. Yang, and Y. S. Zhou. 2015. Design of finger disc residual film recover machine. *Agricultural Engineering*, 5(3): 89–92.

Design and experiment of soil covers rice whole straw machine

Zhou Wenqi[1], Feng Xin[1], Wang Jinwu[1*], Wang Qi[2], Wang Jinfeng[1]

(1. *Engineering College, Northeast Agricultural University, Harbin 150030, China*;
2. *School of Biological and Agricultural Engineering, Jilin University, Changchun 130022, China*)

Abstract: The structure characteristics and working principle of the soil covers rice whole straw machine was described, soil covers rice whole straw machine was developed by designing the knife roller, the blocking rice straw device and analyzing the up-cut rotary mode of operation in theoretical. Based on the test-bed of the laboratory to design the experiment, and using Design-Expert software to analyze the data. The test results showed that the entire width of the soil covers rice whole straw machine was 1m, the power consumption of the machine was 12.56 kW and the returning rate of rice straw was 91.27% when the forward speed was 1.25 km/h and rotation speed was 217 r/min. The performance test of the machine in paddy field showed that the tillage depth was more than 20 cm, the returning rate of rice straw was 86%, the depth of rice straw buried could be 15 cm and the rate of crushed soil was 90.6%. The machine could achieve the functions of the followings, such as cutting up soil, breaking up soil, burying rice straw and pressuring rice straw. The situation of soil after the machine operation is so good that it could directly fulfill agricultural requirements of steeping field and soil preparation.

Keywords: soil covers rice whole straw machine, rice straw, buried rice straw, up-cut rotary mode of operation

Citation: Zhong, W. Q., X. Feng., J. W. Wang, Q. Wang, and J. W. Wang. 2017. Design and experiment of soil covers rice whole straw machine. International Agricultural Engineering Journal, 26(4): 106–115.

1 Introduction

At present, the comprehensive utilization of crop stalks is regarded as a basic national policy of the sustainable agricultural development in China (The Ministry of Agriculture of The People's Republic of China, 2011). The returning way of rice straw to the field can meet the basic requirements fully. It can replenish soil nutrients (Wang et al., 2010; Zhang et al., 2014), promote microbial decomposition, reduce the use of fertilizers (Wang et al., 2008; Lao et al., 2002; Li, 2015), improve soil structure (Jiang et al., 2011), improve the ability of water storage and soil conservation (Wu, 2009), prevent the phenomenon of wind and water erosion occurring, improve crop yield (Zhao et al., 2010; Hu et al., 2016) and promote sustainable agricultural development (Gao et al., 2008; Han et al., 2002; Shen et al., 1998; Gu, 2016). At this stage, the common form of returning the rice straw to the field is using the rotary tiller directly to crush the rice straw and bury it into the soil (Jia et al., 2015; Jian et al., 2015; Li et al., 2011). Another mode of the operation is the rice combine harvester harvests the rice straw and sprays them in the field, then using the plow to bury the rice straw into the soil. Although the plow has a significant effect on burying the crushed rice straw, the mode of operation will take some root stubble out of the soil. In the soak paddy time, the crushed rice straw will be floated out of the water surface. The crushed rice straw will be taken out of the soil during the raking paddy (Wang, 2015). They seriously influence the effect of rice planting. Multi-channel tillage processes can cause a lot of energy consumption, destroy the soil structure, lower the working efficiency and the effect of rice straw return to the paddy (Wang et al., 2009; Wang et al., 2004; Zhang et al., 2006).

In view of these problems, the up-cut rotary theory was analyzed. The theory and data as reference were used to develop the soil covers rice whole straw machine. In order to get the optimal working parameters combination of the machine, the Design-Expert software was used to analyze the reason that influenced the forward speed and

Received date: 2017-01-08 **Accepted date:** 2017-11-16

*** Corresponding author: Wang Jinwu**, PhD, Professor, Research focuses on farm machine and mechanical reliability. Engineering College, Northeast Agricultural University, Harbin 150030, Heilongjiang Province, China. Email: jinwuw@163.com.

rotation speed on the returning rate of rice straw and the power consumption. The performance of the machine was verified by field experiment.

2 Design and working principle of soil covers rice whole straw machine

2.1 Design of soil covers rice whole straw machine

The soil covers rice whole straw machine consists of frame, central reducer, side reducer, blocking rice straw device, knife roller shaft, pedestal of knives, knives, limiting the depth plank and so on, as shown in Figure 1.

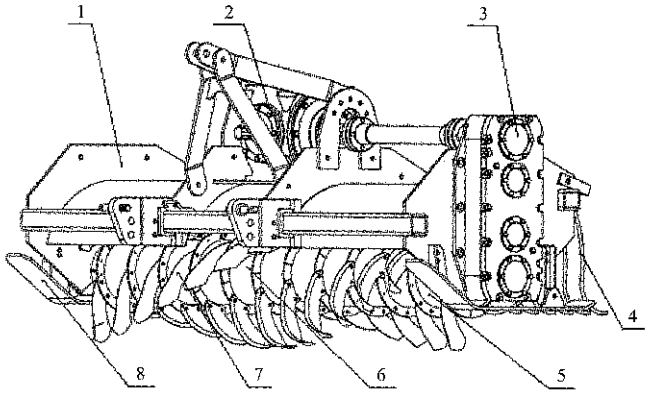

1. Frame 2. Central reducer 3. Side reduce 4. Blocking rice straw device 5. Knife roller 6. Knife seat 7. Knife 8. Limiting the depth plank

Figure 1 Structure of the soil covers rice whole straw machine

The machine is connected to the tractor by a three-point suspension frame, the power direction is changed to 90 degree by the bevel gears of the central reducer, the power is transmitted to the assembly of knife roller by the side reducer. The machine completes the whole rice straw returning to the field by rotation of knife roller. The rice straw is returned to the field in the way of up-cut rotation (Zhong et al., 2010; Xu et al., 2012; Chen et al., 1998). This mode of operation can make the soil and rice straw be fully thrown to increase the returning rate of rice straw and get the soil layer which meets the agronomic requirements. The main structure parameters were shown in Table 1.

Table 1 Parameters of soil covers rice whole straw machine

Parameter	Value
Dimensions, mm	1344×1970×1040
Machine weight, kg	650
Number of knives	35
Working width, mm	1600
Tillage depth, mm	20-23
Matching power, kW	≥66
Operating speed, km/h	1.25

2.2 Working principle of soil covers rice whole straw machine

The soil covers rice whole straw machine works in the way of the up-cut rotary mode of operation (Guo et al., 2016; Wang et al., 2007). The knives throw the soil and the whole rice straw, then they will fall from the top of the knife roller to the rear of the knife roller. The working principle was shown in Figure 2.

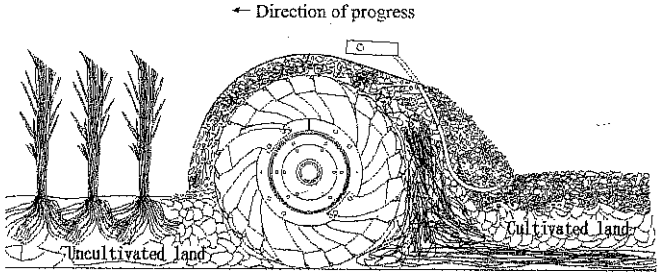

Figure 2 Working principle of soil covers rice whole straw machine

As the quality of the rice straws are lighter than the soil, so the height of the rice straw that is thrown is lower. Due to the impact of air resistance, the time of the rice straws in the air is short. While the height of the broken soil that is thrown is higher, the less impact of air resistance to make it stay a long time in the air (Hao et al,. 2014). Therefore, rice straws and soil fall into the ditch with different time. The rice straws will fall into the ditch before the soil and then be covered with the soil to complete the process of work.

3 Design of the main working parts

3.1 Design of knife roller

Knife roller is one of the key parts of the machine (Details of knife design are given in Ref 20). The diameter parameter of the knife roller directly influences the working performance of the machine. The large diameter knife roller will increase the depth of the machine into the soil. When the machine works, that in front of the achine will appear the phenomenon of bulldozing leads the numbers of repeated cutting and throwing of broken soil to increase. Ultimately that will increase the tractor power consumption. The small diameter knife roller will be entangled by rice straw during the operation. That will influence the work performance of the machine seriously. In order to solve the problem which the knife roller is entangled by whole

rice straw , the perimeter of the knife roller should be longer than the length of the whole rice straw (the length of rice straw is 60-70 cm after half-feed combine harvester working). So the large knife roller was designed to meet the work requirements of the device.

In summary, the diameter parameter of the knife roller was designed with the diameter of 240 mm and its perimeter was 75.36 cm. Through the strength calculation, the thickness of the knife roller was 5 mm. the structure of knife roller was shown in Figure 3.

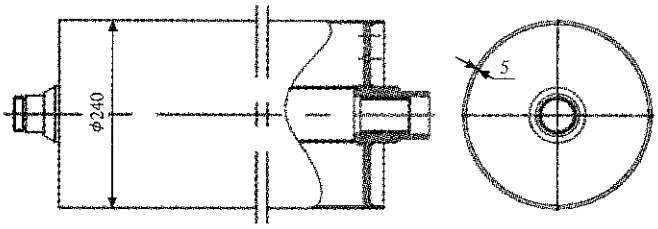

Figure 3 The structure of knife roller

3.2 Design of arc-shaped shell and blocking rice straw device

The operating mode of the device is the way of up-cut rotary. The soil is cut and thrown from the bottom to up during the operation. If the shape of the arc-shaped shell and the relative position with the device are unreasonable, the soil will not be thrown sufficiently and the phenomenon of bulldozing will happen in front of the device. That will seriously influence the returning rate of rice straw and significantly increase the power consumption of the device.

Due to the soil is thrown fast by knives (the diameter of the broken soil is between 20 and 64 cm) and the collision between soil and arc-shaped shell, the arc-shaped shell and knife roller were designed as concentric, and their distance was 66 cm. The collision theory between soil and arc-shaped shell was analyzed. As the soil was thrown fast by the knife, it was assumed that the soil was thrown at an angle with the horizontal straight line. As the Figure 4 shown: the straight line is M, θ_1 and θ_2 are the different angles of arc-shaped shells with horizontal direction, $\theta_1<\theta_2$. OE and OF are the different lines of soil thrown that are come from arc-shaped shells with θ_1 and θ_2, A and C are the collision points of OE and OF with M respectively. Straight line AC and CD are their normal. β_1 and β_2 are the corresponding collision angles. Derivation formula shows: $\beta_1=\omega+\theta_1<\omega+\theta_2$, $\beta_1=90°-\alpha_1$, therefore $\alpha_1>\alpha_2$. So the arc-shaped shell should be designed with a smaller angle in horizontal direction, ensuring that there is a greater collision angle when the soil collides with the arc-shaped shell. The level distance of soil thrown is farther after the collision to ensure that the soil is thrown fully (Yan et al,. 2014). So, the inclined plate was designed as 20° with horizontal direction, its location was tangent with the arc-shaped shell in the offset 20° with the vertical direction. The device improves through performance of soil and rice straws and reduce the soil of repeated cutting and throwing. It was shown in Figure 5.

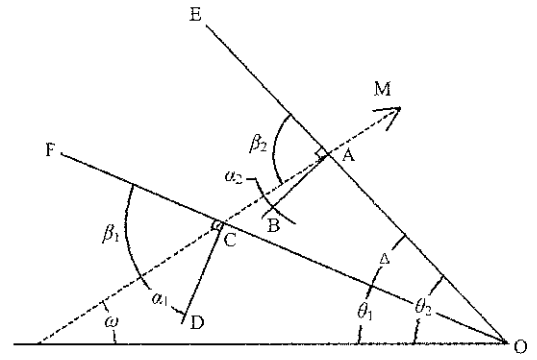

Figure 4 Analysis of collision theroy between soil and arc-shaped shell

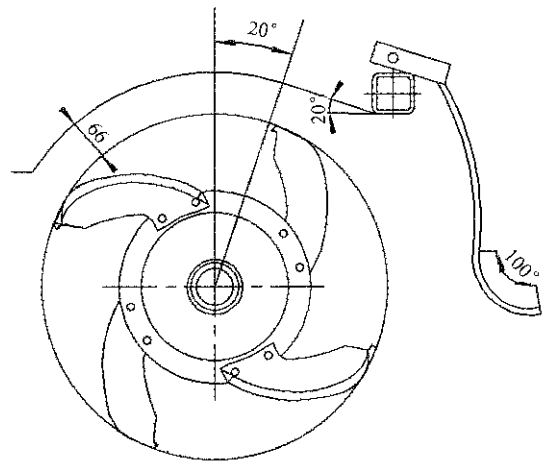

Figure 5 Drc-shaped shell and blocking rice straw device

To design and install the blocking rice straw device in the position of soil thrown, so that the larger soil block can be broken for the second time. Point O was analyzed at the end of the blocking rice straw device. As the Figure 6 shows that the straight line EF is the angle bisector of β at the end of the blocking rice straw device, α is the angle between the thrust of the blocking rice straw device and the horizontal direction. The rice straw was analyzed along the horizontal and vertical directions:

$$\begin{cases} F_1\cos\alpha + f\cos\alpha = F_h \\ G + F_1\sin\alpha - f\cos\alpha = F_v \\ \mu(Gos\alpha + F_1) = f \\ 2\alpha = \beta \end{cases} \quad (1)$$

Finishing Equation (1):

$$(1-\mu\sin\alpha\cos\alpha)G + F_1(\sin\alpha - \mu\cos\alpha) + F_h \quad (2)$$

where, F_1 is the thrust of blocking rice straw device to rice straw, N; f is the friction of blocking rice straw device to rice straw, N; G is the gravity of rice straw, N; α is the angle between thrust of blocking rice straw device and horizontal direction, °; β is the angle of the end of the blocking straw device, °; F_v is the total force of rice straw at the vertical direction, N; F_h is the total force of rice straw at the horizontal direction, N; μ is the coefficient of friction between the blocking rice straw device and the rice straw.

Analysis shows that the greater the value of F_v, the greater the possibility that the rice straw is returned to the field by the thrust of the blocking rice straw device. Because the quality of rice straw is so light that it can be ignored, so α should be greater than 45°. In this paper, α was 50°. Considering that the length of the whole rice straw and the situation of soil crushing, the distance between the two bars of the blocking rice straw device was designed as 100 mm, and the angle of the end of the blocking rice straw device was 100°. That can significantly improve the performance of the whole rice straw buried and the rate of broken soil, and get the high-quality soil layer ultimately. The size of the blocking rice straw device was shown in Figure 5.

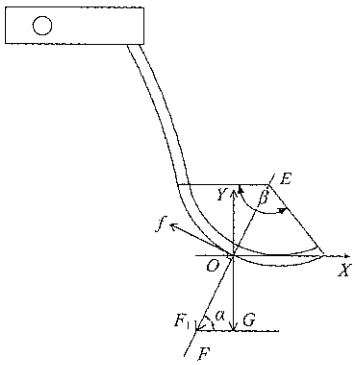

Figure 6 Force analysis of the rice straw at the end of blocking rice straw device

4 Theoretical analysis of soil covers rice whole straw machine

4.1 Theoretical analysis of soil covers rice whole straw

The movements of soil and rice straw were analyzed. There were three processes that rice straw was covered into the soil: the process of soil and straw thrown up, transport process of soil and straw, and the process of soil and straw thrown out, as shown in Figure 7. Due to the characteristics of knife and the interaction between soil and rice straw, the soil layer is located in the up and vicinity of the rice straw layer during the throwing up and transporting stages. Therefore, only the stage of soil and rice straw thrown out was analyzed.

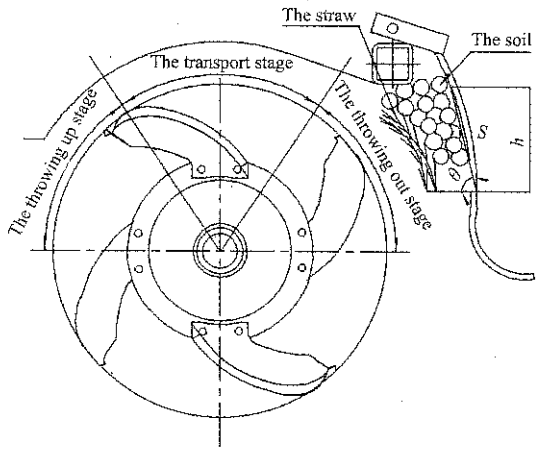

Figure 7 Process of soil covers rice whole straw

In order to achieve the effect of rice straw buried, the method of counter-evidence was used to prove that the soil and rice straw have different heights at the stage of throwing out. Assuming that at the stage of throwing out, the soil and rice straw reach the same height h for a period of time t. Based on the physical characteristics of rice straw at the moment. The formula is as follows:

$$\begin{cases} V_1^2 - V_0^2 = 2gh \\ V_1 = \sqrt{2gh + V_0^2} \end{cases} \quad (3)$$

where, V_1 is the speed of rice straw after time t, m/s; V_2 is the initial speed of rice straw at the throwing out stage, m/s; h is the height of rice straw after time t, m. g is the gravity acceleration, m/s.

The soil was analyzed. When the soil falls, it will be blocked by the blocking rice straw device. The distance was set to s. According to the kinetic energy theorem:

$$\begin{cases} \frac{1}{2}mV_2^2 - \frac{1}{2}mV_0^2 = mgh - 2FS \\ S = \frac{h}{\sin\theta} \\ V_2 = \sqrt{V_0^2 - \frac{2Fh}{m\sin\theta} + 2gh} \end{cases} \quad (4)$$

where, V_2 is the speed of soil after time t, m/s; S is the distance of soil and blocking rice straw device, m; F is the friction between soil and blocking rice straw device, N; θ is the angle between friction and horizontal line, °; m is the quality of soil, kg.

By analyzing Equations (3) and (4), it can be shown that V_1 and V_2 are different. It was proved that there was a speed difference between soil and rice straw in the process of falling. The speed difference of rice straw and soil can be expressed as:

$$\Delta V = V_1 - V_2 = \sqrt{V_0^2 + 2gh} - \sqrt{V_0^2 + 2gh - \frac{2Fh}{m\sin\theta}} \quad (5)$$

The Equation (5) was analyzed. When θ was smaller, ΔV will would be larger. When ΔV is was larger, the gap between the speed of soil and rice straw would be larger. When F was smaller, ΔV will would be larger. When ΔV was larger, the gap between the speed of soil and rice straw would be larger. Increasing the speed gap would allow most of the rice straw to fall into the ditch before the soil. It can ensure that most of the rice straw could fall to a certain depth which met the agronomic requirements.

5 Indoor test bed

5.1 Test equipments and conditions

In order to investigate the performance of soil covers rice whole straw machine and find the best combination of parameters which influences the power consumption and the returning rate of rice straw. Reducing the power consumption of the machine, while to obtain a good operating quality (Zhang, 2008; Liu et al., 2010; Guo et al., 2012; Wang et al., 2016; Zhou et al., 2012; Wang et al., 2010). The experiment of soil covers rice whole straw machine was designed based on the test-bed of Heilongjiang Agricultural Machinery Research Institute. The power consumption and the returning rate of rice straw was studied in the experiment.

The soil of soil tank is typical black loam in Heilongjiang region. The test platform consists of the soil tank, the TCC-III computer monitoring and the auxiliary test vehicle, the track, the measurement and control system. The forward speed, output shaft speed, tillage and the other factors in step-less speed regulation could be adjusted by the measurement and control system, and average-value data such as torque and power consumption were obtained. Due to the restriction of test conditions, the experiment was carried out by soil covers rice whole straw machine with a working width of 1 m. The machine consists of knife roller, knife seats (6), knives (symmetrical 12), reducer, rack, blocking rice straw device and limiting the depth plank, as shown in Figure 8.

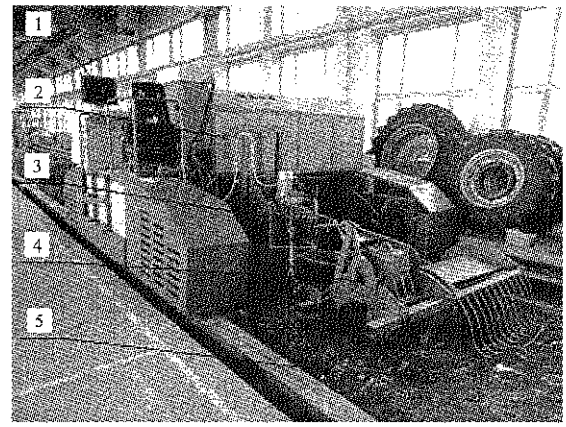

1. Soil tank 2. TCC-III computer monitoring 3. Auxiliary test vehicle
4. Device 5. Measurement and control system

Figure 8 Test bed for the soil covers rice whole straw machine

The machine was connected and tested by the structure of biased suspension. Power was output from the test car, from the universal coupling transmission to the reducer which made power change, drove the roller to achieve the way of up-cut rotary tillage. The main parameters of the machine: operating width was 1 m, tillage depth was 19-22 cm and the roller diameter was 240 mm.

5.2 Experimental design

The performance of the machine was mainly verified by testing. The influences of various factors on the power consumption and the returning rate of rice straw were analyzed. The test car and the machine through the hydraulic three-point suspension was connected to ensure the height that limiting the depth plank and soil surface in each test, which would fix the depth of 200 mm. The test unit area was 2×1 m, as shown in Figure 9. After treatment, the soil moisture was 30%; the soil firmness was 900nKpa; the row spacing of rice straw was 30cm; the spacing of rice straw was 15 cm.

First, the average weight of rice straw in a certain area was calculated before the test, after the test was completed, the weight of rice straw which was cut by

using scissors was measured with an electronic balance. Through the above steps, the returning rate of rice straw was calculated.

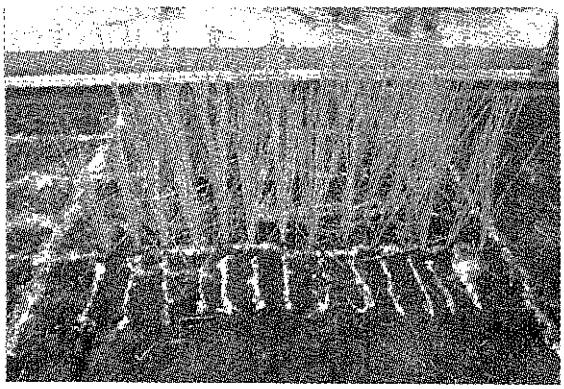

Figure 9 Treatment status of rice straw

The forward speed of machine X_1 and the rotation speed X_2 were selected as the test factors. Each factor was taken five levels. The power consumption of machine Y_1 and the returning rate of rice straw Y_2 were the test indicators. The experiment was carried out by quadratic rotation orthogonal combination design. Table 2 showed the factors level coding table.

Table 2 Coding table of factors level

Levels	Factors	
	Forward speed, km/h	Rotation speed
+1.414	1.50	267.00
+1	1.40	258.00
0	1.25	237.00
−1	1.10	216.00
−1.414	1.00	207.00

The test schedule and results were shown in Table 3, and the average of each test was repeated three times as the test results.

Table 3 Data table of the test using quadratic orthogonal-rotation combination design

Test sequence	Forward speed, km/h	Rotation speed, r/min	Power, kW	The returning rate of rice straw, %
1	1.40	216.00	15.45	92.5
2	1.25	267.00	24.05	91.9
3	1.25	237.00	14.82	93.4
4	1.10	216.00	12.07	86.4
5	1.50	237.00	20.57	91.5
6	1.00	237.00	12.10	89.2
7	1.25	237.00	14.43	93.7
8	1.25	237.00	14.36	92.2
9	1.25	207.00	12.44	89.8
10	1.10	258.00	16.75	90.1
11	1.25	237.00	13.76	93.3
12	1.25	237.00	14.23	93.1
13	1.40	258.00	23.37	91.3

5.3 Analysis of results

5.3.1 The influence of each test factor on the power consumption

Design-Expert software was applied to analyze the data in Table 2 to obtain the variance analysis table about the forward speed and rotation speed of the machine on the power consumption, as shown in Table 4.

Table 4 Variance analysis for the influence of each factor to the power consumption

Source	Sum of square	Freedom	F value	Significance (P>F)
Model	195.7	5	85.74	<0.0001
x_1	60.39	1	132.3	<0.0001
x_2	105.3	1	230.6	<0.0001
x_1^2	5.79	1	12.68	0.0092
x_2^2	24.25	1	53.13	0.0002
x_1x_2	2.61	1	5.73	0.0479
Error	0.59	4		
Sum	198.9	12		

Table 4 shows: when the significance level is 0.05, the effective terms of the models are x_1, x_2, x_1^2, x_2^2, x_1x_2. The influence of the rotation speed on power consumption was significant than the forward speed of the machine. The contour plot and response surface chart for the influence of x_1 and x_2 were obtained, as shown in Figure 10. The influence of each factor on power consumption was analyzed and the regression equation was obtained.

$$y_1 = 327.66 - 143.86x_1 - 2.15x_2 + 40.54x_1^2 + 4.23x_2^2 + 0.26x_1x_2 \quad (6)$$

Figure 10 shows: x_1 and x_2 interacted between the two factors significantly, power consumption increased with the increase of the two factors. When the forward speed and rotation speed of the machine are at a low level, the variation of power consumption is small with the increase of the forward speed and rotation speed. When the forward speed and rotation speed are at a high level, the variation of power consumption is large with the increase of the forward speed and rotation speed. The change of response surface along the direction of rotation speed is faster than that of the forward speed. It indicated that the influence of the rotation speed on power consumption was larger.

Analysis shows when the forward speed and rotation speed of the machine are at a low level, that the soil is cut and thrown by the machine would be more stable. The

power consumption of the machine increases slowly as the forward speed and rotation speed increases. When the machine in the situation of a high forward speed and the rotation speed, the high rotation speed increases the times that the machine cuts and throws soil repeatedly. The machine consumes more energy per unit time. So, the power consumption of machine changes greatly with the increase of the rotation speed.

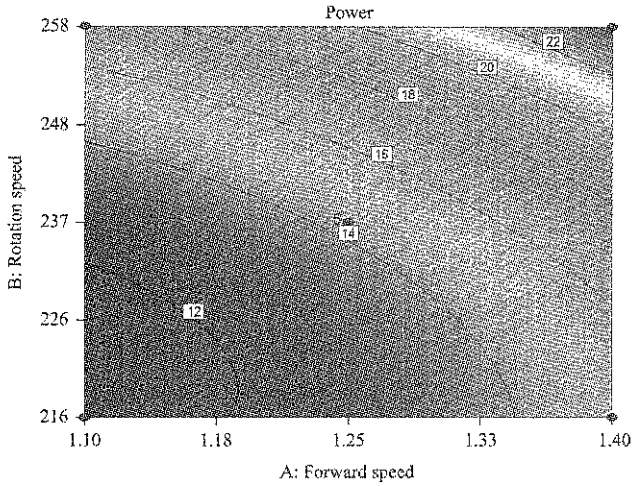

a. Contour plot

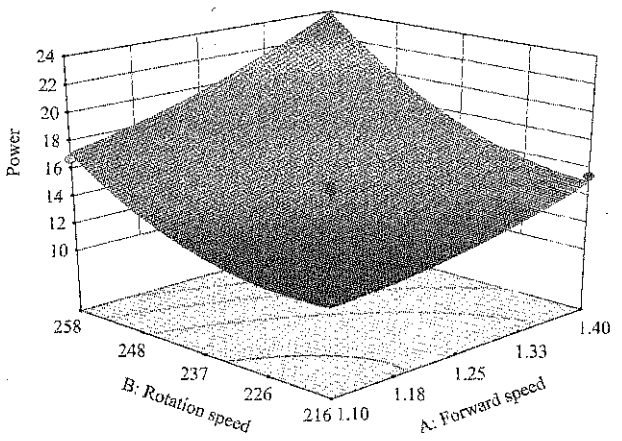

b. Response surface chart

Figure 10 Contour plot and response surface chart for the influence of the forward speed and rotation speed on power consumption

5.3.2 Influence of test factors on the returning rate of rice straw

The data in Table 3 were analyzed by Design-Expert software, the variance analysis table about the forward speed and rotation speed of machine on rice straw covered was obtained, as shown in Table 5.

Table 5 shows: when the significance level is 0.05, the effective term of the models is x_1, x_2, x_1^2, x_2^2, x_1x_2. The influence of the forward speed on the returning rate of rice straw is more significant than that of the rotation speed. The contour plot and response surface chart of the influence of x_1 and x_2 were obtained, as shown in Figure 11. The influence of each factor on the returning rate of rice straw was analyzed and the regression equation was obtained.

$$y_1 = -309.32 + 270.54x_1 + 1.89x_2 - 67.83x_1^2 - 2.89x_2^2 - 0.39x_1x_2 \quad (7)$$

Table 5 Variance analysis for the influence of each factor to the returning rate of rice straw

Source	Sum of square	Freedom	F value	Significance (P>F)
Model	48.08	5	17.18	0.0008
x_1	13.92	1	24.87	0.0016
x_2	3.74	1	6.68	0.0362
x_1^2	16.20	1	28.95	0.0010
x_2^2	11.33	1	20.24	0.0028
x_1x_2	6.00	1	10.72	0.0136
Error	1.29	4		
Sum	52.00	12		

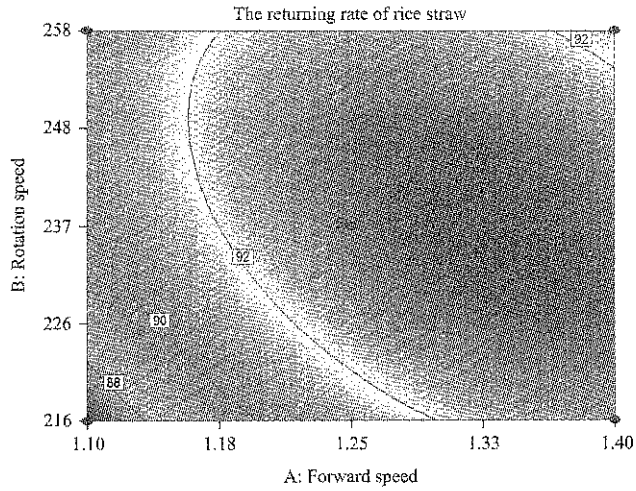

a. Contour plot

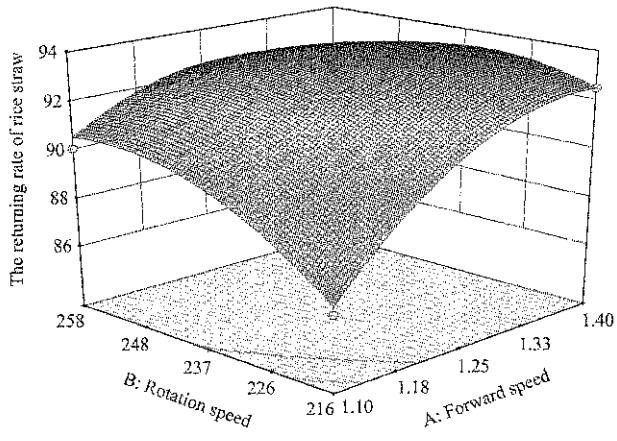

b. Response surfacechart

Figure 11 Contour plot and response surface chart for the influence of the forward speed and rotation speed on the returning rate of rice straw

It can be seen from Figure 11, x_1 and x_2 interacted significantly, the returning rate of rice straw increased with the increase of the factors. When the forward speed and rotation speed of the machine are at a low level, with the increase of the forward speed and rotation speed the variation of the returning rate of rice straw is large. When the forward speed and rotation speed are at a high level, the returning rate of rice straw decreases with the increase of the forward speed and rotation speed, but the trend of decline is slower. The change of response surface is faster than that of the rotation speed along the direction of the forward speed. It indicated that the influence of the forward speed on the returning rate of rice straw was larger.

Analysis shows when the forward speed and rotation speed of the machine are at a low level, the soil and rice straw are fully thrown. The returning rate of rice straw is relatively rapid. But with the increase of the forward speed and rotation speed, the action of excessive rice straw thrown influences the trajectory and position of rice straw. The relative position of soil and rice straw are disrupted to influence the order of their fall, thereby lowering the returning rate of rice straw.

5.3.3 Scheme of optimization parameter combination

The fundamental purpose of the experiment is to find the optimal combination of working parameters, so as to achieve the effect of reducing the power consumption and increasing the returning rate of rice straw. By way of analysis and optimization of Design-Expert software to find the optimal combination of parameters of the forward speed and rotation speed.

The objective functions used in the optimization are the Equations (6) and (7), The constraint of $y_1 \in (12.07,\ 24.05)$, $y_2 \in (90,\ 93.07)$, $x_1 \in (1.00,\ 1.50)$, $x_2 \in (207,\ 266)$ was set up. The optimal combination of parameters was obtained. When the forward speed is 1.25 km/h and the rotation speed is 217 r/min, the power consumption of the machine is 12.56 kW and the returning rate of rice straw is 91.27%. A smaller value was taken in the range of 12.31 to 25.83 kW as described above for the calculation of the power consumption. It is proved that the theoretical analysis is the same as the optimization results. The results showed that the optimal combination of parameters could reduce the power consumption and improve the returning rate of rice straw.

6 Field performance test

6.1 Field test machine

The main technical indicators for the machine: 48 knives were installed, the working width was 2.1 m, the forward speed of the machine was 1.25 km/h, the production efficiency was 0.26 $hm^2\ h^{-1}$, rotation speed was 217 r/min, more than 90 horsepower tractor supported.

6.2 Results of performance test and analysis

Field prototype test was done according to the standard GB/T 5668.3-1995 and JB/T9401.3-2001 and according to the specific test conditions to determine the test indexes: the returning rate of rice straw, tillage depth, the returning depth of rice straw, soil flatness, the crushing rate of soil.

In late September, 2015, the field experiment of soil covers rice whole straw machine was conducted in Jiamusi City, Heilongjiang Province. The state of rice straw is the rice whole straw of semi-fed combine harvester after harvesting as is shown in Figure 12.

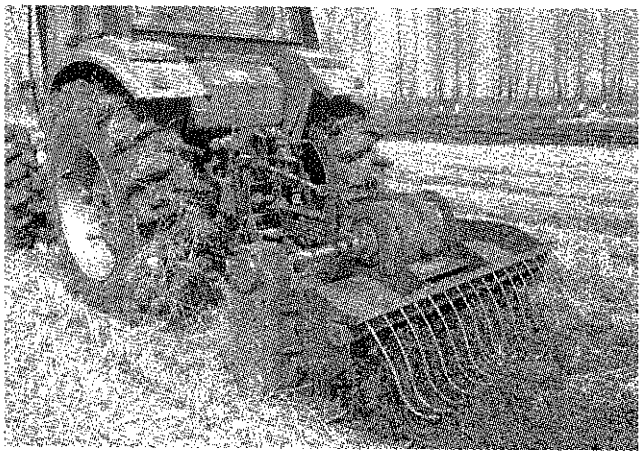

Figure 12 State of the test machine and test ground

The length of rice straw was 70-80 cm, the soil firmness was 700-900 kPa, the length of rice straw was 70-80 cm, the thickness of soil layer was 8-10 cm, the soil firmness was 700-900 kPa and the soil moisture was 35%-45%. The test results are shown in Table 6.

Result analysis: The results of field experiment are in accordance with the results of the test-bed. The soil covers rice whole straw machine can bury rice straw into the ground 15-20 cm and ensure that the returning rate of

rice straw more than 90%. The rate of soil crushing, the stability of tillage depth and surface roughness after tillage can meet the agronomic requirements of rice growth. The tests showed that the machine could complete the rice whole straw deep-buried and rotary-tillage operation at one time.

Table 6 Test results of soil covers rice whole straw machine

Technical indicators	Test Results
Matching power, kW	≥66
Operating speed, km/h	1.25
Working width, m	1.6
Tillage depth, cm	20-23
Stability of tillage depth, %	86
The rate of straw returning, %	92.7
Surface roughness after tillage, cm	1.4
The crushing rate of the soil, %	90.6

7 Conclusions

(1) Based on the theory of up-cut rotary, the soil covers rice whole straw machine was designed and developed. The experimental data were obtained and analyzed by the test-bed and Design-Expert software. The optimal combinations of parameters are as follows: the power consumption is 12.56 kW and the returning rate of rice straw is 91.27%, when the forward speed of the device is 1.25 km/h and the rotation speed of the knife roller is 217 r/min.

(2) Through the field experiments, it showed that the returning rate of rice straw of the soil cover rice whole straw machine could reach more than 90%. The rate of the soil crushing, the stability of tillage depth and surface roughness after tillage could meet the agronomic requirements of rice growth.

Acknowledgements

The authors thank the financial support provided by the National Industry System of Rice Technology of China (CARS-01-44), Heilongjiang Modern Industrial Technology Collaborative Innovation System.

[References]

[1] Chen, X. J., Y. H. Tang, Y. Liu, G. R. Tan, and Z. P. Pu. 1998. Anti-rotary straw stubble field fine effect. *Soil and Fertilizer*, (06): 46.

[2] Gao, H. W., H. W. Li, and W. Y. Li. 2008. Development of conservation tillage. *Transactions of the Chinese Society for Agricultural Machinery*, 39(9): 43–48.

[3] Guo, J., C. Y. Ji, H. M. Fang, Q. Y. Zhang, and C. Zhang. 2016. Experimental analysis of soil and straw displacement after up-cut and down-cut rotary tillage. *Transactions of the Chinese Society for Agricultural Machinery*, 47(5): 21–26.

[4] Guo, X. M. 2012. Key points on orthogonal test design and application of DPS, *Modern Agricultural Science & Technology*, 3: 40–41.

[5] Gu, X. L.,and G. X. Hao. 2016. Promotion of conservation tillage, sustainable agriculture.*Agricultural Development and Equipment*, 05: 3.

[6] Han, L. J., Q. J. Yan, X. Y. Liu, and J. Y. Hu. 2002. Straw resources and their utilization in China. *Transactions of the Chinese Society of Agricultural Engineering*, 18(3): 87–91.

[7] Hao, X. Z., Z. Q. Li, S. G. Huang, S. Z. Li, and W. Y. Ning. 2014. Tiller rotary blade knife roll and its parameters to optimize the design and test. *Agricultural Machine*, 9: 155–158.

[8] Hu, N. J., B. J. Wang, Z. H. Gu, B. R. Tao, Z. W. Zhang, S. J. Hu, L. Q. Zhu, and Y. L. Meng. 2016. Effects of different straw returning modes on greenhouse gas emissions and crop yields in a rice–wheat rotation system. *Agriculture, Ecosystems & Environment*, 223(1): 115–122.

[9] Jiang, J., H. Chen, and X. L. Zhao. 2008. The application actuality and methods of meliorated soil with crop stalks. *Chinese Agricultural Science Bulletin*, 24(8): 420–423.

[10] Lao, X. R., Z. Y. Wu., and Y. C. Gao. 2002. Comprehensive effect of straw returning on soil fertility in long time. *Transactions of the Chinese Society of Agricultural Engineering*, 18(2): 49–52.

[11] Li, Y. M. 2015. Effects of straw pretreatment on soil water and fertilizer factors and crop yield. Ph.D. diss., *College of Water Resources and Architetural Engineering., Northwest Agriculture and Forestry University*, Yang Ling.

[12] Jia, H. L., X. M. Jiang, M. Z. Guo, X. L. Liu, and L. C. Wang. 2015. Design and experiment of V-L shaped smashed straw blade. *Transactions of the Chinese Society of Agricultural Engineering*, 31(1): 28–33.

[13] Jian, S. C., N. N. Zhang, X. Y. Wang, Z. F. Di, Q. J. Peng, and Q. K. Fu. 2015. Design and experiment on straw returning rotary tillage and fertilization maize planter. *Journal of Agricultural Mechanization Research*, 37(8): 177–180.

[14] Li, Y. L., J. N. Song, J. C. Wang, J. K. Zhang, and X. Q. Dong. 2011. Design and experiment of SGTN-180 type rotary tillage-straw returning-fertilization combine machine. *Journal of China Agricultural University*, 16(02): 143–147.

[15] Liu, R. J., W. Y. Zhang, C. W. Wen, and J. Tang. 2010. Orthogonal experimental design and analysis methods. *Experimental Technology and Management*, 27(9): 52–55.

[16] Shen, Y. H., X. G. Huang, and H. Q. Wang. 1998. Field effects of straw mulching. *Agricultural Research in the Arid Area*, 16(1): 48–53.

[17] The Ministry of Agriculture of the People's Republic of China. 2011. National Agricultural Mechanization Development Twelfth Five-Year Plan (2011-2015). Beijing. *Ministry of Agriculture of the People's Republic of China.*

[18] Wang, C. Y., and X. W. Zhan. 2004. A brief discussion on agricultural ecosystem environment and paddy production mechanization. *Chinese Agriculture Mechanization*, 6: 26–27.

[19] Wang, H. B., Y. P. Qing, and K. Yu. 2008. Utilization, distribution and exploitation tactics of crop stalk resources in China. *Territory and Natural Resources Study*, 13(2): 92–93.

[20] Wang, J., D. J. Wang, and G. Zhang. 2010. Effect of incorporated straw-nitrogen fertilizer on nutrient leaching in paddy soils. *China Ecological Agriculture*, 18(18): 316–321.

[21] Wang, J. W., D. Q. Yin, Y. J. Han, W. Y. Ji, Y. Song, and T. J. Zhao. 2007. Design and experiment of whole rice straw returning machine. *Transactions of the Chinese Society for Agricultural Machinery*, 38(10): 54–56.

[22] Wang, J. W., Q. Wang, H. Tang, Q. W. Zhou, Y. T. Duo, and Y. Zhao. 2015. Design and experiment of rice straw deep buried and whole straw returning device. *Transactions of the Chinese Society for Agricultural Machinery*, 46(9): 112–117.

[23] Wang, L., Y. Zang, and X. W. Luo. 2009. Development countermeasure of rice production mechanization in China. *Journal of Agricultural Mechanization Research*, 31(6): 1–4.

[24] Wang, R. L., G. X. Pan, P. Yang, Q. H. Zhang, S. Dou, and D. J. Liu. 2016. Design and experiment of straw deep returning rotary ditching machine. *Shenyang Agricultural University*, 42(2): 185–191.

[25] Wang, Z. S., J. F. Xia, Q. C. Xu, and R. W. Hu. 2010. Power consumption experiment of rotary tillage and stubble mulch knife roller. *Transactions of the Chinese Society for Agricultural Machinery*, 41(12): 44–47.

[26] Wu, Y. Q., M. Qu, F. Sun, and Z. F. Chen. 2009. Effect of straw mulching on soil physical and chemical properties soil microorganism and environment. *Chinese Agricultural Science Bulletin*, 25(14): 263–268.

[27] Xu, L. C., Y. Cai, and N. Zhang. 2012. Virtual prototype modeling and simulation of reverse straw returning machine transmission. *Journal of Agricultural Mechanization Research*, 34(11): 33–36.

[28] Yan, J. C., H. J. Li, and J. P. Hu. 2014. Study on calculation of the up-cut rotary's throwing soil volume and distribution. *Journal of Agricultural Mechanization Research*, 36(11): 29–33.

[29] Zhang, J. 2003. The effects of application of treated rice straw on soil nitrogen supply and crop growth. M.S. thesis., *Department of Plant Science., Nanjing Agricultural University.*, Nanjing.

[30] Zhang, M. Q. 2008. The experimental study and the optimizing design of parameters on rice straw return machine. M.S. thesis, *Engineering College, Northeast Agricultural University, Harbin.*

[31] Zhang, P., T. Wei, Z. K. Jia, Q. F. Han, and X. L. Ren. 2014. Oil aggregate and crop yield changes with different rates of straw incorporation in semiarid areas of northwest China. *Geoderma*, 230-231(7): 41–49.

[32] Zhang, X. F., D. Y. Wang, and H. Li. 2006. Research progress and developing strategy in paddy-field conservation tillage in the south of China. *Chinese Journal of Soil Science*, 37(02): 2346–2351.

[33] Zhao, P., F. Chen, X. M. Ma, and S. P. Xiong. 2010. Effect of integrated straw crop yield and nitrogen balance in winter wheat & summer maize. *Agricultural Research in the Arid Area*, 28(2): 162–166.

[34] Zhao, W., J. Y. Chen, H. Y. Wang, C. B. Li, C. B. Liu and H. Gao. 2012. Impact of different straw return systems on nitrogen and physical characters in black soil. *Maize Sciences*, 20 (6): 98–102.

[35] Zhong, J., J. D. Jiang, T. Jiang, Z. F. Zhao, X. Qiao, and X. Zhang. 2010. Deep-tillage rotavator technology based on smoothed particle Hydrodynamics simulation. *Journal of Mechanical Engineering*, 46(19): 63–69.

[36] Zhou, Y., S. S. Yu, and J. F. Xia. 2012. Design and experiment of cultivator for high straw returning in paddy field. *Transactions of the Chinese Society for Agricultural Machinery*, 43(8): 46–49.

Analysis and comparison on the discharging flow of coal particles through hyperbolic funnel

Li Bo[1], Wang Xuewen[1], Yang Zhilong[1], Cai Tongxiang[1], Yang Zhaojian[1], Chen Jun[2]

(1. *Shanxi Key Laboratory of Fully Mechanized Coal Mining Equipment, College of Mechanical Engineering, Taiyuan University of Technology, Taiyuan 030024, China*;
2. *College of Mechanical and Electronic Engineering, Northwest A & F University, Yangling 712100, China*)

Abstract: The problem of poor particle flow during the actual production of coal bunker can be effectively alleviated by hyperbolic funnel. In order to study the mechanical and discharging characteristics of hyperbolic funnel, the calculation methods of hyperbolic funnel curve equation, sectional shrinkage, and inclination angle of funnel wall were analyzed, and an example calculation was made based on a coal bunker funnel model. According to the hyperbolic funnel model within the example calculation, three funnel models, hyperbolic funnel, conical funnel and pyramid funnel were designed. The discrete element software-EDEM was applied to establish the model of coal particles, and simulate the charging and discharging process of three kinds of funnel. Results showed that the hyperbolic funnel was the fastest in discharging among these three funnels, while the conical funnel was the slowest one. The particle flow was funnel flow near the discharging port, and the upper part was the overall flow state within the hyperbolic funnel. This study can provide scientific guidance for the design and optimization of coal bunker.

Keywords: hyperbolic funnel, coal particles, discharging flow

Citation: Li, B., X. W. Wang, Z. L. Yang, T. X. Cai, Z. J. Yang, and J. Chen. 2017. Analysis and comparison on the discharging flow of coal particles through hyperbolic funnel. International Agricultural Engineering Journal, 26(4): 116–123.

1 Introduction

Silo is widely used in mining, machinery, metallurgy, coal, grain, fertilizer, food, cement and other industrial fields for storing loose material because of its advantages of simple structure, low cost, convenient access, circulation space saving and good stability (González-Montellano et al., 2011; Tejchman, 2013; Schulze, 2007; Wang et al., 2013). Generally, the main structure of overhead silo includes straight silo and funnel part. The straight silo is mainly used for storing material, and the funnel part is mainly used for discharging. The object of this study was the funnel part. According to the shape of section, silo can be made into circular or rectangular. Discharging funnel is also designed as cone or pyramid. In bunker applications, flow problems of arching and blocking often occur in these two kinds of discharging funnels. Especially, when the coal particles have large viscosity, high moisture content, and the number of pulverized coal particles is relatively large, the flow and discharging problems are particularly significant.

Generally, the physical properties of loose materials will have a significant impact on the discharge status. For the coal bunker fields, which are different from other loose materials (such as grain, soil, gravel), the size composition and distribution of coal particles changed and destroyed in different degrees due to the shear friction between particles and particles, particles and equipment (Cleary et al., 2009; Fernandez et al., 2011; Cleary et al., 2009). Therefore, a large number of small particles would be formed during the coal particles charging, discharging and transporting. Since the different fluidity of particles in different sizes and the infiltration of fine particle, the segregation of coal

Received date: 2017-07-25 **Accepted date:** 2017-11-16
* **Corresponding author: Li Bo,** Shanxi Key Laboratory of Fully Mechanized Coal Mining Equipment, College of Mechanical Engineering, Taiyuan University of Technology, Taiyuan, China. Email: libo@tyut.edu.cn.

particles easily occurs when coal particles flow slowly in the discharging funnel. Fine particles will concentrate in the center of the hopper and outflow first, and the larger particles concentrate closing to the inner wall of the funnel and discharge finally. It would easily lead to funnel arch, suspension, until blockage. In order to eliminate blocking, arch broken solutions such as steel tapping and poking have been used by engineers. But it would cause the damage or even collapse of the funnel, which is bad for the equipment and production safety management. Finite element method (FEM) has been tried for analyzing the mass and funnel flow modes, the mass flow rate and the wall pressure (Zheng and Yu, 2015; Li et al., 2014) However, FEM usually treated the material as a whole, which was not suitable for loose material.

The discrete element method (DEM), mainly deals with particle problems, has been widely used in many fields including the filling and discharging of silos. The material flow state had been simulated by DEM (González-Montellano et al., 2012; Yu and Saxén, 2011; Liu et al., 2013; Oldal and Safranyik, 2015). The underlying mechanisms of segregation during filling and discharge of silos have been studied by Garcia et al. (2016). Zeng et al. (2017) studied the relationship between particle velocity fluctuations and contact force. The distribution of the load in silos was studied by researchers (Horabik et al., 2016; Acevedo et al., 2014; Vidyapati et al., 2013). Kobyłka et al. (2017) simulated the discharge initiation of a grain silo. It was found that the passage of the rarefaction wave resulted in dynamic changes of all considered micro- and macro- variables describing the behavior of the bulk of solids. The loads in the silo were also analyzed (Kobyłka and Molenda, 2014). The shape of the blast furnace sector would influence the solid flow state (Yang et al., 2015), similarly, funnel design has an important impact on the loose material flow found by application engineers and design engineers. Through the locale practice, the flow resistance of the coal particles is small when conic hyperbolic funnel is arranged at the bottom of the coal bunker, and the problem of poor flow can be alleviated to a certain extent in the application field of the coal bunker.

In order to further understand the mechanical characteristics of the hyperbolic funnel and the discharging characteristic relative to other forms of funnel, the detailed theoretical analysis and example analysis of hyperbolic funnel were carried out in this study. In addition, the discharging flow simulation and comparison of conical funnel, pyramidal funnel and hyperbolic funnel were carried out using EDEM. This study would provide theoretical basis for the application in mine, hydroelectricity, metallurgy and other fields.

2 Discharging theory and example analysis of hyperbolic funnel

The section of the hyperbolic funnel is shown in Figure 1. The solid line presented the hyperbolic funnel while the dashed line presented conic funnel, and the cross section is circular.

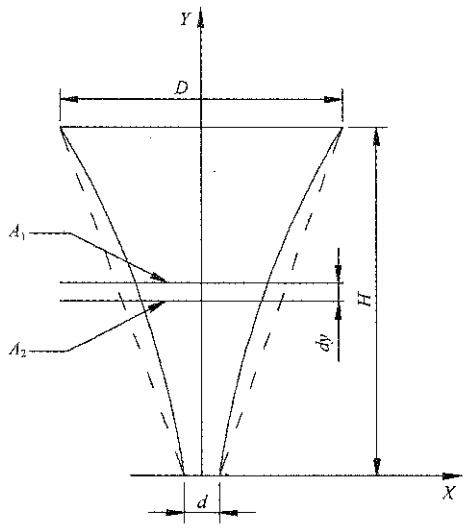

Figure 1 Hyperbolic funnel

The calculation methods of hyperbolic funnel curve equation, sectional shrinkage C, and inclination angle α of funnel wall are shown as follows:

(1) Determine the hyperbolic funnel curve equation (Figure 1)

Calculate according to the constant section shrinkage:

$$\frac{A_1 - A_2}{A_1 dy} = \frac{dA}{A_1 dy} = KC = \text{constant} \quad (1)$$

where, dA = sectional area reduction (m^2); A_1, A_2 = sectional area (m^2); C = constant sectional shrinkage; K = section shape coefficient (circular, K=1; pyramid, K=0.75-1); dy = micro height of particles falling.

For the hyperbolic funnel of circular section in this

paper:

$$\frac{dA}{A_1 dy}=\frac{2\pi x dx}{\pi x^2 dy}=KC \Rightarrow \frac{dx}{x}=\left(\frac{KC}{2}\right)dy \quad (2)$$

After integral:

$$\int_{\frac{d}{2}}^{x}\frac{dx}{x}=\int_0^y\frac{KC}{2}dy \quad (3)$$

After simplify:

$$x=\frac{d}{2}e^{\frac{KC}{2}y} \quad \text{or} \quad y=\frac{2}{KC}\ln\frac{2x}{d} \quad (4)$$

(2) Calculate section shrinkage C

Integrate Equation (2) again:

$$\int_{\frac{d}{2}}^{\frac{D}{2}}\frac{dx}{x}=\int_0^H\frac{KC}{2}dy \quad (5)$$

Then:

$$C=\frac{2}{KH}\ln\left(\frac{D}{d}\right) \quad (6)$$

(3) Calculate inclination angle α of funnel wall

$$\alpha=\arctan\frac{2}{KCx} \quad (7)$$

2.1 Discharging theory

Compared with the conical funnel, the hyperbolic funnel had two main characteristics in its structure: 1. constant section shrinkage (the shrinkage ratio of conical funnel increased gradually from top to bottom, and reached the maximum near the discharging outlet); 2. inclination angles at different heights of funnel varied and increased gradually from charging port to discharging outlet (the inclination angles of conical funnel wall were constant).

When discharging, particles in the funnel moved slowly downward under the action of gravity to overcome the frictional resistance between particles themselves and the funnel wall. When the particles in the funnel dropped from the section A_1 flowing to the next section A_2, the extrusion between the particles became more serious and the particle position was redistributed with the decreasing of the section area. Sectional shrinkage C was used to indicate the decrease of section. The actual test showed that the greater of sectional shrinkage C would lead to more severe extrusion of particles at next section. What's more, the resistance became greater, and the discharging was getting worse. When the resistance was equal to the particle's gravity, the particles stopped flowing downward, and then a funnel jam occurred.

Generally, increasing the cone angle of the funnel until it was larger than friction angle of the wall between coal particle and the inner wall of the silo, then the wall friction of particles would be reduced and the flow of particles would be easier. Decreasing the section is generally not conducive to discharge, but the inclination angle of the hyperbola funnel wall is different at any height. The inclination angle $-\alpha$ was greater when closing to the discharging port. To a certain extent, the inter particle resistance increment caused by the decrease of section was compensated.

The resistance of particles from the top to the bottom was almost constant and the overall particles flow in the funnel was almost the uniform velocity. Problems such as arch and suspending were not easy to appear.

Therefore, the two characteristics of hyperbolic funnel, unlike conical funnel, were apparently helpful for discharging.

2.2 Example analysis

Base on the coal bunker hyperbolic funnel of a coal preparation plant, the inner diameter of the upper and lower openings of funnel were 8and 1m, respectively. The funnel height H was 10m (H=1.25D), and the cross section was circular (K=1).

According to Equation (6), the sectional shrinkage C=0.415 was obtained. In order to get the inclination angle-α and curvature radius-x of each height of the hyperbolic funnel, the height of the funnel was divided into 10 sections on average, each of which was 1m high (Figure 2).

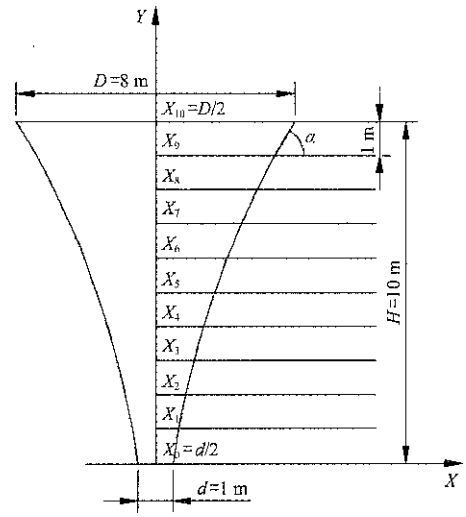

Figure 2 Subsection sketch map of the hyperbolic funnel

According to Equations (4) and (7), the corresponding curvature radius–x and inclination angle -α in each section were calculated in turn. The specific results were shown in Table 1. The inclination angle -α reached the maximum at the discharging port of the hyperbolic funnel. Under the same conditions, the conical funnel had a constant angle of 70°42′36″(= arctan $D/(D–d)$). Although the inclination angle of the upper part was small in the hyperbolic funnel, the gradual increase of inclination angle in the lower part could partially offset the resistance between particles, which was easy to discharge.

Table 1 Subsection parameters of hyperbolic funnel

Ordinate value - y, m	Curvature radius - x, m	Inclination angle -α, (°)	Sectional shrinkage- C
10	4.000	50°25′51″	0.415
9	3.236	56°07′04″	0.415
8	2.630	61°22′46″	0.415
7	2.137	66°05′10″	0.415
6	1.736	70°11′02″	0.415
5	1.411	73°40′45″	0.415
4	1.150	76°36′56″	0.415
3	0.932	79°03′23″	0.415
2	0.757	81°04′13″	0.415
1	0.615	82°43′25″	0.415
0	0.500	84°04′35″	0.415

3 Discrete element analysis

3.1 Funnel model

Refer to the hyperbolic funnel model analyzed in the above example, three funnel models were designed: hyperbolic funnel, conical funnel and pyramidal funnel. The wall thickness was 0.2 m for these three funnels. The opening and outlet section area of these three kinds of funnel were equal, in which the shape of pyramidal funnel section was square, and the inner diameter was its side length. The specific geometric structure parameters were listed in Table 2.

Table 2 Geometric parameters of three funnels

Parameters	Hyperbolic funnel	Conical funnel	Pyramidal funnel
Opening inner diameter, m	8	8	7.1
Outlet inner diameter, m	1	1	0.89
Height., m	10	10	10
Inclination angle	Increase gradually	Constant	Constant
Sectional shrinkage	constant	Increase gradually	Increase gradually

In order to compare the discharging of these three funnels, the calculation and analysis parameters were set equally. Three models of funnel were established using three-dimensional modeling software Pro/E and then imported into Hyper mesh for meshing and numbering. The mesh types were triangular units with size of 250 mm. The mesh numbers were hyperbolic funnel (1-5002), conical funnel (1-5114) and pyramidal funnel (0-6096). After adding funnel material parameters, it was saved as.msh format and imported into EDEM for discrete element discharging simulation (EDEM, 2016).

3.2 Coal particle discrete element model

The generation of coal particle was essential in the whole simulation process, which greatly influenced the simulation results. Because of the uncertainty caused by cutting coal wall of coal mining machine, the shapes of bulk coal were different from each other. It was not similar to the loose materials such as chemical fertilizer or grain whose particle shape was similar to each other. Therefore, it was not easy to define the true shape of coal with accurate data in modeling software. To simplify calculation, the coal particles were simulated by the method of circle filling by EDEM software in this study. The material properties of the coal particle are shown in Table 3.

Table 3 Material parameters of coal particle

Material	Poisson's ratio	Shear modulus, Pa	Density, kg/m^3
Coal	0.25	3×10^7	1300

In order to meet the actual situation as much as possible, the standard coal particle model was built by four combined spheres, and the dimensions of the model were 95.1091 mm long, 85.5912 mm wide and 80.0494 mm high. The coordinates of four sphere center were (–5.18227, –3.17466, –0.027229), (7.55455, 0.107193, 0.0247), (–5.77856, 2.79558, –0.001594) and (5.56446, –0.091541, 0.018026), respectively.

Calculation results showed the quality of the standard coal particle model was 0.564549 kg, the volume was 0.000353 m^3 and the moment of inertia relative to X, Y, Z axis was 0.000401, 0.000448 and 0.000465 kgm^2, respectively.

The generation mode of the particle factory was a dynamic model. The minimum computational mesh radius was 2.6 R and the mesh number was 87412. The target iteration data storage interval was 0.05 s, and the

time step was 0.002 s.

After the model imported into EDEM and the relevant settings finished, a circular baffle was added to the discharging outlet. The particles were blocked at the discharging outlet after they were generated. The establishment of the baffle model was consistent with the funnel. The particle factory (round shape with diameter of 3.4 m) was set at 0.3 m below the upper openings of funnel. The particle generation rate was 5000 per second, and the total number of particles was 30000. When all the particles reached the stable state, the particles began to move down under their own gravity to overcome the frictional resistance.

3.3 Contact model

There were two kinds of contacts in the model, one was the contact between coal, the other one was the contact between coal and the funnel wall. The coal particles broke and deformed, and the wall of the silo also had micro deformation during discharging. The two kinds of contacts should be soft-soft contact. The actual situation could be reflected when two contact bodies were deformed.

The contact state between particles and the contact between the particles and the silo wall were complicated (Weinhart et al., 2016; González-Montellano et al., 2011). To simplify the calculation, two non-slip-contact models of Hertz-Mindlin were established according to the analysis model and the actual working conditions. The gravitational acceleration was set to 9.81 m s^{-1}, and the material parameters were shown in Table 4.

Table 4 Material parameters (Reimbert and Reimbert, 1976; Gai, 2009)

Parameters	Coal particle	Silo wall
Elastic recovery coefficient of coal particles	0.1	0.15
Static friction coefficient of coal particles	0.45	0.5
Dynamic friction Coefficient of coal particles	0.1	0.15
Normal stiffness, Pa	0.5×10^8	1.0×10^8
Tangential stiffness, Pa	0.3×10^8	0.9×10^8

3.4 Result analysis

Figures 3, 4 and 5 were the discrete element simulation results for three funnel discharging processes.

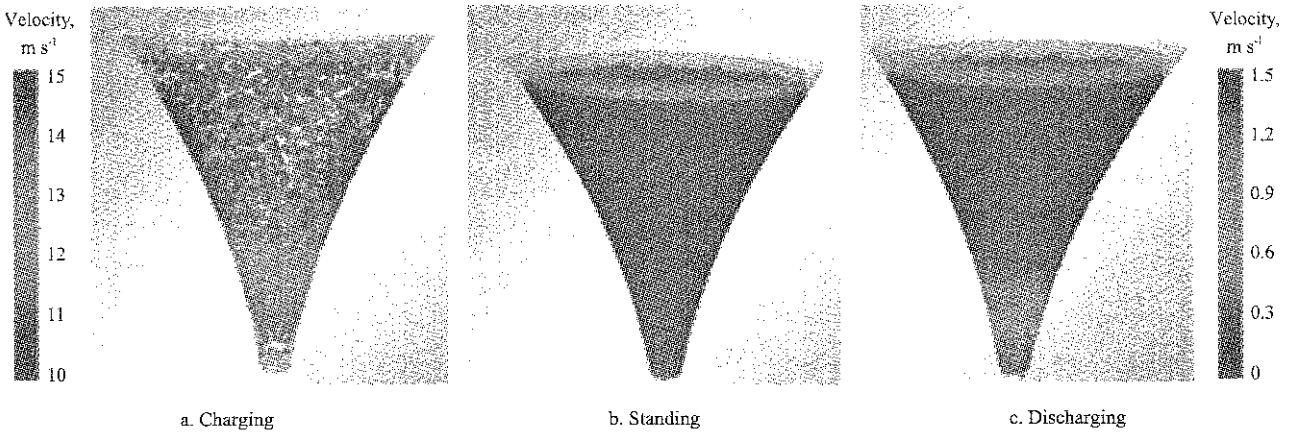

a. Charging b. Standing c. Discharging

Figure 3 Charging and discharging processes of the hyperbolic funnel

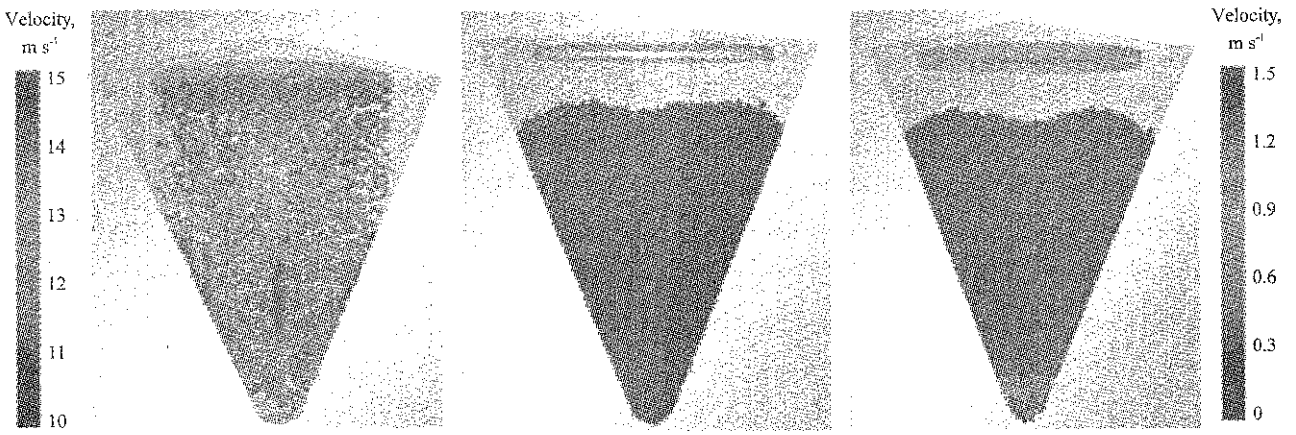

a. Charging b. Standing c. Discharging

Figure 4 Charging and discharging processes of the pyramidal funnel

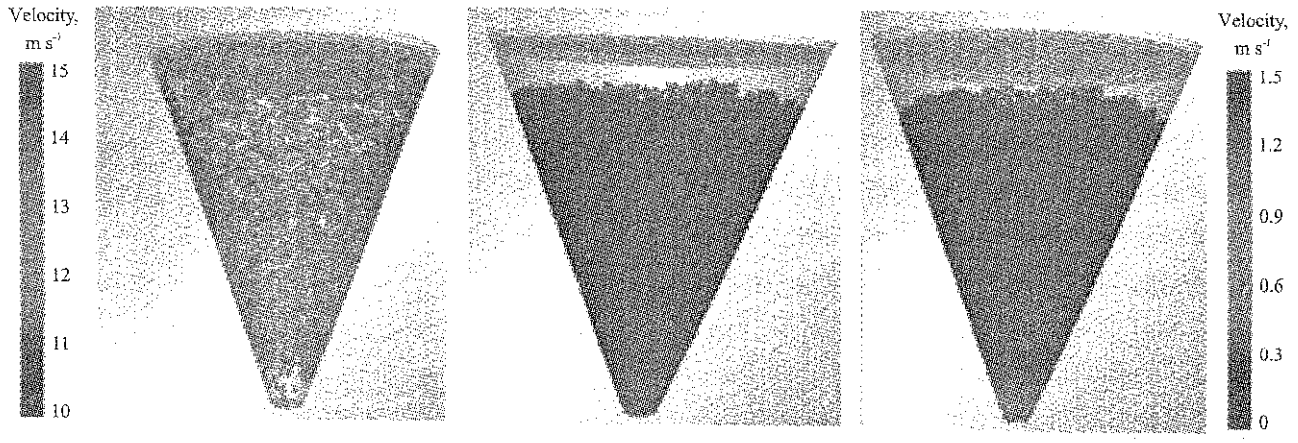

a. Charging b. Standing c. Discharging

Figure 5 Charging and discharging processes of the conical funnel

3.4.1 Charging analysis

Particles moved to the bottom of the funnel under gravity during charging. As the section of funnel shrinking, particles around the edge would first contact with the silo wall, and particle velocity would decrease. This phenomenon was most prominent for the hyperbolic funnel. At the same height, the wall of hyperbolic funnel was closest to the central axis, followed by the conical funnel. In the pyramidal funnel, the frictional contact between particles near the junction of adjacent walls was relatively serious, and the descending velocity of particles was also slow, which was not conducive to charging (Figure 4).

During the process of charging, crushing and collision of particles near the silo wall were more serious for hyperbolic funnel, comparing with conical funnel and pyramidal funnel. Conical funnel was most suitable for loading. It was easy to form suspended material at the junction of wall for the pyramidal funnel.

3.4.2 Charging capacity at standing state

When standing, as shown in Figures 3, 4 and 5, pyramidal funnel could be charged the most under the same condition, followed by the conical funnel, and the hyperbolic one was the least charged.

3.4.3 Discharging analysis

Obviously, when discharging, the velocity of particles in discharging outlet of hyperbolic funnel was higher than that in the other two kinds of funnels, followed by the velocity in pyramidal funnel, and the velocity of particles in conical funnel was the slowest. Under the same conditions, according to the numerical results of funnel discharging, all the particles in the conical funnel flowed out when time was 109.25 s. At the time of 103.5 s, all the particles in the pyramidal funnel flowed out. Particles in the pyramidal funnel used the least time (76.75 s), saving 32.5 s, almost one third of the time compared with the conical funnel.

When discharging, particles in three kinds of funnels showed the form of funnel flow. However, the hyperbolic funnel was more prominent. Particles near the center flowed out first, but funnel flow with particles appeared only in a certain range above the discharging port. Particles closing to the upper discharging port were still in the overall flow state.

The hyperbolic funnel had two main characteristics in its structure: (1) constant sectional shrinkage; (2) the inclination angle of funnel walls varied at different heights, gradually increasing from the loading port to the discharging port. By example analysis and discrete element simulation, the two characteristics of hyperbolic funnel were obviously favorable for unloading.

4 Conclusion

Three kinds of funnels: hyperbolic funnel, conical funnel and pyramid funnel was designed. DEM was used to establish the coal particle model and the charging and discharging processes of three kinds of funnels were simulated. The conclusions were as follows.

(1) The conical funnel was the most suitable for charging materials among these three.

(2) The hyperbolic funnel use the least time in discharging because of its two characteristics in structure: constant sectional shrinkage and the inclination angle of funnel walls varied at different heights.

The results of this study could provide the basis for further design and optimizing the coal bunker according to the actual requirements. However, these studies only compared three kinds of funnels and the coal particles were simplified. More conditions should be considered in the future.

Acknowledgements

The project was supported by the merit funding for the returned overseas personnel sci-tech activities, Shanxi Province, China (Grant No.2016), the Open Research Fund of Shanxi Key Laboratory of Fully Mechanized Coal Mining Equipment (No. mkzczb201602), Youth Foundation of Taiyuan University of Technology (No. 1205-04020203).

[References]

[1] Acevedo, M., I. Zuriguel, D. Maza, I. Pagonabarraga, F. Alonso-Marroquin, and R. C. Hidalgo. 2014. Stress transmission in systems of faceted particles in a silo: the roles of filling rate and particle aspect ratio. *Granular Matter,* 16(4): 411–420.

[2] Cleary, P. W., M. D. Sinnott, R. D. Morrison. 2009. Separation performance of double deck banana screens - Part 1: Flow and separation for different accelerations. *Minerals Engineering,* 22(14): 1218–1229.

[3] Cleary, P. W., M. D. Sinnott, and R. D. Morrison. 2009. Separation performance of double deck banana screens - Part 2: Quantitative predictions. *Minerals Engineering,* 22(14): 1230–1244.

[4] EDEM. EDEM user guide. Edinburgh, UK, DEM Solutions. 2016.

[5] Fernandez, J. W., P. W. Cleary, M. D. Sinnott, and R. D. Morrison. 2011. Using SPH one-way coupled to DEM to model wet industrial banana screens. *Minerals Engineering,* 24(8): 741–753.

[6] Gai, G. S. 2009. Powder Technology.Tsinghua University Press, Beijing.

[7] Garcia, M. C., H. J. Feise, S. Strege, and A. Kwade. 2016. Segregation in heaps and silos: Comparison between experiment, simulation and continuum model. *Powder Technology,* 293(1): 26–36.

[8] González-Montellano, C., E. Gallego, Á. Ramírez-Gómez, and F. Ayuga. 2012. Three dimensional discrete element models for simulating the filling and emptying of silos: Analysis of numerical results. *Computers and Chemical Engineering,* 40(40): 22–32.

[9] González-Montellano, C., F. Ayuga, and J. Y. Ooi. 2011. Discrete element modelling of grain flow in a planar silo: Influence of simulation parameters. *Granular Matter,* 13(2): 149–158.

[10] Horabik, J., P. Parafiniuk, and M. Molenda. 2016. Experiments and discrete element method simulations of distribution of static load of grain bedding at bottom of shallow model silo. *Biosystems Engineering,* 149 :160–171.

[11] Kobyłka, R., J. Horabik, and M. Molenda.2017. Numerical simulation of the dynamic response due to discharge initiation of the grain silo. *International Journal of Solids and Structures,* 106-107: 27–37.

[12] Kobyłka, R., and M. Molenda. 2014. DEM simulations of loads on obstruction attached to the wall of a model grain silo and of flow disturbance around the obstruction. *Powder Technology,* 256: 210–216.

[13] Li, Z. Q., I. A. Oyeliran, C. Tang, R. L. Hu, and Y. X. Zhou. 2014. FEM application to loess slope excavation and support:case study of Dong Loutian coal bunker, Shuozhou, China. *Bulletin Of Engineering Geology and The Environment,* 73: 1013–1023.

[14] Liu, G. D., Y. N. Zhang, H. L. Lu, E. You, and X. Li. 2013. Numerical simulation of particle flow motion in a two-dimensional modular pebble-bed reactor with discrete element method. *Science and Technology of Nuclear Installations,* 2013(3): 178–182.

[15] Oldal, I., and F. Safranyik. 2015.Extension of silo discharge model based on discrete element method. *Journal of Mechanical Science and Technology,* 29(9): 3789–3796.

[16] Reimbert, M. L., and A. M. Reimbert. 1976. Silos theory and practice.Germany, *Trans Tech Publications*

[17] Schulze, D. 2007. Powders and bulk solids: Behavior, characterization, storage andflow. Heidelberg: *Springer Science & Business Media.*

[18] Tejchman, J. 2013. Confined granular flow in silos: Experimental and numerical investigations. New York:*Springer Science & Business Media.*

[19] Vidyapati, V., and S. Subramaniam. 2013. Granular flow in silo discharge: discrete element method simulations and model assessment. *Industrial & Engineering Chemistry Research,* 52(36): 13171–13182.

[20] Wang, X. W., Z. J. Yang, X. F. Shu, and J. L. Feng. 2013. The static contact statuses between granular materials and flat-bottomed steel silos. *Powder Technology,* 235:

1053–1059.

[21] Weinhart, T., S. Luding, C. Labra, and Y. O. Jin. 2016. Influence of coarse-graining parameters on the analysis of DEM simulations of silo flow. *Powder Technology*, 293: 138–148.

[22] Yang, W. J., Z. Y. Zhou, and A. B. Yu. 2015. Discrete particle simulation of solid flow in a three-dimensional blast furnace sector model. *Chemical Engineering Journal*, 278: 339–352.

[23] Yu, Y. W., and H. Saxén. 2011. Discrete element method simulation of properties of a 3D conical hopper with mono-sized spheres.*Advanced Powder Technology,* 22(3): 324–331.

[24] Zeng, Y., F. G. Jia, Y. X. Zhang, X. Y. Meng, Y. L. Han, and H. Wang. 2017. DEM study to determine the relationship between particle velocity fluctuations and contact force disappearance. *Powder Technology*, 313: 112–121.

[25] Zheng, Q. J., and A. B. Yu. 2015. Finite element investigation of the flow and stress patterns in conical hopper during discharge. *Chemical Engineering Science,* 129: 49–57.

Working process analyses of direct insert hill-device with corn whole plastic-film mulching on double ridges based on EDEM

Dai Fei[1], Zhao Wuyun[1*], Song Xuefeng[1], Zhang Fengwei[1], Feng Fuxue[2]

(1. *College of Mechanical and Electrical Engineering, Gansu Agricultural University, Lanzhou 730070, China*;
2. *College of Water Conservancy and Hydropower Engineering, Gansu Agricultural University, Lanzhou 730070, China*)

Abstract: The furrow sowing with whole plastic-film mulching on double ridges has been widely used in the arid region of northwest China, because it can resist drought and increase production. So, the mechanical sowing on film is an inevitable trend in farming. In order to solve the problems of picked film and tore film and kind of holes with seedlings dislocation, the method of direct hill sowing was presented. The simulation model of corn whole plastic-film mulching on double ridges was built with EDEM, and the dynamic operation process of planting in furrow was simulated with the corn direct insert hill-device. The stress curves were measured with the moved soil opener and the fixed soil opener, and the posture change of the moved soil opener and the fixed soil opener in the sowing process numerical simulation of the direct insert hill-device were mastered. The maximum extrusion pressures of the moved soil opener and the fixed soil opener were 7.89 N and 6.71 N respectively. Verification test showed that it was feasible to analyze the direct insert hill-device with corn whole plastic-film mulching on double ridges based on EDEM. The research methods would provide reference for the design and development of corn direct insert hill-device with corn whole plastic-film mulching on double ridges in the northwest dry area of China.

Keywords: corn whole plastic-film mulching on double ridges, direct insert hill-device, sowing process numerical simulation, EDEM

Citation: Dai, F., W. Y. Zhao, X. F. Song, F. W. Zhang, and F. X. Feng. 2017. Working process analyses of direct insert hill-device with corn whole plastic-film mulching on double ridges based on EDEM. International Agricultural Engineering Journal, 26(4): 124–131.

1 Introduction

The furrow sowing technique with whole plastic-film mulching on double ridges is a breakthrough innovative technology that has been developed in recent years (Zhou et al., 2012; Qin et al., 2014; Yang et al., 2010; Zhang et al., 2014), which is mainly aimed at corn production. Its main characteristics are of the advanced good width, narrow and alternate type double ridges, at the same time, it uses the plastic-film to cover the double ridges completely in late autumn or early spring season, and sows corn in the furrow in due time (Zhao et al., 2013). So, the mechanical sowing on film is an inevitable trend in farming. It is one of the key links that make the whole mechanization process of the whole plastic-film mulching on double ridges (Dai et al., 2016). At present, the related sowing machines with whole plastic-film mulching on double ridges are wheel dibber and hand type dibbler, which have the problems of picked film and tore film and kind of holes with seedlings dislocation, and also high labor intensity and low seeding efficiency (Yang et al., 2013; Wang et al., 2011). The enhancement effect of production system with whole plastic-film mulching on double ridges and its promotion demonstration are restricted.

In order to adapt the demand of sowing above the film and solving the problems of picked film and tore film and kind of holes with seedlings dislocation which existed in the traditional sowing machine, the method of direct hill sowing was presented by the domestic scholar, the complete set of equipment was developed, the working

Received date: 2017-09-05 **Accepted date:** 2017-10-12

* **Corresponding author: Zhao Wuyun,** Ph.D. Professor, College of Mechanical and Electrical Engineering, Gansu Agricultural University, Lanzhou 730070, China. Email: zhaowy@gsau.edu.cn, Tel: +09317632472.

parameters were optimized and studied in recent years (Dai et al., 2016; Shi et al., 2017). However, it is not clear in the seedbed soil system if the microcosmic interaction between the seedbed and the cavitation device is confined, the cavitation device is blocked, and kind of holes with seedlings are dislocated, which is key to influencing the sowing quality with whole plastic-film mulching on double ridges.

For this purpose, the simulation model of corn whole plastic-film mulching on double ridges was built with EDEM, the dynamic operation process of planting in furrow was simulated with the corn direct insert hill-device, the key parameters of the direct insert sowing method were clarified, the stress curve was measured with the moved soil opener and the fixed soil opener, and the posture change of the moved soil opener and the fixed soil opener in the sowing process numerical simulation of the direct insert hill-device were mastered. It would provide reference for the design and development of direct insert hill-device with corn whole plastic-film mulching on double ridges.

2 Direct insert sowing process

2.1 Working process

As shown in Figure 1, the direct insert corn precision hill-seeder is sowing with whole plastic-film mulching on double ridges.

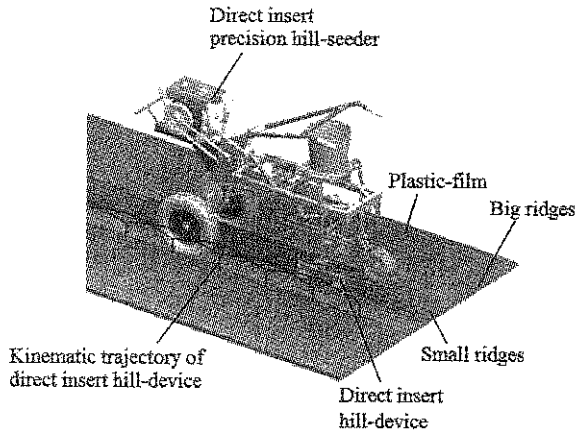

Figure 1 Sowing process of direct insert corn precision hill-seeder

The direct insert hill-device horizontal velocity component is zero in sowing period and in excavating period, the planting distance can be adjusted within a certain range, the arrangement of the soil hole and the hole-former motion trajectory is all reasonable, which can meet the requirements of agronomic techniques of dry-land corn furrow seeder with whole plastic-film mulching on double ridges (Zhao et al., 2013). Thereinto, the direct insert hill-device is instantaneous contact with the small ridge furrow, and it fulfills the dynamic operation process of direct insert, punctures film, and cavitation with corn whole plastic-film mulching on double ridges.

2.2 Operating system principle

As shown in Figure 2, the direct insert hill-device is mainly composed of moved soil opener and fixed soil opener, and the two soil openers are pressed together with a torsion spring. The two hill-devices are symmetric arranged and the openings of the moved soil opener depend on the stretching of the flexible cord.

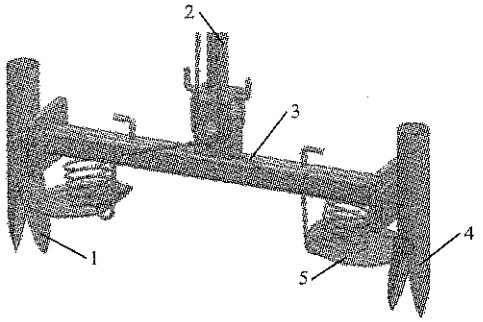

1. Moved soil opener 2. Cavitation rod 3. Flexible cord 4. Fixed soil opener 5. Torsion spring

Figure 2 Structure diagram of moved and fixed soil openers

As shown in Figure 3, when the sowing device with reciprocating works, the direct insert hill-device moves up and down in the vertical direction, and it uses this movement to design open mechanism of hole-former (Chen et al., 1993; Hu et al., 2016). It connects the proper position between the moved soil opener and the top rod with a flexible cord. By adjusting the length of the flexible cord, the cavitation device can be opened precisely at the optimum depth of sowing, which also completes the sowing operation.

The factors of dislocation of soil hole, mechanical damage of daylighting mulch and direct insert hill-device opening failure are restricted the operating performance of the direct insert corn precision hill-seeder. The direct insert hill-device opening failure after burrowing into the soil is the major factor which reduced the yield effect of whole plastic-film mulching on double ridges. In order to analyze operation process of corn direct insert hill-device,

and avoid the occurrence of leakage sowing and soil opener blockage, it is important to realize visualization for the interaction between the seedbed and the direct insert hill-device.

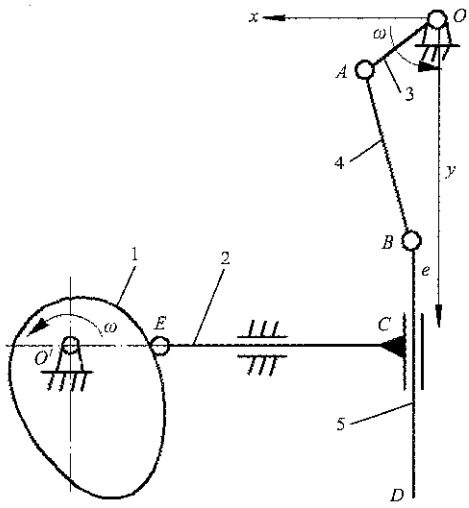

1. Cam 2. Push rod 3. Crank 4. Connecting rod 5. Cavitation rod

Figure 3 Schematic diagram of kinematic analysis of direct insert hill-device

According to the description of the motion equation of cavitation rod in literature we have the motion displacement of the cavitation rod in the vertical direction (Zhao et al., 2013):

$$y = a_1 \sin(wt) + \sqrt{b^2 - \left(e - vt - a_1 \cos(wt)\right)^2} \quad (1)$$

where, y is the motion displacement of the cavitation rod in the vertical direction, m; a_1 is the length of the crank, m; b is the length of connecting rod, m; v is the speed of the hill-seeder, m/s; t is the sowing time, s; e is the x direction of connecting rod point B start getting into the soil, m; w is the rotation angular velocity of crank, rad/s.

The relation among y, a_2 and t is:

$$y = v_0 t + \frac{1}{2} a_2 t^2 \quad (2)$$

where, v_0 is the initial velocity of the cavitation rod, m/s (which is 0 m/s, because the cavitation rod instantaneous downward direct initial velocity is 0); a_2 is the acceleration of cavitation rod with the direct insert planting (m/s^2).

That contact force produce between hill-device and seedbed in sowing process was defined as F, which, can be expressed as:

$$F = ma_2 \quad (3)$$

where, m is the quality of the cavitation rod (kg).

From the integration of the Equations (1), (2) and (3), we have the mechanical model of contact force produced between hill-device and seedbed in sowing process:

$$F = 2m \frac{a_1 \sin(wt) + \sqrt{b^2 - \left(e - vt - a\cos(wt)\right)^2}}{t^2} \quad (4)$$

As is shown in Equation (4), for given a_1, b, v, e, w, and m, the contact force produced between hill-device and seedbed is F, and it can be determined by changing the sowing time t in experiment. Therefore, we obtained the complete mathematical model of contacting force produced between hill-device and seedbed in sowing process.

3 Process analyses of direct insert hill-device

3.1 Modeling of corn kernel

In view of the corn kernel shape is irregular modeling, it is difficult to describe the shape of corn kernel with spherical particles directly. Therefore, the discrete element model of corn kernel was established by multi-spherical clustering in EDEM (Figure 4), and the single corn kernel model includes 13 spherical particles (Shi et al., 2014). The corn kernel model was simplified, which was ignored the collision plastic deformation of grain-grain and grain-wall, and also ignored its contact time, the Hertz-Mindlin's no slip contact model with corn kernel was adopted in this study.

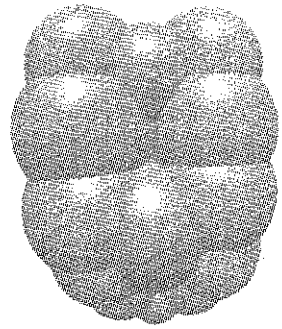

Figure 4 Discrete element model of corn kernel

3.2 Modeling of seedbed and direct insert hill-device

The establishment of accurate seedbed and direct insert hill-device model is the basis to ensure the effectiveness of simulation results. In order to guarantee the accuracy of the simulation analysis, according to the proportion of 1:1, the software of the Pro/E 4.0 was adopted to establish the three-dimensional structure model of the soil opener, and saved as a *.step format, and would build a good model

import to EDEM software (Huang et al., 2016). In EDEM software, a cube of 1120×210×165 mm was created and named as wall. The material of wall is steel, the 3D model material of seedbed was used as virtual, and the seedbed model was completely surrounded by the cube (Zheng et al., 2016). The soil particles with diameter of 4 mm are generated in the wall by static particle generation, and the filling height of the particles reached the edge of wall $+z$ toward. The material type of seedbed model was selected as physical, its material is steel, and wall material type was chosen as virtual.

As is shown in Figure 5, after the simulation, the granule outside the ridge was out of the calculation domain, and the simulation model of whole plastic-film mulching on double ridges was generated. A total of 338019 particles were included in the building, the number of granule bond is 1052494, and the average granule has 3.1 bonds in contact with each other. The seedbed soil simulation adopted the Hertz-Mindlin with JKR contact model.

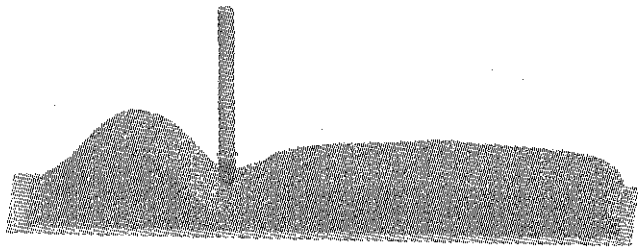

a. Granular model

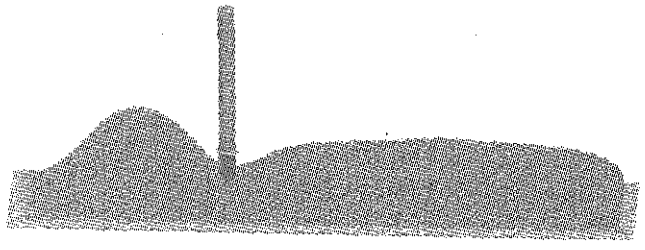

b. Bond distribution

Figure 5 Seedbed simulation model of EDEM

The discrete element simulation parameters mainly include material parameters and contact parameters. The related material properties and contact parameters of whole plastic-film mulching on double ridges are illustrated in Table 1 (Shi et al., 2015; Ji et al., 2014; Ucgul et al., 2014a).

The granule bonding parameters of whole plastic-film mulching on double ridges are illustrated in Table 2 (Jia et al., 2016; Liu et al., 2015; Ucgul et al., 2014b).

Table 1 Parameters of materials and contact in EDEM

Item	Parameter	Value
Soil	Poisson ratio	0.25
	Shear modulus, Pa	1×10^{7}
	Density, kg/m^3	2600
Corn	Poisson ratio	0.4
	Shear modulus, Pa	2.6×10^{6}
	Density, kg/m^3	1250
Steel	Poisson ratio	0.3
	Shear modulus, Pa	7.0×10^{10}
	Density, kg/m^3	7800
Soil-Soil	Coefficient of restitution	0.1
	Coefficient of static friction	0.5
	Coefficient of dynamic friction	0.05
Soil-Corn	Coefficient of restitution	0.2
	Coefficient of static friction	0.5
	Coefficient of dynamic friction	0.01
Soil-Steel	Coefficient of restitution	0.2
	Coefficient of static friction	0.5
	Coefficient of dynamic friction	0.05

Table 2 Granule bonding parameter

Item	Parameter	Value
Soil granule	Normal stiffness per unit, N/m^3	5.0×10^{9}
	Shear stiffness per unit, N/m^3	6.0×10^{9}
	Normal critical stress, Pa	8.0×10^{8}
	Shear critical stress, Pa	5.0×10^{8}
	Bond radius, mm	2.6

3.2 Simulation of sowing process

During the simulation, the granule began to bond at 0.01 s, the fixed time step for simulation is 4×10^{-6} s which is 5% for rayleigh time step, the core i7 and 6 core processor was used for simulation calculation. The simulation time lasted 0.80 s. The cavitation device was inserted to seedbed at a speed of 30 mm/s and its acceleration is 30 mm/s^2. At the same time, the moved soil opener opened with the angular speed of 20 deg/s and its acceleration is 20 deg/s^2. As is shown in Figure 6, there is the simulation of sowing process at different moments.

The operation of the direct insert hill-device is mainly completed in furrow. After the hill-device is partly inserted into the seedbed, the corn seeds in the prototype seed case are entered into the grain tube (0.47 s) and as its own gravity falls (0.58-0.72 s). The corn seeds near the soil opener are discharged to complete the sowing operation in 0.77 s. Through the forward speed compensation mechanism, the vertical insertion and extraction of the direct insert hill-device are realized,

which avoids to pick film, tear film as well as avoid the kind of holes with seedlings dislocation. After the completion of the directly insert planting process, the forced condition of moved soil opener and fixed soil opener can be obtained.

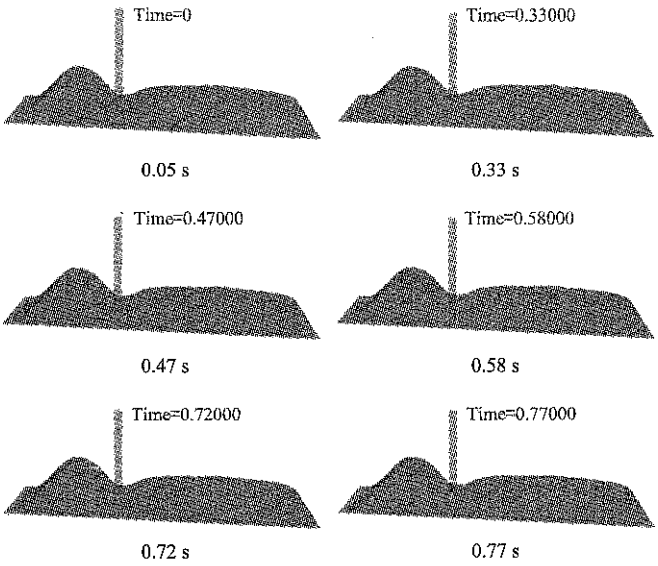

Figure 6 Process of mechanical sowing on whole plastic-film mulching on double ridges

4 Simulation results and discussion

4.1 Cavitation condition analysis

As is shown in Figure 7, using the software of EDEM, we visualized the interaction between the seedbed and the direct insert hill-device. The establishment of the model with corn whole plastic-film mulching on double ridges conducted a cross-sectional view, and also can obtain the dynamic force analysis of the cavitation device in sowing process.

When the direct insert hill-device is moving vertically down in 0.05 s, the mutual contact force is produced between hill-device and seedbed. With the further downward movement of the hill-device (0.18-0.33 s), the growing of the bed holes gradually increase, and the soil around the hill-device gradually becomes loose. At 0.47 s, the corn is discharged by a seed box as the vertical hill-device is relatively falling (0.58 s), and the force between the soil opener and the soil is further increased. The stress of hill-device and its interaction with the seedbed can be seen in 0.72 s, when the moved soil opener of hill-device starts to open, the lateral extrusion force of the left soil granule is obviously transmitted, and the soil on the right side of the fixed soil opener is squeezed significantly less than the moved soil opener. When the moved soil opener and fixed soil opener of hill-device are cut and squeezed in the surrounding soil, the sowing hole is basically formed, and the sowing operation is completed.

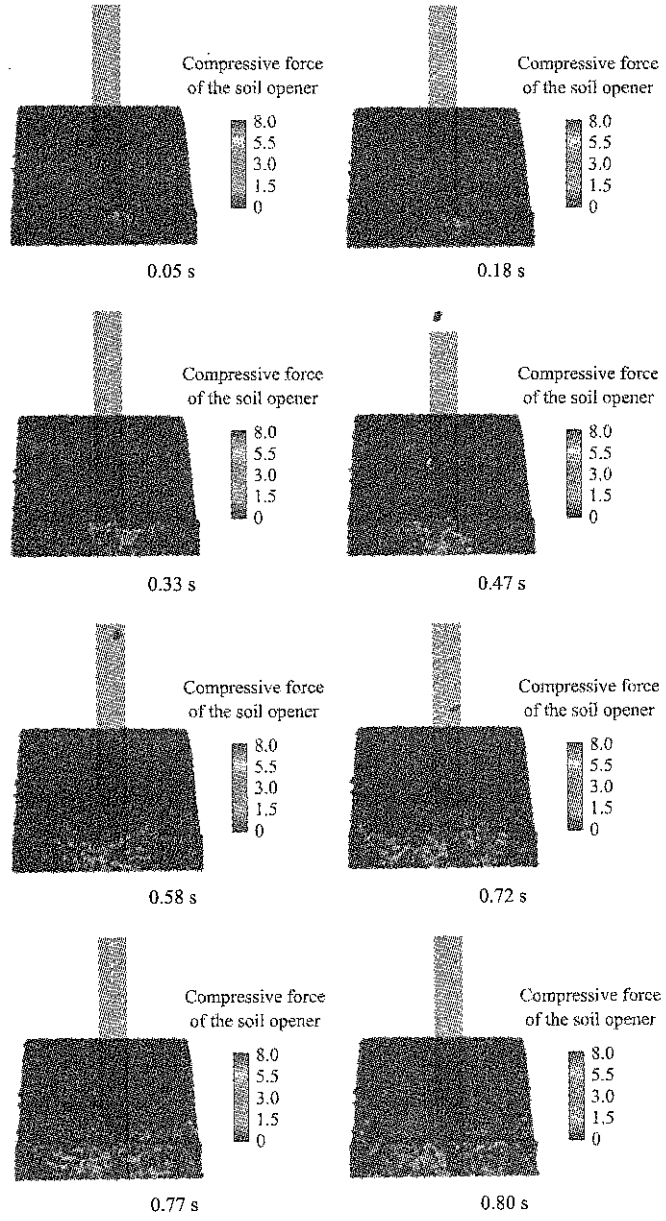

Figure 7 Force process analysis of the hill-device

4.2 Stress curve analysis of soil opener

As is shown in Figure 7, the shape of the soil opener affects the size of the sowing hole and soil disturbance quantity (Dai et al., 2016). At the same time, during the operation of the direct insert hill-device, the top of the soil opener contacts the seedbed surface. Then, with the forced mechanism action of the machine, the moved soil opener starts to enlarge hole slowly, and the directly insert sowing operation is completed.

Therefore, as is shown in Figure 8, the determination of stress curve of the moved soil opener and the fixed soil opener will provide some reference to the design and optimization of the direct insert hill-device. The red curve is the force curve of the moved soil opener and the blue curve is the force curve of the fixed soil opener in the diagram.

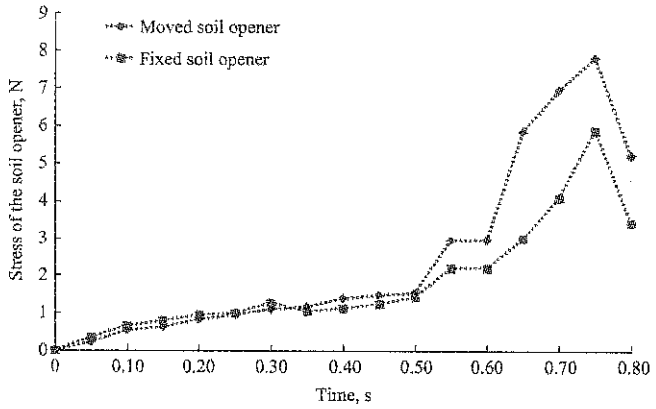

Figure 8 Stress curve of the moved soil opener and the fixed soil opener

The force curve of the soil opener can be seen when the hill-device inserted only vertically in the seedbed but not opens (before 0.3 s), the force applies to the moved soil opener and the fixed soil opener basically tend to be consistent (between 0 and 1.5 N). When the hill-device inserted to the certain depth of seedbed, with the forced mechanism action of the machine, the moved soil opener starts to open and gradually increases, which is subjected to soil reaction extrusion force greater than the fixed soil opener. At 0.75 s the hill-device opens maximum (Figure 9), the corn seeds fall into the hole of the seedbed to complete the sowing operation, and the maximum extrusion forces of the moved soil opener and the fixed soil opener are 7.89 N and 6.71 N respectively. Then the hill-device is closed immediately, and the extrusion force of the soil opener is reduced instantly. Therefore, the direct insert hill-device must be opened after inserting to the certain depth of seedbed, which can effectively prevent the soil opener from blocking and improve the quality of the sowing operation.

4.3 Experimental verification

To verify the accuracy of EDEM simulation model, the field cavitation performance test was performed by the direct insert corn precision hill-seeder with whole plastic-film mulching on double ridges. The characteristics and regularities of the direct insert hill-device and seedbed furrow were observed. The experiment was carried out in a demonstration experimental field with the corn whole plastic-film mulching on double ridges in Gansu Academy of Agricultural Sciences (Dai et al., 2016). The simulation of sowing process and the field sowing operation test (Figure 10) were basically the same, which showed that the numerical setting of correlation model was reliable and effective. The research results would provide reference for the design and development of direct insert hill-device with corn whole plastic-film mulching on double ridges.

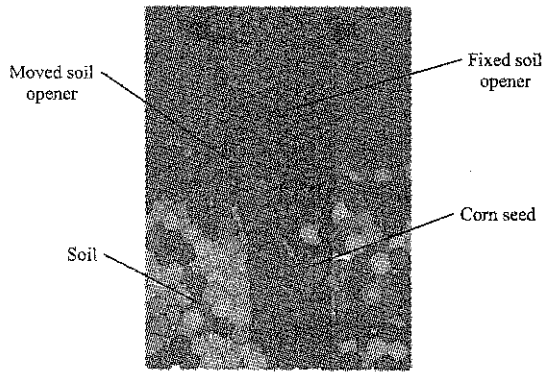

Figure 9 Maximum opened of hill-device

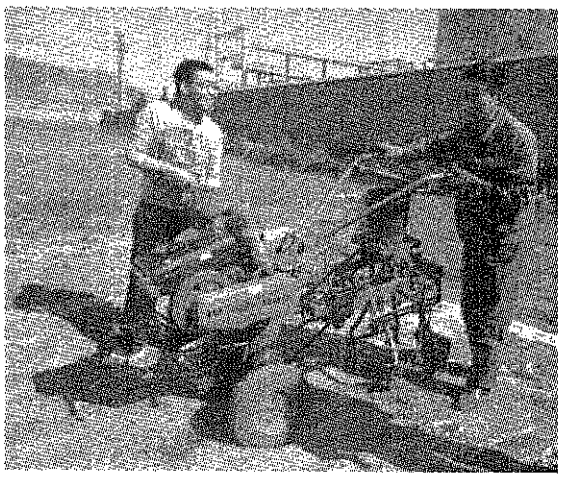

Figure 10 Field test verification

The results of sowing performance in field are illustrated in Table 3.

Table 3 Field sowing performance test results

Parameter	Experimental value	Technical requirements
Empty seed rate, %	0.66	≤2
Qualification rate of sowing depth under the film, %	95.2	≥75
Dislocation of soil hole rate, %	0.46	≤6
Mechanical damage area of daylighting mulch, mm/m^2	42.8	≤55

Field experiment showed that when the direct insert corn precision hill-seeder was planting operation with

whole plastic-film mulching on double ridges, the hole-former horizontal velocity component was zero in sowing period and excavating period, the arrangement of the soil hole and the hole-former motion trajectory was all reasonable, which met the requirements of relevant standard and agronomic techniques of dry-land corn furrow seeder with whole plastic-film mulching on double ridges.

5 Conclusions

On the basis of analyzing the corn direct insert hill-device operation principle, the simulation model of corn whole plastic-film mulching on double ridges, direct insert hill-device and corn seed were built with EDEM, and the dynamic operation process of sowing in furrow was simulated with the corn direct insert hill-device. From the simulation and experimental analysis, we had the following conclusions:

(1) The dynamic operation process of sowing in the small ridges furrow was simulated with the corn direct insert hill-device, the stress curve was measured with the moved soil opener and the fixed soil opener, and the EDEM software was used for simulation the interaction stress distribution between the soil openers and the seedbed soil. The research identified the posture change of the moved soil opener and the fixed soil opener in the process of the direct insert sowing, and the maximum extrusion forces of the moved soil opener and the fixed soil opener were 7.89 and 6.71 N respectively.

(2) The characteristics and regularities of the direct insert hill-device and seedbed furrow interaction were observed by combining the results of the field experiment, which verified the accuracy of EDEM simulation model and provided reference for the design and development of corn direct insert hill-device with corn whole plastic-film mulching on double ridges in the northwest dry area of China.

Acknowledgements

This project was supported by National Natural Science Foundation of China (Grant No. 51405086 and No. 51775115), and the Special Fund for Agroscientific Research in the Public Interest (No. 201503105).

[References]

[1] Chen, X. G., C. C. Zuo, and F. Gao. 1993. Study on the direct insert planter (I)-the research and the principal study of the direct insert hole former of planter. *Transactions of the Chinese Society of Agricultural Engineering*, 9(3): 66–70. (In Chinese with English abstract)

[2] Dai, F., W. Y. Zhao, F. W. Zhang, Z. W. Wu, X. F. Song, and Y. F. Wu. 2016. Operating performance optimization and experiment of collector for corn whole plastic film mulching on double ridges. *Transactions of the Chinese Society of Agricultural Engineering*, 32(18): 50–60. (In Chinese with English abstract)

[3] Dai, F., W. Y. Zhao, L. R. Shi, X. P. Tang, J. X. Wang, and X. L. Liu. 2016. Design and experiment of hill-seeder with whole plastic-film mulching on double ridges for corn based on mechanism with approximate constant speed. *Transactions of the Chinese Society for Agricultural Machinery*, 47(11): 74–81. (In Chinese with English abstract)

[4] Hu, H., H. W. Li, Q. J. Wang, J. He, Y. F. Zhang, W. Z. Chen, and X. L. Wang. 2016. Design and experiment of targeted hole-pricking and deep-application fertilizer applicator between corn rows. *Transactions of the Chinese Society of Agricultural Engineering*, 32(24): 26–35. (In Chinese with English abstract)

[5] Dai, F., W. Y. Zhao, M. Y. Ma, J. X. Wang, L. R. Shi, and J. M. Ma. 2016. Parameters optimization of operation machine for tillage-fertilization and spraying-filming on double ridges. *Transactions of the Chinese Society for Agricultural Machinery*, 47(1): 83–90. (In Chinese with English abstract)

[6] Dai, F., W. Y. Zhao, J. M. Ma, J. X. Wang, L. R. Shi, and X. L. Liu. 2016. Operation performance test of hill-seeder based on mechanism with approximate constant speed for corn whole plastic-film mulching. *Transactions of the Chinese Society for Agricultural Machinery*, 47(S1): 47–56. (In Chinese with English abstract)

[7] Huang, Y. X., C. G. Hang, M. C. Yuan, B. T. Wang, and R. X. Zhu. 2016. Discrete element simulation and experiment on disturbance behavior of subsoiling. *Transactions of the Chinese Society for Agricultural Machinery*, 47(7): 80–88. (In Chinese with English abstract)

[8] Ji, Y. J., M. Yu, and C. H. Li. 2014. Establishment and parameter verification of farmland soil model in uniaxial compression based on discrete element method. *Journal of Jiangsu University: Natural Science Editions*, 35(1): 40–43. (In Chinese with English abstract)

[9] Jia, F. G., L. N. Yao, Y. L. Han, H. Wang, Y. F. Shi, Y. Zeng, and L. W. Jiang. 2016. Simulation test for metering process of horizontal disc precision metering device based on discrete element method. *Transactions of the Chinese Society of Agricultural Engineering*, 32(4): 235–241. (In Chinese with

English abstract)

[10] Liu, Y., Y. L. Han, F. G. Jia, L. N. Yao, H. Wang, and Y. F. Shi. 2015. Numerical simulation onstirring motion and mixing characteristics of ellipsoid particles. *Acta Physica Sinica*, 64(11): 258–265.

[11] Qin, S. H., J. L. Zhang, H. L. Dai, D. Wang, and D. M. Li. 2014. Effect of ridge-furrow and plastic-mulching planting patterns on yield formation and water movement of potato in a semi-arid area. *Agricultural Water Management*, 131(1): 87–94.

[12] Shi, L. R., J. M. Wu, W. Sun, F. W. Zhang, B. G. Sun, Q. W. Liu, and W. Y. Zhao. 2014. Simulation test for metering process of horizontal disc precision metering device based on discrete element method. *Transactions of the Chinese Society of Agricultural Engineering*, 30(8): 40–48. (In Chinese with English abstract)

[13] Shi, L. R., J. M. Wu, W. Y. Zhao, W. Sun, F. W. Zhang, and B. G. Sun. 2015. Establishment and parameter verification of farmland soil model in uniaxial compression based on discrete element method. *Transactions of the Chinese Society for Agricultural Machinery*, 20(4): 174–182. (In Chinese with English abstract)

[14] Ucgul, M., J. M. Fielke, and C. Saunders. 2014a. 3D DEM tillage simulation: validation of a hysteretic spring (plastic) contact model for a sweep tool operating in a cohesionless soil. *Soil and Tillage Research*, 144(4): 220–227.

[15] Ucgul, M., J. M. Fielke, and C. Saunders. 2014b. Three-dimensional discrete element modelling of tillage: determination of a suitable contact model and parameters for a cohesionless soil. *Biosystems Engineering*, 121(2): 105–117.

[16] Wang, J. K., K. Q. Guo, X. M. Lv, W. Fu, and C. S. Qi. 2011. Experiment and improvement on clamping cotton precision seeding dibbler. *Transactions of the Chinese Society for Agricultural Machinery*, 42(4): 43–47. (In Chinese with English abstract)

[17] Yang, Q. F., G. C. Liu, C. R. Xiong, C. R. Zhang, and Y. Y. Zhu. 2010. Study on highly efficient water utilizing mechanisms on techniques of whole plastic-film mulching on double ridges and planting in catchment furrows of dry-land maize. *Research of Agricultural Modernization*, 31(1): 113–116. (In Chinese with English abstract)

[18] Yang, Z., W. Y. Zhao, F. Dai, and X. R. Li. 2013. Development situation of ancillary seeding machine with whole plastic-film mulching on double ridges and planting in catchment furrows of dry-land maize. *Mechanical Research and Application*, 26(4): 191–192, 195. (In Chinese with English abstract)

[19] Zhang, P. L., T. W. Guo, S. T. Li, M. S. Ma, and Y. H. Xie. 2014. Effects of different coverage cultivation and balanced fertilization on yield and water use efficiency of spring corn in the dryland. *Agricultural Research in the Arid Areas*, 32(4): 169–173. (In Chinese with English abstract)

[20] Zhao, W. Y., F. Dai, J. Yang, Z. L. Shi, Z. Yang, and L. R. Shi. 2013. Design and experiment of direct insert precision hill-seeder with corn whole plastic-film mulching on double ridges. *Transactions of the Chinese Society for Agricultural Machinery*, 44(11): 91–97. (In Chinese with English abstract)

[21] Zheng, K., J. He, H. W. Li, P. S. Diao, Q. J. Wang, and H. B. Zhao. 2016. Research on polyline soil-breaking blade subsoiler based on subsoiling soil model using discrete element method. *Transactions of the Chinese Society for Agricultural Machinery*, 48(8): 87–94. (In Chinese with English abstract)

[22] Zhou, L. M., S. L. Jin, C. A., Liu, Y. C. Xiong, J. T. Si, X. G. Li, Y. T. Gan, and F. M. Li. 2012. Ridge-furrow and plastic-mulching tillage enhances maize-soil interactions: opportunities and challenges in a semiarid agroecosystem. *Field Crops Research*, 126(1): 181–188.

Experiment of pot seedling planting process based on high-speed photography

Jin Xin[1], Ji Jiangtao[1*], Liu Weixiang[1], Du Xinwu[1], Pang Jing[1], He Yakai[2]

(1. *College of Agricultural Equipment Engineering, Henan University of Science and Technology, Luoyang471003, China*;
2. *Chinese Academy of Agricultural Mechanization Sciences, Beijing 100083, China*)

Abstract: In order to address the problems of seedling lodging and missing caused by speed increase of the duckbilled planting device, the whole falling process of seedlings during transplanting was studied to find out the motion status and interactive relation between the falling seedlings and the duckbilled planting device. The whole motion process of seedlings from falling into the duckbilled planting device to the soil was analyzed, with the intention to explore the key factors of the emergence of lodging status and seedling loss during high-speed seedling transplanting. The planting mechanism with plexiglass duckbilled planting device and a cross-shaped planetary gear train planting mechanism were adopted. Under the rotating speed of 40 r/min, 60 r/min and 80 r/min, the motion status and instantaneous status of seedlings were observed through high-speed photography, and the trajectory of some key points were recorded. After video processing and analysis, six stages in the motion were divided: free falling, collision between seedling and wall surface of planting device, oblique projectile motion in the planting device, collision between seedling and wall surface of the nozzle, planar motion within the nozzle and gliding along the wall surface of the nozzle. When the rotating speed of the duckbilled planting device increased, other than the falling process, the moving time of seedlings in the duckbilled planting device increased, and the seedlings were relatively static or even going upward to the planting device; when the rotating speed increased to a certain degree, the seedlings failed falling to the bottom of the planting device when the nozzles penetrated into the soil, resulting in seedling loss and lodging.

Keywords: pot seedling planting, duckbilled planting mechanism, high-speed photography, seeding lodging

Citation: Jin, X., J. T. Ji, W. X. Liu, X. W. Du, J. Pang, and Y. K. He. 2017. Experiment of pot seedling planting process based on high-speed photography. International Agricultural Engineering Journal, 26(4): 132–139.

1 Introduction

Duckbilled planting mechanism is a commonly applied pot seedling planting mechanism for transplanters. It doesn't have to clamp the pot seedlings in operation; after pot seedlings fall into the duckbilled planting device, the duckbilled nozzle opens to let seedlings fall into soil under the effect of gravity (Jin et al., 2012; Prasanna et al., 2011; Zhang et al., 2011). The planting process finishes after soil covering and compaction. The function of the duckbilled planting device is catching seedlings and keeping seedlings erect when falling down to designated position (Chen et al., 2010; Jin et al., 2012; Xiao et al. 2014). The seedlings do free motion during the whole process of planting, so the seedlings rarely get damaged. However, the state of motion of seedlings in the planting device (friction, collision and rotation) may influence the time of falling. When the planting speed increases, the pot seedlings fail to fall to the bottom of the planting device at the planting point. The delay of falling may result in lodging status or seedling loss, which seriously affect planting quality (Chen et al., 2015; He et al., 2016).

Therefore, it bears great significance to find out the state of motion of pot seedlings in improving seedling planting quality and working efficiency. At present, related studies have been made on the planting device of transplanters with guide tube, to analyze the state of motion of seedlings at different stages of motion in the guide tube and establish the dynamics model of seedlings in guide tube (Peng et al., 2006; Yu et al., 2011; Zhang

Received date: 2017-09-25 **Accepted date: 2017-11-07**

* **Corresponding author: Ji Jiangtao,** Professor, College of Agricultural Engineering, Henan University of Science and Technology. Email: jjt0907@163.com, Tel: +860379-64877837.

et al., 2009). The working principle of transplanters with guide tube and duckbilled planting mechanism are different, for the former one, the guide tube is set on a fixed position, and the duckbilled planting device rotates around the body frame during working, so the seedlings have more complicated state of motion in the duckbilled planting mechanism with unclear stages and state of motion, and there are much fewer related studies on duckbilled planting mechanism. Therefore, a plexiglass duckbilled planting nozzle and a cross-shaped planetary gear train planting mechanism were established in this paper. By observing the state of motion of seedlings in the duckbilled planting device with high-speed photography, the study seeks to provide reference for improving transplanting efficiency and working quality.

2 Design of high-speed planting device

2.1 Design requirements

(1) Planting frequency of the planting device ≥120/min;

(2) It should meet the principle of zero-speed seedling dropping to satisfy the characteristic value of the trajectory of planting device $\lambda=R\omega/v_m\geq1$, where, R is the distance from center of the planet wheel to the center of rotation of the planting device; ω is the angular velocity of the planting device; v_m is the advancing speed of the transplanter (Feng et al., 2002; Jin et al., 2015);

(3) The duckbilled planting device keeps planar motion all the time;

(4) The opening and closing direction of the duckbilled planting device is the same with that of the advancing direction of the transplanter.

2.2 Configuration scheme

The transplanting device with planetary gear train was adopted in this study, including a planet carrier, a central gear (sun gear), intermediate gear, planet gear, duckbilled planting device, and duckbilled opening and closing nozzles. The planetary gear train planting mechanism has four duckbilled planting nozzles in a cross-shaped structure. The nozzles were made of plexiglass, which is ideal for observing the moving status of seedlings and the interaction process between seedlings and the duckbilled planting nozzles. The testbed for the planetary gear train planting mechanism is shown in Figure 1.

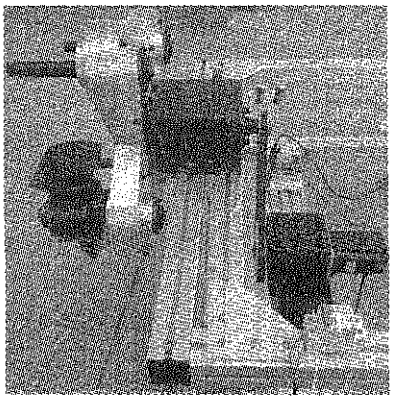

Figure 1 Testbed for the duckbilled planetary gear train planting mechanism

The duckbilled planting device has a three-phase hybrid stepping motor of HollySys 110 series (110BYG350DH-SAKSMA-0501, with torque of 16 N·m) as the power source. The output end of the stepping motor was connected with a speed reducer to realize high torque output, the reduction ratio of the speed reducer i_1=12, and there was a synchronous belt driving device between the speed reducer and planting device to transmit the power from the stepping motor to the planting device, the transmission ratio was i_2=0.5.

2.3 Working principle of the planting device and key parameter design

The central gear of the duckbilled planetary gear train planting device was fixed; the planet carrier was connected with the center axis by a spine, then transmit the power to the center axis through chain drive, and later to the planet carrier to drive it to rotate around the center axis. The intermediate gear was fixed on the planet carrier. In the rotating process of the planet carrier, the intermediate gear also rotated around the sun gear with the planet carrier, and meanwhile, it rotated the planet wheel. The duckbilled planting device was fixed on one end of the planetary shaft through key joint. To ensure the perpendicular status of the duckbilled planting nozzle in transplanting, the transmission ratio between the planetary gear and the planet carrier should be zero. The opening and closing of the duckbilled planting nozzles were controlled by the motion of swinging rod typed cam mechanism and tension spring, meanwhile, to ensure timely and precise opening and closing of the nozzles under normal working conditions, the phase angle was set as adjustable to avoid

seedling loss or damages because of failing in timely opening or closing.

2.3.1 Distance between the center of planet wheel and center of rotation of the planting device

The ratio between the rotating speed of the planting mechanism and the advancing velocity of the transplanter was λ, which wasthe characteristic parameter of the motion trajectory of the planting mechanism, and:

$$\lambda=\frac{Rw}{V_m}=\frac{R\cdot\frac{\pi f}{30N}}{\frac{f\cdot L}{60}}=\frac{2\pi R}{NL} \tag{1}$$

where, w is the rotating angular velocity of the planting mechanism, rad/s; V_m is the advancing velocity of the transplanter; m/s; f is the transplanting frequency of the transplanter, number of seedlings/min; L is seedling distance, mm; N is the number of duckbilled planting nozzles, and N=4 in this study.

Based on the design requirements of the planting devicetestbed, the following equation can be obtained:

$$R\geq\frac{NL}{2\pi} \tag{2}$$

Pepper seedlings were selected as the object. Based on agronomic requirements, L was determined as 30 cm, and R≥0.191.

2.3.2 Determination of key parameters of the planetary gear train transmission mechanism

The plan of the transmission mechanism of the planetary gear train is shown in Figure 2, which consists mainly of the sun gear 1, the intermediate gear 2, the planetary wheel 3 and the carrier H.

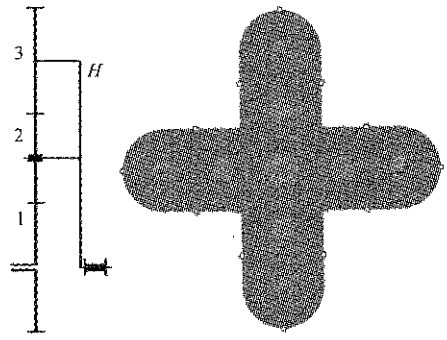

Figure 2 Transmission mechanism of the planetary gear train planting mechanism

The transmission mechanism of the planetary gear train planting mechanism is shown in Figure 2, including an intermediate gear, a sun gear, a planet wheel and a planet carrier.

The transmission ratio of the planetary gear train is:

$$i_{13}^{H}=\frac{n_1-n_H}{n_3-n_H}=\frac{1}{1-\frac{n_3}{n_H}}=\frac{z_3}{z_1}\quad(n_1=0) \tag{3}$$

where, n_1 is the rotating speed of the sun gear, r/min; z_1 is number of teeth on the sun gear; n_3 is the rotating speed of the planet gear, r/min; z_3 is number of teeth on the planetary gear; n_H is the rotating speed of the planet carrier, r/min; z_2 is the teeth number of the intermediate gear.

According the design requirements for the test bed of planting device, the duckbilled planting nozzle should be in planar and translational motion, and:

$$i_{3H}=\frac{n_3}{n_H}=0 \tag{4}$$

Therefore, z_1=z_3.

The distance Rbetween the center of rotation of the planting mechanism to the planet axis center is:

$$R=\frac{m}{2}\cdot(z_1+2z_2+z_3)\geq 191\ \text{mm} \tag{5}$$

where, m is the module of gear.

And let m=2, z_1=z_3=56, z_2=45。

2.3.3 Determination of key parameters of the duckbilled opening and closing mechanism

In order to ensure the real-time opening and closing of the duckbilled planting nozzles, in this paper, end cam with oscillating follower was adopted as the controlling mechanism for the opening and closing of the nozzles, and the movement was sine acceleration movement in lifting and constant acceleration and deceleration motion in return stroke. Figure 3 shows the structure of the duckbilled opening and closing mechanism.

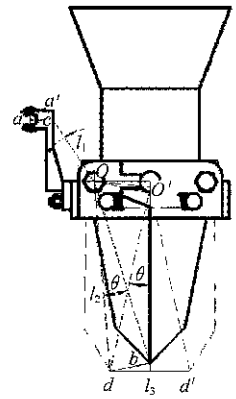

Figure 3 Structure diagram of the duckbilled opening and closing mechanism

Where, the thick solid lines indicate the position of the nozzle when it is closed, the dashed lines show its position when it is opening, $l_{dd'}$ is the degree of opening of the nozzle. Based on the size of the planting object, $l_{dd'}$ was determined as 70 mm. The geometric relation in this figure shows that:

$$l_{o'd} = l_{od} = l_2 \tag{6}$$

$$l_3 = 2l_2 \cdot \sin\theta \tag{7}$$

$$\angle a'ac = \frac{\pi - 2\theta}{4} \tag{8}$$

$$l_{ac} = l_{aa'} \cdot \cos\angle a'ac \tag{9}$$

$$\cos\theta = \frac{2l_1^2 - l_{aa'}^2}{2l_1^2} \tag{10}$$

Solve the simultaneous Equations (6) to (10) and got:

$$l_{ac} = \frac{l_1}{2l_2} \cdot \sqrt{4l_2^2 + 2l_2 \cdot l_3 - 2l_2 \cdot \sqrt{4l_2^2 - l_3^2} - l_3 \cdot \sqrt{4l_2^2 - l_3^2}} \tag{11}$$

where, l_1 is length of O_a, mm; l_2 is length of O_d, mm; l_3 was length of dd', namely the opening degree of the nozzle, mm; θ is the swinging angle of the roller-oscillating follower, (°); $l_{aa'}$ is length of aa', mm; l_{ac} is the length of ac, namely the route of the roller-oscillating follower, mm.

Based on the size of the transplanting object and agronomic requirements, the related parameters of the duckbilled planting nozzle were determined as follows: l_1=31 mm, l_2=68 mm, l_3=60 mm. Substitute the parameters into Equation (11) and got the route of the roller-oscillating follower l_{ac}=11.9193 mm, after rounding off, l_{ac}=12 mm.

The motion equation of the roller-oscillating follower was established:

$$\begin{cases} s = l_{ac} \cdot [(\delta/\delta_1) - \sin(2\pi\delta/\delta_1)/2\pi] & (0 \le \delta \le \delta_1) \\ s = l_{ac} & (\delta_1 \le \delta \le \delta_2) \\ s = l_{ac} \cdot \left[1 - 2(\delta - \delta_2)^2 / (\delta_3 - \delta_2)^2\right] & (\delta_2 \le \delta \le (\delta_2 + \delta_3)/2) \\ s = 2l_{ac} \cdot (\delta_3 - \delta)^2 / (\delta_3 - \delta_2)^2 & ((\delta_2 + \delta_3)/2 \le \delta \le \delta_3) \\ s = 0 & (\delta_3 \le \delta \le 2\pi) \end{cases} \tag{12}$$

The basic parameters of the end cam are: route l_{ac}= 12 mm; motion angle for rise travel $\delta_1'=\pi/9$, farthest dwell angle $\delta_2'=\pi/2$, motion angle for return travel $\delta_3'=\pi/6$, nearest dwell angle $\delta_4'=11\pi/9$.

The whole structure of the planting device was designed based on the basic parameters of the planetary gear train planting mechanism. To avoid the interference of seedling in the nozzles when it is planted into the soil and also to avoid lodging, the opening and closing direction of the nozzles should be perpendicular to the forward direction of the transplanter. The 3D model of the planetary gear train planting mechanism is shown in Figure 4. Among them, 2 planetary gear trains achieve rotation about center of duckbilled planting, and4 roller swing follower end cam mechanism achieve duckbilled planting according to certain rules of opening and closing.

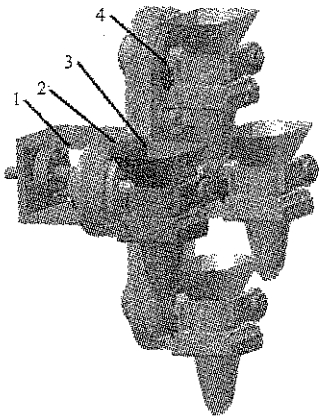

1. Holder of planting mechanism 2. Planetary gear train transmission mechanism 3. Duckbilled planting nozzle 4. End cam with roller-oscillating follower

Figure 4 3D model of the planetary gear train planting mechanism

3 High-speed photography test for seedling falling process

3.1 Test materials

The object in transplanting was pepper pot seedlings of 601 type. The seedling plug tray had 128 grids, the cultivation substrate was composed of peat, vermiculite and perlite, with volume ratio of 3:1:2. The seedling age was 40 d, moisture content was 55%. The morphology of a seedlingis shown in Figure 5.

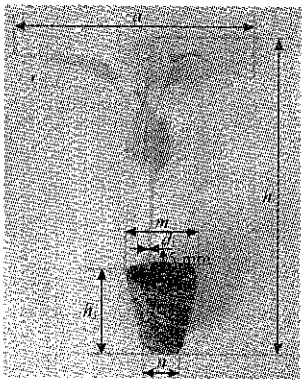

d_1: stem diameter
a: seedling width
h: seedling height
m: upper side width of the pot
n: bottom width of the pot
h_1: pot height

Figure 5 Morphological parameters of the pot seedlings

3.2 Test equipment

The test system for the whole high-speed photography process of the seedlings in duckbilled planting nozzles is shown in Figure 6. The system is mainly composed of the high-speed photography system and planetary gear train planting mechanism.

(1) The high-speed photography system, including: Phantom series high-speed photographer, Phantom camera control application and image processing software, lens, computer, light, tripod head and data cables and wires;

(2) The planetary gear train planting device, including plexiglass duckbilled planting nozzles for direct observation of the interaction between seedlings and duckbilled planting nozzles.

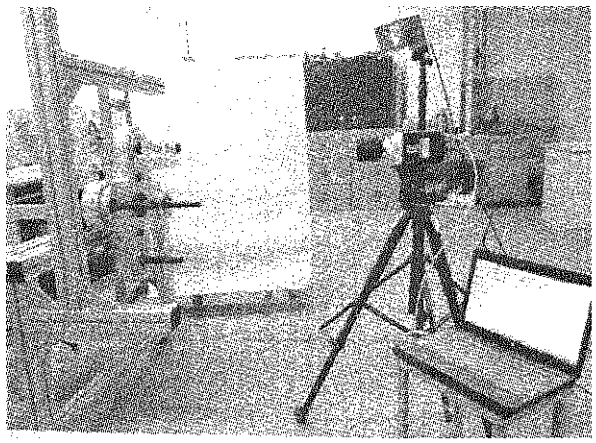

Figure 6 High-speed photography system for observation of seedling falling process

3.3 Test method

(1) Equipment testing

Under normal operating conditions of the planetary gear train planting device, the high-speed photography system was fixed and connected with the high-speed camera and computer through Ethernet cabling, then the camera and light were powered on for position adjustment, to let the planting device show the whole planting device, then the parameters of the camera, such as resolution, shooting rate, time of exposure by PCC and image processing software, meanwhile the focal length of the camera was adjusted to ensure the sharpness of the images for future analysis.

(2) Scheme plan

First, the planting speed was divided into three levels: low speed, intermediate speed and high speed, and respective rotating speed was selected for the three speed levels. By comparing the relative motion between the seedlings and planting device under three levels of speed, the motion rules of seedlings under different levels of speed and reason for lodging status under high speed can be explored.

(3) Implementation method

The rotating speed of the electric motor was adjusted to 40 r/min, 60 r/min, 80 r/min, as that mean the planting frequency was 160 plants/min, 240 plants/min and 320 plants/min, then the motion process of the seedling in the duckbilled planting nozzles was filmed and recorded under the three levels of speed. Based on the video that showed the motion process of seedlings in the plexiglass duckbilled planting device, the play speed of the video was set by the Phantom camera control application to observe and analyze the interaction between seedlings and duckbilled planting nozzles and the motion of seedlings with precision.

4 Test results and analysis

Based on the motion of seedling under three different levels of rotating speed, the whole motion process can be divided into six stages, and one or two pictures of each stage were selected to form a whole motion process of the seedling in the planting device with eight pictures under different levels of rotating speed (pictures were labeled with numbers 1-8 based on sequence of motion), as is shown in Figure 7 (the seedling was tagged with a white square).

After comparison and analysis on the video of the whole motion process in high-speed photography under three levels of speed, it was clear that the motion of seedlings in the planting device was made up of six stages.

(1) Free falling

Under different levels of rotating speed, the motion process in this stage is shown in the first pictures of Figures 7a, 7b and 7c. This stage is the free falling process of seedlings till they reached the wall surface of the planting device.

(2) Collision between seedlings and wall surface of planting device

Under different levels of rotating speed, the motion process in this stage is shown in the first pictures of

Figures 7a, 7b and 7c. This stage is the free falling process of seedlings till they reached the wall surface of the planting device.

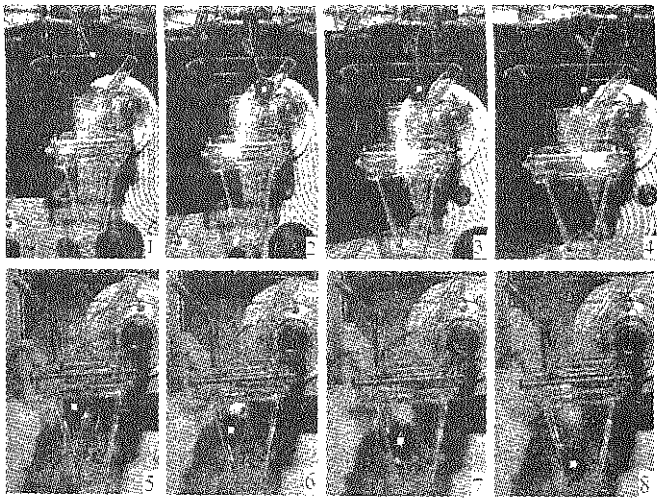

a. Motion of seedlings under high-speed photography at rotating speed of 40 r/min of the planting device

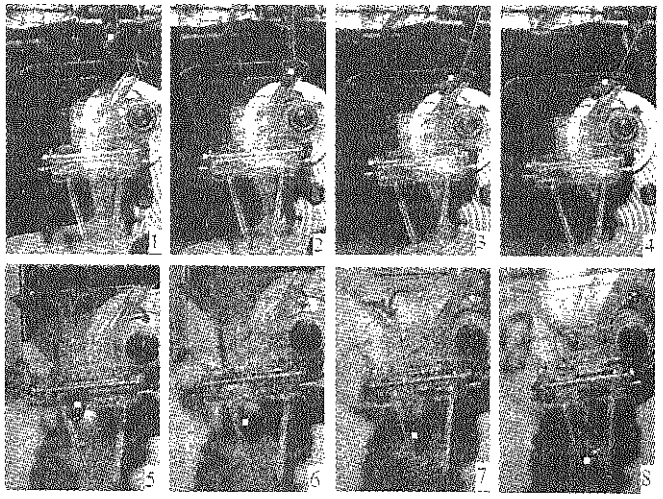

b. Motion of seedlings under high-speed photography at rotating speed of 60 r/min of the planting device

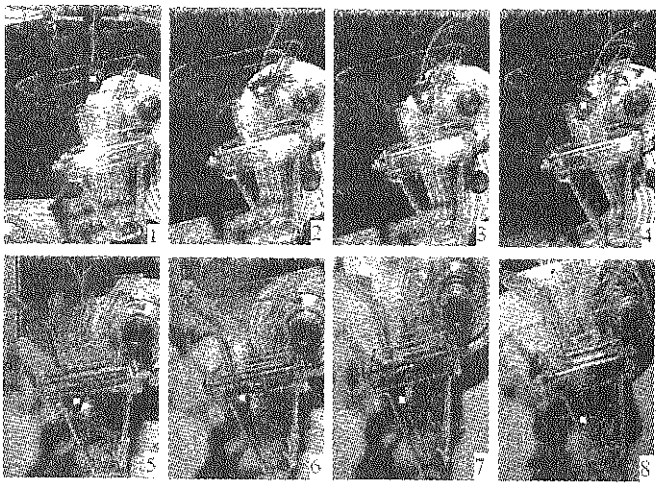

c. Motion of seedlings under high-speed photography at rotating speed of 80 r/min of the planting device

Figure 7 High-speed photography system for observation of seedling planting and falling process

(3) Oblique projectile motion of seedlings in the planting device

Under different levels of rotating speed, the motion process in this stage is shown in the third and fourth pictures of Figures 7a, 7b and 7c. In this stage, the collision between seedlings and the planting device finished, and the seedlings were bounced up in oblique projectile motion in the planting device.

(4) Collision between seedlings and wall surface of the duckbilled planting nozzles

Under different levels of rotating speed, the motion process of seedlings in this stage is shown in the fifth pictures of Figures 7a, 7b and 7c. In this stage, the seedlings collided with the planting device, however, as the relative speed of the seedlings and planting device at the direction perpendicular to the planting device was very low, and the seedlings rotated around the touch point of the seedlings and planting device immediately after it collided with the planting device, therefore, the process was simplified and the bouncing motion after collision was ignored.

(5) Planar motion between seedlings and the duckbilled planting nozzles

Under different levels of rotating speed, the motion process of seedlings in this stage is shown in the sixth pictures of Figures 7a, 7b and 7c. In this stage, since the springback was very slight between the seedlings and the duckbilled planting nozzles, for simplicity of motion process, the springback between seedlings and the planting was ignored, namely, one the one hand, the seedlings rotated around the touch point with the wall surface of the duckbilled planting nozzle after collision; on the other hand, the seedlings glided downward till the pot fit closely with the wall of the duckbilled planting nozzle, and the planar motion came to an end.

(6) Seedling gliding process along the wall surface of the duckbilled planting nozzles

Under different levels of rotating speed, the motion process in this stage is shown in the seventh and eighth pictures of Figures 7a, 7b and 7c. In this stage, the seedlings was gliding along the all of the duckbilled planting nozzle till it falls to the bottom of the nozzle.

Meanwhile, the result of the seedling gliding stage

along the wall surface of the nozzle shows that, when the rotating speed of the planting device was at 40 r/min and 60 r/min respectively, seedling glided downward relative to the nozzle; and when the rotating speed was 40 r/min, the seedling fell to the bottom when the planting device was still far from the lowest point; when the rotating speed was 60 r/min, the seedling fell to the bottom when the planting device reached the lowest point. When the rotating speed was 80 r/min, the seedling kept static or moved upwards relative to the nozzle for one period, and didn't fall to the bottom when the planting device reached the lowest point.

The analysis on the motion process of the seedling above shows that, when the seedling was moving in the nozzle, with the increase of rotating speed, the seedling also changed its motion process. When the rotating speed became higher, the seedling kept static or moved upwards relative to the planting device, and the seedling failed falling to the bottom when the planting device reached to the planting point, resulting in seedling loss and serious lodging status of the seedling.

5 Conclusions

(1) According to the morphological characteristics of pepper seedlings and agronomic requirements, in this paper, a cross-shaped planetary gear train planting mechanism and a plexiglass duckbilled planting device were designed; also the whole process test system with high-speed photography was established for observation of seedling planting, for the precise observation of motion and instantaneous status of seedling.

(2) After treatment and analysis on the video, the whole motion process of seedling in the planting device could be divided into six stages, namely, free falling, collision between seedling and wall surface of planting device, oblique projectile motion in the planting device, collision between seedling and wall surface of the nozzle, planar motion within the nozzle and gliding along the wall surface of the nozzle. When the rotating speed of the duckbilled planting nozzles increased, other than the falling process, the moving time of seedlings in the duckbilled planting nozzles increased, seedlings had the seedlings were relatively static or even going upward to the planting device; when the rotating speed increased to a certain degree, the seedlings failed falling to the bottom of the planting device when the nozzles penetrated into the soil, and seedling loss and lodging occurred as a result.

Acknowledgements

This project was supported by National Natural Science Foundation of China (Grant No.51505130), the National Key Research and Development Program of China Sub-project (No. 2017YFD0700800 & No. 2016YFD0700103), the Innovation Scientists and Technicians Troop Construction Projects of Henan Province (No.184200510017), the Research Project of Science and Technology of Henan Province (No. 172102110021).

[References]

[1] Chen, J. N. B. H. Wang,and G. Y. Ren. 2010. Kinematics modeling and parameters analysis of seven-linkagevegetable seedlingtransplanting mechanism. *Transactions of the Chinese Society for Agricultural Machinery*, 41(12): 48–53.

[2] Chen, J. N., X. D. Xia, and Y. Wang. 2015. Motion differential equations of seedling in duckbilled planting nozzle and itsapplication experiment. *Transactions of the Chinese Society of Agricultural Engineering*, 31(3): 31–39.

[3] He Yakai, S. J. Li, and X. J. Yang. 2016. Kinematic analysis and performance experiment of cam-swing link planting mechanism. *Transactions of the Chinese Society of Agricultural Engineering*, 32(6): 34–41.

[4] Feng, J., G. Qin, and W. T. Song. 2002. The kinematic analysisand design criteria of the dibble-type transplanters. *Transactions of the Chinese Society for Agricultural Machinery*, 33(5): 48–50.

[5] Jin, X., S. J. Li, and X. J. Yang. 2012. Motion analysis and parameter optimization for pot seedling planting mechanism based on up-film transplanting. *Transactions of the Chinese Society for Agricultural Machinery*, 43(s1): 29–34.

[6] Jin, X., S. J. Li, H. Yan, and X. J. Yang. 2012. Optimization of working parameters of tobacco transplanter to achieve higher erectness of block seedlings. *International Agricultural Engineering Journal*, 21(2): 50–56.

[7] Jin, X., X. W. Du, and G. S. Geng. 2015. Experiment on planting system of 2ZDJ-2 transplanter. *Transactions of the Chinese Society for Agricultural Machinery*, 46(7): 97–101.

[8] Peng, X., J. N. Song, and Y. B. Huang. 2006. The dynamicsanalysis of the vegetable potted seedling in

theseedling-guiding tube. *Journal of Agricultural Mechanization Research*, 37(8): 54–59.

[9] Prasanna K. G., andH.Raheman. 2011. Development of awalk-behind type hand tractor powered vegetable transplanterfor paper pot eedlings. *Biosystems Engineering*, 110(26): 189–197.

[10] Xiao M. T., S. L. Sun, and H. F. Luo.2014. Kinematic analysis and experiment of dual parallelogram multi-pole planting mechanism. *Transactions of the Chinese Society of Agricultural Engineering*, 30(17): 25–33.

[11] Yu, G. H., B. H. Liu, and Y. Zhao. 2011. Kinematic principle analysis of transplanting mechanism with planetary elliptic gears in automatic vegetable transplanter. *Transactions of the Chinese Society for Agricultural Machinery*, 42(4): 53–57.

[12] Zhang, G. F., Y. Zhao, and J. N. Cheng. 2009. Characteristicanalysis of rice plotted-seedlings motion in air and onturbination-type guide-canal. *Journal of Zhejiang University (Engineering Science)*, 43(3): 529–534.

[13] Zhang, Z. L., J. L. Wang, and W. Z. Zhang. 2011. Kinematicanalysis and performance experiment of cantilever cupvegetabletransplanter. *Transactions of the Chinese Society of Agricultural Engineering*, 27(11): 21–25.

EDEM-based numerical simulation and analysis on filling performance of centralized seed metering device

Li Zhaodong[1], Liao Yitao[2], Zhang Wenyu[2], Liao Qingxi[2*]

(1. *College of Engineering, Anhui Agricultural University, Hefei 230036, China*;
2. *College of Engineering, Huazhong Agricultural University, Wuhan 430070, China*)

Abstract: In order to improve the filling performance of centralized hole-wheel seed metering device, in this paper, average hole particle number and filling rate were used as the evaluation indexes to simulate the filling performance of hole shape, cone angle of holes, lateral width of the seed-filling room and filling height by EDEM. In the bench test, experiment seed was the rapeseed variety "Hua oil Hybridization 62", the variable coefficient of seeding stability and seed damage rate were used as the evaluation indexes to the influence of ratio between filling height and lateral width of seed-filling room, and seeding cylinder's rotating speed on seed metering performances were studied. The simulation results showed that the average hole particle number and filling rate increased with the increase ratio between filling height h and lateral width of the seed-filling room M, the average hole particle number of inverted pyramid holes more than the average hole particle number of inverted circular cone, filling rate increased and then dropped with the increase of cone angle, the blockage rate decreased with the increase of cone angle, and the seeding performance of cubic hole with cone angle of 50°-55° and the ratio between filling height h and lateral width of the seed-filling room M should be no less than 0.475 as this was better for the improvement of seeding performance. Bench test showed that the variable coefficient of seeding stability and seed damage rate had no significant changes, the variable coefficient of seeding stability was no higher than 2.5%, and seed damage rate was less than 0.1%. The above test results showed that when holes of inverted square cone with cone angle of 50°-55° and ratio of filling height h and lateral width of seed-filling room M was $0.475 \leq h/M \leq 0.675$, it was good to improve filling performance. The study can serve as a reference for structure improvement of centralized hole-wheel seed metering device and its parameter optimization.

Keywords: centralized hole-wheel seed metering device, filling performance, numerical simulation and analysis, filling rate

Citation: Li, Z. D., Y. T. Liao, W. Y. Zhang, and Q. X. Liao. 2017. EDEM-based numerical simulation and analysis on filling performance of centralized seed metering device. International Agricultural Engineering Journal, 26(4): 140–148.

1 Introduction

Precision rape seeding technology means seeding the rape seeds into field in rows with precision. It is suitable for mechanized harvesting, and for its advantages of labor and time saving, cost saving and high efficiency with small risks in lodging (Su et al., 2011; Tian et al., 2008; Wu et al., 2007), it has become the trend for rape planting. The seed metering device as the core working unit directly affects the quality of rape seeding (Cao et al., 2015; Zhang et al., 1982).

Seed-filling as the primary stage in seeding is an efficient method for improving seeding performance and seeding efficiency (Cong et al., 2014), and there are some studied in this field. Anantachara et al. (2011) and Karayel et al. (2006) studied optimization seed-filling room structure to improve filling performance. Ryu et al. (1998) designed a special hole wheel-type rice precision metering device in order to improve the quality of rice direct seeding. Wang et al. (2009) studied the seed-filling posture of rice seeds by applying high-speed photography technology. Tang et al. (2010) realized precision seeding of hybrid rice by air-blowing seed metering device, and carried out experiments on three shapes of holes of circular cone, elliptic cone and oblong cone based on waxen model technology. In order to improve the seed suction performance of air-suction seed metering device, Chen et al. (2007) analyzed shape, size of seeding holes

Received date: 2017-11-09 **Accepted date:** 2017-11-28
***Corresponding author: Liao Qingxi.** College of Engineering, Huazhong Agricultural University, Wuhan 430070, China. Email: liaoqx@mail.hzau.edu.cn, Tel: 027-87282121.

and the influence of air traveling distance on suction performance. Shi et al. (2015) studied the influence of seeds' interference intensity on pneumatic seed-metering device with combined holes and analyzed seeds' interference intensity of four shapes of holes, namely, cylinder, circular cone, holes with inverted sawteeth and holes without sawteeth, and verified the rationality of analysis by taking seed leakage rate into consideration. Lei et al. (2016) studied the influence of seed layer thickness on seed filling performance of seed metering device for rapeseed and wheat by EDEM simulation technology. The studies listed above had filling performance experiments on hole structure, seed-filling room structure and filling height through high-speed photography, waxen modeling, and simulation technology, however, the experimental study with combination of filling height and lateral width of the seed-filling room of seeding performance for rapeseed centralized hole-wheel seed metering device has few been done .

In order to improve the seed filling performance of centralized hole-wheel seed metering device, in this paper, discrete element method was applied to study the influence of hole shape, cone angle, filling height and lateral width of seed-filling room on seed filling performance, with the aim to provide reference to structure improvement of such kind of rapeseed metering device.

2 Filling process analysis of rapeseed metering device

2.1 Structure and working principles of metering device

The rapeseed centralized pneumatic seed metering device is mainly composed of a seed box, a shell body, a seed-filling room, a seeding cylinder, a seeding shaft, seed protection device, chamber protection plate, seed cleaning device, seed tube and transmission and driving chain wheel, as was shown in Figure 1.

The centralized seed-metering device has four working stages, namely seed filling, seed cleaning, seed protecting and seed throwing, as was shown in Figure 2. The working principles of the seed metering device are as follows: in working, under the influence of gravity, the seeds in the seed box flow into the seed-filling room through the seed tube, then the seeds fill into the holes under lateral extrusion force, friction between the cylinder and seeds, and inertial centrifugal force. The seeding hole with seeds goes through the seed cleaning area and seed protecting area: in seed cleaning, the air flow from the cleaning air tap blows the surplus seeds in the holes out of the seed-filling room, and the remaining seeds in the holes are sent to seed protecting area with the cylinder. With the protection of the seed protecting device, the seeding holes with seeds goes to the seed throwing area. Under the influence of gravity and inertial centrifugal force, it goes into seed tube to finish a cycle of seed metering.

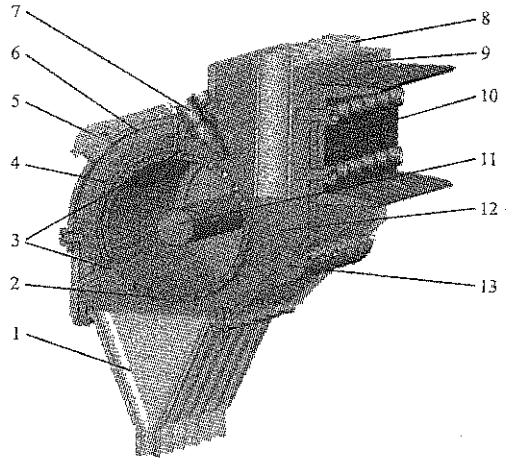

1. Seeding device 2. Cylinder 3. Hole passage 4. Seed protecting device 5. Chamber protecting stopper 6. Chamber protecting plate 7. Seed cleaning device 8. Inlet branch pipe 9. Shell body 10. Connection plate 11. Seeding shaft 12. Seed-filling room 13. Seed unloading stopper

Figure 1 Structure of rapeseed centralized hole-wheel seed metering device

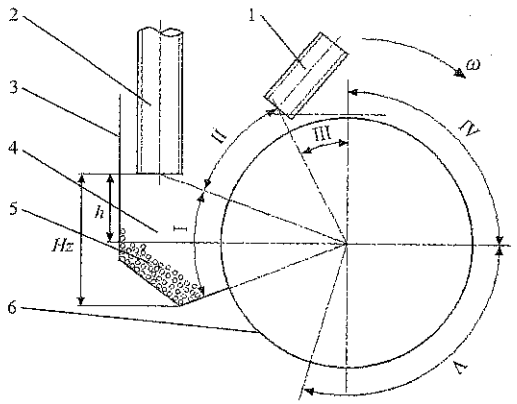

1. Seed cleaning air tap 2. Inlet branch pipe 3. Shell body 4. Seed-filling room 5. Rapeseeds 6. Seeding cylinder

Note: *Hz* is seed layer thickness, mm; *h* is filling height, mm; *M* is lateral width of the seed-filling room, mm; Ⅰ is seed filling area; Ⅱ is seed cleaning area; Ⅲ is seed protecting area; Ⅳ is seed throwing area; Ⅴ is transitional area.

Figure 2 Working principles of the seed metering device

2.2 Filling process analysis

For the convenience of mechanical analysis, hypothesized the rapeseed was homogeneous material rigid body without considering vibration and friction between single rapeseed Q and seed-population, chosen the critical condition of single rapeseed Q filled into hole as research object, the force analysis model was shown in Figure 3. The auxiliary coordinate system was built on horizontal and vertical directions, the following equation could be established.

$$\begin{cases} F_{f2}\sin\dfrac{\varepsilon}{2}+N_2\cos\dfrac{\varepsilon}{2}=F_{f1}\sin\dfrac{\varepsilon}{2}+N_1\cos\dfrac{\varepsilon}{2}+G\cos\sigma \\ N_1\sin\dfrac{\varepsilon}{2}+N_2\cos\dfrac{\varepsilon}{2}F_l\le F_{f1}\cos\dfrac{\varepsilon}{2}+F_{f2}\cos\dfrac{\varepsilon}{2}+G\sin\sigma+N_p \\ F_{f1}=\mu N_1 \\ F_{f2}=\mu N_2 \\ F_l=m\omega^2R \\ G=mg \\ \omega=\pi n_p/30 \\ R\approx(d_p-d_a)/2 \end{cases} \tag{1}$$

where, N_p is the lateral extrusion force which rapeseeds act on seeds of filling into type hole, N; N_1 is braced force which type hole lateral wall 1 acts on rapeseed, N; N_2 is braced force which type hole lateral wall 2 acts on rapeseed, N; F_l is inertial centrifugal force, N; F_{f1} is friction force which rapeseed and type hole lateral wall 1, N; F_{f2} is friction force which rapeseed and type hole lateral wall 2, N; G is gravity of rapeseed, N; μ is surface friction coefficient which rapeseed and cylinder; σ is filling angle, (°); ε is cone angle of hole, (°); m is quality of single seed, kg; ω is angular velocity of cylinder, rad·s^{-1}; n_p is cylinder rotating speed, r·min^{-1}; R is distance between which rapeseed mass center and rotation center of cylinder, m; d_p is diameter of cylinder, m; d_a is diameter of rapeseed, m.

$$\sigma\ge\arccos\frac{\left(\cos\dfrac{\varepsilon}{2}-\mu\sin\dfrac{\varepsilon}{2}\right)\omega^2R}{g\sqrt{1+\mu^2}}+\arctan\frac{\cos\dfrac{\varepsilon}{2}-\mu\sin\dfrac{\varepsilon}{2}}{\sin\dfrac{\varepsilon}{2}+\mu\cos\dfrac{\varepsilon}{2}} \tag{2}$$

As shown in Equation (2), filling angle σ was related to diameter of rapeseed d_a, diameter of cylinder dp, cone angle of hole ε and cylinder rotating speed np. The prototype was mounted on 2BFQ-6 model, a precision combined planter for rapeseed, and driven by the power of DFH LX-854. The forward speed of tractor was 2.1 km·h^{-1}, cylinder rotating speed n_p was 18 r·min^{-1} and cone angle of hole ε was 55°, it could be calculated that the initial filling angle σmin was approximately equal to 7° by Equation (2).

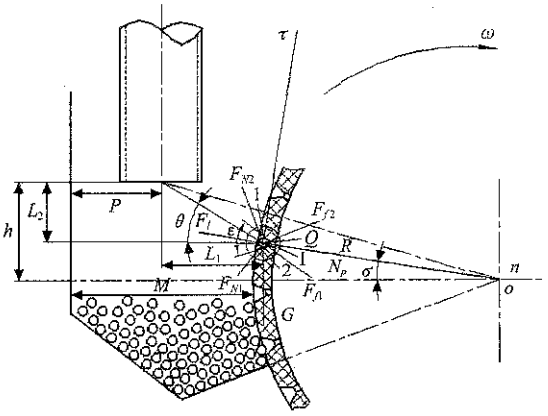

a. Force diagram of rapeseed at filling place

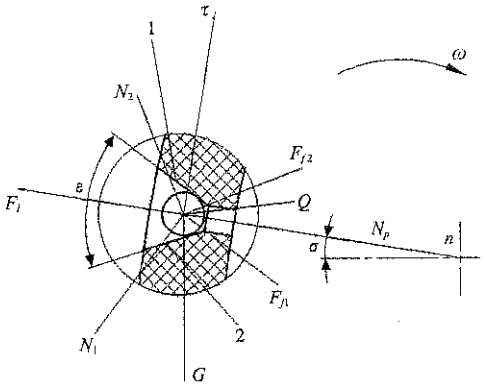

b. Enlarged drawing of I

Figure 3 Force simplified model of rapeseed at filling place

Regardless of interaction force among rapeseeds and braced force which type hole lateral wall 1 acts on rapeseed, from Equation (1), we obtained that:

According to Figure 3a, the relationship between filling height h and lateral width of seed-filling room M and filling angle σ could be analyzed.

$$\begin{cases} L_1=M+R(1-\cos\sigma_{\min})-P \\ L_2=h-R\sin\sigma_{\min} \\ \tan\theta=\dfrac{L_2}{L_1} \end{cases} \tag{3}$$

where, $\sigma_{\min}$ is initial filling angle,(°); θ is natural angle of repose, (°); L_1 is horizontal distance which rapeseed geometry center and branch pipe center, m; L_2 is longitudinal distance which bottom surface of branch

pipe center and rapeseed geometry center, m; M is lateral width of seed-filling room, m; P is horizontal distance which branch pipe center and sidewall of seed-filling room, m; h is filling height, m.

From Equation (3), we obtained that:

$$h=(M+R-P)\tan\theta+\frac{R}{\cos\theta}\sin(\sigma_{\min}-\theta) \quad (4)$$

As shown in Equation (4), there was a remarkable positive correlation between filling height h and lateral width of seed-filling room M and initial filling angle σmin. The experiment seed was the rapeseed variety "Hua oil Hybridization 62". Set lateral width of seed-filling room M ranged from 40 to 70 mm, horizontal distance which branch pipe center and sidewall of seed-filling room P was 25 mm, natural angle of repose θ was 26.7° and diameter of rapeseed da was 1.83 mm, we obtained that the minimum filling height $hmin$ was ranged of 13.7 to 28.5 mm from Equation (4).

3 Filling performance simulation and analysis based on EDEM

3.1 Establishment of the simulation model

3.1.1 Material characteristics

For convenience of simulation and calculation, the EDEM simulation model was simplified and composed of a shell body, a seeding cylinder and an inlet branch pipe, as was shown in Figure 4a. In the simulation model, the seeding shell body and inlet branch pipe were made from steel, and the seeding cylinder was made from ABS engineering plastics.

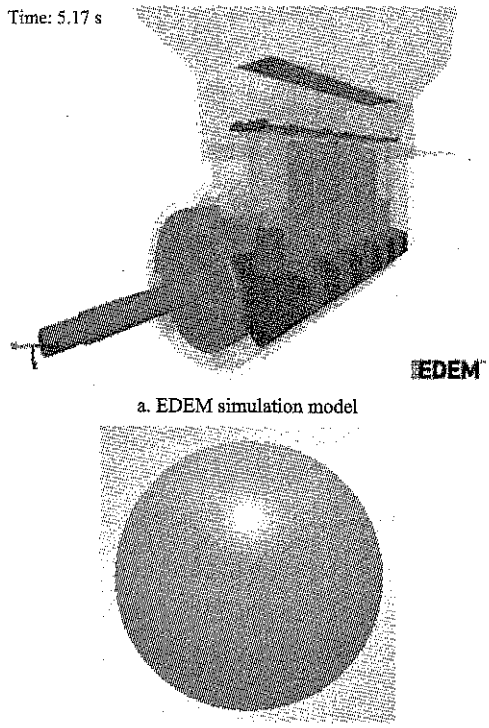

a. EDEM simulation model

b. Rapeseed model

Figure 4 Simulation model of the seed metering device

The rapeseed particle model was built based on the normal size of rapeseeds, as was shown in Figure 4b. Since rapeseeds have high degree of sphericity and smoothness, and commercial seeds adopted in safe storage period were adopted for mechanized seeding (moisture content ≤9%), and the adhesive force between seeds can be ignored. Therefore, Hertz-Mindlin non-sliding contact model was adopted in this paper (Zhao et al., 2013; Li et al., 2009). Related parameters for physical and dynamic characteristics of the simulation analysis (Liao et al., 2014; Lei et al., 2016) were shown in Table 1.

Table 1 Material parameters of physical and mechanical characteristics

Material characteristics	Poisson's ratio	Shear modulus, Pa	Density, g cm^{-3}	Collision coefficient of restitution (with seeds)	Static friction coefficient (with seeds)	Dynamic friction coefficient (with seeds)
Rapeseeds	0.25	1.1×10^{7}	680	0.6	0.5	0.01
Engineering material	0.394	8.96×10^{8}	1060	0.75	0.5	0.01
Steel	0.3	7.94×10^{10}	7800	0.6	0.3	0.01

3.1.2 Determination of the other parameters

It is supposed in the discrete element method that the external force of particles kept constant in one-time step. If the time step is too long, the contact process of particles cannot be described in precision. If the time step is too short, too much calculation is required. In this study, the time step of Rayleigh time was 1.45×10^{-5} s, the exported time step was 0.05 s and running time was 10 s. In order to ensure sustainable seed flow from the seed-filling room within a given period, namely keep seed filling height unchanged, the production rate of rapeseed particles was set as 7500 particles/s, and 15000 particles in total.

3.1.3 Verification of the simulation model

In order to test the reasonability of the simulation model and its parameters, a comparison

experiment was made on results of the simulation and the bench test. Taking rapeseed metering device as the test object, the filling status of the seeding holes under different conditions of filling height were studied. The rotating speed was set as 20 r·min^{-1}, range of filling height was set as 11-23 mm (four levels of 11, 15, 19 and 23 mm), and each situation was repeated for 50 times, and the relative error of average seed particle number was taken as the evaluation index of the model.

$$\lambda = \frac{|n_s - n_z|}{n_s} \times 100\% \quad (5)$$

where, λ is the relative error of the average seed particle number, %; n_s is the actual seed particle number in the holes. n_z is the average seed particle number filled into simulated holes.

Table 2 Comparison between simulation test and bench test

Filling height h/mm	Simulation value n_Z	Measured value n_s	Relative error λ, %
11	0.618	0.600	3.33
15	0.980	1.036	5.41
19	1.680	1.824	7.90
23	2.520	2.696	6.53

In Table 2, a comparison on the average seed particle number between the simulation and the bench test showed that within the range of the filling height listed above, the average seed particle number in the holes in seed filling area increased with the increase of filling height. The conclusion was in line with the existing research results (Lei et al., 2016): the relative error between simulation value and measured value of average seed particle number in the holes was below 8%, which showed that the model and its parameters were consistent with the experiment.

3.2 Experimental design

In order to find out the influence of holes on seed-filling performance, the rotating speed of the seeding cylinder was set as 20 r min^{-1}, lateral width of the seed-filling room was 40 mm, and filling height was 15-27 mm (four levels of 15, 19, 23 and 27 mm). There were two shapes of holes, inverted circular cone and inverted pyramid; and six levels of cone angles were 35°, 40°, 45°, 50°, 55° and 60°. In simulation, the cylinder rotated at 2 s, and stopped at 10 s. The seed particle number filled in the holes during 2-10 s was exported. After the test area was defined, the seed particle number filled into each hole in the area was recorded, taking the point of seed-filling hole leaving seed layer as the starting point, and the beginning end of seed cleaning area as the end. The case of not filling seeds into the hole was recorded as failure in seed filling. The point of holes leaving seed protecting device was taken as the start, and the lowest point of the holes was taken as the end of the seed throwing area. The case of filling seeds into the hole and failure in seed throwing was recorded as blockage. Hereby, the average seed particle number, filling rate and blockage rate can be calculated.

In order to study the influence of lateral width of the seed-filling room, and the ratio between feeding height and lateral width of the seed-filling room on seed filling performance, in the simulation model, the cylinder rotating speed was set as 20 r min^{-1}, the holes were inverted pyramid with cone angle of 55°, filling height was 15-35 mm (six levels of15, 19, 23, 27, 31 and 35 mm), the lateral width of the seed-filling room was 40-70 mm (four levels of 40, 50, 60 and 70 mm). In the same way, the average hole particle number and filling rate during the period of 2-10 s under different treatments were exported.

3.3 Evaluation indexes and calculation method

Based on GB/T 6973-2005 *Testing method of single seed drills (Precision drills)*, in this study, filling rate η_c and blockage rate η_d were taken as the evaluation indexes in the virtual experiment, and the equations of them are as follows respectively:

$$\eta_c = \frac{n_c}{n} \times 100\% \quad (6)$$

$$\eta_d = \frac{n_d}{n_q} \times 100\% \quad (7)$$

where, n is number of holes passing through the seed-filling area; n_c is number of holes filled with seeds; n_q is number of holes that passed through the seed throwing area; n_d is number of holes that passed through the seed throwing area but failed in seed throwing.

3.4 Simulation results and analysis

3.4.1 The influence of holes on seeding performance

Table 3 showed that, when filling height was among 15-27 mm, the average hole particle number of inverted

pyramid holes more than the average hole particle number of inverted circular cone; filling rate increased and then dropped with the increase of cone angle; the blockage rate decreased with the increase of cone angle; under the same condition, the inverted pyramid holes had better seeding performance than that of inverted circular cone, and the blockage rate of inverted pyramid holes was lower than that of inverted circular cone. The reason might be that, the contacting method of inverted pyramid holes and rapeseeds with quasi-circular intersectional surface was point contact, which was good for rolling of the rapeseeds, and thus reduced or got rid of seed blockage. While the holes with inverted circular cone had round intersectional surface and had linear contact with rapeseeds, thus greater friction was produced, hindered seed charging and caused seed blockage and miss-seeding. It is thus clear that, in order to improve the seeding performance of the seed metering device, the inverted pyramid holes with cone angle between 50°-55° can be adopted.

Table 3 Influence of hole structure on seeding performance

Hole structure	Cone angle, (°)	Filling height of 15 mm			Filling height of 19 mm			Filling height of 23 mm			Filling height of 27 mm		
		Average hole particle number	Filling rate, %	Blockage rate, %	Average hole particle number	Filling rate, %	Blockage rate, %	Average hole particle number	Filling rate, %	Blockage rate, %	Average hole particle number	Filling rate, %	Blockage rate, %
Inverted pyramid	35	0.81	81.43	100	0.86	85.71	100	0.89	88.57	100	1.12	95.59	100
	40	0.84	84.51	100	1.04	95.71	100	1.17	94.20	100	1.63	100	100
	45	1.06	91.55	88.68	1.39	97.14	62.1	1.75	100	31.7	2.10	100	32.8
	50	0.96	85.71	0	1.46	95.71	0	1.97	98.55	0	2.56	100	0
	55	1.06	78.26	0	1.56	91.43	0	2.32	100	0	3.09	100	0
	60	0.88	71.01	0	1.77	90	0	2.48	97.10	0	3.54	100	0
Inverted circular cone	35	0.61	61.43	100	0.86	85.71	100	0.81	81.43	100	0.99	94.20	100
	40	0.80	80	100	0.91	91.43	100	0.9	89.86	100	1.10	98.55	100
	45	0.89	87.14	100	0.94	85.71	100	1.22	97.10	100	1.46	100	100
	50	0.97	82.86	95.65	1.24	91.43	90	1.43	95.65	88.5	1.77	100	89.6
	55	0.67	62.86	0	1.11	87.14	0	1.61	97.10	0	2.07	100	0
	60	0.66	58.57	0	1.07	85.51	0	1.61	97.10	0	2.31	100	0

3.4.2 Influence of lateral width of seed-filling room on seeding performance

Figure 5 showed when filling height was among 15-35 mm, the lateral stress of seed group reduced with the increase of lateral width of the seed-filling room, while the lateral stress of seed group and filling rate had positive correlation with the average hole particle number. Results showed that with the same filling height, lateral stress of seed group can be increased by reducing lateral width of seed-filling room, and the seeding performance can be improved.

3.4.3 The influence of filling height on seeding performance

Figure 6 showed that with the same lateral width of the seed-filling room, the lateral stress of seed group had positive correlation with filling height, and average hole particle number and filling rate increased with the increase of lateral stress of seed group. It showed that with the same lateral width of seed-filling room, seed filling performance could be improved by increasing filling height. To avoid miss-seeding, at least one particle of seed should be filled into hole, and filling height h should be no lower than 15 mm.

3.4.4 The influence of h/M on seed filling performance

Figure 7 showed that both average hole particle number and filling rate increased with the increase of h/M; when $h/M \leq 0.375$, the average hole particle number and filling rate stayed at low level; when $0.375 < h/M < 0.475$, the average hole particle number and filling rate took on a fluctuant increasing process. When $h/M \geq 0.475$, the average hole particle number increased significantly and filling rate was in a stable status (≥95%). The analysis above showed that after determining the lateral width of the seed-filling room, better seeding performance can be achieved by adjusting the ratio between filling height h and lateral width of seed-filling room M, namely, $h/M \geq 0.475$. Therefore, adjusting seed-filling height with inlet branch pipe can ensure the stability of seed feeding amount in the seed-filling room and improve the performance of centralized seeding.

To sum up, in order to improve the seeding performance of the hole-wheel seed metering device and avoid seed blockage, the inverted pyramid holes with cone angle between 50°-55° can be adopted and the ratio between filling height h and lateral width of the seed-filling room M should be adjusted as $(h/M)\geq 0.475$.

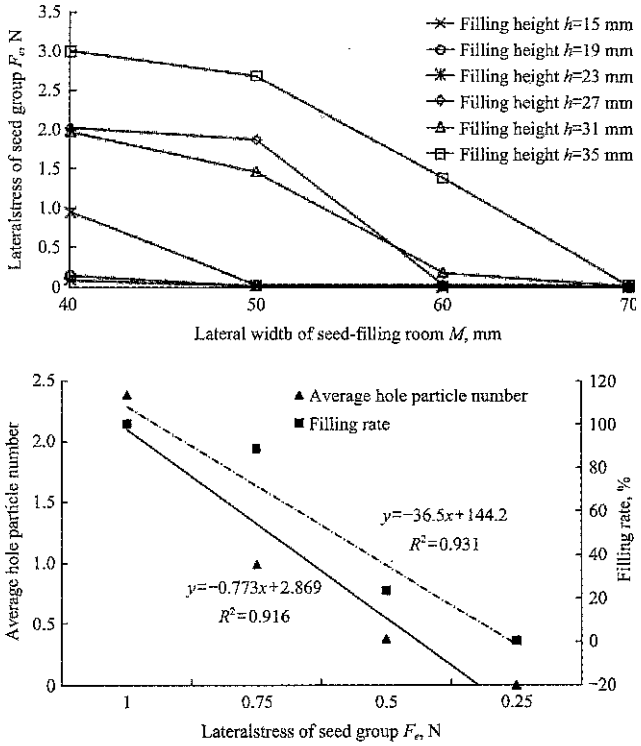

Figure 5 Influence of lateral width of seed-filling room on seeding performance

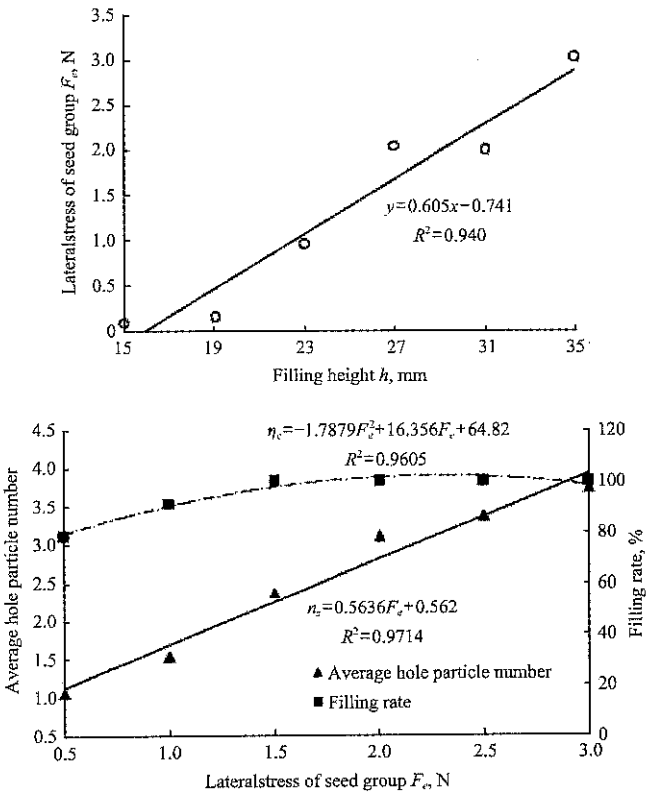

Figure 6 Influence of filling height on seeding performance

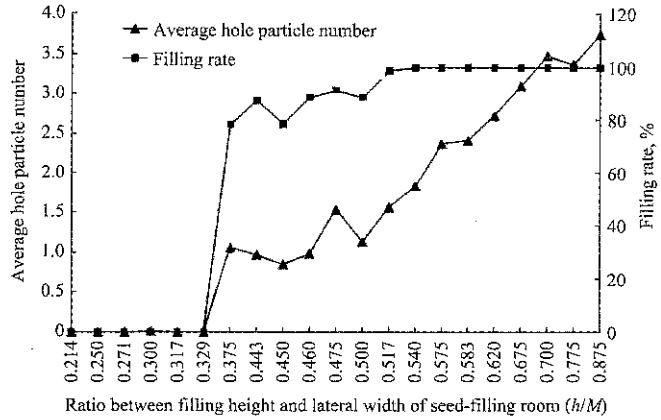

Figure 7 Influence of ratio between filling height and lateral width of seed-filling room on seed-filling performance

4 Performance experiment

4.1 Materials and method

Rape Huayouza 62 was adopted as the experimental material. Its chief characteristics are as follows (Cong, 2014): the mean size of length × width × thickness was 2.01×1.84×1.67 mm; degree of sphericity was 91.25%; natural angle of repose was 26.7°; sliding friction angle was 22.7°; 1000-grain weight was 4.45 g. The experiment was carried out on the testbed of the centralized hole-wheel seed metering device (Figure 8). In the experiment, the inverted pyramid holes with cone angle of 55° were adopted, and air-blowing velocity was 9 m s^{-1}, lateral width of the seed-filling room was 40 mm, filling height was among 19-29 mm, and rotating speed of the cylinder was 20-40 r min^{-1}.

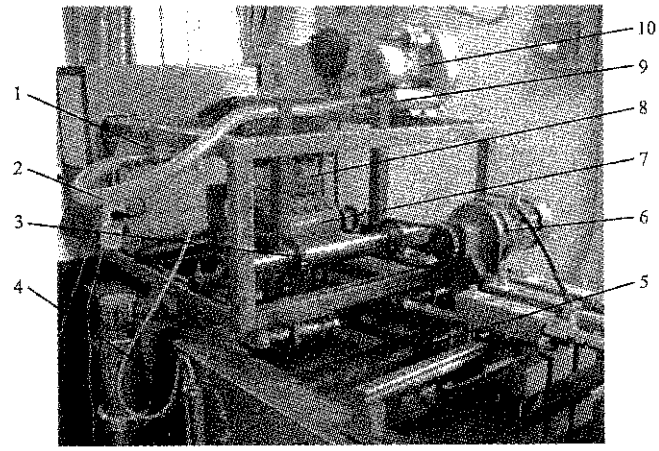

1. Control valve of wind pressure 2. Pneumatic tube 3. Transmission chain 4. U-shaped manometer 5. JPS-12 experimental platform of metering device 6. Driving Motor 7. Pneumatic-typed precision centralized metering device 8. Seed cleaning tube 9. Air-bleed hole 10. Air pump

Figure 8 Composition diagram of experimental device

By taking variable coefficient of seeding stability and seeds damage rate as evaluation indexes, and based on

GB/T 9478-2005 *Testing methods of sowing in lines* (Lei et al., 2013), an experiment on the influence of filling height and rotating speed on seeding performance was carried out. The experiment data were collected for six times, and once every two minutes, then the seeding quantity, variable coefficient of seeding stability and damage rate were calculated.

4.2 Results and analysis

Tables 4 and 5 showed when the ratio between filling height h and lateral width of seed-filling room M was among 0.475-0.725, the seeding amount increased with the increase of h/M. The reason might be the increase of average hole particle number along with the increase of h/M. When $0.475 \leq h/M \leq 0.675$, the variable coefficient of seeding stability was no more than 2.5%, seed damage rate was less than 0.1%; When rotating speed of the cylinder was among 20-40 r min^{-1}, the seeding quantity increased with the increase of cylinder rotating speed, and the variable coefficient of seeding stability was not more than 2%, seed damage rate was less than 0.1%.

Table 4 Influence of h/M on seeding performance

h/M h, mm	0.475	0.525	0.575	0.625	0.675	0.725
Seeding quantity, g	11.069	13.603	14.604	16.994	20.232	22.728
Stability of seeding quantity, %	1.836	2.159	1.156	1.666	1.748	8.588
Damage rate, %	0.005	0.018	0.002	0.041	0.080	0.220

Table 5 Influence of rotating speed on seeding performance

Rotating speed of the seeding shaft, r min^{-1}	20	30	40
Seeding quantity, g	11.410	14.665	20.232
Stability of seeding quantity, %	0.766	0.435	1.748
Damage rate, %	0.020	0.041	0.080

5 Conclusions

1) Tests showed that the average hole particle number and filling rate increased with the increase ratio between filling height h and lateral width of the seed-filling room M, the average hole particle number of inverted pyramid holes more than the average hole particle number of inverted circular cone, filling rate increased and then dropped with the increase of cone angle, the blockage rate decreased with the increase of cone angle, and the seeding performance of cubic hole with cone angle of 50°-55° and ratio between filling height h and lateral width of the seed-filling room M should be no less than 0. 475 as it was better for the improvement of seeding performance.

2) Tests showed that the variable coefficient of seeding stability and seed damage rate had no significant changes, the variable coefficient of seeding stability was no higher than 2.5% and seed damage rate was less than 0.1%.

Acknowledgements

The authors acknowledge that this study was provided by the National Natural Science Foundation of China (51275197) and Modern Agro-industry Technology Research Systems (CARS-13).

[References]

[1] Su, W., J. W. Lu, G. S. Zhou, X. K. Li, Z. H. Han, and H. X. Lei. 2011. Effect of no-tillage and direct sowing density on growth, nutrient uptake and yield of rapeseed. *Scientia Agricultura Sinica*, 44(7): 1519–1526. (In Chinese with English abstract)

[2] Tian, B. P., Q. X. Liao, H. D. Huang, C. X. Shu, H. B. Duan, and J. B. Li. 2008. Design of 2BFQ-6 precision planter for rapeseed. *Transactions of the Chinese Society for Agricultural Machinery*, 39(10): 211–213. (In Chinese with English abstract)

[3] Wu, M. L., C. Y. Guan, C. Z. Tang, S. Y. Chen, H. F. Luo, G. H. Wang, F. P. Xie, M. X. Li, and W. M. Yang. 2007. Experimental research on 2BYF-6 type no-tillage rape combine seeder in paddy stubble field. *Transactions of the Chinese Society of Agricultural Engineering*, 23(11): 172–175. (In Chinese with English abstract)

[4] Cao, X.Y., Y. T. Liao, Q. X. Liao, Z. D. Li, and X. L. Lei. 2015. Design and experiment on value-branch distributor of centrifugal precision metering device for rapeseed. *Transactions of the Chinese Society for Agricultural Machinery*, 46(9): 77–84. (In Chinese with English abstract)

[5] Zhang, D. W., L. Li, and H. M. Wang. 1982. Precision Planter. Beijing: Agricultural Publishing House.

[6] Cong, J. L., Q. X. Liao, X. Y. Cao, Y. T. Liao, J. J. Yu, and L. Wang. 2014. Seed filling performance of dual-purpose seed plate in metering device for both rapeseed & wheat seed. *Transactions of the Chinese Society of Agricultural Engineering*, 30(8): 30–39. (In Chinese with English abstract)

[7] Anantachara, M., G. V. Prasanna Kumarb, and T. Guruswamy. 2011. Development of artificial neural network models for the performance prediction of an inclined plate seed metering device. *Applied Soft Computing*, 11(4): 3753–3763.

[8] Karayel, D., M. Wiesehoff, A. Özmerzi, and J. Müller. 2006.

Laboratory measurement of seed drill seed spacing and velocity of fall of seeds using high-speed camera system. *Computers and Electronics in Agriculture*, 50(2): 89–96.

[9] Ryu, I. H., and K. U. Kim. 1998. Design of roller type metering device for precision planting. *Transactions of the ASAE*, 41(4):923–930.

[10] Wang, Z. M., X. W. Luo, S. X. Huang, W. T. Chen, and J. H. Li. 2009. Rice seeds feeding process in cell wheel based on high-speed photography technology. *Transactions of the Chinese Society for Agricultural Machinery*, 40(12): 56–61. (In Chinese with English abstract)

[11] Tang, C.Z., H. F. Luo, M. L. Wu, and M. Li. 2010. Design and test on seed metering device with variable capacity model-hole roller. *Transactions of the Chinese Society of Agricultural Engineering*, 26 (12): 114-119. (In Chinese with English abstract)

[12] Chen, J., Y. M. Li, X. Q. Wang, and Z. Zhao. 2007. Finite element analysis for the sucking nozzle air field of air-suction seeder. *Transactions of the Chinese Society for Agricultural Machinery*, 38(9): 59–62.(In Chinese with English abstract)

[13] Shi, S., D. X. Zhang, L. Yang, T. Cui, and K. H. Li. 2015. Simulation and verification of seed-filling performance of pneumatic-combined holes maize precision seed-metering device based on EDEM. *Transactions of the Chinese Society of Agricultural Engineering*, 31(3): 62–69. (In Chinese with English abstract)

[14] Lei, X. L., Y. T. Liao, Z. D. Li, W. Y. Zhang, X. Y. Cao, S. S. Li, and Q. X. Liao. 2016. Effects of seed layer thickness on filling performance of seed feeding device for rapeseed and wheat. *Transactions of the Chinese Society of Agricultural Engineering*, 32(6): 11–19. (In Chinese with English abstract)

[15] Zhao, Z., Y. M. Li, Z. W. Liang, and Z. Q. Gong. 2013. DEM simulation and physical testing of rice seed impact against a grain loss sensor. *European Polymer Journal*, 41 (10) :2216-2223.

[16] Li, Y. M., Z. Zhao, J. Chen, and L. Z. Xu. 2009. Discrete element method simulation of seeds motion in vibrated bed of precision vacuum seeder. *Transactions of the Chinese Society for Agricultural Machinery*, 40(3): 56–59. (In Chinese with English abstract)

[17] Liao, Q. X., P. L. Zhang, Y. T. Liao, J. J. Yu, and X. Y. Cao. 2014. Numerical simulation on seeding performance of centrifugal rape-seed metering device based on EDEM. *Transactions of the Chinese Society for Agricultural Machinery*, 45(2): 109–114. (In Chinese with English abstract)

[18] Lei, X. L., Y. T. Liao, Z. D. Li, W. Y. Zhang, S. S. Li, and Q. X. Liao. 2016. Design of seed churning device in air-assisted centralized metering device for rapeseed and wheat and experiment on seed filling performance. *Transactions of the Chinese Society of Agricultural Engineering*, 32(18): 26–34. (In Chinese with English abstract)

[19] Cong, J. L. 2014. Study on seeding system and mechanism of pneumatic precision metering device for wheat and rapeseed. Ph.D. diss. Wuhan: Huazhong Agricultural University. (In Chinese with English abstract)

[20] Lei, X. L., Y. T. Liao, Z. D. Li, X. Y. Cao, S. S. Li, Y. P. Wei, and Q. X. Liao. 2015. Design and experiment of seed feeding device in air-assisted centralized metering device for rapeseed and wheat. *Transactions of the Chinese Society of Agricultural Engineering*, 31(20): 10–18. (In Chinese with English abstract)

Physical properties of mechanical covering film seedbed with corn whole plastic-film mulching on double ridges

Dai Fei[1], Zhao Wuyun[1*], Wang Jiuxin[1], Zhang Fengwei[1],
Feng Fuxue[2], Zhang Fangyuan[1]

(1. *College of Mechanical and Electrical Engineering, Gansu Agricultural University, Lanzhou 730070, China*;
2. *College of water conservancy and hydropower engineering, Gansu Agricultural University, Lanzhou 730070, China*)

Abstract: The furrow sowing with whole plastic-film mulching on double ridges has been widely used in the arid region of northwest China, since it can resist drought and increase production. So the mechanical sowing on film is an inevitable trend in farming. In order to further study the working mechanism and the determination of working parameters of the direct insert precision hill-seeder with corn whole plastic-film mulching on double ridges, to research on the physical properties of 3 kinds of mechanical covering film seedbed with corn whole plastic-film mulching on double ridges. Which included the different types of covering film seedbed soil temperature, soil moisture and plastic-film mechanics properties of furrow in the corn growth period, as well as the soil density of seedbed each several part in the sowing time. The experimental results showed that, when the 3 kinds of mechanical covering film seedbed soil depth increased, the soil temperature of furrow gradually decreased. The 3 kinds of covering film seedbed soil moisture content showed a tendency to decrease firstly and then increase. And the soil moisture (18.57%-21.76%) was the largest in seedbed of corn sowing stage. Meanwhile, the thickness of the seedbed mulching plastic-film had significant effect on the average tensile load of torn apart at right angles and the average fracture elongation displacement of torn apart at right angles. The furrow soil density was the largest in different kinds of covering film seedbed each part, the soil density of all 3 kinds of seedbed furrows was reached 334-549 kPa in the sowing depth of 50 mm. According to the rainfall in different regions, it was advisable to select the 2 types (film mulching in early spring and film mulching in autumn) of covering film seedbed, and the thickness of the cover film was greater than 0.008 mm in northwest arid of China.

Keywords: corn whole plastic-film mulching on double ridges, physical properties, mechanical covering film seedbed, parametric measurement

Citation: Dai, F., W. Y. Zhao, J. X. Wang, F. W. Zhang, F. X. Feng, and F. Y. Zhang. 2017. Research on the physical properties of mechanical covering film seedbed with corn whole plastic-film mulching on double ridges. International Agricultural Engineering Journal, 26(4): 149–156.

1 Introduction

The furrow sowing technique with whole plastic-film mulching on double ridges is a breakthrough innovative technology that has been developed in recent years (Zhou et al., 2012; Qin et al., 2014; Yang et al., 2010; Zhang et al., 2014), which is mainly aimed at corn production and planting, to require ridging and mulching plastic-film, and then finish the sowing on the plastic-film in the double ridges furrow (Zhao et al., 2013; Dai et al., 2016). The cultivation method of the whole plastic-film mulching on double ridges can promote the growth of corn nutrition by improving the ridge furrow microenvironment of soil-water-thermal. In the end, the results show that the yield and water utilization efficiency are significantly improve, and also enrich the adaptive strategies of crop active drought avoidance under drought conditions (Liu et al., 2012; Borut et al., 2011).

The furrow sowing with whole plastic-film mulching

Received date: 2017-08-12 **Accepted date:** 2017-12-03
* **Corresponding author: Zhao Wuyun,** Ph.D. Professor, College of Mechanical and Electrical Engineering, Gansu Agricultural University, Lanzhou 730070, China. Email: zhaowy@gsau.edu.cn, Tel: +09317632472.

on double ridges has been widely used in the arid region of northwest China, since it can resist drought and increase production. So the mechanical sowing on film is an inevitable trend in farming. It is one of the key links that make the whole mechanization process of the whole plastic-film mulching on double ridges. The mechanical covering film seedbed with corn whole plastic-film mulching on double ridges is an important link to connect the equipment of agricultural machinery and agricultural technology (Dai et al., 2016). Therefore, it is necessary to study the physical properties of mechanical covering film seedbed with corn whole plastic-film mulching on double ridges, to research on the physical properties of 3 kinds of mechanical covering film seedbed with corn whole plastic-film mulching on double ridges. Which include the different types of covering film seedbed soil temperature, soil moisture and plastic-film mechanics properties of furrow in the corn growth period, as well as the soil density of seedbed each several part in the sowing time.

There are few reports of the physical properties of mechanical covering film seedbed with corn whole plastic-film mulching on double ridges. So the research results will provide reference for the study of the operation mechanism of the direct insert precision hill-seeder and its working parameters.

2 Materials and methods

2.1 Test materials

The parametric measurement experiment of the physical properties of mechanical covering film seedbed with corn whole plastic-film mulching on double ridges was carried out in the Sanjiaocheng town of Yuzhong county in Lanzhou city. The area of the test site was 0.60 hm^2, the ground was flat and the soil property was loessal soil. According to the agronomic requirements of the whole plastic-film mulching on double ridges, the different film thickness (0.008 mm, 0.010 mm and 0.012 mm) and different types (film mulching in early spring, film mulching in autumn and film mulching in two-year) of seedbed correlation indexes will be measured. As shown in Figure 1, the different types of seedbed have mechanized constructed by operation machine for tillage-fertilization and spraying-filming on double ridges (Dai et al., 2016).

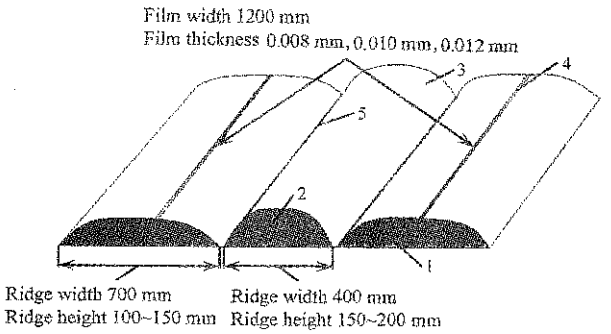

a. Seedbed agronomic requirements

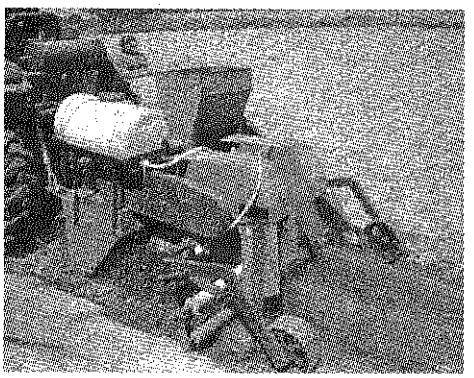

b. Seedbed mechanized construction

1. Big ridges 2. Small ridges 3. Plastic-film 4. Strip of covering film soil 5. Furrow

Figure 1 Agronomic requirements and mechanized construction of whole plastic-film mulching on double ridges

2.2 Experimental apparatus and methods

Combined the operation characteristics of the direct insert precision hill-seeder with corn whole plastic-film mulching on double ridges, and considered the interaction with sowing mechanism and mechanized covering seedbed (Zhao et al., 2013; Wang et al., 2011). The selection measurement of physical properties parameters of whole plastic-film mulching on double ridges were included the soil temperature of seedbed furrow in corn growth stage, the soil moisture of seedbed each part in corn growth stage, the soil moisture of seedbed furrow in corn seedling stage, the film mechanics properties of seedbed furrow in corn growth stage and the soil density of seedbed each part in corn sowing stage. The test sampling and test data were all measured at 10 a.m.

As shown in Figure 2, the soil temperature of seedbed furrow is observed with the curved tube ground temperature meter, which is produced by Taizhou Diao Pu Optics Instrument Co. Ltd, and also can measure the soil depth of 0-600 mm.

a. Soil temperature testing in seedling stage b. Soil temperature testing in elongation stage

Figure 2 Measurement of soil temperature of seedbed furrow

As shown in Figure 3, the soil density of seedbed each part is measured with the soil compactness meter, which is produced by Shanghai AICE Electronic Technology Co. Ltd, it can measure the soil depth of 0-450 mm and the measuring range is 0-7000 kPa.

a. Determination of soil density in sowing stage b. Determination of soil density in seedling stage

Figure 3 Measurement of density of seedbed each part

Gravimetric method is used to carry out the soil moisture measurement with the support of apparatus of soil-drilling, the electronic balance, and the 101 electronic oven, which are produced by Shanghai Lichen Technology Co. Ltd, as shown in Figure 4. Among them, the soil-drilling bit length is 163 mm, the 101 electronic oven drying temperature in the range of 10-250°C, and the accuracy of the electronic balance is 0.1 g.

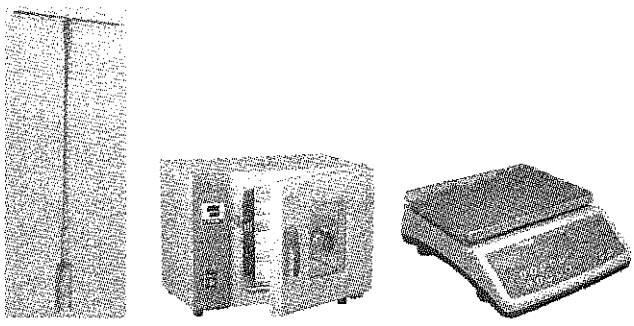

a. Soil-drilling b. 101 electronic oven c. Electronic balance

Figure 4 Measurement of density of seedbed each part

3 Results and discussion

Enhancing film thickness manages to improve soil temperature and moisture status, but it results in different yield responses depending on crops (Zhang et al., 2017). Combination with the common application of film thickness in Gansu province, the white film thickness of 0.010 mm is used when measuring the soil temperature, soil moisture and soil density.

3.1 Soil temperature of seedbed furrow in corn growth stage

The soil temperature of seedbed furrow in corn growth stage is one of the key factors affecting the crop yield and soil environment (Yang et al., 2013). To measure the soil temperature of the 3 types (film mulching in early spring, film mulching in autumn and film mulching in two-year) of covering film seedbed with the different furrow soil depths (0-50 mm, 50-100 mm, 100-200 mm, 200-400 mm) in corn growth stage (sowing stage April 23, 2015, seedling stage May 9, 2015, elongation stage June 16, 2015, bell-mouthed stage July 8, 2015, grain filling stage August 6, 2015, ripeness stage September 9, 2015). Figure 5 shows the field test data with different soil depth of ridge furrows.

The experimental results show that, when the 3 kinds of mechanical covering film seedbed soil depth increases, the soil temperature of furrow gradually decreases. The soil temperature of covering film seedbed furrow with film mulching in autumn is slightly higher than the others two types. The highest soil temperature of furrow all appear in elongation stage, bell-mouthed stage and grain filling stage, and the 3 kinds of mechanical covering film seedbed furrow soil temperature change from 31.4°C to 33.4°C, which meet the heat demand of the corn growth stage.

3.2 Soil moisture of seedbed each part in corn growth stage

The biggest effect of corn whole plastic-film mulching on double ridges is efficient preserving soil moisture. Therefore, the soil moisture of seedbed each part in corn growth stage directly determines the corn growth potential and its final yield. As shown in Figure 6, there is the whole variation trend of soil moisture of the 3 types of covering film seedbed with different furrow soil depths in corn growth stage.

As shown in Figure 6, the soil moisture of the 3 types of covering film seedbed both show the trend of decreasing firstly and then increasing. The soil moisture (18.57%-21.76%) of furrow is the largest in the sowing stage, and then gradually decreases. At the same time,

after the corn is growing through the bell-mouthed stage, the soil moisture of furrow increases gradually, which can effectively solves the problems of water supply and demand caused by seasonal drought (Zhang et al., 2014; Wang et al., 2011). So the utilization rate of water resources in dry farming is greatly improved, the spatial and temporal distribution of precipitation resources is realized. The soil moisture of furrow with film mulching in two-year is high overall, which is mainly related to the film with longer covering time.

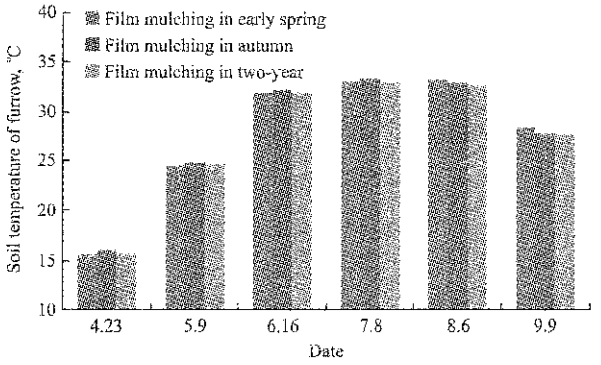

a. Soil depth of furrow is 0-50 mm

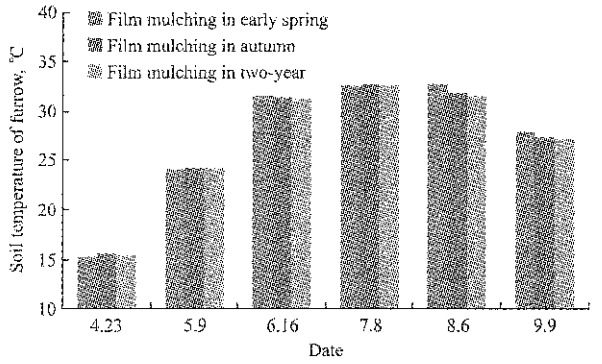

b. Soil depth of furrow is 50-100 mm

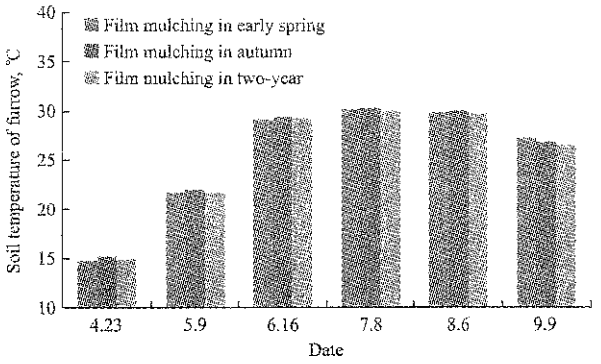

c. Soil depth of furrow is 100-200 mm

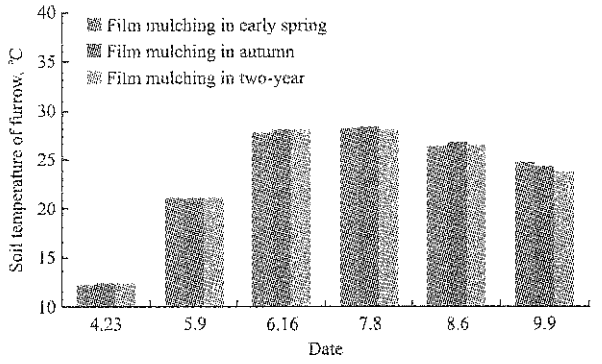

d. Soil depth of furrow is 200-400 mm

Figure 5 Soil temperature of seedbed furrow in corn growth stage

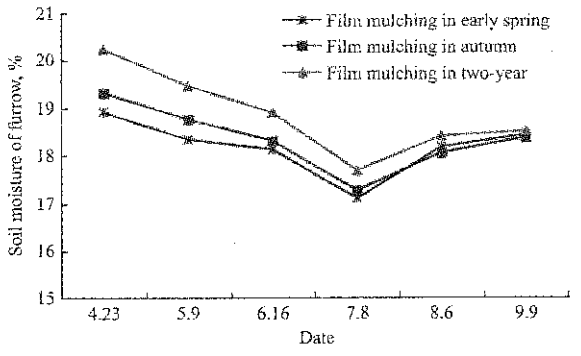

a. Soil depth of furrow is 0-50 mm

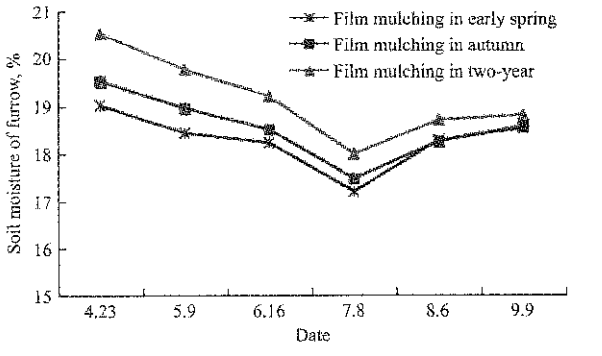

b. Soil depth of furrow is 50-100 mm

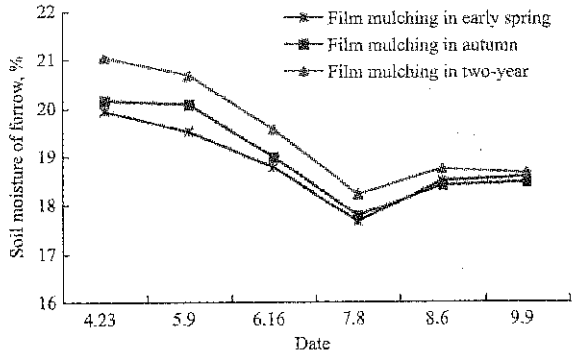

c. Soil depth of furrow is 100-200 mm

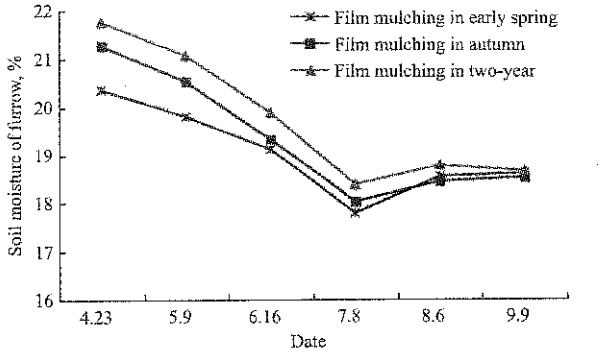

d. Soil depth of furrow is 200-400 mm

Figure 6 Soil moisture of seedbed furrow in corn growth stage

The big ridge body and small ridge body of corn whole plastic-film mulching on double ridges are the effective carrier with the water supply for the seedbed furrow. The seedling stage has high demand for soil moisture of various parts (big ridge, small ridge and furrow) of seedbed. The soil moisture of seedbed each part in corn seedling stage are illustrated in Table 1.

Table 1 Soil moisture of seedbed each part in corn seedling stage

Film mulching modes	Soil depth of seedbed, mm	Soil moisture of seedbed each part, %		
		Big ridge	Small ridge	Furrow
Film mulching in early spring	0-50	16.86	16.04	18.13
	50-100	17.51	16.82	18.56
	100-200	17.72	18.19	19.52
	200-400	19.44	19.46	19.81
Film mulching in autumn	0-50	17.05	16.33	18.38
	50-100	17.83	17.11	19.16
	100-200	18.22	18.68	20.09
	200-400	19.98	20.02	20.53
Film mulching in two-year	0-50	18.12	17.38	19.21
	50-100	18.75	18.26	20.06
	100-200	20.03	19.72	21.32
	200-400	21.18	21.24	21.86

Form the above test data, it can be seen that the soil moisture of seedbed increases when the soil becomes deeper with the 3 kinds patterns of mechanical covering film. Combine with the covering film seedbed function of covering film to inhibit evaporation, collecting rainwater with film surface and rainwater infiltration in furrow (Hu et al., 2016). The soil moisture (18.13%-21.86%) of seedbed furrow is the largest in 3 kinds of operating patterns, and the soil moisture (16.04%-21.24%) of the small ridge is the lowest, the seedbed soil is not easy to bond and collapse under the covering plastic-film. Therefore, when the direct insert precision hill-seeder is designed, the tail wheel could walk on the surface of the small ridge.

3.3 Film mechanics properties of seedbed furrow in corn growth stage

Figure 7 is the process of mechanical sowing on whole plastic-film mulching on double ridges. As shown in Figure 7, the acting force of the hole-former on the surface of the plastic-film is represented as F, the direct insert, puncture film, and cavitations with hole-former, which is directly affected the sowing performance and working quality of the hill-seeder. The interaction between the hole-former and the furrow film, which has important influence for dislocation of soil hole and mechanical damage of daylighting mulch (Wang et al., 2017). Combine of the process of sowing on the film in actual, the film mechanics properties of seedbed furrow need to be measured in corn growth stage.

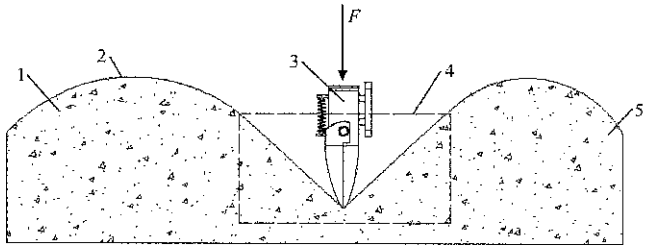

1. Big ridges 2. Plastic-film 3. Hole-former 4. Sowing area 5. Small ridges

Figure 7 Process of mechanical sowing on whole plastic-film mulching on double ridges

When the hole-former inserts into the hole-former seedbed directly for sowing, the furrow film and seedbed soil are all affected by the acting force. In the process of sowing, the hole-former directly inserts into the covering film furrow, which is similar to torn apart the covering film at right angles. Therefore, to measure the average tensile load of torn apart at right angles and average fracture elongation displacement of torn apart at right angles with the 3 types (film mulching in early spring, film mulching in autumn and film mulching in two-year) of covering film seedbed with the different film thickness (0.008 mm, 0.010 mm and 0.012 mm) in corn growth stage (sowing stage April 23, 2015, seedling stage May 9, 2015, elongation stage June 16, 2015, bell-mouthed stage July 8, 2015, grain filling stage August 6, 2015, ripeness stage September 9, 2015). As shown in Figure 8 and Figure 9, it is the field test data with different film thickness of ridge furrow. It is important to optimize the work parameters of the direct insert precision hill-seeder.

3.3.1 Average tensile load of torn apart at right angles

Figure 8 shows that when the three kinds of seedbed covering film thickness increase, the average tensile load of torn apart at right angles of furrow gradually decreases in corn growth stage. The average tensile load of torn apart at right angles of furrow with film mulching in two-year is slightly less than the others two types. In ripeness stage, the three kinds of the average tensile load of torn apart at right angles of furrow are only 0.35-0.44 N, which restricts the collecting mode of the rewinding film.

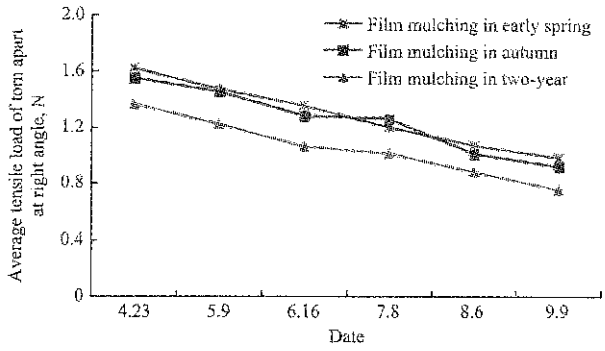

a. Film thickness is 0.008 mm

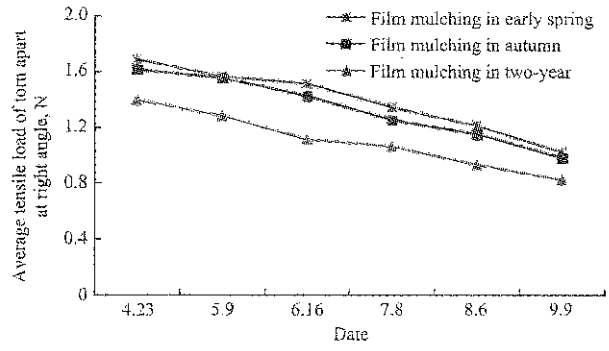

b. Film thickness is 0.010 mm

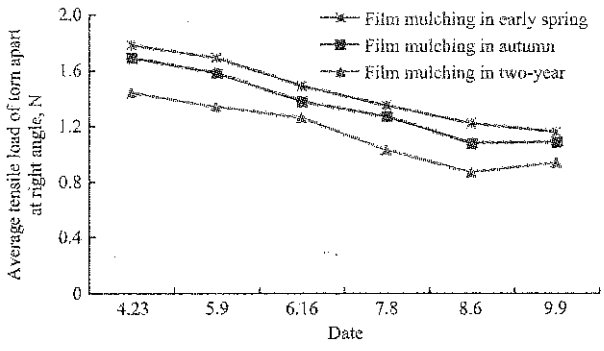

c. Film thickness is 0.012 mm

Figure 8 Average tensile load of torn apart at right angles in corn growth stage

3.3.2 Average fracture elongation displacement of torn apart at right angles

Figure 9 shows that the average fractures elongation displacement of torn apart at right angles following the change of the growth cycle is decreasing in corn growth stage. Among them, the film mulching in two-year mode is the most prominent. The thickness of the seedbed mulching plastic-film has significant effect on the average fracture elongation displacement (the maximum value of three kinds of covering film is reached 61.7-101.3 mm) of torn apart at right angles (Zhang et al., 2015; Zhang et al., 2017). Due to that the time interval is 5-6 months between the film mulching in early spring and film mulching in autumn, the average fracture elongation displacement of torn apart at right angles of these two kinds of covering film has little difference, and the basic difference is between 3.1-5.8 mm.

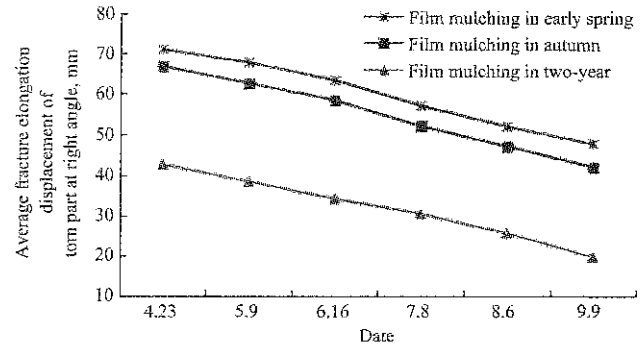

a. Film thickness is 0.008 mm

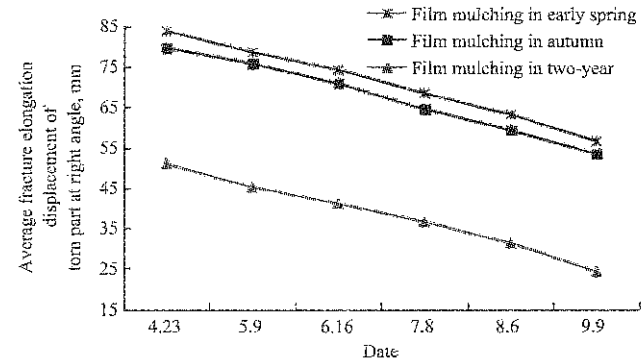

b. Film thickness is 0.010 mm

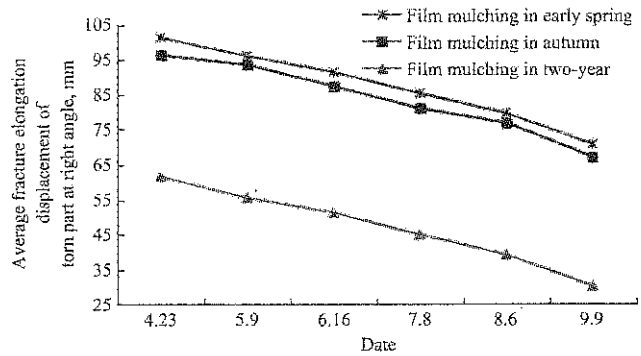

c. Film thickness is 0.012 mm

Figure 9 Average fracture elongation displacement of torn apart at right angles in corn growth stage

3.4 Soil density of seedbed each several part in the sowing time

Taking the each group of the small ridge as a unit, when the direct insert corn precision hill-seeder is planting operation with whole plastic-film mulching on double ridges, the walking wheel walks in both side of the furrow, and the hole-former can force open and sowing in furrow fixed-point. Based on the center line of the small ridge, the tail wheel can walk on the surface of the small ridge, which has a function of the walking, sowing and three-point support. Therefore, the soil density of seedbed each several part (furrow, big ridge

and small ridge) in the sowing time need to be measured, which will provide a reference for calculating the operating machine quality and the cavitation mechanism power of the direct insert corn precision hill-seeder.

As is shown in Figure 10, the soil density of seedbed each several part increases as the 3 kinds of seedbed soil depth increases in the sowing time. Because of the seedbed soil is not cultivated for two years, the soil density of seedbed each several part with film mulching in two-year is higher than the others two types. The dual function of the hill-seeder walking wheel and its cavitation mechanism, the furrow soil density is the largest in different kind of covering film seedbed each part, the soil density of all 3 kinds of seedbed furrows is reached 334-549 kPa in the sowing depth of 50 mm. By reason of the big ridge surface has been covered and suppressed twice, so the soil density of the big ridge of mechanical covering film seedbed is higher than its small ridge. Therefore, when the direct insert corn precision hill-seeder is planting operation with whole plastic-film mulching on double ridges, the operator should not handle the machine walk on the small ridge.

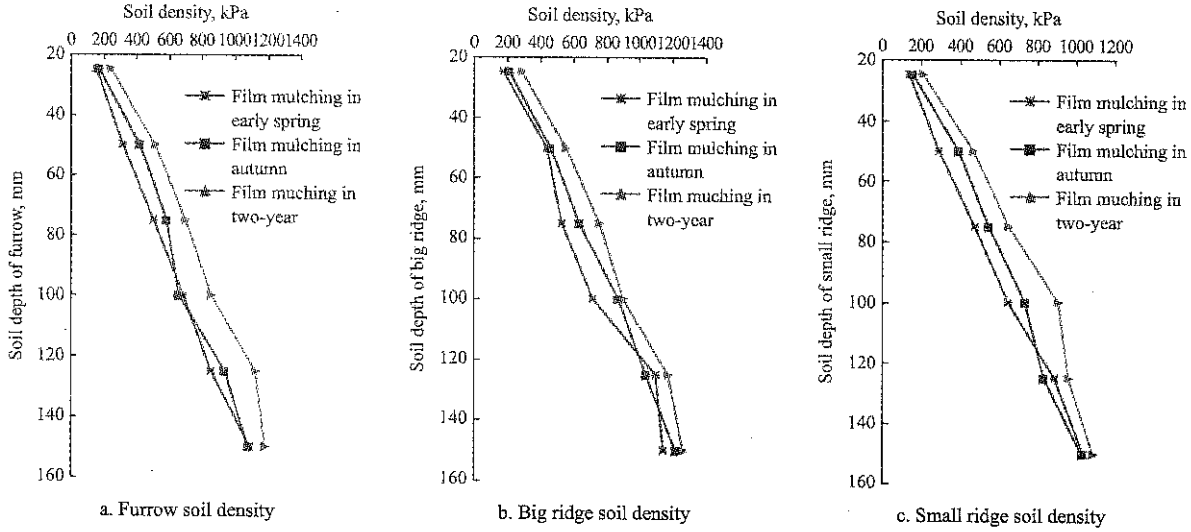

a. Furrow soil density b. Big ridge soil density c. Small ridge soil density

Figure 10 Soil density of seedbed each several part in the sowing time

4 Conclusions

In order to further study the working mechanism and the determination of working parameters of direct insert precision hill-seeder with corn whole plastic-film mulching on double ridges, we researched on the physical properties of 3 kinds of mechanical covering film seedbed with corn whole plastic-film mulching on double ridges. From the experimental analysis the following conclusions can be made:

(1) The experimental results showed that, when the three kinds of mechanical covering film seedbed soil depth increased, the soil temperature of furrow gradually decreased. The highest soil temperature of furrow all appeared in elongation stage, bell-mouthed stage and grain filling stage, and the three kinds of mechanical covering film seedbed furrow soil temperature reached 31.4°C-33.4°C, when its soil depth in 0-100 mm, which met the heat demand of the corn growth stage.

(2) The soil moisture of the three types of covering film seedbed both showed the trend of decreasing firstly and then increasing. The soil moisture (18.57%-21.76%) of furrow was the largest in the sowing stage, which could effectively solve the problems of water supply and the demand caused by seasonal drought.

(3) The thickness of the seedbed mulching plastic-film had significant effect on the average tensile load of torn apart at right angles and the average fracture elongation displacement of torn apart at right angles. The average tensile load of torn apart at right angles of furrow with film mulching in two-year was slightly less than the others two types, which restricted the collecting mode of the rewinding film.

(4) The furrow soil density was the largest in different kinds of covering film seedbed each part, the soil density of all three kinds of seedbed furrows reached 334-549 kPa at the sowing depth of 50 mm.

(5) According to the rainfall in different regions, it

was advisable to select the two types (film mulching in early spring and film mulching in autumn) of covering film seedbed, and the thickness of the cover film was greater than 0.008 mm in northwest arid of China.

Acknowledgements

This project is supported by National Natural Science Foundation of China (Grant No. 51775115 and No. 51405086), and the Special Fund for Agroscientific Research in the Public Interest (No. 201503105).

[References]

[1] Borut, G., and Dea B. 2011. Incorporation of a ridge-furrow-ridge rainwater harvesting system with mulches in high-value plant production. Irrigation and Drainage, 60(4): 518–525.

[2] Dai, F., W. Y. Zhao, F. W. Zhang, H. Zhang, and F. X. Feng. 2016. Current status of mechanization planting technology and equipment for corn whole plastic-film mulching on double ridges in the arid of Northwest China. *Journal of Chinese Agricultural Mechanization*, 37(8): 217–222. (In Chinese with English abstract)

[3] Dai, F., W. Y. Zhao, F. W. Zhang, Z. W. Wu, X. F. Song, and Y. F. Wu. 2016. Operating performance optimization and experiment of collector for corn whole plastic film mulching on double ridges. *Transactions of the Chinese Society of Agricultural Engineering*, 32(18): 50–60. (In Chinese with English abstract)

[4] Dai, F., W. Y. Zhao, M. Y. Ma, J. X. Wang, L. R. Shi, and J. M. Ma. 2016. Parameters optimization of operation machine for tillage-fertilization and spraying-filming on double ridges. *Transactions of the Chinese Society for Agricultural Machinery*, 47(1): 83–90. (In Chinese with English abstract)

[5] Hu, G. R., Q. Wang, X. Y. Song, F. C. Li, D. K. Zhang, E. H. Zhang, Q. L. Liu, and H. L. Wang. 2016. Effects of furrow-mulching materials on soil temperature, crop yield and water use efficiency in ridge-furrow rainwater harvesting systems. *Chinese Journal of Eco-Agriculture*, 24(5): 590–599. (In Chinese with English abstract)

[6] Liu, X. W., B. L. He, and T. W. Guo. 2012. Effects of full mulching on double ridges with different mulching methods on soil water content and maize yield in dryland. *Journal of Nuclear Agricultural Sciences*, 26(3): 602–609. (In Chinese with English abstract)

[7] Qin, S. H., J. L. Zhang, H. L. Dai, D. Wang, and D. M. Li. 2014. Effect of ridge-furrow and plastic-mulching planting patterns on yield formation and water movement of potato in a semi-arid area. *Agricultural Water Management*, 131(1): 87–94.

[8] Wang, H. L., X. C. Zhang, S. Y. Song, Y. F. Ma, X. F. Yu, and Y. L. Liu. 2011. Effects of whole field-surface plastic mulching and planting in furrow on soil temperature, soil moisture, and corn yield in arid area of Gansu Province, Northwest China. *Chinese Journal of Applied Ecology*, 22(10): 2609–2614. (In Chinese with English abstract)

[9] Wang, X. F., C. Hu, B. Lu, J. Y. Jiang, and S. L. Hou. 2017. Wind tunnel test on damages of plastic film under the wind-sand effect in south Xinjiang of China. *International Agricultural Engineering Journal*, 26(1): 16–23.

[10] Yang, F. K., L. M. Wang, and G. H. Zhang. 2013. Effects of plastic film mulching with double ridges and furrow planting on soil moisture and temperature and soybean yield on a semiarid dryland of Gansu Province, Northwest China. *Chinese Journal of Applied Ecology*, 24(11): 3145–3152. (In Chinese with English abstract)

[11] Yang, Q. F., G. C. Liu, C. R. Xiong, C. R. Zhang, and Y. Y. Zhu. 2010. Study on highly efficient water utilizing mechanisms on techniques of whole plastic-film mulching on double ridges and planting in catchment furrows of dry-land maize. *Research of Agricultural Modernization*, 31(1): 113–116. (In Chinese with English abstract)

[12] Zhang, D., H. Y. Wang, W. L. Hu, H. D. Yang, Y. Xu, X. W. Ma, P. Y. Zhao, and H. B. Liu. 2017. Effect of filmthickness on crop yield and soil environment. *Journal of Agro-Environment Science*, 36(2): 293–301. (In Chinese with English abstract)

[13] Zhang, J. X., L. Zhang, X. F. Liu, Y. X. Jiang, and J. K. Wang. 2017. Mechanical analysis and contrast experiment on collecting residual plastic film with different side-film shovels. *Transactions of the Chinese Society of Agricultural Engineering*, 33(4): 10–15. (In Chinese with English abstract)

[14] Zhang, J. X., X. N. Wang, L. Zhang, X. Yu, Y. X. Jiang, H. C. Zhang, X. F. Liu, Y. Y. Qiao, X. J. Wang, S. S. Zhang, and S. L. Hou. 2015. Effects of mechanical tensile properties of plastic film on plastic recycling method. *Transactions of the Chinese Society of Agricultural Engineering*, 31(20): 41–47. (In Chinese with English abstract)

[15] Zhang, P. L., T. W. Guo, S. T. Li, M. S. Ma, and Y. H. Xie. 2014. Effects of different coverage cultivation and balanced fertilization on yield and water use efficiency of spring corn in the dryland. *Agricultural Research in the Arid Areas*, 32(4): 169–173. (In Chinese with English abstract)

[16] Zhao, W. Y., F. Dai, J. Yang, Z. L. Shi, Z. Yang, and L. R. Shi. 2013. Design and experiment of direct insert precision hill-seeder with corn whole plastic-film mulching on double ridges. *Transactions of the Chinese Society for Agricultural Machinery*, 44(11): 91–97. (In Chinese with English abstract)

[17] Zhou, L. M., S. L. Jin, C. A., Liu, Y. C. Xiong, J. T. Si, X. G. Li, Y. T. Gan, and F. M. Li. 2012. Ridge-furrow and plastic-mulching tillage enhances maize-soil interactions: opportunities and challenges in a semiarid agroecosystem. *Field Crops Research*, 126(1): 181–188.

Design and test of shift system for tractor hydro-mechanical continuously variable transmission

Zhang Haijun[1,2*], Wang Jiabo[1], Xiao Maohua[1], Lu Zhixiong[1], Wang Guangming[3], Wang Yuewen[1], Wang Shuai[1]

(1. *College of Engineering, Nanjing Agricultural University, Nanjing 210031, China*;
2. *Institute of mechanical transmission technology of Nanjing Agricultural University Nanjing 210031, China*;
3. *College of Mechanical and Electronic Engineering, Shandong Agricultural University, Tai'an 271018, China*)

Abstract: In order to meet the needs of the power-split hydrostatic continuously variable transmission in shifting process, the wet clutch and its control system were designed. Experiment and simulation of the wet clutch and its system were carried out. Results of the experiment and simulation show that the model can reflect the actual situation of the wet clutch. The simulation shows that the overlapping shift and the flow rate can improve the shift quality in a certain range. The experiment shows that the control system meets the demand of power-split hydrostatic continuously variable transmission. The research in this paper provides a theoretical and experimental basis for the design and application of the control system of power-split hydrostatic continuously variable transmission.

Keywords: tractor; power-split hydrostatic continuously variable transmission; shift system; wet clutc

Citation: Zhang. H. J., Wang, J. B., Xiao, M. H., Lu, Z. X., Wang, G. M., Wang, Y. W., and Wang, S. 2017. Design and test of shift system for tractor hydro-mechanical continuously variable transmission. International Agricultural Engineering Journal, 26(4): 157–165.

1 Introduction

The hydro-mechanical continuously variable transmission (HMCVT) (Böhl and Küçükay, 2004) is a kind of transmission that commonly used in high-horsepower tractor. With the mechanical transmission system and control implemented by the hydraulic pump motor drive system in parallel, axis gears (or planet gears) are fixed to shunt the engine power and then the planet gears (or fixed axis gears) is used to realize the confluence of hydraulic and mechanical power. The HMCVT makes full use of the pump-motor's stepless speed and regulation characteristics (Fu, 2011), thereby obtaining an output speed of the transmission variable.

Received date: 2017-06-20 **Accepted date:** 2017-09-29

* **Corresponding author: Zhang Haijun**, Ph.D., Associate Professor of Engineering College, Nanjing Agricultural University, Nanjing 210031, China. Email: zhhj@njau.edu.cn. Tel: +86 15852918769.

In order to avoid the problem of large shift due to overload when the tractor is working in the field, HMCVT usually uses the wet clutch to shift (Jeong and Kunsan, 2000). Therefore, domestic and foreign researchers have already done a lot of research on the wet clutch. For example, the Heon-Sul Jeong's team (Hu, 2008) has a detailed study in the characteristics of the smooth shift of the clutch steering mechanism and the Agusmian Partogi Ompusunggu's team (Huwendiek, Bailly, and Grad, 2004) has established a clutch model based on generalized Maxwell sliding extension friction model. In addition, the Yang Shujun's team (Kong and Wang, 2010) has established a multistate dynamic model to describe the process of wet clutch coupling and the correctness of the model has been verified using bench test and Hu Hongwei's team (Luoyang Tractor Research Institute and Ministry of machinery and electronics industry. 1994) has studied several key problems such as the automatic control of the wet clutch, the chattering in the combined process and the heat load of the clutch.

The various researches in the past provided different methods to study the shift of wet clutch.

Based on the HMCVT, this paper will design and test the shift system. Firstly, the correctness of the wet clutch model is determined by using experiment and simulation. Then, based on the simulation model, a single factor flow and overlap timing test is carried out to find out the relationship between the size of the flow (or the change of the overlap time sequence) and the shift quality. Finally, the bench test is carried out to verify the validity of the model and the effectiveness of the control system.

2 Design of wet clutch

2.1 Analysis of clutch load

2.1.1 Design of transmission scheme

Figure 1 is the HMCVT that our team independently developed. It is equipped with high-powered tractor, of which the tire diameter is 1835 mm. In addition, the engine is the Weifang WP6T180E21 type high pressure common rail diesel engine, of which the power is 132.5 kW and the rated speed is 2200 r/min and the calibration of torque is 620 N·m.

As shown in Figure 1, i_1-i_{12} stands for transmission ratio and C_0-C_4 stands for wet clutch. The power of the engine is divided into two ways after the fixed gear pair i_1. In order to achieve the variable pump-quantitative motor speed control loop, the first way, which is used as a hydraulic path, transfers the power to the solar wheel which is shared by the P_1 and P_2 planetary rows. The other way, which is used as a mechanical road, transfers the power to the P_1 planet rack and P_2 gear ring. Then, the power is gathered in the double planetary row. Finally, through the shift control system, the power is transferred to the C_1-C_4 clutch and the power outputs. The speed regulating circuit can continuously output power and the speed ratio of the whole gearbox can be changed continuously with the change of the displacement of the variable pump, such that the continuous change of the speed can be realized. It should be noted that the C_0 clutch is located in the pure hydraulic power output section.

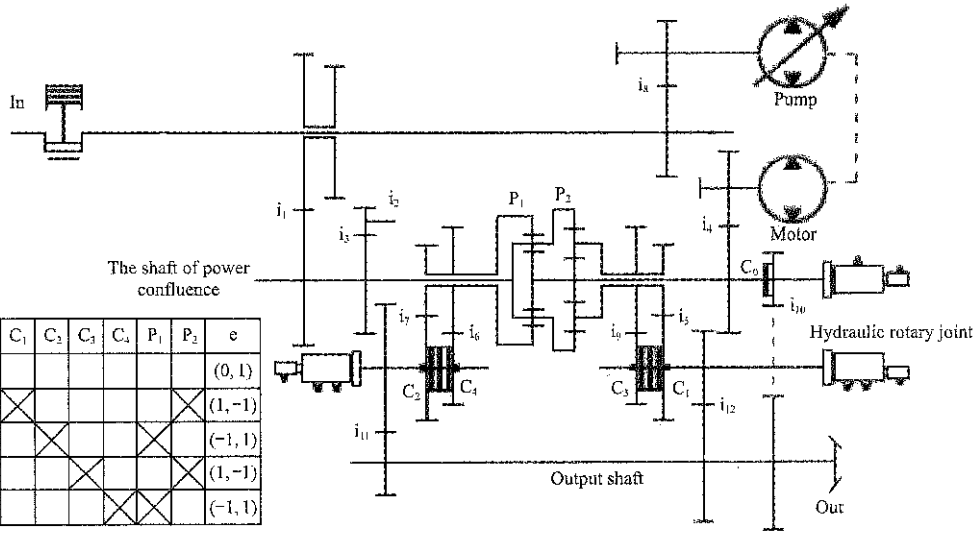

Speed	Section	C_0	C_1	C_2	C_3	C_4	P_1	P_2	e
(0,4)	H	×							(0, 1)
(4,8)	HM_1		×					×	(1, -1)
(8,15)	HM_2			×			×		(-1, 1)
(15,28)	HM_3				×			×	(1, -1)
(28,51)	HM_4					×	×		(-1, 1)

Figure 1 Diagram of power-split hydrostatic continuously variable transmission

2.1.2 Calculation of the load of C_0-C_4 clutch under full load working condition

It is known from the literature that the nominal load T_j can be calculated using the following two equations (Ompusunggu, Sas and Brussel, 2013). Then, the smaller value should be selected.

$$T_j = T_0 i' \eta' T = K_A T_j \quad (1)$$

$$T_j = \frac{n \cdot Q \cdot \phi \cdot r_d}{i'' \cdot \eta''} \quad (2)$$

where, T_j is nominal load; T_0 is engine calibration torque; T is equivalent load; K_A is tractor gear coefficient; i' is transmission ratio of the engine to calculated part; η' is transmission efficiency of the engine to calculated part; i'' is transmission ratio from calculated part to drive shaft; η'' is transmission efficiency from calculated part to drive shaft; n is the number of tires or tracks; Q is the bearing capacity of the driving wheel when the tire pressure is 100 kPa; r_d is drive wheel radius, and ϕ is adhesion

coefficient.

2.1.3 Calculation of the speed of C_0-C_4 clutch under full load condition

Through the HMCVT diagram (Figure 1) and referring to the related literature, the transmission ratio can be calculated in each section and then the full speed of each clutch can be calculated. At the same time, the calculated clutch's torque and speed should meet the following conditions, as shown in Table 1.

Table 1 Torque and speed requirements of clutch

Control element	C_0	C_1	C_2	C_3	C_4
Torque, N·m	1850	3200	3200	1850	1000
Speed, r min^{-1}	4000	3200	3200	4000	4000

2.2 Design of clutch structure

2.2.1 Structure and working principle of the wet clutch

The cooling method of the wet clutch designed and used in this paper is oil cooling. Because the cooling oil cannot only protect the friction plate but also make the power transmission smooth and soft. The structure of wet clutch is shown in Figure 2.

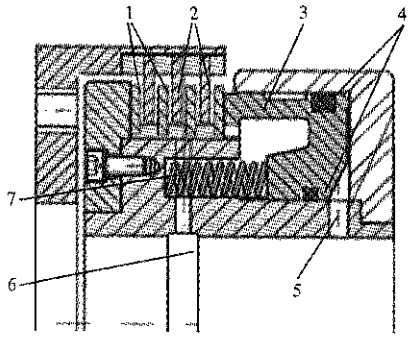

1. Dual steel 2. Friction plate 3. Piston 4. Gasket ring 5. Hydraulic oil inlet 6. Cooling oil inlet 7. Return spring

Figure 2 Structure of wet clutch

(1) Engage process of wet clutch is as follows

The hydraulic oil enters the cylinder through the axial oil pipeline to push the piston forward. When the piston is contacted with the steel sheet, the steel sheet is squeezed into the friction state with the friction plate. With the increase of the oil pressure, the piston continues to squeeze the steel sheet, which makes the friction torque between the steel plate and the friction plate bigger. When the torque generated by the sliding friction force generated by the friction plate and the steel plate is the same as the load of input shaft, the friction plate and the steel sheet enter a static friction state. At this time, the engage process of the wet clutch is finished.

(2) Separation process of wet clutch

When the pressure of the working oil is less than that of the return spring, the spring pushes the piston back to separate the steel sheet and the friction plate, and the power is cut off.

2.2.2 Main parameters of wet clutch

The main parameters of wet clutch include clutch reserve factor β, friction surface pressure P, friction surface diameter D_2, inner diameter D_1, and friction plate number Z.

2.2.2.1 Clutch reserve factor β

The clutch reserve factor is the ratio of the maximum friction torque to the engine torque. The reserve coefficient has a great influence on the working performance of the clutch. Wet clutch reserve factor β is 2.0-2.5, when the workload is heavy or the engine speed is high, the reserve factor should be taken larger.

2.2.2.2 Selection of friction plate used in wet clutch

Because the working condition of tractor is similar to that of the general engineering machinery, the choice of the clutch material can refer to the selection of clutch material used in the engineering machinery. The material of the friction plate is copper based powder metallurgy and the material of dual steel sheet is cast iron and steel.

2.2.2.3 Friction surface pressure P

The pressure on the friction plate can be calculated as;

$$P=\frac{T_c}{R_v \mu m} \tag{3}$$

where, $T_c=T_j\beta$, R_v is equivalent friction radius; μ is friction coefficient, m is friction face number, $m=Z-1$.

2.2.2.4 Friction surface diameter D_2 and inner diameter D_1

The inner diameter of the friction plate can be calculated formulas:

$$D_1=(1.5-2)d \tag{4}$$

where, d is the diameter of the clutch shaft.

The outer diameter of the friction plate can be calculated by the following formula.

$$D_2=(1.25-2)D_1 \tag{5}$$

2.2.3 Friction plate number Z

$$z=\frac{3T_c}{2\pi\mu(p)(R_2^3-R_1^3)K_z} \tag{6}$$

where, K_Z is the friction face number correction factor; p is the allowable pressure of friction plate.

2.2.4 The verification of wet clutch calculation

The friction torque on the friction surface of the clutch can be calculated according to the following formula.

$$T_\mu = z\int_{R_1}^{R_2} \mu p 2\pi R^2 dR = 2\pi\mu pz(R_2^3 - R_1^3)/3 \quad (7)$$

In the formula, R_1 - inner radius of friction plate, R_2 - outer radius of friction plate. Other parameters as described above.

The friction torque calculated by the above should be greater than or equal to the calculated torque of the clutch.

$$T_\mu \geq T_C \quad (8)$$

According to the above formulas and the clutch design manual, the key parameters of the clutch are shown in Table 2.

Table 2 Parameters of clutch

Clutch	Outer radius of friction plate, mm	Inner radius of friction plate, mm	Number of friction plates	Return spring stiffness, N·mm	Friction material
C_0, C_3	164	135	8	438	Copper-based Metal Part by Laser Powder Sintering
C_1, C_2	198	165	5	438	Copper-based Metal Part by Laser Powder Sintering
C_4	164	135	5	438	Copper-based Metal Part by Laser Powder Sintering

The corresponding three-dimensional model and the clutch is shown in Figure 3.

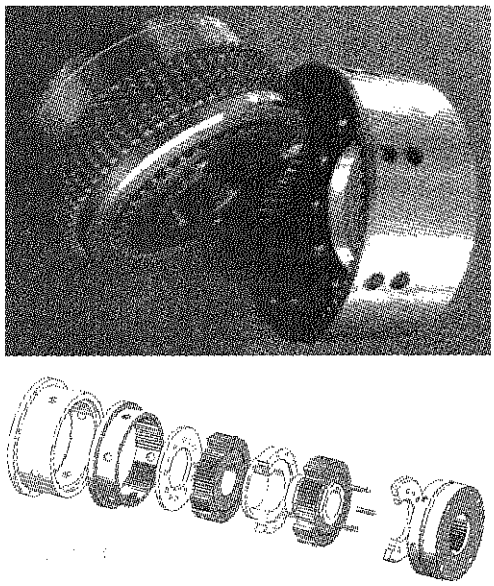

Figure 3 Pictures of clutch and its 3D model

3 Design of oil circuit for shift control

3.1 Design of oil circuit

The control and cooling system of clutch is shown in Figure 4 below.

In Figure 4, when the solenoid valve is energized, the electromagnetic coil generates a suction force to open the valve core so that the oil inlet pipe is connected. When the power is off, the valve core is reset and the oil outlet is connected. As can be seen from the schematic, the main entrance is divided into two passages. One cooling passage is used for cooling the clutch friction plate and the dual steel plate, and the other is a pressure oil passage, which is used for overcoming the spring force to make the combination of the clutch friction plate and the steel sheet.

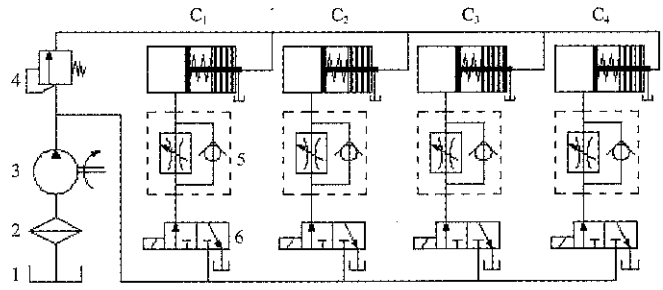

1. Tank 2. Filter 3. Pump 4. Relief valve 5. Speed control valve 6. Solenoid valve

Figure 4 Principle diagram of hydraulic control for clutch

The shift process is as follows. When the pump starts to work, the overflow valve will adjust to the oil inlet pressure, and then the left solenoid valves in three two-way solenoid valves will be energized to make the hydraulic oil enter the speed regulating valve, and finally the hydraulic oil enters the pressure oil passage, thus controlling the combination of the clutch. When the solenoid valve is powered off, the oil outlet is opened and the clutch is separated. It can be seen from this process that, for a clutch, as long as the left side of the solenoid valve powers on or off, the clutch engagement and separation can be controlled. Therefore, as long as we control the power of a solenoid valve, the power can be switched to the corresponding level.

3.2 Design of control system

The hydraulic control system of clutch is shown in Figure 5.

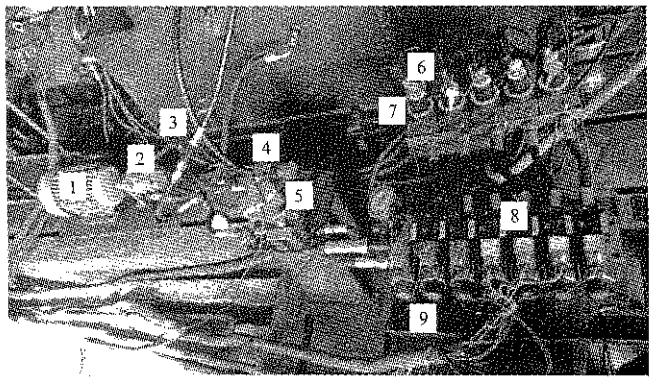

1. Oil pump motor 2. Oil pump 3. Check valve 4. Overflow valve 5. Flow sensor 6. Pressure transducer 7. Speed regulating valve 8. Solenoid valve 9. Integrated valve plate

Figure 5 Clutch oil circuit control system

The oil pressure control system of the clutch is driven by an external motor. Relief valve controls the main oil pressure of clutch. Five solenoid valves mounted on the integrated valve plate are used to control the oil channel on or off. The oil flow rate of the clutch is controlled by five speed regulating valves. The speed control valve is fixed on a valve plate. The pressure sensors are installed in each clutch oil circuit to measure the hydraulic characteristics of each clutch. The flow sensors installed in the main oil circuit are used for detecting the oil flow rate of the clutch. The parameters of the main parts of the clutch shift control system are shown in Table 3.

Table 3 Main components parts of test bench

Name	Performance parameter
Electric machinery	1450 r/min
Vane pump	6.3 mL/r
Speed regulating valve	0-10 L/min
Pressure transducer	0-10 MPa; 0-5 V
Flow sensor	0-0.4 m^3/h; 4-20 mA

The on-off of each clutch is controlled by the electromagnetic valves. The control of the solenoid valve is realized by shift register. The STC12C5A60S2 microcontroller is chosen for control and the controller is shown in Figure 6.

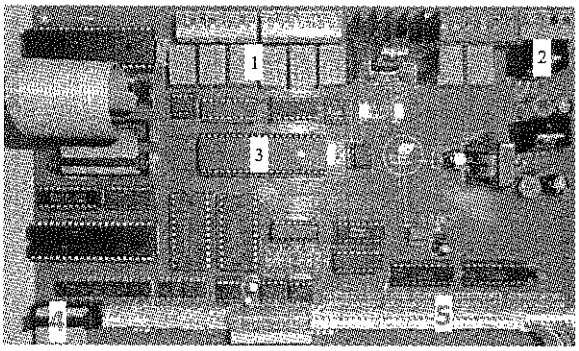

1. Electric relay 2. Power and communication port 3. Master Chip 4. Acquisition port 5.Analog acquisition port

Figure 6 Picture of controller

3.3 Simulation analysis

3.3.1 Establishment and verification of simulation model

In this paper, the modeling and simulation experiments are carried out in AMESim (Shamshirband, Petkovic and Amini, 2014) software. The model of wet clutch driven by hydraulic pressure is mainly composed of the following parts: (1) inertia of the active part of the clutch; (2) inertia of clutch follower; (3) friction torque of clutch; (4) piston mass and clutch; (5) friction torque of sealing ring; (6) piston and return spring. Based on the above analysis, the wet clutch model is shown in Figure 7. The simulation of the clutch model is carried out, and the results are compared with the clutch test data of the bench test.

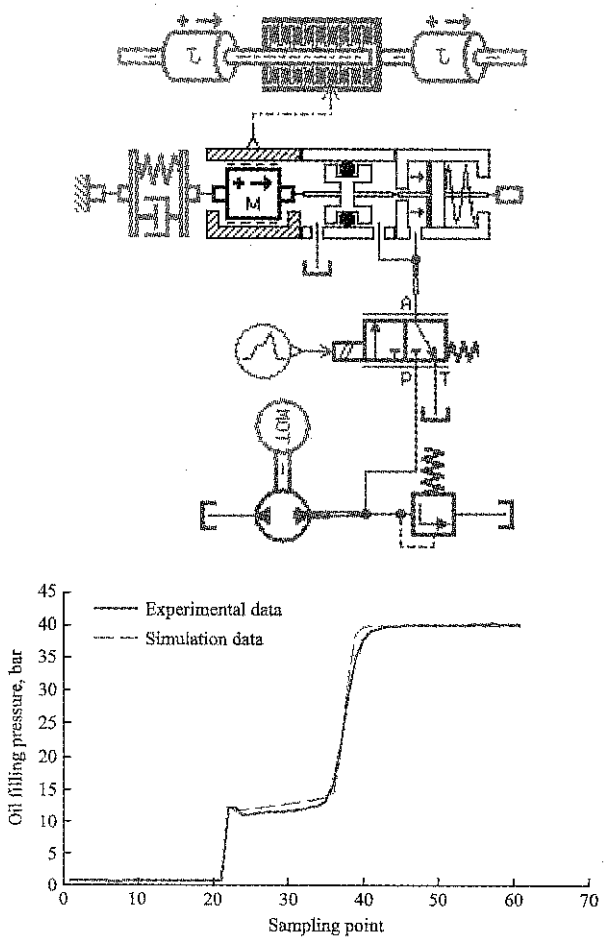

Figure 7 Comparison of experimental and simulated results of clutch in AMESim

According to the above figure, the clutch engagement process can be divided into four stages (Shi, 2011). In the first stage, there is no movement interference between the clutch friction plate and the steel plate before the combination, and the original state is operated independently. The pressure oil flows into the hydraulic cylinder with a certain flow rate and pressure. The second

stage is that the pressure oil is filled with the hydraulic cylinder and the cylinder starts to move. The third stage is that the hydraulic cylinder under the action of the pressure oil is to move, overcoming the return spring force, pressing the friction plate and the steel plate until there is no relative slip. The fourth stage is the pressure maintaining stage, which is the continuation of the third stage. The clutch is in full working state, and the power is transmitted continuously and smoothly.

The experimental results show that the model can reflect the actual clutch combination. In addition, the model can also be used to simulate the clutch combination and torque characteristics.

3.3.2 Overlapping timing and flow's influence on shift quality

Based on the above model, we study the influence of overlap timing and flow rate in the main oil circuit on speed in the process of clutch shifting. Because of the same action mechanism of the five wet clutches, this paper only studies the case of the first gear shift to the second gear.

With the help of the batch function of AMESim, the research of shift timing and flow rate on the shift time is carried out. For the convenience of analysis, the clutch simulation model in Figure 7 is transformed into a super element. The new simulation model is shown in Figure 8.

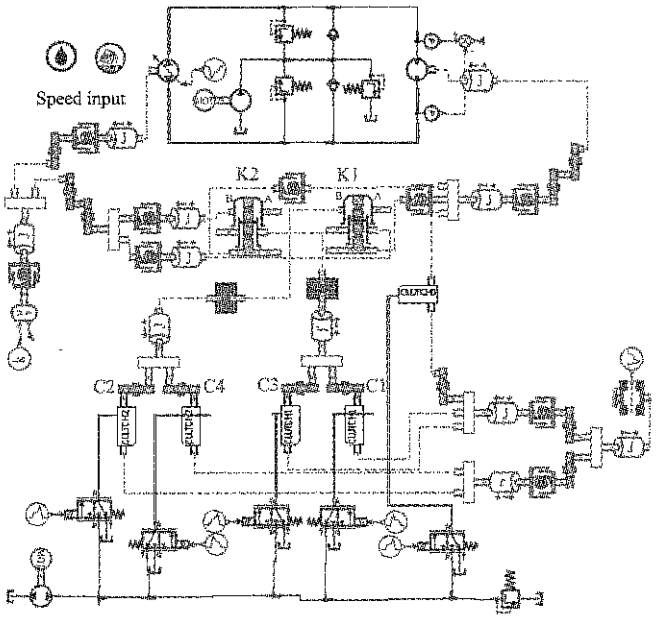

Figure 8 Simulation model of HMCVT transmission system

3.3.2.1 Simulation of shift timing

The engine speed is set to 750 rev/min, and the load is set to 200 N·m. The main oil flow rate is set to 5 cc/min, and the main oil pressure is set to 5 MPa. The overlapping timing varies from 80 ms to 0 ms, and its interval is 40 ms. At this point, we get three sets of simulation curves, as shown in Figure 9.

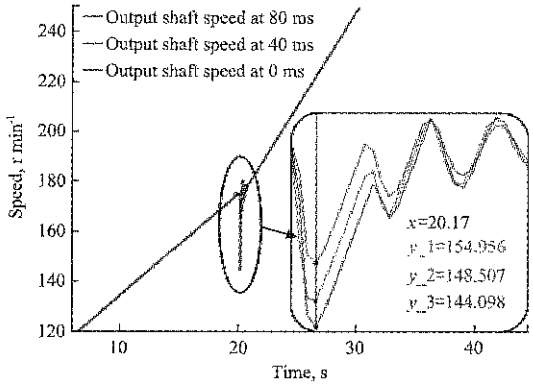

Figure 9 Different overlapping shift time in AMESim simulation model (Speed-Time)

In Figure 9, the local amplification is used to show the change of output shaft speed. It can be seen that at 20.170 s, the output shaft speed is reduced to 144.098 rev/min when the overlap timing is 0 ms, and the output shaft speed is reduced to 148.507 rev/min when the overlap timing is 40 ms, and the output shaft speed is reduced to 154.956 rev/min when the overlap timing is 80 ms. According to the above results, a conclusion can be drawn that with the increase of the overlapping time, the value of the speed drop after shift is reduced within a certain range.

3.3.3.2 Simulation of flow rate

The engine speed is set to 750 rev/min, and the load is set to 200 N·m. The main oil pressure is set to 5 MPa. The main oil flow varies from 3 cc/min to 5cc/min, and the interval is 1 cc/min. At this point, we get three sets of simulation curves, as shown in Figure 10.

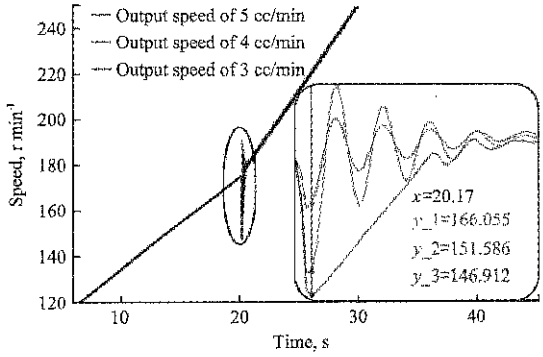

Figure 10 Different flow rate on shift base on Clutch AMESim simulation model (Speed-Time)

After magnifying the simulation graphics locally, we clearly see that at 20.170 s, the output shaft speed is reduced to 166.005 rev/min when the flow rate is 5 cc/min, and the output shaft speed is reduced to 151.586 rev/min when the flow rate is 4 cc/min, and the output shaft speed is reduced to 146.912rev/min when the flow rate is 3 cc/min. According to the above data, a conclusion can be drawn that with the increase of the oil flow rate, the value of the speed drop after shift is reduced within a certain range.

Finally, from the above two experiments, a conclusion is drawn as follows: when the gears is shifted in a certain range of flow, a larger flow may improve the quality of the shift, and when the gears is shifted in a certain overlap timing range, a larger overlap timing may improve the quality of the shift.

4 Experiment and verification

4.1 Construction of test bench

The design of the test bench is shown in Figure 11.

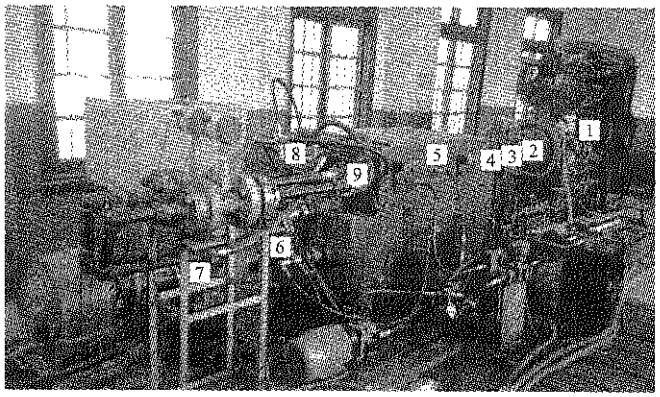

1. Diesel engine 2, 4, 6. Elastic coupling 3. Transmission speed indicator 1 5. Transmission case 7. Transmission speed indicator 2 8. Hydraulic variable pump 9. Hydraulic quantitative motor

Figure 11 Structure of test bench

The platform is composed of a diesel engine, an elastic coupling, a rotational speed torque meter, a hydraulic variable pump, a hydraulic quantitative motor and a flow and pressure sensor. The measurement and control system includes the independently developed tractor control center TCU and host computer. The performance parameters of the main equipment are shown in Table 4.

4.2 Load shifting test

The bench test of the clutch and the hydraulic shift control system of hydraulic mechanical continuously variable transmission is carried out.

Table 4 Equipment parameters

Name	Main performance parameters
Electric machinery	1450 r/min
Transmission case	6.3 mL/r
Rotational speed meter	0-3000 r/min, 0-5000 N·m
Measurement and control system	Independent development
Magnetic particle brake	500 N·m

According to the simulation test, the bench test is divided into two types. One is to study the relationship between overlap timing and shift quality. The other one is to study the relationship between flow and speed fluctuation.

The process of changing the timing sequence is as follows. We adjust the engine accelerator pedal to stabilize the engine speed at 750 rev/min and adjust the speed control valve so that the main circuit oil flow rate is 5 cc/min. We adjust the pressure of the relief valve to control the main oil circuit pressure at 5 MPa and change the current of the magnetic particle brake to ensure that the load is 200 N·m. The overlap timing is set from 80 ms to 0ms and the interval is 40 ms. The simulation curves of three groups are shown in Figure 12.

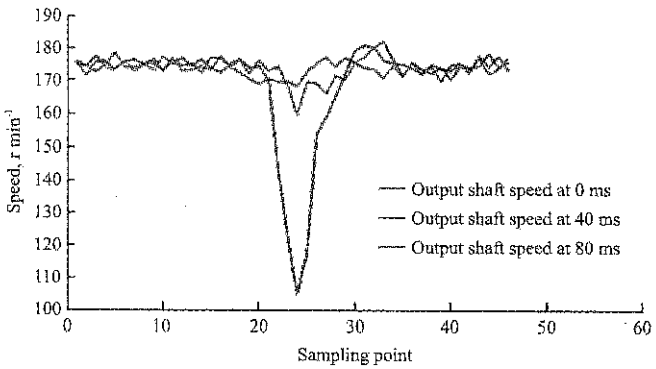

Figure 12 Different overlapping shift time in AMESim simulation model (Speed-Sampling point)

The process of changing the flow rate is as follows. The engine accelerator pedal is adjusted to stabilize the engine speed at 750 rev/min and adjust the pressure of the relief valve to control the main oil circuit pressure at 5 MPa and change the current of the magnetic particle brake to ensure that the load is 200 N·m. The position of the valve is changed so that the main oil flow rate is from 3 cc/min to 5 cc/min and the interval is 1 cc/min. The simulation curves of three groups are shown in Figure 13.

From the simulation curves of the bench tests, it can be seen that there are fluctuations and speed drop in shift

whether to change the flow rate or change the overlapping timing and the speed drop will become small with the increase of overlapping timing and the flow rate in main circuit.

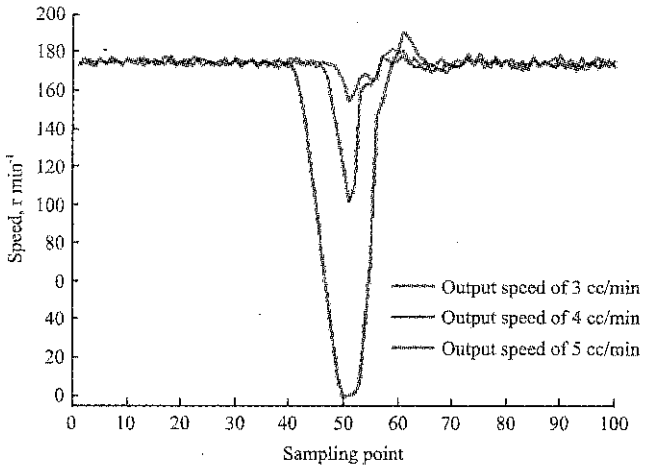

Figure 13 Different flow rates on shift based on Clutch AMESim simulation model (Speed-Sampling point)

5 Conclusion

(1) Through the establishment of a single clutch model and after the comparison between simulation and experiment, it could be inferred that the simulation model can be used to meet the requirements of the dynamic characteristics of the clutch and simulation test also lays a foundation for the subsequent study of bench test.

(2) Through the simulation of the shift timing and the flow rate and the bench test, it can be inferred that the larger overlap timing and the larger oil flow rate in a certain range can help to improve the shift quality.

(3) This paper adopts the electromagnetic directional valve to control the clutch, but the size of the flow has important influence on the shift quality, which provides theoretical and practical basis for the adoption of proportional solenoid valve that can be used to linearly control the flow rate later.

(4) Through the bench test, it is proved that the design of the gear shifting system can meet the shift requirements of the CVT developed by our research group. Although there is a speed drop and fluctuation of speed after the shift, it reflects that the design of the HMCVT meets the standard of power shift, which provides the theoretical and practical basis for the design of the shift system of the high-powered tractor.

Acknowledgments

The research is funded partially by the National Key Research and Development Program of China (2016YFD0701103), Jiangsu Provincial Natural Science Foundation of China (BK20140727), Jiangsu Province Science and Technology Support Program (BE2014134), Science and Technology Foundation of Outstanding Young Talents of Nanjing Agricultural University (YQ201605), and the Fundamental Research Funds for the Central Universities fund (KYZ201760).

[References]

[1] Böhl, J. and F. Küçükay. 2004. Shifting comfort studies using automatic gear shifts. *VDI Berichte*, 1827: 203–216.

[2] Fu, Y. L. 2011. *LSM Imagine. Lab AMESsim system modeling and simulation examples tutorial*. Beijing: Beihang University Press.

[3] Jeong, H. S. and Kunsan. 2000. Shift characteristics analysis and smooth shift for an automatic power transmission. *KSME International Journal*, 14(5): 499–507.

[4] Hu, H. W. 2008. Study on the characteristics of wet automatic clutch engagement. M.S. thesis. Hangzhou: Zhejiang University.

[5] Huwendiek, O., G. Bailly, and K. Grad. 2004. Continuously variable transmission ZF-Eccom: components and control structures. *VDI Berichte. German: VDI Verlag GMBH*: 17–22.

[6] Kong, H. F. and Y. Wang. 2010. Design of TCU for vehicle six-speed automatic transmissions. *2nd International Conference on Information Science and Engineering, ICISE2010-Proceedings. Hangzhou, China: IEEE Computer Society*: 6541–6544.

[7] Luoyang Tractor Research Institute, and Ministry of machinery and electronics industry. 1994. Tractor design manual. *Beijing: China machine press*.

[8] Molari, G. and E. Sedoni. 2008. Experimental evaluation of power losses in a power-shift agricultural tractor transmission. *Biosystems Engineering*, 100(2): 177–183.

[9] Ompusunggu, A. P., P. Sas and H. V. Brussel. 2013. Modeling and simulation of the engagement dynamics of a wet friction clutch system subjected to degradation: An application to condition monitoring and prognostics. *Mechatronics*, 23: 700–712.

[10] Renius, K. T. and R. Resch. 2005. Continuously variable tractor transmissions. *Agricultural Equipment Technology Conference. Louisville*: ASME: 1–37.

[11] Shahaboddin, S., P. Dalibor, A. Amineh, B. A. Nor, N. Vlastimir, Ć. Žarko, L. M. K. Miss and G. Abdullah. 2014. Support vector regression methodology for wind turbine

reaction torque prediction with power-split hydrostatic continuously variable transmission. *Energy,* (67): 623–630.

[12] Shi, J. L. 2011. Design of hydraulic mechanical continuously variable transmission for non road vehicle and control performance of variable pump. *Nanjing: Nanjing Agricultural University.*

[13] Wang, G. M., S. H. Zhu, and S. H. Wang, L. X. Shi, X. D. Ni and D. Y. Ouyang. 2013. Speed ratio control of tractor hydraulic mechanical continuously variable transmission. *Journal of agricultural engineering*, 29(7): 17–23.

[14] Yang, S. J., S. H. Yuan and J. B. Hu. 2005. The dynamic characteristics of wet clutch shift process. *Journal of agricultural machinery*, 36(11): 38–41.

[15] Zhang, W. Q. 2011. Design and performance simulation of a new type of shift clutch. *Zhengzhou: Zhengzhou University.*

[16] Zhang, X. S. 2011. Research on hydraulic mechanical stepless speed change and control strategy. Jilin: Jilin University.

[17] Zhong, Z. M., H. Jing and Y. Ma. 2011. The coordination work between engine management system and TCU in transmission control. *International Conference on Consumer Electronics, Communications and Networks, CECNet 2011-Proceedings. Xian Ning, China: IEEE Consumer Electronics Society*: 5357–5360.

[18] Xu, X. M., Y. P. Jiang, N. Chen and H. P. Lee. 2017. Dynamic behavior of a vehicle with rear axle compliance steering. *Journal of Vibro engineering*, 18(4): 4483–4497.

[19] Xu, X. M., N. Chen and H. P. Lee. 2016. A Review on the applied research of rear wheel compliance steering. *Automobile Technology*, (07): 1–6, 16.

Design and experiment of 4UM-2 potato harvester

Qi Jiangtao[1,2], Li Yaping[1,2], Meng Hewei[1,2*], Kan Za[1,2], Wang Lihong[1,2], Chen Shaojie[1,2], Gong Weidi[3]

(1. *College of Mechanical and Electrical Engineering, Shihezi University, Shihezi, 832000 China*;
2. *Key Laboratory of Northwest Agricultural Equipment, Ministry of Agriculture, Shihezi, 832000 China*;
3. *China Coal Energy Xinjiang Coal Electrochemical Co., Ltd, Urumqi, 830000 China*)

Abstract: Based on the requirements in mechanized potato harvesting, in this study, a 4UM-2 potato harvester with adjustable working parameters such as conveying velocity, vibration velocity and vibration amplitude was designed. The harvester was mainly composed of a digging device, velocity adjustable conveying and separating device, a parameter adjustable vibration device, a hydraulic driver and a control system. The results of the field test of the harvester showed that, the order of effects on potato-exposing rate was amplitude>vibration velocity>conveying velocity. Amplitude had the significant fluence on potato-exposing rate (P=0.046<0.05); the order of effects on breakage rate was conveying velocity>vibration velocity>amplitude; conveying velocity P=0.013<0.05, vibration velocity P=0.015<0.05, showing a significant effect of conveying velocity on breakage rate. Analysis showed that, the optimal factors of the harvester were: conveying velocity = 90 r min^{-1}, vibration velocity = 120 r min^{-1}, amplitude was low. The results of the verification of the factor combination showed that potato-exposing rate was 92.11% and potato breakage rate was 3.22%. The study can provide a basis for studying intelligent potato harvesting technology and equipment.

Keywords: potato, harvester, parameter adjustable, field test

Citation: Qi, J. T., Y. P. Li, H. W. Meng, Z. Kan, L. H. Wang, S. J. Chen, and W. D. Gong. 2017. Design and experiment of 4UM-2 potato harvester. International Agricultural Engineering Journal, 26(4): 166–174.

1 Introduction

In recent years, potato has become one of the chief food crops in China. With the increasing demand on potato products, the whole process mechanization and automation of potato production has been improved, meanwhile, various kinds of machinery for potato harvesting have been continuously upgraded (Yang et al., 2016; Shi et al., 2015). Harvesting is one of the key stages in the whole working system of potato production. Traditional harvesting methods were completed by human labor, including vine cutting, digging, collecting, packaging and transportation, which were labor intensive with low working efficiency and high costs (Zhao et al.,2016; Liu et al., 2013; Lv et al., 2015).

To solve the problems stated above, some institutions, companies and their experts did researches on technology and equipment of mechanized potato harvesting. Toyo Agricultural Machinery Manufacturing Co., Ltd. in Japan designed a self-walking potato harvester with two-grade separation device and hydraulic conveyor tuber box (Sun et al.,2012). Kvernel and Narbo AS in Norway produced a series of UN2600 type two-line potato harvesters with mechanical, hydraulic and electronic control. GRIMME in Germany produced RL1700 potato harvester and SE140-type potato harvester (Wu et al., 2015). Gansu Academy of Mechanical Sciences developed side output potato combine harvester, and 1710 potato combine harvester developed by Modern Agricultural Northern (Beijing) Agricultural Machinery Co., Ltd. (Yang et al., 2007), and Scholar Li Yang designed a potato combine harvester consisting of digging mechanism, conveying device, separating mechanism and side output lifting loading mechanism (Li et al., 2015). Shi Linrong developed a disc grille type potato digger (Shi et al., 2012). Li Yimin designed the 4U-55 potato harvester which was

Received date: 2017-10-27 **Accepted date:** 2017-12-13

* **Corresponding author: Meng Hewei,** Associate Professor, College of Mechanical and Electrical Engineering, Shihezi University, Shihezi, 832000 China. Email: mhw_mac@shzu.edu.cn.

matched with the hand tractor and could be used to dig, separate and lay of potato (Li et al., 2014). Meng Li designed a vertical swing - type tuber - soil separation device for small potato harvesters (Meng et al., 2012). Based on the researches listed above and the current problems of high power consumption and low separation efficiency in potato harvesting, also by taking into consideration of the potato planting model and agronomic requirements in potato harvesting in Xinjiang, a kind of 4UM-2 potato harvester was designed by integrating a digging device, speed adjustable conveying and separating device, parameter adjustable vibration device, a hydraulic driver and a control system. The parameters of the harvester such as conveying velocity, vibration velocity and amplitude can be adjusted and this study may provide a basis for the study of intelligent potato harvesting technologies and equipment.

2 Whole structure and working principle

2.1 Whole structure

The harvester is mainly composed of a digging device, a speed adjustable conveying and separating device, a parameter adjustable vibration device, a hydraulic driver and a control system. The speed adjustable conveying and separating device is mainly composed of a closed rotary sieve, a driving wheel and a driven wheel; the parameter adjustable vibration device is mainly made up of a V-shaped vibration device, an adjustments panel and an adjustment screw; the hydraulic driver is mainly made up of a hydraulic pump, a hydraulic proportion valve and a hydraulic motor, as is shown in Figure 1.

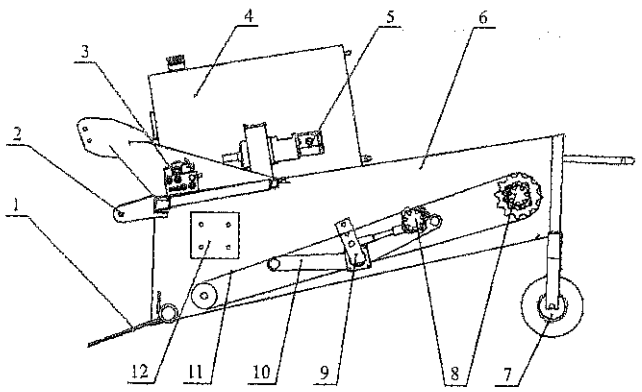

1. Digging device 2. Traction frame 3. Hydraulic proportion valve 4. Hydraulic fluid chamber 5. Hydraulic pump 6. Body frame 7. Land wheel 8. Hydraulic motor 9. Adjustments panel 10. V-shaped vibration device 11. Closed rotary sieve 12. Electronic control system

Figure 1 Structural diagram of the potato harvester

2.2 Working principles

Before working, vine cutting was finished. The harvester was connected with a tractor through three-point suspension. In operation, the potato-soil compounds were dug by the digging device, and then conveyed and separated by the conveying and separating device. In this process, the V-shaped vibration device vibrated the closed rotary sieve to move up and down, and the soil blocks in the potato-soil compounds were separated and fell on the ground through the grids of the sieve, then the potato tubers were conveyed backward and laid on the ground in a line. The transporting velocity and vibration velocity of the harvester were controlled by a programmable control system. After inputting different control signals, the hydraulic proportion valve adjusted the rotating speed of the hydraulic motor, and then adjusted the conveying velocity of the closed rotary sieve and the vibration velocity of the V-shaped vibration device. The adjustment of amplitude was determined by the position of adjustment screw and adjustments panel.

2.3 Main technical parameters

Main technical parameters of the potato harvester are shown in Table 1.

Table 1 Main technical parameters of the potato harvester

Parameters	Values
Size, mm×mm×mm	2350×1300×1250
Power, kw	≥33
Number of rows	2
Ridge distance, mm	300-400
Digging depth, mm	180
Working speed, km h	2.4

3 Design of key components

3.1 Design of the digging device

Digging device is an important component in potato harvester. It mainly realizes digging the soil-potato compounds from ridges. The design should ensure the machine to dig out all potatoes on the basis of reducing whole machine power (Liu et al., 2009; Liu et al., 2004), including bar shovel, triangle convex shovel, triangle groove shovel and flat shovel. After comparing the characteristics of the shovels and considering the soil conditions of potato planting in Xinjiang, in this paper, triangle flat shove was selected and the main factors that influence digging performance were horizontal inclination

and length of the digging shovel, etc.

3.1.1 Horizontal inclination of the shovel surface

When the digging device digs the potato-soil compounds, the compounds would move on the surface of the shovel, and the force status of the compounds is shown in Figure 2.

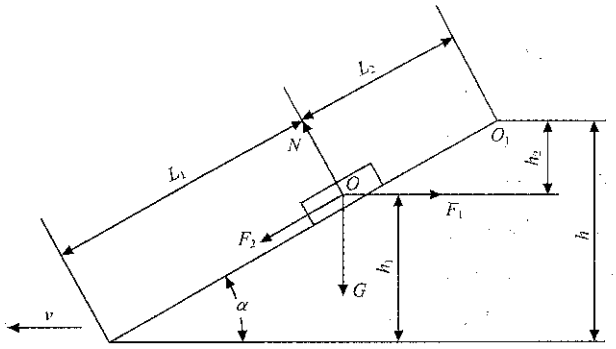

Figure 2 Force status of digging shovel

According to the equation of force balance, the following Equations (1), (2) and (3) can be obtained:

$$F_1\cos\alpha - F_2 - G\sin\alpha = 0 \quad (1)$$

$$N - G\cos\alpha - F_1\sin\alpha = 0 \quad (2)$$

$$F_2 = \mu N \quad (3)$$

where, F_1 is the force needed for the potato-soil compounds moving along the shovel surface, N; F_1 is the friction between the potato-soil compound and shovel surface, N; μ is the friction coefficient of the potato-soil compounds on the shovel; G is the gravity of the potato-soil compounds, N; N is the counterforce of shovel surface on the compound, N; α is the angle between the shovel surface and level ground, °.

Based on Equations (1) to (3) and the following equation can be obtained:

$$\alpha = \arctan\frac{F_1 - \mu G}{\mu F_1 + G} \quad (4)$$

The high inclination of shovel surface α is good for soil pulverization, but it may also result in soil hilling and the length of shovel surface and working resistance may also be increased. Therefore, considering the practical working situation and based on Equation (4), the angle between the shovel surface and level ground was 20°, and flush bolt was used to fix the digging shovel on the rack for convenience of shovel changing.

3.1.2 Length of the digging shovel

Figure 2 showed that, the length of the shovel had two sections, L_1 and L_2 and $L=L_1+L_2$, L_1 was determined by the inclination of the shovel surface and average digging depth h_1, namely $L_1=h_1/\sin\alpha$. L_2 can be calculated by the principle of conservation of energy, the kinetic energy of the compound at point O was $mv^2/2$, and the total work of the compound at point O_1 was the sum of work by friction and work by gravity, which was $GL_2\tan\varphi\cos\alpha+GL_2\sin\alpha$, and:

$$mv^2/2=GL_2\tan\varphi\cos\alpha+GL_2\sin\alpha$$

It can be simplified as: $L_2 = \dfrac{v^2\cos\varphi}{2g\sin(\alpha+\varphi)}$ (5)

where, v is the advancing speed of the tractor, m s^{-1}; φ is the friction angle of soil on shovel surface, °.

Based on the analysis above and the real working situation, the length of digging shovel was determined as 20 cm.

3.2 Design of conveying and separation device

During the mechanized harvesting of potatoes, the efficient conveying and separation of potato-soil compounds is an important aspect in the working performance of the harvester (Xie et al., 2016; Boac et al., 2010; Wei et al., 2014). The conveying and separating work is mainly realized by adjustable conveying and separating device, adjustable parametric vibration device, and the structure diagram is shown in Figure 3. It can improve working performance by improving the adaptability of the equipment under different soil conditions. In the process of conveying and separating potato-soil compounds, the indexes such as potato-exposing rate and breakage rate could reveal the working performance (Bentini et al., 2006; Wu et al., 2011), and the main factors that influence the indexes are vibration velocity, conveying velocity and amplitude. Therefore, the three factors were selected to be analyzed in this study.

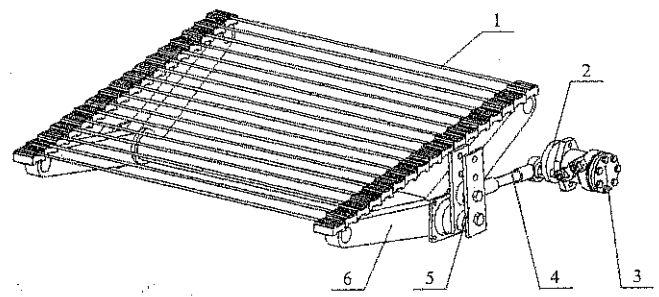

1. Closed rotary sieve 2. Eccentric disc 3. Hydraulic motor 4. Adjustment screw 5. Adjustments panel 6. V-shaped vibration device

Figure 3 Conveying and separating device

3.2.1 Determination of conveying velocity

The average size of a potato is 45-55 mm in length, 40-50 mm in width, and 40-45 mm in thickness (Jia et al., 2011). Considering farmers' demands in harvesting (potatoes less than 25 mm in any size are excluded from harvesting), the material of the grates of the closed rotary sieve was round steel with diameter of 10 mm and the grates were spaced at 38 mm. The angle between the sieve surface and ground during working was 20° for the convenience sieving potato-soil compounds. Conveying velocity refers to the linear velocity of the closed rotary sieve. When the speed of the tractor kept constant, the high value of conveying velocity will result in delayed separation of compounds, and some potato tubers may be buried by soil in potato laying. The low conveying velocity may result in stacking of potato-soil compounds on the sieve surface, and the consumption power of the harvester may increase. The high or low values of transporting velocity may affect the quality of potato-soil separation, and reduce the working performance of the harvester. Therefore, in designing the conveying velocity, its value should be slightly higher than the advancing velocity of the harvester, and it should be about 2.4 km h^{-1} (40 m min^{-1}). According to Equation (6), the rotating speed of hydraulic motor on driving wheel should be higher than 68 r min^{-1}. Combined with the actual production effect of the previous experience, the three levels of conveying velocity were determined, they were 70 r min^{-1}, 90 r min^{-1} and 110 r min^{-1} respectively.

$$v = \frac{\pi n r}{30} \tag{6}$$

where, v is conveying velocity, m min^{-1}; n is the rotating speed of the rotary sieve, r min^{-1}; r is the radius of the driving wheel, m.

3.2.2 Determination of vibration velocity

The vibration device applies an acting force on the sieve surface in conveying the potato-soil compounds and cause up and down motion of the sieve surface to realize separation of the compounds. In this study, the vibration device is a V-shaped structure under the surface of the closed rotary sieve. The hydraulic motor vibrates the closed rotary sieve up and down, and the potato-soil compounds are thrown up and then fall on the sieve surface. After repeating the motion for several times, the crumbling soil may fall on the ground after crashing and the potato tubers will be conveyed along with the closed rotary sieve to finish potato-soil separation. The high vibration velocity (rotating speed of the hydraulic motor) may increase breakage rate of the potatoes, while low vibration velocity may result in poor effects of potato-soil separation. Therefore, reasonable vibration velocity may ensure the high quality of potato-soil separation. During working, the vibration velocity should be slightly higher than conveying velocity; therefore, based on the three levels of the conveying velocity of 70 r min^{-1}, 90 r min^{-1} and 110 r min^{-1}, combined with the actual production effect of the previous experience to determine that the three levels of vibration velocity should be 80 r min^{-1}, 100 r min^{-1} and 120 r min^{-1} respectively. Vibration velocity can be converted to vibration frequency according to Equation (7), which is also the number of vibration within 1 s, then the influence of vibration frequency on the working performance (potato-exposing rate and damage rate) of the harvester will be analyzed.

$$f = \frac{1}{T} \tag{7}$$

where, f is vibration frequency, Hz; T is time of finishing a vibration process for the V-shaped vibration device (time for the hydraulic motor to make a turn), s.

3.2.3 Determination of amplitude

Amplitude refers to the extreme positions of the V-shaped vibration device in vibration. It determines the distance between the highest and the lowest points of the sieve surface in vibration and also plays a vital role in the working performance of potato-soil separation. The high amplitude can throw the potato-soil compounds higher, and the decrease of gravity of the compounds and the increase of instantaneous force between the compounds and the sieve surface may result in higher damage rate. The low amplitude may throw the potato-soil compounds lower, and the potato tubers and soil may go together up and down, resulting in insufficient separation. The output shaft of the hydraulic motor is connected with the central shaft of the eccentric disc. One end of the adjustment screw is connected with the eccentric shaft of the eccentric disc, and the other end is connected with the adjustments panel, which is fixed at its bottom. There are three holes on the adjustments panel and the connection between one of

the holes and the adjustment screw can realize the adjustment of amplitude. The eccentric disc, adjustment screw and adjustments panel form the crank-rocker mechanism, in which the eccentric disc is crank AB, adjustment screw is the connecting rod BC, and the adjustments panel is side link rocker CD, point A is set fixed with point D to form the rack AD. Rack AB is a driving link. Driven by the hydraulic motor, it rotates and becomes collinear with the connecting rod BC twice when the rocker CD is at extreme positions C_1D and C_2D. Since the V-shaped vibration device is fixed with the adjustments panel, the motion of the two devices is synchronous. When CD is at two extreme positions, the V-shaped vibration device is also at extreme positions, E_1F_1 and E_2F_2. The motion process is shown in Figure 4a. Therefore, the V-shaped vibration device moves between the two extreme positions, E_1F_1 and E_2F_2. It vibrates the sieve surface up and down and realizes separation of the potato-soil compounds.

When the adjustment screw is connected with the upper hole on the adjustments panel (as shown in Figure 4a), the amplitude of the V-shaped vibration device T_1=(97+103)/2=100 mm. In the same way, the motion process of the adjustment screw and adjustments panel is shown in Figure 4b, and the amplitude of the V-shaped vibration device is T_2=(213+283)/2=247 mm. Calculation and analysis showed that, the amplitude range of the V-shaped vibration device was 100-247 mm.

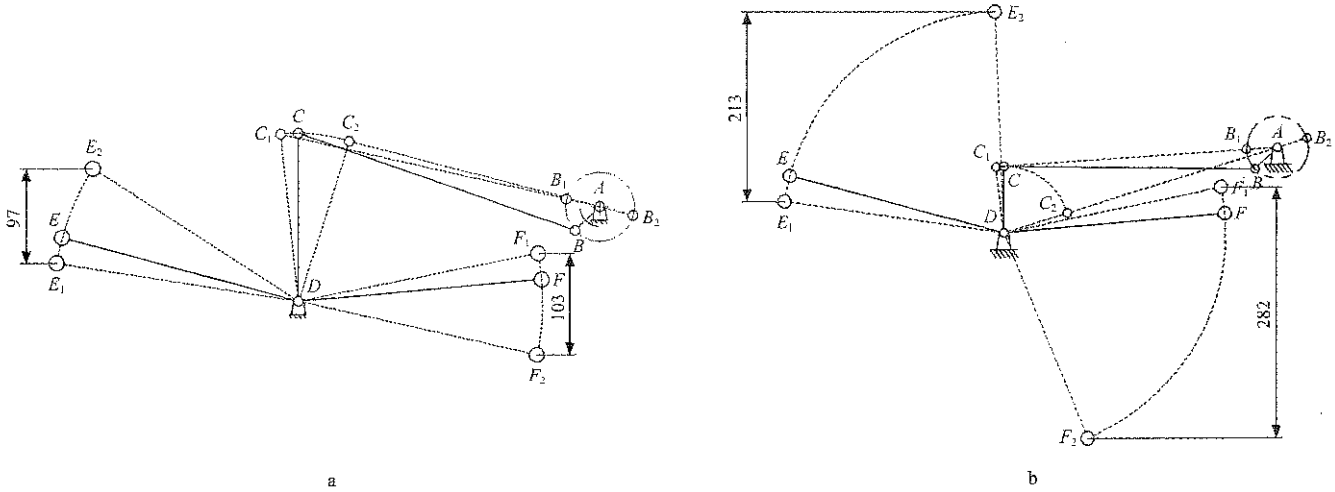

a b

Figure 4 Sketch map of motion process

4 Experimental analysis

4.1 Experimental conditions

The experiment on the 4UM-2 potato harvester took place in Wugong village of Shihezi, Xinjiang Autonomous Region of China (Figure 5). The variety of potatoes in the test field was Holland No.7, which has good adaptability, and easily gets damaged on skin. Planted in wide double ridges, the potatoes had a test field area of 3 hm^2. Drip irrigation was applied on the field and the vine cutting was finished seven days before the experiment. The harvester was matched with a John-Deere 454 tractor working at third gear.

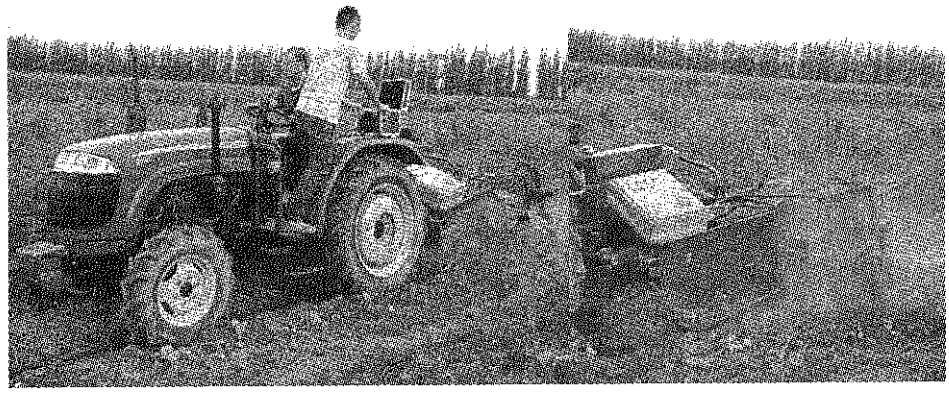

Figure 5 Performance test

4.2 Evaluation indexes

According to the test method listed in *NY/T1130-2006 Potato Harvesting Machinery*, by taking potato-exposing rate, breakage rate as the indexes for evaluation for harvester performance, Potato-exposing rate (T_0) and breakage rate (T_P) are calculated based on Equations (8) and (9).

$$T_0 = \frac{W_0}{W} \times 100\% \quad (8)$$

$$T_P = \frac{W_P}{W} \times 100\% \quad (9)$$

where, W_0 is the weight of the exposed potatoes, kg; W_P is the weight of the broken potatoes, kg; W is the total weight of potatoes, kg.

4.3 Experimental design and result analysis

In this experiment, the three-factor three-level orthogonal test design was adopted. The conveying velocities were 70 r min^{-1}, 90 r min^{-1}, 110 r min^{-1}; the vibration rotating speeds were 80 r min^{-1}, 100 r min^{-1}, 120 r min^{-1}, the amplitude had three levels: high, medium and low levels. The factors and levels of the experiment are shown in Table 2. Nine groups of experiments were made according to $L_9(3^3)$ orthogonal table, and each experiment was repeated for five times, the average values were selected as the experimental results, as shown in Table 3.

Table 2 Experimental factors and levels

Level factors	Transporting velocity A, r min^{-1}	Rotating speed in vibration B, r min^{-1}	Amplitude C
1	70	80	High
2	90	100	Medium
3	110	120	Low

Table 3 Experimental data

Test No.	Transporting velocity A, r min^{-1}	Rotating speed in vibration B, r min^{-1}	Amplitude C	Experiment result of the indexes	
				Potato-exposing rate, %	Breakage rate, %
1	1	1	1	43.61	15.78
2	1	2	2	67.53	18.44
3	1	3	3	91.38	5.4
4	2	1	2	66.99	23.2
5	2	2	3	83.33	24.68
6	2	3	1	64.67	18.62
7	3	1	3	77.69	8.87
8	3	2	1	59.1	18.2
9	3	3	2	72	2.22

Potato exposingrate	K_1	202.52	188.29	167.38	Breakage rate	K_1	39.62	47.85	52.6
	K_2	214.99	209.96	206.52		K_2	66.5	61.32	43.86
	K_3	208.79	228.05	252.4		K_3	29.29	26.24	38.95
	K_1	67.51	62.76	55.79		K_1	13.21	15.95	17.53
	K_2	71.66	69.99	68.84		K_2	22.17	20.44	14.62
	K_3	69.60	76.02	84.13		K_3	9.76	8.75	12.98
	R	4.15	13.26	28.34		R	12.41	11.69	4.55

Table 3 showed that the order of factors influencing potato-exposing rate was amplitude>vibration velocity> conveying velocity, which showed that amplitude had the greatest impacts on potato-exposing rate before vibration velocity and conveying velocity; the order of factors influencing breakage rate was conveying velocity> vibration velocity>amplitude, showing that conveying velocity had the greatest impacts on breakage rate before vibration velocity and amplitude.

Then the test results were analyzed by SPSS, and the influence of different levels of conveying velocity, vibration velocity and amplitude on potato-exposing rate and breakage rate are shown in Table 4.

Table 4 showed that the influence of amplitude on potato-exposing rate was P=0.046<0.05, showing that amplitude had significant influence on potato-exposing rate. Results of pairwise comparison on the three levels of the amplitude are shown in Table 5. The level of amplitude C_1 and C_2 was P=0.097>0.05, the level of C_1 and C_2 was P=0.073>0.05, showing no significant differences between the two groups of levels, and the level of C_2 and C_3 was P=0.023<0.05, showing significant difference

between the two groups of levels.

It can be concluded in Table 4, for the factors that influenced breakage rate, conveying velocity P=0.013< 0.05, vibration velocity P=0.015<0.05, showing that conveying velocity had the greater influence on breakage rate. Pairwise comparison was made on the three levels of conveying velocity and the results are shown in Table 6. The level of conveying velocity A_1 and A_3 was P=0.078> 0.05, showing no significant difference between the two groups of levels. The level between A_1 and A_2 P=0.013< 0.05 and A_2 and A_3 P=0.007<0.05, showing significant differences between the two groups of levels.

Table 4 Variance analysis

Source	Dependent variable	Type III Sum of Square	df	Meansquare	F	Sig.
Calibration model	Potato-exposing rate	0.150[a]	6	0.025	8.621	0.108
	Breakage rate	0.049[b]	6	0.008	51.630	0.019
Intercept	Potato-exposing rate	4.359	1	4.359	1505.332	0.001
	Breakage rate	0.204	1	0.204	1297.677	0.001
Conveying velocity	Potato-exposing rate	0.003	2	0.001	0.448	0.691
	Breakage rate	0.025	2	0.012	78.306	0.013
Vibration velocity	Potato-exposing rate	0.026	2	0.013	4.562	0.180
	Breakage rate	0.021	2	0.010	66.425	0.015
Amplitude	Potato-exposing rate	0.121	2	0.060	20.853	0.046
	Breakage rate	0.003	2	0.002	10.160	0.090
Error	Potato-exposing rate	0.006	2	0.003		
	Breakage rate	0.000	2	0.000		
Total	Potato-exposing rate	4.514	9			
	Breakage rate	0.253	9			
Total after correction	Potato-exposing rate	0.156	8			
	Breakage rate	0.049	8			

Note: a. R square = 0.963 (Adjusted R square = 0.851); b. R square = 0.994 (Adjusted R square = 0.974).

Table 5 Comparison of amplitude level

Potato-exposing rate
LSD

(I) C	(J) C	Mean value-different value,I-J	Standard error	Sig.	95% confidence interval	
					Lower limit	Upper limit
High (C_1)	Medium	–13.0467	4.39157	0.097	–31.9421	5.8487
	Low	–28.3400*	4.39157	0.023	–47.2354	–9.4446
Medium (C_2)	High	13.0467	4.39157	0.097	–5.8487	31.9421
	Low	–15.2933	4.39157	0.073	–34.1887	3.6021
Low (C_3)	High	28.3400*	4.39157	0.023	9.4446	47.2354
	Medium	15.2933	4.39157	0.073	–3.6021	34.1887

Table 6 Comparison of conveying velocity levels

Breakage rate
LSD

(I) A	(J) A	Mean value-different value,I-J	Standard error	Sig.	95% confidence interval	
					Lower limit	Upper limit
70(A_1)	90	–8.9600*	1.02368	0.013	–13.3645	–4.5555
	110	3.4433	1.02368	0.078	–0.9612	7.8479
90(A_2)	70	8.9600*	1.02368	0.013	4.5555	13.3645
	110	12.4033*	1.02368	0.007	7.9988	16.8079
110(A_3)	70	–3.4433	1.02368	0.078	–7.8479	.9612
	90	–12.4033*	1.02368	0.007	–16.8079	–7.9988

It can be concluded that the optimal combination of parameters that influences potato-exposing rate was $A_2B_3C_3$, and the optimal combination of parameters that influences breakage rate was $A_3B_3C_3$. Based on the integrated balance method, and taking full consideration of the importance of potato-exposing rate and breakage rate

as well as the influence of each factor, the optimal combination of parameters was determined: $A_2B_3C_3$, namely, when the conveying velocity was 90 r min^{-1}, vibration velocity was 120 r min^{-1}, amplitude was low. Then the conveying velocity, vibration velocity and amplitude were adjusted based on the combination $A_2B_3C_3$ for five times of experiments. The experimental data are shown in Table 7. Results showed that potato-exposing rate was 92.11% and breakage rate was 3.22%.

Table 7 Experimental data

Test No.	Potato-exposing rate, %	Breakage rate, %
1	92.25	3.25
2	91.63	2.99
3	92.45	3.65
4	92.38	2.89
5	91.86	3.33
Mean value	92.11	3.22

5 Conclusions

In view of the existing problems of potato harvest, the potato planting pattern and harvest agronomic requirements were fully considered in Xinjiang. 4UM-2 potato harvester, integrating digging device, adjustable parametric vibration device, velocity adjustable conveying and separating device, hydraulic driver and controlling system, was designed in this paper. The working parameters such as conveying velocity, vibration velocity and amplitude could be adjusted. The study obtained the following conclusions:

(1) Based on the analysis of horizontal inclination and length of digging shovel, structure and parameters of adjustable parametric vibrator and speed adjustable conveying and separating device were designed. Combined with the actual production effect of the previous experience to determine the factors and levels that influence the quality of potato-soil separation, then took conveying velocity, vibration velocity and amplitude as the experiment factors, potato-exposing rate and breakage rate as the experiment indexes, a three-factor and three-level orthogonal experiment was made on the harvester.

(2) Field test results showed that the order of the three factors that influence potato-exposing rate of the harvester was amplitude>vibration velocity>conveying velocity, and amplitude had the significant influence on potato-exposing rate (P=0.046<0.05); the order of the three factors in influencing breakage rate was conveying velocity>vibration velocity>amplitude, in which conveying velocity (P=0.013<0.05) and vibration velocity (P=0.015<0.05) had the significant influence on breakage rate, and the influence of the former was more significant. Analysis on the results showed that the optimal parameters combination was: conveying velocity = 90 r min^{-1}, vibration velocity = 120 r min^{-1}, and the amplitude was low. Experimental verification of the parameters combination showed that the potato-exposing rate was 92.11% and damage rate was 3.22%.

Acknowledgment

This research was supported by the National Youth Science Foundation of China (51705343), project of industry and hi-tech scientific attack and commercialized findings plan of Xinjiang Production and Construction Corps (2016AB003).

[References]

[1] Bentini, M., C. Caprara, and R. Martelli. 2006. Harvesting damage to potato tubers by analysis of impacts recorded with an instrumented sphere. *Biosystems Engineering,* 94(1): 75–85.

[2] Boac, J. M., M. E. Casada, R. G. Maghirang, and J. P. I. Harner. 2010. Material and interaction properties of selected grains and oil seeds for modeling discrete particles. *Transactions of the ASABE,* 53(4): 1201–1216.

[3] Jia, J. X., D. Q. Yang, and D. X. Zhang. 2011. Simulation and analysis of tuber movement during potato harvesting. *Journal of Agricultural Mechanization Research,* 38(08): 38–41, 50. (In Chinese with English abstract).

[4] Li, Y., B. Gao, J. Y. Yan, J. H. Wang, and Z. F. He. 2015. Development of potato harvester with elevator loading function. *Journal of Chinese Agricultural Mechanization,* 36(05): 50–53, 66. (In Chinese with English abstract)

[5] Li, Y. M., C. J. Wang, and X. Y. Wang. 2014. Design of 4U-55 potato harvester. *Agricultural Equipment & Vehicle Engineering,* 52(09): 69–71. (In Chinese with English abstract)

[6] Liu, B., D. X. Zhang, and J. Li. 2009. Design on MZPH-820 single-row potato harvester. *Transactions of the Chinese Society for Agricultural Machinery,* 40(05): 81–86. (In Chinese with English abstract)

[7] Liu, J. F., X. Yang, Y. J. Ma, and J. X. Jia.2004. Design of 4U-1A potato harvester. *Transactions of the Chinese Society for Agricultural Machinery*, 35(02): 181–183, 186. (In Chinese with English abstract)

[8] Liu, X. 2013. Improved design of lifting system of 4UFD-1400 potato combine harvester. Gansu Agricultural University, Gansu. (In Chinese with English abstract)

[9] Lv, J. Q., Z. E. Tian, J. E. Wu, Y. Yang, Q. Q. Shang, Y. B. Wang, and Z. X. Liu. 2015. Design and experiment on 4U1Z vibratory potato digger. *Transactions of the Chinese Society of Agricultural Engineering*, 31(12): 39–47. (In Chinese with English abstract)

[10] Meng, L., and W. Meng. 2012. Design of potato soil separation unit for small potato digger. *Beijing Agriculture*, (03): 199–200. (In Chinese with English abstract)

[11] Shi, L. R., J. M. Wu, W. Y. Zhao, W. Sun, D. Wang, H. Li, and Q. W. Liu. 2012. Development and experiment of disc type potato digger. *Transactions of the Chinese Society of Agricultural Engineering*, 28(24): 15–21. (In Chinese with English abstract)

[12] Shi, Z. H., L. L. Hu, N. Wu, Z. C. Hu, and B. Wang. 2015. Potato and sweet potato planting and harvesting machinery. *Journal of Agricultural Mechanization Research*, 37(04): 265–268. (In Chinese with English abstract)

[13] Sun, G. H. 2012. Design and experimental study on 4UFD-1400 potato seedling separator of potato combine. Gansu Agricultural University, Gansu. (In Chinese with English abstract)

[14] Wei, H. A., J. L. Zhang, X. P. Yang, X. P. Huang, L. X. Dai, G. H. Sun, and X. Liu. 2014. Improved design and experiment of 4UFD-1400 potato combine harvester. *Transactions of the Chinese Society of Agricultural Engineering*, 30(03): 12–17. (In Chinese with English abstract)

[15] Wu, J. M., H. Li, W. Sun, X. P. Huang, and W. Zhang.2011. Test of wheeled potato digger. *Transactions of the Chinese Society of Agricultural Engineering*, 27(07): 173–177. (In Chinese with English abstract)

[16] Wu, Q. F. 2015. Grimme company GT170 series traction potato harvester. *Agricultural Engineering*, 5(03): 161–164. (In Chinese with English abstract)

[17] Xie, S. S., C. G. Wang, J. G. Meng, S. H. Qi, G. D. Ma, and B. Ji. 2016. Experimental study on the movement law of potatoes on separating screen. *Journal of Agricultural Mechanization Research*, 38(09): 197–200, 205. (In Chinese with English abstract)

[18] Yang, D. Q., X. M. Hao, and J. X. Jia. 2007. Development of mechanized potato harvesting technology. *Agricultural Technology & Equipment*, (07): 8–9. (In Chinese with English abstract)

[19] Yang, R. B., H. G. Yang, S. Q. Shang, P. X. Xu, G. P. Cui, and L. H. Liu. 2016. The design and test of roller push potato harvester. *Transactions of the Chinese Society for Agricultural Machinery*, 47(07): 119–126. (In Chinese with English abstract)

[20] Zhao, D., S. J. Wang, X. Q. Li, Y. S. Wen, Z. Y. Yang, and L. Cheng. 2016. Design and research of side output potato harvester. *Journal of Agricultural Mechanization Research*, 38(08): 101–104. (In Chinese with English abstract)

Experiment on mechanical properties of pepper seedlings based on high-speed and low-loss planting

Ji Jiangtao[1], Li Mingyong[1], Jin Xin[1*], Pang Jing[1], Lv Huangzhen[2]

(1. *College of Agricultural Engineering, Henan University of Science and Technology, Luoyang 471003, China;*
2. *Chinese Academy of Agricultural Mechanization Sciences, Beijing 100083, China*)

Abstract: Planting methods, operating speed and its own characteristics of seedlings were important factors for transplanting quality, this paper aimed to study the problem which produce planting seedlings lodging damaged in high-speed transplanting focus on the mechanical properties of the seedlings and interaction between duckbilled planter and seedlings. The pepper seedlings were selected as the research objects, the substrate moisture content, matrix composition, seedling age as the test factors; orthogonal test method was used to analyze the pressure resistance and friction characteristics of the seedling. The results showed that compressive strength of the seedlings first increased and then decreased with the increase of the substrate moisture content, and the change with the matrix composition was L4>L3>L2>L1; the friction coefficient increased with the increase of substrate moisture content, and the change with the matrix composition was L4<L1<L2<L3; the compressive strength and friction coefficient of the seedlings all increased with the seedling age increase. In order to achieve a smaller friction coefficient among the seedlings body and the duckbilled planting and a greater compressive strength, weighted comprehensive evaluation method was used and the best parameters combination of mechanical properties of pepper seedlings was obtained as the follows: the substrate moisture content was 55%, the matrix composition was L4 (Peat: Vermiculite: Perlite = 3: 1: 2), the seedling age was 40 days.

Keywords: transplanting, pepper seedling, matrix composition, moisture content, seedling age, coefficient friction

Citation: Ji, J. T., M. Y. Li, X. Jin, J. Pang, and H. Z. Lv. 2017. Experiment on mechanical properties of pepper seedlings based on high-speed and low-loss planting. International Agricultural Engineering Journal, 26(4): 175–183.

1 Introduction

High-speed transplanting technology broke the limits of the artificial frequency of take seedlings and casting seedlings and has laid a foundation for the realization of an efficient and stable planting target of automatic transplanter. It has become the research focus of transplanting machinery field (Yu et al., 2014; Jiang et al., 2017; Han et al., 2014). The high-speed mechanized transplanting technology is still at a low level in China at present, the main reason for the limitation of high-speed transplanting is that as the planting speed increases, easy to produce seedlings damaged, drop seedling rewind and so on in the process of planting, which reduced the transplanted survival rate (Wang et al., 2014; Han et al., 2013; Miao et al., 2013; Han et al., 2013). The main reason for this problem is that the mechanical strength and sliding friction coefficient of the seedlings cannot match the high-speed planting requirements (Liang et al., 2015; Song et al., 2003; Zhang et al., 2009; Wang et al., 2014; Tang et al., 2016; Chen et al., 2014). Therefore, in order to meet matching requirements of agronomic and agriculture machinery, and to reduce the rate of seedlings damaged and rewind, there is an urgent need to carry out the research on the mechanical properties of pot seedlings for high-speed planting.

In the previous reported studies, most researches were aimed at optimizing the mechanical structure of transplanting, and did not carry out the research of pot seedling mechanical characteristics to planting mechanism movement characteristics effecting, cannot meet the requirements of the combination of agronomic

Received date: 2017-10-21 **Accepted date:** 2017-12-23

* **Corresponding author: Jin Xin,** Associate Professor, College of Agricultural Engineering, Henan University of Science and Technology, Luoyang 471003, China. Email: jx.771@163.com.

and agriculture machinery. (Jin et al., 2016; Wang et al., 2014; Han et al., 2013; Miao et al., 2013)

In view of this, this paper selected pepper seedlings as the research object, through the experiment to analysis pepper seedlings properties of pressure resistance and friction coefficient. The aim is to get the best combination of parameters of seedlings for high-speed transplanting, and to reduce the rate of seedlings damage and clogging in high-speed planting movement. This study can provide a theoretical support for the realization of high-speed and low-loss transplanting technology.

2 Pepper seedlings anti-compressive test

In the process of high-speed planting, the collision between the seedling and the planting machine will damage the pot seedlings, and decrease the transplanted survival rate, therefore, the transplanting pot seedlings requires a large compressive strength to avoid damage. The seedlings compressive strength is mainly affected by the yield limit and elasticity magnitude, the greater value of the two showed that the pot seedlings allowed withstanding the greater pressure.

In order to reduce the broken rate of seedlings and improve transplanting survival rate when it is planting, the yield limit and elasticity magnitude were taken as test indexes to analyze the compression characteristics of seedlings.

2.1 Materials and instruments

2.1.1 Test material

Pepper variety was 601 type peppers, the nursery substrates consist of peat and vermiculite and perlite, according to the volume ratio, four substrates were: L1=3:1:1, L2=3:0:1, L3=6:2:1, L4=3:1:2, seedling tray was a 128-hole square cone body (diameter was 35, and 20 mm, depth was 42 mm). Under the same matrix composition, the seedling ages were taken as 30, 35, 40 and 45 days, respectively, and the moisture content was taken as 45%, 55%, 65% and 75%.

2.1.2 Test equipment

Electronic universal testing machine used DNS series, measuring range: 0-500 N, measurement accuracy: 0.5%, 101A-1 type electric constant temperature oven, temperature range: 10°C-300°C.

2.2 Test method

This test was based on the anti-pressure and compression curve of seedlings in the compression process to define the yield limit and elasticity magnitude of the seedlings. Orthogonal experiment was used to analyze the compressive characteristics of the seedlings.

At the beginning, placed the seedling which was to be tested on the sloping platform (As the pot seedling was a square vertebral body, by constructing a sloping platform to achieve the plane contact between the seedlings and the compression plate of machine, shown as Figure 1). Set the electronic universal testing machine loading speed of 1 mm s^{-1} and compression plate down distance of 18 mm, and repeated the test 10 times. The computer automatically generated the seedling anti-pressure and compression curve. Seedlings compression test was shown in Figure 1.

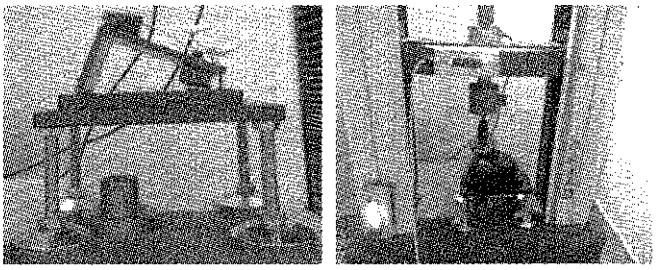

a. The sloping platform b. Seedlings compression test

Figure 1 Seedlings anti-compressive test

Defined the A point (which was the curve slope showed a mutation in first) in anti-pressure and compression curve as compression starting point, the B point (which was the curve slope showed a mutation in second) in the curve as compression yield limit point, and the slope K_{AB} of the straight line A to B was defined as the elasticity magnitude of the seedlings as shown in Figure 2b.

Using orthogonal experimental method to design the test, the matrix composition and seedling age and moisture content were as the test factors, every test factor was taken four levels. The factors level was shown in Figure 1. The yield limit and the elasticity magnitude were as test indicators, and selected $L_{16}(4^5)$ type orthogonal table to arrange the test program. Using the repeat test method of single-factor and single-level and each test was repeated for 10 times, the computer can automatically record data and curves.

Table 1 Factors level table of test

Level	Factors		
	Seedlings age (A)	Matrix composition (B)	Moisture content (C)
1	30	L1 (3:1:1)	45%
2	35	L2 (3:0:1)	55%
3	40	L3 (6:2:1)	65%
4	45	L4 (3:1:2)	75%

2.3 Test results analysis

2.3.1 Seedlings anti-pressure and compression curve

Under the conditions of seedling age was 30 days, matrix composition was L1, moisture content rate was 45%, and test was repeated for 10 times. The anti-pressure and compression curve was shown in Figure 2a. Polynomial regression analysis of a curve which was taken randomly from Figure 2a was shown in Figure 2b.

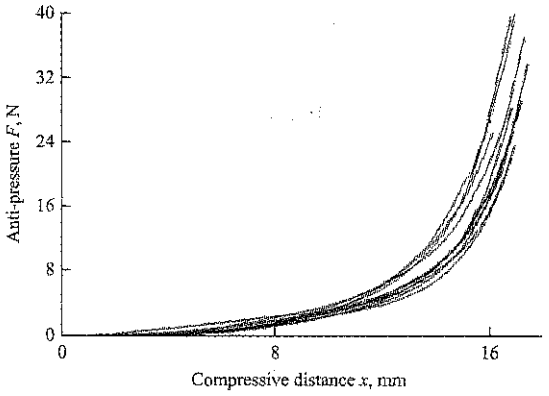

a. Anti-pressure-compressive curves

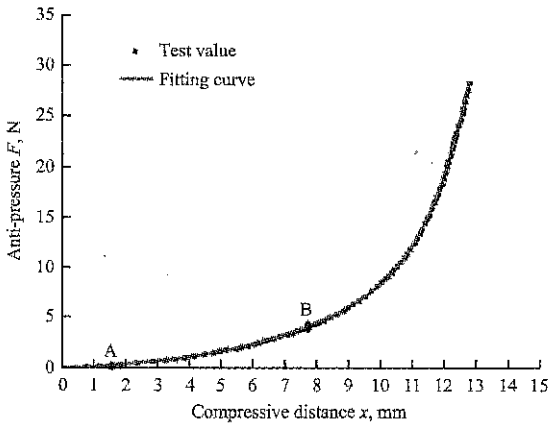

b. Experimental data regression analysis

Figure 2 Relation curves of anti-pressure and compressive distance of soil block

As can be seen from Figure 2b, the change of pot seedlings anti-pressure with the amount of compression was mainly divided into three stages. The initial stage of compression, anti-pressure and compression curve slope was changeable, anti-pressure and compression were non-linear relationship, they increased slowly with compression increasing. When the bowl body compression reached 1.5115 mm (is compression start point A), the contact change of seedling and compression plate was from point into surface, in the next period of the curve, anti-pressure and compression was an approximate linear relationship, it increased linearly with compression increasing. When the compression reached 7.8157 mm (is yield point B), it increased with the compression increasing, and showed an index upward trend.

In the compression test, as the amount of compression increased, the changes of seedlings characteristic was from elasticity into compaction. When the compression range was between A point and B point, the seedling showed deformation but no matrix collapsed or cracking occurred, seedling performance for the elasticity (Tang et al., 2016; Chen et al., 2014) (remove the pressure, the pot seedling deformation can be backed to its original state). Continue pressing until the amount of compression exceeded the yield point of the seedling, pot seedling damage rupture, the performance of seedling characteristic was compaction (Gao et al., 2016) (at this time to remove the pressure, the bowl deformation cannot be restored). A seedling has a greater yield point shows that it has the better pressure resistance. It shows that the pot seedlings can bear bigger deformation when they collide with the wall of the planter during planting, and is conducive to high-speed low-loss planting requirements.

2.3.2 Seedlings elasticity magnitude and yield limit

The seedlings compressive strength is mainly affected by yield limit and elasticity magnitude. When the amount of compression does not exceed the yield limit, the seedlings are deformed but no damage; when it is beyond, the seedlings will damage and cannot be restored. The compression resistance of the seedlings corresponded to the destruction of the internal structure of the matrix, which mainly showed that the seedling root adhered to the matrix particles slipped, collapsed and rearranged. The greater of the elasticity magnitude indicated that in a certain amount of compression seedlings allowed withstanding the greater pressure. The elasticity magnitude corresponds to the seedlings strength; seedlings can withstand the range of pressure when it has the performance of elasticity.

Orthogonal test was used to analyze the influence of the test factors on yield limit and elasticity magnitude. The orthogonal test results were shown in Table 2, and the results of orthogonal test variance analysis were shown in Table 3.

Table 2 The orthogonal test result analysis of the anti-compressive properties of pot seedling

Test number	Seedlings age (A)	Matrix composition (B)	Moisture content (C)	Yield limit (F_{max}), N	Elasticity magnitude (K)
1	1	1	1	4.0356	0.6247
2	1	2	2	4.7413	0.7060
3	1	3	3	4.3849	0.6848
4	1	4	4	4.2289	0.6784
5	2	1	2	4.5452	0.6708
6	2	2	1	4.1541	0.6575
7	2	3	4	4.1565	0.6472
8	2	4	3	4.7596	0.7246
9	3	1	3	4.1352	0.6312
10	3	2	4	4.0534	0.6188
11	3	3	1	4.3093	0.6814
12	3	4	2	5.2445	0.8162
13	4	1	4	3.8451	0.5975
14	4	2	3	4.2831	0.6714
15	4	3	2	4.9729	0.7699
16	4	4	1	4.6716	0.7174
Order of factors		Yield limit		C>B>A	
		Elasticity magnitude		C>B>A	
Prefer proposal		Yield limit		$A_4B_4C_2$	
		Elasticity magnitude		$A_4B_4C_2$	

Table 2 showed that seedling yield limit and elasticity magnitude increased with the growth of ages. That was because about 35 days bowl bodies of seedlings were covered by the root. Although the root has increased with the growth of seedling age, the impact on the seedlings strength was not large, so changes of the yield limit and elastic magnitude with the age growth of seedlings was not significant. Under different matrix components, the yield limit and elasticity magnitude of seedlings was L4>L3>L2>L1. The largest of yield limit and the elasticity magnitude was in the matrix component L4, because of the large content of peat in the matrix L4, that increased the air permeability of the seedlings and helped the root growth and made the bowl body more tightly wrapped by the root, which enhanced the compressive strength of pot seedlings; followed by the yield limit and elasticity magnitude was in matrix component L3, because the proportion of peat and vermiculite was larger, which made the matrix porosity smaller, and combined all components closely, it enhanced the compressive strength of the pot seedlings. The changes of the yield limit and elasticity magnitude was increasing first and then decreasing with the increase of the moisture content of pot seedlings, because it was difficult for the seedling matrix particles to combine tightly with each other when the moisture content was low. Pot seedlings body can be easily to loose and dry crack damage when it was in the compression; when the moisture content was too high, it was easy to cause the matrix particles of seedlings body to stagger, thus reduced the compressive strength of the seedlings.

According to P value in Table 3, the influence of seedling age on the yield limit and elasticity magnitude was generally (P>0.1), and the influence of matrix composition and moisture content was significant (P<0.01). Therefore, if the seedlings in the planted process appear damage phenomenon, we should preferential control the moisture content and matrix composition to enhance the pot seedlings strength.

Table 3 Variance analyses of the anti-compressive properties of pot seedling

Difference source	Difference source	Square deviation of the sum (SS)	Degree of freedom (df)	Mean square (MS)	F	Regression coefficients (P)
Seedling age	Yield limit	0.2262	3	0.0754	0.98	0.405
	Elasticity magnitude	0.0077	3	0.0026	1.76	0.158
Matrix composition	Yield limit	7.4077	3	2.4692	32.01	0.000
	Elasticity magnitude	0.2340	3	0.0780	53.36	0.000
Moisture content	Yield limit	13.8479	3	4.6160	59.84	0.000
	Elasticity magnitude	0.2304	3	0.0768	52.55	0.000
Error	Yield limit	11.5707	150	0.0771		
	Elasticity magnitude	0.2193	150	0.0015		
Sum	Yield limit	33.0542	159			
	Elasticity magnitude	0.6914	159			

3 Pot seedlings friction coefficient test

If the planter was moved to the planting seedlings position but the seedling did not fall to the planter bottom (because the seedling sliding friction resistance was too large to drop seedlings) when the seedling slide along the planter wall in the process of seedlings planting, it caused planting failure. The friction coefficient affected the change of sliding frictional resistance; therefore, in order to achieve high-speed planting, it is necessary to reduce the friction coefficient as much as possible to reduce the sliding friction resistance, so as to improve the success rate of high-speed planting.

In order to reduce the movement time of planting seedlings, and reduce sliding frictional resistance, the friction coefficient was taken as the index and the test was designed to analyze the frictional characteristics of the seedling.

3.1 Materials and instruments

3.1.1 Test material

The materials used were the same as test in Section 2.1.

3.1.2 Test equipment

The high-speed camera system of Phantom series, including lens, lighting, computer, tripod PTZ, PCC processing software; Friction test slope, length was 60 cm, width was 20 cm, height was 50 cm, scale range was 0-50 cm, adjustable angle, function: provide downhill and friction for the test. The seedling friction coefficient test device was shown in Figure 3.

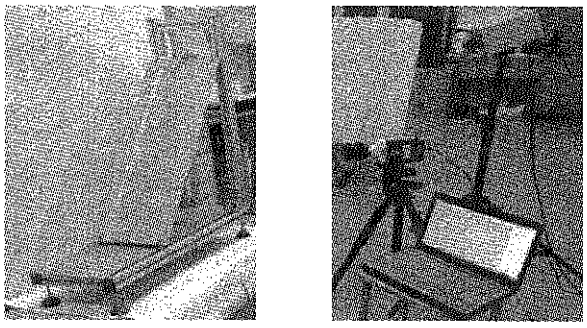

a. Friction test slope b. High-speed camera system

Figure 3 Seedling friction coefficient test device

3.2 Test method

In order to improve the situation of plugs block during the high-speed planting process and study the effects of pot seedlings self-characteristics on the sliding friction coefficient, the test selected seedling age and matrix composition and moisture content as the experimental factors, and the level of factors were in Table 1. Orthogonal test method was used to analyze the influence of the factors on sliding friction coefficient. The experimental scheme was the same as that in Section 1.2.

Adjusted the slope angle to 55°, and placed the pot seedling at the beginning of the slope, then let it down by its own gravity. Took high-speed camera system to record the seedlings sliding process, through the PCC software to analysis time t of seedlings falling distance $x=30$ cm. According to Newton's kinematical theory, the seedlings sliding acceleration $a=2x/t2$, and the sliding friction coefficient $\mu=(g\sin55°-a)/g\cos55°$, the g was the gravitational acceleration.

3.3 Test results analysis

The orthogonal test results were shown in Table 4; And the variance analysis results were shown in Table 5.

Table 4 Orthogonal test result analysis of friction coefficient

Test number	A	B	C	Average friction coefficient (μ)
1	1	1	1	0.4684
2	1	2	2	0.5614
3	1	3	3	0.6396
4	1	4	4	0.6488
5	2	1	2	0.5476
6	2	2	1	0.4861
7	2	3	4	0.7058
8	2	4	3	0.5841
9	3	1	3	0.6185
10	3	2	4	0.6907
11	3	3	1	0.5255
12	3	4	2	0.5389
13	1	1	1	0.6738
14	1	2	2	0.6444
15	1	3	3	0.5849
16	1	4	4	0.4740
Order of factors			C>B>A	
Prefer proposal			A1B4C1	

Table 5 Variance analysis of friction coefficient

Difference source	SS	df	MS	F	P
A	0.0099	3	0.0033	1.96	0.123
B	0.0597	3	0.0199	11.84	0.000
C	0.8403	3	0.2801	166.70	0.000
Error	0.2520	150	0.0017		
Sum	1.1619	159			

In the friction coefficient test, the change of frictional resistance was more significant with the change of the moisture content and the matrix composition when

seedlings slipped along the slope, but not significantly with the seedling age. When pot seedlings matrix moisture content increased, the sliding resistance increased too. The friction coefficient between pepper seedlings and duckbill planters was L4<L1<L2<L3, and under the condition of matrix composition L4 was the smallest. Pot seedlings resistance has increased with the growth of seedling age, but the changes were not significant.

Table 4 showed that the influence of each factor on the friction coefficient was C>B>A (moisture content> matrix composition>seedling age). The moisture content has the greatest effect on the friction coefficient; this was because the increased moisture content and the adhesion between the substrate and the planter wall increased, which led to the friction coefficient increase. Followed was the matrix composition, each component of the matrix body with different density, which was resulting in different weight and surface roughness of seedlings. The smallest friction coefficient was L4. Since the volume ratio of perlite in its composition was the largest, the contact surface between the seedling body and the planter wall was reduced, which was reducing the contact area and thus reducing the adhesion effect between seedling and planter, so the friction coefficient decreased. The last was the seedling age, the surface attached root of the seedlings body increased with the increase of seedling age, and the roots stick to the wall of the planter when the seedling was sliding down, which caused the friction coefficient increase.

According to P value of the variance analysis in Table 5, the seedling age had a certain influence on the friction coefficient between the seedlings and the planter wall (P>0.1), while the matrix composition and moisture content had a significant effect on the friction coefficient (P<0.01). Therefore, when it appears blockage and seedlings back to tape in the planting process, we may give priority control to the moisture content of seedlings.

4 Determine the best parameters

In order to achieve the requirements of high-speed and low-loss planting, the seedlings need to meet the requirements of larger pressure resistance and smaller sliding frictional resistance to avoid the seedling damage and lagging. In the selection of seedlings parameters, firstly, increase the yield limit to ensure the seedlings with better pressure resistance, reduce the damage rate during planting. Secondly, reduce the sliding friction coefficient to ensure the reliability of high-speed planting movement. However, these two conditions cannot be met at the same time. Therefore, this paper weighed the yield limit and the elasticity magnitude and friction coefficient of pot seedling to obtain the best combination of parameters.

Before calculating the weighted composite score, it is needed to calculate the normalized score y'_{ij} of these three indicators to ensure the three indicators in the same order of magnitude. The formula to calculate the normalized score is shown in Equation (1).

$$y'_{ij} = \frac{y_{ij} - y_{j\min}}{y_{j\max} - y_{j\min}} \quad (1)$$

where, y_{ij} is the test index value; $y_{j\min}$ is the minimum value of each test index; $y_{j\max}$ is the maximum value of each test index.

High-speed low-loss planting must improve the survival seedlings rate and ensure the transplanting efficiency. Lower damage rate is the prerequisite to improve the survival rate; prevent seedlings lagged and planter plugged was an important condition to ensure the reliability of high-speed planting. Therefore, in this paper, the weighted coefficient of yield limit and elasticity magnitude was taken as 0.6, and friction coefficient was taken as 0.4. The following function was used:

$$y_i^* = 0.6(y_{i-F} + y_{i-K}) + 0.4y_{i-\mu} \quad (2)$$

The results of the comprehensive evaluation of the yield limit and the elasticity magnitude were shown in Table 6. The order of the three factors affect from main to secondary was soil moisture content, matrix composition and seedling age. The highest score combination was the number 12, it was determined that the best parameters of pepper bowl seedlings for high-speed and low-loss planting are: seedling age is 40 days, matrix composition is L4, and moisture content is 55%.

Table 6 Comprehensive scoring results of mechanical features of pot seedling

Test number	A	B	C	Yield limit (F_{max}), N	Elasticity magnitude (K)	Average friction coefficient (μ)	Overall rating (y^*)
1	1	1	1	4.0356	0.6247	0.4684	0.1563
2	1	2	2	4.7413	0.7060	0.5614	0.8386
3	1	3	3	4.3849	0.6848	0.6396	0.7594
4	1	4	4	4.2289	0.6784	0.6488	0.6905
5	2	1	2	4.5452	0.6708	0.5476	0.6347
6	2	2	1	4.1541	0.6575	0.4861	0.3269
7	2	3	4	4.1565	0.6472	0.7058	0.6699
8	2	4	3	4.7596	0.7246	0.5841	0.9357
9	3	1	3	4.1352	0.6312	0.6185	0.4697
10	3	2	4	4.0534	0.6188	0.6907	0.5223
11	3	3	1	4.3093	0.6814	0.5255	0.5254
12	3	4	2	5.2445	0.8162	0.5389	1.3188
13	4	1	4	3.8451	0.5975	0.6738	0.3461
14	4	2	3	4.2831	0.6714	0.6444	0.6871
15	4	3	2	4.9729	0.7699	0.5849	1.1528
16	4	4	1	4.6716	0.7174	0.4740	0.6927
K1	2.4448	1.6068	1.7013				
K2	2.5672	2.3749	3.9449				
K3	2.8362	3.1075	2.8519				
K4	2.8787	3.6377	2.2288				
R	0.4339	2.0309	2.2436				

5 High-speed planting test

In order to further verify the operation effect of the optimal parameter combination, high-speed planting test was designed to verification the combinations effect on planting by using the first four combinations with the highest scores which were based on the comprehensive score method..

5.1 Test equipment

High-speed camera system was the same as the test in Section 2.1, function: record the entire process of planting, and get pot seedlings dropping time.

Planetary gear planting device was shown in Figure 4a, including duckbill planters, planet gear rotary planting mechanism, and stepper motor. Function: rotate a week planting 4 times to complete high-speed planting process.

5.2 Test plan

Let pot seedlings in the distance 0.1 m above the planters fall, planting speed was set to 30 r min^{-1} (planting frequency was 120 strains min^{-1}), the seedlings total test number was 80, recorded the number of damaged pot seedlings to analysis the matrix breakage rate, recorded seedling dropping time to analysis the rewind rate. The process of seedling planting is shown in Figure 4b.

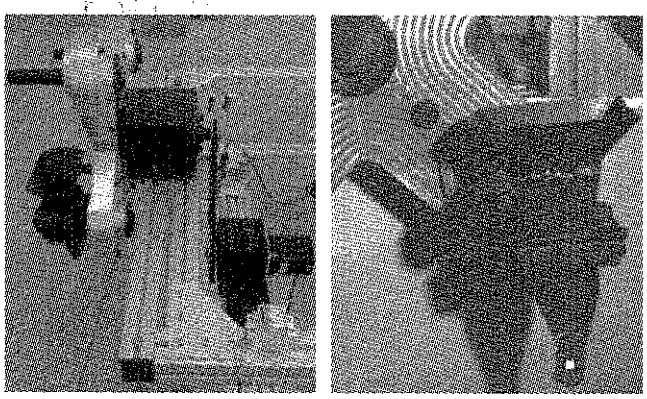

a. Planetary gear planting device b. Planting process

Figure 4 High-speed planting test

5.3 Analysis of test results

The high-speed planting test results were shown in Table 7, no damaged seedlings occurred during the planting test, it showed that the seedlings compressive strength of experimental selection met the high-speed planting requirements; Test No. 15, the planting rewind rate was 0, the others test combinations appeared the phenomenon of seedlings rewind, because the seedlings sliding resistance was larger in the planter, pot seedling movement lagged to planter movement in planting

process, which caused the seedlings dropping to fail. In the high-speed planting test, seedling age was 45 days, matrix composition was L3, moisture content was 55%, pepper seedlings did not appear rupture and rewind, which was most suitable for high-speed mechanized planting. The test results were consistent with the comprehensive score test.

Table 7 High-speed planting test

Test number	A	B	C	Breakage rate, %	Rewind rate, %
2	30d	L2	55%	0	60
8	35d	L4	65%	0	57
12	40d	L4	55%	0	38
15	45d	L3	55%	0	0

6 Conclusion

(1) The yield limit and elasticity magnitude of pepper seedlings were significantly affected by matrix composition and moisture content (P<0.01), and generally affected by seedling age (P>0.1). Under different matrix conditions, the yield limit and elasticity magnitude was L4>L3>L2>L1. Both of yield limit and elasticity magnitude increased with seedling age, but the changes were not obvious.

(2) The friction coefficient of the seedlings was more affected by matrix composition and moisture content (P<0.01), and generally on its age (P>0.1). The friction coefficient was L4<L1<L2<L3 in different matrix conditions, and increased with the moisture content and seedling age increasing.

(3) The optimal combination of pepper seedlings for high-speed and low-loss planting was obtained by the weighted comprehensive evaluation method and the test of physical and mechanical properties of pepper seedlings, and it is: the seedling age was 40 days, the matrix composition was L4, and the moisture content was 55%.

Acknowledgements

This project was supported by National Natural Science Foundation of China (Grant No.51505130), the National Key Research and Development Program of China Sub-project (No. 2017YFD0700800), the Innovation Scientists and Technicians Troop Construction Projects of Henan Province (No.184200510017), and the Research Project of Science and Technology of Henan Province (No. 172102110021).

[References]

[1] Chen, X. L., J. H. Wang, and S. Y. Li. 2014. Elastoplastic simulation for undrained cyclic stress-strain responses of soft clays. *Chinese Journal of Geotechnical Engineering*, 36(5): 934–941.

[2] Gao, C. L., Z. Y. Yan, J. J. Li, B. X. Wang, and M. Q. Zhang. 2016. Effect of grain size distribution on compaction property of cohesionless soil. *Journal of Wuhan University of Technology* (Transportation Science & Engineering), 40(2): 227–232.

[3] Han, L. H. 2014. Mechanical analysis of the root lumps and development of a robotic transplanter for vegetable plug seedlings. Ph.D. diss. Jiangsu University.

[4] Han, L. H., H. P. Mao, J. P. Hu, J. Y. Xu, Z. R. Zhao, and G. X. Ma. 2016. Design and test of automatic transplanter for greenhouse plug seedlings. *Transactions of the Chinese Society for Agricultural Machinery*, 11(47): 59–67. (In Chinese with English abstract)

[5] Han, L. H., H. P. Mao, J. P. Hu, X. H. Miao, K. P. Tian, and X. J. Yang. 2013. Experiment on mechanical property of seedling pot for automatic transplanter. *Transactions of the Chinese Society of Agricultural Engineering*, 29(2): 24–29. (In Chinese with English abstract)

[6] Han, L. H., H. P. Mao, X. H. Miao, J. P. Hu, and X. J. Yang. 2013. Design of automatic picking up seedling end-effector based on mechanical properties of plug seedlings. *Transactions of the Chinese Society for Agricultural Machinery*, 44(11): 260–265. (In Chinese with English abstract)

[7] Jiang, Z. H. 2017. Optimal design of automatic transplanter in greenhouse and force analysis for transplanting process. Ph.D. diss. Hangzhou: Zhejiang University.

[8] Jin, X. 2014. Research on automatic transplanting technology and device for vegetable plug seedling. Ph.D. diss. Beijing: China Agricultural University.

[9] Jin, X., X. W. Du, C. H. Yang, J. T. Ji, S. G. Wang, and H. Yan. 2016. Design and experiment on crank-chute planting mechanism of transplanting machine. *Transactions of the Chinese Society for Agricultural Machinery*, 47(5): 83–90. (In Chinese with English abstract)

[10] Liang, X. F., Y. Y. Cai, and Y. W. Wang. 2015. Experiment on physical and mechanical properties of tomato seedling pot for automatic vegetable transplanter. *Journal of Zhejiang University* (Agriculture and Life Sciences), 05(41): 616–622.

[11] Miao, X. H., H. P. Mao, L. H. Han, H. Sun, X. J. Yang, and H. Huang. 2013. Analysis of influencing factors on force of

picking plug seedlings and pressure resistance of plug seedlings. *Transactions of the Chinese Society for Agricultural Machinery*, 44(Supp.1): 27–32. (In Chinese with English abstract)

[12] Song, J. N., P. Wang, W. J. Wei, and L. C. Wang. 2003. Experimental research on tensile strength of rice seedlings and force of pulling out seedlings from trays. *Transactions of the Chinese Society of Agricultural Engineering*, 19(6): 10–13. (In Chinese with English abstract)

[13] Tang, J. Z., C. C. Fu, W. Wan, W. J. Wang, and S. L. Luo. 2016. Rheological test of separation between viscoelastic-plastic strains and creep damage model. *Chinese Journal of Rock Mechanics and Engineering*, 35(7): 1297–1308.

[14] Wang, Y. 2014. Optimization and experiment on planting parameters for high upright rate. Ph.D. diss. Hangzhou: Zhejiang Sci-Tech University.

[15] Wang, Y., J. N. Chen, J. W. Wu, and Y. Zhao. 2014. Mechanics property experiment of oil seedling oriented to mechanized planting. *Transactions of the Chinese Society of Agricultural Engineering*, 30(24): 1–10. (In Chinese with English abstract)

[16] Yu, X. X., Y. Zhao, B. C. Chen, M. L. Zhou, H. Zhang, and Z. C. Zhang. 2014. Current situation and prospect of transplanter. *Transactions of the Chinese Society for Agricultural Machinery*, 45(8): 44–53. (In Chinese with English abstract)

[17] Zhang, G. F., Y. Zhao, and J. N. Chen. 2009. Characteristic analysis of rice plotted-seedling's motion in air and on turbination-type guide-canal. *Journal of Zhejiang University* (Engineering Science), 43(3): 529–534. (In Chinese with English abstract)

Optimal hedging strategies for an agricultural exporting firm

Yu Xing[1], Wang Laibin[2*], Wen Kun[3]

(1. *Department of Mathematics & Applied Mathematics, Hunan University of Humanities, Science and Technology, Loudi, 417000, China*; 2. *Management and Law Department, Chizhou University, Chizhou Anhui, 247000, China*; 3. *Jiangxi Administrative Institute, Jiangxi, 330000, China*)

Abstract: Suppose that an agricultural exporting firm faces uncertainties of the export commodity price, the exchange rate and production. The expected utility maximization problem is examined when the firm has access to both futures and option markets of commodity and currency. In the presence of unbiased futures and option markets, we showed that the firm's optimal output was such that the marginal cost equal to the price (in domestic currency). Furthermore, if the random spot exchange rate and the output price are independent, options are redundant and future is full-hedged. When the random spot exchange rate and the random output price are negatively correlated, it is optimal to long put currency options, short put commodity options for a prudent firm and under-hedge futures position. Our results thus offered a systematic analysis for hedging agricultural exporting risk with multiple derivative instruments.

Keywords: agricultural exporting, exchange rate, agricultural exporting risk

Citation: Yu, X., L. B. Wang, and K. Wen. 2017. Optimal hedging strategies for an agricultural exporting firm. International Agricultural Engineering Journal, 26(4): 184–192.

1 Introduction

With the expansion of international financial relationships and the development of economic globalization, agricultural firms have become more and more exposed to the risks associated with foreign exchange operations and the export commodity price under uncertainty production. A large number of studies have examined in great detail the issue of import/export risk (Allayannis and Ofek, 2001; Mun and Morgan, 2003; Shi et al.2015). The question that naturally arises is how to hedge the currency and output price risk. The forward / futures and option markets have provided the export firms, among others, with a vehicle for hedging against unanticipated changes. Lien and Tse (2000) compared the hedging effectiveness of currency futures vs. currency options on the basis of the lower partial moments (LPMs). Other relative studies can refer to Amüller and Nolte (2011), Cimoli et al. (2016). Although there is a large literature dealing with currency futures markets, few attempts have been made to incorporate futures or forward trading in the theory of the firm which calls for further study. Because in the real case, the true and concrete utility function, exchange rate and output distributions are unknown, results derived from particular examples may be misleading and lack generality. In the general utility function framework, Broll and Wahl (1996) showed that the exporting firm could eliminate the foreign currency risk through imperfect hedging. Wong (2001) examined the production and hedging decisions of a competitive exporting firm under exchange rate uncertainty. It is shown that the separation theorem does not hold under export flexibility, the export-flexible firm under-hedges its exchange rate risk exposure in a currency forward market where in the forward exchange rate contains a non-positive risk premium. Later, Wong (2002) considered a firm export flexible in that it could distribute its output to either the domestic market or a foreign market, after observing the realized spot exchange rate. It is shown that the separation theorem holds if selling exclusively in the domestic market is suboptimal even under the most unfavorable spot exchange rate.

Received date: 2017-09-02 **Accepted date:** 2017-10-17

* **Corresponding author: Wang Laibin**, Lecturer, Management and Law Department, Chizhou University, Chizhou Anhui, 247000, China. Email: 28276062@qq.com

Otherwise, the firm's optimal output depends on its preference and on the underlying exchange rate uncertainty. Furthermore, the export-flexible firm under hedges its exchange rate risk exposure in a currency forward market where in the forward exchange rate contains a non-positive risk premium. To name just a few, some other literatures could see to Broll and Eckwert (1998), Boll and Eckwert (2000), Borll and Zilcha (1991), Viaene and Zilcha (1998). In recent study, Wong (2013) examined the behavior of a competitive exporting firm under joint price and exchange rate uncertainty. It showed that the firm's optimal production and hedging decisions depend crucially on the degree of forward market incompleteness, and on the correlation structure of the price and exchange rate risk.

Surprisingly, the widespread advocacy of using currency options in foreign exchange risk management, the question concerning their proper application as a hedging instrument remains largely unexplored, especially under the theoretical framework. To fill this gap, Machnes (1992) examined the behavior of the competitive firm in the presence of commodity options and price uncertainty. Confined to Machnes' model, Wong (2002) showed that it was always optimal for the firm to use the commodity option for hedging purpose. Adam-Müller (2004) assumed orthogonal price and exchange rate risk when hedged with derivative. Wong (2002) extended the model of Adam-Müller where in a competitive exporting firm faced concurrently hedgeable exchange rate risk and non-hedgeable price risk and expanded the firm's risk-sharing choice set to include currency options. He examined the optimal hedging decision of the firm in the presence of unbiased currency futures and options market using two-stage optimization method. Chang and Wong (2003) discussed the cross-hedging with currency options and futures and offered analytical insights into the optimal cross-hedging strategies of the firm. The questions that naturally also arise are whether and how the export firms with exposure to both export commodity price and foreign exchange risks hedge and can improve its risk-return performance by hedging the two sources of risks simultaneously both futures and options for commodity and currency relative to hedging them separately. A systematic analysis of this question, to our knowledge, does not exist in the literature. We address this question by developing a theoretical hedging model that accommodates both risks, with four hedge instruments, i.e. currency futures and option, commodity futures and option and evaluating hedging performance for the export firms when foreign exchange risks and price risk are hedged separately versus simultaneously.

The rest of this paper was organized as follows. Section 2 proposed a model of an agricultural exporting firm facing joint price and exchange rate uncertainty, in which we also considered uncertain output and the cost function. Section 3 analyzed the firm's optimal production and hedging decisions when both commodity and currency futures and option markets were present. Section 4 gave results that compared depending on the several cases of futures and option market incompleteness. The final section is the conclusion.

2 Hedging model

Firstly, we presented some assumptions. Factors at the micro level (such as hedging, accounting standards, bank interest rates, settlement time matching, etc.) were not considered. There are some reasons why we do not discuss the microcosmic problems. One is that, due to the lack of mature options markets, literature and practice about the choice of options hedging in importing is relatively scarce in China. Therefore, the agricultural firm in this paper is fiction rather than actual existence. We assumed that an agricultural exporting firm wanted to export agricultural products to the foreign market. It does not mean that firm exports crude to the foreign market better than in domestic market. There may be some objective reasons why the firm has to do so. For example, the domestic demand of agricultural products may not be enough to meet the firm's supply. Based on this analysis, the domestic CNY products price series have no effect on the model in this paper. Since the firm has to export agricultural products to the foreign market, then it faces risk of agricultural products price denominated in foreign currency. Further, it faces exchange rate risk. To cope with price and exchange rate risk, based on the

completeness of markets of oil option and exchange rate option, the enterprise may choose commodity and currency options for hedging. Consider an agricultural exporting firm exports a single agricultural output Q, to a foreign country for one period with date, 0 and 1. There are two sources of uncertainty, the first is the output price per unit denominated in the foreign currency. The second is the spot exchange rate expressed in units of the domestic currency per unit of the foreign currency. It is assumed that the firm was chosen both among entering commodity and currency futures and option markets. The decision variables are output Q, positions of commodity futures and option H_p, Z_p and positions of currency futures and option H_s, Z_s.

It is possible to replicate the payoff of any combination of futures, puts, and calls with any two of these three assets (Broll and Wahl, 1992). Thus, we ignored calls in the following analysis. For simplicity, only one strike price for put options was considered and this strike price was assumed to be the current futures price. Throughout this paper, random variables have a tilde(~) while their realizations do not. The mean value of the random variables has a tilde(–). As such, the random profit at time 1 denominated in the home currency, is therefore written as

$$\begin{aligned}\tilde{\Pi} = {} & \tilde{S}\tilde{P}Q + \tilde{S}(p^f - \tilde{P})H_p + (s^f - \tilde{S})H_s + \\ & \tilde{S}[p - (K_p - \tilde{P})^+]Z_p + [s - (K_s - \tilde{S})^+]Z_s - C(Q)\end{aligned} \tag{1}$$

where, $\tilde{S}$ and $\tilde{P}$ denote random variables of the agricultural product price and exchange rate at date 1, respectively; p^f and s^f are the given commodity futures price and the exchange rate at date 0, p and s are called as option premium that the firm should pay for put options for commodity and exchange rate, which are known by the firm ex ante. $(K_p - \tilde{P})^+$ is the terminal value of a commodity put option, defined as $(K_p - \tilde{P})^+ = \begin{cases} 0, \ if \ P \geq K_p \\ K_p - P, \ if \ P < K_p \end{cases}$, where P is a realization of the random variable $\tilde{P}$. K_p is the strike price of commodity put option. It is similarly for $(K_s - \tilde{S})^+$. $C(Q)$ is a strictly convex cost function dual to a concave production function, $C(0)\geq 0$, $C'(Q)>0$, and $C''(Q)>0$. The firm's utility is a strictly concave function defined over profit $U(\tilde{\Pi})$, such that $U'>0$ and $U''<0$, where $\tilde{\Pi}$ is given by (1). Thus, the firm is risk averse, but no other restrictions are placed on its preferences. Following the standard model of hedging under expected-utility maximization, the firm makes decision strategies on the five variables Q, H_p, Z_p, H_s, Z_s. The optimal hedging model is

$$\max_{Q,H_p,Z_p,H_s,Z_s} \Re = E[U(\tilde{\Pi})] \tag{2}$$

where, E denotes the mathematical expectation operator.

Since the firm is, by assumption, risk-averse, the maxim and is strictly concave in the profit, and the cost function is strictly convex in output, the second-order conditions are satisfied. Hence, the first order conditions require $\Re_Q' = \Re_{H_p}' = \Re_{Z_p}' = \Re_{H_s}' = \Re_{Z_s}' = 0$, where the subscripts to $\Re$ denote arguments of partial differentiation, that is

$$E[U'(\tilde{S}\tilde{P} - C'(Q))] = 0 \tag{3.1}$$

$$E\{U'[\tilde{S}(p^f - \tilde{P})]\} = 0 \tag{3.2}$$

$$E[U'(s^f - \tilde{S})] = 0 \tag{3.3}$$

$$E\{U'\tilde{S}[p - (K_p - \tilde{P})^+]\} = 0 \tag{3.4}$$

$$E\{U'[s - (K_s - \tilde{S})^+]\} = 0 \tag{3.5}$$

3 Complete markets

In this part, for the pure sake of simplicity, we considered only one strike price. Furthermore, the option premium together with strike price equal to the mean value, that is, $K_p = E(\tilde{P}) = \bar{P}$, and $K_s = E(\tilde{S}) = \bar{S}$. Specifically, if the firm's expectation of the end-of-period price equals the current price, which is also called unbiased, i.e., $E(\tilde{P}) = p^f = \bar{P}$, $E(\tilde{S}) = s^f = \bar{S}$, $E(\bar{P} - \tilde{P})^+ = p$ and $E(\bar{S} - \tilde{S})^+ = s$. Holthausen (1992) showed that when futures were biased the optimal hedge depended on the hedger's degree of risk-aversion. Hence, unbiased prices assumption is a necessary condition for utility-free hedge ratios.

Proposition 1. When futures and option markets are unbiased, then (a) the firm's optimal output Q^* makes the marginal cost equal to the price in the home currency, i.e. $C'(Q^*)=E(\tilde{S})E(\tilde{P})$; (b) If the random spot exchanging rate and agricultural product price are independent, options are not used as hedging instruments and the optimal hedging strategy is the opts for full-hedge that eliminates risk exposure are $H_p=Q^*$, $H_s=p_fQ^*$.

Proof: We first proof that $C'(Q^*)=p^fs^f$. In fact, due to the unbiased markets, Equations (3.1), (3.2) and (3.3) are in terms of covariance as

$$EU'[E(\tilde{S})E(\tilde{P})+\mathrm{cov}(\tilde{S},\tilde{P})-C'(Q^*)]+\mathrm{cov}(U',\tilde{S}\tilde{P})=0 \tag{3.1'}$$

$$\mathrm{cov}(U'\tilde{S},\tilde{P})=0 \tag{3.2'}$$

$$\mathrm{cov}(U',\tilde{S})=0 \tag{3.3'}$$

The second term of Equation (3.1') can be transformed as

$$\begin{aligned}&\mathrm{cov}(U',\tilde{S}\tilde{P})=E(U'\tilde{S})E(\tilde{P})+\mathrm{cov}(U'\tilde{S},\tilde{P})-\\&E(U')E(\tilde{S})E(\tilde{P})-E(U')\mathrm{cov}(\tilde{S},\tilde{P})\end{aligned} \tag{4}$$

Substituting Equations (3.2'), (3.3'), and (4) into Equation (3.1') yields $C'(Q^*)=E(\tilde{S})E(\tilde{P})$. We then proof that (b) in proposition 1. In fact, Equation (1) can be rewritten as the following equation

$$\begin{aligned}&\tilde{\Pi}=s^fp^fQ-C(Q)+\tilde{S}[\tilde{P}-p^f](Q-H_p)+(\tilde{S}-s^f)\\&(p^fQ-H_s)+\tilde{S}[p-(\bar{P}-\tilde{P})^+]Z_p+[s-(\bar{S}-\tilde{S})^+]Z_s\end{aligned} \tag{1'}$$

the candidate solutions are $H^*_p=Q^*$, $H^*_s=p^fQ^*$, $Z^*_p=Z^*_s=0$. In fact, substitute the candidate solutions into Equation (1'), we find that the profit is certainty, not random anymore, i.e. $\tilde{\Pi}^*=s^fp^fQ^*$. Due to the independence, Equations (3.1) - (3.5) are obviously satisfied under the assumed conditions of unbiased and independent prices.

The intuition of proposition 1 is as follows. When futures and option markets both for commodity and currency are available, the firm's optimal output makes the marginal cost equal to the price in the home currency. The optimal positions not only access to the optimal utility but to eliminate the risk exposure completely as well. It seems not in conformity with the intuitive understanding because in a realistic hedging environment, we would expect commodity and currency options to be an integral part of the optimal hedge position of a firm. The major cause of this is the unduly restrictive to assume conditions of independent prices between commodity and currency.

To characterize the solution of these equations, it is necessary to be specific about the relationship between commodity price and exchange rate in the following manner adopted from that of Moschini and Lapan (1995):

$$\tilde{P}=\alpha+\beta\tilde{S}+\tilde{\varepsilon} \tag{5}$$

where, α and β are scalars, and $\tilde{\varepsilon}$ is a zero-mean random variable independent of $\tilde{S}$. Since any pass-through to exchange rate movements would imply a negative correlation between $\tilde{P}$ and $\tilde{S}$, in the sequel we focus on the case where $\beta<0$.

Proposition 2. Given that the futures and options markets are unbiased. If the firm is prudent, i.e. $U''>0$, and the relation between commodity and currency described as Equation (5), then the firm opts for buying currency put options and selling commodity put options for the exchange rate and the agricultural product price $Z^*_s<0$, $Z^*_p>0$.

Proof: $E[U(\tilde{\Pi})]$ is strict concavity of Z^*_s due to $U''<0$, as such it is necessary to prove that $\left.\frac{\partial\{E[U(\tilde{\Pi})]\}}{\partial Z_s}\right|_{Z_s=0}<0$. In fact, $\left.\frac{\partial\{E[U(\tilde{\Pi})]\}}{\partial Z_s}\right|_{Z_s=0}=E\{U'(\tilde{\Pi}^0)[s-(\bar{S}-\tilde{S})^+]\}$, where

$$\begin{aligned}&\tilde{\Pi}^0=s^fp^fQ-C(Q)+\tilde{S}[\tilde{P}-p^f](Q-H_p(0))+(\tilde{S}-s^f)\\&(p^fQ-H_s(0))+\tilde{S}[p-(\bar{P}-\tilde{P})^+]Z_p(0)\,.\end{aligned}$$

The following steps to proof $Z^*_s<0$ is similar to Chang and Wong. (2003) as such we omit the details.

Next to prove $Z^*_p>0$. Let $\bar{S}-\tilde{S}=t$. Due to $\mathrm{cov}(U',\bar{S}-t)=0$, we have $\mathrm{cov}(U',t)=0$, or $\mathrm{cov}(E(U')|t,t)=0$. According to Adam-Muller (2004), for $U''\neq0$, the covariance is zero only if there exists at

one interval of t in which $\frac{\partial[E(U')|t]}{\partial t}$ is positive and at least one in which the derivative is negative.

$$\frac{\partial[E(U')|t]}{\partial t}=E(U''|t)E\frac{\partial\Pi}{\partial t}+\operatorname{cov}\left(U'',\frac{\partial\Pi}{\partial t}|t\right)$$

$$=E(U''|t)E\frac{\partial\Pi}{\partial t}+\operatorname{cov}(U'',-\varepsilon Q+\varepsilon H_p+(\beta t-\varepsilon)^+Z_p|t)$$

The sign of $\operatorname{cov}(U'',-\varepsilon Q+\varepsilon H_p+(\beta t-\varepsilon)^+Z_p|t)$ is the same as

$$\frac{U'''\frac{\partial\Pi}{\partial\varepsilon}}{\frac{\partial[-\varepsilon Q+\varepsilon H_p+(\beta t-\varepsilon)^+Z_p]}{\partial\varepsilon}}=U'''(t-\bar{S})$$

And

$$\frac{\partial\Pi}{\partial t}=(-\alpha-2\bar{S}\beta+2\beta t)Q+(\bar{S}\beta-2\beta t+\varepsilon)H_p+H_s$$
$$+\left[(\beta t-\varepsilon)^+-p-(\bar{S}-t)\frac{\partial(\beta t-\varepsilon)^+}{\partial t}\right]Z_p-\frac{\partial(t^+)}{\partial t}Z_s$$

Then

$$E\left(\frac{\partial\Pi}{\partial t}\right)=(-\alpha-2\bar{S}\beta)Q+\bar{S}\beta H_p+H_s-$$
$$E\left[(\bar{S}-t)\frac{\partial(\beta t-\varepsilon)^+}{\partial t}\right]Z_p-E\left[\frac{\partial(t^+)}{\partial t}\right]Z_s$$

So, when $t>\bar{S}$, we have $E\left(\frac{\partial\Pi}{\partial t}\right)<0$; when $t\le\bar{S}$, we have $E\left(\frac{\partial\Pi}{\partial t}\right)>0$. In addition, $sign\left(\frac{\partial(\beta t-\varepsilon)^+}{\partial t}\right)<0$ because of $\beta<0$; it is obvious that $sign\left(\frac{\partial(t^+)}{\partial t}\right)\ge0$. We have the following two inequations

$$H_s-\alpha Q+\bar{S}\beta(H_p-Q)-\bar{S}\beta Q-\Delta_{11}Z_p-\Delta_{12}Z_s<0 \quad (6)$$

$$H_s-\alpha Q+\bar{S}\beta(H_p-Q)-\bar{S}\beta Q-\Delta_{21}Z_p-\Delta_{22}Z_s>0 \quad (7)$$

where, $\Delta_{11}=E\left[(\bar{S}-t)\frac{\partial(\beta t-\varepsilon)^+}{\partial t}\right]$ when $t>\bar{S}$, so $\Delta_{11}>0,\Delta_{21}=E\left[(\bar{S}-t)\frac{\partial(\beta t-\varepsilon)^+}{\partial t}\right]$; when $t\le\bar{S}$, so $\Delta_{21}\le0,\Delta_{12}=\Delta_{22}=E\left[\frac{\partial t^+}{\partial t}\right]\ge0$. It is easy to yield $Z^*_p>0$ from Equation(6)and Equation(7) and the fact of $Z^*_s>0$.

The intuition of proposition 2 is as follows. For a prudent firm, in the purpose of hedging the exposed risk of exchange rate and the commodity price, the firm is wise to buy currency put option and sell commodity put option. The reason can be explained by quoting Chang and Wong's words (2003): Given prudence (i.e. $U'''>0$), the firm is more sensitive to low realizations of its domestic currency income than to high ones (Kimball 1989, 1993). The firm as such has incentives to avoid the low realizations of its domestic currency income. Inspection of Equation (1) reveals that the firm can achieve this goal to long put currency option and short put commodity option as $Z^*_s<0$, $Z^*_p>0$. Next, we examine the currency and commodity futures positions.

Proposition 3. Given that the futures and options markets are unbiased. If the firm is prudent, i.e. $U'''>$, and the relation between commodity and currency described as Equation (5), then the firm opts for commodity futures positions $H^*_p<Q^*$ and currency futures positions $H^*_s<\bar{P}Q^*+pZ^*_p$.

***Proof*:** Substitute Equation(5) into Equation(1), the profit can be rewritten as

$$\tilde{\Pi}=(\bar{S}+\theta)(\bar{P}+\beta\theta+\varepsilon)Q-(\bar{S}+\theta)(\beta\theta+\varepsilon)H_p-\theta H_s+$$
$$(\bar{S}+\theta)[p+(\beta\theta+\varepsilon)a]Z_p+[s+\theta b]Z_s-C(Q) \quad (8)$$

where, $a=\begin{cases}0, \text{ if } p^f<\tilde{P}\\ 1, \text{ if } p^f\ge\tilde{P}\end{cases}$ and $b=\begin{cases}0, \text{ if } s^f<\tilde{S}\\ 1, \text{ if } s^f\ge\tilde{S}\end{cases}$.

Equation (3.3') means that $\operatorname{cov}(U'(\Pi),\theta)=0$. A random variable y is conditionally independent of another random variable z if and only if $\operatorname{cov}[y,l(z)]=0$ for all functions $l(\cdot)>0$. We have that $Q^*-H^*_p+aZ^*_p=0$ and $\bar{P}Q^*-H^*_s+pZ^*_p+bZ^*_s=0$. According to the obtained results of $Z^*_s<0,Z^*_p>0$, we have $H^*_p<Q^*$ and $H^*_s<\bar{P}Q^*+pZ^*_p$.

4 Special compared examples

In order to reveal the advantages of adopting both futures and options markets of commodity and currency for hedging purpose, it is necessary to specify the utility

functions and the distributions of the random variables. Similar to Chang and Wong (2003), given that $\tilde{\theta}$ is symmetrically distributed over support $[-\Theta,\Theta]$ with cumulative distribution function G, where $0<\Theta\le\infty$.

Suppose that $\tilde{S}=\bar{S}+\tilde{\theta}$, where $\bar{S}$ is the expected value of $\tilde{S}$, and $\tilde{\theta}$ is a zero mean variable. Furthermore, suppose that $\tilde{P}=\alpha+\beta\bar{S}+\beta\tilde{\theta}$, which is the special case of (5) with $\tilde{\varepsilon}=0$.

Note first that the put option premium is perceived as unbiased by the firm. That is $s=E(\bar{S}-\tilde{S})^+$, $p=E(\bar{P}-\tilde{P})^+$. Write the first equation in integral form as $s=E(-\theta)^+=\int_{-\Theta}^{0}-\theta dG(\theta)$. Since $\tilde{\theta}$ is symmetrically distributed over support $[-\Theta,\Theta]$ with cumulative distribution function G, then $dG(\theta)=dG(-\theta)$ for all $\theta\in[-\Theta,\Theta]$. Using this fact, we have $s=\int_0^{\Theta}\theta dG(\theta)$. Then, we have $p=-\beta E(\theta)^+=-\beta\int_0^{\Theta}\theta dG(\theta)=-\beta s$. Therefore, we have $p=-\beta s$.

The firm's utility function, U, is said to be quadratic if it takes the generic form of $U(\Pi)=\Pi-b\Pi^2$, where b is a positive constant.

Proposition 4. Suppose that the futures and options markets are unbiased. If the firm has a quadratic utility function and if $\tilde{S}$ is symmetrically distributed. When only currency futures and option markets are present, then the firm's optimal hedging strategy is given by $H_s^*=(\bar{P}+\bar{S}\beta)Q^*+\frac{Z_s^*}{2}$, $Z_s^*=2\beta Q^*\frac{K-s\sigma^2}{\sigma^2/2-2s^2}$, where $\sigma^2=E(\tilde{\theta}^2)$, $K=\int_0^{\Theta}\theta^3dG(\theta)$.

Proof: According to Equations (3.3), (3.5), and the quadratic utility function, we have

$$E(\tilde{\Pi}^*\tilde{\theta})=0 \tag{9}$$

$$E\{\tilde{\Pi}^*[s-(-\tilde{\theta})^+]\}=0 \tag{10}$$

where, $\tilde{\Pi}^*$ is the special case of missing commodity futures and option of Equation (1),

$$\tilde{\Pi}^*=(\bar{S}+\tilde{\theta})(\bar{P}+\beta\tilde{\theta})Q^*-\tilde{\theta}H_s^*+[s-(-\tilde{\theta})^+]Z_s^*-C(Q^*) \tag{11}$$

By calculating directly toward Equation (9), we have

$$\int_{-\Theta}^{0}[\theta(\bar{S}+\theta)(\bar{P}+\beta\theta)Q^*-\theta^2H_s^*+\theta(s+\theta)Z_s^*-C(Q^*)\theta]dG(\theta)+\int_0^{\Theta}[\theta(\bar{S}+\theta)(\bar{P}+\beta\theta)Q^*-\theta^2H_s^*+\theta sZ_s^*-C(Q^*)\theta]dG(\theta)=0 \tag{12}$$

Since $\tilde{\theta}$ is symmetrically distributed over support $[-\Theta,\Theta]$ with cumulative distribution function G, then Equation (12) equals to $\int_0^{\Theta}[(2\beta\bar{S}\theta^2+2\bar{P}\theta^2)Q^*-2\theta^2H_s^*+\theta^2Z_s^*]dG(\theta)=0$. It is easy to yield

$$(2\bar{S}\beta+2\bar{P})Q^*-2H_s^*+Z_s^*=0$$

According to the result of proposition 4, the first part of proposition 4 is solved easily as

$$H_s^*=(\bar{P}+\bar{S}\beta)Q^*+\frac{Z_s^*}{2}=(\alpha+2\bar{S}\beta)Q^*+\frac{Z_s^*}{2}$$

The similar process to proof the second part of proposition 3. We divided it into three steps. The first step is to calculate

$$\begin{aligned}E(\tilde{\Pi}^*)&=\int_{-\Theta}^{0}[(\bar{S}+\theta)(\bar{P}+\beta\theta)Q^*-\theta H_s^*+(s+\theta)Z_s^*-C(Q^*)]dG(\theta)+\int_0^{\Theta}[(\bar{S}+\theta)(\bar{P}+\beta\theta)Q^*-\theta H_s^*+sZ_s^*-C(Q^*)]dG(\theta)\\&=\int_0^{\Theta}[2\bar{S}\,\bar{P}Q^*+2\beta\theta^2Q^*+2sZ_s^*-\theta Z_s^*-2C(Q^*)]dG(\theta)\\&=(\bar{S}\,\bar{P}+\beta\sigma^2)Q^*-C(Q^*)\end{aligned} \tag{13}$$

The second step is to calculate

$$E[\tilde{\Pi}^*(-\theta)^+]=\left(s\bar{S}\,\bar{P}-\frac{1}{2}\beta\sigma^2\bar{S}-\frac{1}{2}\bar{P}\sigma^2+\beta K\right)Q^*+\frac{1}{2}\sigma^2H_s^*+\left(s^2-\frac{1}{2}\sigma^2\right)Z_s^*-sC(Q^*) \tag{14}$$

At last, submitting Equation (13) and H_s^* in the given result into Equation (10), we have $Z_s^*=2\beta Q^*\frac{K-s\sigma^2}{\sigma^2/2-2s^2}$.

Proposition 5. Suppose that the futures and options markets are unbiased. If the firm has a quadratic utility function and if $\tilde{S}$ is symmetrically distributed. When both currency and option for currency and commodity markets are present, then under the condition of Equations (9) and (10), we have:

(a) If $K = s\sigma^2$ and $4s^2 \neq \sigma^2$, then commodity and currency options are redundant, and $H_p^* < Q^*$ if $H_s^* < \bar{P}Q^*$.

(b) $K=s\sigma^2$ and $4s^2=\sigma^2$, the positions are satisfied as

$$(\beta\bar{S} + \bar{P})Q^* - \bar{S}\beta H_p^* - H_s^* + \frac{1}{2}\bar{S}\beta Z_p^* + \frac{1}{2}Z_s^* = 0$$

(c) If $K\neq s\sigma^2$ and $4s^2=\sigma^2$, then commodity and currency futures are redundant, i.e. $H_p^* = 0$, $Z_p^* = 0$ and $\bar{P}Q^* - H_s^* + \frac{1}{2}Z_s^* = 0$.

(d) If $K\neq s\sigma^2$ and $4s^2\neq\sigma^2$, then the positions are satisfied as the following equations:

$$(\beta\bar{S} + \bar{P})Q^* - \bar{S}\beta H_p^* - H_s^* + \left(\frac{1}{2}\bar{S}\beta + p + \frac{\beta K}{\sigma^2}\right)Z_p^* + \frac{1}{2}Z_s^* = 0$$

and

$$\left(\beta\bar{S} + \bar{P} + 2s\beta - 2\frac{\beta K}{\sigma^2}\right)Q^* - \left(2s\beta + \bar{S}\beta - 2\frac{\beta K}{\sigma^2}\right)H_p^* - H_s^* + 2\frac{\bar{S}s^2\beta}{\sigma^2}Z_p^* - \left(2\frac{s^2}{\sigma^2} - 1\right)Z_s^* = 0$$

Proof: We still begin with the equivalent formulation of Equation (1)

$$\tilde{\Pi} = (\bar{S} + \tilde{\theta})(\bar{P} + \beta\tilde{\theta})Q^* - \left(\bar{S} + \tilde{\theta}\right)\beta\tilde{\theta}H_p^* - \tilde{\theta}H_s^* + (\bar{S} + \tilde{\theta})[p + \beta(\tilde{\theta})^+]Z_p^* + [s - (-\tilde{\theta})^+]Z_s^* - C(Q^*)$$

Equation (3.3) is equal to $E(\tilde{\Pi}^*\tilde{\theta}) = 0$, submit the above equation to it, we have

$$(\bar{S}\beta + \bar{P})\sigma^2 Q^* - \bar{S}\beta\sigma^2 H_p^* - \sigma^2 H_s^* + \left(\frac{1}{2}\bar{S}\beta\sigma^2 + p\sigma^2 + \beta K\right)Z_p^* + \frac{1}{2}\sigma^2 Z_s^* = 0$$

Thus, we have the first important result as

$$(\beta\bar{S} + \bar{P})Q^* - \bar{S}\beta H_p^* - H_s^* + \left(\frac{1}{2}\bar{S}\beta + p + \frac{\beta K}{\sigma^2}\right)Z_p^* + \frac{1}{2}Z_s^* = 0 \quad (15)$$

Equation (3.5) is equal to $E[\tilde{\Pi}^*(-\tilde{\theta})^+] - sE(\tilde{\Pi}^*) = 0$, submit the above equation to it, we have

$$E(\tilde{\Pi}^*) = (\bar{S}\,\bar{P} + \beta\sigma^2)Q^* - \beta\sigma^2 H_p^* + \left(\bar{S}p + \bar{S}s\beta + \frac{\beta}{2}\sigma^2\right)Z_p^* - C(Q^*)$$

$$E[\tilde{\Pi}^*(-\theta)^+] = \left(\bar{S}\,\bar{P}s - \frac{1}{2}\beta\sigma^2\bar{S} - \frac{1}{2}\bar{P}\sigma^2 + \beta K\right)Q^* + \left(\frac{1}{2}\bar{S}\beta\sigma^2 - \beta K\right)H_p^* + \frac{1}{2}\sigma^2 H_s^* + \left(\bar{S}ps - \frac{1}{2}p\sigma^2\right)Z_p^* + \left(s^2 - \frac{1}{2}\sigma^2\right)Z_s^* - sC(Q^*)$$

Thus, we have the second result as

$$\left(\beta\bar{S} + \bar{P} + 2s\beta - 2\frac{\beta K}{\sigma^2}\right)Q^* - \left(2s\beta + \bar{S}\beta - 2\frac{\beta K}{\sigma^2}\right)H_p^* - H_s^* + 2\frac{\bar{S}s^2\beta}{\sigma^2}Z_p^* - \left(2\frac{s^2}{\sigma^2} - 1\right)Z_s^* = 0 \quad (16)$$

If $K=s\sigma^2$, then Equations (15) and (16) are reduced as $\bar{S}\beta Z_p^* + Z_s^* = 0$ and $2\bar{S}s^2\beta Z_p^* - (2s^2 - \sigma^2)Z_s^* = 0$. Furthermore, when $4s^2\neq\sigma^2$, it yields $Z^*_p=Z^*_s=0$, i.e. the commodity option and currency option are redundant. And the positions of commodity and currency futures are satisfied $(\beta\bar{S} + \bar{P})Q^* - \bar{S}\beta H_p^* - H_s^* = 0$, which is equal to $\bar{S}\beta(Q^* - H_p^*) + \bar{P}Q^* - H_s^* = 0$. So, $H_p^* < Q^*$ if and only if $H_s^* < \bar{P}Q^*$.

When $K=s\sigma^2$ and $4s^2=\sigma^2$, the positions are satisfied as

$$(\beta\bar{S} + \bar{P})Q^* - \bar{S}\beta H_p^* - H_s^* + \frac{1}{2}\bar{S}\beta Z_p^* + \frac{1}{2}Z_s^* = 0$$

If $K\neq s\sigma^2$, then according to Equations(15) and (16), we have

$$Q^* - H_p^* + \frac{4\bar{S}s^2 - \bar{S}\sigma^2 + 4s\sigma^2 - 4K}{4(s\sigma^2 - K)}Z_p^* - \frac{4s^2 - \sigma^2}{4(s\sigma^2 - K)}\frac{Z_s^*}{\beta} = 0$$

Furthermore, if $4s^2=\sigma^2$, the positions are satisfied as $Q^* - H_p^* + Z_p^* = 0$ and $Q^* - H_p^* + \frac{1}{2}Z_p^* = 0$. As such $H_p^* = Q^*$, $Z_p^* = 0$. $\bar{P}Q^* - H_s^* + \frac{1}{2}Z_s^* = 0$. If $4s^2\neq\sigma^2$, the positions are satisfied as Equations (15) and (16).

Next, we shall evaluate the potential usefulness of hedging with currency and commodity futures and options. Given that the futures and option markets are unbiasedness, the firm's utility is the quadratic utility function, so the firm's expected utility is a linear function of the variance. In other words, the hedge effectiveness of the optimal positions as such that can be gauged by the difference between the variances with single spot exchange rate futures and option and with both futures and option for currency and commodity.

To compare the performance of adopting commodity futures and option with currency for hedging purpose, we need to estimate the variances of the two different cases with and without commodity futures and option. Assume that $\tilde{\theta}$ is normally distributed with mean zero and variance 1, the rest parameters are $Q^*=1$, $\bar{S}=1$, $\bar{P}=1.5$.

Then we have $s=\int_0^\infty \theta \frac{e^{-\theta^2/2}}{\sqrt{2\pi}}d\theta=\frac{1}{\sqrt{2\pi}}$ and $K=\int_0^\infty \theta^3 \frac{e^{-\theta^2/2}}{\sqrt{2\pi}}d\theta=\frac{\sqrt{2}}{\sqrt{\pi}}$. For simply, we neglected the term of $C(Q^*)$, which has no effect on the compared results. When the market is incomplete without commodity futures and options, only with currency futures and options, the expected profit is $E_1=E[(\bar{S}+\tilde{\theta})(\bar{P}+\beta\tilde{\theta})]Q^*$. The variance is

$$V_1=Var\{(\bar{S}+\tilde{\theta})(\bar{P}+\beta\tilde{\theta})Q^*-\tilde{\theta}H_s^*+[s-(-\tilde{\theta})^+]Z_s^*\}$$

When the market is complete with commodity and currency futures and options, the expected profit is

$$E_2=E[(\bar{S}+\tilde{\theta})(\bar{P}+\beta\tilde{\theta})]Q^*-\beta E[(\bar{S}+\tilde{\theta})\tilde{\theta}]H_p^*+$$

$E[(\bar{S}+\tilde{\theta})(p+\beta\tilde{\theta}^+)]Z_p^*$, and the variance is

$$V_2=Var\{(\bar{S}+\tilde{\theta})(\bar{P}+\beta\tilde{\theta})Q^*-\beta\tilde{\theta}(\bar{S}+\tilde{\theta})H_p^*-\tilde{\theta}H_s^*+$$
$$(\bar{S}+\tilde{\theta})(p+\beta\tilde{\theta}^+)Z_p^*+[s-(-\tilde{\theta})^+]Z_s^*\}$$

There are some comparison results:

(1) Comparing E_1 and E_2, we found that for an export firm, it has $E_1 \le E_2$ if he sells commodity put options. It means adding commodity futures and option may increase the hedging profit.

(2) Since it includes four decision variables in Equation (14) and Equation (15), it is impossible to give the explicit expressions for them. In order to discuss the hedging results, we supposed the positions of currency futures and option were as the same proportion of ones only existed currency derivatives market.

As the numerical example result shows, using commodity futures and option integrated with currency futures and option for both price and exchange rate risk hedging, the hedging efficiency is enhanced by higher propositions compared to the case of only using currency futures and option. In fact, the improvements in hedge effectiveness can be substantial with different correlation coefficient between commodity price and exchange rate.

5 Conclusions

This paper generalized the existing results on decision rules for optimal agricultural export commodity price and currency hedging in the presence both of commodity and currency futures and options and examined the optimal hedging decision. Given that unbiased commodity and currency futures markets, the firm's optimal output level satisfies that the marginal cost equal to the price in the home currency. Options played no role as a hedging instrument only under restrictive conditions of independent between output price and spot exchange rates. If the price risk is negatively correlated with the exchange rate risk and if the firm is prudent, we have shown that short put option position for commodity option while long put currency option is part of the firm's optimal hedging strategy with under-hedge for commodity and currency futures. It gives the explicit positions under the case of only entrance to currency futures and option with the condition that the firm has a quadratic utility function and the exchange spot is symmetrically, which is called as a benchmark. Then, we discussed the hedging strategy of different situations under the case two entrances both to commodity and currency futures and option market. Furthermore, some comparing results were presented relative to the benchmark for discussing the hedging efficiency. It found that if the investor improved propositions of the currency futures and option positions compared to the benchmark case, the firm would have benefits from the strategy of hedging both with commodity and currency futures and options. We thus offered new insights into the strategy of hedging in the context of multiple derivative instruments.

Acknowledgements

This paper was supported by Hunan Provincial Natural Science Foundation of China (No. 2016JJ6046); Hunan Provincial Social Science Foundation of China (No. 16YBA220).

[References]

[1] Adam-Müller, A. F. A. 2004. Export and hedging decisions under revenue and exchange rate risk: a note. *European Economic Review*, 41(7): 1421–1426.

[2] Adam-Müller, A. F. A. 2011. Cross hedging under multiplicative basis risk. *Journal of Banking & Finance*, 35(11): 2956–2964.

[3] Allayannis, G., and E. Ofek. 2001. Exchange rate exposure, hedging, and the use of foreign currency derivatives. *Journal of international Money Finance*, 20(2): 273–296.

[4] Broll, U., and B. Eckwert.1998. Export and hedging decision with state-dependent utility. *International Review of Economics and Finance*, 7(3): 247–253.

[5] Broll, U., and B. Eckwert. 2000. Market structure and multiperiod hedging. *International Review of Economics and Finance*, 9(4): 291–298.

[6] Broll, U., and I. Zilcha. 1991. Exchange rate uncertainty, futures markets and the multinational firm. *European Economic Review*, 36(4): 815–826.

[7] Broll, U., and J. E. Wahl. 1996. Imperfect hedging and export production. *Southern Economic Journal*, 62(3): 667–674.

[8] Broll, U. F., and J. E. Wahl. 1992. Hedging with synthetics, foreign-exchange forwards, and export decision. *Journal of Futures Markets*, 12(5): 511–517.

[9] Chang, E. C., and K. P. Wong. 2003. Cross-hedging with currency options and futures. *Journal of Financial and Quantitative Analysis*, 38(3): 555–574.

[10] Cimoli, M., G. T. Lima, and G. Porcile. 2016. Input substitution, export pricing, and exchange rate policy. *Structural Change and Economic Dynamics*, 37: 13–26.

[11] Devereux, M. B., and J. Yetman. 2010. Price adjustment and exchange rate pass-through. *Journal of International Money Finance*, 29(1): 181–200.

[12] Holthausen, D. M. 1992. Hedging and the competitive firm under price uncertainty. *American Economic Review*, 69(5): 989–995.

[13] Kimball, M. S. 1989. Precautionary saving in the small and in the large. *Nber Working Papers*, 58(1): 53–73.

[14] Kimball, M. S. 1993. Standard risk aversion. *Econometrica*, 61(3): 589-611.

[15] Lien, D., and Y. K. Tse. 2001. Hedging downside risk: futures vs. options. *International Review of Economics and Finance*, 10(2): 159–169.

[16] Machnes, Y. 1992. Production decisions in the presence of options. *International Review of Economics and Finance*, 1(4): 341–345.

[17] Moschini, G., and H. Lapan. 1995. The hedging role of options and futures under joint price, basis, and production risk. *International Economic Review*, 36(4): 1025–1049.

[18] Mun, K. C., and G. E. Morgan. 2003. Bank foreign exchange and interest rate risk management: simultaneous versus separate hedging strategies. *Journal of Financial Intermediation*, 12(3): 277–297.

[19] Shi, K., J. Y. Xu, and X. P. Yin. 2015. Input substitution, export pricing, and exchange rate policy. *Journal of International Money and Finance*, 51: 26–46.

[20] Viaene, J. M., and I. Zilcha. 1998. The behavior of competitive exporting firms under multiple uncertainty. *International Economic Review*, 39(3): 591–609.

[21] Wong, K. P. 1997. Currency hedging with options and futures. *European Economic Review*, 47(5): 833–839.

[22] Wong, K. P. 2001. Currency hedging for export-flexible firms. *International Economic Journal*, 15(1): 165–174.

[23] Wong, K. P. 2002. Export-flexible firms and forward markets. *International Economic Journal*, 16(3): 81–95.

[24] Wong, K. P. 2002. Production decisions in the presence of options: a note. *International Review of Economics and Finance*, 11(1): 17–25.

[25] Wong, K. P. 2013. International trade and hedging under joint price and exchange rate uncertainty. *International Review of Economics & Finance*, 27(2): 160–170.

Mechanical properties and compression damage simulation by finite element for kiwifruit

Tian Kunpeng, Shen Cheng, Li Xianwang, Huang Jicheng, Chen Qiaomin, Zhang Bin*

(*Nanjing Research Institute for Agricultural Mechanization, Ministry of Agriculture, 210014 China*)

Abstract: In order to reduce the mechanical damage of kiwifruit in the process of picking, packaging and transporting and to understand the mechanism of kiwifruit damage, the mechanical properties of kiwifruit peel, flesh and placenta were tested by universal testing machine. The average of elastic modulus, tensile strength and tensile force of kiwifruit peel's axial and radial tensile were measured, which are 12.04 MPa, 1.26 MPa, 5.27 N and 12.85 MPa, 1.21 MPa, 5.28 N, respectively. The average of elastic modulus, tensile strength and tensile force of kiwifruit flesh's axial and radial compression were also measured, which are 3.96, 0.70, 0.42 and 1.71, 0.45, 0.33 MPa, respectively. The average of elastic modulus, tensile strength and tensile force of kiwifruit flesh's axial and radial compression were also determined, which are 5.33, 2.24, 1.63 and 4.32, 1.75, 1.54 MPa, respectively. Based on the geometric structure and mechanical properties of the components, the finite element model of the kiwifruit was established. The stress distribution and variation rule of the whole fruit under compressive load were simulated and analyzed by using Workbench ANSYS software. The results showed that when the kiwifruit was subjected to continuous radial compression and the compressive strain reached 0.060, the stresses in the contact area between the seed chamber and the placenta of kiwifruit first reached its stress yield limit, and when the kiwifruit is subjected to axial compression, the compressive strain reaches 0.068, the stress in the end region of the placenta is first reached the yield stress limit. Finally, the whole fruit of kiwi was tested by plate compression test, the results showed that under different compression directions, the stress-strain curves of whole kiwifruit's actual compression and finite element simulation compression were similar, and the simulation by finite element for kiwifruit was feasible.

Keywords: kiwifruit, mechanical properties, mechanical damage, stress-strain curve, finite element simulation, compression test

Citation: Tian, K. P., C. Shen, X. W. Li, J. C. Huang, Q. M. Chen, and B. Zhang. 2017. Mechanical properties and compression damage simulation by finite element for kiwifruit. International Agricultural Engineering Journal, 26(4): 193–203.

1 Introduction

Fresh, tender and nutritious, the kiwifruit is one of the most characteristic fruit in China (Xu et al., 2003). Owing to the soft texture, the kiwifruit will suffer mechanical compression damage easily in various kinds including picking, packaging, transporting, and marketing. The damaged fruit will deteriorate and rot rapidly, which might seriously influence the fruit quality and economic benefit (Chen et al., 2011 b; Ortiz et al., 2011; Ma et al., 2012; Li et al., 2012). The study on mechanical properties of the kiwifruit will help to understand the compression damage mechanism of kiwifruit, and provide references for reducing mechanical damages of kiwifruit in picking, packaging, transporting, and marketing processes and for developing production equipment.

In recent years, there were many studies on mechanical properties of common fruits and vegetables like citrus, pear, grape, and tomato, and the research on kiwifruit was also involved (Singh et al., 2006; Goyal et al., 2007; Kılıçkan et al., 2008; Pallottion et al., 2011; Sirisomboon et al., 2007; Chen et al., 2011 a; Wu et al., 2012; Li, 2014; Liu et al., 2016; Lu et al., 2016). In foreign countries, Talens P measured the physical and compressive mechanical properties of kiwifruit before

Received date: 2017-05-07 **Accepted date:** 2017-09-12

* **Corresponding author: Zhang Bin,** Associate Professor of Nanjing Research Institute for Agricultural Mechanization, Ministry of Agriculture, 210014 China. Email: xtsset@hotmail.com. Tel: +86-25-84346291, Fax: +84-25-84346291.

and after refrigeration, and determined the storage temperature and pressure to maintain the optimal physical and mechanical properties of kiwifruit after freezing and thawing (Talens et al., 2002). Besides, Razavi studied physical and mechanical properties of "Hayward" kiwifruit, and measured parameters like outline dimension, volume, density, static friction coefficient, compactness, and adhesive power of kiwifruit, providing important mechanical parameters for the design of mechanical equipment in the production link of kiwifruit (Razavi et al., 2007). In China, Ji et al. (2010) conducted a compression test on the whole kiwifruit, analyzed the mechanical behaviors of kiwifruit in the compression process, and offered the creep-time curve. Meanwhile, Chen et al. (2012) measured the anti-extrusion property and other relevant physical parameters of kiwifruit, providing a parameter reference for the end effector design of kiwifruit picking robot.

Through the induction analysis, we can find that all the above researches were aimed at mechanical properties of the whole kiwifruit, and the damage studied was restricted to apparent damage that can be observed by naked eyes, but there was no corresponding study on the internal stress variation and damage law of kiwifruit under extrusion load. The kiwifruit flesh is more delicate than peel, so the internal part might be damaged earlier than the surface under the extrusion of external force, which will result in qualitative change of flesh. It is not easy to measure the internal stress distribution and variation of kiwifruit with conventional methods. Therefore, the finite element simulation method will be used in this paper to analyze the compression damage mechanism of kiwifruit, so as to find an effective solution for reducing the compression damage in the process of kiwifruit production.

2 Test on mechanical properties of kiwifruit

2.1 Test materials

The kiwifruits used in this test were China's major kiwifruit variety "Jinkui" kiwifruit. Fresh damage-free kiwifruits with uniform growth conditions at the mature stage were selected as test specimens. According to the measurement result of moisture content detector, the moisture content of kiwifruits is 83.3%-85.5%. The outline of kiwifruits approximate ellipsoid, and the axial size (i.e. the connection line direction of carpopodium and umbilical region) is longer than the radial size. It is gained via vernier caliper that the axial size and radial size of kiwifruits are 53.1-62.7 mm and 40.8-51.6 mm respectively. The kiwifruits were cut open along the axial direction and radial direction respectively, as shown in Figure 1. According to the figure, the middle part of kiwifruit is placenta, and seed chamber is located between placenta and flesh. The seed chamber is filled with seeds and mucilage coating the seeds.

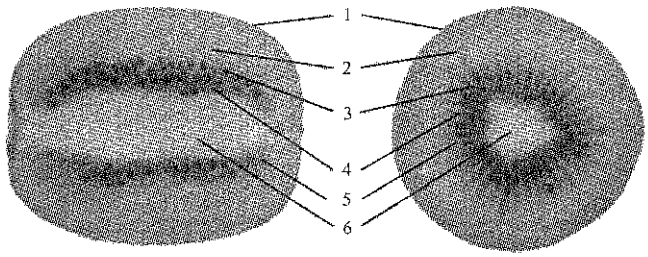

a. Axial section view b. Radial section view

1. Peel 2. Flesh 3. Seeds 4. Matrix mucilage 5. Seed room 6. Placenta

Figure 1 Internal structure of kiwifruit

2.2 Test instruments and equipment

The test on compressive mechanical properties of kiwifruits should be conducted via universal testing machine, and SUNS UTM6503 microprocessor control electronic universal testing machine was adopted in this test. The power range of this universal testing machine is 100 N-5 KN, the accuracy grade is grade 0.5, the indication error of test force is within ±0.5%, the adjustable range of loading speed is 0.001-500 mm min^{-1}, the displacement resolution is 0.04 μm, and the indication error of displacement is within ±0.2%. Other auxiliary instruments and tools needed in the test include vernier caliper, calibrated scale, moisture content detector, knife, etc.

2.3 Test methods

2.3.1 Tensile test on kiwifruit peel

In order to analyze the similarities and differences between axial and radial mechanical properties of kiwifruit peel, the kiwifruit peel was made into axial and radial tensile specimens respectively. When axial tensile specimens were made, a gel pen was used to mark out several equally distributed longitudes on the kiwifruit

peel along the axial direction, and the maximum interval between adjacent longitudes was 15 mm. Later the art knife was used to cut the kiwifruit into slices with the same size along the longitudes, and then the flesh was removed from the peel with art knife (the flesh was standby). Finally, the peel was made into 30 specimens with the width of 10±0.8 mm and length of 45±2 mm. The making of radial tensile specimens was similar to that of axial tensile specimens. Firstly, a gel pen was used to draw latitudes with the interval of 12 mm along the radial direction of kiwifruit, and the flesh kiwifruit flesh was removed from the peel after ring incision along the latitudes (the flesh was standby). Similarly, the peel was made into 30 specimens with the width of 10±0.8 mm and length of 45±2 mm. According to the measurement results of vernier caliper, the peel thickness is 0.38-0.46 mm. The kiwifruit peel is relatively thin, so the universal testing machine fixture with rubber gasket was used to clamp both ends of the specimens for stretching, so as to prevent the peel from being damaged. During the test, the loading speed was set as 5 mm min^{-1}. Peels rupturing in the middle between upper and lower chucks were selected as effective tensile specimens, and the universal testing machine was used to take down corresponding stress-strain curves and test data.

2.3.2 Compression test on kiwifruit flesh

The remaining flesh of the peel tensile test produced in the previous section was cut along the radial and axial direction, the flesh was made into axial compression specimens (length 10±1 mm; width 7±0.6 mm; height 10±1 mm) and radial compression specimens (length 10±1 mm; width 10±1 mm; height 7±0.6 mm). Each stick was divided into 4 compression specimens. The two kinds of specimens were placed in the center of compression test bed of universal testing machine along the height direction. The space between seaming chuck and specimen was finely adjusted through displacement adjustment button, and the compressing force and displacement were reset when the seaming chuck touched the upper surface of specimen slightly. At this time, the original gauge length of universal testing machine along the compression direction was the specimen height. The loading speed of universal testing machine was set as 5 mm min^{-1}, and the load button was initiated. When the flesh specimens underwent compression failure, loading was stopped if the stress value decreased to the minimum and began to increase gradually. Corresponding stress-strain curves and test data were taken down via the universal testing machine.

2.3.3 Compression test on kiwifruit placenta

In order to measure the axial and radial compression characteristics of kiwifruit placenta, the kiwifruit placenta was made into 30 axial and radial compression specimens (length 10±1 mm; width 10±1 mm; height 10±1 mm) respectively. The compression tests were conducted on placenta according to the test methods for kiwifruit flesh in the above section, and corresponding stress-strain curves and test data were taken down via the universal testing machine.

2.4 Basis of solving mechanical property parameters

When peel tensile tests and flesh compression tests were conducted for kiwifruits, interactional force will be generated between various parts in the peel and flesh. The internal force assumed by the peel and flesh in unit area is called stress, and its formula is as follows:

$$\sigma=F/S \quad (1)$$

where, σ means the stress, N mm^{-2}; F indicates the tensile force (pressure), N; S denotes the cross-sectional area of the material at the tensile (compression) direction, mm^2.

Deformation will happen to the peel and flesh under external force, the deformation degree is called strain, and its formula is as follows:

$$\varepsilon=\Delta L/L \quad (2)$$

where, ε means the tensile (compression) strain capacity, %; ΔL indicates the length after deformation, mm; L denotes the original gauge length before deformation, mm.

At the elastic deformation stage, the material stress is in direct proportion to strain, and the proportional coefficient is called elastic modulus, whose formula is as follows:

$$E=\sigma/\varepsilon=FL/S\Delta L \quad (3)$$

where, E means the elastic modulus of the material, N mm^{-2} or MPa.

According to the constitutive relation of material, elastic modulus and shear modulus have the following

relation (Shen et al., 2013):

$$G=E/2(1+\mu) \quad (4)$$

where, G indicates the shear modulus, N mm^{-2} or MPa; μ is Poisson's ratio.

2.5 Results and analysis

2.5.1 Results and analysis of tensile test on kiwifruit peel

The comparison before and after fracture of the kiwifruit peel is shown in Figure 2. The tensile stress-strain curves gained were presented in Figure 3, the test data are shown in Table 1.

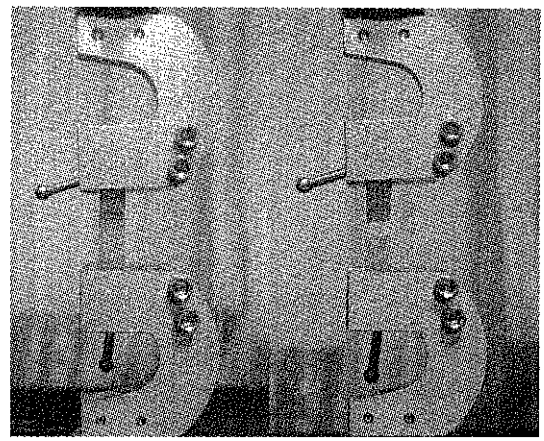

Figure 2 Figures of kiwifruit peel before and after fracture

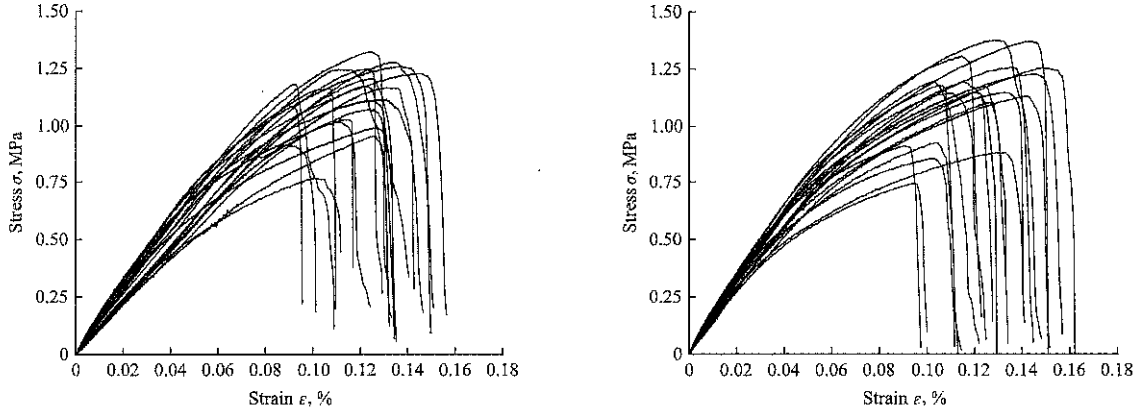

a. Axial tension b. Radial tension

Figure 3 Tensile stress-strain curves of the kiwifruit peel

Table 1 Tensile test data of kiwifruit peel

Loading direction	No.	L_d, mm	L_h, mm	L_o, mm	E_t, MPa	R_m, MPa	F_m, N	Loading direction	No.	L_d, mm	L_h, mm	L_o, mm	E_t, MPa	R_m, MPa	F_m, N
Axial direction	1	10.20	0.42	25.62	13.15	1.21	5.20	Radial direction	1	10.26	0.40	34.12	12.98	0.95	3.91
	2	10.12	0.40	27.08	11.90	1.37	5.40		2	10.80	0.44	34.30	14.44	1.12	5.34
	3	10.50	0.42	31.40	11.28	1.30	5.59		3	10.54	0.40	36.00	11.65	1.04	4.39
	4	10.04	0.40	32.06	10.73	1.30	5.19		4	10.00	0.46	30.82	13.62	0.99	4.55
	5	10.36	0.38	26.12	10.21	1.15	4.73		5	10.02	0.40	30.28	11.51	1.32	5.31
	6	10.40	0.40	26.48	12.79	1.38	5.73		6	10.06	0.48	30.34	13.79	1.30	6.30
	7	10.16	0.44	26.94	13.63	1.31	5.44		7	10.12	0.42	35.16	12.12	1.26	5.37
	8	10.00	0.40	26.46	13.48	1.46	5.82		8	10.40	0.46	35.20	12.62	1.12	5.36
	9	10.60	0.40	26.50	10.64	1.41	6.12		9	10.36	0.38	29.64	13.85	1.46	5.74
	10	10.52	0.40	26.10	12.56	1.04	4.38		10	10.50	0.40	33.00	14.39	1.39	5.80
	11	10.02	0.44	26.32	12.04	1.28	5.49		11	10.18	0.38	29.82	11.42	1.25	3.82
	12	9.82	0.40	24.56	10.44	1.00	4.02		12	10.00	0.42	27.60	11.43	1.16	4.90
	13	10.06	0.38	26.70	11.68	1.20	4.81		13	10.04	0.44	27.36	13.08	1.38	6.09
	14	10.10	0.40	24.90	13.93	1.36	5.50		14	10.18	0.42	28.40	13.58	1.36	5.81
	15	10.30	0.40	26.08	13.28	1.26	5.33		15	10.04	0.40	28.52	12.16	1.26	5.04
	16	10.32	0.42	24.58	12.12	1.41	5.30		16	10.24	0.42	32.26	11.72	1.05	5.45
	17	10.28	0.40	26.72	10.03	1.10	5.24		17	10.50	0.40	30.22	12.65	1.37	6.13
	18	10.20	0.42	28.30	13.47	1.32	5.97		18	9.78	0.38	30.64	13.32	1.19	4.80
	19	9.94	0.38	26.74	10.16	1.23	4.75		19	10.16	0.44	31.00	12.37	1.24	5.70
	20	10.06	0.40	30.12	13.30	1.19	5.32		20	10.08	0.40	27.86	14.22	1.03	5.72
	x	10.20	0.41	26.99	12.04	1.26	5.27		x	10.21	0.42	31.13	12.85	1.21	5.28
	S	0.21	0.02	2.08	1.32	0.12	0.52		S	0.24	0.03	2.70	1.03	0.15	0.70

Note: L_d is the specimen width, L_h is the specimen thickness, L_o is the original gauge length, E_t is the elasticity modulus, R_m is the tensile strength, F_m is the tensile force, x is the average value, S is the standard deviation.

According to the axial and radial tensile stress-strain curves of kiwifruit peel in Figure 3, when the kiwifruit peel is under tension, its axial and radial tensile stress-strain curves are nonlinear, and no obvious tensile

bioyield point appears in the stretching process. With the gradual increase of load and deformation, after the tensile limit of peel was reached, the kiwifruit peel was snapped rapidly, and the stress dropped suddenly.

According to the test data in Table 1, the average values of axial tensile elastic modulus, tensile strength, and tensile force of kiwifruit peel are 12.04 MPa, 1.26 MPa, and 5.27 N respectively; the average values of radial tensile elastic modulus, tensile strength, and tensile force of kiwifruit peel are 12.85 MPa, 1.21 MPa, and 5.28 N respectively. By comparing the above test data, we can know that there is a relatively small difference between axial and radial tensile mechanical property parameters of kiwifruit peel, and the kiwifruit peel can be approximately deemed as isotropic material.

2.5.2 Results and analysis of compression test on kiwifruit flesh

The comparison before and after compression of the kiwifruit flesh was shown in Figure 4. The stress-strain curves of kiwifruit flesh gained were presented in Figure 5. The test data were shown in Table 2.

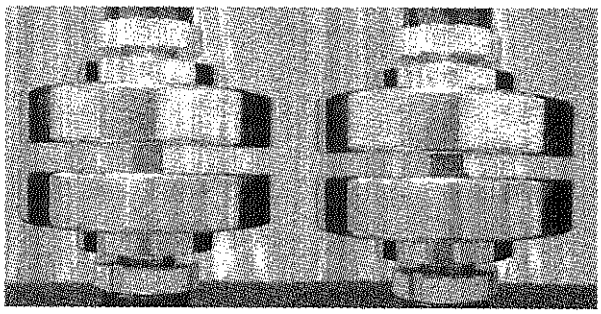

Figure 4 Comparison figures of kiwifruit flesh before and after compression

According to the axial compression stress-strain curves of kiwifruit flesh in Figure 5a, at the initial stage of axial compression, the stress-strain curves present a certain linear variation characteristic, showing that kiwifruit has elastic strain characteristic when bearing tiny compression. With the increase of load, axial compressive stress rises gradually. When the stress reaches the compressive strength of flesh, the original tissue structure of flesh will be destroyed, and the whole flesh will be crushed. Later, with the increase of strain capacity, the stress value decreases gradually, rather than increases. Such phenomenon shows that the flesh has compressive yielding during the later period of compression stage. According to the radial compression stress-strain curves of kiwifruit flesh in Figure 5b, the nonlinear variation characteristic at the initial stage of radial compression is more obvious than that of axial compression, but their general variation trend is similar, showing that the radial direction and axial direction of flesh have similar compression characteristics.

According to the test data in Table 2, the average values of axial compression elastic modulus, upper yield strength, and lower yield strength of kiwifruit flesh are 3.96, 0.70, and 0.42 MPa respectively; the average values of radial compression elastic modulus, upper yield strength, and lower yield strength of kiwifruit flesh are 1.71, 0.45, and 0.33 MPa respectively. By comparing various mechanical property parameters of kiwifruit peel, we can know that there is a relatively big difference between axial and radial compression mechanical property parameters of kiwifruit flesh. By combining with the mechanic constitutive model characteristics of biological materials (Shen et al., 2013), we can deem kiwifruit flesh as orthotropic material.

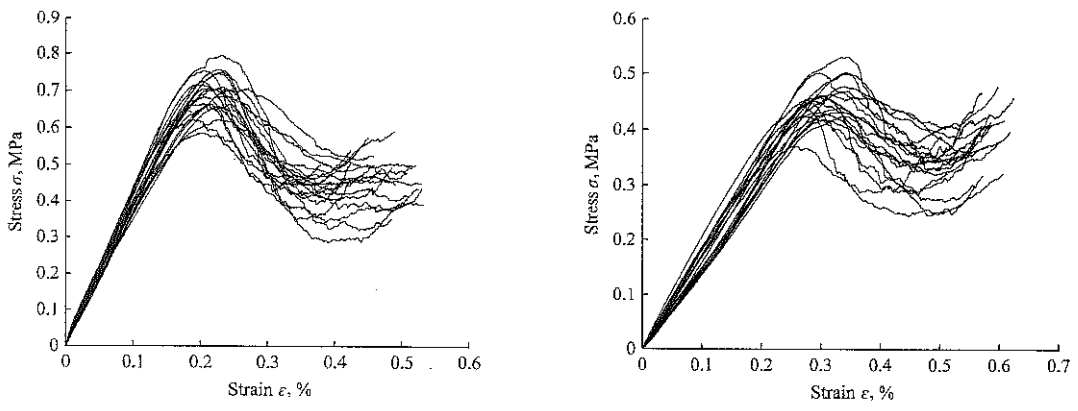

a. Axial tension b. Radial tension

Figure 5 Stress-strain curves of kiwifruit flesh compression

Table 2 Compression test data of kiwifruit flesh

Loading direction	No.	L_1, mm	L_2, mm	L_3, mm	E_c, MPa	*ReH* MPa	*ReL*, MPa	Loading direction	No.	L_1, mm	L_2, mm	L_3, mm	E_c, MPa	*ReH* MPa	*ReL*, MPa
Axial direction	1	10.20	6.60	10.12	3.95	0.73	0.47	Radial direction	1	10.42	10.46	7.00	1.72	0.49	0.43
	2	10.82	7.16	10.10	3.71	0.65	0.42		2	10.52	10.40	6.74	1.92	0.45	0.36
	3	10.02	6.90	9.86	4.27	0.62	0.43		3	10.06	10.32	6.72	1.75	0.50	0.39
	4	9.80	6.72	10.30	3.83	0.70	0.38		4	9.82	9.94	7.08	1.85	0.51	0.34
	5	10.54	6.84	9.52	3.90	0.68	0.36		5	10.40	9.90	6.82	1.63	0.41	0.29
	6	10.32	6.80	10.48	3.54	0.62	0.47		6	10.32	10.08	7.16	1.74	0.42	0.30
	7	10.20	7.36	9.92	4.17	0.72	0.43		7	9.64	10.36	7.30	1.67	0.47	0.39
	8	10.10	7.00	10.40	3.69	0.68	0.47		8	10.20	10.40	7.48	1.74	0.50	0.32
	9	9.72	7.30	9.76	3.92	0.58	0.46		9	10.26	10.00	7.22	1.82	0.43	0.25
	10	10.38	6.76	10.24	3.60	0.70	0.51		10	9.98	9.82	7.14	1.49	0.39	0.30
	11	10.00	7.18	10.06	3.87	0.66	0.41		11	10.44	9.62	6.92	1.51	0.47	0.41
	12	10.26	6.84	10.30	4.22	0.65	0.44		12	10.32	10.38	7.28	1.76	0.40	0.27
	13	10.80	7.42	10.20	4.45	0.72	0.31		13	9.86	9.90	7.00	1.54	0.36	0.24
	14	10.64	7.56	10.22	4.40	0.75	0.48		14	10.00	9.90	6.84	1.48	0.50	0.34
	15	10.38	6.78	9.86	3.89	0.75	0.46		15	9.82	10.02	6.86	1.40	0.44	0.29
	16	10.20	7.06	10.10	4.19	0.74	0.40		16	10.44	10.30	7.20	1.83	0.50	0.39
	17	10.08	7.04	10.32	4.11	0.79	0.32		17	10.52	10.40	7.38	1.98	0.45	0.28
	18	9.86	7.00	9.84	3.72	0.71	0.35		18	10.06	10.00	7.02	1.84	0.48	0.39
	19	10.28	7.26	10.06	4.11	0.76	0.50		19	10.28	10.16	7.10	1.83	0.46	0.37
	20	9.86	7.02	9.92	3.70	0.71	0.42		20	10.44	10.02	6.98	1.83	0.45	0.34
	x	10.22	7.03	10.08	3.96	0.70	0.42		x	10.19	10.12	7.06	1.71	0.45	0.33
	S	0.31	0.26	0.24	0.27	0.05	0.06		S	0.27	0.24	0.21	0.16	0.04	0.06

Note: L_1 is the specimen length, L_2 is the specimen width, L_3 is the specimen thickness, L_o is the original gauge length, E_c is the compression elastic modulus, *ReH* is the upper yield strength, *ReL* is the lower yield strength, x is the average value, S is the standard deviation.

2.5.3 Results and analysis of compression test on placenta

The stress-strain curves of kiwifruit placenta gained were presented in Figure 6. The test data were seen from Table 3.

According to the axial and radial compression stress-strain curves of kiwifruit placenta in Figure 6, at the initial stage of compression, the stress-strain curves present an obvious linear variation characteristic. Afterwards, it is similar to the compression characteristic of flesh. With the increase of load, when the stress reaches the compressive strength of kiwifruit placenta, the original tissue structure of flesh will be destroyed, and the whole placenta will be crushed. Later, with the increase of strain capacity, the stress value decreases gradually, rather than increases, and compressive yielding phenomenon appears.

According to the test data in Table 3, the average values of axial compression elastic modulus, upper yield strength, and lower yield strength of kiwifruit placenta are 5.33, 2.24, and 1.63 MPa respectively; the average values of radial compression elastic modulus, upper yield strength, and lower yield strength of kiwifruit placenta are 4.32, 1.75, and 1.54 MPa respectively. By comparing the above mechanical property parameters, we can know that there is a certain difference between axial and radial compression mechanical property parameters of kiwifruit placenta. By combining with the mechanic constitutive model characteristics of biological materials, we can deem kiwifruit placenta as orthotropic material.

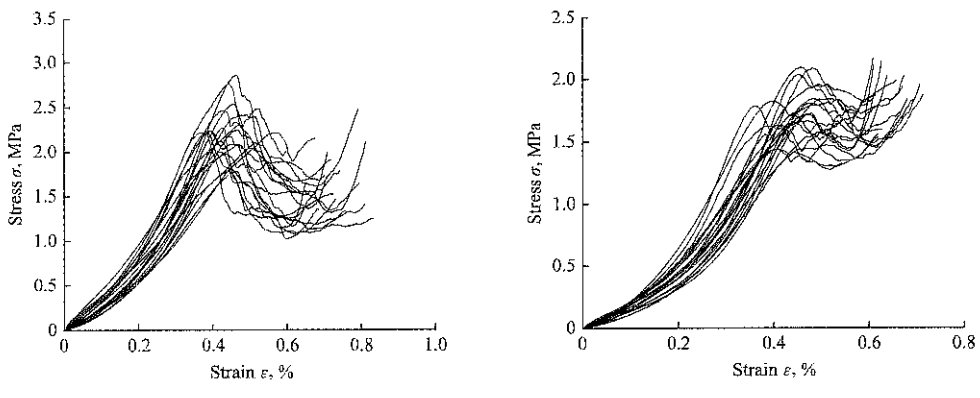

a. Axial tension b. Radial tension

Figure 6 Stress-strain curves of kiwifruit placenta compression

Table 3 Compression test data of kiwifruit placenta

Loading direction	No.	L_1, mm	L_2, mm	L_3, mm	E_c, MPa	*ReH*, MPa	*ReL*, MPa	Loading direction	No.	L_1, mm	L_2, mm	L_3, mm	E_c, MPa	*ReH*, MPa	*ReL*, MPa
Axial direction	1	10.54	9.78	10.14	4.40	2.25	1.67	Radial direction	1	10.50	9.84	10.46	3.95	1.44	1.37
	2	10.45	10.06	10.24	4.31	2.23	2.03		2	10.22	10.06	9.88	4.22	2.09	1.71
	3	10.80	9.64	10.32	4.99	2.23	1.82		3	10.54	10.42	9.60	4.42	1.83	1.76
	4	1.05	9.86	9.96	5.28	2.10	1.26		4	10.60	10.50	9.78	4.38	1.93	1.83
	5	10.70	10.36	10.08	3.55	1.77	1.33		5	10.07	10.05	10.18	3.72	1.63	1.42
	6	10.68	10.12	9.90	6.13	1.78	1.38		6	10.27	10.05	9.50	5.24	1.66	1.62
	7	10.30	10.22	9.96	4.42	2.00	1.65		7	10.34	10.28	9.86	3.82	1.43	1.30
	8	10.06	10.02	9.28	4.51	2.21	2.08		8	10.70	10.04	9.80	4.13	1.81	1.47
	9	10.08	9.98	10.74	5.92	2.22	1.90		9	10.68	10.45	10.00	3.56	1.84	1.55
	10	10.20	10.06	10.44	5.71	2.47	1.68		10	10.26	10.14	10.06	4.03	1.82	1.34
	11	10.40	9.72	10.16	4.81	1.97	1.31		11	10.74	10.20	10.20	3.57	1.44	1.34
	12	10.32	10.00	10.14	5.51	2.53	1.09		12	10.22	9.96	9.86	4.81	1.73	1.51
	13	10.06	9.98	10.08	5.35	2.26	1.11		13	10.88	9.68	9.52	4.06	1.71	1.52
	14	10.80	9.22	9.56	7.47	2.41	1.61		14	10.92	10.54	10.28	3.93	1.78	1.52
	15	9.85	9.70	9.48	4.91	2.09	1.53		15	10.52	10.36	10.03	4.84	1.72	1.51
	16	10.42	10.00	10.48	4.93	2.08	1.77		16	10.76	10.40	8.60	5.02	1.79	1.49
	17	10.46	10.04	10.36	6.99	2.83	1.54		17	10.30	10.14	10.00	4.25	2.04	1.94
	18	10.03	10.00	9.64	5.97	2.75	2.28		18	10.56	10.24	9.50	4.85	2.09	1.69
	19	10.56	10.32	10.06	4.78	2.29	2.04		19	10.82	9.88	10.16	5.48	1.57	1.44
	20	10.22	10.10	9.98	6.58	2.25	1.43		20	10.30	10.22	10.34	4.31	1.63	1.50
	x	10.35	9.96	10.05	5.33	2.24	1.63		x	10.51	10.17	9.88	4.32	1.75	1.54
	S	0.28	0.26	0.36	0.97	0.27	0.33		S	0.25	0.23	0.41	0.54	0.19	0.17

Note: L_1 is the specimen length, L_2 is the specimen width, L_3 is the specimen thickness, L_o is the original gauge length, E_c is the compression elastic modulus, *ReH* is the upper yield strength, *ReL* is the lower yield strength, x is the average value, S is the standard deviation.

3 Compression simulation analysis by finite element

In order to further know about the internal stress distribution and variation rule of the whole kiwifruit under the action of external load, a finite element elastomeric model of kiwifruit compression was established according to the geometric structure and mechanical properties of the components, and compression characteristics and compression damage mechanism of kiwifruit were analyzed via finite element method.

3.1 Kiwifruit model establishment

According to the structural features and dimension parameters of kiwifruit measured above, the three-dimensional structure model of kiwifruit was established via PTC Creo software (as shown in Figure 7). Besides, compression plates were constructed at axial and radial ends of kiwifruit respectively, so as to simulate the actual compression situations of kiwifruit. When the kiwifruit model was established, in order to reduce the operation time of computer, the placenta was simplified into a fusiform shape. Moreover, only seed chamber wall with the same mechanical properties was constructed in the connection part of flesh and placenta, in order to simplify the internal chamfer of seed chamber. In addition, the seed and matrix mucilage coating the seed were omitted.

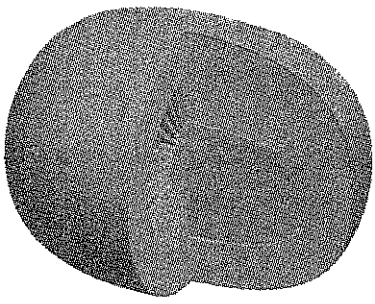

Figure 7 Three-dimensional structure model section of kiwifruit

3.2 Pretreatment setting

The plate compression three-dimensional model of kiwifruit established was imported into the finite element analysis software ANSYS Workbench. According to the mechanical property parameters of kiwifruit peel, flesh, and placenta measured above, the kiwifruit peel was treated as isotropic material, and the average values of axial and radial mechanical property parameters of peel

were taken as mechanical property parameters of kiwifruit peel. Besides, the flesh and placenta were deemed as orthotropic materials, and the mechanical property parameters of flesh and placenta were set according to the actual numerical values gained in the axial and radial compression tests. By referring to Poisson's ratio of other fruits, we set Poisson's ratio of various kiwifruit components as 0.3 (Zhou, 1994). By substituting this value into Formula (4), we obtained axial and radial shear modulus values of peel, flesh, and placenta. Then the peel, flesh, and placenta materials were endowed with values after these parameters were input into Engineering Data. During mesh generation, curvature and approximate size can be used for refinement in key areas in the tetrahedral mesh, and the expansion function can be applied to refine grids near the solid boundary. It is applicable to division of models with complex structures. Therefore, Tetrahedrons (tetrahedral mesh) division method was adopted for the kiwifruit model. The upper and lower platens were regular plates, so sizing (to set the size of unit grid) division method was used, and the grid size was set as 5 mm. In setting of contact type, the upper and lower platens were treated as the target surfaces, to set the contact between peel and flesh as well as flesh and placenta as bonded contact. Moreover, the contact between peel and upper and lower plates was frictional contact, and the friction coefficient was 0.4 (Razavi et al., 2007). When load and constraint were imposed, fixed constraint was imposed on the lower platen, a downward initial velocity of 5 mm min^{-1} was imposed on the upper platen, and the loading time was set as 100 s. The axial and radial compression models after mesh generation were presented in Figure 8.

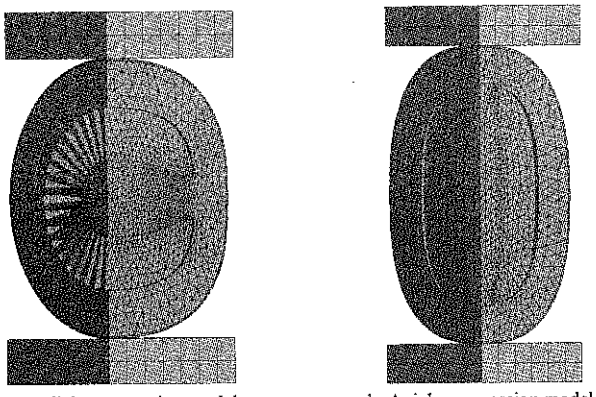

a. Radial compression model b. Axial compression model

Figure 8 Compressed model mesh of kiwifruit

3.3 Analysis on solution results

Figure 9 and Figure 10 respectively show the equivalent stress solutions of radial and axial kiwifruit compression via finite element analysis.

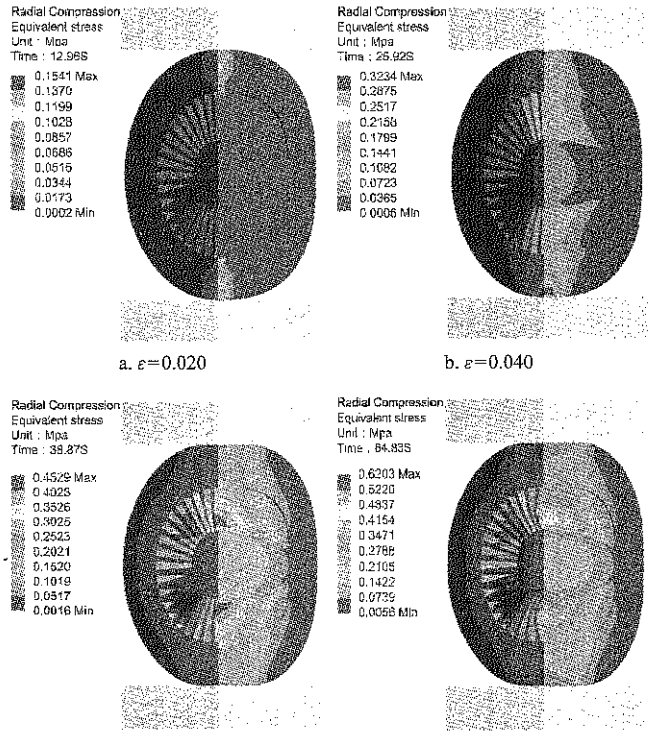

a. ε=0.020 b. ε=0.040

c. ε=0.060 d. ε=0.100

Figure 9 Stress nephogram of radial compression

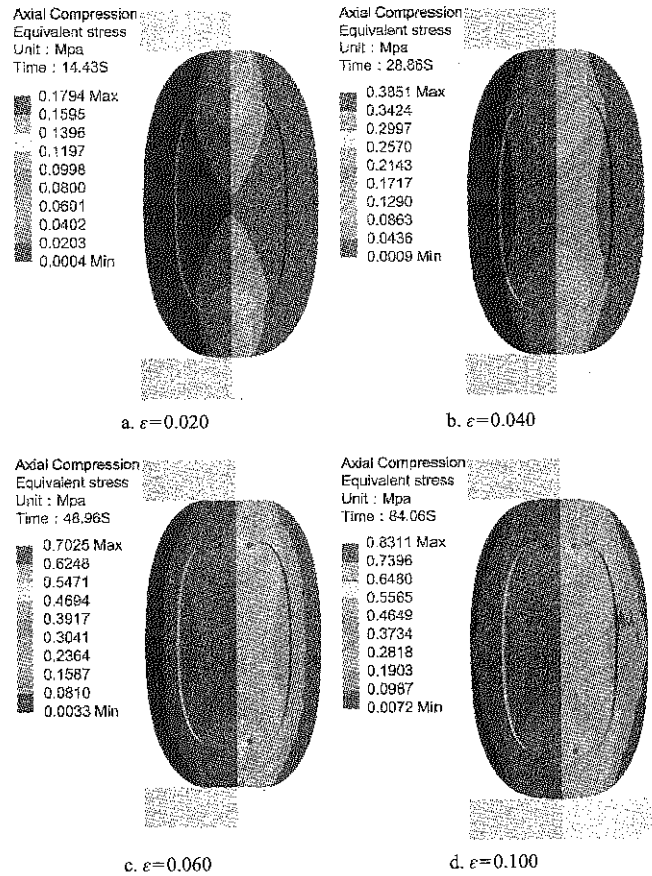

a. ε=0.020 b. ε=0.040

c. ε=0.060 d. ε=0.100

Figure 10 Stress nephogram of axial compression

According to the stress nephograms of radial compression at different moments in Figure 9, at the initial stage of compression, the stress of kiwifruit mainly concentrates upon the contact area between the fruit and upper and lower platens at the compression direction. At this time, the stress of peel and flesh is small. As shown in Figure 9a, when the compressive strain becomes 0.020, the maximum stress appears in the flesh near upper and lower platens, but the maximum stress value is 0.1541 MPa, which is far smaller than the yield stress of peel and flesh. This compressive strain capacity will not damage the kiwifruit.

With the increase of loading time, the compression amount rises gradually. The internal stress assumed by kiwifruit extends from the small scope of contacting the platen to the placenta part. As shown in Figure 9b, when the compressive strain reaches 0.040, the stress in a large scope between platen and placenta has already changed. At this time, the maximum stress still appears in the flesh near the platen, and this maximum stress value is 0.3234 MPa, which is also smaller than yield strength of flesh. It will not damage the kiwifruit.

When loading is continued, the maximum stress assumed by the kiwifruit begins to transfer to the contact area between seed chamber and placenta in the flesh, and the region of stress variation in the flesh also extends to the axial direction and horizontal direction vertical to the compression direction gradually. As shown Figure 9c, when the compressive strain becomes 0.060, the maximum stress appears in the contact area between seed chamber and placenta in the flesh first, and the maximum stress value is 0.4529 MPa, which reaches the ultimate yield strength of flesh, showing that the kiwifruit flesh begins to suffer compression damage under this strain capacity.

Under the action of follow-up loading, the region in which stress near seed chamber in the flesh exceeds the ultimate yield strength of flesh increases gradually, and relatively great folding deformation phenomenon appears. According to Figure 9d, when the compressive strain reaches 0.100, the stress value exceeds the ultimate yield strength in most areas near the seed chamber, showing that the internal part of kiwifruit has suffered compression damage in a large area under this compressive strain capacity.

According to the radial compression process of kiwifruit in Figure 9, when the continuous radial loading and compressive strain capacity reaches 0.060, the stress assumed by the contact area between seed chamber and placenta in the kiwifruit flesh reaches the stress yield limit first. When this part of flesh suffers compression damage, the peel and flesh in other parts still maintain a good condition.

According to the stress nephogram of radial compression at different moments in Figure 10, at the initial stage of compression, the stress of kiwifruit mainly concentrates upon the axial contact area between the fruit and upper and lower platens, and extends to the central zone gradually. At this stage, the stress of peel and flesh is small. As shown in Figure 10a, when the compressive strain becomes 0.020, the maximum stress appears in the flesh contacting upper and lower platens, and its value is 0.1794 MPa, which is far smaller than the yield strength of kiwifruit peel and flesh. This compression amount will not damage the kiwifruit.

With the increase of compression amount, the region of stress variation in the kiwifruit continues to extend toward the central and radial directions, and the maximum stress also transfers from the peel to the internal part of flesh contacting it. According to Figure 10b, when the compressive strain becomes 0.040, the maximum stress appears in the axial contact area between flesh and peel. At this time, the maximum stress value is 0.3851 MPa, which is smaller than yield strength of the flesh.

When loading is continued, the maximum stress assumed by the kiwifruit transfers from the flesh area near the platens to the end of placenta gradually, and the region of stress variation in the kiwifruit extends to the surrounding area along the radial direction. According to Figure 10c, when the compressive strain becomes 0.068, the stress value at the end of placenta reaches the yield strength value of flesh (0.7025 MPa) first, showing that the region at the end of kiwifruit placenta will suffer compression damage first under this compressive strain capacity.

If compression is continued when the yield limit of flesh is reached, the region of exceeding the yield strength of flesh at the end of placenta will expand. According to Figure 10d, when the compressive strain becomes 0.100, the stress value in most regions at the end of placenta has exceeded the yield limit of flesh, showing that the internal part of flesh has suffered compression damage in a large area.

According to the axial compression process of kiwifruit in Figure 10, when the continuous axial loading and compressive strain capacity of kiwifruit reaches 0.068, stress at the end of fruit placenta flesh reaches the yield limit first. When this part of flesh suffers compression damage, the peel and flesh in other parts still maintain a good condition.

4 Verification test on kiwifruit compression

It is not easy to observe the microscopic damage of kiwifruit, so a contrastive analysis was made on the stress-strain curves of kiwifruit gained via finite element analysis and the stress-strain curves obtained in actual compression in this paper, in order to verify the accuracy of finite element model establishment for kiwifruit compression and the feasibility of finite element simulation analysis. It presents the stress-strain curves gained by actual kiwifruit compression and compression simulated by finite element in Figure 11.

According to Figure 11, under different compression directions, the stress-strain curves gained in actual kiwifruit compression and compression simulated by finite element present the similar trend. Under actual compression situations, when the radial compressive strain capacity and axial compressive strain capacity approach 0.060 and 0.068, stress yield phenomenon will happen, which is similar to the results of finite element simulation analysis. Moreover, according to the calculation, the maximum deviation between two groups of data is 13.2%, and the difference is relatively small. The contrast test verifies the feasibility of kiwifruit compression damage simulation via finite element method. Reasons for errors in this test might include error of test data, difference between simple finite element model of kiwifruit and actual shape, and difference of maturity between different individual kiwifruit.

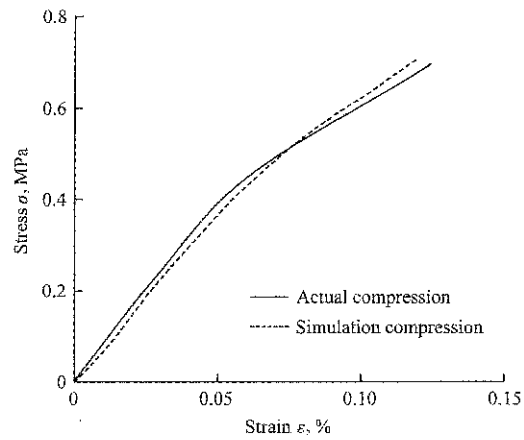

a. Radial compression

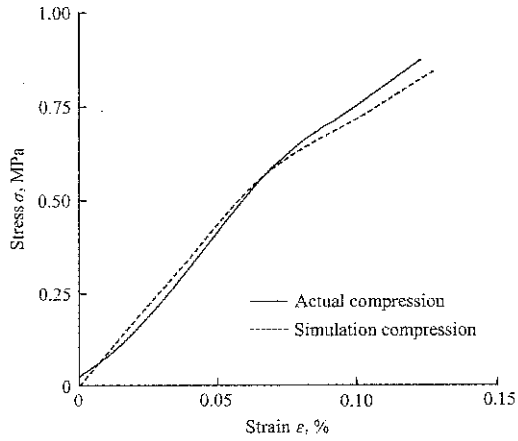

b. Axial compression

Figure 11 Comparison of stress-strain curves between practical compression and finite element simulation

5 Conclusions

1) Mechanical properties of kiwifruit peel, flesh, and placenta were measured in this paper, and the elastic modulus, tensile strength, and yield strength of major kiwifruit components were obtained. In addition, the constitutive model attributes of various major constituent materials were determined.

2) The compressive strain capacity and damage area of kiwifruit during compression damage were acquired, the analysis results showed that the kiwifruit flesh would suffer compression damage earlier than peel under the loading action.

3) Plate compression verification tests have been conducted for the whole kiwifruits, the results showed that compression characteristics gained via finite element method were similar to the actual compression characteristics, which verified the feasibility of applying finite element method to simulate kiwifruit compression damage.

Acknowledgements

We greatly appreciate the careful and precise reviews by the anonymous reviewers and editors. This study has been financially supported by the Special Fund for Agro-scientific Research in the Public Interest of China (201503142).

[References]

[1] Chen, J., H. Wang, H. R. Jiang, H. Gao, W. L. Lei, and G. R. Dang. 2012. Design of end-effector for kiwifruit harvesting robot. *Transactions of the Chinese Society of Agricultural Machinery*, 43(10): 151–154, 199. (In Chinese with English abstract)

[2] Chen, Y., W. L. Cai, X. J. Zou, and H. P. Xiang. 2011a. Extrusion mechanical properties of fresh litchi. *Transactions of the Chinese Society of Agricultural Engineering*, 27(8): 360, 362–364. (In Chinese with English abstract)

[3] Chen, Y., W. L. Cai, X. J. Zou, H. P. Xiang, T. H. Liu, and F. Y. Xu. 2011b. Mechanical properties test and finite element analysis for litchi. *Transactions of the Chinese Society of Agricultural Engineering*, 27(12): 358–363. (In Chinese with English abstract)

[4] Goyal, R. K., A. R. P. Kingsly, P. Kumar, and H. Walia. 2007. Physical and mechanical properties of aonla fruits. *Journal of Food Engineering*, 82(4): 595–599.

[5] Ji, H. W., W. Q. Shao, and X. W. Meng. 2010. Experimental research on compression mechanical behaviors and creep property of kiwifruit. *Journal of Anhui Agricultural Sciences*, 38(3): 1107–1109, 1121. (In Chinese)

[6] Kılıçkan, A., and M. Güner. 2008. Physical properties and mechanical behavior of olive fruits (*Olea europaea* L.) under compression loading. *Journal of Food Engineering*, 87(2): 222–228.

[7] Li, P. 2014. Studies on the mechanical damage and quality deterioration of huanghua pears caused by simulating transport vibration. MS Dissertation. Hangzhou: *College of Biosystems Engineering and Food Science, Zhejiang University*. (In Chinese)

[8] Li, Y. H., E. L. Lü, H. Z. Lu, J. M. Guo, and J. H. Zhao. 2016. Effects of carpopodium treatment on storage characteristics of litchi fruit at am bient temperature. *Journal of Chinese Institute of Food Science and Technology*, 6(4): 191–197. (In Chinese)

[9] Liu, L. L., H. Hu, Y. Wang, S.X. Song, X.Q. Yang, and T. L. G. Dong. 2016. Effect of vibration parameters on the damage characteristics and viscoelasticity of pears. *Journal of Vibration and Shock*, 35(10): 139–144.

[10] Lu, B., C. Hu, X. F. Wang, X. Y. Tang, R. K. Niu, C. F. Li. 2016. Compressive mechanical properties test and finite element analysis of winter jujube during crisp ripe period in south Xinjiang, China. *International Agricultural Engineering Journal*, 25(4): 245–256.

[11] Ma, X. L., X. Y. Chen, Y. S. Yan, and X. Y. Jiang. 2012. Mechanical damage test and biomechanical characteristics of red bayberry fruit. *Transactions of the Chinese Society of Agricultural Engineering*, 28(16): 282–287. (In Chinese with English abstract)

[12] Ortiz, C., J. Blasco, S. Balasch, and A. Torregrosa. 2011. Shock absorbing surfaces for collecting fruit during the mechanical harvesting of citrus. *Biosystems engineering*, 110(1): 2–9.

[13] Pallottino, F., C. Costa, P. Menesatti, and M. Moresi. 2011. Assessment of the mechanical properties of tarocco orange fruit under parallel plate compression. *Journal of Food Engineering*, 103(3): 308–316.

[14] Razavi, S. M. A., and M. BahramParvar. 2007. Some physical and mechanical properties of kiwifruit. *International Journal of Food Engineering*, 3(6): 1–16.

[15] Shen, G. L., G. K. Hu, and B. Liu. 2013. Mechanics of Composite Materials. Beijing: *Tsinghua University Press*. (In Chinese)

[16] Singh, K. K., and B. S. Reddy. 2006. Post-harvest physico-mechanical properties of orange peel and fruit. *Journal of Food Engineering*, 73(2): 112–120.

[17] Sirisomboon, P., P. Kitchaiya, T. Pholpho, and W. Mahuttanyavanitch. 2007. Physical and mechanical properties of Jatropha curcas L. fruits, nuts and kernels. *Biosystems Engineering*, 97(2): 201–207.

[18] Talens, P., N. Martınez-Navarrete, P. Fito, and A. Chiralt. 2002. Changes in optical and mechanical properties during osmodehydro freezing of kiwifruit. *Innovative Food Science & Emerging Technologies*, 3(2): 191–199.

[19] Wu, J., K. Q. Guo, Y. Ge, and Y. Y. Wang. 2012. Contact pressure distribution characteristics of Korla pear fruit at moment of drop impact. *Transactions of the Chinese Society of Agricultural Engineering*, 28(1): 250–254. (In Chinese with English abstract)

[20] Xu, X. B., and Q. M. Zhang. 2003. Researches and utilizations of germplasm resource of kiwifruit in china. *Chinese Bulletin of Botany*, 20(6): 648–655. (In Chinese)

[21] Zhou, Z. E. 1994. Physical Properties of Agricultural Materials. Beijing: *China Agricultural Press*. (In Chinese)

Shear properties test of sweet potato vine in mature period

Zheng Wenxiu[1], Lü Zhaoqin[1,2*], Lu Yao[1], Liu Zhengduo[1],
Shi Wenting[1], Cheng Xiangxun[1]

(1. *College of Mechanical and Electronic Engineering, Shandong Agricultural University, Tai'an, 271018, China*;
2. *Shandong Provincial Key Laboratory of Horticultural Machinery and Equipment, Tai'an, 271018, China*)

Abstract: In order to understand the shear mechanical properties of sweet potato vine and provide related data for sweet potato vine crushing and collecting machine, Shangshu 19 sweet potato vine in mature period was used as the test materials. Single factor test and central composite test were used to study the single factor effect and comprehensive effect of moisture content, sampling position and shearing rate on the shear mechanical properties of sweet potato vine. The regression model between the test factors and the shear mechanical properties of sweet potato vine was established. The results showed that the moisture content and sampling position had a significant effect on the target values, while the shearing rate had no significant influence. In the interaction of the two factors, the interaction between moisture content and sampling position has a significant effect on the target values, and the effect of other interaction items is not significant. With the increase of moisture content and sampling position, the target values showed a downward trend as a whole. When the moisture content is more than 80% and the sampling position is above the middle part, the change of the target values is not significant. The single factor test data curve and the model curve were compared, and the fitting degree of the two curves is better, which proved that the regression model is credible and the regression model can be used to predict the change of the target values. This study provided data support and theoretical basis for the establishment of the mechanical model of sweet potato vine and the design of sweet potato vine crushing and collecting machine.

Keywords: sweet potato vine, shear properties, moisture content, sampling position, shearing rate

Citation: Zheng, W. X., Z. Q. Lü, Y. Lu, Z. D. Liu, W. T. Shi, and X. X. Cheng. 2017. Shear properties test of sweet potato vine in mature period. International Agricultural Engineering Journal, 26(4): 204–212.

1 Introduction

China is the largest producer of sweet potatoes in the world. Sweet potatoes can not only be processed into many kinds of food, but also are an important industrial raw materials and a new type of energy materials (Ma et al., 2012; Richard., 2013; Saiful-Islam et al., 2002; Smith et al., 1994). Sweet potato vines are very long, grow flourishing and cover the entire ridge (He et al., 2009; Wang et al., 2014). Therefore, the mechanization of sweet potato harvest must take into account the handling problems of sweet potato vine. The vines must be cleaned up before sweet potatoes are harvested, otherwise the subsequent harvest work can't be carried out (Zhao et al., 2012; Wang et al.,2012; Xia et al., 2011; Liu et al., 2014). The mechanical properties of sweet potato vine during mature period affect the main operation indicators of sweet potato vine crushing and collecting machine, such as the qualified rate of sweet potato vine crushing length, the ridge top stubble length and so on. So research the mechanical properties of sweet potato vine is of great significance for the related structural design of sweet potato vine crushing and collecting machine.

In recent years, the study on the mechanical properties of crop stalks has been paid more and more attention, and the related studies are also increasing (Liu et al., 2007; Yuan et al., 2002). At present, domestic experts, Hu et al. (2015) studied the mechanical properties of sweet potato vine during harvest, revealed the relationship between vine moisture content, shear

Received date: 2017-07-31 **Accepted date:** 2017-10-12

* **Corresponding author: Lü Zhaoqin,** Professor, College of Mechanical and Electronic Engineering, Shandong Agricultural University, Tai'an, 271018, China. Email: lzqsdau2003@126.com.

strength and quality of mechanical crushing work; Chen et al. (2016) used the universal testing machine to analyze the sorghum straw compression, bending, shear test, the results showed that the presence of section affected the mechanical properties of sorghum straw obviously, moisture content and shear area also had an effect on it; Yan et al. (2012) studied the correlation between microstructure of soybean stem and stem mechanical properties, the results showed that soybean stem bottom shear stress and bending stiffness were higher than the other two parts; Lu et al. (2011) studied the clover stems mechanical properties with TA-XT2i texture analyzer and other instruments, found the relationship between the diameter and tensile strength, shear strength; Zhang et al. (2014) studied the mechanical properties and the microstructure of the cucumber vine straw; Zhang et al. (2016) studied the mechanical properties of soybean stalks for the design of comb soybean, soybean straw cutting, and plastic film recycling machines and provided the fundamental equipment and mold design data.

Although the study on mechanical properties of straw started relatively early, while the study on the shear properties of sweet potato vine has not yet appeared. In this paper, the effects of moisture content, sampling position and shearing rate on the shear properties of sweet potato vine were studied by using single factor test and central composite test. And the regression model between the test factors and shear properties of sweet potato vine was established. This study provided theoretical basis for the design of sweet potato vine crushing and collecting machine.

2 Materials and methods

2.1 Test materials

The sweet potato vine samples were taken from sweet potato planting base of Shandong Agricultural University, the type of sweet potato Shangshu 19 was regarded as testing object. The sweet potato vines during mature period are shown in Figure 1. They were planted in early May and harvested in middle to late October. Its planting patterns are single ridge cultivation, ridge distance is 90 cm and planting distance is 23 cm. The samples require no obvious defects, and the epidermis is not damaged or cracked. After sampling, the branches and leaves were removed in the laboratory, leaving the main stem part as the test object. The sampling position is five equal from the root of sweet potato vine to the top, which is the lower part (root), middle-lower part, middle part, middle-upper part, upper part (top). The sampling position is shown in Figure 2.

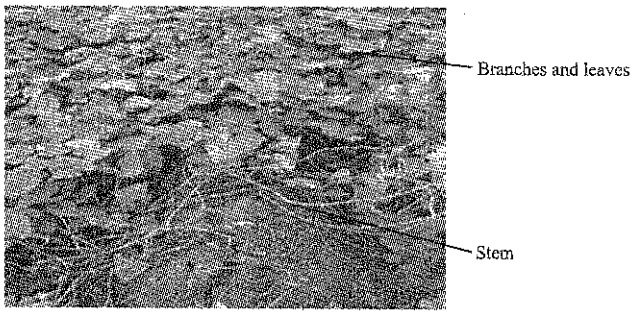

Figure 1 Sweet potato vines during mature period

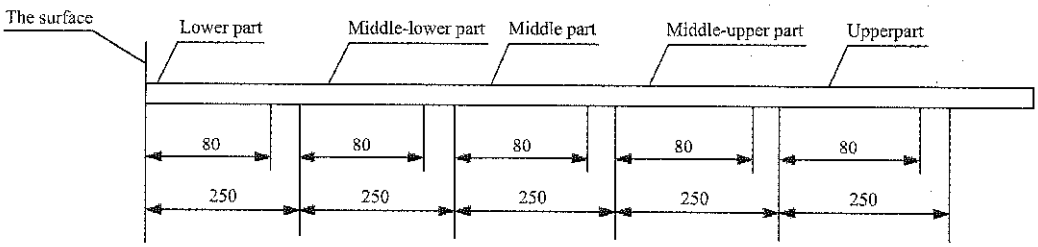

Figure 2 Sampling position map (Unit: mm)

Before test, the moisture content of sweet potato vine was measured randomly. The moisture content was between 68.9% and 88.7%. In order to make the moisture content of the test materials closer to the natural condition, the range of moisture content of the test samples was determined from 70% to 90%. In order to reduce the influence of moisture content regulation on the internal structure of sweet potato vine, all the samples should be stored in the temperature and humidity regulator to unify the moisture content after the sweet potato vines were collected from the fields, and to adjust the parameters of the temperature and humidity regulator for the normal temperature and high humidity environment (temperature is 20°C, relative humidity is 95%). After the samples

were stored for three days, ten samples were selected and weighed for the first time. In later time, the samples were weighed once every day until the quality of the sweet potato vine samples kept unchanged (Chen et al., 2012; Yu et al., 2012; Gao et al., 2016), then the moisture content of the samples reached the maximum in the temperature and humidity regulator, while the moisture content at this time could not meet the requirement of the test. So the next step is to soak the samples in water for 24-36 h according to the requirements of moisture content of different sweet potato vine samples. Finally, the samples were dried in the drying oven at 40°C. The quality of the samples was measured every 1-5 min during the drying process until the moisture content of each sample reached the required value (Guo, 2016; Zhang, 2015; Ding et al., 2016).

2.2 Test equipment

The equipment used in the test mainly include: micro controlled electronic universal testing machine (WDW-5E, Jinan Shijin Group Limited Company), vacuum drying oven (202-2, Shanghai Second Hardware Factory), temperature and humidity regulator (302A, Shanghai Experimental Instrument General Factory), electronic balance (0.001 g, JA5003A, Shanghai Jingtian Electronic Instrument Limited Company), as is shown in Figure 3. In addition, vernier caliper and ruler are needed.

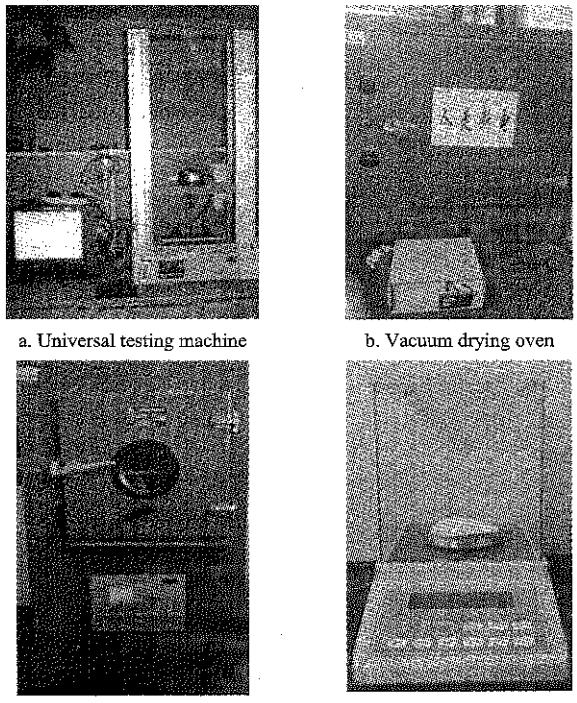

a. Universal testing machine b. Vacuum drying oven

c. Temperature and humidity regulator d. Electronic balance

Figure 3 Test equipment

2.3 Test method

2.3.1 Shear test

According to the requirement of the mechanical design optimization of the sweet potato vine crushing and collecting machine, the test was carried out with taking moisture content, sampling position and shearing rate as test factors, taking maximum shear force per unit diameter and shear strength as target values. The shear test of sweet potato vine was carried out on the micro controlled electronic universal testing machine. The length of each sample is 80 mm. According to the test plan, the sample was placed in the V-shaped locating block and the acquisition system was adjusted to zero. The test data was automatically collected by the test software, and the force-displacement curve was obtained. Through the force-displacement curve, the maximum shear force $F_{j\max}$ can be obtained. The shear test is shown in Figure 4. Each test was repeated 5 times and the average value was taken at last.

The maximum shear force per unit diameter was calculated according to Equation (1):

$$P_j = \frac{F_{j\max}}{d} \tag{1}$$

where, P_j represents the maximum shear force per unit diameter, N mm^{-1}; $F_{j\max}$ represents the maximum shear force, N; d represents the diameter, mm.

The shear strength was calculated according to Equation (2):

$$\sigma_j = \frac{4F_{j\max}}{d^2} \tag{2}$$

where, σ_j represents shear strength, MPa.

Figure 4 Shear test of sweet potato vine

2.3.2 Single factor test design

The factors and levels of single factor test of sweet potato vine are shown in Table 1.

Table 1 Factors and levels of single factor test

Levels	Factors		
	Moisture content A, %	Sampling position B	Shearing rate C, mm/min
1	70	Lower part	5
2	75	Middle-lower part	10
3	80	Middle part	15
4	85	Middle-upper part	20
5	90	Upper part	25

When the single factor test of moisture content on shear properties of sweet potato vine was carried out, the moisture content was taken 70%, 75%, 80%, 85%, 90% respectively, the sampling position was all taken the middle part and the shearing rate was all taken 15 mm/min; When the single factor test of sampling position was carried out, the sampling position was taken lower part, middle-lower part, middle part, middle-upper part, upper part respectively, the moisture content was all taken 80% and the shearing rate was all taken 15 mm/min; When the single factor test of shearing rate was carried out, the shearing rate was taken 5, 10, 15, 20, 25 mm/min respectively, the moisture content was all taken 80% and the sampling position was all taken the middle part. Each test was repeated 5 times and the average value was taken at last.

2.3.3 Central composite test design

In order to further study the effect of the interaction between the factors on the shear properties of sweet potato vine, general effects of sweet potato vine moisture content, sampling position and shearing rate on the shear properties were studied by using central composite test (Pan et al., 2008; Zhao et al., 2006). The response surface method was used to analyze the test results. And the regression model between the test factors and shear mechanical properties of sweet potato vine was established. The corresponding relationship between the coded value and the actual value of the design scheme is shown in Table 2.

Table 2 Relation of actual value and coded value

Coded value	Actual value		
	Moisture content A, %	Sampling position B	Shearing rate C, mm/min
−1.682	70	Lower part	5
−1	74	Middle-lower part	9
0	80	Middle part	15
1	86	Middle-upper part	21
1.682	90	Upper part	25

3 Test results and analysis

3.1 Results and analysis of single factor test

3.1.1 Effect of moisture content on shear properties of sweet potato vine

According to the factor level of moisture content in Table 1, shear test was carried out at a shearing rate of 15 mm/min on the middle part sweet potato vine. The effect of moisture content on the target values was studied. The test results are shown in Figure 5.

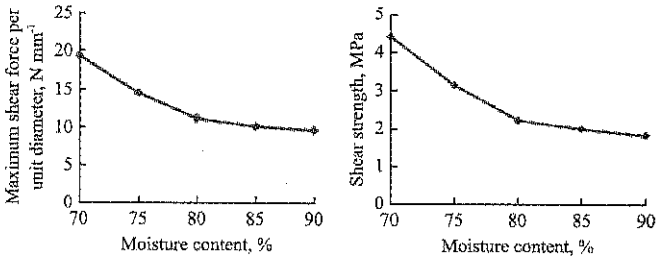

Figure 5 Relationship between shear properties and moisture content of sweet potato vine

When the moisture content was 70%, the target values were the largest, 19.36 N/mm and 4.41 MPa respectively; when the moisture content was 90%, the target values were the smallest, 10.06 N/mm and 1.85 MPa respectively. It indicated that the maximum shear force per unit diameter and shear strength of sweet potato vine decreased with the increasing of the moisture content. The reason was that, with the decreasing of the moisture content, sweet potato vine gradually has been aging and lost activity (Lee et al., 2006), and vine toughness has been increasing, so the maximum shear force per unit diameter and shear strength increased.

3.1.2 Effect of sampling position on shear properties of sweet potato vine

According to the factor level of sampling position in Table 1, shear test was carried out on sweet potato vine with moisture content of 80% and at a shearing rate of 15 mm/min. The effect of sampling position on the target values was studied. The test results are shown in Figure 6.

When the sampling position was the lower part, the target values were the largest, 18.12 N/mm and 4.13 MPa are respectively; when the sampling position was the upper part, the target values were the smallest, 8.61 N/mm and 1.77 MPa respectively. The maximum shear force per unit diameter and shear strength were gradually decreased from the lower part of the sweet potato vine to the upper

part. This is because the sweet potato vine closer to the top, its internal organizational structure was more dispersed; the closer to the root, its internal organizational structure was more compact, the degree of lignifications was increased, so the sweet potato vine was closer to the top, the weaker the shearing ability would be; the closer it was to the root, the stronger the shearing ability would be.

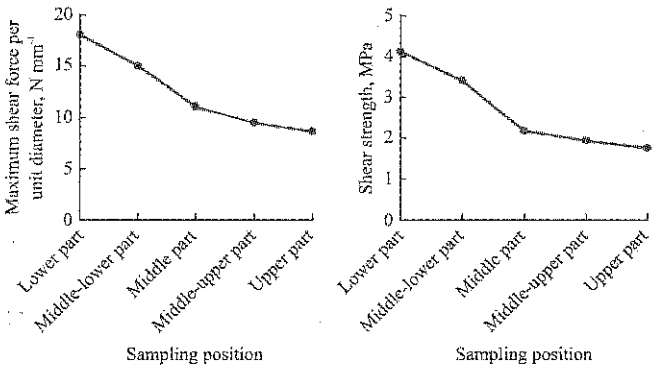

Figure 6 Relationship between shear properties and sampling position

3.1.3 Effect of shearing rate on shear properties of sweet potato vine

According to the factor level of shearing rate in Table 1, shear test was carried out on the middle part sweet potato vine with moisture content of 80%. The effect of shearing rate on the target values was studied. The test results are shown in Figure 7.

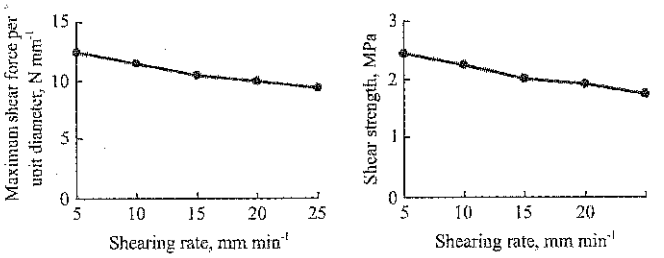

Figure 7 Relationship between shear properties and shearing rate

When the shearing rate was 5 mm/min, the target values were the largest, 12.48 N/mm and 9.42 MPa respectively; when the shearing rate was 25 mm/min, the target values were the smallest, 9.42 N/mm and 1.75 MPa respectively. It indicated that the maximum shear force per unit diameter and shear strength of sweet potato vine decreased with the increasing of the shearing rate, but the downward trend of the two is not obvious. When the shearing rate increased, the time of stem transfer deformation decreases and the required peak cutting force decreased (Sang, 1988). So, the target values decreased with the increasing of the shearing rate.

3.2 Results and analysis of central composite test

According to the level of each factor in Table 2, the test was carried out three times in each group and the average value was taken finally. The central composite test adopted the ternary quadratic regression orthogonal rotation combination test design table. The test plan and the results are shown in Table 3.

Table 3 Test plan and results

Test number	Test factors			Test target values	
	Moisture content A, %	Sampling position B	Shear rate C, mm/min	Maximum shear force per unit diameter P_j, N/mm	Shear strength σ_j, MPa
1	1	1	1	8.61	2.18
2	1	1	−1	9.90	2.30
3	1	−1	1	10.30	2.66
4	1	−1	−1	10.93	2.51
5	−1	1	1	14.64	3.20
6	−1	1	−1	14.85	3.39
7	−1	−1	1	18.57	4.51
8	−1	−1	−1	19.58	4.67
9	−1.682	0	0	17.46	4.50
10	1.682	0	0	9.12	2.21
11	0	−1.682	0	17.59	3.68
12	0	1.682	0	14.47	2.43
13	0	0	−1.682	12.41	2.41
14	0	0	1.682	10.45	1.92
15	0	0	0	11.67	2.01
16	0	0	0	12.06	2.35
17	0	0	0	12.16	1.95
18	0	0	0	11.97	2.45
19	0	0	0	10.35	2.35
20	0	0	0	12.34	2.03
21	0	0	0	10.75	2.50
22	0	0	0	10.46	2.25
23	0	0	0	10.58	1.93

3.2.1 Effect of test factors on the maximum shear force per unit diameter of sweet potato vine

According to the test data in Table 3, the test data of the maximum shear force per unit diameter was analyzed by using the Design Expert8.0 software (Ding, 2015; Ge, 2015; Xu, 2010). The regression model of each factor coding value and the maximum shear force per unit diameter P_j of sweet potato vine was obtained, as shown in Equation (3).

$$P_j = 11.22 - 3.89A - 3.12B - 0.75C - 0.07AB - 0.33AC + 1.26BC + 2.04A^2 + 0.92B^2 - 0.19C^2 \quad (3)$$

The variance analysis was carried out and the results are shown in Table 4.

Table 4 Variance analysis results of the maximum shear force per unit diameter

Model items	Mean square	*F* value	*P* value	Significance
Model	22.48	28.62	<0.0001	**
A	128.71	163.86	<0.0001	**
B	20.24	25.77	0.0002	**
C	3.03	3.86	0.0711	
AB	4.41	5.61	0.0340	*
AC	0.061	0.078	0.7844	
BC	0.002	0.003	0.9563	
A^2	6.05	7.71	0.0157	*
B^2	39.97	50.88	<0.0001	**
C^2	0.026	0.033	0.8588	
Lack of fit	0.97	1.44	0.3064	

Note: * means significant $p<0.05$; ** means highly significant $p<0.01$.

From Table 4, it can be seen that the model of relationship between the maximum shear force per unit diameter of sweet potato vine and the test factors is very significant ($p<0.01$), and the lack of fit is not significant ($p>0.05$), which indicated that there was no significant effect of other factors in the study and the regression model is reasonable. In the single factor effect, the single term of the moisture content A ($p<0.01$), the single term of the sampling position B ($p<0.01$) and the quadratic term of the sampling position B ($p<0.01$) have highly significant effect on the maximum shear force per unit diameter; the quadratic term of the moisture content A ($p<0.01$) has significant effect. The effect of other items ($p>0.05$) is not significant.

In the two-factor interaction effect, the interaction between the two factors is different. The interaction between moisture content A and sampling position B ($p<0.05$) has significant effect on the maximum shear force per unit diameter, and the effect of other interaction items is not significant ($p>0.05$). Taking the coded value of shearing rate C as 0, the regression model of the effect of moisture content A and sampling position B on the maximum shear force per unit diameter was obtained, as shown in Equation (4), the response surface is shown in Figure 8.

$$P_j=11.22-3.89A-3.12B-0.07AB+2.04A^2+0.92B^2 \quad (4)$$

It can be seen from Figure 8 that with the increasing of the sampling position and the moisture content, the maximum shear force per unit diameter of sweet potato vine showed a downward trend as a whole. When the moisture content is more than 80% and the sampling position is above the middle part, the change of the maximum shear force per unit diameter of sweet potato vine is not significant.

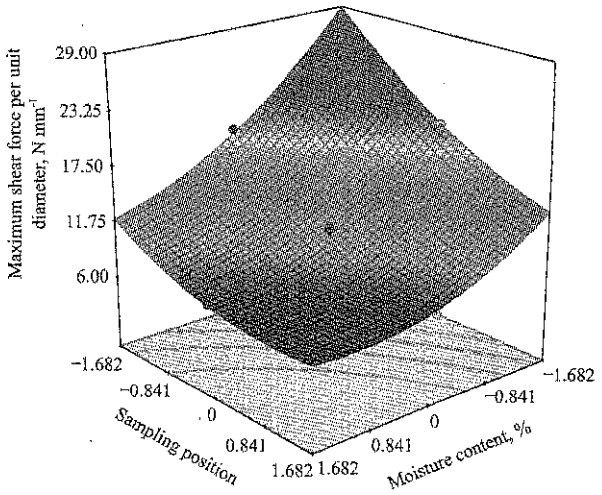

Figure 8 Effect of moisture content and sampling position on maximum shear forceper unit diameter

3.2.2 Effect of test factors on the shear strength

According to the test data in Table 3, the test data of the shear strength was analyzed by using the Design Expert 8.0 software. The regression model of each factor coding value and the shear strength σ_j of sweet potato vine were obtained, as is shown in Equation (5).

$$\sigma_j=2.29-0.51A-1.12B-0.53C+0.063AB-0.04AC+0.02BC+0.24A^2+0.27B^2+0.13C^2 \quad (5)$$

The variance analysis was carried out and the results are shown in Table 5.

Table 5 Variance analysis results of the shear strength

Model items	Mean square	*F* value	*P* value	Significance
Model	1.72	30.92	<0.0001	**
A	87.28	131.02	<0.0001	**
B	2.12	38.17	<0.0001	**
C	0.096	1.72	0.2118	
AB	0.45	8.12	0.0137	*
AC	0.018	0.32	0.5784	
BC	0.011	0.20	0.6601	
A^2	3.44	61.96	<0.0001	**
B^2	2.05	36.94	<0.0001	**
C^2	0.032	0.57	0.4625	
Lack of fit	0.064	1.29	0.3570	

Note: * means significant $p<0.05$;** means highly significant $p<0.01$.

From Table 5, it can be seen that the model of relationship between the shear strength of sweet potato vine and the test factors is very significant ($p<0.01$), and the lack of fit is not significant ($p>0.05$), which indicated that there was no significant effect of other factors in the

study and the model is reasonable. In the single factor effect, the single term and quadratic term of the moisture content A ($p<0.01$), the single term and quadratic term of the sampling position B ($p<0.01$) have highly significant effect on the shear strength. The effect of other items ($p>0.05$) is not significant.

In the two-factor interaction effect, the interaction between the two factors is different. The interaction between moisture content A and sampling position B ($p<0.05$) has significant effect on the shear strength, and the effect of other interaction items is not significant ($p>0.05$).Taking the coded value of shearing rate C as 0, the regression model of the effect of moisture content A and sampling position B on the shear strength was obtained, as is shown in Equation (6), the response surface is shown in Figure 9.

$$\sigma_j=2.29-0.51A-1.12B+0.063AB+0.24A^2+0.27B^2 \quad (6)$$

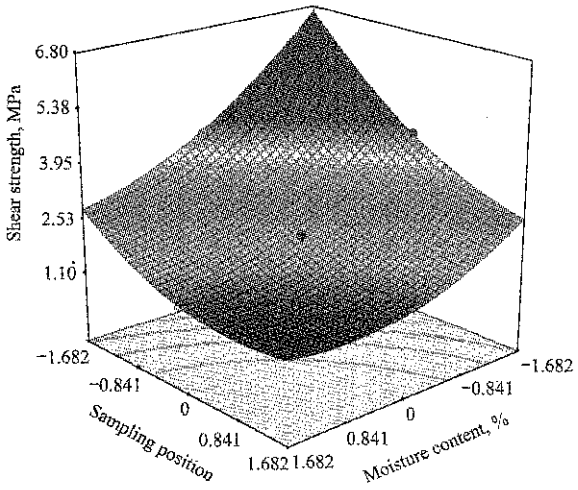

Figure 9 Effect of moisture content and sampling position on shear strength

It can be seen from Figure 9 that with the increasing of the sampling position and the moisture content, the shear strength of sweet potato vine showed a downward trend as a whole. When the moisture content is more than 80% and the sampling position is above the middle part, the change of the shear strength of sweet potato vine is not significant.

3.3 Test verification

After the model was established, the single factor test data curve was compared with the model curve. Taking the single factor test curve and model curve of moisture content as an example, the contrast diagrams are shown in Figure 10. .

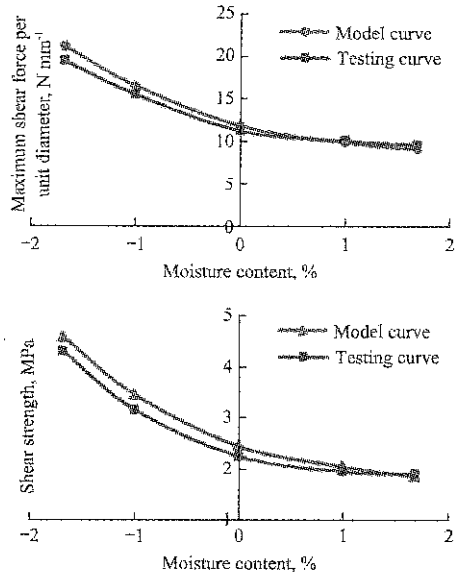

Figure 10 Shear property model verification of sweet potato vine

It can be seen from Figure 10 that the fitting degree of the model curve and the single factor test curve is better. The decision coefficients of the regression model can also be obtained by Design Expert 8.0 software, $R^2_{pj}=0.96$, $R^2_{\sigma j}=0.97$ respectively. It is shown that fitting degree of the regression model and the test results is better, and it can be used to predict the changes of maximum shear force per unit diameter and shear strength.

4 Conclusions

In this paper, single factor test and central composite test were used to study the single factor effects and comprehensive effects of moisture content, sampling position and shearing rate on the mechanical properties of sweet potato vine. The regression model between the test factors and the target values was established. The test results showed that:

(1) In the single factor test, the maximum shear force per unit diameter and shear strength of sweet potato vine decreased with the increasing of the moisture content, sampling position and shearing rate, and the change trend of shearing rate on target values is not obvious.

(2) In the central composite test, the moisture content and sampling position have a significant effect on the maximum shear force per unit diameter and the shear strength, while the shearing rate has no significant influence. In the interaction of the two factors, the interaction between moisture content and sampling position has a significant effect on the target values, and

the effect of other interaction items is not significant. With the increasing of moisture content and sampling position, the target values showed a downward trend as a whole. When the moisture content is more than 80% and the sampling position is above the middle part, the change of the target values is not significant.

(3) In order to verify the reliability of the regression model between the test factors and the target values, single factor test data curve and model curve were compared, and the fitting degree of the two curves is better, which proved that the regression model was credible. This study provided data support and theoretical basis for the establishment of the mechanical model of sweet potato vine and the design of sweet potato vine crushing and collecting machine.

Acknowledgement

This work was supported by the Foundation of Modern Agricultural Technology System Innovation Team Expert in Shandong Province (No.SDAIT10-22-10), the Agricultural Equipment Research and Development Innovation Program of Shandong Province (No.2017YF002).

[References]

[1] Chen, K. C., F. D. Li, Y. F. Yan, T. H. Gao, Y. D. Li, and Z. H. Song. 2016. Experimental study on sorghum stalks mechanics characteristics. *Journal of Chinese Agricultural Mechanization,* 37(5): 130–136.

[2] Chen, Z. G., D. F. Wang, L. Q. Li, and R. X. Shan. 2012. Experiment on tensile and shearing characteristics of rind of corn stalk. *Transactions of the Chinese Society of Agricultural Engineering,* 28(21): 59–65. (In Chinese with English abstract)

[3] Ding, L. P. 2015. Design and experimental study on saw type cotton stalk cutting test bench. M. S. thesis, College of Mechanical and Electrical Engineering, Shihezi University, Shihezi.

[4] Ding, L. P., Y. C. Chen, Y. Ge, and L. Wang. 2016. Research on the shear mechanical properties of cotton stalk. *Journal of Chinese Agricultural Mechanization,* 37(2): 116–118, 122. (In Chinese)

[5] Gao, T. H., Y. F. Yan, F. D. Li, Y. D. Li, F. Y. Tian, K. C. Chen, and Z. H. Song. 2016. Shear mechanical properties of cotton stalks at the harvesting time based on response surface methodology. *China Science Paper,* 11(22): 2542–2547.

[6] Ge, Y. Y. 2015. Experimental design method and Design-Expert software application. *Harbin: Harbin Institute of Technology Press.*

[7] Guo, Q. 2016. Experimental research on the cutting mechanism and performance of rattan straw. Ph.D.diss., *College of Mechanical Engineering., Jiangsu University, Zhenjiang.*

[8] He, Y. J., X. Z. Yang, W. P. Sun, Y. Xia, and W. Z. Wang. 2009. Design and experiment on the sweet potato vine chopping and returning machine. *Journal of Henan Agricultural University,* 43(6): 639–641. (In Chinese)

[9] Hu, L. L., G. P. Wang, X. Y. Ling, B. Wang, and B. K. Wang. 2015. Mechanical properties of sweet potato vine and stalk during harvest. *Transactions of the Chinese Society of Agricultural Engineering,* 31(9): 45–48. (In Chinese with English abstract)

[10] Lee, S., T. F. Shupe, and C. Y. Hse. 2006. Mechanical and physical properties of agro-based fiberboard. *European and Life Sciences,* 64(1): 74–79.

[11] Liu, L. M., J. D. Xu, Y. Huang, Z. X. Ji, and M. Q. Lü. 2014. Development and varieties screening of sweet potato harvester in hilly region. *Hubei Agricultural Sciences,* 53(15): 3647–3649. (In Chinese)

[12] Liu, Q. T., Y. G. Qu, S. L. Qing, and W. Z. Wang. 2007. Study progress on mechanics properties of crop stalks. *Transactions of the Chinese Society for Agricultural Machinery,* 38(7): 172–176. (In Chinese with English abstract)

[13] Lu, Q., S. R. Chen, and J. W. Li. 2011. The Experiment study on mechanical properties of clove. *Journal of Agricultural Mechanization Research,* 7(3): 174–177.

[14] Ma, D. F., Q. Li, and Q. H. Cao. 2012. Development and prospect of sweet potato industry and its technologies in China. *Jiangsu Journal of Agricultural Sciences,* 28(5): 969–973. (In Chinese)

[15] Pan, L. J., and J. S. Chen. 2008. Experimental design and data processing. *Nanjing: Southeast University Press.*

[16] Richard, G. 2013. How sweet potato varieties are distributed in Uganda: actors, constraints and opportunities. *Food Security,* 5(6): 781–791.

[17] Saiful-Islam, A. F. M., C. Kubota, M. Takagaki, and T. Kozai. 2002. Sweet potato growth and yield from plug transplants of different volumes, planted intact or without roots. *Crop Science,* 42(3): 822–826.

[18] Sang, Z. Z. 1988. Agricultural mechanics. *Beijing: China Agricultural Machinery Press.*

[19] Smith, S. L., and M. E. Wright. 1994. A preharvest vine disposal machine for sweet potatoes. *Applied Engineering in Agriculture,* 10(3): 321–326.

[20] Wang, B., L. L. Hu, L. J. Tian, Z. C. Hu, and F. L. Ji. 2012.

Design of 1JHSM-800 sweet potato vine profiling crushing machine. *Chinese Agricultural Mechanization,* 242(4): 103–107. (In Chinese)

[21] Wang, C. J., Y. M. Li, and X. Y. Wang. 2014. The design of 4U-60 sweet potato harvester. *Agricultural Equipment and Vehicle Engineering,* 52(8): 55–57.

[22] Xia, Y., Y. J. He, W. Z. Wang, and X. Z. Qin. 2011. Experiment on the multiple steps mechanized sweet potato harvest. *Chinese Agricultural Mechanization*, 238(6): 70–72. (In Chinese)

[23] Xu, X. H. 2010. Experimental design and application of design-expert software. *Beijing: Science Press.*

[24] Yan, Y. X., S. H. Zhao, Y. Q. Yang, and B. L. Tian. 2012. Study on mechanics properties of soybean stems in mature stage. *Journal of Northeast Agricultural University*, 43(5): 46–49.

[25] Yu, Y., Y. Lin, M. Mao, W. M. Wang, F. Tian, J. M. Pan, and Y. B. Ying. 2012. Experimental study on tensile properties of corn straw. *Transactions of the Chinese Society of Agricultural Engineering*, 28(6): 70–76. (In Chinese with English abstract)

[26] Yuan, Z. H., B. P. Feng, A. Q. Zhao, and A. Q. Liang. 2002. Dynamic analysis and comprehensive evaluation of crop-stem lodging resistance. *Transactions of the Chinese Society of Agricultural Engineering,* 18(6): 30–31. (In Chinese with English abstract)

[27] Zhang, H. 2015. Study on the shear properties and cutting parameters of alfalfa stem. Ph.D.diss., *Engineering College, China Agricultural University., Beijing.*

[28] Zhang, X. L., X. J. Sun, Y. F. Xu, P. P. Li, Q. Guo, and S. Q. Zhang. 2014. Mechanicalcharacteristics and microstructure of cucumber vine straw. *Journal of Agricultural Mechanization Research,* 12(4): 156–159.

[29] Zhang, K. F., H. Li, Y. J. He, W. Z. Wang, and Y. C. Yu. 2016. Experimental study on mechanical properties of soybean straw. *Soybean Science,* 35(2): 306–309.

[30] Zhao, D. W., and Z. W. Gao. 2012. Research on the development in the sweet potato stem leaves treatment and harvesting machines at home and abroad. *Agricultural Science Technology and Equipment,* 216(6): 19–20.

[31] Zhao, X. M. 2006. Experimental design method. *Beijing: Science Press.*

Analysis and optimization of microwave drying process of germinated brown rice

Liu Chenghai[1], Lu Shuwen[2], Liu Chai[1], Xu Hao[1], Zhu Guanghao[1], Shen Liuyang[1], Zheng Xianzhe[1*]

(1. *College of Engineering, Northeast Agricultural University, Harbin, Heilongjiang Province, 150030, China*;
2. *Food Research Institute, Heilongjiang Academy of Agricultural Sciences, Harbin Heilongjiang Province, 150030, China*)

Abstract: To analyze the effects of microwave drying parameters on the drying characteristics of germinated brown rice (GBR), the microwave intensity (W), surface ventilate velocity (m/s), each circular drying time (min) were selected as the influencing factors. The response curve surface method was employed to investigate the effects of influencing factors on the drying properties. The microwave intensity had the most significant positive effect on the drying rate and grain temperature of GBR. The drying rate tends decreasing followed by increasing trend with drying time, while the changes of temperature of GBR showed reverse trends. The surface ventilate velocity has a significant negative correlation with the temperature of GBR. A three-stage drying process was proposed which included the microwave drying of 4-5 W/g microwave intensity at first stage with drying duration of 9-12 min, followed by second stage of tempering process with duration of three times of drying time, and third stage and finial microwave drying of 2.5-4 W/g microwave intensity, and the surface ventilate velocity is 3.5-4.5 m/s for all drying stages. The results can provide theoretical basis for microwave drying of germinated brown rice.

Keywords: germinated brown rice, microwave drying, drying processing parameters, drying properties

Citation: Liu, C. H., S. W. Lu, C. Liu, H. Xu, G. H. Zhu, L. Y. Shen, and X. Z. Zheng. 2017. Analysis and optimization of microwave drying process of germinated brown rice. International Agricultural Engineering Journal, 26(4): 213–227.

1 Introduction

GBR comes from ordinary brown rice by soaking in water under a suitable temperature and time conditions to initiate budding (Lin et al., 2015). Compared to polished rice, GBR is highly nutritional and has many bioactive compounds (Han et al., 2016) including the γ-aminobutyric acid (GABA) (Chungcharoen et al., 2012; Chenet al., 2016), dietary fibre (Chungcharoen et al., 2014; Esa et al., 2013), phenolic compounds (Tianet al., 2004), oligosaccharides (Sirisoontaralak et al., 2015), vitamins and minerals (Komatsuzaki et al., 2007). In cooking rice, GBR has shorter cooking time, softer texture, and higher digestion rate than that of brown rice (Zhang et al., 2014, Cheevitsopon and Noomhorm, 2015). Therefore, GBR has been recommended as a healthy food (Chunget al., 2012) and consumed as an alternative of brown rice in Japan and Korea (Chung et al., 2014). Moisture content of GBR is as high as 30% (wet basis, w.b.) (Komatsuzaki et al., 2007) or 52% (drybasis, d.b.) (Srisang et al., 2010), which is easy to cause the microbial growth and reproduce bad odor. It is necessary to dry it to safe moisture content of 14.0%-15.0% (w.b.) as soon as possible (Srisang et al., 2016) for the safe storage and milling of parboiled paddy (Pruengam et al., 2016). In addition, the real-time drying is helpful to improve the drying efficiency and to ensure the quality of GBR (Yang, 2004).

Microwave volumetric heating (Chandrasekaran et al., 2013) may meet the requirement of real-time and rapid drying GBR (Zheng et al., 2013). Previous study indicated that microwave drying could improve the drying rate of 3-5 times, and effectively avoid the degradation of the γ-aminobutyric acid (GABA) compared to hot air drying method (Zhang et al., 2016).

Received date: 2017-08-14 **Accepted date:** 2017-09-24

*** Corresponding author: Zheng Xianzhe, Professor,** College of Engineering, Northeast Agricultural University, Harbin. Email: zhengxz@neau.edu.cn, Tel: +0086-451-55191021, Fax: +0086-451-55190667.

However, microwave drying method easily led to unstable quality of GBR including cracking and uneven color (Seo et al., 2016). Zheng et al. (2015) found that the microwave drying conditions including the microwave intensity, surface ventilate velocity (SV), the ratio between drying time and tempering time had significant effects on the microwave drying rate and temperature. Existing studies about the microwave drying of GBR focus on the microwave drying characteristics, drying quality and parameters optimization of drying process, which could provide the basis for the reasonable design of drying mode (Wang, 2016). However, it is difficult to analyze the changes of the drying process involving in the drying rate and quality based on the final temperature and moisture content. In the continuous microwave drying, distribution of temperature of the material is uneven due to the changes of dielectric properties, thermal properties of the material.

In order to determine the reasonable input mode of microwave power and reveal the mechanism of the quality changes, the temperature changes of GBR were systematically studied by measuring and analyzing the maximum temperature, as well as drying rate during the continuous microwave drying process. It is helpful to essentially reveal the influence mechanism of drying process parameters on drying characteristics and quality by investigating the changes of temperature and moisture during the continuous microwave drying process. The influence mechanism is useful to provide the control model for the design of automatic control system of microwave drying process, and is also the basis for the research and development of microwave dryer. According to the current research of microwave drying technology and the requirements of drying GBR, the main objectives of this study are as follows:

(1) To analyze the influence of microwave drying parameters on the drying characteristics of GBR. (2) To propose an optimum drying condition for microwave drying of GBR.

2 Material and method

2.1 Preparation of germinated brown rice

Fresh GBR was provided by Jindu Rice Company in Harbin of China. The embryo brown rice with high taste value obtained by hulling was selected as the experimental samples. GBR with 3 mm bud length could be produced by soaking brown rice in water at 37°C±1°C germination temperature for 36 h germination duration. GBR were packed by using polyvinyl chloride (PVC) bags with mass of 5 kg, and then were cool stored in 4°C-5°C. Before the experiment of microwave drying, the packaging bags with GBR were taken out and placed at the room temperature (~22.5°C) about 4-5 h until GBR temperature arriving at room temperature.

2.2 Experimental procedure

According to the preliminary experimental results from microwave drying of GBR, the microwave intensity (MI), defined as the ratio of output power to processing weight of initial material, had the most important effect on the drying rate (DR) and temperature. The MI characterizes the influence ability of microwave power on material, and effect on the relationship between drying efficiency and drying quality. In order to control the level of the experimental factors, the initial microwave intensity (IMI) is defined as the influence factor due to the reduction of material weight led to water evaporation of GBR during drying process. The experiment was implemented in continuous microwave dryer. Ventilation may improve the uniformity of temperature distribution in the microwave field and promote the evaporation rate of the surface water of GBR, such SV was selected as an experimental factor in microwave drying GBR. The drying technology was used with multi-stage circulation combining the tempering and the microwave drying process, which could reduce the fissure of grains. Each circular drying time (CT) was also chosen as the influence factor of experiment because CT had the significant influence on the drying rate and temperature of GBR, and the suitable CT was helpful to balance the relation between drying efficiency and quality of GBR. According to the preliminary experimental results and the drying requirements of microwave drying process, the ranges of experimental factors were determined: 0.5-5.0 W/g IMI, 0-5 m/s SV, 2-10 min CT. The objective indexes were developed as moisture content of each circulation (MCEC), material temperature, temperatures

before and after tempering, total drying time (TDT), and the finial moisture content (FMC).

The ratio of circular times and total drying time (RCT) represents the index of drying efficiency and capability for dryer and drying process, which was calculated by dividing circular times to the total drying time. The circular times (n) was equal to the duration of microwave drying process of GBR from initial moisture content to the finial moisture content below 16%. While the total drying time (T) was the sum of microwave drying time and tempering time at each circular stage, and could be calculated by Equation (1):

$$T=nt_i+3(n-1)t_i \quad (1)$$

where, t_i and 3 t_i were the microwave drying time and tempering time at each circular stage respectively.

The finial moisture content of GBR, as an important target of drying process, was measured by the grain moisture meter (DP-5, KANEKO Co., LTD., Japan). The drying rate represented the capability of water removed under different drying conditions and drying characteristics, and could be obtained by dividing the difference between initial and finial moisture contents to drying continuous time. The drying temperature was measured at the end of each drying stage by the infrared thermometer (GM1150, Dongguan Zhixuan Equipment and Instrument Corporation, China), and the maximum temperature (MT) was got by comparing the above measuring temperature values. The mean grain temperature (MGT) was defined as ratio of the measuring temperature accumulation at the end of each drying circular stage to the duration of microwave drying at each stage. MGT is used to present the temperature level of GBR under the different drying processes. Rising temperature mean deviation (RTMD) was defined as the deviation of temperature at the end of each drying stage. This term represents the fluctuating level of temperature during the microwave drying GBR, and could be used to evaluate the rising temperature process and stability at the different drying stages. The ratio between rising temperature deviation and grain temperature mean (RRG) was defined as ratio of rising temperature deviation to average temperature, which is the index to compare the temperature stability at the different microwave drying conditions.

The operation parameters of microwave drying of GBR were as follows (1) the microwave power was 4 kW, (2) the weight of GBR was determined by setting the IMI at each experiment, (3) the tempering time was three times as high as drying time according to the results from preliminary experiment.

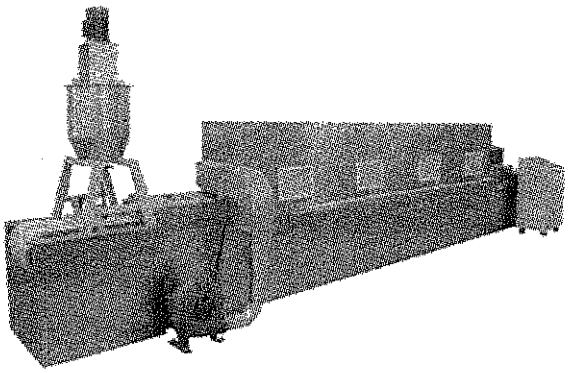

Figure 1 Continuous microwave dryer

The continuous microwave dryer (WXD10S-17, Nanjing Sanle Microwave Technology Development Co., Ltd., China), as is shown in Figure 1, was employed to obtain the process optimization for drying GBR, and to verify the experimental results of production scale. The size of dryer is 7200×520×1500 mm^3, and the microwave power includes 4, 7 and 10 kW. The number of magnetron is 15 and these magnetrons are divided into two lines (one line contains 7 magnetrons and the other is 8 magnetrons) and arranged in parallel. The belt speed was 120 m/h in this experiment and the thickness of material was 5 mm. While microwave work station (MWS, FISO Technologies Inc., Canada) was used to analyze the drying characteristics of GBR.

2.3 Data processing

All experimental design scheme, statistical analysis and parameter optimization were obtained by using Expert Design Software (Ver 7.0, Stat-Ease, Inc., Minneapolis, USA). The response surface method (RSM) was employed to optimize drying parameters according to the report by several previous researchers which the RSM technique had successful utilization for drying parameters of products (Han et al., 2010; Liu et al., 2014).

3 Results and discussion

All experiments of microwave drying of GBR were

carried out according to the experimental factors and levels in Table 1. The experiments of microwave drying of GBR last until the moisture content of GBR in range of 14.0%-16.0% (w.b.). The experimental results were shown as Table 2. The dried samples were stored in plastic encapsulated packages with vacuum condition.

Table 1 Experimental factor coding table

Coding value	IMI, W/g	SV, m/s	Unit drying time, min
1.68	5.00	5.00	10.00
1	4.34	4.27	8.83
0	2.75	2.50	6.00
−1	1.16	0.73	3.17
−1.68	0.50	0	2.00

Table 2 Temperature, moisture and drying time of GBR in each stage during microwave drying process

Order number	Stage	0	1	2	3	4	5	6	7	TDT, min
1	T, °C	18.1	70.8	75.6	83.5	NA	NA	NA	NA	79.5
	M, %	28.8	21.7	16.5	14.8	NA	NA	NA	NA	
2	T, °C	18.1	54.8	58.6	61.2	73.2	74.1	NA	NA	34.0
	M, %	28.8	23.6	21.7	19.4	16.5	15.1	NA	NA	
3	T, °C	18.1	56.2	63.0	70.1	NA	NA	NA	NA	79.5
	M, %	28.8	24.4	20.1	16.0	NA	NA	NA	NA	
4	T, °C	18.1	68.1	89.2	88.1	89.8	NA	NA	NA	78.0
	M, %	28.8	24.0	20.6	17.8	15.0	NA	NA	NA	
5	T, °C	18.1	60.6	70.8	90.0	91.1	NA	NA	NA	78.0
	M, %	28.8	23.1	20.5	17.0	15.3	NA	NA	NA	
6	T, °C	18.1	59.6	68.2	93.4	92.1	NA	NA	NA	78.0
	M, %	28.8	23.1	20.6	17.1	13.7	NA	NA	NA	
7	T, °C	18.1	59.4	69.2	92.8	93.2	NA	NA	NA	78.0
	M, %	28.8	22.9	19.7	16.8	14.1	NA	NA	NA	
8	T, °C	18.1	67.8	98.5	NA	NA	NA	NA	NA	50.0
	M, %	28.8	21.1	15.6	NA	NA	NA	NA	NA	
9	T, °C	18.1	60.2	71.2	90.6	91.4	NA	NA	NA	78.0
	M, %	28.8	23.3	21.0	17.9	15.6	NA	NA	NA	
10	T, °C	18.1	58.6	70.4	92.8	95.1	NA	NA	NA	78.0
	M, %	28.8	22.8	19.2	17.1	15.0	NA	NA	NA	
11	T, °C	18.1	61.2	73.2	91.6	93.2	NA	NA	NA	78.0
	M, %	28.8	23.8	19.7	17.3	14.9	NA	NA	NA	
12	T, °C	18.1	60.8	70.2	92.4	94.1	NA	NA	NA	78.0
	M, %	28.8	22.9	19.1	16.9	14.5	NA	NA	NA	
13	T, °C	18.1	50.4	59.2	61.6	64.8	66.8	68.7	70.2	79.3
	M, %	28.8	26.5	23.0	21.7	19.8	17.2	15.8	14.2	
14	T, °C	18.1	69.6	73.5	NA	NA	NA	NA	NA	44.2
	M, %	28.8	19.7	15.5	NA	NA	NA	NA	NA	
15	T, °C	18.1	53.4	60.5	65.9	NA	NA	NA	NA	79.5
	M, %	28.8	24.2	19.5	15.1	NA	NA	NA	NA	
16	T, °C	18.1	60.9	70.4	76.9	79.6	NA	NA	NA	41.2
	M, %	28.8	22.8	20.1	16.9	14.5	NA	NA	NA	
17	T, °C	18.1	47.3	57.3	58.6	59.4	61.1	65.5	NA	66.6
	M, %	28.8	25.3	22.7	21.2	18.9	16.1	14.7	NA	
18	T, °C	18.1	65.2	74.9	76.8	NA	NA	NA	NA	54.0
	M, %	28.8	20.3	17.0	14.1	NA	NA	NA	NA	
19	T, °C	18.1	62.3	72.8	93.5	92.1	NA	NA	NA	78.0
	M, %	28.8	21.5	18.9	16.0	14.1	NA	NA	NA	
20	T, °C	18.1	58.2	67.4	75.9	79.8	NA	NA	NA	78.0
	M, %	28.8	22.8	18.9	16.4	14.7	NA	NA	NA	
21	T, °C	18.1	65.0	72.1	79.9	81.2	NA	NA	NA	41.2
	M, %	28.8	24.7	20.6	17.3	15.1	NA	NA	NA	
22	T, °C	18.1	59.9	68.9	88.3	90.8	NA	NA	NA	78.0
	M, %	28.8	23.9	20.3	17.9	15.0	NA	NA	NA	
23	T, °C	18.1	46.4	53.2	69.3	70.6	72.8	73.4	NA	126.0
	M, %	28.8	25.9	23.1	19.8	18.1	16.4	15.8	NA	

Note: T and M represent temperature (°C) and moisture content (%,w.b.), respectively. NA represents no value.

From Table 2, it could be seen that the finial moisture content of GBR was less than 16.0%. For a part of experiment, the finial moisture content was above 14.5% of the desired level. This was because for microwave drying, the drying rate was rapid and was difficult to control, and the finial moisture content of GBR might be less than 14.0% by further microwave drying when moisture content below 16.0%, which result in the quality deterioration of GBR in darker color and fissure increment as well as high energy consumption. The objective values were calculated and listed in Table 3 according to the temperature and moisture content of GBR during microwave drying process shown in Table 2.

Statistical analysis was employed to determine the influence of every factor under microwave drying condition on target value of drying GBR according to the data in Table 3, and the analysis results were shown in Table 4.

From Table 4, it was shown that the influence of MI was extremely significant on total drying time, DR and MGT of GBR. The SV had a significant effect on DR and MGT. While there was an extremely significant influence of each circular drying time on DR and a significant influence on RCT.

Table 3 Target value of microwave drying GBR

	Technology factors			Objective factors						
	MI X_1, W/g	SV X_2, m/s	CT X_3, min	RCT, min	FMC, % (w.b.)	DR, %/min	MT T_{max}, °C	MGT, °C	RTMD	RRG
1	4.34	0.73	8.83	3/80	14.8	0.18	83.5	76.6	4.6	6.0%
2	2.75	2.50	2.00	5/34	15.1	0.34	74.1	64.4	7.4	11.5%
3	1.16	0.73	8.83	3/80	16.0	0.16	70.1	63.1	4.7	7.4%
4	2.75	0.00	6.00	4/78	15.0	0.18	89.8	83.8	7.9	9.4%
5	2.75	2.50	6.00	4/78	15.3	0.17	91.1	78.1	12.4	15.9%
6	2.75	2.50	6.00	4/78	13.7	0.19	92.1	78.3	14.4	18.4%
7	2.75	2.50	6.00	4/78	14.1	0.19	93.2	78.7	14.4	18.2%
8	2.75	2.50	10.00	2/50	15.6	0.26	98.5	83.2	15.4	18.5%
9	2.75	2.50	6.00	4/78	15.1	0.18	91.4	78.4	12.7	16.1%
10	2.75	2.50	6.00	4/78	15.0	0.18	95.1	79.2	14.7	18.6%
11	2.75	2.50	6.00	4/78	14.9	0.18	93.2	79.8	12.6	15.8%
12	2.75	2.50	6.00	4/78	14.5	0.18	94.1	79.4	13.9	17.5%
13	1.16	0.73	3.17	7/79	14.2	0.18	70.2	63.1	5.2	8.2%
14	4.34	4.27	8.83	2/44	15.5	0.30	73.5	71.6	2.0	2.7%
15	1.16	4.27	8.83	3/80	15.1	0.17	65.9	59.9	4.4	7.3%
16	4.34	4.27	3.17	4/41	14.5	0.35	79.6	72.0	6.3	8.8%
17	1.16	4.27	3.17	6/67	14.7	0.21	65.5	58.2	3.9	6.8%
18	5.00	2.50	6.00	3/54	14.1	0.27	76.8	72.3	4.7	6.5%
19	2.75	2.50	6.00	4/78	14.1	0.19	92.1	80.2	12.6	15.7%
20	2.75	5.00	6.00	4/78	14.7	0.18	79.8	70.3	7.5	10.7%
21	4.34	0.73	3.17	4/41	15.1	0.33	81.2	74.6	6.0	8.0%
22	2.75	2.50	6.00	4/78	15.0	0.18	90.8	77.0	12.6	16.3%
23	0.5	2.50	6.00	6/126	15.8	0.10	73.4	64.3	9.7	15.0%

Table 4 Statistical analysis (ANOVA) with the influence of process parameters on the target volume during microwave drying process

		RCT, min		DR, %/min		MT T_{max}, °C		MGT, °C		RTMD		RRG	
		F	p	F	p	F	p	F	p	F	p	F	p
MI A, W/g	A	53.98	**	110.65	**	5.22	*	15.33	**	0.58	ns	1.73	ns
	A^2	1.99	ns	0.48	ns	25.55	**	18.82	**	18.91	**	9.41	**
SV B, m/s	B	2.54	ns	6.80	*	2.71	ns	5.53	*	0.21	ns	0.02	ns
	B^2	0.45	ns	0.10	ns	7.99	*	2.40	ns	16.73	**	11.1	**
CT C, min	C	5.86	*	32.69	**	2.74	ns	4.57	ns	0.59	ns	0.058	ns
	C^2	40.69	**	87.85	**	6.16	*	6.68	*	4.75	*	2.22	ns
$A\times B$		1.09	ns	3.58	ns	0.02	ns	0	ns	0	ns	0	ns
$A\times C$		1.48	ns	7.03	**	0.06	ns	0	ns	0.54	ns	0.53	ns
$B\times C$		1.09	ns	2.29	ns	0.21	ns	0	ns	0.06	ns	0.07	ns
R^2		0.89	**	0.95	**	0.79	ns	0.80	**	0.76	**	0.66	**

Note: ns represents no significant difference, $p>0.05$; * represents the significant level, $0.01<p<0.05$; ** represents the extremely significant level, $p<0.01$.

3.1 Effects of microwave drying parameters on drying characteristics of GBR

To research the microwave drying process of GBR, it is primary to ensure the quality of GBR during drying process, and then to consider improving the drying efficiency. The multi-circular drying process combining microwave heating and tempering insulation was carried out, and the drying time, drying rate and maximum temperature were chosen as the characteristic indexes. The heat and mass transfer processes were analyzed during drying process according to the effects of drying parameters on drying characteristics of GBR, which provided the theoretical basis for the processing optimization by the microwave drying GBR.

(1) Effect of microwave drying condition on the total drying time of GBR

According to the operation mode of microwave dryer and the requirement of drying quality, multi-stage process

combining microwave drying and tempering insulation for drying GBR was developed. This multi-stage process may improve the color and drying quality, reduce the fissuring produce, and ensure active component content, such as γ-aminobutyric acid (GABA), and vitamins C (VC). However, tempering stage could result in prolonging the drying time, and declining the drying efficiency, as well as increasing the complexity of drying process and the site area of dryer. The primary question for designing drying process and developing (or choosing) the drying equipment is to consider how to ensure and improve the drying quality of GBR. Total drying time represents the drying efficiency to evaluate the ratio of drying and tempering. According to the total drying time of microwave drying of GBR, the drying efficiency was improved on the premise of ensuring GBR quality, thus the contradiction between the drying efficiency and the drying quality of GBR may be balanced. During the process of microwave drying GBR, the effects of microwave intensity, SV and each stage time on total drying time are shown in Figure 2a, b, c.

From Figure 2a, it could be seen that the total drying time decreased with the increase of MI and SV. This is because the microwave volumetric heating could accelerate the evaporation rate of moisture inside the material to improve the evaporation rate of GBR, and accelerate the SV to increase the removing capacity of wet air. Because the interaction between microwave intensity and SV made the match between rapid evaporation of the high-humidity GBR and the rapid convective migration of the surface, and thus the drying rate could be improved. The drying time, required to reduce the moisture content from initial moisture content (32.0%-33.0%) to finial moisture content (14.0%-15.0%), was shortened as shown in Figure 2a, so the total drying time was shortened. There was an insignificant change of drying time with increasing of SV in lower MI. The reason is lowering MI could result in the evaporation capability of moisture reduced inside the GBR, and all vapor was taken away with the lower ventilate velocity, and increasing SV could not improve the removing capability of moisture during drying process of GBR.

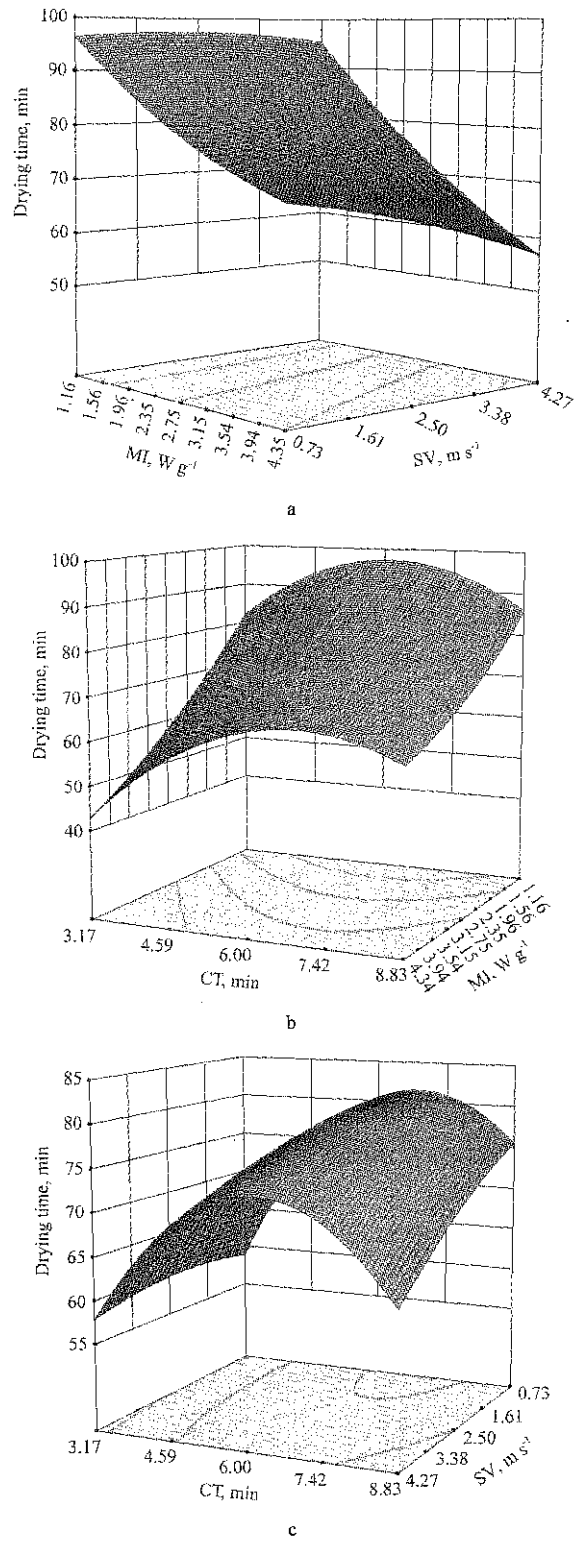

Figure 2 Effect of microwave drying conditions on the drying time of GBR

From Figure 2b, it was shown that the total drying time was prolonged with the microwave irradiation time from 2 to 7 min in the drying stage, and it is because the initial moisture content of GBR is high and most of the moisture is present in the form of unbound water in the surface of the material. Extension of the drying time could increase the water removal ability of GBR. In later

drying stage, the future prolonging drying time did not improve the ability of water removal because most of unbound water had been removed. The ratio between drying and tempering was kept at 1:3 in the experimental design, and the total drying time was prolonged when the finial moisture content arriving at 14.0%-15.0%, but the bound water within GBR kernel could be removed only when the temperature reached 70°C-80°C at the heating stage with the time of each drying stage extending from 7 to 10 min. The ability of water removal increased at each drying stage, and total drying time required by which the moisture content decreased to 14%-16% was shortened, as well as drying rate was improved and the total drying time was reduced as shown Figure 2b.

From Figure 2c, drying rate was improved and total drying time was reduced with the SV increasing, but it resulted in the drying rate increasing firstly and then decreasing with drying time at each stage. This reason was mentioned as above. It was an effective method to improve the drying rate and ensure the drying quality of GBR by selecting the suitable the ratio of drying time and tempering time.

(2) Effect of microwave drying condition on the drying rate of GBR

Drying rate represents the decline range of moisture content of material in unit time, and reflects the effect of the drying condition on ability water removed of material. The appropriate drying rate could ensure the drying efficiency and drying quality, but the excessive rapidly drying rate may result in wet and thermal stress to form fissure.

In drying characteristics, the drying rate reflects the effect of the drying condition on ability of removing water of material, and depends on the physical indicators including material composition, and heat and mass transfer. In the drying process, the high drying efficiency suggests the high rate of removal water during the drying process, but it could result in the quality deterioration of dried material, such as fissure and deformation. Furthermore, it could also cause more serious quality deterioration phenomenon of de-color and degradation of quality due to accelerating drying rate by virtue of improving temperature method. Therefore, it will be helpful to control the drying process and quality of material according to the microwave drying rate of GBR, and it provides a theoretical basis to ensure the drying process with the high efficiency and quality. From Figure 3a, it could be seen that the drying efficiency of GBR significantly increased with increasing of MI and SV during microwave drying process, and there was a significant positive correlation between the drying rate and the interaction of MI and SV, and the improvement of the drying rate by MI was greater than that by SV. In the microwave drying process, the GBR was put on the conveyor belt of a microwave dryer. This was one drying stage in which GBR was transported from the inlet to the outlet of dryer. The unit mass material absorbs much more energy with the MI increasing in one drying stage to cause more moisture evaporated by volumetric heating produced inside the GBR. Increasing SV enhances the airflow convective effect at the surface of material to take away the vapor from interior of GBR. While the increase of SV reduces the pressure of wet air at the surface of material, and improves the pressure difference between the surface of GBR and its interior. It is beneficial to accelerate the movement of moisture vapor. Therefore, the drying rate of GBR was improved by increasing the MI and SV.

The interaction between CT and MI was described during the microwave drying GBR process as shown in Figure 3b. The drying rate of GBR increased with the MI in the conditions of 10 min CT and 2.5 m s^{-1} SV. It was because the increasing MI resulted in the moisture evaporation increasing of GBR in unit time, so the drying rate was improving. But the drying rate decreased firstly and then increased with the drying time. The drying rate was calculated by using dividing the removal water amplitude of GBR by the total drying time which included the microwave drying time (the run time of material in the drying chamber) and tempering insulation time. The ratio between microwave drying time and tempering time was 1:3. The temperature of GBR and the moisture reduced in the microwave drying process which formed the moisture gradient between surface and interior of GBR grain. The moisture inside GBR diffused toward its surface due to the difference of moisture contents at

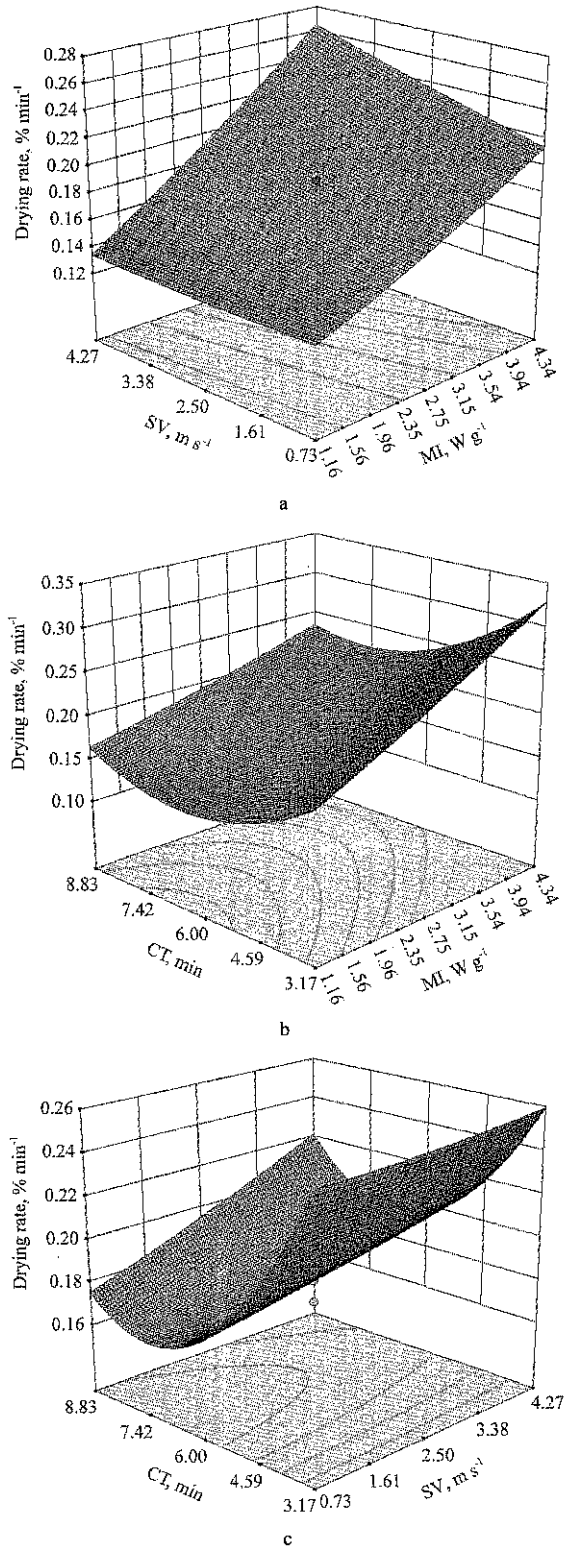

Figure 3 Effect of microwave drying conditions on the drying rate of GBR

the interior and surface at the tempering stage after the microwave drying stage. The microwave volumetric heating caused the evaporation of moisture in GBR surface. The ratio between microwave drying time and tempering time was kept at 1:3 and the initial moisture content reduced from 33.0% (w.b.) to 15.0% (w.b.). The corresponding tempering time, matching with the shorter each circular drying time, was shortened, and the total drying time was also reduced. The drying rate was higher if the reduction range of GBR moisture was similar. The drying rate decreased and the total drying time increased with the microwave drying time. When each circular drying time prolonged by 7 min, the moisture of GBR dried by microwave heating had enough time to diffuse inside GBR in the tempering stage, and the remove of moisture was improved at the following drying stage. The increasing degree of removing moisture amplitude was higher than that of total drying time, and then the drying rate slightly increased. The increasing degree of drying rate in the low MI was larger than that in the high MI. This result was attributed to the higher removing moisture capability by the evaporation of GBR interior than that by water diffusion in the tempering stage with the MI increasing. The promoting effect of removing moisture by tempering was relatively weak at the high MI.

The interaction between each CT and SV is shown as Figure 3c in the microwave drying condition. The drying rate decreased firstly and then increased with increasing CT. Thus, the change trend was the same with the effect reason of CT in Figure 3b. SV increasing was helpful to improve the drying rate of GBR, and the reason resulting in the phenomenon was also the same with the explanation of corresponding part in Figure 3a.

(3) Effect of microwave drying condition on the drying temperature of GBR

The drying temperature is an important index to evaluate the drying technology and control drying process, and it is an index of process controlling to ensure drying quality and reflects the effects of drying condition on the change capability of drying rate of material. The maximum drying temperature generally occurs the final stage in each group drying process. This temperature was measured at the outlet of microwave dryer to record the temperature rising process and calculating the maximum heat accumulation in GBR.

The change trend was described by the effect of factor's interaction of the drying conditions on maximum drying temperature of GBR in Figure 4. It could be seen from Figure 4a that the maximum drying temperature of GBR showed a trend of increasing firstly and then

decreasing with the increasing of SV and MI in the range of experimental parameters. The increasing MI resulted in the drying temperature rising due to the high dissipation of volumetric heating inside the GBR. So the corresponding maximum temperature was also increasing. However, the increasing MI led to further increasing of the drying rate when MI is higher than 2.75 W/g as shown in Figure 3a, and the drying time decreased. Thus, the total drying time was also shortened as shown by Figure 2b, as well as the time of microwave irradiation was reduced. The level of maximum temperature would decrease when the level of MI was high. In the microwave drying GBR, the increasing SV enhanced the convection transfer effect on material surface. The increasing SV may increase the material temperature and improve distribution of the heat uniform. The higher temperature caused the bound water to transfer into unbound water within the material, and the increasing unbound water resulted in the increase of dielectric loss factor. Therefore, more microwave energy could be absorbed and transferred into the heat energy. This process was defined as ventilation and heat accumulation effect. The ventilation in heat convection process not only removed water vapor from GBR, but also took away the heat in the material surface and declined the material temperature. When SV was in the low level (0 to 2.5 m/s), the ventilation and heat accumulation effect was stronger than that of the ventilation and heat dissipation effect. The maximum drying temperature represented the increasing trend. With SV increasing from 2.5 to 5 m/s, the ventilation and heat dissipation effect was stronger than the effect of ventilation and heat accumulation, to decline the maximum temperature.

It was shown in Figure 4b that the maximum drying temperature of GBR was increasing firstly and then decreasing with the increasing of microwave intensity (MI) and each circular time (CT). This change was the same with that of the effect of MI on the maximum drying temperature in Figure 4a. The drying time of GBR was prolonged in the microwave dryer with the CT increase, and the highest drying temperature was increasing, but the total drying time decreased with the further increasing of CT, and the irradiation time was also shortened, so the maximum drying temperature decreased.

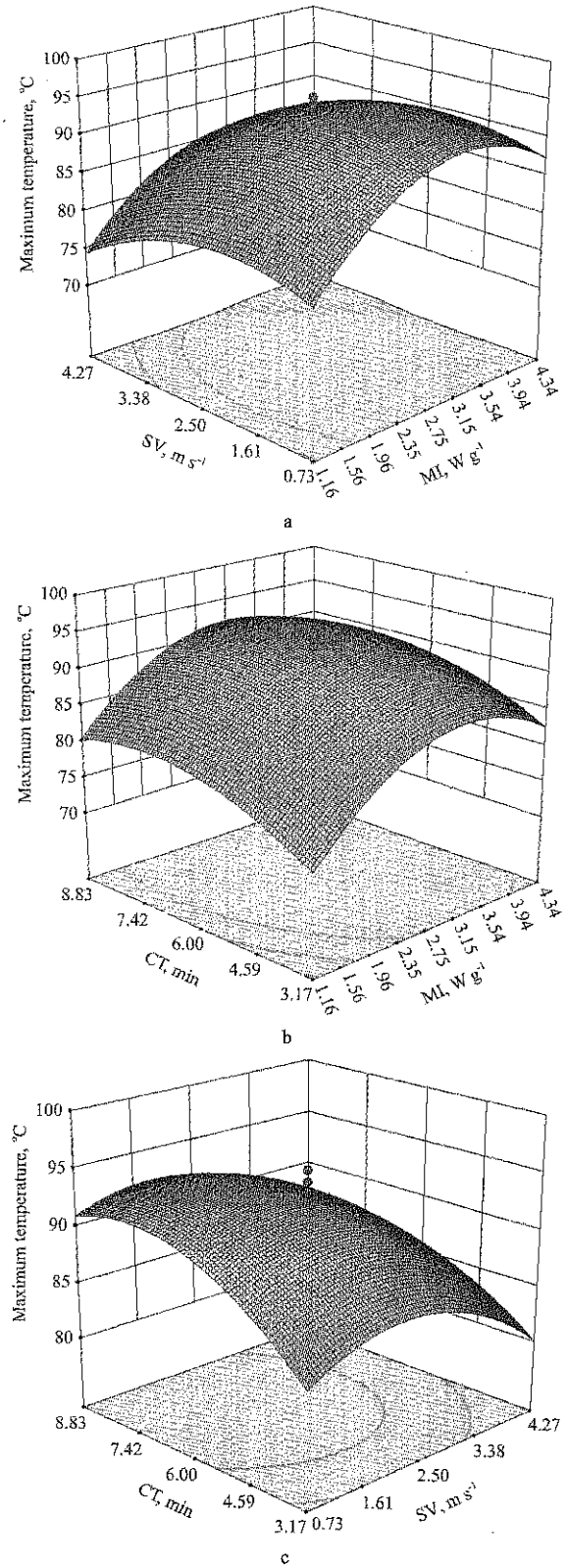

Figure 4 Effects of microwave drying conditions on the maximum temperature of GBR

Figure 4c described the coupling effect of the SV and each circular drying time (CT) on the maximum drying temperature of GBR during microwave drying. The maximum drying temperature showed the increasing trend and then decreasing with the increase of SV and CT. These trends were explained by the corresponding

analysis as shown in Figures 4a and 4b.

Figure 5a showed that the average temperature of GBR raised from 65.2°C to 82.0°C with the microwave intensity increasing from 1.16 to 3.15 W/g. It was maintained in a stable state when the MI arrived at 4.34 W/g level. The average temperature had a positive correlation with unit drying time (3.17-7.42 min), and then had a non-significant correlation (7.42-8.83 min), as well as had a negative correlation with SV. It was because the removal moisture of GBR increased with the increase of MI and unit drying time. The time reaching the target moisture content was shortened, and the heat consumed by the moisture evaporation was equal to the heat supplied by microwave energy. The temperature kept constant till the internal heat of GBR accumulated to a certain extent. The temperature of GBR was shown a trend of increasing followed by stabilization.

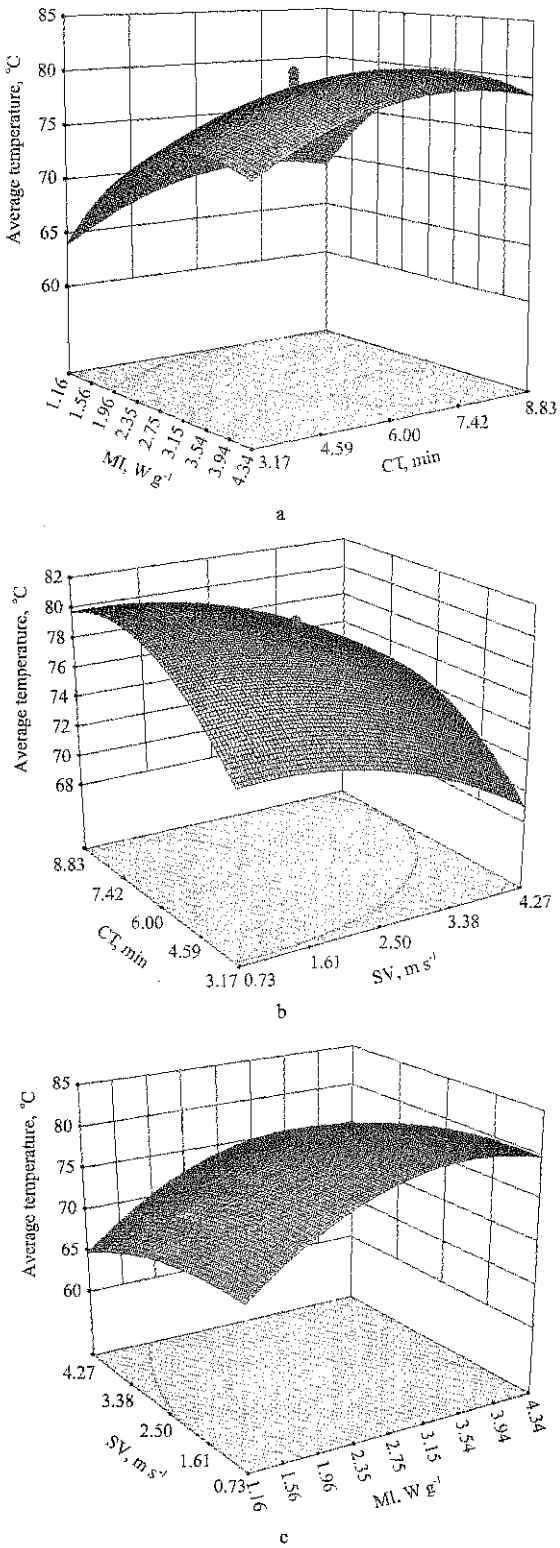

Figure 5 Effects of microwave drying conditions on the average temperature of GBR

The concept of deviation from the average temperature was proposed in this study. It referred to the difference between the real-time temperature and the average temperature during the microwave drying GBR process, which reflected the variation degree and change trend of the instantaneous temperature of the material. Deviation from the average temperature depends on the drying characteristics of the material and the effect of the drying conditions on temperature. This provided the basis to analyze the influence of temperature on the heat-sensitive components in the drying process. The deviation from the average temperature discriminated the effect capability of each factors as shown in Figures 6a, 6b and 6c. The ratio of the average to the deviation of the temperature reflects the effect of the average temperature on the temperature rise. As a dimensionless ratio, this ratio could be used to compare the effect ability of each experimental factor on this ratio as shown in Figures 7a, 7b and 7c. The results from Figure 6 and Figure 7 were used to analyze the influence of microwave drying conditions on the temperature change of the material, and to determine the temperature change characteristics of GBR, which provided a basis for controlling the drying temperature according to the microwave drying condition and reducing the thermal degradation of the heat-sensitive components of GBR. It could be known from Figure 6 that in the range of experimental factors, the degree of temperature deviation from the mean arrived at the highest level with the parameter level increasing from the initial value to near the intermediate level. It indicated that the two-coupling effects among the three factors arrived at the highest values when to approach the middle level of parameter. As shown in Figures 6a and 6c, the

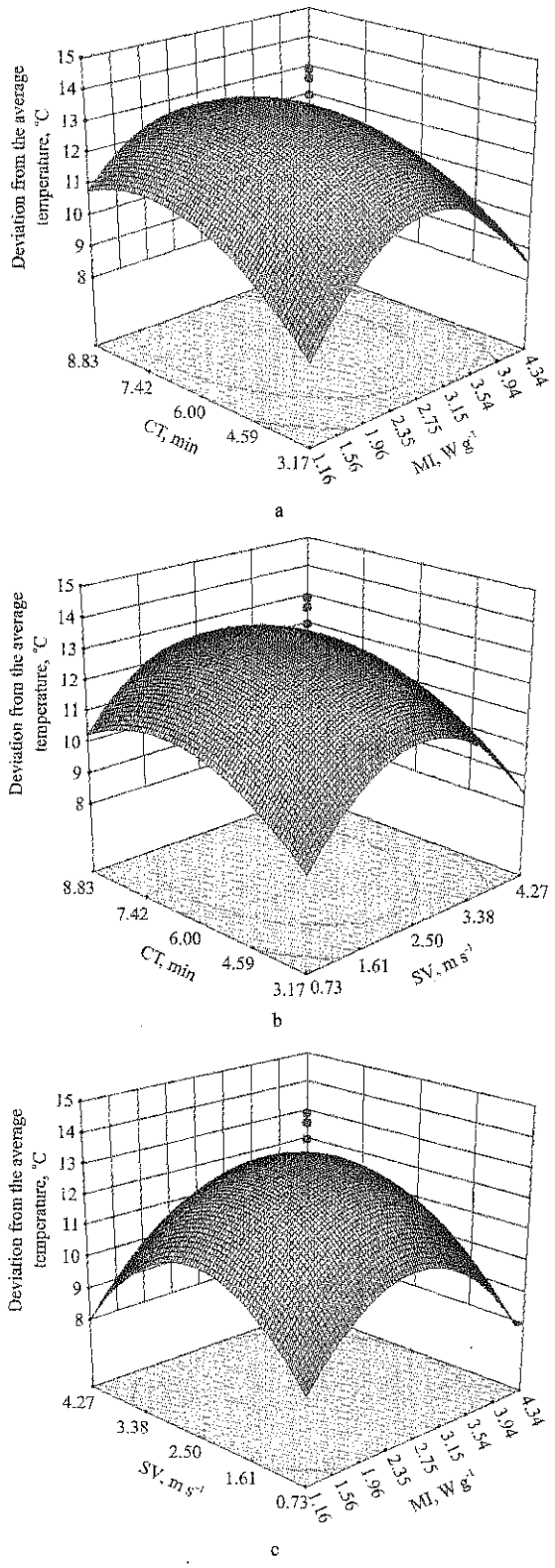

Figure 6 Effects of microwave drying conditions on deviation between the average temperature and drying temperature of GBR

microwave energy absorbed by GBR increased at first with the increase of MI, which indicated that the increase of MI had a positive effect on the material temperature rise, and then microwave energy showed a decreasing trend. This was because the increase amplitude was decline (as shown in Figures 5a, 5c) when GBR temperature arrived at a certain level, but the amount heat of GBR increased with the increase of CT, and SV increased and the convective heat transfer was enhanced. Meanwhile, the heat loss was also increase in drying GBR, and the temperature deviation arrived at peak value when the temperature was at the maximum value. It could be seen from Figure 6b that the temperature deviations caused by CT and SV decreased because the temperature was relatively stable when reaching the highest value. Comparing the effects of the microwave drying conditions on the ratio of average and deviation of temperature in Figures 7a, 7b and 7c, it was determined that the effect of MI on temperature of GBR was the highest, then followed by SV, and CT was the least. The above analysis results suggested that the temperature of GBR was significantly higher than the average level in the microwave drying process when the drying parameters approached the middle level (MI at 2.75 W/g, SV at 2.5 m/s, CT at 6 min). It was helpful to improve the drying rate, but the higher temperature could also cause the quality deterioration phenomenon, degradation of sensitive components (GABA), brown colors and fissure. Therefore, in order to full select microwave drying parameters and correctly analyze the influence of drying parameters on drying characteristics and quality of GBR, it was necessary not only to consider the influence of the average temperature of the material, but also to take into account the effect of temperature over the average level.

According to the changes of the water and temperature of GBR in Figure 1 to Figure 7 and F value in Table 4, it indicated that MI had the most significant positive effect on the DR and MGT of GBR, but the grain temperature rose slowly when MI exceeded 2.75 W/g. With the increase of CT, the drying rate of GBR showed a decreasing followed by increasing trend, while the temperature had an increasing followed by decreasing tendency. CT of 6-10 min was helpful for ensuring the drying efficiency and quality of GBR. SV had a significant negative correlation with the temperature of GBR, and the coupling effect with MI had a significant positive correlation effect on drying rate, and the suitable SV was 2.5-5.0 m/s. According to the influence law of MI, CT and SV on the drying process of GBR, the input

of dynamic parameters was used in microwave drying process to achieve the higher drying rate with the lower grain temperature, and it was helpful to improve drying efficiency and ensuring drying quality of GBR.

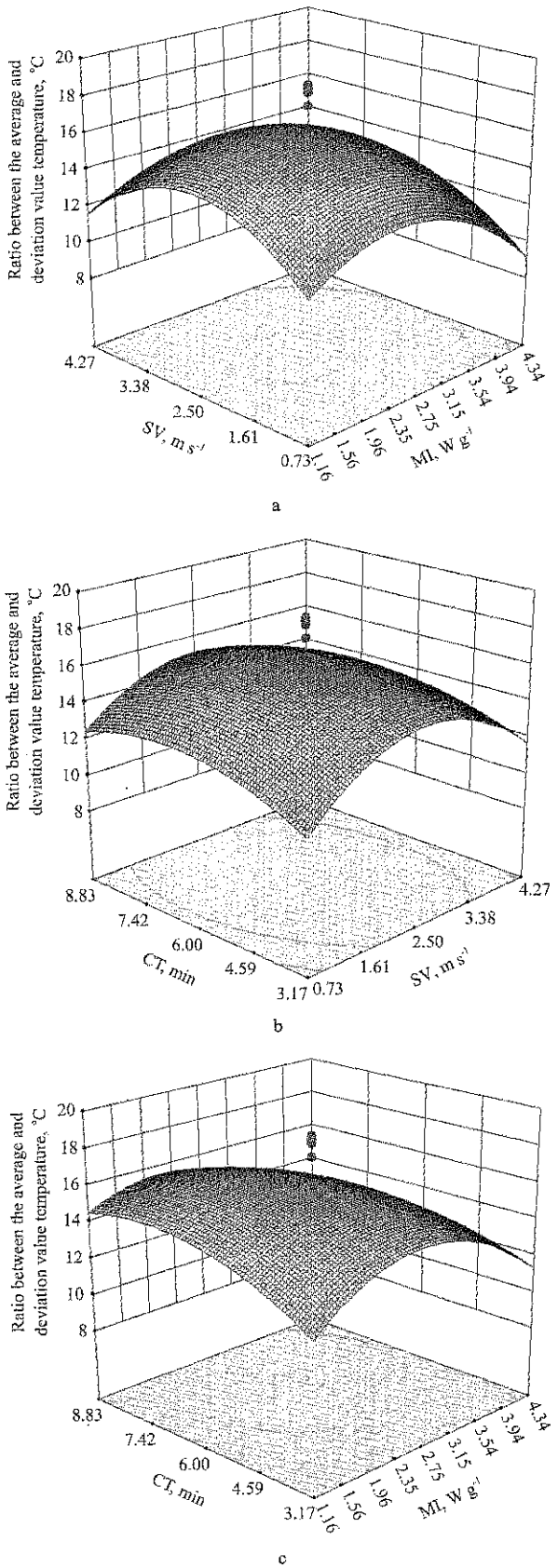

Figure 7 Effects of microwave drying conditions on the ratio between the average and deviation value of temperature of GBR

3.2 Process parameters optimization of microwave drying GBR

Drying efficiency and quality of product are two important aspects to evaluate the advanced technology and applicability of drying process, and are the target values to optimize the drying parameters in the process of drying agricultural products such as grains, fruits and vegetables. From the above analysis for the microwave drying characteristics of GBR, the increase of temperature and the decline of moisture during the microwave drying process were very significant in the initial stage and then were relative stabilization. It was seen from Figure 4a that the average temperature of GBR increased from 65.2°C to 82.0°C with MI increasing from 1.16 to 3.15 W/g, and the average temperature maintained in a stable state when MI increasing to the level of 4.34 W/g. According to the influence of microwave drying parameters on the increase of temperature and the decline of moisture, the structure characteristics with the two-stage drying process and three-layer drying conveyer in each drying stage were considered to design a continuous microwave dryer. A drying technology with MI changeability ranging from high (4-5 W/g) to low (2.5-4 W/g) was employed in order to meet the requirement of the production efficiency and drying quality.

Figure 2b showed that the total drying time increased with the microwave irradiation time from 2 to 7 min during the drying stage. This was attributed to high initial moisture content of GBR at the form of non-bound water in the surface of GBR. The drying time was shorter, and the prolonging heating time could increase the removal moisture in each drying stage including the microwave heating and the tempering process. The further prolonging the drying time would not increase the removal moisture because the most of the non-binding water was removed. Therefore, the drying time was determined with 9-12 min in each stage in order to ensure the drying rate.

It was seen from Figure 2a that the total drying time was shortened with the increase of microwave intensity and SV. This was because the microwave volumetric heating resulted in the rapid evaporation of moisture

inside the material, and the MI increase could improve the evaporation rate and evaporation capability of internal water. The increase of SV could improve the capacity of removing wet of flowing air. By the interaction of MI and SV, the rapid evaporation of internal moisture for high humidity GBR matched with the rapid migration of the surface. As shown in Figure 2a, the drying time required the moisture content reducing from the initial moisture (32.0%-33.0%) to the final moisture content (14.0%-15.0%) was shortened, and the total drying time was also reduced. The SV was determined as 3.5-4.5 m/s to improve the drying rate and reduce the uneven distribution of GBR temperature.

Table 5 showed that the drying parameters was 4 W g^{-1} microwave intensity, 3.50 m s^{-1} SV and 10.22 min drying time in the first drying stage of the microwave drying GBR. When meeting all constraints, it could be obtained with 0.28% min^{-1} drying rate, 82°C maximum drying temperature, 6.5°C temperature deviation, and 0.844 fitness.

Table 5 Optimization results of the first drying stage during microwave drying GBR

(1) Constraint conditions

Constraint condition	Target	Minimum	Maximum	Minimum	Maximum	Importance
		Limiting value	Limiting value	Weight	Weight	
A:IMI	Range	4	5	1	1	3
B:SV	Range	3.5	4.5	1	1	3
C:CT	Range	10	12	1	1	3
Drying time	Minimum	50	60	1	1	3
Drying rate	Maximum	0.1	0.35	1	1	3
Maximum temperature	82°C	75.5	85.5	1	1	4
Temperature deviation	Minimum	2	15.4	1	1	3

(2) Optimization results

Optimum combination	IMI	SV	CT	Drying time	Drying rate	Maximum temperature	Temperature deviation	Expectation
1	4.00	3.50	10.22	44.0116	0.281665	81.9999	6.53526	0.844

Table 6 Optimization result of the second drying stage during microwave drying GBR

(1) Constraint condition

Constraint condition	Target	Minimum	Maximum	Minimum	Maximum	Importance
		Limiting value	Limiting value	Weight	Weight	
A:IMI	Range	4	5	1	1	3
B:SV	Range	3.5	4.5	1	1	3
C:CT	Range	10	12	1	1	3
Drying time	Minimum	50	60	1	1	3
Drying rate	Maximum	0.1	0.35	3.2893	1	3
Maximum temperature	82°C	75.5	85.5	1	1	4
Temperature deviation	Minimum	2	15.4	1	1	3

(2) Optimization results

Optimum combination	IMI	SV	CT	Drying time	Drying rate	Maximum temperature	Temperature deviation	Expectation
1	4.00	3.50	10.38	42.06	0.29	81.42	6.26	0.715

It could be seen from Table 6 that the drying parameters was 4 W/g MI, 3.50 m/s SV and 10.38 min drying time in the second drying stage of the microwave drying GBR. When meeting all requirements of constraints, it could be obtained with 0.28% min^{-1} drying rate, 81°C maximum drying temperature, 6.3°C temperature deviation, and 0.715 fitness.

The two-stage verification experiment was carried out in the drying condition with 4 W/g MI, 3.50 m/s SV and 10.3 min drying time. The measured results were 0.31% min^{-1} drying rate, 85.2°C maximum temperature and 8.2°C temperature deviation. It indicated that the optimizing parameters can be used for microwave drying process of GBR.

4 Conclusion

The influences of microwave drying parameters are different on the drying characteristics of germinated brown rice (GBR). The MI has the most significant positive effect on the drying rate and grain temperature of GBR, but the temperature rising trend is slow when MI over 2.75 W/g. The drying rate decreases firstly and then increases with each circular drying time, while the change of temperature is inverse. Each circular drying time of 6-10 min is helpful to ensure the drying efficiency and quality of GBR. The SV has a significant negative correlation with the temperature of GBR, and the coupling effect with MI has a significant positive effect on the drying rate, and the SV is suitable for 2.5-5.0 m/s. A three-stage drying process was proposed as microwave drying +tempering insulation +microwave drying. The optimal parameters of drying process include the variable range of MI of 4-5 W/g in the first microwave drying stage and 2.5-4 W/g at the second microwave drying stage, and the drying time of 9-12 min and tempering time with the third times than that of drying time, as well as the SV of 3.5-4.5 m/s. The three-stage microwave drying technology and optimal parameters may ensure the drying efficiency and quality of GBR.

Acknowledgments

The authors gratefully thank the financial support provided by National Public Welfare Industry (Agriculture) Research Project of China (201403063-4), Natural Science Foundation of Heilongjiang Province of China (590028), Science and Technology Project of Harbin in Heilongjiang Province of China (2017RAXXJ028) and Young Talents" Project of Northeast Agricultural University of China (518076) for this research project.

[References]

[1] Chandrasekaran, S., S. Ramanathan, and T. Basak. 2013. Microwave food processing—A review. *Food Research International,* 52(1): 243–261.

[2] Cheevitsopon, E., and A. Noomhorm. 2015.Effects of superheated steam fluidized bed drying on the quality of parboiled germinated brown rice.*Journal of Food Processing & Preservation,* 39(4): 349–356.

[3] Chen, H. H., H. C. Chang, Y. K. Chen, C. L. Hung, S. Y. Lin, and Y. S. Chen. 2016. An improved process for high nutrition of germinated brown rice production: Low-pressure plasma. *Food Chemistry,* 191(15): 120–127.

[4] Chung, H.J., A. Cho, and S.T. Lim. 2012. Effect of heat-moisture treatment for utilization of germinated brown rice in wheat noodle. *LWT - Food Science and Technology,* 47(2): 342–347.

[5] Chung, H.J., A. Cho, and S.T. Lim. 2014. Utilization of germinated and heat-moisture treated brown rices in sugar-snap cookies. *LWT - Food Science and Technology,* 57(1): 260–266.

[6] Chungcharoen, T.,S. Prachayawarakorn,S. Soponronnarit, andP. Tungtrakul. 2012. Effect of drying temperature on drying characteristics and quality of germinated rices prepared from paddy and brown rice. *DryingTechnology,*30(16): 1844–1853.

[7] Chungcharoen, T., S. Prachayawarakorn, P. Tungtrakul, and S. Soponronnarit. 2014. Effects of germination process and drying temperature on Gamma-Aminobutyric Acid (GABA) and starch digestibility of germinated brown rice. *Drying Technology,* 32(6): 742–753.

[8] Esa, N. M., K. K. A. Kadir, Z. Amom, and A. Azlan. 2013. Antioxidant activity of white rice, brown rice and germinated brown rice (*in vivo and in vitro*) and the effects on lipid peroxidation and liver enzymes in hyperlipidaemic rabbits. *Food Chemistry,* 141(2): 1306–1312.

[9] Han, A., J. R. Jinn, A. Mauromoustakos, and Y. J. Wang. 2016.Effect of parboiling on milling, physicochemical, and textural properties of medium- and long-grain germinated brown rice. *Cereal Chemistry.,* 93(1): 47–52.

[10] Han, Q. H., L. J. Yin, S.J.Li, B.N.Yang, and J.W. Ma. 2010. Optimization of process parameters for microwave vacuum drying of apple slices using response surface method. *Drying Technology,* 28(4): 523–532.

[11] Komatsuzaki, N., K. Tsukahara, H. Toyoshima, T. Suzuki, N. Shimizu, and T. Kimura. 2007. Effect of soaking and gaseous treatment on GABA content in germinated brown rice. *Journal of Food Engineering,* 78(2): 556–560.

[12] Lin, Y. T., C. C. Pao, S. T. Wu, and C. Y. Chang. 2015. Effect of different germination conditions on antioxidative properties and bioactive compounds of germinated brown pice.*Biomed Research International,* 2015, (4): 608761.

[13] Liu, C. H., L. B. Zhang, C. Srinivasakannan, J. H. Peng, B. G. Liu, and H. Y. Xia. 2014. Dielectric properties and optimization of parameters for microwave drying of petroleum coke using response surface methodology. *Drying Technology,* 32(3): 328–338.

[14] Pruengam, P., S. Soponronnarit, S. Prachayawarakorn, and S.

Devahastin. 2016. Evolution of mechanical properties of parboiled brown rice kernels during impinging stream drying. *Drying Technology,* 34(15): 1843–1853.

[15] Seo, D. H., M. S. Kim, H. W. Choi, J. M. Sung, J. D. Park, and J. S. Kum. 2016. Effects of millimeter wave treatment on the germination rate and antioxidant potentials and gamma-aminobutyric acid of the germinated brown rice. *Food Science & Biotechnology,* 25(1): 111–114.

[16] Sirisoontaralak, P., N. N. Nakornpanom, K. Koakietdumrongkul, and C. Panumaswiwath. 2015. Development of quick cooking germinated brown rice with convenient preparation and containing health benefits. *LWT - Food Science and Technology,* 61(1): 138–144.

[17] Srisang, N., S. Prachayawarakorn, W. Varanyanond, and S. Soponronnarit. 2010. Germinated brown rice drying by hot air fluidization technique. *Dry. Technol.,* 29(1): 55–63.

[18] Srisang, N., S. Soponronnarit, R. Thuwapanichayanan, and S. Prachayawarakorn. 2016. Modeling heat and mass transfer-induced stresses in germinated brown rice kernels during fluidized bed drying. *Drying Technology,* 34(6): 619–634.

[19] Tian, S., K. Nakamura, and H. Kayahara. 2004.Analysis of phenolic compounds in white rice, brown rice, and germinated brown rice. *Journal of Agricultural & Food Chemistry.,* 52(15): 4808–4813.

[20] Wang, L. 2016. Study on microwave drying germinated brown rice system. M. S. Thesis. : College of Engineering. Northeast Agricultural University.Harbin

[21] Yang G. F. 2004. A Summary of mechanism about fissure formation in rice kernel. *Food Science,* 25(10): 384–387. (In Chinese)

[22] Zhang, Q., J. Xiang, L. Z. Zhang, X. F. Zhu, J. Evers, W. V. D. Werf, and L. S. Duan. 2014. Optimizing soaking and germination conditions to improve gamma-aminobutyric acid content in japonica and indica germinated brown rice. *Journal of Functional Foods,* 10(10): 283–291.

[23] Zhang, Y. Z. 2016. Quality nondestructive detection andevaluation research of germinated brownrice based on NIS.M. S. Thesis.: College of Engineering. Northeast Agricultural University. Harbin

[24] Zheng, X. Z., Y. K. Wang, C. H. Liu, J. K. Sun, B. X. Liu, B. H. Zhang, Z. Lin, Y. Sun, and H. J. Liu. 2013. Microwave energy absorption behavior of foamed berry puree under microwave drying conditions. *DryingTechnology,* 31(7): 785–794.

[25] Zheng, X. Z., J. Yu, Y. Z. Zhang, L. Wang, Y. Y. Wang, and C. H. Liu. 2015. Study on drying characteristics and quality of germinated brown rice under microwave drying conditions. *Journal of Northeast Agricultural University,* 46(11): 86–94. (In Chinese)

Effects of storage temperature and humidity on equilibrium moisture content of brown rice

Zhang Qiang[1,2*], Liu Nian[1,2], Tu Ming[1,2], Wang Shuangshuang[1,2], Zheng Xianzhe[3]

(1. *College of Engineering, Huazhong Agricultural University, Wuhan 430070, China*;
2. *Key Laboratory of Agricultural Equipment in Mid-lower Yangtze River, Ministry of Agriculture, Wuhan 430070, China*;
3. *College of Engineering, Northeast Agricultural University, Harbin 150030, China*)

Abstract: This paper aimed to solve the problem of moisture content changing with the storage temperature and humidity during the storage of brown rice. The static weighing method was used to study the change law of the equilibrium moisture content (EMC) of brown rice under different storage conditions. Software SAS was used to analyze the experimental data. Several models for EMC were compared in their abilities to fit the experimental results. The effects of temperature and relative humidity on EMC of brown rice were analyzed. The results showed that modified Guggenheim-Anderson-Boer model and its optimum parameter combination provided the best agreement with the EMC curves for both the absorption and desorption of brown rice. Compared with the adsorption and desorption law of the paddy rice of the same variety, the lag range of the brown rice moisture absorption was larger. The adsorption and desorption of the brown rice had higher EMC. The isotherms of the adsorption and desorption were relatively moderate. Therefore, the mathematical model of EMC of brown rice can evaluate the temperature and relative humidity conditions of the brown rice under storage conditions objectively and effectively, which can contribute to a good quality of the brown rice.

Keywords: brown rice, equilibrium moisture content, storage, model, quality

Citation: Zhang, Q., N. Liu, M. Tu, S. S. Wang, and X. Z. Zheng. 2017. Effects of storage temperature and humidity on equilibrium moisture content of brown rice. International Agricultural Engineering Journal, 26(4): 228–233.

1 Introduction

The brown rice is the product after the paddy rice hulling. It is an existing form that still maintains the life energy (Wu et al., 2013; Zhang et al., 2015; Cho and Lim, 2016). The storage and circulation of the brown rice has advantages of decreasing the depot content, saving the transportation and storage expenses, improving the rice taste attributes and reducing urban environmental pollution. And it is also beneficial to deep processing of paddy rice and comprehensive utilization of secondary product (Zhou et al., 2014). The brown rice storage has become the development trend of rice storage in the world (Zhou et al., 2011). The moisture content of the brown rice is closely related to the speed and the way of the quality change during the period of the brown rice storage (Nimmol and Devahastin, 2010; Zheng et al., 2011; Zhang et al., 2014). When the moisture content of the brown rice is too high, the physiological metabolism will be strong and the nutrients will be easy to decompose, causing fever, mildew, birth of worms and other quality deterioration (Champagne et al., 2004; Sablani et al., 2009). When the moisture content of the brown rice is too low, the freshness will decrease (Genkawa et al., 2008). The minimum life activities can not be maintained, so the metabolism stops. Therefore, it is necessary to study the influence law of storage conditions on the EMC of brown rice.

Some researchers have researched the classical equation of EMC and isotherm models of farm products (Prasantha and Amunogoda, 2013; Chen and Danao, 2015). Henderson (1952) deduced that the classical model of EMC was based on relations of material adsorption energy. Ajibola (1986) investigated that the modified

Received date: 2017-09-04 **Accepted date:** 2017-10-26

* **Corresponding author: Zhang Qiang**, PhD, lecturer, College of Engineering, Huazhong Agricultural University. Email: zq604@mail.hzau.edu.cn.

Halsey model was the best desorption isotherm model for winged bean seed. Saravacos et al. (1986) found that EMC of Sultana raisins at water activities up to 0.70 decreased as the temperature was increased from 20°C to 35°C. Hubinger et al. (1992) observed that the three fruits temperature had practically no effect on the isotherms. Sun and Woods (1994) noted that the Modified-Chung-Pfost and the Modified-Oswin equations gave the best fit for isotherm data of wheat. Shivhare et al. (2004) investigated Chung and Pfost model showed the best fit for the moisture adsorption isotherms of mushrooms. At present, the study of the adsorption and desorption laws of some grains mainly uses paddy rice as the raw material. The relevant models suitable for describing its isotherm were obtained by fitting research of the isotherm data. Brown rice is another form of paddy rice after shelling. Rice husk has an important influence on its water absorption characteristic, so the water absorption characteristic of brown rice is different from that of paddy rice. Systematic studies considering the effects of storage conditions on the EMC of brown rice are limited.

Based on the above-mentioned reviews, it is necessary to study the effects of storage conditions on EMC of brown rice and obtain the best fit model for the brown rice under storage conditions.

2 Materials and methods

2.1 Brown rice samples

Paddy, variety of Early 944, was supplied by experiment station of the Huazhong Agricultural University, Wuhan, China. After 24 h from harvesting, it was dried to about 14 g/100 g moisture content (wet basis) and was stored for 2 months at temperature of 20°C±2°C and in relative humidity of 55%-65%. After hulling by a sheller (THU-35B type, Satake, Tokyo, Japan) before the experiment, the brown rice was processed. Then the samples were selected impurities-free and stored in airtight containers at room temperature for the further experiments.

2.2 Experimental procedure

The EMC experimental temperatures were fixed at 5°C (Low temperature storage), 15°C (Quasi low temperature storage), and 25°C (Room temperature storage). The EMC experimental relative humidity were fixed at 15%, 25%, 35%, 45%, 55%, 65%, 75%, 85%, and 95%. The brown rice grain for adsorption of EMC experiment was dried to about 4 g/100 g moisture content (wet basis) (Hu and Zhang, 2006). The brown rice grain for desorption of EMC experiment was humidified to about 25 g/100 g moisture content (wet basis). Considering the moisture conditioning treatment process, moisture content of brown rice was increased by 1.5% by way of adjunction with once amount of water solution in this condition (Jia et al., 2006). The prepared samples were sealed in plastic bags and then put in a temperature-humidity chamber (CTHI-150(A) B type, temperature fluctuation ±0.2°C, Shi Dukai Equipment Co., Ltd., Shanghai, China) at 4°C. And they were shaken up regularly to reach equilibrium and used in reserve. Take 400 g for each sample, and the measured average value was the EMC of the brown rice under this condition of temperature and humidity. All tests were performed in triplicate.

2.3 Static weighing method

The EMC of brown rice is based on the static weighing method (Speciss and Wolf, 1987). In a constant-closed-system space, a standard relative humidity environment was created using saturated salt solution. After a certain period of time, the difference between the two consecutive weighing results before and after the equilibrium was less than 2 mg under certain condition of temperature and humidity. Then the moisture content was determined to reach equilibrium. The moisture content of the brown rice in equilibrium state could be determined.

2.4 Data analysis

All analyses were performed in triplicate. The best fitting mathematical model for adsorption and desorption isotherm equations of brown rice based on the fitting of available data was selected by using the highest coefficient of determination (R^2) and the lowest standard error of estimate (*SEE*) (Rohitha Prasantha and Amunogoda, 2013). The results of model parameters were obtained by using SAS software (Ver. 9.4, SAS Institute, INC., Cary, NC, USA).

3 Results and discussion

3.1 Effects of storage environmental temperatures and humidity on the EMC curves of brown rice

The results in Figure 1 indicated the adsorption and desorption EMC curves of brown rice under different storage conditions.

Figure 1a-c showed that adsorption and desorption isotherms of brown rice presented the typical inverse "S" curve. The desorption EMC was higher than adsorption EMC under given temperature and humidity. There was hysteresis between the adsorption and desorption curves. To achieve the same EMC, the environmental relative humidity of the adsorption should be higher than that of the desorption at the same temperature. Hence, brown rice was stored after being dried to less than the adsorption EMC. The relative humidity of the storage environment was controlled as the corresponding humidity value of the adsorption EMC, which could prevent the moisture change of the brown rice during the storage.

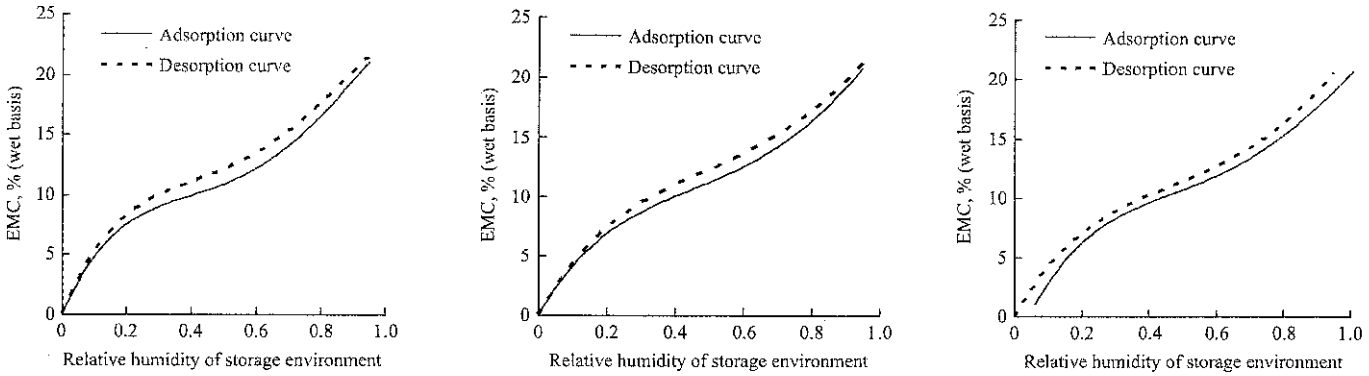

a. EMC curves of brown rice at 5°C b. EMC curves of brown rice at 15°C c. EMC curves of brown rice at 25°C

Figure 1 EMC curves of brown rice at three different temperatures

3.2 Change curves for hysteresis range of brown rice

The moisture difference in adsorption and desorption EMC of brown rice at different temperatures was shown in Figure 2. The increase of temperature caused the decrease of hysteresis range of brown rice hysteresis range. The biggest changing range of the hysteresis was at the relative humidity scope of 40%-80%.

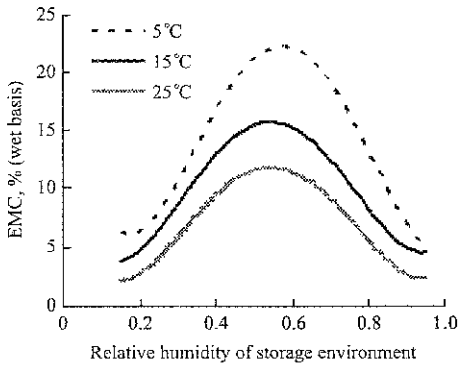

Figure 2 Change curves for hysteresis range of brown rice

3.3 Comparison of adsorption and desorption EMC curves and hysteresis range in brown rice and paddy rice

Figure 3a-c indicated the adsorption and desorption EMC curves of brown rice and paddy rice under different test conditions.

As seen in Figure 3a-b, compared with the adsorption and desorption law of paddy rice and brown rice of the same variety, the adsorption and desorption isotherms of the brown rice were relatively gentle. The change of brown rice EMC was less affected by environmental relative humidity. That was because the moisture content of the rice husk was greatly affected by the external environmental conditions. The rice husk could easily absorb or release moisture from the external environment to change the moisture content of the paddy rice. Therefore, the adsorption and desorption isotherms of the brown rice were more gentle than those of the paddy rice, and the EMC was relatively stable.

From Figure 3c, we can see the change curves for hysteresis range of the brown rice and paddy rice. Figure 3a-c showed that the hygroscopic hysteresis range of the brown rice was larger than that of the paddy rice. Under the same relative humidity condition, the EMC of the brown rice was higher than that of the paddy rice. That was because paddy rice was composed of rice husks and the brown rice. In each component of the paddy rice, the

rice husk had the lowest water content, the worst hydrophilic property and the lowest EMC (Juliano, 1964; Lu and Siebenmorgen, 1992). Therefore, the EMC of the brown rice was higher than that of the paddy rice.

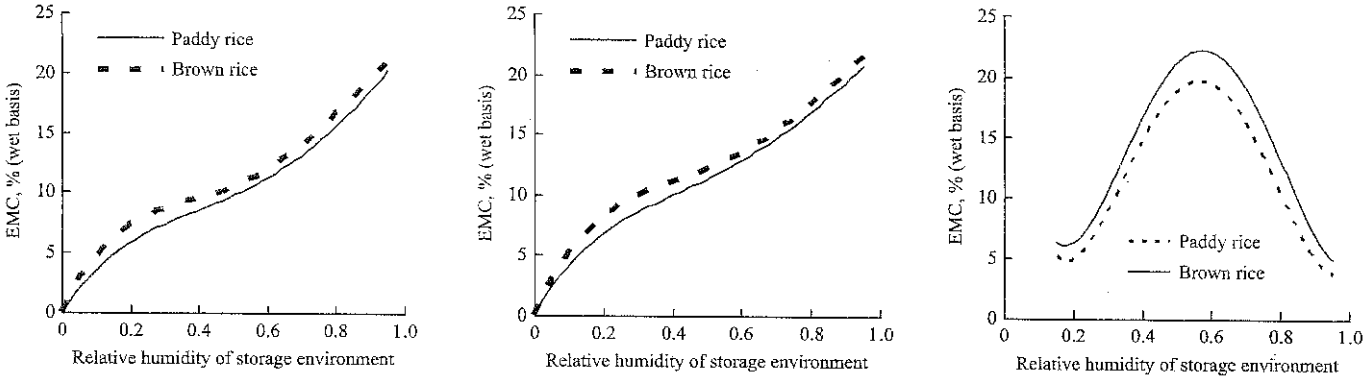

a. Equilibrium curves for adsorption of paddy rice and brown rice of the same cultivars

b. Equilibrium curves for desorption of paddy rice and brown rice of the same cultivars

c. Change curves for hysteresis range of the paddy rice and brown rice of the same cultivars

Figure 3 Comparisons of EMC and hysteresis range variation curves of paddy rice and brown rice

3.4 Effects of temperature and relative humidity on EMC of brown rice

Figures 4a and 4b presented the adsorption and desorption EMC curves of the brown rice grain at different temperatures. Both temperature and relative humidity affected the EMC of the brown rice. Temperature had a more significant effect than relative humidity. Under the same relative humidity condition, both the adsorption and desorption EMC decreased with the increase of the temperature. While under the same temperature condition, the adsorption and desorption EMC increased with the rising of the relative humidity. In different relative humidity intervals, the changing rates of the EMC were different.

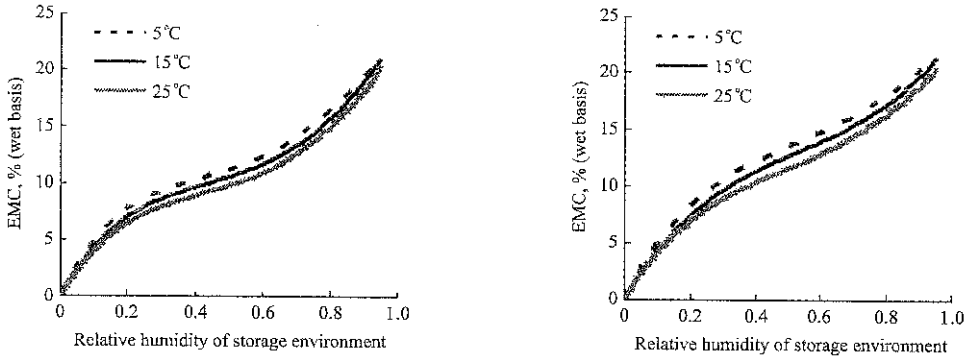

a. EMC curves for adsorption of brown rice

b. EMC curves for desorption of brown rice

Figure 4 EMC curves of brown rice under different storage environments

3.5 Fitting EMC model of brown rice

Modified Henderson model, modified Chung-Pfost model, modified Halsey model, modified Oswin model, and modified Guggenheim-Anderson-Boer (GAB) model were analyzed for goodness of fit for the experimental data of brown rice adsorption and desorption, which were summarized in Table 1 (Wen et al., 1998). According to the measured value of EMC of the brown rice grain, the parameters in each model were fitted by using the non-linear regression method in SAS software package. The five models for brown rice were evaluated by means of estimated standard deviation *SEE* and determination coefficient R^2. The estimated parameters and fitting indexes of adsorption and desorption EMC model for brown rice were shown in Table 2.

The GAB model gave the best fit for adsorption and desorption isotherm data of brown rice (Table 2). The adsorption EMC model parameters obtained for R^2 and *SEE* were 0.9983 and 0.3319 respectively. The R^2 and *SEE* found on the desorption EMC model parameters were 0.9977 and 0.5181 respectively. Therefore, the GAB model was selected as the best model for brown rice. The modified GAB model was revised by the BET model (Yang, 1991). Each of its constants has definite physical

meaning. Therefore, the modified GAB model was selected as the adsorption and desorption model of the brown rice grain.

Table 1 Fitting model and model expression

Model	Model expression
Modified Henderson model	$1-ERH=EXP[-A\cdot(T+C)\cdot(M_e)^B]$
Modified Chung-Pfost model	$ERH=EXP[-\frac{A}{T+C}\cdot EXP(-B\cdot M_e)]$
Modified Halsey model	$ERH=EXP[-EXP(A+B\cdot T).M_e^{-C}]$
Modified Oswin model	$M_e=(A+B\cdot T)(\frac{ERH}{1-ERH})^C$
Modified GAB model	$M_e=\frac{(\frac{A}{T})\cdot A_w}{(1-B\cdot A_w)[1-B\cdot A_w+(\frac{C}{T})\cdot A_w]}$

Note: ERH represents relative humidity of air; T represents temperature; M_e represents equilibrium moisture content; A, B and C represent constant term.

Table 2 Parameters for adsorption and desorption EMC model of brown rice and their fitting indexes

	Parameters and index	Henders.	Chung-Pfost	Halsey	Oswin	GAB
Adsor-ption	A	0.0108	1246.7	8.3549	11.8203	2837.7
	B	0.4853	0.2479	–0.0054	–0.0420	0.6722
	C	135.2	103.6	–3.6360	0.2263	373.2
	$S.E$	2.4121	0.3586	1.6702	1.6542	0.3319
	R^2	0.9877	0.9844	0.9915	0.9918	0.9983
Desor-ption	A	0.0125	925.9	9.4073	12.5996	2243.1
	B	0.4923	0.2453	–0.0116	–0.0394	0.6196
	C	91.5990	56.8795	–3.8975	0.2152	248.7
	$S.E$	1.8399	0.6477	2.2833	1.0598	0.5181
	R^2	0.9919	0.9729	0.9897	0.9953	0.9977

Putting the data of Table 2 (A=2837.7, B=0.6722 and C=373.2) into the modified GAB model, the adsorption isotherms model of the brown rice was obtained:

$$M_{ea}=\frac{2837.7\frac{A_w}{T}}{(1-0.6722A_w)(1-0.6722A_w+373.2\frac{A_w}{T})} \quad (1)$$

where, M_{ea}—adsorption EMC, %; A_w—water activity; T—environment temperature, °C.

Putting the data of Table 2 (A=2243.1, B=0.6169 and C=248.7) into the modified GAB model, the desorption isotherms model of the brown rice was obtained:

$$M_{ed}=\frac{2243.1\frac{A_w}{T}}{(1-0.6169A_w)(1-0.6169A_w+248.7\frac{A_w}{T})} \quad (2)$$

where, M_{ed}—desorption EMC, %; A_w—water activity; T— environment temperature, °C.

To meet the requirements of the storage quality and optimum storage moisture content of brown rice, the storage temperature was 5°C-15°C and the relative humidity of the storage environment was 55%-70% according to the EMC model of the brown rice.

4 Conclusions

Compared with the adsorption and desorption law of paddy rice of the same variety, hygroscopic hysteresis range of the brown rice was larger than that of the paddy rice. The adsorption and desorption EMC of the brown rice was higher than that of the paddy rice. The adsorption and desorption isotherms of the brown rice were more gentle than those of the paddy rice. The change of brown rice EMC was less affected by environmental relative humidity. The effects of temperatures and relative humidity on the EMC of brown rice were significant. The modified GAB model and its optimum parameters combination are the most suitable for describing the EMC curve of the brown rice grain. The EMC model of brown rice can evaluate the temperature and relative humidity conditions of the brown rice objectively and effectively, which can contribute to a good quality of the brown rice.

Acknowledgments

The authors express their acknowledgment to the Fundamental Research Funds for the Central Universities (2662015QD043), Opening Subject for Key Laboratory of Modern Agriculture, Tarim University (TDNG20160102) and Industrial Science and Technology Project of Xinjiang Production and Construction Corps (2015AB039) for financial support and all of the persons who assisted in this writing.

[References]

[1] Ajibola, O. O. 1986. Equilibrium moisture properties of winged bean seed. *Transactions of the ASAE*, 29(5): 1485–1487.

[2] Champagne, E. T., J. F. Thompson, K. L. Bett-Garber, R. Mutters, J. A. Miller, and E. Tan. 2004. Impact of storage of freshly harvested paddy rice on milled white rice flavor. *Cereal Chemistry*, 81(4): 444–449.

[3] Chen, S. F., and M. G. C. Danao. 2015. Modeling the equilibrium moisture content (*EMC*) of *Miscanthus sinensis*, miscane, energy cane, and energy sorghum. *Fuel*, 147(1):

18–26.

[4] Cho, D. H., and S. T. Lim. 2016. Germinated brown rice and its bio-functional compounds: A review. *Food Chemistry*, 196(1): 259–271.

[5] Genkawa, T., T. Uchino, S. Miyamoto, A. Inoue, Y. Ide, F. Tanaka, and D. Hamanaka. 2008. Development of mathematical model for simulating moisture content during the re-wetting of brown rice stored in film packaging. *Biosystems Engineering*, 101(4): 445–451.

[6] Henderson, S. M. 1952. A basic concept of equilibrium moisture. *Agriculture Engineering*, 33: 29–32.

[7] Hu, K., and J. N. Zhang. 2006. Selection of fitting models of adsorption and desorption isotherms of rice and optimization of their parameters. *Transactions of the Chinese Society of Agricultural Engineering*, 22(1): 153–156. (In Chinese with English abstract)

[8] Hubinger, M., F. C. Menegalli, R. J. Aguerre, and C. Suarez. 1992. Water vapor adsorption isotherms of guava mango and pineapple. *Journal of Food Science*, 57(6): 1405–1407.

[9] Jia, F. G., H. L. Deng, X. Z. Zheng, S. G. Bai, and F. L. Wang. 2006. Effect of moisture conditioning treatment on milling characteristic of brown rice. *Transactions of the Chinese Society of Agricultural Engineering*, 22(5): 180–183. (In Chinese with English abstract)

[10] Juliano, B. O. 1964. Hygroscopic equilibria of rough rice. *Cereal Chemistry*, 41(5): 191–197.

[11] Lu, R., and T. J. Siebenmorgen. 1992. Moisture diffusivity of long-grain rice components. *Transactions of the ASAE*, 35(6): 1955–1961.

[12] Nimmol, C., and S. Devahastin. 2010. Evaluation of performance and energy consumption of an impinging stream dryer for paddy. *Applied Thermal Engineering*, 30(14-15): 2204–2212.

[13] Prasantha, B. D. R., and P. N. R. J. Amunogoda. 2013. Moisture adsorption characteristics of solar-dehydrated mango and jackfruit. *Food and Bioprocess Technology*, 6(7): 1720–1728.

[14] Rohitha Prasantha, B. D., and P. N. R. J. Amunogoda. 2013. Moisture adsorption characteristics of solar-dehydrated mango and jackfruit. *Food and Bioprocess Technology*, 6(7): 1720–1728.

[15] Sablani, S. S., L. Bruno, S. Kasapis, and R. M. Symaladevi. 2009. Thermal transitions of rice: Development of a state diagram. *Journal of Food Engineering*, 90(1): 110–118.

[16] Saravacos, G. A., D. A. Tsiourvas, and E. Tsami. 1986. Effect of temperature on the water adsorption isotherms of sultana raisins. *Journal of Food Science*, 51(2): 381–383.

[17] Shivhare, U. S., S. Arora, J. Ahmed, and G. S. V. Raghavan. 2004. Raghavan. Moisture adsorption isotherms for mushroom. *LWT-Food Science and Technology*, 37(1): 133–137.

[18] Speciss, W. E., and W. Wolf. 1987. Critical evaluation of methods to determine moisture sorption isotherms. Rocland L B, Beuchat L R. Water activity: Theory and Application to food. New York. *Marcel Dekker*, 215–233.

[19] Sun, D. W., and J. L. Woods. 1994. The selection of sorption isotherm equations for wheat based on the fitting of available data. *Journal of Stored Products Research*, 34(1): 27–34.

[20] Wu, F. F., N. Yang, A. Touré, Z.Y. Jin, and X. M. Xu. 2013. Germinated brown rice and its role in human health. *Critical Reviews in Food Science and Nutrition*, 53(5): 451–463.

[21] Yang, Q. X. 1991. Adsorption of real gases in multimolecular layers. *Chinese Journal of Chemical Physics*, 4(6): 458–463

[22] Zhang, Q., F. G. Jia, Y. J. Zuo, Q. Fu, and J. T. Wang. 2015. Optimization of cellulase conditioning parameters of germinated brown rice on quality characteristics. *Journal of Food Science and Technology*, 52(1): 465–471.

[23] Zheng, X. Z., C. H. Liu, Z. Y. Chen, N. Y. Ding, and C. J. Jin. 2011. Effect of drying conditions on the texture and taste characteristics of rough rice. *Drying Technology*, 29(11): 1297–1305.

[24] Zhou, Y. L., F. G. Jia, Q. Fu, Q. Zhang, J. T. Wang, and S. Han. 2011. Influence regularity of storage conditions on brown rice moisture changes. *Transactions of the Chinese Society of Agricultural Engineering*, 27(7): 383–386. (In Chinese with English abstract)

[25] Zhou, Z., X. S. Chen, M. Zhang, and C. Blanchard. 2014. Phenolics, flavonoids, proanthocyanidin and antioxidant activity of brown rice with different pericarp colors following storage. *Journal of Stored Products Research*, 59: 120–125.

[26] Wen, Y. X., J. N. Zhang, J. Y. Liu, Z. F. Zhao, and H. T. Chen. 1998. Using the computer software to construct sorption isotherms. *Transactions of the Chinese Society for Agricultural Machinery*, 29(3): 95–98. (In Chinese with English abstract)

[27] Zhang, Q., F. G. Jia, C. H. Liu, J. K. Sun, and X. Z. Zheng. 2014. Rapid detection of aflatoxin B_1 in paddy rice as analytical quality assessment by near infrared spectroscopy. *International Journal of Agricultural and Biological Engineering*, 7(4): 127–133.

Application of NIRS to determine the quality of potato and potato products: A review

Xing Li, Zhang Xiaoyan, Li Shaoping, Cao Youfu, Zhao Qingliang*

(*Chinese Academy of Agricultural Mechanization Sciences, Beijing 100083, China*)

Abstract: Potato (*Solanum tuberosum* L.) is one of the major agricultural crops in the world. It contains a variety of chemical constituents which are highly valuable to people health, including starch, carbohydrate, protein, calcium and potassium. The potato quality test is an area that both market section and technology concern about. Near infrared spectroscopy (NIRS) is a rapid, nondestructive and precise technology can be used in determination of raw potato and potato products. This paper summarized recent advances in NIRS in predicting chemical composition, texture characteristics and sprouting capability in potato or potato products. The results indicated that high potential of NIRS is an efficient tool for monitoring the chemical composition, texture and sprouting capability of potato or potato products. Future prospects and needs related to increasing the feasibility of the industrial application of NIRS in potato composition test were discussed.

Keywords: potato, potato products, NIRS, quality, nondestructive

Citation: Xing, L., X. Y. Zhang, S. P. Li, Y. F. Cao, and Q. L. Zhao. 2017. Application of NIRSto determine the quality of potato and potato products: A review. 2017. International Agricultural Engineering Journal, 26(4): 234–245.

1 Introduction

Potato (*Solanum tuberosum* L.) is one of the major agricultural crops in the world. It is rich in many kinds of nutriments, such as starch, carbohydrate, protein, calcium and potassium, so it is called 'underground apple' or 'second bread' in Europe (Pedreschi et al., 2005). Potato plays a particularly important role in agriculture in the world because it is grown in approximately 80%of all countries and occupies the fourth position after rice, wheat and maize in the world (Otto, 2010). In many developing countries, rising levels of income are driving a 'nutrition transition' toward more energy-dense foods and prepared food products. As part of that transition, demand for potato is increasing. Traditionally potato was generally used as staple food, while nowadays with the development of food industry, potato could be used in many ways such as source of starch, chips and French fries (Gökmen et al., 2005). The quality of potato test is an area that both market and processing industry concerned about.

Potato quality includes many kinds of aspects, such as physicochemical property, security feature and quality characteristic. Grading and sorting of potatoes ensured the derived products meet the defined grade requirements for sellers, and the expected quality for buyers. Except for consumers, industries also need more studies for the quality determination technology, for chemical composition, and internal qualities are also important indicators for transportation, storage and other handlings (Marchi, 2013). Therefore, different analysis methods and techniques including chemical method, instrumental methods, and sensory analysis were appeared. Although traditional analyses in the laboratory provided high accuracy, while most of them involved time-consuming, laborious, costly and unsuitable for on-line application. Compared to the traditional methods, some nondestructive technologies have been used in food assessment (Abbott et al., 1997), like NIRS. So, this review focused on the application of NIRS for potato quality.

NIRS is a rapid, non-destructive method. It requires little or no sample preparation and can evaluate several

Received date: 2017-06-26 **Accepted date:** 2017-10-18

* **Corresponding author: Zhao Qingliang,** Chinese Academy of Agricultural Mechanization Sciences, Beijing 100083, China. Email: xingliclj@163.com.

components simultaneously. It is based on spectral absorption at near infrared wavelengths by the molecules constituting the sample. It has been extensively used in many areas, including agricultural (Pedro et al., 2005;Vincent etal., 2009; Wanget al., 2013; Lebot and Malapa, 2013), food (Coppaet al., 2012; Shen et al., 2012), and medical (Guo et al., 2011), etc. It was first used in agricultural applications by Norris (1964) to measure grain moisture. Since then it has begun to be used in agricultural products and food area to measure chemical components (Dong, 2013; Bevilacqua, 2013; Wang et al., 2013), control food quality (Keller et al., 1993; Kasemsumran, 2007) and ensure food safety (Marchi, 2013; Alexandrakis, 2011).

In the last years, NIRS technology became a powerful tool in predicting and estimating the main compositions of vegetable and fruit (Nicolaï, 2007; Pissard et al, 2013), but only few potato models existed. Except for the high water content overlays spectral information of other constituents, compositions are not homogenously distributed within and between tubers, and wide ranges of size and shape exist. Measurement of whole tubers noted those problems. NIRS is increasingly being applied to determine the chemical composition of potato. Some papers reported on slices, discs from cylinders, and crude mash from single tubers.

Quality of potato such as moisture, starch, protein can be demonstrated by the NIRS directly. Other attributes such as firmness, bruises, inner disease can also be demonstrated by the distinction of near infrared spectra indirectly.

In the past, an excellent review showing the ability of NIR spectroscopy to predict potato chemical composition and quality could be found in Lopez (2013). This paper reviewed the major advances of the NIRS method, as applied to quality inspection and determination of chemical composition.

2 Application of NIRS to predict potato tuber and potato crisp quality

2.1 Potato tuber chemical composition

2.1.1 Dry matter

Many studies showed NIRS had the ability to predict the content of major chemical components such as moisture (Li et al., 2010), dry matter (DM), starch (Hacisalihoglu, 2010), and carbohydrate (Chen et al., 2004). Moisture content determination was the first application of NIRS in the analysis of food. In potato, the moisture content reaches about 70%-90%, it is one of the most important composition and will affect its nutritive value (http://ndb.nal.usda.gov/ndb/search/list). Therefore, the monitoring of moisture content is notably important for potato processing.

Moisture concentration is a prime candidate for measurement using NIRS, with vibration for C-H and O-H bonds responsible for strong absorption features (Lin et al., 2009). Dry matter concentration is a useful index for potato quality, containing information on both moisture and carbohydrate concentration.

Dull et al. (1989) firstly used NIRS to determine potato dry matter contents including thin tissue slices, thick slices and intact potato tubers. The coefficients of correlations of prediction (r_p) were 0.975, 0.952 and 0.918 with a standard error of calibration (SEC) of 0.91 for thin tissue slices, SEC and standard error of prediction (SEP) of 1.28, 1.69, 1.04and 1.52 for thick slices and intact potato tubers, respectively. The results showed that NIRS is a fast way to determine the DM content of potato.

Hartmann and Büning-Pfaue (1998) further collected 116 samples of potato and scanned the samples from 1100 to 2500 nm using a NIR Systems 5000 (Perstorp Analytical Co.). The NIRS calibration models of DM were developed using modified partial least square (MPLS) regression. The results indicated that the NIR technique had the ability to determine DM content with a root mean square error (RMSE) of prediction (RMSEP) of 0.19% and with a coefficient of determination in validation (r_v^2) of 0.97.

Scanlon et al. (1999) investigated the influence of time and conditions of storage on the calibration equations. The researchers used excised 'coins' (48mm diameter and 10 mm thick, periderm removed) of potato tissue. A NIR spectrum was acquired in the 770-2498 nm range at intervals of 2 nm with A NIR Systems (Silver Spring, MD) Model 6500 scanning

spectrophotometer. Calibrations for DM were not affected by time, conditions of storage and robust with coefficient of determination in calibration (r_c^2) = 0.75-0.84 and root mean square error of calibration (RMSEC) of 1.1%-1.2%.

Under-water weightand oven-drying are common methods to determine DM in potato industry. Dijk et al. (2002) studied the relationships between DM obtained by means of underwater weight analysis (DM_{uww}), oven-drying (DM_{dry}) and near-infrared spectra. The result of DM_{uww} has indicated that the NIRS technique could provide good quantitative predictions (DM_{uww}: r_v=0.94, RMSEP=8.46). For DM_{dry} content, the result only showed calibration model (r_c=0.96, $RMSEP_{cal}$=9.37).

Haase (2003) further compared NIRS and an optimized procedure of the under-water weightto identify the best technique in offering a fast and reliable information about the DM concentration of potato. NIR spectra of 837 samples were recorded with a NIRS 6500 instrument (Foss Company, Hamburg, Germany) by scanning the mash twice (400-2500 nm). Models were calculated with the whole NIR spectrum (850-2500 nm). Spectra were used as original, as first derivative (1^{st}) and as second derivative (2^{nd}). The results showed NIRS technology with less divergence than the techniques of under-water weighting, the r^2 of calibration and validation were 0.96, 0.98; 0.96, 0.98; 0.96, 0.97 under original, 1^{st} and 2^{nd} derivatives, respectively.

Fernández-Ahuma et al. (2006) collected 275 samples and used a FT-NIR (ABB Bomem MB160D) spectrometer to develop the DM calibration of mashed potatoes. The equations for the prediction of DM presented an accuracy and precision acceptable for routine analysis according to its ratio of SEP to the standard sample of the reference data in validation value (RPD) 4.2.

Calibrations of potato moisture content were also established by Subedi and Walsh (2009). Spectra were acquired using a Carl Zeiss (Jena, Germany) MMS1/NIR enhanced spectrometer. Short-wavelength near-infrared spectroscopy from 750 to 950 nm was studied in the research. Two kinds of potatoes, including intact, whole tubers and sliced tubers, were used. The results showed the prediction accuracy of r_p^2 of 0.85 with RMSEP of 1.52% for intact, whole tubers and r_p^2 of 0.95 and RMSEP of 0.50% for sliced tubers was achieved.

Brunt and Drost (2010) used an off-line NIR to explore the possibility of determining DM of potato samples. The results showed that NIR model was valid with RMSE of 0.5%.

Helgerudet al. (2010) studied the feasibility of using high speed industrially available 1D and 2D NIR interactance instrumentation for DM content assessment in single potato tubers. The performance of the 1D NIR interactance instrument exceeded the performance of a 2D NIR interactance instrument (r^2=0.95, Root mean square error of cross validation (RMSECV)=0.91 and r^2=0.83, RMSECV=1.65, respectively).

Haase (2011) collected 2517 ground raw potatoes from nine growing seasons and four to five locations. Spectral information was obtained from 850 to 2500 nm with a NIR 6500 monochromator (FOSS). The best r_v^2 within independent validation sets were about 0.99 for DM, RPD was up to 8.5.

The summaries of NIRSapplications for evaluation moisture and dry mattercontents in raw potato were shown in Table 1.

2.1.2 Starch

Starch concentration as important as DM is a significant property of potato food industry, because the quality of final products and efficiency of processing are directly linked to them. Starch content affects the taste, method of cooking and processing of potato tubers. Traditionally, starch concentration of tubers determination method is under-water weight. Hartmann and Büning-Paue et al. (1998) used NIRS technology to estimate the starch content. Spectral data were collected by measurement of diffuse reflectance from the homogenized sample in the NIR region within 1100-2500 nm using a NIR Systems 5000 (Perstorp Analytical Co.). The results showed that SEC, SECV, SEP and r of validation were 0.21%, 0.46%, 0.28% and 0.93, respectively. Meanwhile, Thygesen et al. (2001) researched a set of 97 potato starch samples by NIR technology, RMSECV of 0.006%. Dijk et al. (2002) also studied the relationships between starch and NIRS. The

result showed the potential calibration model (r_{cal}=0.91, $RMSEP_{cal}$=12.4; r_{val}=0.89, $RMSEP_{val}$=13.8). Fernández-Ahumada et al. (2006) scanned 233 mashed potato samples in NIR range (4000-10000 cm^{-1}) using FT-NIR spectrometer (model MB160D, ABB BOMEM, Quebec, Canada; instrument at-line). The NIR model of starch content based on the modified PLS1 method provided moderately successful predictions with r_{cv}^2 of 0.92, standard error of cross-validation (SECV) of 5.0 and a RPD of 3.10.

Table 1 Summary of NIRSapplications for evaluation moisture and dry matter contents in raw potato

Sample description	Wavelength range, nm	Multivariate calibration	Model statistics		References
			Calibration	Validation	
Slices (thin) *n*=52, Slices (thick) *n*=80, Intact *n*=60	800-1000	Linear regression	Slices (thin) (SEC=0.91) Slices (thick) (SEC=1.28) Intact (SEC=1.04)	Slices (thin) (r_v=0.97, SEP=N) Slices (thick) (r_v=0.95, SEP=1.69) Intact (r_v=0.92, SEP=1.52)	Dull et al., 1989
Mashed *n*=116	1100-2500	MPLS	*SEC*=0.07	r_{cv}^2=0.97, SECV =0.24, *SEP*=0.19	Hartmann and Büning-Pfaue, 1998
Coin slice *n*=200	770-2500	MLR	Year 1993-1994 (r_c^2=0.84, SEC=1.1) Year 1994-1995 (r_c^2=0.75, SEC=1.2)	Year 1993-1994 (r_v^2=0.77, SEC=1.3) Year 1994-1995 (r_v^2=0.58, SEC=1.5)	Scanlon et al., 1999
Mashed *n*=81	1100-2500	PLS		DM (r_v^2=0.91, RPD=3.22)	Dijk et al., 2002
Mashed *n*=275	1000-2500	PLS	r_c^2=0.92,	*SECV*=4.5, *RPD*=4.18	Fernández-Ahumaet al., 2006
Unwashed *n*=100, Washed *n*=100, Peeled *n*=100, Sliced *n*=100	750-950	PLS	Unwashed (r_c^2=0.87, MSECV=0.86) Washed (r_c^2=0.87, MSECV=0.87) Peeled (r_c^2=0.92, MSECV=0.70) Sliced (r_c^2=0.92, MSECV=0.72)	Unwashed (r_v^2=0.85, RMSECV=1.52) Washed (r_v^2=0.81, RMSECV=1.64) Peeled (r_v^2=0.90, RMSECV=1.13) Sliced (r_v^2=0.86, RMSECV=1.08)	Subedi and Walsh, 2009
Mashed *n*=356	1100-2500	PLS	r_c^2=0.98, RMSEC=0.44	r_v^2=0.97, RMSEP=0.47	Brunt and Drost , 2010
Intact	760-1040	PLS	/	1D Interactance Measurements (r_v^2=0.95, RMSECV=0.91); 2D Interactance Measurements (r_v^2=0.83, RMSECV=1.68)	Helgerud et al., 2010
Mashed *n*=2517	850-2500	MPLS	/	r_v^2=0.99, SEP=0.39, RPD=8.5	Haase, 2011

Notes: MLR - multiple linear regression; r_{cv}^2 - coefficient of determination in crossvalidation.

Starch content of potato tubers could be predicted successfully by NIR scans of the crude mash in the research of Haase (2006). Three types of pretreatment methods, including original (none), 1st and 2nd, were constructed to predict starch content. The results indicated that three calibration models were no significant differences among these calibration models (none: r_c^2=0.98, 1st: r_c^2=0.98, 2nd: r_c^2=0.98). The prediction results were more reliable based on model evaluation criteria (none: r_v^2=0.90, RPD=2.97; 1st: r_v^2=0.90, RPD= 2.93; 2nd: r_v^2=0.98, RPD=2.78). Haase (2006) further studied the phosphorus content of the potato starch. The data sets investigated were between 0.0265% and 0.1242%. The results obtained showed that precise prediction by NIR-model were not possible, but models pointed out the potentiality of a rough estimation. In order to enable the introduction of sorting machines based on the starch content of potato tubers, Komiyama et al. (2007) investigated nondestructive determination of starch content using visible and NIRS under practical conditions. It indicated that the visible and NIR transmittance method was effective for the accurate and rapid selection of potato tubers based on starch content. Brunt and Drost (2010) collected spectral data from 1100to 2500 nm to detrmine starch content of potato samples. The validation model was equipped with r_v^2 of 0.92, RMSEP of 0.06. It showed that off-line measurements of starch were feasible.

The summaries of NIRS applications for evaluation starch contents in raw potato were shown in Table 2.

2.1.3 Protein

Protein content of potato is smaller than dry matter and starch content. However, protein played an important role in the potato process. Hartmann and Pfaue (1998) studied the possibility of using the NIRS technology to measure the erude protein (CP) in potato. The results demonstrated that it was possible to obtain high precision and accuracy equation for the prediction of CP (r_v^2=0.86, SEP=0.06%). In the following research, Fernández-Ahumada et al. (2006) further studied CP and recoverable

protein (RP) contents using FT-NIR spectrometer(model MB160D, ABB BOMEM, Quebec, Canada; instrument at-line), obtained the reflectance spectral data from 4000 to 10000 cm^{-1}. The r_v^2 and RPD values are low for both CP and RP, they are only 0.62, 1.45 and 0.46, 1.58. Haase (2006) further established calibration and validation models of protein and coagulable protein using NIRS under three different pre- processing methods. The results indicated that total protein content could be predicted (62% confidence), whereas the amount of coagulable protein was not predictable (r^2=0.25). Brunt and Drost (2010a) studied the coagulating protein content using optical fiber NIR probe (EDAPT-1) connected to the NIR spectrophotometer (Technicon Infralyzer IA 500) from 1100 to 2500 nm. The results showed that for the total raw protein concentration, no satisfactory NIR model could be developed. In the further study, Brunt and Drost (2010b) focused on coagulating protein. The tentative PLS calibration model for coagulating protein concentration was very promising, the average difference between NIR-predicted and the chemically measured concentration was 0±0.06%. The summaries of NIRS applications for evaluation of protein contents in raw potato were shown in Table 3.

Table 2 Summary of NIRS applications for evaluation starch contents in raw potato

Sample description	Wavelength Range, nm	Multivariate calibration	Model statistics		References
			Calibration	Validation	
Mashed n=116	1100-2500	MPLS	SEC=0.21	r_v^2=0.93, *SECV*=0.46, *SEP*=0.28	Hartmann and Büning-Pfaue, 1998
Mashed n=275	1000-2500	PLS		*SECV*=5.0, *RPD*=3.10	Fernández-Ahumaet al., 2006
Mashed n=368	850-2500	/	None (r_c^2=0.98, SEC=0.33) 1st Der (r_c^2=0.98, SEC=0.32) 2nd Der (r_c^2=0.98, SEC=0.32)	None (r_v^2=0.90, SEP=0.74, RPD=2.97) 1st Der (r_v^2=0.89, SEP=0.75, RPD=2.93) 2nd Der (r_v^2=0.97, SEP=0.79, RPD=2.78)	Haase, 2006
Mashed n=72	1100-2500	PLSR	r_c=0.91, RMSEP=12.4	r_v=0.89, RMSEP=13.8	Dijk et al, 2002
Mashed n=283	1100-2500	PLS	r_c^2=0.97, RMSEC=0.50	r_v^2=0.92, RM*SEP*=0.63	Brunt and Drost , 2010

Note: None- no pre-processing.

Table 3 Summary of NIRS applications for evaluation of protein contents in raw potato

Sample description	Wavelength Range, nm	Multivariate calibration	Model statistics		References
			Calibration	Validation	
Mashed n=114	1100-2500	MPLS	SEC=0.10	r_v^2=0.86,SECV =0.10, SEP=0.06	Hartmann and Büning-Pfaue, 1998
Mashed n=275	1000-2500	PLS	/	CP (r_v^2=0.62, SECV=2.4, RPD=1.45) RP (r_v^2=0.46, SECV =1.7, RPD=1.58)	Fernández-Ahuma, et al., 2006
Protein (none: n=176; 1st Der: n=174; 2nd Der: n=173) Coagulable protein (none: n=187; 1st Der: n=190; 2nd Der: n=188)	850-2500	MPLS	Protein None (r_c^2=0.83, SEC=0.13) 1st Der (r_c^2=0.89, SEC=0.10) 2nd Der (r_c^2=0.94, SEC=0.07) Coagulable protein None (r_c^2=0.64, SEC=0.070) 1st Der (r_c^2=0.65, SEC=0.070) 2nd Der (r_c^2=0.73, SEC=0.06)	Protein None (r_v^2=0.62, SEC=0.20) 1st Der (r_v^2=0.60, SEC=0.21) 2nd Der (r_v^2=0.59, SEC=0.21) Coagulable protein None (r_v^2=0.25, SEC=0.09) 1st Der (r_v^2=0.23, SEC=0.09) 2nd Der (r_v^2=0.13, SEC=0.11)	Haase, 2006
Mashed n=165	1100-2500	PLS	Coagulating protein (r_c^2=0.88, *RMSEC*=0.09)	Coagulating protein (r_v^2=0.92, *RMSEP*=0.06)	Brunt and Drost, 2010a

2.1.4 Carbohydrate

The color of potato chips is the first quality parameter evaluated by consumers and is critical for the acceptance of the product (Pedreschi et al., 2006). It depends on the content of amino acids, reducing sugar and the heating of the system (Pedreschi, et al., 2005).In the past researches, potato chip color is affected by the Maillard reaction that mainly depends on the content of reducing sugars and amino acids at the surface as well as the frying temperature and time (Márquez and Añón, 1986). Therefore, sugar contents were an important index for the potato processing industry. At the same time, NIR has the ability to assess these quality parameters, so there have been investigations for NIR to determine the contents of sugar in potatoes.

Mehrubeoglu and Cote (1997) used PLS statistical analysis tools to develop the total reducing sugar content of sliced potato samples. The results indicated that NIR

spectroscopy was accurate enough to determine total reducing sugar. On the other hand, Scanlon et al. (1999) studied if a robust NIR calibration could be developed that would screen out tubers having unacceptably high levels of reducing sugars. In the study, a NIR Systems (Silver Spring, MD) Model 6500 scanning spectrophotometer was used to scan the area of 1017 mm^2 of the surface of the coin. A NIR spectrum (no visible region) was acquired in 770-2498 nm range at intervals of 2 nm for a total of 100 spectra. For sugar calibrations, the group of 68 spectra used to develop the screening calibrations covered the whole range of glucose content. Separate calibrations were developed for fructose and for glucose. However, the result showed reflectance NIR spectroscopy didn't appear to be able to screen tubers for unacceptable sugar contents. The results differed from those reported by the former authors. Hartmann and Bijning-Pfaue (Hartmann and Büning-Pfaue, 1998) used NIR technology to predict individual sugar components such as glucose, fructose and sucrose, and it was uncertain. This came from both the low sugar contents and their narrow concentration range in potato tubers. The results showed that the prediction of the individual component had to be improved. The estimation of total reducing sugar was with better results than the prediction of individual sugar content. This result also indicated that totally reducing sugar content seemed to be technologically more important than the content of the single compounds. Chen et al. (2004) examined the performance of NIRS for determination of carbohydrate content in potatoes. The results showed good calibration model with reasonable accuracy (r_v^2=0.93 and SEP=0.98%). This model was developed using PLS regression.

Mehrubeoglu and Cote (1997) indicated that the sugar concentration of thin slices of potato could be determined using NIRS in transmittance geometry. However, only calibration results were presented, with no prediction of an independent data set attempted. Thus, the results may represent over fitting of the data.

Haase (2011) has studied the reducing sugar, sucrose and total sugar in potatoes by NIR technology. The best coefficients of determination (r^2) within independent validation sets were 0.43 for reducing sugars, 0.71 for sucrose and 0.66 for total sugar.

The RPD statistic was unacceptably low in the case of reducing sugars (1.7) and low for sucrose (2.4) and total sugar (2.3).

The sugar assessment by NIRS is impossible, given the relatively low sugar concentration of the potato tuber (approximately 1%-2% w/v of tissue juice) (Walsh et al., 2004).

The summaries of NIRS applications for evaluation carbohydrate contents in raw potato were shown in Table 4.

Table 4 Summary of NIRS applications for evaluation carbohydrate contents in raw potato

Sample description	Wavelength Range, nm	Multivariate calibration	Model statistics		References
			Calibration	Validation	
Mashaed Glucose, n=116	1100-2500	MPLS	SEC=0.034	r_v^2=0.70, SECV =0.050, SEP=0.041	Hartmann and Büning-Pfaue, 1998
Mashaed Fructose, n=100			SEC=0.022	r_v^2=0.89, SECV=0.038, SEP=0.028	
Mashaed Sucrose, n=109			SEC=0.036	r_v^2=0.62, SECV =0.054, SEP=0.037	
Mashaed Σ red. Sugars, n=134			SEC=0.046	r_v^2=0.82, *SECV* =0.069, SEP=0.061	
Sliced n=39	/	PLS	/		
Mashed n=2517	850-2500	MPLS	/	Reducing Sugar (r_v^2=0.43, SEP =38.9×10^{-6}, RPD=0.061) Sucrose (r_v^2=0.71, SEP =96.9×10^{-6}, RPD=2.4) Total Sugar (r_v^2=0.66, SEP =135×10^{-6}, RPD=2.3)	Haase, 2011
Intact	700-1100	PLS	None (r_c^2=0.90, SEC=0.89) 2nd Der (r_c^2=0.91, SEC=0.84)	None (r_v^2=0.87, SEC=0.98) 2nd Der (r_v^2=0.87, SEC=0.98)	Chen, 2004

2.2 Potato products

2.2.1 Physicochemical property

Potato chips are considered as one of the most important products among all the snack industry. The contents of dry matter, oil and acrylamide are some of the most relevant parameters in the quality control of potato chips.

In 2000, the suitability of Fourier transform infrared photoacoustic spectroscopy (FTIR-PAS) for analyzing potato chips was investigated (Sivakesava and Irudayaraj, 2000). The result showed that FTIR-PAS with its depth-profiling capability could be used for qualitative analysis.

Shiroma and Rodriguez-Saona (2009) invested the feasibility of developing a technique for rapid monitoring of potato chip quality by using infrared spectroscopy combined with multivariate analysis. Cross-validated (leave-one-out) PLSR models were developed to determine the fat and moisture content in potato chip products. Satisfactory results for moisture and fat calibrations were obtained with r_c^2=0.98, 0.99 and SEC=1.12, 0.17, respectively. Pedreschi et al. (2010) investigated the possibility of using on-line NIR monitoring of acrylamide, moisture and oil content in potato chips. On-line NIR interactance was found to predict fat and dry matter of potato chips with high accuracy, i.e. prediction errors of 0.99% and 0.86% (w/w), respectively. The corresponding correlations between predicted values and reference values were 0.99 and 0.97 for fat and DM. Ni (2011) further compared different models for fat, moisture, acid and peroxide value. Three types of NIRS calibration models, including PLS, Kernel PLS (KPLS), and Least Squares-Support Vector Machines (LS-SVM) methods were constructed to predict fat, moisture, acid and peroxide content. More positive prediction results of fat, moisture, acid and peroxide content were obtained using LS-SVM than with other methods. The prediction of potato crisp moisture, the use of PMSC leads to improved results over MSC (Nigel, 2001).

The summaries of NIRS applications for evaluation chemical compositions in potato products are shown in Table 5.

Table 5 Summary of NIRS applications for evaluation chemical compositions in potato products

Sample description	Wavelength range, nm	Multivariate calibration	Model statistics		References
			Calibration	Validation	
Potato chips n=15	1000-2500	PLSR	Moisture (r_c=0.99, SEC=0.17) Fat (r_c=0.98, SEC=1.21)	Moisture (r_v=0.98, SECV=0.20) Fat (r_v=0.97, SECV=1.54)	Shiroma and Rodriguez-Saona, 2009
Potato chips n=80	800-2500	PLS	/	Fat(r_v=0.95, SECV =0.35) Moisture (r_v =0.95, SECV =0.15) Acid value (r_v =0.94, SECV =0.26) Peroxide (r_v =0.79, SECV =0.26)	Ni et al., 2011
		KPLS	/	Fat (r_v =0.98, SECV =0.24) Moisture (r_v =0.99, SECV =0.10) Acid value (r_v =0.98, SECV =0.12) Peroxide (r_v =0.93, SECV =0.53)	
		LS-SVM	/	Fat (r_v =0.993, SECV =0.22) Moisture (r_v =0.995, SECV =0.07) Acid value (r_v =0.994, SECV =0.09) Peroxide (r_v=0.947, SECV=0.42)	
Potato chips Fat: n=60, DM: n=58 Acrylamide: n=55	460-1040	PLS		Fat(r_v=0.99,RMSECV=0.99, RPD=6.0); DM(r_v=0.97, RMSECV=0.84, RPD=4.8); Acrylamide(r_v=0.83, RMSECV=0.03, RPD=1.85)	Pedreschi et al., 2010

2.2.2 Acrylamide

Determination of acrylamide contents in potato chips is currently necessary due to its potentially toxic attributes, and the fact that very high concentrations can be produced in amylaceous fried foodstuffs (Rosen and Hellenäs, 2002). Acrylamide is one of the reaction products in the Maillard reaction between the acrylamide precursors, amino acids and reducing sugars (Becalski, et al., 2004). Segtnan et al. (2006) established NIRS analytical method to monitor the acrylamide content during processing or in the finished products. All potato crisp samples were ground and analyzed on a NIR Systems 6500 near-infrared spectrometer. The acrylamide contents were modeled by NIR spectra using PLS regression. Different NIR spectral region models were compared, the result showed that NIR spectra could give satisfying results with r values ranging from 0.928 to 0.952. It means that the prediction models can explain between 86.1% and 90.6% of the acrylamide variation. As well as NIR spectra alone, the calibration model in

combination with the process variable settings also can give the better prediction models for acrylamide.

Pedreschi et al. (2010) further investigated the possibility of using on-line NIR to monitor the content of acrylamide in potato chips. Sixty samples of potato chips from individual frying runs were measured on-line using a VIS/NIR interactance line scanner. For acrylamide, an average prediction error of 266 μg kg^{-1} was achieved using NIR and VIS signals in combination. The correlation between predicted values and reference values was 0.83 for this model. The system may be used to separate samples with very high acrylamide contents from samples with average to low contents. The special results were shown in Table 5.

2.3 Texture

Texture is very important for the consumer's perception of potato quality. Not only consumers were concerned about the texture of potatoes, but also the potato processing industry which produces various products with highly dependent on the rheological properties of the cooked product.

Boeriu et al. (1998) evaluated the ability of NIRS for the assessment of sensory texture properties of steam-cooked potatoes. The spectra of 87 samples were obtained from 1100 to 2500 nm. Among the sensory parameters, moist, waxy, firm and mealy were best predicted, with SEC ranging from 7.4 to 10.5 and correlation coefficients (r_c) between 0.89 and 0.94.

Thybo et al. (2000) studied the relationship between nine sensory texture parameters and NIRS in raw and cooked potatoes. Twenty-four samples from six different varieties were used for this assessment. The spectra were collected at ambient temperature over the wavelength range of 400-2498 nm at 2 nm intervals.

Van Dijk et al. (2002) established quantitative model between spectral data of fresh potato samples and sensory perceived texture attributes of raw samples based on PLS regression. Among the sensory parameters, moist, waxy, firm and mealy were best predicted, with SEC ranging from 7.4 to 10.5 and r_c between 0.89 and 0.94.

Compared the results of above studies, firmness, mealiness and moistness were higher obtained by Boeriu et al. (1998) than the other results. The special results were shown in Table 6.

Table 6 Summary of NIRS applications for evaluation texture and sprouting capability in potato products

	Hardness	Firmness	Springiness	Adhesiveness	Graininess	Mealiness	Moistness	Chewiness	Sprouting capability	References
R_{cooked}	0.50	0.67	0.67	0.54	0.77	0.83	0.82	0.67	/	Thybo et al., 2000
R_{raw}	0.69	0.71	0.62	0.25	0.66	0.73	0.67	0.63	/	
SEP_{cooked}	0.40	0.43	0.32	0.26	0.51	0.75	0.56	0.32	/	
SEP_{raw}	0.28	0.38	0.36	0.36	0.70	1.12	0.33	0.34	/	
$R_{prediction}$	/	0.82	/	/	/	0.89	0.91	/	/	Boeriu et al., 1998
SEP	/	8.64	/	/	/	11.28	8.72	/	/	
R	0.88	0.82	/	/	0.85	0.88	0.92		/	Van Dijk et al., 2002
SEP	/	/	/	/	/	/	/	/	/	
2004 Superior r_c, SEC	/	/	/	/	/	/	/	/	0.97, 0.36	Cheol Jeong et al., 2008
2004 Superior r_v, SECV									0.88, 0.68	
2005 Superior r_c, SEC	/	/	/	/	/	/	/	/	0.95, 0.40	
2005 Superior r_v, SECV									0.88, 0.60	
2005 Atlantic r_c, SEC	/	/	/	/	/	/	/	/	0.87, 0.37	
2005 Atlantic r_v, SECV									0.69, 0.47	
Total r_c, SEC	/	/	/	/	/	/	/	/	0.96, 0.31	
Total r_v, SECV									0.9.3, 0.40	

2.4 Sprouting capability

Predicting the sprouting capacity of potato tubers was very useful because the optimum planting data of seed potatoes can be timely obtained. At the same time, the sprouting potential of raw potatoes during the storage can be estimated. With the development of NIRS technology, except for traditional chemical properties, the scope of NIRS has been expanded to include the determination of the physiological indices of crops.

Cheol Jeong et al. (2008) studied the potential of NIRS for predicting the sprouting capacity of potato tubers. This research included 380 potato tubers (200,

'Superior'; 180, 'Atlantic') which were divided into four groups. Three groups were classified according to the cultivars or years as follows: Superior, 2004; Superior, 2005; Atlantic, 2005; the fourth group contained the total number of samples. For the four groups, the prediction ability of each of the calibration equations was determined based on r_v^2 and SEP. Cross validation revealed a close relationship between NIRS and the reference values for the sprouting capacity with an acceptable coefficient of determination ranging from 0.724 to 0.904. The RPD in NIRS calibration exceeded 1.5 for all sample sets, indicating good performance.The special results were shown in Table 6.

3 Conclusions

A number of applications of NIRS for the analyses of chemical composition, texture and sprouting capability in raw potato and potato products have been summarized and evaluated. Most of the chemical constituents of raw potato and potato products could be predicted accurately, whereas reducing sugar and total sugar required further research to improve their related prediction precision.

4 Future outlook

Although these studies demonstrated the potential of NIRS for the analysis of the chemical composition of potato, the applications of NIRS in monitoring potato warrant need further research. A major challenge is that most of the previous studies were performed in the laboratory with stationary NIR instruments that provide discontinuous spectral information for potato samples. The production and use of potato, including potato crisps, are continuous and in real-time procedures. There is a need to develop on-line NIRS systems for the analysis of potato. Therefore, more studies should be conducted to close the gap between the stationary-state NIR technique at the laboratory level and the on-line dynamic-state NIR technique at the industrial level. The factors complicating the development of on-line NIR techniques include sample inhomogeneity, sample instability, and complex other parameters. Potato is non-homogeneous. It can be mixed thoroughly to ensure homogeneity and stability in laboratory NIR analyses, whereas the homogeneity and stable properties of potato are difficult to achieve in on-line NIR analysis due to the rapid and dynamic-state processes.

Another area for future research is the application of advanced chemometrics methods to further improve the prediction precision of the chemical composition of potato. The NIR spectral information used in the analysis is encoded as an electrical signal from the spectrometer. In addition to the desirable information, the signal usually contains an undesirable component termed noise that can interfere with the accurate extraction and interpretation of the analytical data. The noise contained in the spectral information is one of the key factors significantly influencing the prediction of NIRS analysis. Chemometrics, which involves spectra preprocessing and multivariate calibration methods, is an efficient tool to eliminate or reduce spectra noise and improve NIRS prediction (Azzouz et al., 2003;Vidal et al., 2010). In most previous studies, the most common preprocessing methods, such as standard normal variate (SNV), multiplicative scatter correction (MSC), derivative, and smoothing, were usually employed. Nevertheless, several advanced preprocessing methods may have a greater ability to address the noise effects.

Acknowledgements

This study was supported by National Natural Science Fund (project number 31401582) and China Postdoctoral Science Fund (project number 2014M550894).

[References]

[1] Abbott, J. A., R. F. Lu, B. L. Upchurch, R .L. Stroshine, and R. F. Lu. 1997. Technologies for nondestructive quality evaluation of fruits and vegetables. *Horticultural Reviews*, 20: 1–120.

[2] Ainara, L., A. Silvia, G. Ignacio, M. Jesús, and J. Carmen. 2013. A review of the application of near-infrared spectroscopy for the analysis of potatoes. *Journal of Agricultural & Food Chemistry*, 61(23): 5413–5424.

[3] Alexandrakis, D., G. Downey, and A. G. M. Scannell. 2011. Detection and identification of selected bacteria, inoculated on chicken breast, using NIRSand chemometrics. *Sensing and Instrumentation for Food Quality and Safety*, 5(2): 57–62.

[4] Becalski, A., Y. B. P. Lau, D. Lewis, S. W. Seaman, S.

Hayward, M. Sahagian, M. Ramesh, and Y. Leclerc. 2004. Acrylamide in french fries: influence of free amino acids and sugars.*Journal of Agricultural & Food Chemistry*, 52(12): 3801–3806.

[5] Bevilacqua, M., R. Bucci, S. Materazzi, and F. Marini. 2013. Application of near infrared (NIR) spectroscopy coupled to chemometrics for dried egg-pasta characterization and egg content quantification. *Food Chemistry*, 140(4): 726–734.

[6] Boeriu, C. G., D. Yuksel, R. Van der Vuurst de Vries, T. Stolle-Smits, and C. Van Dijk. 1998. Correlation between near infrared spectra and texture profiling of steam cooked potatoes. *Journal of Near Infrared Spectroscopy*, 6(1): 291–297.

[7] Brunt, K., and W. C. Drost. 2010a. Design, construction, and testing of an automated NIR in-line analysis system for potatoes. Part I: Off-line NIR feasibility study for the characterization of potato composition. *Potato Research*, 53(1): 25–39.

[8] Brunt, K., and W. C. Drost. 2010b. Design, construction, and testing of an automated NIR in-line analysis system for potatoes. Part II: development and testing of the automated semi-industrial system with in-line NIR for the characterization of Potatoes. *Potato Research*, 53(1): 41–60.

[9] Chen, J. Y., Y. L. Miao, H. Zhang, and R. Matsunaga. 2004. Non-destructive determination of carbohydrate content in potatoes using near infrared spectroscopy. *Journal of Near Infrared Spectroscopy*, 12(5): 311–314.

[10] Coppa, M., B. Martin, C. Agabriel, C. Chassaing, C. Sibra, I. Constant, B. Graulet, and D. Andueza. 2012. Authentication of cow feeding and geographic origin on milk using visible and near-infrared spectroscopy. *Journal of Dairy Science*, 95(10): 5544–5551.

[11] Dijk, C. V., M. Fischer, J. R. Holm, J. G. Beekhuizen, T. Stolle-Smits, and C. Boeriu. 2002. Texture of cooked potatoes (Solanum tuberosum). 1. Relationships between dry matter content, sensory-perceived texture, and Near-Infrared Spectroscopy. *Journal of Agricultural & Food Chemistry*, 50(18): 5082–5088.

[12] Dong, W., Y. Ni, and S. Kokot. 2013. A near-infrared reflectance spectroscopy method for direct analysis of several chemical components and properties of fruit, for example, chinese hawthorn. *Journal of Agricultural & Food Chemistry*. 61(3): 540–546.

[13] Dulp, G. G., G. S. Birth, and R. G. Leffler. 1989. Use of near infrared analysis for the nondestructive measurement of dry matter in potatoes. *American Potato Journal*, 66(4): 215–225.

[14] Fernandez-Ahumada, E., A. Garrido-Varo, J. E. Guerrero-Ginel, A. Wubbels, C. Van der Sluis, and M. Van der Meer. 2006. Understanding factors affecting near infrared analysis of potato constituents. *Journal of Near Infrared Spectroscopy*, 14(1): 27–35.

[15] Haase, N. U. 2003. Estimation of dry matter and starch concentration in potatoes by determination of under-water weight and near infrared spectroscopy. *Potato Research*, 46(4): 117–127.

[16] Haase, N. U. 2006. Rapid estimation of potato tuber quality by near-infrared spectroscopy. *Starch–Stärke*, 58(6): 268–273.

[17] Haase, N. U. 2011. Prediction of potato processing quality by near infrared reflectance spectroscopy of ground raw tubers. *Journal of Near Infrared Spectroscopy*, 19(1): 37–45.

[18] Gökmen, V., H. Z. Şenyuva, J. Acar, and K. Sarıoğlu. 2005. Determination of acrylamide in potato chips and crisps by high-performance liquid chromatography, *Journal of Chromatography A*, 1088(1-2): 193–199.

[19] Guo, L. P., L. Q. Huang, X. P. Zhang, L. Bittner, C. Pezzei, J. Pallua, S. Schonbichler, V. A. Huck-Pezzei, G. K. Bonn and C. W. Huck. 2011. Application of Near-infrared spectroscopy (NIRS) as a tool for quality control in traditional Chinese medicine (TCM). *Current Bioactive Compounds*, 7(2): 75–84.

[20] Hacisalihoglu, G., B. Larbi, and A. M. Settles. 2010. Near-Infrared Reflectance Spectroscopy predicts protein, starch, and seed weight in intact seeds of common bean (*Phaseolus vulgaris* L.). *Journal of Agricultural & Food Chemistry*, 58(2): 702–706.

[21] Hartmann, R., and H. Büning-Pfaue. 1998. NIR determination of potato constituents. *Potato Research*, 41(4): 327–334.

[22] Helgerud, T., V. H. Segtnan, J. P. Wold, S. Ballance, S. H. Knutsen, E. O. Rukke, and N. K. Afseth. 2012. Near-infrared spectroscopy for rapid estimation of dry matter content in whole unpeeled potato tubers. *Journal of Food Research*, 1(4): 55–65.

[23] Jeong, J. C., H. C. Ok, O. S. Hur, and C. G. Kim. 2008. Prediction of sprouting capacity using near-infrared spectroscopy in potato tubers. *American Journal of Potato Research*, 85(5): 309–314.

[24] Kasemsumran, S., W. Thanapaseand A. Kiatsoonthon. 2007. Feasibility of near-infrared spectroscopy to detect and to quantify adulterants in cow milk. *Analytical Sciences*, 23(7): 907–910.

[25] Keller, S., T. Lochte, B. Dippel, and B. Schrader. 1993. Quality-control of food with near-infrared-excited raman-spectroscopy. *Fresenius Journal of Analytical Chemistry*, 346(6-9): 863–867.

[26] Komiyama, S., J. Kato, H. Honda, and K. Matsushima. 2007. Development of sorting system based on potato starch content using visible and Near-Infrared Spectroscopy. *Nippon Shokuhin Kagaku Kogaku Kaishi*, 54(6): 304–309.

[27] Lebot, V., and R. Malapa. 2013. Application of near infrared reflectance spectroscopy for the evaluation of yam

(Dioscorea alata) germplasm and breeding lines. *Journal of the Science of Food & Agriculture*, 93(7): 1788–1797.

[28] Li, S. F., X. Zhang, Y. Shan, and Z. H. Li. 2010. Prediction analysis of soluble solids content and moisture in honey by near infrared spectroscopy. *Spectroscopy and Spectral Analysis*, 30(9): 2377–2380.

[29] Lin, H. J., and Y. B. Ying. 2009. Theory and application of NIRSin assessment of fruit quality: a review. *Sensing & Instrumentation for Food Quality & Safety*, 3(2): 130–14.

[30] Marchi, M. D. 2013. On-line prediction of beef quality traits using near infrared spectroscopy. *Meat Science*, 94(4): 455–460.

[31] Márquez, G., and M. C.Añón. 1986. Influence of reducing sugars and amino acids in the color development of fried potatoes. *Journal of Food Science*, 51(1): 157–160.

[32] Mehrubeoglu, M., and G. Cote. 1997. Determination of total reducing sugars in potato samples using near-infrared spectroscopy. *Cereal Foods World*, 111(49): 12466–12470.

[33] Ni, Y. G., M. H. Mei, and S. Kokot. 2011. Analysis of complex, processed substances with the use of NIR spectroscopy and chemometrics: Classification and prediction of properties - The potato crisps example.*Chemometrics and Intelligent Laboratory Systems*, 105(2): 147–156.

[34] Nicolaï, B. M., K. Beullens, E. Bobelyn, A. Peirs, W. Saeys, K. I. Theron, and J. Lammertyn. 2007. Nondestructive measurement of fruit and vegetable quality by means of NIR spectroscopy: A review. *Postharvest Biology and Technology*, 46(2): 99–118.

[35] Nigel, Y. 2001. Potato crisp moisture estimation using near infrared spectroscopy. *International Journal of Food Properties*, 4(2): 247–260.

[36] Norris, K. H. 1964. Design and development of a new moisture meter. *Agric. Eng.* 45(7): 370–372.

[37] Otto, I. A. 2010. Research on organic potato cultivation. *Agricultura, Agricultural Practice and Science Journal*, 73(1-2): 21–25.

[38] Pedreschi, F., P. Moyano, K. Kaack, and K. Granby. 2005. Color changes and acrylamide formation in fried potato slices. *Food Research International*, 38(1): 1–9.

[39] Peterson, C. L., R. Wyse, and H. Neuber. 1981. Evaluation of respiration as a tool in predicting internal quality and storability of potatoes. *American Journal of Potato Research*, 58(5): 245–256.

[40] Pissard, A., J. A. Fernández Pierna, V. Baeten, G. Sinnaeve, G. Lognay, A. Mouteau, P. Dupont, A. Rondia, and M. Lateur. 2013. Non-destructive measurement of vitamin C, total polyphenol and sugar content in apples using near-infrared spectroscopy.*Journal of the Science of Food & Agriculture*, 93(2): 238–244.

[41] Pedreschi, F., P. Moyano, K. Kaack, and K. Granby. 2005. Color changes and acrylamide formation in fried potato slices. *Food Research International*, 38(1): 1–9.

[42] Pedreschi, F., V. H. Segtnan, and S. H. Knutsen. 2010. On-line monitoring of fat, dry matter and acrylamide contents in potato chips using near infrared interactance and visual reflectance imaging. *Food Chemistry*, 121(2): 616–620.

[43] Pedro, A. M. K., and M. M. C. Ferreira. 2005. Nondestructive determination of solids and carotenoids in tomato products by near-infrared spectroscopy and multivariate calibration. *Analytical Chemistry*, 25(77): 2505–2511.

[44] Rosen, J., and K. E. Hellenăs. 2002. Analysis of acrylamide in cooked foods by liquid chromatography tandem mass spectrometry. *Analyst*, 127(7): 880–882.

[45] Scanlon, M. G., M. K. Pritchard, and L. R. Adam. 1999. Quality evaluation of processing potatoes by near infrared reflectance. *Journal of the Science of Food and Agriculture*, 79(5): 763–771.

[46] Segtnan, V. H., A. Kita, M. Mielnik, K. Jorgensen, and S. H. Knutsen. 2006. Screening of acrylamide contents in potato crisps using process variable settings and near-infrared spectroscopy. *Molecular Nutrition & Food Research*, 50(9): 811–817.

[47] Shen, F., D. T. Ynag, Y. B. Ying, B. B. Li, Y. F. Zheng, and T. Jiang. 2012. Discrimination between shaoxing wines and other chinese rice wines by Near-Infrared spectroscopy and chemometrics. *Food and Bioprocess Technology*, 5(2): 786–795.

[48] Shiroma, C., and L. Rodriguez-Saona. 2009. Application of NIR and MIR spectroscopy in quality control of potato chips. *Journal of Food Composition and Analysis*, 22(6): 596–605.

[49] Sivakesava, S., and J. Irudayaraj. 2000. Analysis of potato chips using FTIR photoacoustic spectroscopy. *Journal of the Science of Food and Agriculture*, 80(12): 1805–1810.

[50] Subedi, P. P., and K. B. Walsh. 2009. Assessment of potato dry matter concentration using short-wave near-infrared spectroscopy. *Potato Research*, 52(1): 67–77.

[51] Thybo, A. K., I. E. Bechmann, M. Martens, and S. B. Engelsen. 2000. Prediction of sensory texture of cooked potatoes using uniaxial compression, NIRSand low field H NMR spectroscopy. *LWT - Food Science and Technology*, 33(2): 103–111.

[52] Thygesen, L. G., S. B. Engelsen, M. H. Madsenb, and O. B. Sørensenc. 2001. NIR spectroscopy and PLS regression for the determination of phosphate content and viscosity behaviour of potato starch. *Journal of Near Infrared Spectroscopy*, 9(2): 133–139.

[53] Van Dijk, C., M. Fischer, J. Holm, J. G. Beekhuizen, T. Stolle-Smits, and C. Boeriu. 2002. Texture of cooked potatoes (Solanum tuberosum). 1. Relationships between dry

matter content, sensory-perceived texture, and Near-Infrared Spectroscopy. *Journal of Agricultural & Food Chemistry*. 50(18): 5082–5088.

[54] Vidal, M., J. M. Amigo, R. Bro, M. Ostra, and C. Ubide. 2010. Quantitative determination of additives in a commercial electroplating nickel bath by spectrophotometry and multivariate analysis. *Analytical Methods*, 2(1): 86–92.

[55] Vincent, L., C.Antoine, M. Roger and S. Dan. 2009. NIR determination of major constituents in tropical root and tuber crop flours. *Journal of Agricultural and Food Chemistry*, 57(22): 10539–10547.

[56] Walsh, K. B., M. Golic, and C. V. Greensill. 2004. Sorting of fruit using near infrared spectroscopy: application to a range of fruit and vegetables for soluble solids and dry matter content. *Journal of Near Infrared Spectrosc*,12(1): 141–148.

[57] Wang, L., Q. Wang, H. Z. Liu, L. Liu, Y. Du. 2013. Determining the contents of protein and amino acids in peanuts using near-infrared reflectance spectroscopy. *Journal of the Science of Food and Agriculture*, 93(1): 118–124.

[58] Wang, S. S., L. J. Luo, Y. Q. Li, R. Cai, and W. J. Zhao. 2013. Qualitative and quantitative analysis of effective components in Fructus Ligustri Lucidi by near infrared spectroscopy. *Analytical Methods*, 5(12): 3045–3049.

[59] United States Department of Agriculture. USDA Nutrient Database. USDA 2011. Available at: http://ndb.nal.usda.gov/ndb/search/list) (24/02/2013).

[60] Zzouz, T., A. Puigdoménech, M. Aragay, and R. Tauler. 2003. Comparison between different data pre-treatment methods in the analysis of forage samples using near-infrared diffuse reflectance spectroscopy and partial least-squares multivariate calibration method. *Analytica Chimica Acta*, 484(1): 121–134.

Discussion on big data statistical analytics application in agriculture

Jia Jingdun[1,2,3], Kang Bohan[1,3], Gao Wanlin[1,3], Zhang Li[1,3]

(1. *College of Information and Electrical Engineering, China Agricultural University, Beijing 100083, China*;
2. *National Rural Technology Development Center, Ministry of Science and Technology, Beijing 100862, China*;
3. *Key Laboratory of Agricultural Informatization and Standardization of Ministry of Agriculture, Beijing 100083, China*)

Abstract: With the production of the technologies of parallel computing, the Internet of Things and the software applications for smart phones have been occurred numerously. It has produced huge amounts and various forms of data in our social networking applications. In one sense, we can say that with the rapid development of our society, we have already come into the era of big data. And besides the cloud computing, and the Internet of Things, big data has become another technology innovation to the information technology industry due to its great potential values. Big data has turned to a current research priority in every walk of life, and the arrival of big data era has created the concept of the agricultural big data. This paper made some analytics on big data statistical analytics application in agriculture. At first, it introduced the relevant concept, the background and the key feature of the big data; then it plunged into the explanations for relevant concepts of the agricultural big data, and introduced the main applied technologies of agricultural big data as well; next it stated how the agricultural big data being applied in the field of agricultural informatization; and at last it pointed out the problems that the agricultural big data has been facing at the present stage and its application prospect, some suggestions and thoughts were given, especially regarding the field of wisdom agriculture.

Keywords: big data, big data statistical analytics application in agriculture, agricultural informatization, Internet of Things, wisdom agriculture

Citation: Jia, J. D., B. H. Kang, W. L. Gao, and L. Zhang. 2017. Discussion on big data statistical analytics application in agriculture. 2017. International Agricultural Engineering Journal, 26(4): 246–256.

1 China agriculture has already come into the big data era

1.1 Review of big data analytics and research

With the rapid development of internet technology in recent years, the storage and the processing scale of data has become more complicated. Back in 1980, Alvin Toffler, the famous futurologist, pointed out in " The 3rd Wave" that big data would be the third wave of the future, and the sole certainty was that the development of big data would surprise us all (Guo et al., 2014). Now the application of big data has entered into every walk of life, and it has become one of the key factors in production. In the past few years, big data has become widely used in many aspects of business and finance. Yet it has not unified a standard concept on big data. McKinsey, The global well-known consulting firm has come up with an idea that big data is a data set which could not be collected, stored, analyzed and processed its contents by traditional database software tools for a certain time (Manyika et al., 2011; Zhang et al., 2014). But the relative standard concept, which has been generally accepted by many researchers, is that the big data is diversified and massive information assets which can produce much more effective decisive values, value explorations and optimization capabilities by the new-type processing methods (Zhang et al., 2014). At the earliest, people were accustomed to using "3V" to explain

Received date: 2017-09-01 **Accepted date:** 2017-11-24

* **Corresponding author: Gao Wanlin,** Professor of College of Information and Electrical Engineering of China Agricultural University, Beijing 100083, China. Major field: Agricultural big data and informatization, Network and Information Security Technology. Tel: 13910781016. Email: gaowlin@cau.edu.cn.

the characteristic of big data, that is--volume, variety and velocity; shortly afterwards researchers added "value" to "3V", and it has formed "4V"; but now people are used to utilizing the theory of "5V" to make an interpretation of big data: volume, velocity, variety, value and veracity.

Due to the rapid development and popularity of Internet of Things, mobile internet and varieties of cellphone applications, making the big data come into being so quickly. On the one hand, the capacity by which our human society generated data, got data and transmitted data has developed and improved unprecedentedly (Wang et al., 2015); on the other hand, some emerging technologies such as cloud computing and parallel computing have created a platform for big data to make cluster analytics. Moreover, not only do these data have a huge volume, but also the big data exists a diversity of the data structure. Taking Wechat application as an example, when chatting in Wechat, we may send various data including text messages, voice calls, videos and photos to our contact person. And these emerging technologies have upgraded the data storage and processing capacity from GB, TB to PB and even a higher level. So, scientists have predicted that 21th century would be the era of "data explosion", and big data would have become the "new oil" of the future. Therefore, combining big data with agriculture will make a great catalytic influence in the area of agriculture and relevant industries by utilizing the advanced technical analytics to agricultural production management activities.

1.2 Characteristics of agricultural big data

In the domestic agricultural production activities of China, it has produced diversities of big data in tilling, fertilizing, irrigating, product transporting and processing by farmers. Although these massive amounts of data seem to be completely irrelevant, we can provide a systematic way to collect, analyze and summarize the information so as to increase agricultural productivity, reduce the cost of agricultural production and promote the agricultural informationization. Therefore, agricultural big data is the thinking innovation of big data in the embodiment of agriculture.

With rapid development of wisdom agriculture and agricultural Internet of Things, our traditional agriculture has been making a transition to informatization and intelligence. And the relevant information has showed a massive growth in many fields of agriculture, hence this has provided the data foundation for big data statistical analytics using in agriculture. Agricultural big data technology aims to solve a series of problems on acquisition, memory and computation of data in each link in agriculture by using big data technology methods (Sun et al., 2013). And the concept of agricultural big data originated from two parts: big data and agricultural informatization. The statistics and analytics of agricultural big data have become the most important tool to achieve agriculture informationization. And Figure 1 is the technical architecture of big data statistical analytics application in agriculture.

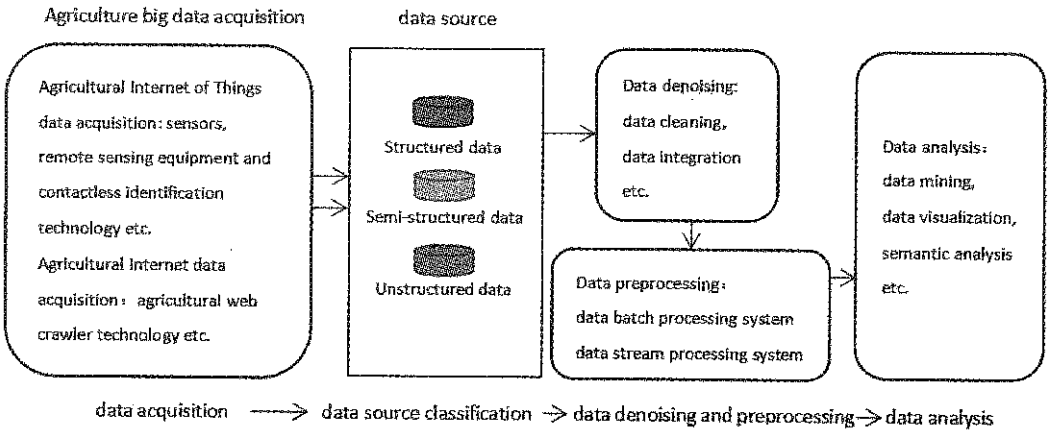

Figure 1 Technical architecture of big data statistical analytics application in agriculture

Compared to modern agriculture, traditional agriculture is more like

"weather-dependent mealtimes", that if we couldn't avoid climate disasters effectively, our crops would be more likely to lose out. But if we make use of big data statistical analytics technology, not only will we forecast

the future environmental conditions accurately by the algorithm pattern, but also, we can get field information and ensure whether the crops and herds are in good conditions.

2 Relevant technologies on agricultural big data

2.1 Collection and acquisition of agricultural big data

The collection and acquisition of agricultural big data are the data source for us to make a big data statistical analytics, and by analyzing the data sets containing spam or fault elements, it will make us get the error to the outcome. In other words, data acquisition is the basic and the key point of all the agricultural big data technologies, and later steps including statistical analytics, data management, conclusion are all built on the data acquisition foundation. However, the gross of the data accumulation is extremely weak, and even less than one tenth of that in foreign countries. The reason causing this kind of phenomenon can be divided into two pieces: on one hand, because of the late development of agriculture big data, deficiencies are still existed both in the understanding and in the direction of development compared to the foreign developed countries. On the other hand, it also depends on our traditional agricultural production factors. Due to the population pressure, small stock of agricultural resources and low level of per capita, and actually it is unavailable for us to take large mechanized formation, intensive management and production specialization, which are widely utilized by western countries. So, it is even more important for our country to have the advanced data acquisition technology. Agricultural big data sources derive from every aspect of our life including from production to consumption, from entity to network. And different data sources of various types have different data acquisition technologies. For now, agricultural big data acquisition and collection technologies are mainly including the following sections.

2.1.1 Agricultural Internet of Things data acquisition technologies

China is a large agricultural country and agriculture in China, is the fundamental industry of the national economy. In traditional Chinese agriculture, getting agricultural production data are quite limited. However, in modern agriculture, we can use contactless identification and sensor technologies, which are the two most important factors in the IOT to acquire and collect agricultural data. In this way our agricultural practices can be gradually updated to software and technology-led rather than people-centered, and so that some automatic, intelligent, remote-controlled of production equipment can be widely used in agriculture. The application of agricultural IOT can collect the information of crop growth and environment exactly, and reduce human consumption effectively as well.

Sensing technology plays a key role in the agricultural IOT. Sensors, remote sensing devices and contactless identification are core technologies of sensing technology (Li, 2012). The application of agricultural sensors is the decider to achieve the modernization of equipment. In the past few years, agriculture sensors products have already covered many fields containing soil, water, weather and plant growth, etc. In addition, some special-purpose sensors such as temperature sensors, humidity sensors, pH sensors have been applied to monitor some decisive factors in agriculture. With the different crossing subjects has been synthetically applied and developed, optical sensors, micro electrical mechanism systems, hyperspectral image detection system and biomimetic sensors technology will be the focus of our research in the field of IOT. By using these new generation of sensor technologies will significantly raise the range and accuracy in data collection.

In data acquisition system, contactless identification technologies mainly contain RFID and barcode technique. RFID has used in many fields for its readability and writability, speed identification, long-distance identification, high-speed movement identification and running in atrocious environment. Generally, RFID system consists of hardware instruments, such as reader, antenna, electronic tag, and software components including data collecting and processing middleware. The tag, attached to the identified object, is typically used to record the information of the object. It will be activated by the reader when entering its magnetic field, the

information carried by the tag will be conveyed to reader and computer system by radio waves so as to achieve the functionality of recognizing objects and collecting information automatically (as shown in Figure 2). With the development of RFID technology, it has being used in field information real-time collecting, field management and agricultural products quality traceability system (Wang et al., 2010).

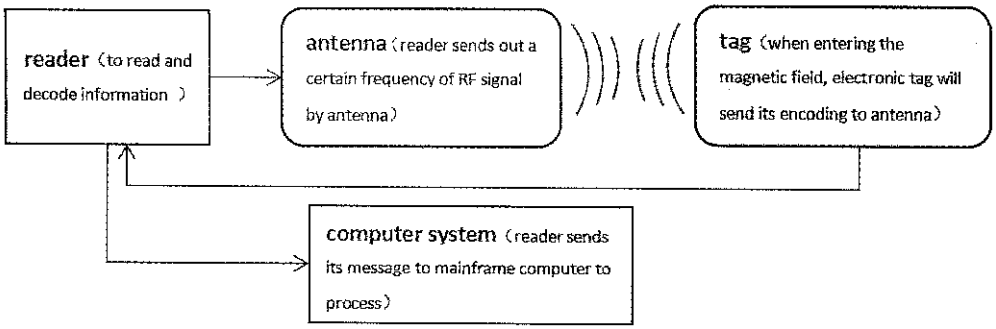

Figure 2 Working principle diagram of RFID

Barcode is one kind of sign composed regularly with a group of bars and spaces, which is used to represent the combination information of characters, numbers and symbols. Barcode is a remote automatic identification technology which has integrated the basis theory of barcode, photovoltaic, computer and communication technologies in a unit (Xing et al., 2014). At first, the most commonly used is one-dimensional code. But as high-speed information and automation techniques were growing and maturing, one-dimensional code is limited in its finite quantity of information, deficiency of error-correcting ability. And people have developed two-dimensional barcode, equipping with larger information density, higher-speed read, larger storage space and powerful error-correcting ability. In agriculture, two-dimensional barcode has widely used in many aspects such as information industry, identity authentication and safe-guarding and anti-counterfeiting in order to supervise and ensure safety of the produce (Liu et al., 2004). In China, two-dimensional barcode has become the most pervasive technology to establish the agricultural product traceability system.

In addition, the research of remote sensing started late in China, and it has been in rapidly developing stage now. Remote sensing technology can collect the ground information periodically in different electromagnetic spectrums. At present, the remote sensing technology represented by mini-micro UAS application has been widely used in agriculture, which is one of the principal methods to collect the field-crop data quickly (Wang et al., 2014). Yang et al. (2015) have developed a set of multi-load agricultural UAV based remote sensing system for assisting crop breeding information acquisition, different kinds of sensors such as digital camera, multi-spectral camera and infrared thermal imager, could be loaded on the UAV at the same time. The above characteristics made multi-rotor UAV most suitable to acquire different kinds of farmland spatial information at different scales readily. Zhao et al. (2008) have designed a visible light remote sensing system based on CMOS image sensor for micro UAV, and the remote sensing system substituted CMOS sensor for CCD, the drive timing module, data buffer and color interpolation module were realized on the hardware platform based on FPRA. Finally, they put the device to the UAV to acquire information in agriculture.

2.1.2 Agricultural web crawler technology

Along with the network popularization, world wild web has become the biggest information carrier and how to pick up and make full use of big data effectively is a great challenge. A web-crawler is a program/software or automated script which browses the World Wide Web in a methodical, automated manner (Yu et al., 2011; Cho, 2013) and it is an important search engine component. The basic working of a web-crawler can be shown as Figure 3.

Agricultural network data is the objective reflection of agricultural aspects at the internet layer. Now China has many websites covering agriculture, which have their own separate technology features and market resources.

But with no standardized form, they couldn't be functioning well. Agriculture data based on the Microblogs, Forums, BBS can be dynamically monitored and oriented collected by web crawler. Some specific search engines like Chinese Sounong and Nongsou are agricultural data acquisition platforms based on web crawler (Wang et al., 2015).

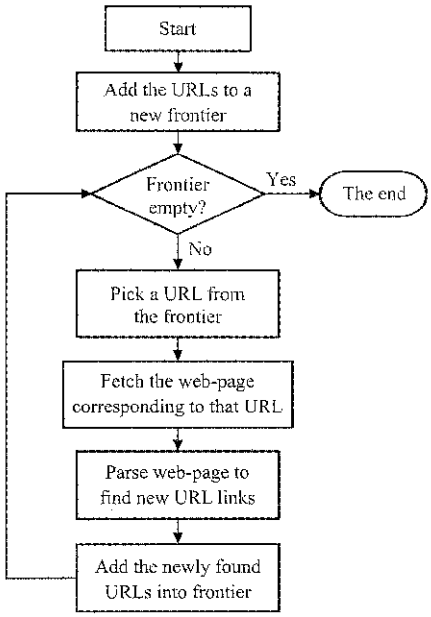

Figure 3 Basic working of a web-crawler

2.2 Pre-processing of agricultural big data

Agricultural big data came from not only limited to the field production, planting and processing in agriculture, but also originated in retail sales figures, agricultural technology database and agricultural market data information (Li, 2015). Therefore, agricultural big data contain structured data type, which is a form of user-defined data type that contains a sequence of attributes, each of which has a data type, for instance some texts and reports. It includes unstructured data as well such as images, audio, video, and web pages and even semi-structured data, which refers to data with some form of structure but not enough structure to fit gracefully into a relational model. So, in order to ensure large data sets with high quality, the first step is to preprocess the collected data.

There are various sources of agricultural big data. But not all of the mass data are necessary for us. In order to ensure the authenticity and accuracy of agricultural big data, we should firstly do data denoising, and by which we can restore realistic data so that a relatively accurate outcome can be calculated by the following steps of data analyzing and processing. For this, some foreign researchers came up with cleaning technologies for semi- and unstructured data due to the different characteristics of big data (Feng et al., 2014).

At present, the forms processing of big data mainly are data batch processing system and data stream processing system. Most of the data, with lower demand for real-time of the outcome, possess huge volume and could be stored before computation are applicable to take data batch processing system, but others with higher demand for timeliness and lower demand for outcome accuracy could be calculated directly without storage, and they are more suitable for data stream processing system. It has basically evolved into a stable system with the programming model of MapReduce and the architecture of Hadoop, which have been widely used in the real production. But for the research of the data stream processing system, it is mainly about stream calculation, which was concentrated on doing stream calculation in the database environment in the early research (Sun et al., 2014). Due to the data continuity, complex format and the low diversity of data value of stream data, it is a key problem on how to develop a data stream processing system with high performance, low-latency and good scalability. Now the Storm of Twitter, the Scribe of Facebook and the Nutch of Apache are typically stream processing system.

2.3 Agricultural big data analytics

Data analytics is one of the core contents in the research of big data (Labrinidis et al., 2012). Data analytics mainly contains data mining, data visualization etc. Data mining makes boost the large scale of big data, which can help people to make better decisions. Traditional data mining algorithm focus mainly on relational database, and the research on which is comparatively mature (Feng et al., 2014). But the research on data mining algorithm of semi and unstructured data including pictures, videos or HEML, XML documents are relatively few. So the literature came up with a newly web text clustering algorithm based on non-structured data mining structure model, which cluster the text resource information collected from

all kinds of remote education websites (Hu et al., 2008), and Zhu et al., (2016) developed the management of semi-structured data in electric information acquisition system, using different for different kinds of data mining algorithms to different kinds of data such as text, video and audio, and Yang (2015) put forward web data mining algorithm based on segmentation of semi-structured features. In order to improve the purity of data mining and the anti-interference performance, using feed-forward modulation filter data interference filter, and extracting data features by using semi-structural feature segmentation (Yang, 2015).

In agriculture, data mining technology has been widely used in agricultural production, environmental monitoring and agricultural Internet economy. But most of our agricultural data have been archived by documents. The data, which have been effectively utilized and analyzed only occupying 17% of total amount and it has appeared the phenomenon described as "data rich but information poor" (Li et al., 2004). The relevant researches have been discussed on that. For example, in order to control insect pests in North China, by monitoring of the crop growth and acquiring the farmland eco-environmental situation, we can effectively predict and prevent the occurrence of plant diseases and insect pests. Zhang et al. (2008) used Apriori algorithm (which is a famous algorithm for mining association rules) to find out the valuable association of each item, and by establishing knowledge base of agricultural expert system based on crop insect pests, it has verified that mining association rules play an important role in decision-making (Liu et al., 2009).

As for agricultural big data, another analytical dimension is mainly represented by data visualization, especially emphasizing human interaction. Based on enormous processing capacity of computer, primary algorithms in computer graphics and visualization algorithms, data visualization could present a static or dynamic image in front of people from data, and through interactive methods, the intrinsic relation and the change rule of the data can be understood more accurately, so it provides the powerful method for people to analyze the data, form the concepts and discover the rules (Ren et al., 2004). Data visualization technologies, facing big data, mainly contain text visualization, network visualization, spatiotemporal data visualization and multidimensional data visualization etc. (Ren et al., 2014). Now, agricultural data visualization analytics are mainly provided for building model to simulate the growth of animals and plants, display 3D agricultural information and monitor agricultural environment condition etc (Ren et al, 2014). Liu et al., (2009) proposed a model-based visualization system for rice growth, initially realized dynamic simulation and fidelity display of the growth of rice with different species, environment conditions and production techniques; and Lin et al., (2012) built the agricultural products data information management system, and the model for the evaluation of agricultural products safety state and early warning, which eventually realized the visualization of staple agricultural products data information by using the GIS technology integration, and making the products map to the database and the map; and Lin et al., (2015) constructed a visual monitoring system of farmland micro-climate environment based on GIS, a certain kind of techniques was explored including IOT perception, the information fusion and data visualization. Furthermore, a unified interface specification was established to fuse IOT data with geographic information system seamlessly. In order to display and visualize the multidimensional environmental data, a series of visual methods were developed. It is convenient for farmers to monitor the environment visually by the form of web GIS.

3 Agricultural big data applications in informatization

Agricultural informatization refers to the process in which human being resorts to the high technologies such as communications technology and network technology to develop and utilize agricultural information resources more thoroughly and more effectively in agricultural production and social practice, so as to push the sustainable development of agricultural economy and social progress of rural region. At present, agricultural informatization has been integrated into the agricultural industry, becoming one of the most active factors of

production. Promoting agricultural informatization and realizing cooperative service of agricultural information have become the important trend to develop agriculture in the developed countries. Given this background, the British government launched "agricultural technology strategy", using big data and IT to raise its agricultural productivity. The USA collected, organized and saved agricultural data resources which concerned for the domestic and international level managed mainly by the government. France is focusing on creating a "Big Agriculture" data system, including some industries that seem to be "detached" from the agriculture, like the development of high and new technologies, business market consultancy, law and policy guarantees, the application of the internet, etc.

In conclusion, agricultural information construction has become a long-term strategy for the developed countries in recent years, and under this background, big data statistical analytics technologies have become widely used in the field of agricultural informatization in foreign countries. For instance, the Solum, a service provider on soil analytics in USA, has invested $17 million to determine the problems of the usage of chemical fertilizer and pesticides by big data statistical analytics technologies, so as to help the farmers to reduce costs and increase output. Farmeron company in Europe aims to provide a data tracking and analysis service, which is similar to Google Analytics, to analyze some agricultural data specifically those are seemingly irrelevant in order to help producers to make reasonable production planning.

Since the 12th Five-Year Plan, the Chinese government has been attaching the great importance to use big data statistical analytics agricultural informatization. When visiting Inspur Group in 2014, Chinese Premier Li Keqiang stressed that from streamlining administration and delegating power to the lower levels to promote industrialization, urbanization and agricultural modernization, all these cannot be achieved without big data and cloud computing. They represent the general trend and they are the tide of time that we must follow. In 2015, the State Department of China issued "Outline of the Action Plan for the Big Data Development", making full arrangements to develop agricultural big data. In 2016, the Ministry of Agriculture, China has approved a pilot program based on agricultural big data development in rural area, aiming to provide decisions in agricultural industry chain for the enterprises and government. The application system of agricultural big data in agricultural informatization industry chain is clearly showed in Table 1.

Table 1 Application system of agricultural big data in agricultural informatization industry chain

	Data generation	Data acquisition	Data storage and analysis	Data application
Agricultural informatization industry chain	Cultivation Production	Soil information; Cultivated land information; Fertilizer information	Data screening; Data sharing and fusion analysis	Develop new products and new technologies; Optimal configuration; Optimize configurations
	Processing logistics	Processing information Logistics information		Precision detection; Agricultural products quality traceability; Logistics route optimization
	Sales	Supply and demand info Price information Consumer information		Demand forecasts; Precision marketing; Personalized recommendation

Under the guidance of national policy in China, some colleges and enterprises have begun the relevant practice especially in the field of the wisdom agriculture, for instance, Isoftstone company associates with China Agricultural University to set up the agricultural IOT and Big Data Research Center, focusing on wisdom IOT and big data application, agricultural informatization system, overall solution on internet agriculture, and some key technologies of wisdom agriculture were studied under field condition by some businesses, which utilized wireless sensor and camera to acquire and collect essential factors in crop growing, then uploaded them to the cloud to be analyzed and managed in real time, cellphone and pad were also provided for farmers in order to monitor the crops more conveniently (Zhang et al., 2015).

4 Current problems in agricultural big data

4.1 The complexity and heterogeneity of agricultural big data

Agriculture big data face with the complexity of its

model. they are no longer restricted to simply static data, but corresponding to dynamic data with rapid data generation, data propagation and shorter duration. All of these come up with higher challenges for us to record, index and query the dynamic data. Computation patterns can be divided into two forms: batch computing and stream computing. Batch computing system works in a "storage first, computing later" mode, the first requirement is to make the significant amount of static data save to the disk before computing and analysis (Li et al., 2016). The advantages of batch processing are that we can get a relatively full scale, accurate search results, but a major disadvantage is that it has a poor real-time performance due to batching massive amounts of data (usually with the petabyte level) simultaneously. However, a stream processing system is opposite to the features of those, as a result of data continuity and complication of streaming data, so, no storage is required that they can be computed directly, and they have advantages of short response time and high real-time performance, but with disadvantage of comparatively lower precision. How to combine the two processing systems to realize the features of precise computing and available response time is one of the key research directions for us in the future.

Moreover, the problems of the query and index. Due to the increasing share of the unstructured and semi-structured data on big data, perhaps it is unavailable for us to simply use traditional two-dimensional table to query, store and index big data. So NOSQL technology has been rising in research. NOSQL is a data storage system which is non-relational, distributed and perhaps doesn't comply with the ACID principles (NOSQL 2009) Facing this, much attention has been paid to the key-value storage, which has already become the symbol of NOSQL research. For example, focusing on the key-value type of database, Wang et al., (2012) has been trying to optimize its query performance. But there are also existing some application problems: although most of the NOSQL data storage system have been deployed on the practical application, no standards have been formed for many key-value database products, and with poor compatibility and versatility (Chang et al.,2006; Lakshman et al., 2009; Shen et al., 2013), some products has no global transaction support so that they cannot be used under certain conditions (Stonebraker et al., 2011), and moreover, due to the lack of formally official support, there may be exist some potential risks in usage. And these disadvantages will be the main bottlenecks of the development of the key-value storage in the future, and how to deal with these problems have become one big topic for the researchers.

4.2 Integration and management issues on agricultural big data

China is a big agricultural country in the world with more than 50% of the agricultural population, and possesses a large number of potential agricultural data resources. But in fact, there are only 3.6 T total data now stored in our National Agricultural Science Data Center, only accounting for 7% in USA and 60% in Japan (Wen, 2013). Moreover, the data which have been utilized by scientific research effectively only take 17% in total, and in other word, more than 80% of the data have been wasted. The main reason is that due to the lack of favorable integration and management of various types of data. It is popular that the data resources are unevenly distributed in different areas, and the level of cooperative founding and sharing is relatively low, so that data fusion has its difficulties. For instances, The Ministry of Agriculture, China has successively constructed many agricultural databases including agricultural product price, agricultural policy database etc, and each local agricultural department has constructed its own database with its actual situation (Wang, 2015). It is lack of data fusion that these databases have been stored separately, that they can't be related and complemented to each other (Guo et al., 2014).

Before the rise of big data, we were used to acquiring "micro-elements data" to study on agriculture, and by analyzing small range of transverse or longitudinal data, we may get the "point" conclusion in the process of agricultural production. But now we have been coming into the era of big data, when facing so much complex data information, we firstly need to change our mind and processing mode. Only a large number of data can be calculated and analyzed by big

data processing methods; only fused data have potential to make data mining. From a macroscopic view to increase the utilization of agricultural big data, the key point is to make a comprehensive planning and integration on acquisition, storage and utilization of agricultural big data, constructing agricultural data information center and database with large scale and influence by government in order to avoid the problems about information islands.

5 Application prospects on agricultural big data

Since the big data came into being, IBM company has launched a campaign called "Smarter Planet", touting digital technology that would make energy, transport, cities and many other areas more intelligent. In 2009, IBM put forward the proposal of "Smarter Planet, Win in China", which has formally opened the strategy of "wisdom China". The development of big data will touch off a cycle of "wisdom revolution". And now, with the advent of some new industries such as smart city, wisdom agriculture, intelligent transportation and wisdom treatment, "Big data + wisdom" strategic thought has been widely accepted by every developed country, and that has become the new direction of reform, technology innovation and industrialization of technology achievements in China.

As the concept of "wisdom agriculture" came into being in a shorter time, the wisdom agriculture, judging from what we have thought so far, is to use big data, cloud computing and IOT techniques into traditional agriculture, and apply sensors and software to control and manage the agricultural production via mobile platform or computer, aiming to make traditional agriculture become more "wisdom" (Lu et al., 2016). And along with "wisdom agriculture" embed ceaselessly, fully fusing the knowledge base, the model base, using theoretical analysis and logical reduction in all areas, and using key techniques (big data, cloud computing) to make computational analysis. Aiming to provide high-intelligent controlling, prediction and decision management is the future trend for wisdom agriculture.

6 Conclusion

The emergence of a new generation of information technologies including big data, cloud computing and IOT, have made a great revolution on thinking concept, industrial pattern and technology innovation in every field of our society. China is a big agricultural country with a large population, agriculture is the fundamental industry to support national economy construction and development. Going with the trend of high-speed development of big data and grasping the rallying point of agricultural big data have great significance on the development of agricultural informatization, agricultural modernization and wisdom agriculture. This paper firstly introduced the development situation of big data, and then extended the concept and features of agricultural big data. Secondly, it gave the details on key technologies of agricultural big data including data acquisition, data pre-processing and relevant data analysis. Thirdly, we set forth the application and development of agricultural informatization and wisdom agriculture. Finally, the authors put forward their own thinking based on the existing problems and challenges in agricultural big data at this stage.

[References]

[1] Chang, F., J. Dean, S. Ghemawat, W. C. Hsieh, and D. A. Wallach. 2006. Bigtable: A distributed storage system for structured data. In *Proc. of the OSDI.* New York: ACM Press.

[2] Cho, J. 2013. Crawling the web: discovery and maintenance of large-scale web data. *International Journal of Advances in Engineering Sciences,* 3(3): 62–66.

[3] Feng, D. G., M. Zhang, and H. Li. 2014. Big data security and privacy protection. *Chinese Journal of Computers,* 37(1): 246–258.

[4] Ge, W. J., and C. J. Zhao. 2014. Research on agricultural IOT & application and development countermeasure. *Transactions of the Chinese Society for Agricultural Machinery,* 45(07): 222–230. (In Chinese with English abstract)

[5] GS1 China. 2007. *Technology and Application of Two-deminsion Code.* Beijing: China Measurement Press.

[6] Gu, Y., W. Zhang. 2011. QR code recognition based on image processing. *International Conference on Science & Technology,* 2011: 733–736.

[7] Guo, C. K., Y. Z. Liu, Y. Y. Chen, M. Sun, X. Y. Tu. 2014. Main problems and missions on developing agricultural big data. *Journal of Anhui Agricultural Sciences*, 42(27): 9642–9645. (In Chinese)

[8] Guo, L. F. 2016. Study on the key technolonies of big data for agriculture. Ph.D. diss. Chinese Academy of Agricultural Sciences, Beijing.

[9] Hu, J., B. R. Yang, Z. F. Song, and R. Qian. 2008. Web text clustering algorithm based on the nonstructural data mining model. *Journal of University of Science & Technology Beijing*, 30(2): 217–220.

[10] Kang, E. 2014. A rectification for quick response code image. *Consumer Electronics (ISCE 2014) the 18th IEEE International Symposium on IEEE*, 01–02.

[11] Labrinidis, A., and H. V. Jagadish. 2012. Challenges and opportunities with big data. *PVLDB*, 05(12): 2032–2033.

[12] Lakshman, A., P. M. Cassandra. 2009. A decentralized structured storage system. Available at: http://www.cs.cornell.edu/projects/ladis2009/papers/lakshman-ladis2009.pdf.

[13] Li, D. L. 2012. Internet of Things and wisdom agriculture. *Agriculture Engineering*, 02(01): 01–07.

[14] Li, D. L. 2012. *Introduction of agricultural IOT*. Sciences Press, Beijing.

[15] Li, S., Y. Z. Huang, and H. Y. Chen. 2016. Review of big data stream computing system study. *Journal of Information Engineering University*, 17(01): 88–92.

[16] Li, W. F., C. J. Zhao, and X. Y. Guo. 2004. Data mining based on agricultural information express as data element. *Computer Engineering and Applications*, 40(24): 174–176.

[17] Lin, L. F., R. S. Wang, and P. H. Yu. 2015. GIS Based visual monitoring system of farmland microclimate environment. *Transactions of the Chinese Society of Agricultural Machinery*, 46(03): 254–260.

[18] Lin, W. J., H. F. Shi, J. Mu, D. X. Duan, S. Li, and W. Ma. 2012. Study on the visualization management of staple agricultural products data information based on GIS technology. *Guangdong Agricultural Sciences*, 39(16): 185–188.

[19] Liu, F. E., J. H. Peng, and J. Q. Hu. 2009. Application of data mining in the field of agriculture. *Agriculture Network Information*, 01(01): 55–58.

[20] Liu, H., L. Tang, W. Y. Zhang, Y. L. Wu, and W. X. Cao. 2009. Construction and implementation of model-based visual rice growth system. *Transactions of the Chinese Society of Agricultural Engineering*, 25(9): 148–154.

[21] Lu, J. S., L. Y. Xu, L. B. Zhao, G. H. Wu. 2017. Analysis of the situation of RFID research based on bibliometrics. *Computer Integrated Manufacturing Systems*, 02(03): 01–22.

[22] Manyika, J., M. Chui, B. Brown, J. Bughin, R, Dobbs, C. Roxburgh, and A. H. Byers. 2011. Big Data: The next frontier for innovation, competition and productivity. *Report from the McKinsey Global Institute*, 2011(05): 46–49.

[23] Meng, J. H., B. F. Wu, Q. Z. Li, and X. Du. 2010. Research advances and outlook of crop monitoring with remote sensing at field level. *Remote Sensing Information*, 32(03): 122–128.

[24] NoSQL. 2009. Available at: http://nosql.eventbrite.com/. (Accessed 2017.06.23)

[25] Ren, L., Y. Du, S. Ma, X. L. Zhang, and G. Z. Dai. 2014. Visual analytics towards big data. *Journal of Software*, 25(9): 1909–1936.

[26] Ren, Y. G., and G. Yu. 2004. Research and development of the data visualization techniques. *Computer Science*, 31(12): 92–96.

[27] Shen, D. R., G. Yu, X. T. Wang, T. Z. Nie, and Y. Kou. 2013. Survey on NoSQL for management of big data. *Journal of Software*, 24(8): 1786–1803.

[28] Sheng, D. D. 2016. The research on method optimization of data cleaning in the construction of agricultural domain knowledge base. M.S. thesis. Chinese Academy of Agricultural Sciences, Beijing.

[29] Stonebraker, M., and R. Cattell. 2011. 10 rules for scalable performance in 'simple operation' data stores. *Communications of the ACM*, 54(06): 72–80.

[30] Sun, D. W., G. Y. Zhang, W. M. Zheng, and T. University. 2014. Big data stream computing: technologies and instances. *Journal of Software*, 25(04): 839–862.

[31] Sun, K., H. H. Wu, and P. Lei. 2015. The application of sensor technology in agriculture. *Agriculture Engineering*, 05(02): 32–35.

[32] Sun, L. W., G. H. He, L. F. Wu. 2011. Research on web crawler technology. *Computer Knowledge and Technology*, 06(15): 4112–4115.

[33] Sun, Z. F., K. M. Du, and F. X. Zheng. 2013. The research and application prospect of big data in wisdom agriculture. *Journal of Agricultural Science and Technology*, 15(06): 63–71.

[34] Tai, H. Z. 2013. The key technology's research and optimization of the one-dimensional bar code decoding system. M.S. thesis. University of Electronic Science and Technology of China, Chengdu.

[35] Wang, L. L., J. J. Huang, S. J. Weng, J. Cao, and K. Lu. 2010. Field information collection system for characteristic and tropical farming based on RFID. *Transactions of the Chinese Society of Agricultural Engineering*, 26(14): 98–102. (In Chinese with English abstract)

[36] Wang, P., X. W. Luo, Z. Y. Zhou, Y. Zeng, and L. Hu. 2014. Key technology for remote sensing information acquisition based on micro UAV. *Transactions of the Chinese Society of Agricultural Engineering*, 30(18): 01–12. (In Chinese with English abstract)

[37] Wang, Q. 2015. Application analysis and construction strategy of big data technology in agriculture. *Journal of Xinjiang Agricultural Science and Technology*, 01(01): 1–4.

[38] Wang, W. S., and L. F. Guo. 2015. Agricultural big data and prospect on agricultural application. *Journal of Jiangsu Agricultural Sciences*, 43(09): 01–05. (In Chinese)

[39] Wang, X. B. 2016. Agriculture informationization and big data. *Big Data*, 21(01): 21–27.

[40] Wang, Y. G., W. M. Lu, and B. G. Wei. 2012. Transactional multi-row access guarantee in the key-value store. *Proceedings of the 2012IEEE International Conference on Cluster Computing (CLUSTER)*, 572–575. Beijing, China.

[41] Wang, Z., J. L. Hou, K. Tang, and G. P. Han. 2010. Application of image recognition and GPRS technology in plant grow detection. *Journal of Electronic Measurement & Instrument*, 24(06): 574–579.

[42] Wen, F. J. 2013. The strategic significance and synergistic mechanism of agricultural big data research. *Higher Agricultural Education*, 11(11): 03–06.

[43] Xu, S. W. 2013. The present situation of and countermeasures for agricultural IOT in China. *Journal of Chinese Academy of Sciences*, 28(06): 686–692.

[44] Yang, G. J., C. C. Li, H. Y. Yu, B. Xu, H. K. Feng, L. Gao, and D. M. Zhu. 2015. UAV based multi-load remote sensing technologies for wheat breeding information acquirement. *Transactions of the Chinese Society of Agricultural Engineering*, 31(21): 184–190. (In Chinese with English abstract)

[45] Yang, L. P. 2015. Web data mining algorithm based on semi structure feature segmentation. *Microelectronics & Computer*, 32(08): 154–157.

[46] Zhang, H. R., Z. L. Li, T. F. Zou, X. Y. Wei, G. C. Yang. 2014. Review on agricultural big data. *Computer Science*, 41(11A): 387–392.

[47] Zhang, L., and L. C. Ren. 2015. Study on application mechanism and value creation of big data in agricultural information. *Journal of Anhui Agricultural Sciences*, 43(34): 341–344.

[48] Zhao, P., T. Z. Shen, B. T. Shan. 2008. The application of remote sensing system for micro UAV based on CMOS image sensor. *Acta Photonica Sinica*, 37(08): 1657–1661.

[49] Zhu, E. G., X. Liu, and L. J. Ge. 2016. Management design for unstructured data in electrical information acquisition system. *Proceedings of the CSU-EPSA*, 28(10): 123–128.

Whole process traceability technology of wisdom dairy cattle breeding

Liu Guangli[1], Zong Xiaohui[1*], Liu Shang[2]

(1. *College of Information and Electrical Engineering, China Agricultural University, Beijing 100083, China*;
2. *Beijing-Dublin International College at BJUT, Beijing University of Technology, Beijing 100124, China*)

Abstract: As an important part of food industry, the dairy has been brought to our attention. The security of milk not only concerns consumer's vital interest, but also impacts the development of dairy industry. The quality of milk mainly depends on safe operation of dairy management, nutrition and processing technology of forage, storage of fresh milk, milk processing and packaging technology etc. Based on the above-mentioned background, this paper attempted to present the whole process traceability technology of wisdom dairy cattle breeding. In this study, video was stored in the database by category, time and other information, integrating Global GAP standard, RFID technology, and video compression technology. Through system coding, it achieved some key points tracing of text and video information in the process of dairy farming, and finally realized whole process traceability technology. As compared to the use of tracing text information, adding video information can improve the correctness and authenticity of milk source, and enhance milk quality.

Keywords: wisdom dairy, dairy cattle breeding, traceability, Global GAP

Citation: Liu, G. L., X. H. Zong, and S. Liu. 2017. Whole process traceability technology of wisdom dairy cattle breeding. International Agricultural Engineering Journal, 26(4): 257–262.

1 Introduction

Food security is a big issue for people's livelihood. It is also the guarantee of citizen's healthy life (Zhang, 2004; Zhang and Huang, 2016). With the continuous progress of modern society, citizen's economic level and living standard have been improved. The consumption structure of residents has gradually changed from survival type to enjoyment, development and health, and people pay more attention to food quality (Luo et al., 2007; Sun et al., 2012; Tang et al., 2015). China is one of the largest countries in the dairy production and consumption in the world, the safety of dairy products is not only related to citizen's life and health, but also involved in the development of dairy industry (Bian, 2010; Yang et al., 2012). However, in China, dairy quality and security incidents occurred frequently. Especially it was reported that distributors adulterated milk powder with a substance called "melamine" in 2008. It shocked people at home and abroad, and as a result China's dairy industry was hit (Liu et al., 2015). The quality of milk mainly depends on the security operation of dairy management, nutrition and processing technology of forage, storage of fresh milk, processing and packaging technology of milk etc. Most cattle farms in China still adopt traditional backward mode of production. The process of dairy feeding, quarantine and other operations were not standardized. Weak consciousness of people, unperfect facilities and relatively poor sanitation were all the exiting problems. The above adverse effects led to poor quality of raw milk.

By way of introducing Global GAP standard, this paper integrated RFID and video compression technology to trace some key points tracing of text and video information in the process of dairy farming. As a prompt and effective technique, video traceability technology is playing an increasingly important role in dairy cattle breeding, then fundamentally solves the problems of

Received date: 2017-08-05 **Accepted date:**2017-11-23

* **Corresponding author: Zong Xiaohui,** Master, College of Information and Electrical Engineering, China Agricultural University, Beijing 100083, China. Email: zongxh6@163.com.

dairy diffusion (Bao et al., 2011; Feng et al., 2013; Valdez-Silva et al., 2013).

2 Global GAP and transparent traceability

2.1 Global GAP

Global GAP (Good Agricultural Practice) certification is a global standard for agricultural products and it has been recognized by most countries. Global GAP certification standard covers the whole process of tested products from planting, breeding to harvesting (edible state), and it is a fundamental method of solving the security of edible agricultural products from the root (Li et al., 2013).

The GAP standard has been used in several agricultural industries. Practice showed that good agricultural practices GAP was an effective tool to improve the quality and safety of raw-food materials both at home and abroad (Gao et al., 2013; Zhang and Huang, 2016). Dairy cattle GAP is a scientific tool for the dairy farming to increase the service. The implementation of it can improve comprehensive management level to realize dairy products' safety from cattle breeding to dining table.

2.2 Wisdom cow

Wisdom cow, specifically referred to process of dairy cattle breeding, milk production etc. can ensure the quality and safety of product and promote credibility of enterprises by introducing whole process of monitoring management that could trace back. From the Word Organization for Animal Health (OIE), Japan, New Zealand, Australia to China, there is a clear requirement for the full supervision and traceability of animal products and diseases to ensure the safety of livestock products (Pan et al., 2016). Dairy traceability system can achieve whole process of traceability from feed supply, aquaculture production, milk processing to storage. It can protect consumers' rights and interests, improve the efficiency of enterprise management, promote the level of government for food supervision, and stimulate dairy production more efficient, safe, standardized, sustainable development (Xia et al., 2014).

2.3 Traceability methods and techniques

"Traceability system" refers to a system of product's manufacturing process that could be traced back from the end product to initial raw materials (Liu et al., 2009). It extracted some trace points consumers concerned about from the entire production and consumption process to establish an information database of food safety, such as raw materials, food testing, supervision and consumption etc. Once the food was dug out quality and safety problems, it could perform effective control from root source to ensure consumers' interests based on the key information. The consumers can fully aware of production and circulation process in line with health and safety and this manner can heighten consumers' confidence in food companies (Wang et al., 2012; Zhu et al., 2008).

Radio Frequency Identification (RFID), also known as electronic tags, is a kind of communication technology (Ma and Yu, 2014). It reads or writes relevant data through the radio signal to identify specific targets without establishing mechanical or optical contact between specific objectives. RFID uses dedicated RFID readers and specialized RFID tags that can be attached to the target, to transfer information from tags to RFID readers taking advantage of frequency information (Abed et al., 2013; Hsu et al., 2008; Wang et al., 2008; 20-24). The superiorities of RFID technology are: it can be automatically identified without contact; using radio frequency signal automatically identifies the target and obtains the relevant data; it identifies work without any human intervention; it can adapt to various of harsh environment (Wang et al., 2016). This greatly reduces manual intervention in dairy farming, enabling dairy breeding to be automated. RFID technology recognizes multiple tags at once and improves work efficiency (Huang et al., 2011; Huang et al., 2010).

Most dairy products in the market used RFID technology or barcode technology, and most of them presented to consumers are text messages. The goal of this research was to develop a text and video traceability system that used RFID and video processing and other technologies, which was expected to solve the problems of food safety with higher efficiency. This was only used in a small number of areas, and also a major innovation point of the subject.

3 Design of whole process traceability technology of wisdom dairy cattle breeding

We can obtain dairy environmental information through the sensor and ensure security management of farm by monitoring equipment. Importing dairy basic information and specific events into management system can form a set of dairy farming traceability system. In line with user needs, the traceability system, which was described by this paper, was divided into two parts, the client and database, and adopted B/S structure (Browser/Server mode). Entered the address in the browser bar directly without installing client, you could access dairy real-time video or trace relevant text and video information.

3.1 System overall design

The objective of this study was to complete dairy cattle breeding traceability system mainly using RFID, sensor technology, video monitoring, data mining etc. First, through active tag, RFID obtained the basic dairy cattle information, then it was transmitted by the sensor, receiving device returned all the tag information received at the same time. Afterward system distinguished information in the background according to the unique label ID. Integrating video compression technology, the video would be saved in the database in class, time and other forms. In the end, by means of connecting the system coding with database to realize the function of traceability system extracting relevant text and video information. The overall design of the system is shown in Figure 1.

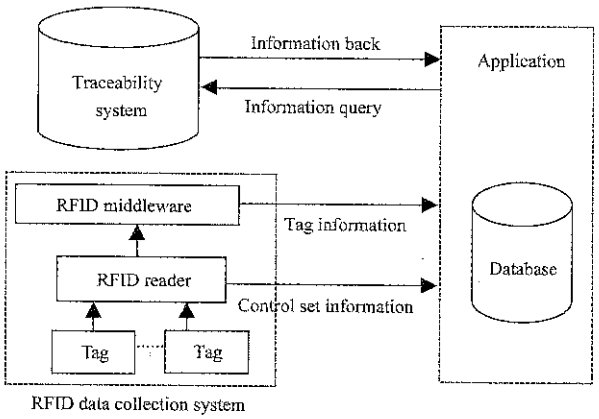

Figure 1 Overall design of system

3.2 System function design

The functions that were available in the browser included viewing real-time video and in the light of trace code tracing text and video information. Experiment was used by infrared camera and the recorded video and was EPG format. Computer system coming with the media player might not play, so it attached a player plug-in download function. Function flow chart is shown in Figure 2.

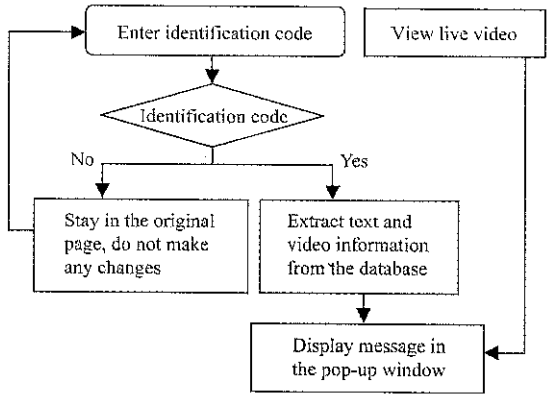

Figure 2 System function flow chart

3.3 System module design

For the purpose of creating system module better, a simple questionnaire was designed in the system demand analysis stage. A total of 43 questionnaires were received, of which 38 were valid. From the consumer's point of view, we set the following function module that people cared about, as shown in Figure 3.

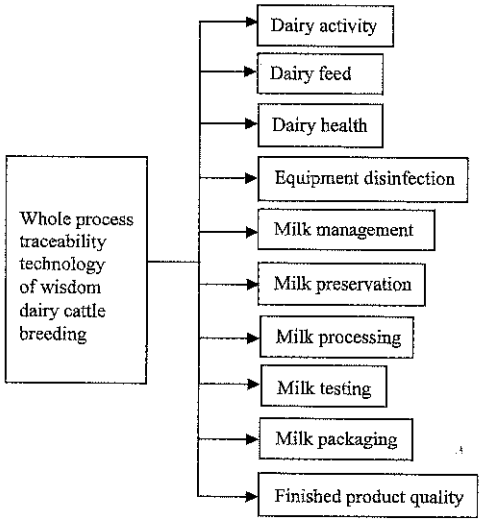

Figure 3 System module design

4 Realization of whole process traceability technology of wisdom dairy cattle breeding

This paper used Myeclipse10.0 as a development software, and JSP, SQL Server 2008 to develop a dynamic web system with an SSH framework based on

MVC (model view controller). After system coding, entered server address in the browser and directly jumped to the login interface of traceability system.

It mainly achieved two aspects of function: one was cattle real-time video viewing interface, you clicked each button on the page to see real-time information corresponding to each area, as shown in Figure 4. The other was tracing the trace code, clicked "tracing milk", then entered trace code on milk packing box and clicked "search" button. When dairy number was entered correctly and data were extracted from the database, the dairy traceability information would be displayed. Specific information included video and text information, and traceability success interface is shown in Figure 5. Compared to the barcode technology, using RFID tags can easily read out the relevant information. Owing to the video format recorded by camera was special, it might not be available on some computers, so we provided a plug-in download function in system. We embed windows media player into video interface. On the player, it had functions of controlling volume, pausing, stopping, and selecting. The traceability interface showed videos of different modules following clicking the "Video" button. The video player interface is shown in Figure 6. It realized the same interface although using different commands. From what has been mentioned above, it greatly reduced amount of codes and made system functions clearer.

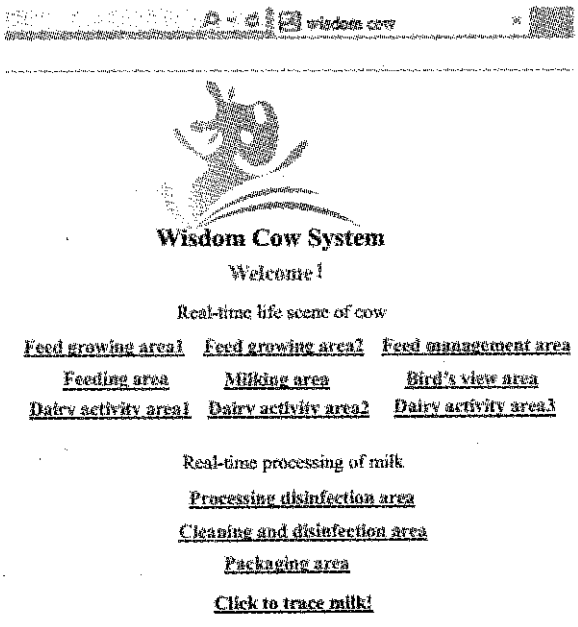

Figure 4 Login success interface

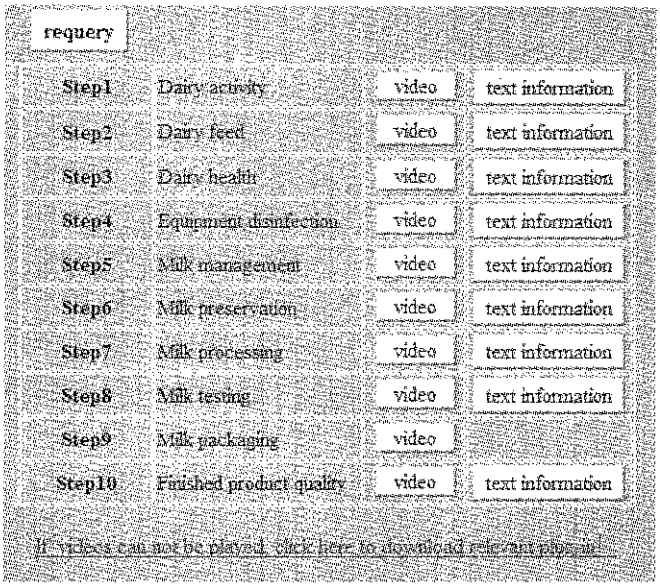

Figure 5 Traceability information interface

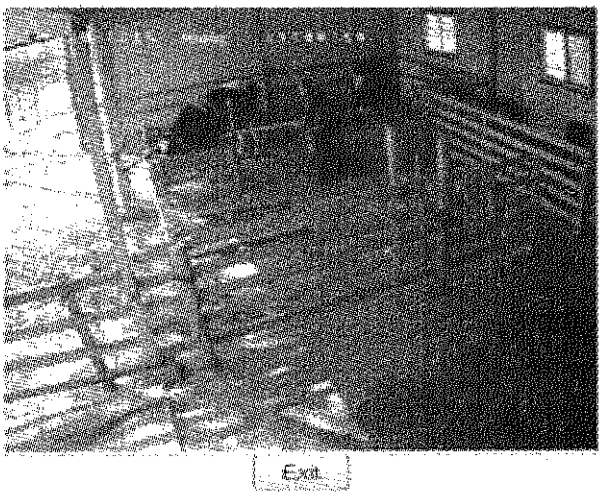

Figure 6 Video player interface

finished product name	Vidham	unit	box
capacity	910	shelf life	6 month at room temperature
identification code	20130301100900	executive standard	GB19645-2010
test item	national quality requirements		test results
sense	milk preservation		fresh, without any smell
net content(ml)	>=900		910
fat (g/ml)	>=3.1		3.4

previous step

Figure 7 Information query interface

In addition, "previous step" and "next step" functions were added in text information interface. Users could view information directly through clicking buttons without cumbersome operations closing original window and opening a new window. Figure 7 just listed finished product quality information interface. Introducing video compression technology, it improved video capacity problems and made video clearer and smoother. As

compared to the information viewing, video viewing can be more clearly view the source of milk to ensure food quality, improve enterprise information management capabilities.

5 Conclusions

In recent years, dairy quality and safety incidents occurred frequently, the consumers' trust in dairy products has been greatly decreased, therefore quality management has become an urgent and priority task in dairy industry. In this study, a whole process traceability technology of wisdom dairy cattle breeding was proposed. Based on the MVC design pattern and Object-oriented thought, we finished this system achieving the goal of tracing text and video information. We focused on video tracing by integrating Global GAP standard, RFID technology, and video compression to improve the correctness and authenticity of milk source. In order to protect consumers' rights and interests, milk production process was transparent by tracing code. people could obtain information and see relevant video they want. Compared with traditional breeding methods, this method is more convenient to achieve transparency and standardization of breeding process, and heighten the credibility of milk quality.

Acknowledgements

This research has been partly supported by Wisdom Agriculture Transparent Traceability System (29014065, 2012-2017). The authors would like to thank the anonymous reviewers for valuable suggestions.

[References]

[1] Abed, M., I. Charfeddine, M. Benaissa, and M. Starostkapatyk. 2013. Intelligent traceability system of containerized goods. *Applied Mechanics and Materials*, 309(6): 241–251.

[2] Bao, X. Y., Q. Lu, Y. Wang, and W. Zheng. 2011. Food traceability: General supervision system and applications. *Eighth International Conference on Fuzzy Systems and Knowledge Discovery*, IEEE, 4: 2514–2517.

[3] Bian, J. 2010. Design of traceability system for the agricultural product based on RFID and Two-Dimensional code technology. *Network Security Technology & Application*, 49–52.

[4] Feng, J., Z. Fu, Z. Wang, M. Xu, and X. Zhang. 2013. Development and evaluation on a RFID-based traceability system for cattle/beef quality safety in China. *Food Control*, 31(2): 314–325.

[5] Gao, Y. M., F. U. Hai-Ying, L. I. Min, R. X. Liang, and R. Q. Zhao. 2013. Application of agricultural products quality and safety traceability system of Chancheng District in Foshan City. *Modern Agricultural Science & Technology*, 15: 306–307.

[6] Hsu, Y. C., A. P. Chen, and C. H. Wang. 2008. A RFID-enabled traceability system for the supply chain of live fish. *IEEE International Conference on Automation and Logistics*, IEEE, 2008: 81–86.

[7] Huang, F., S. Zhang, and H. Zhao. 2011. Design and application of quality traceability system based on RFID technology for red jujubes. *IFIP Advances in Information and Communication Technology*, 68: 371–380.

[8] Huang, Y. C., W. C. Kuo, and M. C. Kao. 2010. A RFID field operation system design for Agricultural traceability. *International Conference on Pervasive Computing IEEE Computer Society*, 2010: 423–426.

[9] Li, F., Y. P. Zhu, and H. R. Wu. 2013. Modeling and optimization of traceability system for agriculture products supply chain. *Advanced Materials Research*, 605-607: 574–579.

[10] Liu, P., W. Liu, L. I. Qiang, Y. R. Wang, M. Duan, and Y. Dai. 2015. Cattle breeding Research traceability system based on RFID technology. *Food Research & Development*, 24: 200–203.

[11] Liu, S. P., Y. P. Zhu, and S. Li. 2009. Research on data acquisition system for agent-based bee product traceability platform. *Computer and Computing Technologies in Agriculture-i--Proceedings of the Third Ifip International Conference on Computer and Computing Technologies in Agriculture*, 2009: 375–381.

[12] Luo, D. C., and J. F. Peng. 2007. Analysis on present situation of ecological safety in China and its protection countermeasures. *China Safety Science Journal*, 17(3): 10–14.

[13] Ma, L., and H. L. Yu. 2014. The establishment of the pork product traceability system based on RFID. *Applied Mechanics & Materials*, 644-650: 3694–3696.

[14] Pan, J., X. Zhu, L. Yang, S. Lian, and N. Zhang. 2016. Research and implementation of safe production and quality traceability system for fruit. *Computer and Computing Technologies in Agriculture V. Springer Berlin Heidelberg*, 368: 133–139.

[15] Sun, A., B. Guan, and F. Wang. 2012. Current situation and countermeasure of food safety in China. *Henan Science*, 09: 199–202.

[16] Tang, Q., J. Li, M. Sun, J. Lv, R. Gai, L. Mei, and L. Xu. 2015. Food traceability systems in China: The current status of and future perspectives on food supply chain databases, legal support, and technological research and support for food safety regulation. *Bioscience Trends*, 9(1): 7–15.

[17] Valdez-Silva, E., P. Y. Reyes, M. A. Alvarez, J. Rojas, and V. Menendez-Dominguez. 2013. Expert system for evaluating learning management systems based on traceability. *Springer New York*, 152(1): 1103–1113.

[18] Wang, H. C., Y. H. Qin, M. C. Zhang, F. Liu, and W. K. Jia. 2016. Study on beef identification and information traceability system based on UHF RFID technology. *Chinese Journal of Agricultural Science*, 37(5): 220–222. (In Chinese with English abstract)

[19] Wang, L. C., S. K. Lin, and L. P. Huang. 2009. A RFID based agile manufacturing planning and control system. *Rough Sets and Knowledge Technology*, 5589: 441–451.

[20] Wang, S., C. Ma, and H. Lv. 2012. Yarn quality tracking system based-on RFID. *International Conference on Computer and Information Application IEEE*, 2012: 103–105.

[21] Xia, X., Y. Qiu, L. Hu, and G. Zhou. 2014. Application of information technology on traceability system for agro-food quality and safety. *Computer and Computing Technologies in Agriculture VIII*, 257–269. Springer International Publishing.

[22] Yang, Z. J., J. J. Gong, G. P. Ren, and F. M. Deng. 2012. Research progress in carbohydrates quality control of raw milk and milk products. *Science & Technology of Food Industry*, 33(22): 409–413.

[23] Zhang, H. B. 2004. Analysis on current situation of food safety in China and its countermeasures. *China Safety Science Journal*, 14(1): 15–17.

[24] Zhang, X. R., and H. N. Huang. 2016. Based on GAP and ACCP to build grass coral beverage quality safety line. *Beverage Industry*, 19(6): 60–65. (In Chinese with English abstract)

[25] Zhu, Y., L. Zeng, L. Hua, and H. Yu. 2008. Design of pork traceability information system. *Computer Science and Computational Technology*, 1: 459–462.

OSGi-based system for power quality monitoring and evaluation

Yu Lina[1,3,6], Zhang Ganghong[2,5], Niu Boya[4], Gao Wanlin[2,5*], Huang Liangji[2,5], Zhao Long[2,5], Wang Yan[2,5], Lin Kequan[2,5], Zuo Min[3*]

(1. *Institute of Semiconductor, Chinese Academy of Sciences, Beijing, 100083, China;*
2. *Key Laboratory of Agricultural Informatization Standardization, Ministry of Agriculture, Beijing 100083, China;*
3. *Beijing Key Laboratory of Big Data Technology for Food Safety, Beijing Technology and Business University, 100048, China;*
4. *College of Information and Computer Engineering, Northeast Forestry University, Harbin, 150040, China;*
5. *College of Information and Electrical Engineering, China Agricultural University, Beijing 100083, China;*
6. *School of Microelectronics, University of Chinese Academy of Sciences, Beijing, 100049, China*)

Abstract: Traditionally, the systems of power quality monitoring and evaluation are usually designed using Client/Server (C/S) two-layer structure. However, with the development of IT and J2EE technology, power quality monitoring and evaluation system, which is based on Browser/Server (B/S) mode and J2EE enterprise structure, has been gradually replacing the software system of traditional C/S structure. Though this mode has solved many practical problems, especially, in the process of system applications when real-time requirements and data communication processing capacity are more essential than the other factors, there are still some limitations such as low efficiency of code execution and lack of supporting for processing bottom layer data. In order to solve these problems, this paper introduces Open Services Gateway Initiative (OSGi) framework specification, integrating dynamic components technology and ideas of OSGi microkernel into power quality monitoring and evaluation system based upon J2EE. It improved the efficiency of program-code execution in the process of power quality monitoring data collection and processing. It also solved problems of slow processing speed of massive data calculation, analysis, storage, and over time of front-end application displaying.

Keywords: power quality, OSGi, J2EE, monitoring and evaluation, dynamic components technology

Citation: Yu L. N., G. H. Zhang, B. Y. Niu, W. L. Gao, L. J. Huang, L. Zhao, Y. Wang, K. Q. Lin, and M. Zuo. 2017. OSGi-based system for power quality monitoring and evaluation. International Agricultural Engineering Journal, 26(4): 263–269.

1 Introduction

Power quality monitoring and evaluation play a very important role in smart grid (Ali et al., 2016; Bionda et al., 2016; Blair et al., 2016; Liu et al., 2016; Su et al., 2016; Vanin et al., 2016; Xavier et al., 2016; Teng et al., 2015). However, for many years, in the field of power quality monitoring, research is mainly concentrated on the design and development of monitoring terminals, including hardware design, method of sampling window, algorithms of data transformation and feature extraction. As for software products, the rate of on-line monitoring system and evaluation and decision system becomes lower (Hu et al., 2016; Seider et al., 2016; Gao et al., 2014); the application effect is not great. What is more, the increase of terminals and detection points made the management of power quality become difficult, and traditional methods cannot meet this demand. We need better management methods.

With the rapid growth of the national economy and the power load, a large amount of non-linear load, impact load and volatility load have been generated in the power grid, which resulted in the serious deterioration of power quality, weakening and hampering the effective operation of power grid (Elphick et al., 2017; Iqtiyaniilham et al., 2017). Technologies of power quality monitoring and evaluation are the main methods to discover and analyze the various power qualities. It can provide important

Received date: 2017-07-05 **Accepted date:** 2017-08-23

* **Corresponding author: Gao Wanlin,** PhD, Professor, Research interests: agricultural informatization and application specific chip. College of Information and Electrical Engineering, China Agricultural University, Beijing 100083 P. R. China. Tel: +86-010-62736755, Email:cau_szmtyjs@163.com.

decision basis for the improvement of power quality and fault diagnosis of electric power system (Ji et al., 2016). Also, it can provide theory and practice basis for the evaluation and management of power quality. Therefore, people are paying more and more attention to the methods of developing power quality monitoring and evaluation system which are increasing widely used in power system (Esparza et al., 2017; Feng et al., 2016; Luo et al., 2016).

Traditional power quality monitoring and evaluation systems generally adopted C/S mode with two layers in commercial database (Moreno-Munoz et al., 2008). With the continuous application of J2EE architecture and B/S mode in automatic electricity power systems, the power quality monitoring and evaluation system gradually turned to multi-layer software architecture system based on J2EE specification (Pichler et al., 2015). The software architecture owned advantages of: the cross-platform of system, browsing without client-side, rich and beautiful display of results, and simple and convenient operation. This promoted the wide application of technical route. J2EE architecture can solve many practical problems, but the requirement of higher real-time data acquisition frequency and larger data capacity made the application of the power quality monitoring and evaluation system based on J2EE less contented with more complex data analysis algorithm. These led to the following deficiencies: (1) The low execution efficiency of server-side code makes the architecture run slowly; (2) There is no unified management in the software life cycle, registration, security guarantee and coupling strategy of the components, and the communication between the components lacking specifications, which resulted in difficult interactions between the threads and poor execution efficiency. This study has found that in the power quality monitoring system based on J2EE, the coupling is poor in the procedures like the module of communication protocol parsing run by the data acquisition server before, service components of real time sampling, statistical analysis components of evaluation data, data storage service components and data push components. Within 3-5 seconds of the sampling frequency, the traffic rate of the threads between the components was greatly reduced, which would easily lead to data congestion, data loss and an abnormal system. So, we have to reduce the demand on system design and shorten the sampling frequency to 1 minute, even less than 30 seconds.

For this kind of situation, in order to deal with the shortage of application of the technical route in the quasi real-time system (between non-real-time system and real-time system, the software system with data sampling frequency of 5 seconds - 1 minute) only based on J2EE architecture, the project first introduced the Open Services Gateway Initiative (OSGi) framework into the design of the power quality monitoring and evaluation system. Combined with the specification of J2EE architecture, with the aid of the Eclipse Equinox OSGi open source framework, from the view of the design of software architecture, it dealt with the limitations and shortcomings of power quality monitoring and evaluation system simply based on J2EE architecture and laid a foundation for the subsequent systematic research and development. At the same time, it offered help and advice for developers of software system using OSGi framework.

2 Software architecture design based on OSGi

OSGi defines architecture for developing and deploying modular applications and libraries, and for modular application development as the Dynamic Module System for Java. OSGi offers the following advantages: to operate different modules of application dynamically without restarting the container; to own multiple versions of a particular module running at the same time; to provide suitable infrastructure for developing complex Java applications divided into modules. As a standard for service-oriented computing environment, it provides an open, component-service-oriented programming model to users, which is easy to deploy (Konstantelos et al., 2017; Kuijs et al., 2016). It allows the user bind a defined service to certain service interface-service at run time, and has features such as dynamically changing behavior, hot-swappable plug-in architecture, high efficiency and reusability, etc. The OSGi alliance released the earliest/first version named as OSGi Service Platform

V1.0 in 2000 and the latest is version 4.3. The OSGi framework V1.0 was not compatible with Java applications. When the most famous Java development tools Eclipse3.0 version gradually migrated Eclipse plugin mechanism to the OSGi framework, which realized an OSGi open source framework named Equinox, and then OSGi successfully entered Java enterprise development flow, and organically combined with J2EE architecture (Aiman et al., 2015).

2.1 Software architecture

The OSGI framework is a set of several specifications/stipulations that defines dynamic system components for Java applications. It provides such capabilities as function modularization where applications are dynamically composed by adopting Eclipse Equinox development tool. The OSGi is based on layered architecture named Security Layer, Module Layer, Life Cycle Layer, and Service Registry as depicted in Figure 1.

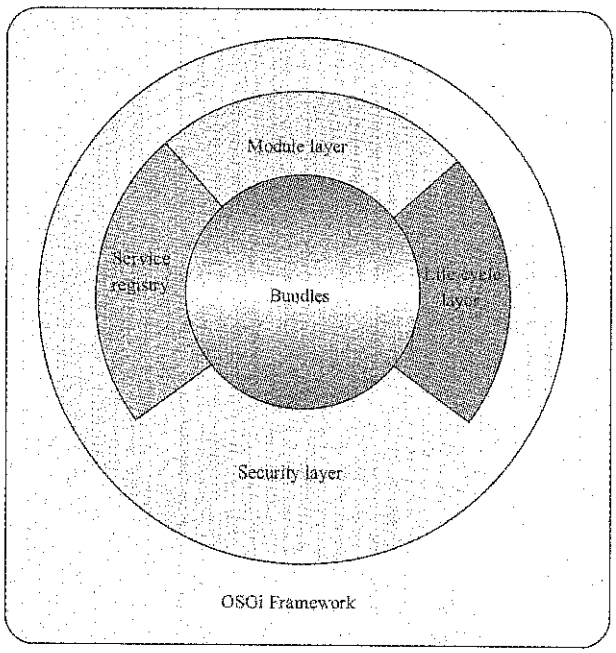

Figure 1 Layering architecture of OSGi

OSGi security layer that handles the security issues and leverages the fine-grained security model because of Java SE security support. It provides one of the most secure application environments with precision control and the basic management framework.

The module layer defines modules concept that how bundle can import and export code (Stusek et al., 2015). To fulfill the system requirements, this layer provides the support of bundle applications of load strategy and Java application integrations for the underlying infrastructure. The OSGi provides dynamic framework architecture for Java modularity. The framework provides a separate class loader for each bundle, which implements the Bundle Activator interface, and makes bundle organization more modularized. Life Cycle Layer provides life cycle management and safety control of the bundle. It also defines how bundles are dynamically installed and managed in the OSGi framework. Bundle is an organization of jar files on Module layer. Service Layer defines programming interface for managing services and provides dynamic interoperability with life cycle.

2.2. Architecture design

The worldwide electricity power system faces radical transformation with the demand to decarbonize. The Smart Grid Technology uses the advanced Information & Communication Technology (ICT) to control the next generation power systems reliably and efficiently. These days the technology is becoming more and more popular. It has put advanced control methods for real-time monitoring, evaluation, decision-making and systematic architecture. Moreover, The OSGi framework specification provides mature and comprehensive compatibility with J2EE architecture, especially the appearance of Equinox, the OSGi open source framework, which is made by Eclipse, the technology framework based on the OSGi specification has well solved the problems in the support of dynamic components technology and in improving the communication efficiency of the underlying data. This project adopted the OSGi framework specifications, and designed a system for power quality monitoring and evaluation. The system has four-layered architecture: data layer, application support layer, business application layer, and client presentation layer as shown in Figure 2.

Data layer: where evaluation and Power Quality Data Interchange Format (PQDIF) event data were stored depending upon the assessment categories in real-time database. The database stored power quality monitoring data in real-time collected by the online monitoring devices based on the commercial relational database; evaluation database is a data collector after classifying, calculating, inducing and processing the real-time data of

power quality, which can be used for the evaluation and analysis of the power quality indicators. PQDIF event library is a series of PQDIF files sent by power quality monitoring device, and a kind of universal power quality data transfer format regulated by IEEE1159. PQDIF event stored all the event information of power quality monitoring device.

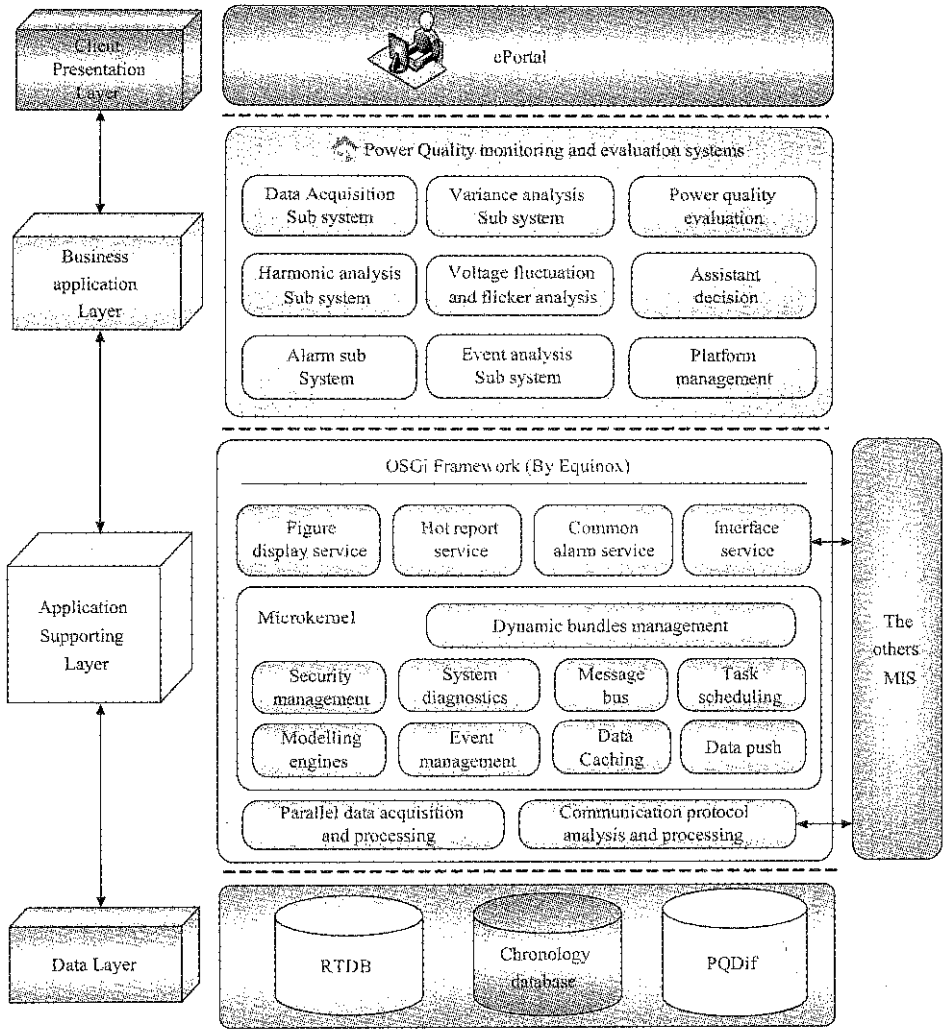

Figure 2 The system of software architecture

Application support layer: Also called OSGi framework platform layer because of OSGi framework component management technology. It halved the platform into two groups named as microkernel components group and special services components group, on the basis of implementing Equinox3.5, microkernel adopted Servlet bridge mode, embedded the OSGi framework to application container, and broke general functions the platform into specific component modules, which made the components form a microkernel framework under the OSGi framework specification and carried out modularization management with model engine. The Microkernel common components incorporate/contain safety control, message bus, system management, task scheduling, engine model, event management, data caching, data pushing and dynamic components management, etc. Special services components group consists of various service components which support the business applications are as parallel data acquisition processing, communication protocols analytic processing, graphical display, impromptu reporting, general alarm and system interface. Microkernel engine and dynamic components management have realized the start-stop management for all components of the platform which includes the module lifecycle management, module service lifecycle management, initialization and management of the spring container, the release and references of module service, registered persistent objects and Web resources register.

Business application layer: syntactically connected with the application support layer, it provides collection of business applications modules for power quality monitoring and evaluation, assessing diagnostic. It has particular functions like monitoring subsystem, auxiliary decision-making management, platform management and modules named as, harmonic, sequence component analysis, incident analysis, deviation analysis, wave flicker analysis, alarm communication management, analysis.

Client presentation layer: it is responsible for providing user interface because it actually interacts-machine interface through Web portal management and performs various activities of power quality monitoring and evaluation system.

2.3 Technical route selection

As shown in Figure 3, system design is based on Web technology (based on B/S access patterns, it supports IE7, FireFox3.6, Chrome 12, and other upper versions) (Ajax, JSP, Flex (version 4.1). The application was developed in Java environment (development kit uses JDK/JRE 1.5, the Servlet/Jsp 2.0 2.4 (1.4 standard Java EE). The component container adopts the mature Spring3.1.1 version based on SSH (Struts + Spring + Hibernate) in order to provide the compatibility with other environments. The architecture is based on the OSGI framework and J2EE specifications. It adopts the hierarchical technology and service-oriented architecture and provides service of RESTful style (Gao et al., 2014). It used HTTP (S) and JSON data format communication protocols. Systems also support Tomcat6. X, Weblogic9.2. X and main middleware. It followed the open source software of agreement like BSD, Apache Licence 2.0. Data persistence layer uses Hibernate technology it has OO features, and it can support database language comprehensively so it provides program portability. Hibernate provides Java DataBase Connectivity (JDBC) connection through SessionFactory to execute SQL directly. Commercial database is compatible with Oracle 10 g, Sql Server and MySql, supports special PQDIF file database in the field of power quality.

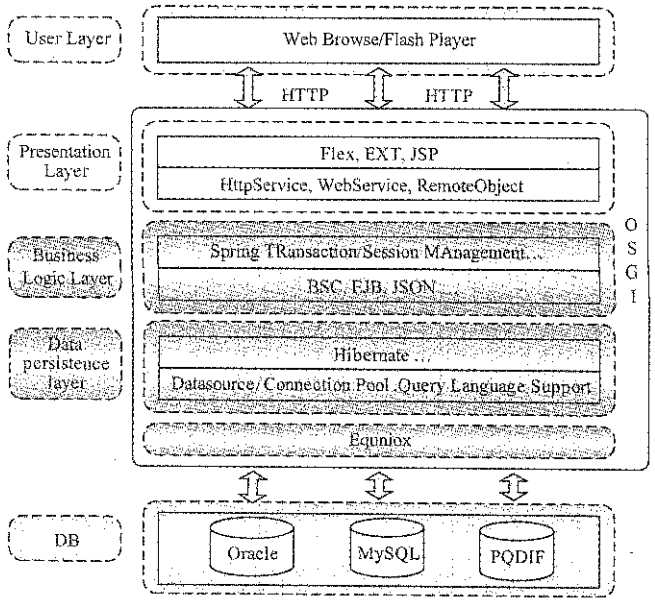

Figure 3 Technical route of the system

3 Architecture application and experiments

This project designed a software framework based on OSGi framework and J2EE specification for power quality monitoring and evaluation systems, and also standardized the selection about the technical route. To verify the design results, a project was tested on two different parameters of OSGi framework and J2EE of power quality monitoring and evaluation system respectively.

(1) Software environment: the two systems were developed at different times, and they have the identical environment such as business application function server deployment, operating system and application software, service middleware of Tomcat7 and Oracle10g database installed by the system. They used system communication protocol and IEC103 specification power quality monitoring device. They were employed after every 300 seconds and all PQDIF data files were uploaded after every 120 minutes. The system data samples after every 5 seconds were stored into the database.

(2) Hardware environment: the system runs on a wide variety of hardware platforms. The following list described the recommended minimum hardware requirements for basic functionality of the system. Actual hardware requirements would be vary, depending on the system configuration and the programs and the features that you install.

Basic hardware requirements

• PC server, 2 CUP, 2 GHZ CPU frequency, 8 nuclear 16 threads

• level 320 MB cache

• 16 GB of system memory

• 1 TB hard disk that has 15 GB of free hard disk space

The numbers of access device are different. The test results are as Table 1.

Table 1 The system performance test correlation

	Test condition	Only with J2EE framework	OSGi combined with J2EE framework
Access to 1 power quality monitoring device (total 256 measurements)	Steady-state CPU load rate	10%-12%	10%-12%
	Steady-state memory occupancy	13%-15%	14%-16%
	Daily statistical report query about the average response time (20 times)	2.7seconds	2.6 seconds
	The average time consuming of power quality assessment in 7 days (20 times)	21.4 seconds	20.5 seconds
	Success rate of daily data acquisition	100%	100%
Access to 10 power quality monitoring device (total 2560 measurements)	Steady-state CPU load rate	35%-37%	18%-20%
	Steady-state memory occupancy	38%-41%	33%-35%
	Daily statistical report query about the average response time (20 times)	18.4 seconds	3.5 seconds
	The average time consuming of power quality assessment in 7 days (20 times)	48.5 seconds	26.4 seconds
	Success rate of daily data acquisition	100%	100%
Access to 50 power quality monitoring device (total 12800 measurements)	Steady-state CPU load rate	98%-100%	28%-31%
	Steady-state memory occupancy	58%-62%	43%-46%
	Daily statistical report query about the average response time (20 times)	More than 1 minute	5.6 seconds
	The average time consuming of power quality assessment in 7 days (20 times)	No response	36.5 seconds
	Success rate of daily data acquisition	<90%	100%

4 Application results

The test results of table 1 depicted the performance indicators and showed that system was underutilized due to less number of devices. If the number of monitoring devices are increased up to 10 (total 2560 measurements) then this will increase the system load rate and there will be significant difference between performance of two systems. The system performance is significantly enhanced after adopting OSGi framework components. When two systems respectively were accessed to 50 sets of power quality monitoring device (total 12800 measurements), The J2EE architecture was on the verge of collapse but the system based on the OSGi framework and having the microkernel on application support layer was still in normal state and has more outstanding performance.

The result showed that a mono server system would not meet the requirements. Therefore, OSGi framework specification reformed the system platform layer, and finally developed a new generation of power quality monitoring and evaluation systems, which solved the problem.

5 Conclusions

Based on the OSGi framework and J2EE specifications, the power quality monitoring and evaluation system was designed. It followed the open source frame work of Eclipse, and Equinox carried out unified management and configuration of various components. At the same time, it employed the microkernel for the layer management and effective real-time interaction of the components which made the system more stable and robust. The architectural pattern will be widely used in the fields of power quality monitoring and evaluation system, enterprise monitoring of energy efficiency and saving management system, etc. Although the system will continue to evolve and provide services for users, the prevailing OSGi framework within the field of power quality monitoring and evaluation is one of optimism. Clearly, the roads leading to the effective management on power quality are still long, and should do something endeavored to implement in cloud platform with the development of big data technology (Kim et al., 2015). However, the research work in this paper provides a promising path to follow.

Acknowledgements

The authors would like to thank their colleagues for the support to this work. The detailed comments from the anonymous reviewers were gratefully acknowledged.

This work was supported by the National Spark Program Key Project (Grant #: 2015GA600002) and the fund of the Beijing Key Laboratory of Big Data Technology for Food Safety, Beijing Technology & Business University (BTBU).

[References]

[1] Aiman, S., B. A. Manjunatha, H. P. Rohith, and P. Gogoi. 2015. Performance evaluation for automated migration of enterprise class JEE applications to OSGi services. *International Conference on Computer and Communication Technology*, 36-40. Allahabad, India, 25-27, September.

[2] Ali, S., K. Wu, K. Weston, and D. Marinakis. 2016. A machine learning approach to meter placement for power quality estimation in smart grid. *IEEE Transactions on Smart Grid*, 7(3): 1552–1561.

[3] Bionda, E., D. Pala, G. Proserpio, L. Tenti, S. Pugliese, and D. D. Giustina. 2016. Integration of power quality information in the framework of a standard semantic model. *IEEE, International Conference on Environment and Electrical Engineering*. Florence, Italy, 7-10 June.

[4] Blair, S. M., C. D. Booth, G. Williamson, A. Poralis, and V. Turnham. 2016. Automatically detecting and correcting errors in power quality monitoring data. *IEEE Transactions on Power Delivery*, (99): 1–1.

[5] Elphick, S., P. Ciufo, G. Drury, V. Smith, S. Perera, and V. Gosbell. 2017. Large scale proactive power-quality monitoring: an example from Australia. *IEEE Transactions on Power Delivery*, 32(2): 881–889.

[6] Esparza, M., J. Segundo, C. Núñez, X. Wang, and F. Blaabjerg. 2017. A comprehensive design approach of power electronic-based distributed generation units focused on power-quality improvement. *IEEE Transactions on Power Delivery*, 32(2): 942–950.

[7] Feng, Y., and Z. Yin. 2016. Comprehensive evaluation of power quality of dc distribution network. *Journal of Shanghai Electric Technology*, 9(2): 1–5. (In Chinese with English abstract).

[8] Gao, S., H. Zhu, X. Zhou, Y. Liu, and L. Sun. 2014. Design and implementation of smart home linkage system based on OSGI and REST architecture. *Advances in Wireless Sensor Networks, Springer Berlin Heidelberg*. 501: 568–582.

[9] Hu, S., C. Tang, F. Liu, and X. Wang. 2016. A distributed and efficient system architecture for smart home. *International Journal of Sensor Networks*, 20(2): 119–130.

[10] Iqtiyaniilham, N., M. Hasanuzzaman, and M. Hosenuzzaman. 2017. European smart grid prospects, policies, and challenges. *Renewable & Sustainable Energy Reviews*, 67: 776–790.

[11] Ji, Z. G., R. C. Hou, and Z. M. Zhou. 2016. A fault diagnostic approach for the OSGi-based cloud platform. Intelligent Computing Methodologies, 9773: 648–657.

[12] Kim, D., C. Lee, and S. Helal. 2015. Enabling elastic services for OSGi-based cloud platforms. *Seventh International Conference on Ubiquitous and Future Networks*, 407–409. Sapporo, Japan, 7-10 July.

[13] Konstantelos, I., S. Giannelos, and G. Strbac. 2017. Strategic valuation of smart grid technology options in distribution networks. *IEEE Transactions on Power Systems*, 32(2): 1293–1303.

[14] Kuijs, H., C. Reich, M. Knahl, and N. Clarke. 2016. A scalable architecture for distributed OSGi in the cloud. *International Conference on Cloud Computing and Services Science*, Closer (2): 109–117.

[15] Liu, D., G. Wang, and Y. Wang. 2016. The monitoring system of electricity quality of intelligent power micro-grid. *Journal of Shenzhen Polytechnic*, 15(3): 16–18.

[16] Luo, A., X. U. Qianming, M. A. Fujun, and Y. Chen. 2016. Overview of power quality analysis and control technology for the smart grid. *Journal of Modern Power Systems & Clean Energy*, 4(1): 1–9.

[17] Moreno-Munoz, A., F. Bellido, D. Oterino, J. J. G. D. L. Rosa. 2008. Power quality monitoring integration into distribution automation through the use of AMR. *IEEE International Conference on Industrial Technology*, 2017: 1–6.

[18] Pichler, M., A. Veichtlbauer, and D. Engel. 2015. Evaluation of OSGi-based architectures for customer energy management systems. *IEEE International Conference on Industrial Technology*, 2455–2460. Seville, Spain, 17-19 March.

[19] Seider, D., A. Schreiber, T. Marquardt, and M. Bruggemann. 2016. Visualizing modules and dependencies of OSGi-based applications. *Software Visualization*, 6–100.

[20] Stusek, M., J. Hosek, D. Kovac, and P. Masek. 2015. Performance analysis of the OSGi-based IoT frameworks on restricted devices as enablers for connected-home. *International Congress on Ultra Modern Telecommunications and Control Systems and Workshops*, 178–183. Brno, Czech Republic, 6-8 Oct.

[21] Su, C. L., J. T. Yu, H. M. Chin, and C. L. Kuo. 2016. Evaluation of power-quality field measurements of an electric bus charging station using remote monitoring systems. *International Conference on Compatibility, Power Electronics and Power Engineering*, 58–63. Bydgoszcz, Poland, 29 June-1 July.

[22] Teng, Z., M. Zhang, T. Jiang, J. Xu, and Q. Zhang. 2015. A power quality online monitoring system oriented zigbee routing optimization strategy. *Wireless Networks*, 22(6): 1–7.

[23] Vanin, A. S., A. V. Valyanski, R. R. Nasyrov, and V. N. Tul'Skii. 2016. Quality monitoring of electrical power to evaluate the operational reliability of power equipment and active–adaptive voltage control in distribution power grids. *Russian Electrical Engineering*, 87(8): 452–456.

[24] Xavier, M. V. E., W. D. C. Boaventura, and M. D. Noronha. 2016. High performance power quality monitoring system. *International Conference on Harmonics and Quality of Power*, 974–979. Belo Horizonte, Brazil, 16-19, Oct.

Vegetable field knowledge representation learning method

Zhao Ming*, Dong Cuicui, Du Huifang, Du Yaru, Chen Ying

(*College of Information and Electrical Engineering, China Agricultural University, Beijing 100083, China*)

Abstract: Knowledge Graph is a sort of knowledge base to describe the entities and relations in the real world. In this study, we used vegetable entries of Baidu encyclopedia and HDwiki as data sources to study the knowledge representation learning models base on vegetable knowledge graph construction. TransE model was adopted to represent vegetable triples, the entities and relations were embedded into a continuous low- dimensional vector space, and the semantic similarity between the entities and relations was measured by computing the vector distance. Facing the complex attribute relations of 1-N, N-1 and N-N, we came up with PTA (path-based TransE for attributes) model, constructed the relation path by combining attribute relations and hyponymy relation, and embedded the relation path into vector space as well. Finally, we took mean rank and Hits@10 as our evaluation metrics to evaluate the link prediction task. The result showed, without taking into account the relations classification, the link prediction results of PTA model was better than TransE models. And in the case of sorting the complex attribute relations, the total value of Hits@10 was higher than TransE model. This study mainly focused on the knowledge representation learning in knowledge graph of Chinese smaller domain. It does not only have a practical value in vegetable fields, but also provides a reference for the other areas in the information extraction, knowledge fusion and knowledge reasoning, etc.

Keywords: vegetable, knowledge graph, knowledge representation learning, TransE, PTA

Citation: Zhao, M., C. C. Dong, H. F. Du, Y. R. Du, and Y. Chen. 2017. Vegetable field knowledge representation learning method. International Agricultural Engineering Journal, 26(4): 270–276.

1 Introduction

Knowledge Graph is a new type of massive knowledge management and service model (Pujara et al., 2013). It is a knowledge base for describing various entities and the relationships between entities in the real world (Wang et al., 2014). According to the characteristics of professional fields, researchers in academia carry out Knowledge Graph in biomedical, news, film and television applications at present (Patrick et al., 2014; Marco et al., 2015; Lin et al., 2015). How to represent and store entities and the relationships between entities to ensure the readability and stability of knowledge are the important subjects of Knowledge Graph construction and application. In recent years, knowledge representation methods mainly include RDF (Resource Description Frame Work) graph model and word embedding-based model.

RDF is a framework proposed by W3C to describe the information on the World Wide Web (Carroll et al., 2004; Brickley et al., 2004). Data are represented by a marked graph, nodes and edges correspond to entities and relations in triples, and the query on large-scale data can be regarded as a graph matching problem. However, the RDF data contain many text information and there are too many associations between the nodes, so that the scale of the graph is huge, which leads to complex and inefficient RDF data query.

Based on word embeddings representation techniques began with One-hot Representation, and gradually the Deep Learning has become the representative (Turian et al., 2010; Xie et al., 2016). The representation learning is a distributed method. It aims to represent the semantic information of the object as dense real embeddings. Compared with the graph, it can effectively solve the problem of data sparseness, and the performance of Knowledge Graph construction is greatly improved

Received date: 2017-09-11 **Accepted date:** 2017-11-22

***Corresponding author**: **Zhao Ming**, MSc, Associate Professor, College of Information and Electrical Engineering, China Agricultural University, Beijing 100083, China. Email: zhaoming@cau.edu.cn.

(Balduccini et al., 2013). In order to better organize the entities and relationships in the Knowledge Graph and make effective use of it, the researchers have devoted themselves to knowledge representation learning and proposed many models, including Structured Embedding (Bordes et al., 2013), Semantic Matching Energy (Haboush et al., 2014; Kim et al., 2016), Latent Factor Model, Neural Network Model (Socher et al., 2013), Matrix Decomposition Model (Nickel et al., 2012) and translation model (Fu et al., 2014). With word2vec put forward, the knowledge of learning technologies gets more and more attention. Word2vec is a tool to transform a word as a real-valued embeddings. The toolkit uses the idea of Deep Learning to train textual content into vectors for information processing. By calculating the Euclidean distance or Cosine distance between word embeddings to measure the semantic similarity (Zhang et al., 2015). On this basis, Bordes et al., (2013) proposed TransE, a translation model for learning. TransE model is a simple and effective representation learning scheme. Its main idea is to regard the relations in the Knowledge Graph as a translation operation from the head entity to the tail entity.

Many studies have extended TransE to process complex relationships, including TransH (Zhang et al., 2014), TransR (Yankai et al., 2015), TransD (Ji et al., 2015). However, different models have different limitations, and need to expand for the characteristics of the study fields and datasets.

However, most of the representation learning techniques are aimed at large-scale global Knowledge Graph of English. At present, there are few reports on the study of knowledge representation of Chinese vegetable domain Knowledge Graph. In particular, the conceptual architecture of the vegetable field is complex and the attribute relations of the entities are complex and diverse. It causes great difficulties to the study, which makes the research on the knowledge representation of the vegetables and even the whole agriculture area relatively weak.

2 Vegetable field knowledge graph

At this stage, the extraction of entities is based on the existing vegetable ontology, and extracts vegetable alias as a supplement. Relations between entities mainly manually recognize the valuable triplet information from form information. And finally build the Knowledge Graph of vegetables to lay the foundation for the follow-up knowledge representation learning stage.

In this study, we used the data from the two mainstream encyclopedias entries, including Baidu Encyclopedia and Interactive Encyclopedia. Vegetable entries involved concepts such as tomato and radish, and the relationships mainly include varieties, branches of the family, and the Latin name, English name, distribution area, cultivation techniques, pests and diseases, nutritional value and medicinal value attribute relationships and non-classification relationships.

3 Representation Learning Model

This study mainly adopted knowledge representation learning translation model, mapped the knowledge graph to the low-dimensional vector space, the triples in the knowledge graph of vegetable field were vectorized.

TransE belongs to the translation model in the knowledge representation learning model, which is derived from semantic translation invariance between word vectors. The model regards the relation in the knowledge graph as a translation vector between two different entities, that is, the translation of the relation vector r as the head vector h to the tail entity vector t, and the vector r can also be viewed as a translation from the vector t to the vector h, so the TransE model is also the translation model.

3.1 TransE model

Because each entity vector only corresponds to a low-dimensional vector, TransE greatly reduces the number of parameters compared with the previous models, to a certain extent simplifies the complexity of the operation. TransE model is a parameterized model method based on translation. Its purpose is to construct a structured vector space. Given a training set of triplets (h, r, t), E is the entity set, and R is the set of relations, where $h,t \in E$. For any triplet (h, r, t) in S, TransE expects $h + r \approx t$ its learning goal to be as shown in Figure 1.

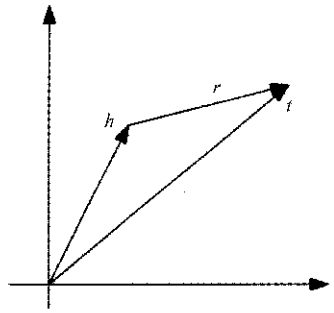

Figure 1 Triples learning objectives

3.2 PTA model

The above TransE is a typical neural network-based method, the main purpose is to map the entities and relationships in the knowledge graph to a low-dimensional vector space. The model has a good effect on the process of knowledge representation learning, but also has some shortcomings, mainly in dealing with different types of relations, the effect of learning is different. From the principle of TransE model, we can see that it is a triplet (h, r, t). It's learning goal is $h+r\approx t$, that is, different tail entities tend to be at the same point in the vector space for the same head entity and relation. For example, (tomatoes, disease is strip rot) and (tomatoes, the disease is bacterial leaf spot), mapping these two triples into the same vector indicates bar rot and bacterial leaf spot of the vectors tend to coincide. Therefore, TransE ignores the semantic difference of the same class vector, it is better when the 1-1 relation is expressed, but the learning effect is worse when dealing with complex relations such as 1-N, N-1, N-N. When the relationship between the different types of their own, there are some limitations.

In this paper, the PTA model was proposed for the entities and relationships of the knowledge graph of vegetable field. This model improved the TransE model, which solved the problem of rich complex attribute relation representation in this domain.

From the vegetable domain knowledge graph construction process can be seen, in addition to the upper and lower relations, the vegetable field includes a lot of non-classification relationships. Among them, non-classification relations among entities (such as crop rotation, intercropping, etc.) account for only a small proportion, and most of them are attribute relationships. Attribute relations include: disease, pests, nutritional value, medicinal value, growth environment and cultivation techniques. Moreover, in this field, attribute relations generally contain two or more attribute values.

In the vegetable field, because the number of entities is small, the relationship path is not so complicated, and the relationship mainly focuses on the attribute relations. Therefore, inspired by path reasoning, the purpose of PTA model is to express the complex attribute relationships in the knowledge graph of vegetable domain, and the paths are also mapped to low-dimensional real-valued vector spaces.

In general, we use multiple path relations $P(h, t)=\{p1,\ldots,pn\}$ to concatenate the header entity h and the tail entity t, and treat them as translations from the head entity to the tail entity. One of the relational paths is defined as $p=\{r_1,\ldots,r_l\}$, the path is represented as $h\xrightarrow{r_1}\ldots\xrightarrow{r_l}t$. Here, the path is composed of multiple relations, and the reasoning model is constructed to explore the hidden relation between the two entities in the knowledge graph.

However, for the complexity of attribute relations in vegetable field, this paper made two basic assumptions: first, the vegetable entity names and attribute values contained in the vegetable field triples were classified as entity categories; second, for the attribute relationship related the upper and lower relationship ISA to increase the direction of the relationship FISA. For example, the semantic relationships between the triples (barley disease, ISA, disease name) and the triples (disease name, FISA, barley disease) are "barley disease is a disease name". The head and tail entities swap positions result in the change of name of the relationship.

Because of the particularity of the vegetable field, it is different from the graph of the relationship between people and the graph of Chinese medicine or the graph of song. The field of vegetables contains less inter-entity relationships, the main relationship for the rotation relation, intercropping relation, in addition, it can be classified as attribute relations. Attribute relations can be classified according to their complexity, mainly contain the following four categories, the following relations are reflected in Figure 2.

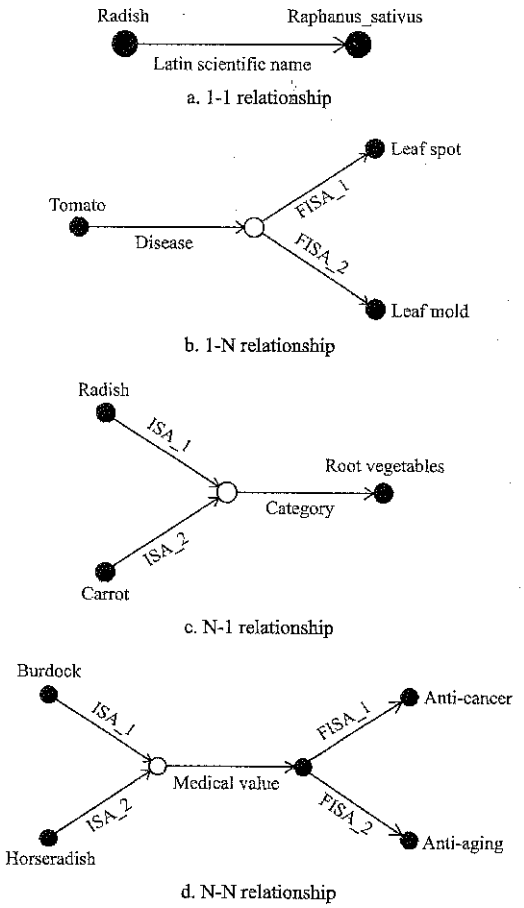

Figure 2 Examples of attribute relationships categories

1 - 1 relationship: Such relation mainly includes the Latin name, English name, etc., mostly for a property name corresponds to a single attribute value, the path relationship directly expressed as a first-order path $h \xrightarrow{r_1} t$. Where r_1 represents the attribute relationship name. For example, potatoes have a Latin name of "Solanum tuberosum", both of which are unique to each other.

1 - N relationship: This kind of relation mainly includes the alias relation, and the category relation, these attribute relations generally contain more than 2 attribute values, but these attribute values only correspond to a certain vegetable, the attribute relation path may express as second order path $h \xrightarrow{r_2} e \xrightarrow{FISA\_i} t$, where r_2 represents the attribute relationship name. For example, the tomato alias includes tomatoes, persimmon, etc., these two aliases can only represent a tomato, a vegetable.

N - 1 relationship: These relations mainly include the boundary, the door, the outline, the head, the branch, the category and so on the classification attribute and the medicinal property, the medicinal smell, the flowering date and so on. These attribute relations have only one attribute value, but contain two kinds or two above kinds of vegetable entities. Its attribute relation path can be expressed as a second-order path $h \xrightarrow{ISA\_i} e \xrightarrow{r_3} t$, where r_3 is the attribute relation name. For example, radish and carrots are root vegetables, root vegetables are a single attribute value, but the corresponding radish and carrots and other vegetable names.

N - N relationship: These relations mainly include the sowing method, cultivation technique, disease relationship, pest relationship, nutritional value, medicinal value, edible value, etc. The attribute relation path can be expressed as the third order path $h \xrightarrow{ISA\_i} e_1 \xrightarrow{r_4} e_2 \xrightarrow{FISA\_i} t$, where r_4 is the attribute relation name. These attribute relationships are characterized by interlude between vegetable entities and attribute values. For example, the medicinal value of burdock and wasabi contains anti-cancer and anti-aging functions.

The four graphs in Figure 2 showed the path planning of the above four attributes. The solid circles represent the entities existing in the knowledge map of the vegetable domain. The hollow circles represent the added attribute fuzzy entities. The increase of fuzzy attribute of the attribute is mainly reflected in the data set of the triples, as shown in Figure 2b, the triples (tomato, alias, tomato) and (tomato, alias, Fan persimmon) are converted into triples (Alias attribute, FISA, Tomato) and (alias attribute, FISA, Fan persimmon), where 'alias attribute' as a property fuzzy entity to deal with.

3.3 PTA relationship path vectorized representation

In this study, the energy function $E(h,p,t)$ of the triple (h,p,t) is defined. Similar to the TransE model, the PTA model also needs to vectorize the relationship path, map the entities, relationships and attribute values to the same vector space. The process relies on the relationship vector in the relationship path.

$$e=\frac{1}{m}(t_1+\ldots+t_m) \tag{1}$$

The relation path vector $p=(r_1, r_2)$ is obtained by the addition operation, which adds all the relation vectors contained in the relation path, as shown in Equation (2)

$$p=r_1+r_2 \tag{2}$$

For the TransE model, $h+r$ and t have similar

semantic relations when (h, r, t) is in existence, and $h+r$ and t are far away from each other when (h, r, t) does not exist. At the same time, the loss function of the model is to calculate the L1 or L2 distance, the specific showed in Equation (3):

$$d(h+r,t) = | h+r-t |_{L1/L2} \quad (3)$$

Correspondingly, for the PTA model, the PTA also defines the corresponding energy function for each triplet (h, r, t)

$$G(h,r,t) = E(h,r,t) + E(h,p,t) \quad (4)$$

where, $E(h,r,t)$ denotes the relativity of the relationships among the triples; $E(h,p,t)$ denotes the energy function of the triplet (h, p, t), and relates to the vectorized representation of the relation path p.

3.4 Optimization of representation learning model

In this paper, TransE model and PTA model were optimized by stochastic gradient descent algorithm. The gradient descent algorithm used the negative gradient direction to determine the new search direction for each iteration, so that each iteration made the objective function value gradually decrease.

4 Methods and results

4.1 Experimental methods

We used TransE model to map entities and relations into an embedding space. In plant domain, we selected 12 different vegetable types as training data, edible fungi (37 types in total) for testing data, and sprouts (25 types in total) as validation data. The detailed dataset description was shown in Table 1.

Table 1 TransE model dataset

Data set	Entities	Relation	Training set	Validation set	Test set	Total entries
Vegeta-ble	8780	187	7550	1850	1250	10650

The hyperparameter setup was as follows: the vector size was chosen from {50:100}; we set the learning rate λ to one of these values – {0.001, 0.01, 0.1}, and the margin γ to {1, 2, 10}. Finally, the optimal parameter combination was given by size = 100, λ=0.001, γ= 1.

In addition to the mappings of entities to an embedding space, we also need to map the relation path to the same space. Second-order translation model can be used for characterize one-to-many and many-to-one relation types, and third-order translation model for many-to-many relation types. i.e. alias information, the relationship between pests and diseases, nutritional value and medicinal value etc. The data we used to evaluate our new model was shown in Table 2. We randomized the data into training, validation, testing as the ratio of 20:1:1.

Table 2 PTA model dataset

Relation types	Entities	Atribute relation	Training set	Validat-ion set	Test set	Total entries
1-1	1764	20	1708	50	50	1808
1-N	2921	85	3608	170	170	3948
N-1	2200	39	2984	140	140	3264
N-N	2105	43	2062	136	136	2334
Total	8990	187	10362	496	496	11354

By comparing Table 1 and Table 2, we noticed that there were extra 210 entities and 704 triples introduced. We used the same parameter setting for both PTA and TransE models.

4.2 Experimental results

As most of the triples were extracted manually, the quality of the dataset could be guaranteed. However, there are some factors that might affect the coverage of knowledge graph which is our on-going work to dynamically update and fulfill the knowledge base.

We evaluated the model performance via knowledge completion task also called link prediction. Given two elements within a triple, linked prediction tries to recover the third element which was missing. i.e. given a head entity tomato and relation alias, the well-trained model should predict the tail entity as either tomatoes or persimmon.

We proposed two evaluation metrics, mean rank and Hits@10. The mean rank is to measure the average rank of the entity to be predicted, and the hit@10 is to measure the probability how often the correct entity is in the top 10 list.

Link prediction without considering relation categories Table 3 showed the link prediction performance for PTA and TransE model in vegetable domain graph.

Table 3 Effects without considering relation categories

Link prediction evaluation index	Mean Rank		Hits@10,%	
	Raw	Filter	Raw	Filter
TransE	79.1	78.7	28.4	28.8
PTA(ADD)	74.8	72.6	32.8	34.3

As we can see from the results, PTA model outperforms TransE model in terms of both mean rank and hit@10 criteria. The value of mean rank decreases to 72.6 and the value of Hits@10 is increased to 34.3%, which gives about 5% improvement. The result implies that the path-based learning scheme provides good complement to the representation learning of knowledge graph.

Link prediction by considering relation categories We constructed the relation path using attribute-type relation and ISA relation to solve one-to-many, many-to-one and many-to-many problems. Table 4 showed the comparison results measured by Hit@10 value on four different relation types, among TransE and PTA models.

We first divided the dataset by category which resulted in different numbers of triples belong to one-to-one, one-to-many, many-to-one, many-to-many case, respectively. Because of that, we were unable to compare the mean rank value. Table 4 showed the prediction performance measured by Hit@10 value on different types of datasets, among TransE and PTA models.

Table 4 Effects with different relation categories

Evaluation	Left Head entity prediction				Right Tail entity prediction				Total
Index	1–1	1–N	N–1	N-N	1–1	1–N	N–1	N-N	
TransE	30.5	25.2	20.6	25.4	31.9	20.1	25.3	24.0	25.4
PTA(ADD)	32.3	36.1	26.5	31.8	33.5	27.0	38.3	30.4	32.0

First consider the correlation between relation category and direction of prediction. The results from Table 4 can be divided into four categories. Because of the symmetric property of one-to-one, many-to-many relations, there is no big difference in terms of performance for the task of predicting head entity and tail entities. On the other hand, we can see the opposite results for prediction of one-to-many and many-to-one relations. i.e. the PTA model gave the predictive accuracy of 36.1% and 38.3% for the task of predicting head entity for one-to-many relation, and tail entity for many-to-one relation, respectively. The results are similar and gave the best performance among others.

However, for the task of predicting head entity for many-to-one relation and tail entity for one-to-many relation, we got the accuracy as low as 25.5% and 26.0%, which gave the worst performance. We can see why by showing the example of predicting for head entity. In this case, the expansion of relation path opposes to the direction of prediction such that each entity maps to multiple attributes which further increases the prediction accuracy of that entity. On the other hand, for the case of many-to-one, multiple entities map to a single attribute value, which results in performance decrease.

5 Discussion

In this paper, we considered the construction and reasoning over the vegetable domain knowledge graph. Because most of the relations are attribute-types, there are significant number of relations belong to one-to-many, many-to-one or many-to-many types, which is inherently different from graph from other domains. In order to handle such special challenges, we proposed a novel method called PTA which constructed the relation path by combining attributes and hyponymy relations, and imbedded them to a lower dimensional space as well. The experimental results showed its superior performance over other competing methods.

Acknowledgements

This research was supported by the National Natural Science Foundation of China under Project 61503386.

[References]

[1] Balduccini, M., C. Baral, and Y. Lierler. 2015. Chapter 20 knowledge representation and question answering. *Foundations of Artificial Intelligence*, 148(07): 779–819.

[2] Bordes, A., J. Weston, R. Collobert, and Y. Bengio. 2011. Learning structured embeddings of knowledge bases. In *Proceedings of the Twenty-Fifth AAAI Conference on Artificial Intelligence.* San Francisco, California, August 7-11

[3] Bordes, A., N. Usunier, A. Garcia-Duran, J. Weston, and O. Yakhnenko. 2013. Translating embeddings for modeling multi-relational data. In *NIPS'13 Proceedings of the 26th International Conference on Neural Information Processing Systems*, 2: 2787–2795. Lake Tahoe, Nevada, December 05 – 10.

[4] Carroll, J. J., I. Dickinson, C. Dollin, D. Reynolds, A. Seaborne, and K. Wilkinson. 2004. Jena: Implementing the semantic web recommendations. In *Proc. of the 13th Int'l*

World Wide Web Conf. on Alternate Track Papers & Posters (WWW 2004), Feldman SI, ed. 74–83. New York: ACM Press.

[5] Fu, R. J., J. Guo, B. Qin, W. X. Che, H. F. Wang, and T. Liu. 2014. Learning semantic hierarchies via word embeddings. *Meeting of the Association for Computational Linguistics*. 1: 1199–1209.

[6] Haboush, A. K. 2014. A hybrid modified semantic matching algorithm based on instances detection with case study on renewable energy. *International Journal of Engineering Trends & Technology*, 8(1): 14–23.

[7] Ji, G. L., S. Z. He, L. H. Xu, K. Liu, and J. Zhao. 2015. Knowledge graph embedding via dynamic mapping matrix. In *Proceedings of the 53rd Annual Meeting of the Association for Computational Linguistics and the 7th International Joint Conference on Natural Language Processing*, 687–696.

[8] Kim, K., G. Kim, D. Yoo, and J. Yu. 2013. Semantic material name matching system for building energy analysis. *Automation in Construction*, 30(1): 242–255.

[9] Lin, Y., Z. Liu, M. Sun, Y. Liu, and X. Zhu. 2015. Learning entity and relation embeddings for knowledge graph completion. In *AAAI'15 Proceedings of the Twenty-Ninth AAAI Conference on Artificial Intelligence*, 2181–2187. Austin, Texas, January 25–30.

[10] Marco, R., M. V. Erp, P. Vossen, A. Fokkens, I. Aldabe, G. Rigau, A. Soroa, T. Ploeger, and T. Bogaard. 2016. Building event-centric knowledge graphs from news. *Web Semantics: Science, Services and Agents on the World Wide Web*, s 37-38: 132–151.

[11] Nickel, M., V. Tresp, H. P. Kriegel. 2012. Factorizing YAGO: Scalable machine learning for linked data. Available at WWW. ACM.org, 2012: 271–280.

[12] Patrick, E., C. Meng, A. Siu, and G. Weikum. 2014. KnowLife: a knowledge graph for health and life sciences. *2014 IEEE 30th International Conference on Data Engineering (ICDE)*, 1254–1257. Chicago, IL, March 31-April 4.

[13] Pujara, J., H. Miao, L. Getoor, W. Cohen. 2013. Knowledge graph identification. *International Semantic Web Conference*, 542–557. Springer-Verlag, New York, Inc.

[14] Socher, R., D. Chen, C. D. Manning, and A. Y. Ng. 2013. Reasoning with neural tensor networks for knowledge base completion. In *NIPS'13 Proceedings of the 26th International Conference on Neural Information Processing Systems*, 1: 926–934. Lake Tahoe, Nevada, December 05 – 10.

[15] Turian, J., L. Ratinov, and Y. Bengio. 2010. Word representations: A simple and general method for semi-supervised learning. In *ACL '10 Proceedings of the 48th Annual Meeting of the Association for Computational Linguistics*, 33(5): 384–394. Appsala, Sweden, July 11-16.

[16] Wang, Z., J. W. Zhang, J. L. Feng, and Z. Chen. 2014. Knowledge graph embedding by translating on hyperplanes. In *Proceedings of the Twenty-Eighth AAAI Conference on Artificial Intelligence*, 1112–1119.

[17] Wang, Z., J. Zhang, J. Feng, and Z. Chen. 2014. Knowledge graph and text jointly embedding. In *Proceedings of the 2014 Conference on Empirical Methods in Natural Language Processing (EMNLP)*, 1591–1601.

[18] Xie, R. B., Z. Y. Liu, J. Jia, H. B. Luan, and M. S. Sun. 2016. Representation learning of knowledge graphs with entity descriptions. *The 30th AAAI Conference on Artificial Intelligence* (AAAI'16). AAAI Publications.

[19] Zeginis, D., Y. Tzitzikas, V. Christophides. 2007. On the foundations of computing deltas between RDF models. *International the Semantic Web and, Asian Conference on Asian Semantic Web Conference*, 7: 637-651. Springer- Verlag.

[20] Zhang, D., H. Xu, Z. Su, and Y. Xu. 2015. Chinese comments sentiment classification based on word2vec and SVM perf. *Expert Systems with Applications*, 42(4): 1857–1863.

Three-dimensional growth modeling of potted tomato root under negative pressure underground irrigation

Ji Ronghua, Liu Qiuxia, Zheng Lihua*, Chen Zhenhai

(*College of Information and Electrical Engineering, China Agricultural University, Beijing 100083, China*)

Abstract: Irrigation method affect crops root growth and spatial distribution. In order to find out the relationship between tomato root growth and irrigation system, the three-dimensional growth modeling of potted tomato root was built. The experiments were done to measure the three-dimensional spatial coordinates and the growth parameters of potted tomato roots at different growth stages. The experimental data were analyzed and the growth functions were defined based on the distribution probability and the directions of potted tomato roots. Based on the differential L-system, a three-dimensional potted tomato root growth model was proposed to describe the roots growth pattern of potted tomato and its boundary. According to the simulation potted tomato root growth modelling, the simulation error increases gradually with the root growth stage. The reason for this is that the faster root development is and the greater root variability will be during the period of late blossom and fruiting. Total root projection area can be calculated accurately. In different growth stages, the emphasis of root growth is different. The number of roots increases greatly at early blossom and the volume of roots increases greatly at fruiting. The root growth at seedling stage can be simulated effectively by the proposed model. The results will provide the foundation for further study of the interaction of soil moisture and root growth.

Keywords: potted tomato, root, three-dimensional growth model, negative pressure underground irrigation

Citation: Ji, R. H., Q. X. Liu, L. H. Zheng, and Z. H. Chen. 2017. Three-Dimensional growth modeling of potted tomato root under negative pressure underground irrigation. International Agricultural Engineering Journal, 26(4): 277–282.

1 Introduction

The crop ability of obtaining resource from soil is determined principally by roots. There are many factors to affect the root growth and distribution, such as crop species, planting patterns and environmental factors. The root growth models are often designed to dig out the relationship between root distribution in soil and the spatio temporal variability of resource supply, especially water.

There are six popular models, RootTyp, SimRoot, ROOTMAP, SPACSYS, R-SWMS, and RootBox, which are used to represent virtual root architectural with high accuracy (Dunbabin et al., 2011). Pagès et al. (2004) claimed the RootTyp model has been developed to simulate the dynamics of root system architecture for a large diversity of plant species (including tree species), as well as developmental stages and soil conditions. Lynch et al. (1997) claimed that SimRoot reconstructed the root architecture based on empirically derived growth rates, branching frequencies and growth angles. Dunbabin et al. (2011) stated the ROOTMAP model could represent root growth responses to 3D dynamic, heterogeneous soil environment and be used to investigate root-soil interactions over a range of spatial and time scales. Wu and Shepherd (2011) stated that SPACSYS model was developed primarily to investigate the interactions between crop root systems and nutrient use efficiency under different soil, fertilizer and crop management regimes. Schroder et al. (2012) claimed that the RSWMS was powerful and used to describe specific processes with different modules: root water flow, soil water flow, solute transport in soils, solute transport in roots, root growth and plant growth. Daniel et al. (2010) stated that the RootBox was used to study the effect of different roots

Received date: 2017-06-30 **Accepted date:** 2017-08-03

* **Corresponding author: Zheng Lihua,** Ph.D., Professor of Department of Computer Engineering, College of Information and Electrical Engineering, Beijing 100083 China. Email: zhenglh@cau.edu.cn. Tel: 010-62736746.

and rhizosphere traits at the root system scale. Root architectural simulation models explicitly simulate the architecture of root systems in 3D space. The crop root growth models are used to simulate root growth in response to heterogeneous soil environments.

The crop root distribution is closely related to soil water distribution. The root distribution is very different with the different irrigation methods. There are many studies about the different crop root distributions under drip irrigation (Li et al., 2017; Sokalska et al., 2009; Zhang et al., 2016).

There are researches for the root growth under different irrigation modes, drip irrigation and sprinkle irrigation are mainly concerned (Ahmadi et al., 2014; Liu et al., 2013; Liu et al., 2014; Rattanapichai and Klem, 2016; Seidel et al., 2016). The root traits, such as length, depth and width radius, were studied with different irrigations (Liu et al., 2014). Artificial intelligence algorithms were implemented to predict the root growth traits in different irrigation strategies. Crop growth model was also used to make the irrigation scheduling strategies (Ahmadi et al., 2014).

Negative pressure underground irrigation is a kind of active irrigation technology and used in greenhouse. The results of study show that negative pressure underground irrigation is effective water saving technology (Ji et al., 2014; Ji et al., 2015).

In order to understand potted tomato root growth and distribution with negative pressure underground irrigation, three-dimensional growth modelling of potted tomato root would be presented in this paper.

2 Materials and methods

2.1 Negative pressure underground irrigation

Negative pressure underground irrigation is a continuous active irrigation technology because the crop can automatically absorb water according to actual crop needs. Negative pressure underground irrigation system includes four parts: soil box, built-in reservoir, water level control tank and reservoir, as shown in Figure 1.

2.2 Potted tomato cultivation experiment setting

The tomatoes were cultivated with loam in the solar greenhouse in Beijing Academy of Agricultural and Forestry Sciences from March 2015 to July 2016.

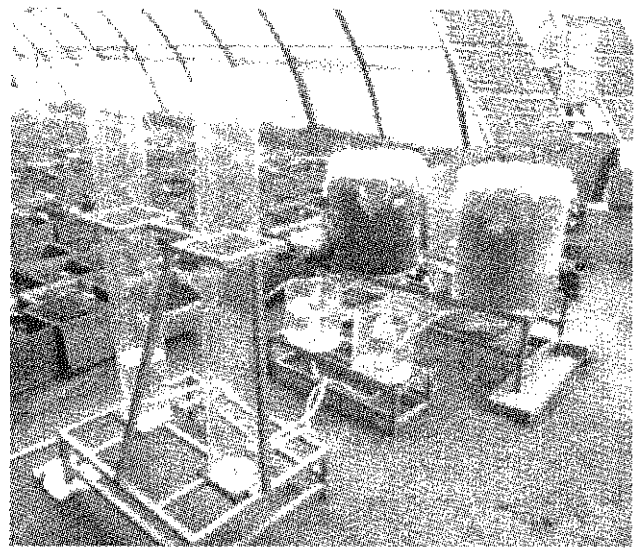

Figure 1 Actual scene of negative pressure underground irrigation

Firstly, setting soil. Soil was sieved and mixed with fertilizer. The mixed soil was filled into the soil box about 20 cm. Secondly, setting up negative pressure underground irrigation system, pour water into the reservoir, open all water valves and start to irrigate. After three days, the soil moisture was distributed evenly in soil box. Finally, transplanting tomato seedlings. The seedlings with good growth, 5 branches and height of about 8-10 cm were selected to be transplanted.

2.3 Potted tomato root parameters measurement

In order to master and model potted tomato root growth under negative pressure underground irrigation, the tomato root spatial coordinates and growth parameters in soil box were measured in different growth stages.

Potted tomato root spatial coordinates measurement. In our experiment, potted tomato root spatial coordinates (X, Y, Z) and orientation coordinate (pitch angle, deflection angle and roll angle) were measured by spatial positioning and tracking system (FASTRAK 3D tracker) .

The measurement process was as the followings. First of all, potted tomato root reference point was calibrated to ensure the smallest measured data error. Then, the coordinate of reference point was measured. After that the three-dimensional coordinate of each lateral root was measured as the followings. In this paper, 5 parameters of tomato root (length, diameter, surface area, volume and number of root tip) were measured by root analysis system (WinRHIZO). The roots to be measured were carefully washed firstly and scanned by the scanner (EPSON V700 Photo) which scanner resolution was set

as 300 dpi, gray level as 24 bit. The root picture was stored as PNG and then processed by WinRHIZO to get the root growth parameters.

Table 1 Tomato roots growth parameters at different growth stages

Days, d	Total root surface area, cm^2	Total root projection area, cm^2	Total root volume, cm^3	Total root length, cm
14	35.9131	11.4315	0.4645	224.4798
25	95.6963	30.4611	1.053	692.2832
37	166.7827	53.0886	2.136	1289.5993
58	1132.2811	360.4164	13.057	7915.6035
79	1380.0634	439.2877	23.157	6608.3731

3 Three-dimensional growth modelling of potted tomato root

In order to build a real and effective root growth model, three-dimensional coordinate of the tomato root was projected in two-dimensional plane separately and selected the appropriate two-dimensional plane. The three-dimensional model of tomato root was built by curve fitting algorithm.

3.1 Potted tomato root growth data analysis

According to the experimental data, potted tomato root growth data traits were analyzed. The growth rate of tomato roots is different at different growth stages, the seedling stage and late fruiting stage is slow, and early blossom stage is the fastest. The roots become thickly at late fruiting stage. The tomato roots gather mainly under 10 cm soil surface and grow slowly in horizontal at the seedling.

Table 2 Growth rate of total root length at different growth stages

Growth stages	Growth rate of total root length, cm/day
Seedling stage	37.5-48.6
Early blossom	285.5-338.6
Late blossom	23.1-36.7

3.2 Project plane selected

In order to select the best project plane to describe potted tomato root growth, the experimental data were projected at three lanes (XOY, XOZ and YOZ) respectively and compared mutually. The results were shown in Figure 2.

From Figure 2 we can find that the root growth information at vertical is missed in the projection at XOY plane, while the root growth information is repeated in the projection at YOZ plane. The projection of tomato root at XOZ plane reflects the actual tomato root growth.

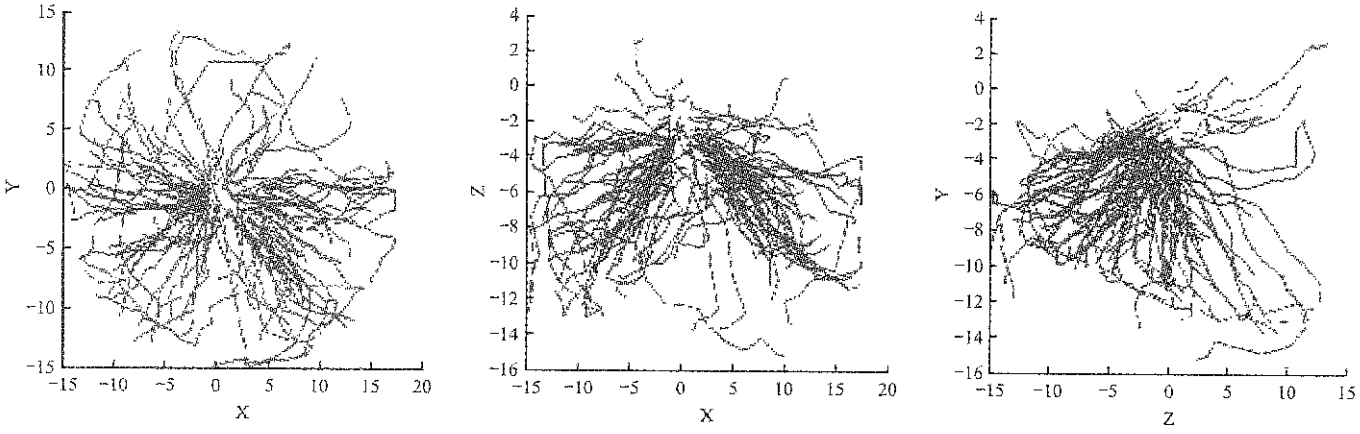

a. XOY b. XOZ c. YOZ

Figure 2 Projection of tomato root at different planes

3.3 Root growth data set generated

The polynomial curve fitting equation can be used to fit most of the root curves well. It is impossible to describe all the root growth curves with the same fitting function because the root spatial distribution so random.

Observed the experimental data, 3, 4 or 5 power polynomials were used to fit almost the root. A dynamic fitting model was proposed to fit the root growth curve with high precision fitting in this paper. For each root, 3, 4 and 5 power polynomials were used to fit it respectively, and the best curve was selected to the fitting polynomials according to the fitness degree (R-square).

According to the selected three-dimensional curve fitting equation, X coordinates of the simulated root key point were calculated. The whole X coordinates were got

by the interpolation algorithm. Y and Z coordinates data were calculated finally. 3D root growth data set were produced. The simulation root at the mainly stages of tomato growth were shown in Figure 3.

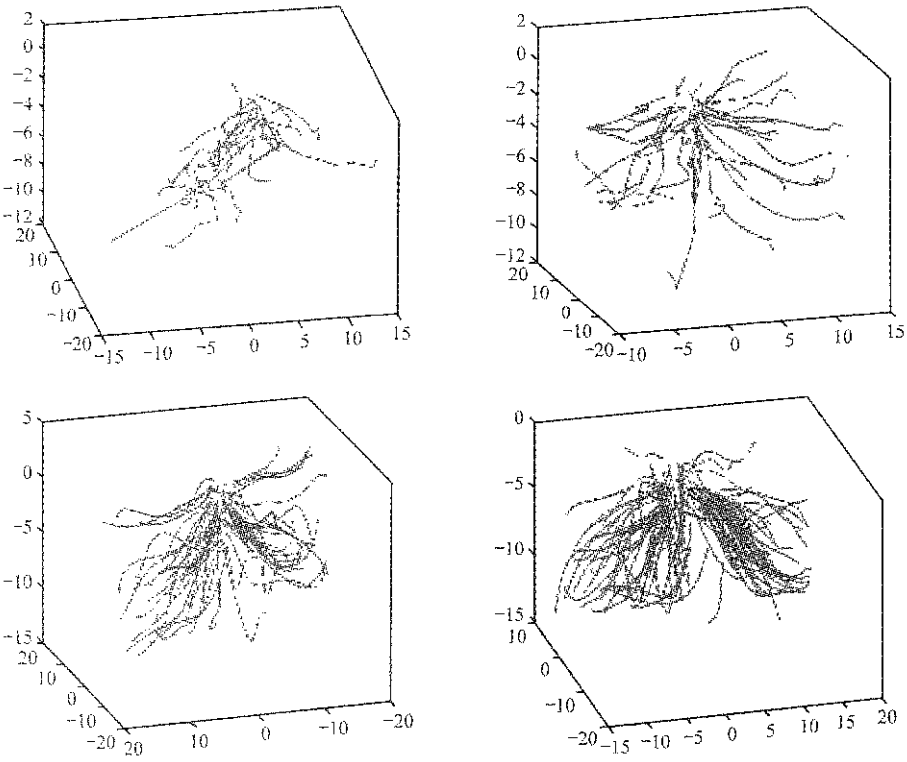

Figure 3 Simulation tomato root at different growth stages

3.4 Growth modelling based on L-system

The growth process of potted tomato root can be mainly described by the change of lengths and directions of main roots, both top lateral root and secondary lateral root in different growth stages. In this paper, an improved differential L-system was used to simulate the root growth process of potted tomato under negative pressure underground irrigation. Three-dimensional growth model of tomato root based on differential L-system was as the following.

V: {Mainroot, FirLa, SecLa}

W: {Mainroot (0), FirLa (0), SecLa (0)}

P: {P1, P2, P3, P4, P5}

P1: Mainroot (l, x, y, z, α, β, γ): <t>

$$\text{Mainroot}\left(1+\frac{dm}{dt}, x', y', z', \alpha', \beta', \gamma'\right)$$

$$\left[\text{nf} * \frac{dm}{dt} * \text{FirLa (0)}\right]$$

P2: FirLa (l, x, y, z, α, β, γ): <t, p_i> FirLa

$$\left(1+\frac{df}{dt}, x', y', z', \alpha', \beta', \gamma'\right)\left[\text{ns} * \frac{df}{dt} * \text{SecLa (0)}\right]$$

P3: FirLa (l, x, y, z, α, β, γ): <t, p_i>

$$\text{SecLa}\left(1+\frac{ds}{dt}, x', y', z', \alpha', \beta', \gamma'\right)$$

P4: FirLa (l, x, y, z, α, β, γ): <X, Y, Z>

$$\text{FirLa}\left(l, z, y, z, \alpha', \beta', \gamma'\right)$$

P5: SecLa (l, x, y, z, α, β, γ): <X, Y, Z>

$$\text{SecLa}\left(l, z, y, z, \alpha', \beta', \gamma'\right)$$

where, V is the root model set which includes main root model (Mainroot), the first lateral root (FirLa) and the second lateral root (SecLa); W is the initial model state set; P1, P2, P3 are the growth rules of taproot, first lateral root and secondary lateral root respectively; P4, P5 are the first and secondary lateral boundary conditions respectively.

The tomato root growth process can be simulated and the simulation root coordinate be generated by the three-dimensional growth simulation system.

4 Results and discussion

Potted tomato root growth simulation parameters at different growth stages (seedling, early blossom, late blossom and fruiting) were calculated by the proposed model and compared with the actual measured data to

verify the effectiveness of the proposed model.

As shown in Table 3, with tomato root growth, the simulation error increases gradually. That is the minimum error occurred at the seedling and early blossom, and the maximum error at late blossom and fruiting. The reason for this is that root development is faster and root variability is greater in these two stages. The minimum simulation error is total root projection area and the maximum simulation error is total root length.

Table 3 Simulation error of tomato roots growth parameters at different growth stages, %

Growth stage	Total root surface area	Total root projection area	Total root volume	Total root length
Seedling	7.32	3.41	5.98	10.43
Early blossom	8.45	4.23	7.32	12.54
Late blossom	9.14	5.44	9.84	13.32
Fruiting	9.8	5.58	10.12	15.12

5 Conclusions

According to the simulation result, potted tomato root growth traits would be concluded as the following:

Potted tomato root growth rate is different at different stages. The fastest is at the blossom and fruiting, and the slowest is at the seedling stage. At the same time, tomato root has higher growth rate in vertical direction during the whole growth process.

In different growth stages, the emphasis of root growth is different. The number of roots increases greatly at the early blossom and the volume of roots increases greatly at the fruiting stage.

The root growth at seedling stage can be simulated effectively by the proposed model.

Acknowledgments

This work was supported by National Key Research and Development Program of China (2017YFD0201500-2017YFD0201501) and National Natural Science Foundation of China Program (31101609 and 31471409).

[References]

[1] Ahmadi, S. H., A. R. Sepaskhah, M. N. Andersen, F. Plauborg, C. R. Jensen, and S. Hansene. 2014. Modeling root length density of field grown potatoes under different irrigation strategies and soil textures using artificial neural networks. *Field Crops Research,* 162(6): 99–107.

[2] Deb, S., A. Morandi, K. Pedersen, S. Riemer-Sorensen, D. M. Goldberg, and H. Dahle. 2011. Simulating the interaction between plant roots, soil water and nutrient flows, and barriers and objects in soil using ROOTMAP. *International Congress on Modelling and Simulation*, 8(1): 975–981.

[3] Dunbabin, V. M., J. A. Postma, A. Schnepf, L. Pagès, and M. Javaux. 2013. Modelling root–soil inter-actions using three–dimensional models of root growth, architecture and function. *Plant & Soil*, 372(1-2): 93–124.

[4] Ji, R., T. Wang, L. Qi, and Z. Yang. 2015. Numerical simulation of soil moisture infiltration under negative pressure irrigation based on HYDRUS-2D. *Transactions of the Chinese Society for Agricultural Machinery*, 46(4): 113–119. (In Chinese with English abstract)

[5] Ji, R., X. Li, L. Qi, and J. Wang. 2014. Three-dimensional growth modelling and realization for potted tomato root system. *Journal of Drainage & Irrigation Machinery Engineering*, 32(9): 795–801.

[6] Leitner, D., S. Klepsch, A. Knieb, and A. Schnepf. 2010. The algorithmic beauty of plant roots an L-System model for dynamic root growth simulation. *Mathematical & Computer Modelling of Dynamical Systems*, 16(6): 575–587.

[7] Li, X., J. Simunek, and H. Shi. 2017. Spatial distribution of soil water, soil temperature, and plant roots in a drip irrigated inter cropping field with plastic mulch. *European Journal of Agronomy,* 83: 47–56.

[8] Liu, K. N., Q. L. Yang, H. Guo, Z. Y. Ge, B. Zhou, and X. G. Liu. 2013. Modeling and visualization of three-dimensional young apple tree root growth under different modes of drip irrigation. *Chinese Journal of Eco- Agriculture*, 21(6): 744–751.

[9] Liu, Z., J. Wang, Y. Xu, and P. Li. 2014. Root growth model of lettuce under different cultivation substrates and irrigation modes. *Transactions of the Chinese Society for Agricultural Machinery*, 45(4): 284–288. (In Chinese with English abstract)

[10] Lynch, J. P., K. L. Nielsen, R. D. Davis, and A. G. Jablokow. 1997. SimRoot: modelling and visualization of root systems. *Plant & Soil*, 188(1): 139–151.

[11] Pagès, L., G. Vercambre, J. L. Drouet, F. Lecompte, C. Collet, and J. Le Bot. 2004. RootTyp: a generic model to depict and analyze the root system architecture. *Plant & Soil*, 258(1/2): 103–119.

[12] Rattanapichai, W., and K. Klem. 2016. Two-dimensional root pheno typing system based on root growth on black filter paper and re-circulation micro-irrigation. *Czech Journal of Genetics & Plant Breeding,* 52(2): 64–70.

[13] Schröder, N., M. Javaux, J. Vanderborght, B. Steffen, and H. Vereecken. 2012. Effect of root water and solute uptake on apparent soil dispersivity: A simulation study. *Vadose Zone Journal,* 11(3): 811–822.

[14] Seidel, S. J., S. Werisch, K. Barfus, M. Wagner, N. Schütze, and H. Laber. 2016. Field evaluation of irrigation scheduling strategies using a mechanistic crop growth model. *Irrigation & Drainage*, 65(2): 214–223.

[15] Sokalska, D. I., D. Z. Haman, A. Szewczuk, J. Sobota, and D. Deren. 2009. Spatial root distribution of mature apple trees under drip irrigation system. *Agricultural Water Management*, 96(6): 917–924.

[16] Wu, L., and A. Shepherd. 2011. Special features of the SPACSYS modeling package and procedures for parameterization and validation. *ASA, CSSA & SSSA, Madison*, 117–154.

[17] Zhang, W., L. H. Li, and X. Li. 2016. Effects of drip irrigation amount on root spatial and temporal distribution, water use efficiency and yield in spring wheat. *Acta Agricultural Boreali-occidentalis Sinica*.

Multi-scale combined prediction model of dissolved oxygen based on EEMD and ELM

Peng Fang[1,2,3], Li Zhenbo[1,2,3*]

(1. *College of Information and Electrical Engineering, China Agricultural University, Beijing 100083, China;*
2. *Key Laboratory of Agricultural Information Acquisition Technology, Ministry of Agriculture, Beijing 100083, China;*
3. *Beijing Engineering and Technology Research Center for Internet of Things in Agriculture, Beijing 100083, China*)

Abstract: Intensive aquaculture has extensive management problem, which increases the risk of water pollution and the outbreak of aquatic disasters. Accurate prediction of water quality can warn in advance, effectively reduce the risk of disaster, and achieve precise control of a variety of breeding equipment, and thus achieve energy conservation and promote the sustainable development of aquaculture. But aquaculture water environment is complex, changing, and non-linear, so it is difficult to realize the accurate prediction of water quality. In this paper, the EEMD-ELM combination forecasting model was proposed to predict dissolved oxygen in the aquaculture water, and the predicted mean square error of the combined model EEMD-ELM is 66% lower than that of single ELM model, 29.2% lower than that of EEMD-BPNN model. The EEMD method was combined with ELM to extract the multi-scale information of time series of water quality data, and the effect of model prediction has been improved.

Keywords: dissolved oxygen, prediction of water quality, EEMD-ELM combination forecasting model

Citation: Peng, F., and Z. B. Li. 2017. Multi-scale combined prediction model of dissolved oxygen based on EEMD and ELM. International Agricultural Engineering Journal, 26(4): 283–292.

1 Introduction

With the further development of China's economy, intensive aquaculture in recent years has gradually become one of the main aquaculture. However, due to the traditional culture model and the blind pursuit of high output, breeders increase the fry blindly, so the breeding density has exceeded the water environment carrying capacity. Feeding bait unscientifically also bring serious pollution problems, ecological balance is broken, which greatly deteriorated water environment, and undoubtedly increase the risk of aquaculture.

Aquaculture water quality is the key factor affecting the production of aquaculture, water quality parameters such as pH, dissolved oxygen, and water temperature will affect the growth and metabolism of aquatic organisms (Xu et al., 2016; Yang et al., 2015). Excessive content of ammonia nitrogen will lead to water quality eutrophication, and will also have a certain degree of toxicity on the aquatic organisms (Song, 2015). It can be said that water quality monitoring and management untimely will trigger the deterioration of water quality, and even lead to disease outbreaks, affecting the normal production (Ma et al., 2013). According to the statistics, China's annual losses directly caused by aquatic disease were up to more than 2 billion dollars. One of the water quality parameters DO (Dissolved Oxygen) is an important indicator of water quality, so figuring out the law of change of the water quality parameters ahead of warning will play a positive role in controlling water quality deterioration, ensuring the sustainable development of aquaculture industry.

US engineers Streeter and Phelps proposed S-P water quality model in 1925 which laid a milestone basis for water quality prediction, and was also called BOD-DO balanced coupling model (Song, 2015). And BOD refers to biological oxygen demand. At the beginning of the

Received date: 2017-09-20 **Accepted date:** 2017-11-22
* **Corresponding author: Li Zhenbo,** Ph.D., Associate Professor of College of Information and Electrical Engineering, China Agricultural University, Beijing 100083, China. Email: zhenboli@126.com. Tel: 18701586839.

study, scholars have tried some simple time series prediction methods, such as exponential smoothing, Markov chain, time series model etc. Traditional methods have some shortcomings, such as the prediction accuracy is not very high, and have poor generalization ability etc. With the development of artificial intelligence technology, Zhang and Gao (2015) used GM (Gray Model) and FNN (Fuzzy Neural Network) for water quality prediction. And Geoffrey Hinton et al. (2006) presented the concept of deep learning in the *Science* in 2006, which attracted wide attention and was given the meaning of crossing time.

The water quality prediction model based on intelligent algorithms such as artificial intelligence and depth learning is becoming a hotspot in the field of water quality prediction. Such as Ma et al. (2014) used Back Propagation Neural Networks as a modeling tool to predict water quality parameters in an intensive shrimp tank. Faruk (2010) proposed a hybrid model based on ANN (Artificial Neural Network) and ARIMA (Autoregressive Integral Moving Average Model) to predict water quality time series data. The results showed that the hybrid model is more predictive than either the simple ARIMA model or the ANN. Sarkar and Pandey (2015) proposed a feed-forward error back propagation neural network to estimate the DO concentrations at the downstream of Mathura city, India, and the experimental results demonstrated its effectiveness. Huang et al. (2015) improved the PSO (Particle Swarm Optimization) for the combined forecasting model, and proved that better prediction results than single model obtained after respectively combining with the SVM (Support Vector Machine), BPNN (Back Propagation Neural Networks) and ARIMA model. Xu et al. (2016) combined EEMD (Ensemble Empirical Mode Decomposition) and the improved ABC (Artificial Bee Colony) to predict the pH value of the intensive culture of *vannamei*, and the prediction accuracy is improved effective.

Since aquaculture water environment is an open and dynamic nonlinear complex system, and the water quality data sequence shows a high degree of nonlinearity and volatility, so direct application of artificial neural network for water quality prediction can't often capture the multi-scale water quality characteristics and local fluctuations. The empirical mode decomposition method can decompose complex signals into a series of IMFs (Intrinsic Modulus Functions) by the filtering process (Chen et al., 2012; Chan et al., 2014). Each IMF component only represents an oscillating pattern embedded in the signal, which is completely different from the other signals on the same scale or frequency band, and it can also reveal patterns and trends hidden in the time series. Therefore, a new prediction model based on EEMD and ELM (Extreme Learning Machine) was proposed in this paper to predict the dissolved oxygen of intensive shrimp culture ponds. And it was compared with the EEMD-BPNN combined model and the standard ELM model in the experimental part.

2 Materials and method

2.1 EEMD (Ensemble empirical mode decomposition)

EEMD (Ensemble Empirical Mode Decomposition) was proposed by Wu and Huang (2005) to solve the problem of modal aliasing in the EMD (Huang, 2001) method (Empirical Mode Decomposition). EEMD is a new adaptive signal time-frequency method. It is difficult to deal with non-stationary and stochastic signals by traditional linear spectrum analysis based on Fourier transform, but EEMD is a stationary method for non-stationary data, so it can be used for various nonlinear and non-stationary problems. Compared with the other decomposition methods, EEMD is intuitive, posterior and adaptive, which decomposes the signal according to the time scale feature of the data itself, can effectively capture the multi-scale water quality characteristics. After decomposition, each IMF component contains the local characteristic signals of the original signal at different time scales, representing an oscillating pattern embedded in the original signal, which is completely different from the other signals on the same frequency band, and it can also reveal the implied trend in the time data sequence.

According to this theory (Huang, 2001), the IMF is a function that represents the hidden oscillation mode embedded in the data sequence, and it must satisfy the following two conditions: (1) the kernel is a function of

the hidden mode, the number of extremes and the number of zero crossings must be equal, or differ at most by one, which is roughly equivalent to finding a "narrow-band" signal or eliminating "riding waves"; and (2) at any point in time, the mean of its upper and lower envelopes equals zero, which ensures that the instantaneous frequency will not have unwanted fluctuations arising from asymmetric wave forms. And the decomposition process of IMFs is as follows:

(1) Find all local maximum and minimum values of the time series data $x(t)$.

(2) Connect all local extrema through a cubic spline to generate the upper envelope $x_{up}(t)$ and the lower envelope $x_{low}(t)$ of the $x(t)$.

(3) The first mean sequence $m_1(t)$ is calculated by using the upper envelope $x_{up}(t)$ and the lower envelope $x_{low}(t)$, i.e.,

$$m_1(t) = [x_{up}(t) + x_{low}(t)] / 2 \tag{1}$$

(4) Calculate the difference between the original time series $x(t)$ and the mean time series to obtain the first IMF $h_1(t)$, i.e.,

$$h_1(t) = x(t) - m_1(t) \tag{2}$$

Check whether $h_1(t)$ meets the two conditions of the IMF feature. If not, repeat steps 1 to 3 until the first IMF is found.

(5) EMD method by applying the above screening process to the residual components to extract the next IMF,

$$r_1(t) = x(t) = c_1(t) \tag{3}$$

where, $c_1(t)$ represents the first IMF.

The decomposition process is repeated until the last residual component $r_n(t)$ has at most one local extremum or becomes a monotonic function, from which no more IMFs can be extracted, then the decomposition program can be halted at that point.

(6) The original time series $x(t)$ can be reconstructed by summing all the IMF components and a residual component as follows (Huang, 2001):

$$x(t) = \sum_{i=1}^{n} c_i(t) + r_n(t) \tag{4}$$

where, n is the number of IMFs; $c_i(t)$ (i = 1,2,...,n) are the values of each IMF that are almost orthogonal to each other, they are different in each frequency band, and change with the variation of the time series signal $x(t)$. The $r_n(t)$ is the final residual component, which represents the central tendency of the time series signal $x(t)$. Thus, each signal can decompose the data series into n-empirical mode functions and one residual component.

However, following the above-mentioned steps only is prone to aliasing, that is, the case where the IMF component and the time scale intersect each other, which means an IMF component contains multiple time scales or a time scale distributed in several IMF components, then the two adjacent IMF waveforms are mixed with each other, and it is difficult to identify. EEMD improves EMD by adding a number of white noise to the original signal to generate a new signal and then decomposing. EEMD takes advantage of the characteristic of uniform distribution of white noise spectrum, when the signal is loaded into the uniform distribution frequency space on the white noise background, the signal at different time scales will automatically match to the appropriate reference scale. Then perform EMD steps for every mixed separately, and finally calculate the average of IMF components and residue to find the approximation of the real mode.

The specific decomposition steps are as follows:

(1) Add white noise $k \cdot \sigma_x \cdot n(t)$ to the original signal, where $n(t)$ is the normalized white noise, σ_x is the standard deviation of the signal, k is the ratio of the standard deviation of the white noise to the original signal. The signal-to-noise mixture $X(t)$ is expressed as follows:

$$X(t) = x(t) + k \cdot \sigma_x \cdot n(t) \tag{5}$$

(2) EMD processing for the signal-to-noise mixture, and $X(t)$ is decomposed into m IMF components and one residue, as shown in Equation (6).

$$X(t) = \sum_{j=1}^{m} c_j + r_m \tag{6}$$

(3) Repeat steps 1 and 2, each time adding a different white noise, as shown in Equation (7).

$$X_i(t) = x(t) + k_i \cdot \sigma_x \cdot n_i(t) \tag{7}$$

EMD processing for $X_i(t)$, which is decomposed into m IMF components and one residue, as shown in Equation (8).

$$X_i(t) = \sum_{j=1}^{m} c_{i,j} + r_{i,m} \tag{8}$$

(4) Repeat N times, calculate the average of IMF components and the residue respectively, as shown in Equations (9) and (10).

$$\overline{c}_j = \frac{1}{N}\sum_{i=1}^{m} c_{i,j} \tag{9}$$

$$\overline{r}_m = \frac{1}{N}\sum_{i=1}^{m} r_{i,m} \tag{10}$$

The final decomposition result is

$$X(t) = \sum_{j=1}^{m} \overline{c}_i + \overline{r}_m \tag{11}$$

Since the white noise has zero mean characteristics, the noise is eliminated to the greatest extent after the average is calculated by multiple decomposition, and the average result can be regarded as the real signal. Throughout the process, the two most critical parameters are the amplitude of the auxiliary white noise and the average number of sets, they will have a great impact on the signal decomposition results.

When amplitude is too low, the phenomenon of modal aliasing can't be eliminated, but when the amplitude is too high, the number of sets will increase, and cause high frequency part difficult to be broken down, white noise residue too large and other issues. Therefore, as mentioned by Wu and Huang (2005), the standard deviation of the amplitude of white noise can be set to 0.2 times of the standard deviation of the original signal. If the original signal is dominated by high frequencies, you need to properly reduce the white noise amplitude, but if it is dominated by low frequencies, increase the amplitude appropriately.

On the other hand, the average number of sets matches the statistical law described in Equation (12).

$$\varepsilon_n = \frac{\alpha}{\sqrt{N}} \quad \text{or} \quad \ln \varepsilon_n + \frac{\alpha}{2}\ln N = 0 \tag{12}$$

where, N is the average number of sets; α is the ratio coefficient of the amplitude standard deviation of white noise; ε_n is the relative error.

Wu and Huang (2005) illuminated that the average number of sets is generally selected as 100 to 300 times, synthetically considering the decomposition effect and calculation cost. In this way, not only the interference error caused by the white noise is low, but also the decomposition effect will not have much impact. In this paper, the standard deviation of white noise amplitude is selected as 0.2, the average number of sets is selected as 150 times. At present, there are some researches on the improvement of these two key parameters, such as Jia and Jiang (2010) put forward white noise amplitude addition criteria from the white noise internal principle; Chen et al. (2011) proposed an adaptive EEMD method, which could automatically obtain the parameters of different signals, and it has adapted to the ECG signal de-noising and heart rate feature extraction successfully.

Figure 1 shows the EMD decomposition flow chart.

Figure 2 shows the EEMD decomposition flow chart.

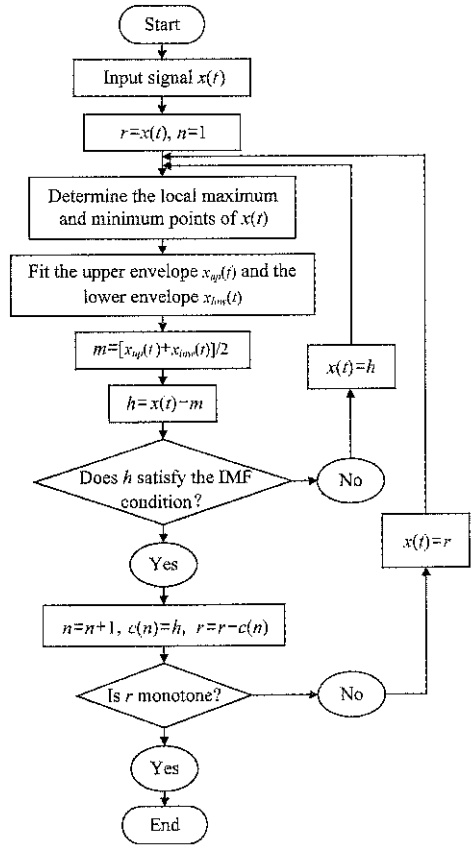

Figure 1 Decomposition flow chart of EMD

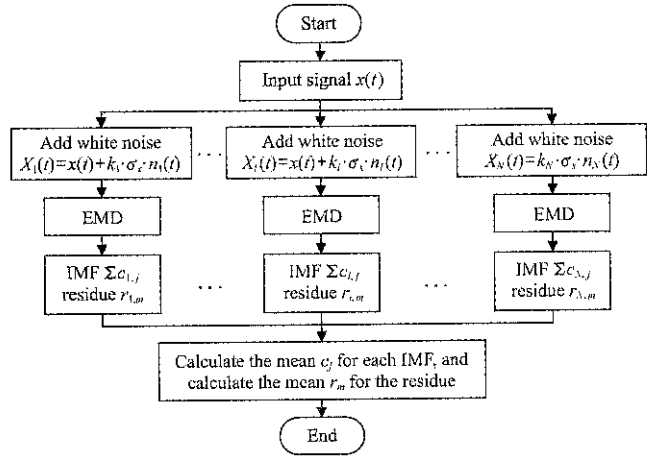

Figure 2 Decomposition flow chart of EEMD

The next prediction model can be established after the EEMD processing.

2.2 ELM (Extreme learning machine)

ELM (Extreme Learning Machine) is a kind of single hidden layer feed-forward neural network algorithm proposed by Huang et al. (2006). Unlike the traditional neural network, ELM does not need to set a large number of training parameters, but randomly generates the threshold of neurons and the weight between neurons, and without the need to adjust them in the training process, you can get a unique optimal solution. The algorithm has the advantages of great adaptability, strong generalization ability and fast operation speed.

Assuming that the number of neurons in the input layer, hidden layer and output layer of the network are respectively m, M and n. $g(x)$ is the activation function of the hidden neuron node, b_i is the threshold. If there are N samples (x_i, t_i) $(1 \le i \le N)$, where x_i represents the data set of the m variables of the input layer, i.e., the matrix $[x_{i1}, x_{i2}, \ldots, x_{im}]^{\mathrm{T}} \in R^m$; t_i represents the data set of the n variables of output layer, i.e., the matrix $[t_{i1}, t_{i2}, \ldots, t_{in}]^{\mathrm{T}} \in R^n$. And the topology of the ELM is shown in Figure 3.

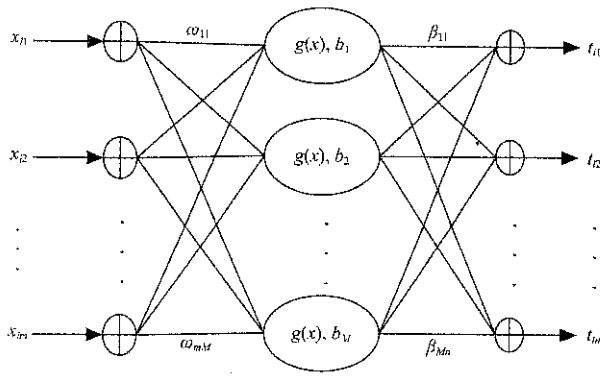

Figure 3 Topology of ELM

ELM algorithm steps are as follows:

(1) Determine the number of neuron nodes in the hidden layer, i.e., M, randomly generates the connection weights between the input layer and the hidden layer, i.e., $w_i=[w_{1i}, w_{2i}, \ldots, w_{mi}]^{\mathrm{T}}$, $(i=1, 2, \ldots, M)$, and the threshold of the neurons of the hidden layer, i.e., $b=[b_1, b_2, \ldots, b_M]^{\mathrm{T}}$.

(2) Determine the activation function of the neurons of the hidden layer, i.e. $g(x)$, which requires infinitely differentiable, and then calculate the output matrix of the hidden layer, i.e., H.

First, the equation is as follows:

$$\sum_{i=1}^{M} \beta_i \cdot g(w_i \cdot x_i + b_i) = o_j, \quad j = 1,2,\ldots,N \tag{13}$$

In Equation (13), o_j represents the output value of the jth node of the current layer, $o_j = [o_{j1}, o_{j2}, \ldots, o_{jn}]^{\mathrm{T}}$. And the cost function E of the ELM is expressed as follows:

$$E(S,\beta) = \sum_{j=1}^{M} \| o_j - t_j \| \tag{14}$$

In Equation (14), S contains the connection weight w_i and the threshold of the neurons of the hidden layer b_i, $S=(w_i, b_i, i=1, 2, \ldots, M)$. And β represents the output weight matrix. According to the literature, the learning goal of ELM is to find the optimal S and β, which can minimize the difference between the output value of the network and the actual value (Huang et al., 2006). And $\min(E(S, \beta))$ is expressed as follows:

$$\begin{aligned} &\min E(S,\beta) = \\ &\min \| H(\omega_1,\ldots,\omega_M,b_1,\ldots,b_M,x_1,\ldots,x_N)\cdot\beta - T \| \end{aligned} \tag{15}$$

In Equation (15), H is the output matrix of the hidden layer, T is the target value matrix, and β is the output weight matrix. H, β, T are separately defined as Equations (16), (17), and (18).

$$\begin{aligned} &H(\omega_1,\ldots,\omega_M,b_1,\ldots,b_M,x_1,\ldots,x_N) \\ &= \begin{bmatrix} g(w_1x_1+b_1) & \cdots & g(w_Mx_1+b_M) \\ \vdots & \ddots & \vdots \\ g(w_1x_N+b_1) & \cdots & g(w_Mx_N+b_M) \end{bmatrix} \end{aligned} \tag{16}$$

$$\beta = \begin{bmatrix} \beta_1^T \\ \vdots \\ \beta_M^T \end{bmatrix}_{M\times n} \tag{17}$$

$$T = \begin{bmatrix} t_1^T \\ \vdots \\ t_N^T \end{bmatrix}_{N\times n} \tag{18}$$

ELM can be simplified as a nonlinear optimization problem. In the case of a given output sample, Equation (15) is the objective function. After w_i and b_i are randomly assigned, the matrix H is calculated as a constant matrix. The training process of ELM network can be equivalent to solving the least squares solution $\hat{\beta}$ of the linear system $H\beta=T$, which is also the only optimal solution.

(3) Solve the least squares solution $\hat{\beta}$ of the weight of output layer as follows:

$$\hat{\beta} = H^{\dagger}T \tag{19}$$

In Equation (19), $H^{\dagger}$ is the MP generalized inverse of the matrix H, and when $\hat{\beta}$ is completed, the training process of the network is completed, without adjusting the parameters. Huang et al. (2006) proved that the ELM algorithm could approximate almost any continuous system, and randomly select the network parameters. Not only it does not weaken the convergence ability of the algorithm, but also greatly shorten the computing time. These excellent features make ELM widely used in the predictive control problem (Bai, 2014; Iosifidis et al., 2013; He, 2014).

2.3 Combination model EEMD-ELM

The prediction model for dissolved oxygen based on EMD-ELM is shown in Figure 4. The detailed calculation steps are described below:

Step 1: Use the EEMD to decompose the original water quality time series into a finite set of IMF sub-sequences and a residue sub-sequence, which can be identified.

Step 2: Construct the ELM prediction model for each sub-sequence, that is, train the network with the previous data set and then use the trained ELM model to predict the future value of these sub-sequences. And the network contains five impact factors as the input layer and the dissolved oxygen as the output layer.

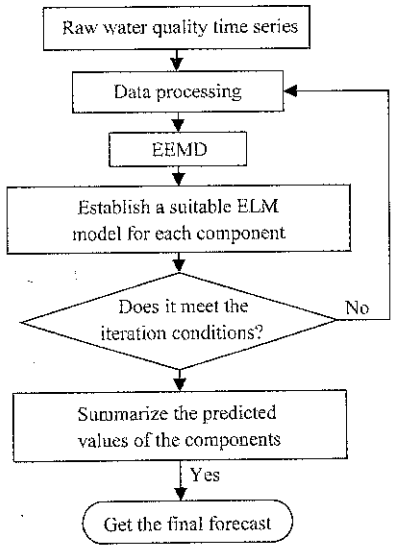

Figure 4 Flow chart of dissolved oxygen prediction model based on EEMD-ELM

Step 3: Summarize the predicted values of the subsequences in step 2 to obtain the final predicted value.

Through the EEMD method, different characteristics of raw water quality data can be displayed on different scales, and multi-scale information can be extracted to capture the local fluctuation of the original water quality data more completely. In addition, each IMF sub-sequence has similar frequency characteristics, simple frequency components and strong regularity. Therefore, this combination model reduces the complexity of ELM modeling and further improves the accuracy of ELM prediction model.

3 Results and discussion

3.1 Experimental data

The data set used in the experiment was measured for 20 consecutive days every ten minutes in a shrimp pond, including five factors: dissolved oxygen, water temperature, oxygen partial pressure, salinity and pH value. It has a total of 2880 sets of data. And the program operating environment is Matlab2014a, based on Windows7 pro 32-bit operating system. The experimental part of this paper was based on the above conditions.

The raw data sequence is shown in Figure 5. The predicted predictor is the dissolved oxygen, i.e., DO.

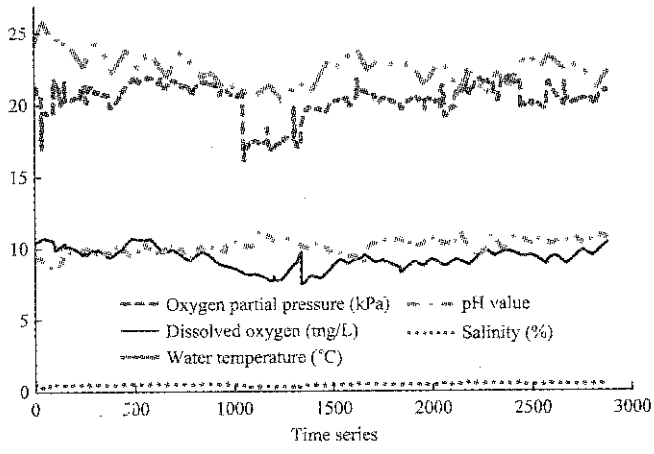

Figure 5 Time series of the influencing factors

The experiment randomly selected a time segment, predicted the amount of dissolved oxygen for a period of future time, the length of time is about 5: 1.

3.2 Analysis of results

The prediction value of EEMD-ELM model was respectively compared with the actual value, the prediction value of EEMD-BPNN model and the single

ELM model. In the EEMD-ELM and ELM algorithm, the number of hidden layer nodes was set to 30. In the EEMD algorithm, the white noise amplitude standard deviation was selected as 0.2, and the average number of sets was 150 times. The number of hidden layers selected in BPNN algorithm was 4, the learning rate was set to 0.1, the momentum factor was set to 0.9, the calculation precision was set to 10^{-6}, the maximum number of iterations was 1000, and the initial weight was set to –0.5-0.5.

The EEMD-ELM algorithm was divided into three steps. Step 1: EEMD. If the 1001th-1750th section of data was selected as the training section, the 1751th-1900th section of the dissolved oxygen would be the prediction section. EEMD was performed on the five factors, such as the EEMD results of the dissolved oxygen and the oxygen partial pressure were shown in Figure 6 and Figure 7, respectively.

Step 2: Predicted the IMF components and the residue of the dissolved oxygen in the 1751th-1900th section respectively, All the forecasting results of the nine components were shown in Figure 8.

Step 3: Summarized the prediction value of each component to get the final prediction result of the 1751th-1900th data section of the dissolved oxygen. And compared the prediction value of EEMD-ELM model with the actual value, the prediction value of EEMD-BPNN model and the single ELM model respectively as shown in Figure 9.

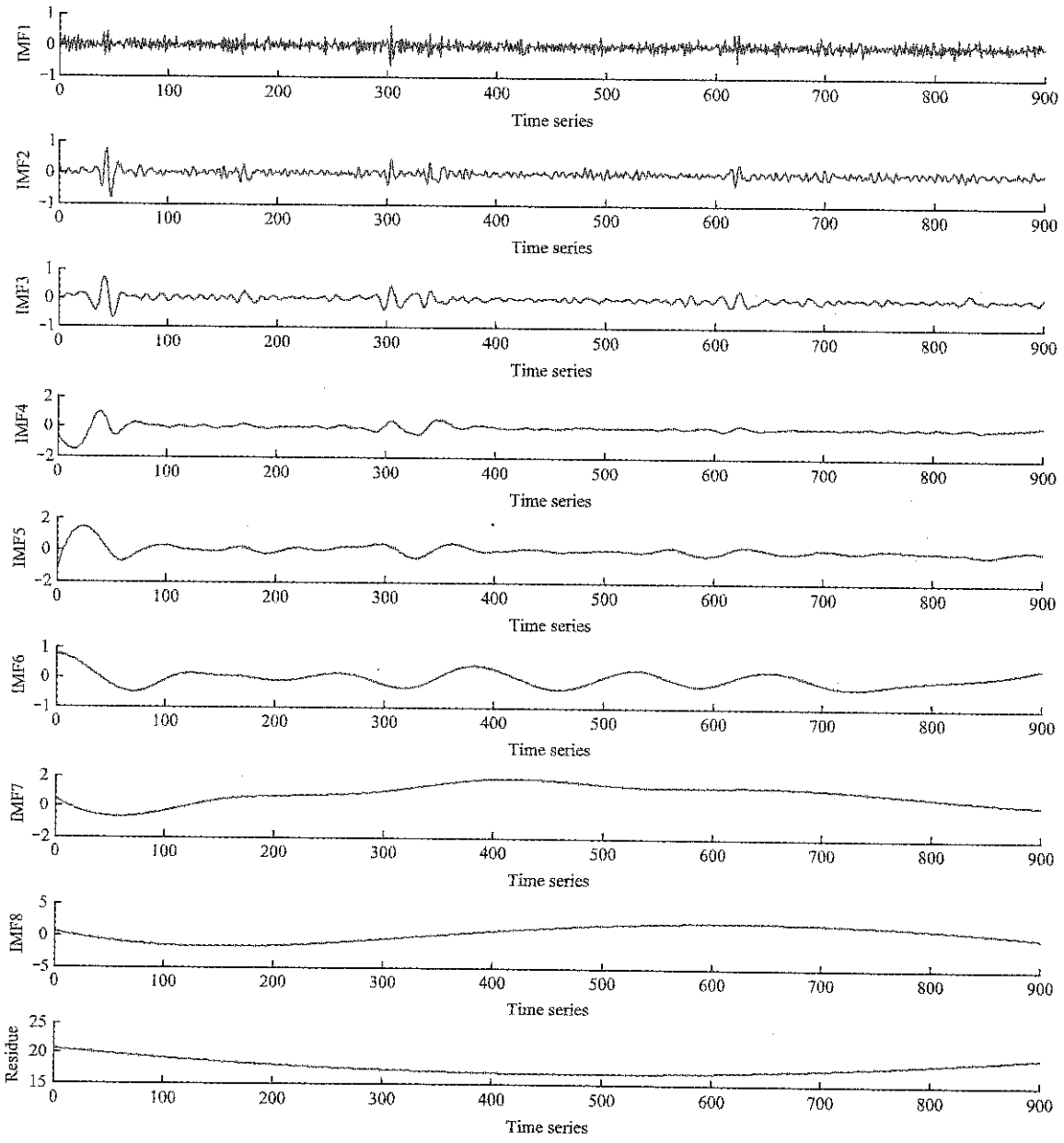

Figure 6 IMF components and the residue of dissolved oxygen decomposed by EEMD

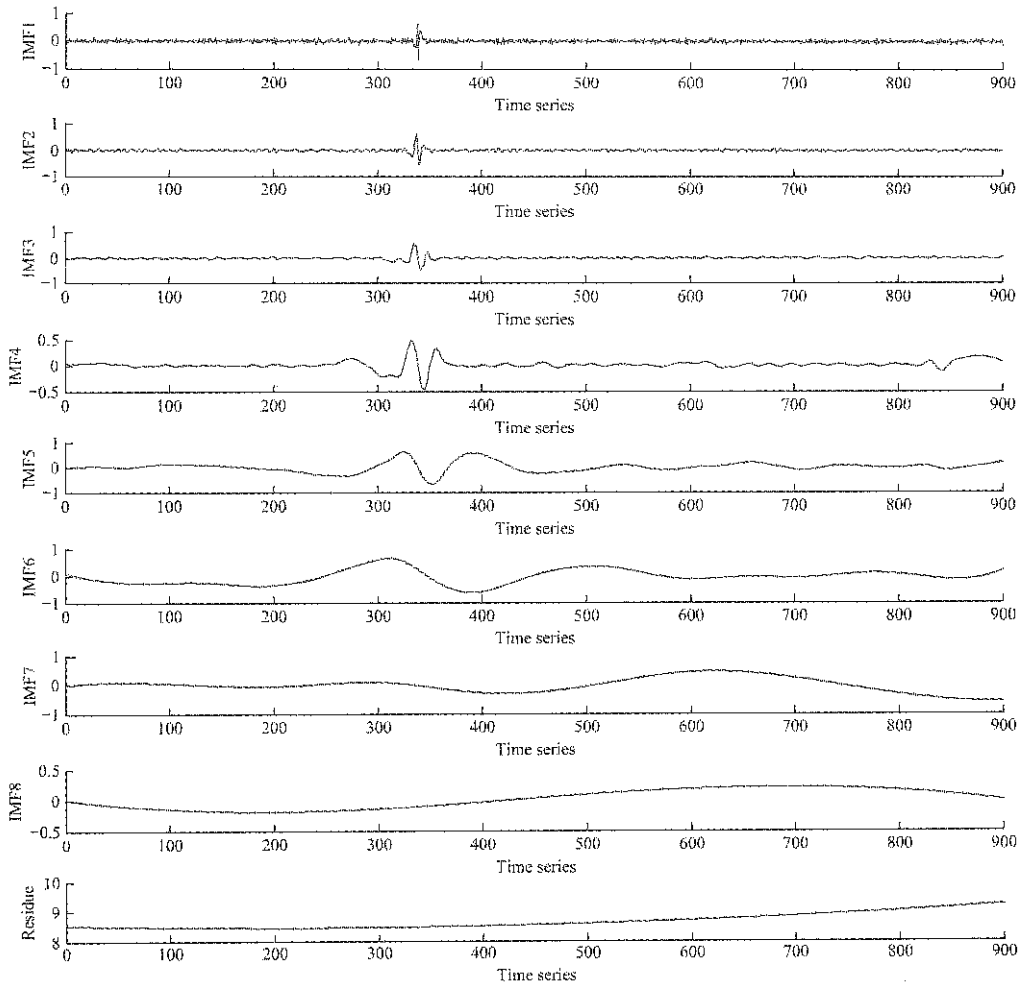

Figure 7 IMF components and the residue of oxygen partial pressure decomposed by EEMD

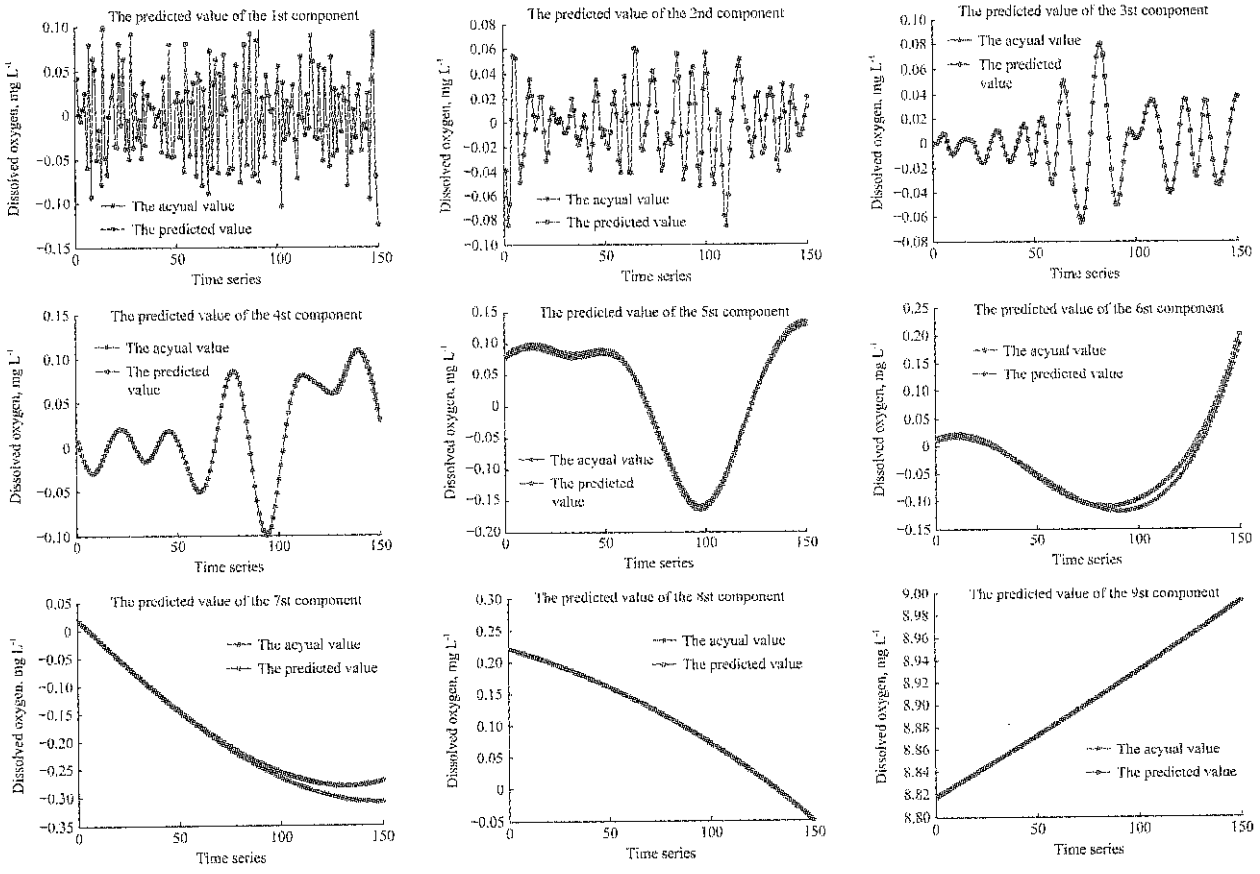

Figure 8 Prediction result of all the components

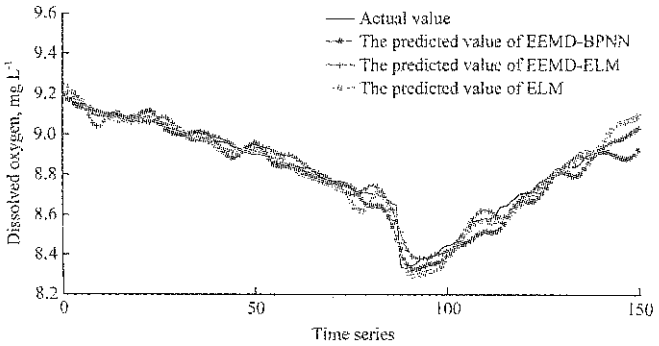

Figure 9 Comparison of predicted results of the three models for dissolved oxygen in the 1751th-1900th period

Repeated the experiments with different time data to test the universality of the algorithm. If the 601th-1350th section of data was selected as the training section, the 1351th-1500th section of the dissolved oxygen would be the prediction section. The result of the EEMD-ELM model, respectively compared with the actual value, the EEMD-BPNN model and the single ELM model was shown in Figure 10.

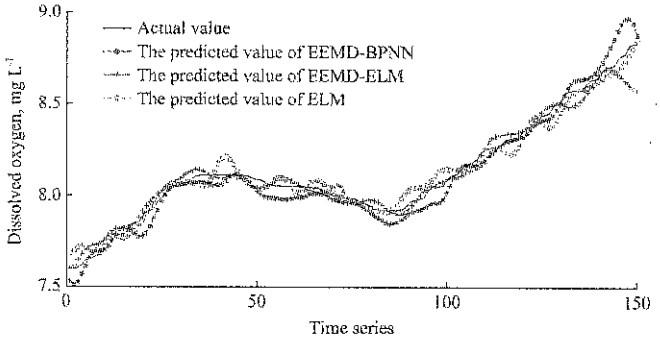

Figure 10 Comparison of predicted results of the three models for dissolved oxygen in the 1351th-1500th period

3.3 Evaluation

Finally, used the mean absolute error, i.e., MAE, mean square error, i.e., MSE, mean absolute percentage error, i.e., MAPE and root mean square error, i.e., RMSE to evaluate the prediction effect of the models.

MAE was defined as follows:

$$\mathrm{MAE}=\frac{1}{n}\sum_{i=1}^{n}|y_i-\hat{y}_i| \tag{20}$$

MSE was defined as follows:

$$\mathrm{MSE}=\frac{1}{n}\sum_{i=1}^{N}(y_i-\hat{y}_i)^2 \tag{21}$$

MAPE was defined as follows:

$$\mathrm{MAPE}(\%)=\frac{100}{n}\sum_{i=1}^{n}\left|\frac{y_i-\hat{y}_i}{y_i}\right| \tag{22}$$

RMSE was defined as follows:

$$\mathrm{RMSE}=\sqrt{\frac{1}{n}\sum_{i=1}^{n}(y_i-\hat{y}_i)^2} \tag{23}$$

where, n was the number of training iterations, y_i and $\hat{y}_i$ were the actual and predicted value, respectively.

In order to reduce the randomness error of the models, we selected the average of errors of 10 experiments to compare as shown in Table 1.

Table 1 Comparison of the average of errors of 10 experiments for the three models

	MAE	MSE	MAPE	RMSE	Run time, s
EEMD-ELM model	0.0311	0.0017	0.0036	0.0402	22.25
EEMD-BPNN model	0.0364	0.0024	0.0042	0.0459	73.65
ELM model	0.0489	0.0050	0.0056	0.0649	17.36

MSE can evaluate the changing degree of data, and the smaller the value of MSE is, the prediction model describes the experimental data with better accuracy. As can be seen from Table 1, the combined model EEMD-ELM is slightly longer than the single ELM model at run time, but the error is much smaller than the single model, such as MSE is reduced by 66%. And in the run-time, the time cost of EEMD-ELM model is much less than that of EEMD-BPNN model, and the MSE is reduced by 29.2%, the MAPE is reduced by 14.3%, so EEMD-ELM is better than EEMD-BPNN in precision performance and error reduction.

4 Conclusions

The problem of aquaculture water quality prediction is the practical problem brought about by the rapid development of intensive aquaculture. If the trend of water quality parameters can be predicted and the deterioration of water quality can be warned in advance, it will provide new decision-making ideas for water quality management and restore economic losses. But the interaction of the influencing factors in the aquaculture water body is complex, changeable and non-linear, so it is difficult to realize the accurate prediction of water quality. The combination model of the new artificial intelligence algorithm and the adaptive time-frequency signal processing method provided a new idea for the research of water quality prediction method, and has become a research hotspot in the field of water quality prediction, and has a wide application prospect.

We chose the key parameter of water quality, i.e.,

dissolved oxygen in the shrimp pond to study. And around the research and implementation of combinatorial model for multi-scale water quality prediction, the main work and conclusions are as follows:

In this paper, EEMD-ELM, EEMD-BPNN and single ELM models were respectively used to predict the same data section, and the experiment was repeated several times by changing data section to verify the universality of the model. The experimental results showed that the EEMD-ELM model is superior to the single ELM model, and EEMD-ELM is superior to EEMD-BPNN in prediction result and time cost. The EEMD method combined with the neural network algorithm could extract the multi-scale information of time series of water quality data, and the prediction effect of the combined model was improved.

Limited by the level of the author, there are some imperfect places in this paper. And in the field of aquaculture water quality prediction, there are still some theoretical and technical problems which haven't yet been resolved:

The combination forecasting model can realize the advantages of multiple forecasting methods, but there is no mature theoretical system to determine how to combine and how to determine the weight, which but also need further research.

Acknowledgements

This research was supported by International Science & Technology Cooperation Program of China (No.2015DFA00530), Key Research and Development Research Project of Shandong Province (No.2016CYJS03A02) and National Nature Science Foundation of China Project (No.61471133).

[References]

[1] Bai, Z. 2014. Sparse extreme learning machine for classification. *IEEE Transactions on Cybernetics*, 44(10): 1858–1870.

[2] Chan, J., H. Ma, T. Saha, and C. Ekanayake. 2014. Self-adaptive partial discharge signal de-noising based on ensemble empirical mode decomposition and automatic morphological thresholding. *IEEE Trans Dielectr Electr Insul*, 21(1): 294–303.

[3] Chen, C. F., M. C. Lai, and C. C. Yeh. 2012. Forecasting tourism demand based on empirical mode decomposition and neural network. *Knowledge-Based Systems*, 26: 281–287.

[4] Chen, L., G. S. Tang, and Y. Y. Zi. 2011. Application of adaptive EEMD method in ECG signal processing. *Signal Acquisition and Processing*, (03): 361–366.

[5] Faruk, D. Ö. 2010. A hybrid neural network and ARIMA model for water quality time series prediction. *Eng Appl Artif Intell*, 23(4): 586–594.

[6] He, Q. 2014. Clustering in extreme learning machine feature space. *Neuro Computing*, 128(5): 88–95.

[7] Huang, G. B., Q. Y. Zhu, and C. K. Su. 2006. The theory of extreme learning machine. *Neuro Computing*, 70–489.

[8] Huang, N. E. 2001. Review of empirical mode decomposition. *Proc SPIE*, 4391: 71–80

[9] Huang, Q., H. R. Zhao, and L. Chen. 2015. Study on combined forecasting model based on improved PSO. *Computer Engineering and Applications*, 51(14): 158–263.

[10] Iosifidis, A., A. Tefas, and I. Pitas. 2013. Dynamic action recognition based on dynemes and extreme learning machine. *Pattern Recognition Letters*, 34(15): 1890–1898.

[11] Ma, Z., X. F. Song, R. Wan, and L. Gao. 2013. A modified water quality index for intensive shrimp ponds of Litopenaeus vannamei. *Ecological Indicators*, 24: 287–93.

[12] Ma, Z., X. F. Song, R. Wan, L. Gao, and D. W. Jiang. 2014. Artificial neural network modeling of the water quality in intensive Litopenaeus vannamei shrimp tanks. *Aquaculture*, 433(5): 307–312.

[13] Sarkar, A., and P. Pandey. 2015. River water quality modelling using artificial neural network technique. *Aquat Procedia*, 4: 1070–1077.

[14] Song, Y. C. 2015. Application of intelligent algorithm in water quality prediction of aquaculture. M.S. thesis. Wuxi: Jiangnan University.

[15] Wu, Z. H., and N. E. Huang. 2009. Ensemble empirical mode decomposition: a noise assisted data analysis method. *Advances in Adaptive Data Analysis*, 1(1): 1–41.

[16] Xu, L. Q., J. Zhang, and Q. C. Li. 2016. Combination forecasting model of industrialized nursery based on EMD and ELM. *Journal of Agricultural Mechanization*, (04): 265–271, 308.

[17] Xu, L. Q., Q. C. Li, and S. Y. Liu. 2016. Preliminary prediction of industrialized aquaculture based on aggregate empirical mode decomposition and artificial bee colony algorithm. *Journal of Agricultural Engineering*, 32(3): 202–209.

[18] Yang, Q. H., B. P. Tan, X. H. Dong, S. Y. Chi, and H. Y. Liu. 2015. Effects of different levels of Yucca schidigera extract on the growth and nonspecific immunity of Pacific white shrimp (Litopenaeus vannamei) and on culture water quality. *Aquaculture*, 439: 39–44.

[19] Yeh, J. R., J. S. Shieh, N. E. Huang. 2010. Complementary ensemble empirical mode decomposition: A novel noise enhanced data analysis method. *Advances in Adaptive Data Analysis*, 2(2): 135–156.

[20] Zhang, Y., Q. Q. Gao. 2015. Research on integrated water quality prediction model based on Gray Model and Fuzzy Neural Network. *Journal of Environmental Engineering*, 9(02): 537–545.

A DLMS/COSEM Protocol-based data acquisition system for smart sensors

Zhang Ganghong[1,3], Yu Lina[2,4], Xiao Wanang[2,4,5*], Gao Wanlin[1,3*], Zhang Guofeng[1,3], Tao Sha[1,3], Yu Limin[1,3]

(1. *Key Laboratory of Agricultural Informatization Standardization, Ministry of Agriculture, Beijing 100083, China*;
2. *Institute of Semiconductor, Chinese Academy of Sciences, Beijing, 100083, China*;
3. *College of Information and Electrical Engineering, China Agricultural University, Beijing 100083, China*;
4. *School of Microelectronics, University of Chinese Academy of Sciences, Beijing, 100049, China*;
5. *Shenzhen Dapu Microelectronics Co. Ltd, Shenzhen, 518100, China*)

Abstract: Smart sensor plays a crucial role in the process of agricultural informatization, especially for agricultural Internet of Things (IoT). However, the lack of standardized data transmission protocol for communication has hampered the pace of progress and that resulted in applications of smart sensors are not unified, and replacement and maintenance become very arduous in the field of agricultural informatization. At present, the process of standardization and development about agricultural information move forward relatively slowly. In view of this, this paper presented a smart sensor data acquisition system based on Device Language Message Specification / Companion Specification for Energy Metering (DLMS/COSEM) model under the international standard architecture named IEC62056. With good interconnectivity and interoperability, the system showed it can realize the traceability and conformance of original measurement data, and unify data transmission communication protocol between data acquisition server and smart sensors. Using DLMS/COSEM based on object-oriented method to define the information model of smart sensors, namely COSEM object model, and format the message content in a standardized way. The acquisition side gets sensor data in the same format, decoupling of manufacturers, device types, and types of communication channel. This object-oriented thinking is of great significance for the market promotion of smart sensors. It can handle more complicated user requirements flexibly and adapt to implement the requirements of development of smart sensor in the future.

Keywords: DLMS, COSEM, smart sensor, data acquisition system, IEC62056

Citation: Zhang G. H., L. N. Yu, W. A. Xiao, W. L. Gao, G. F. Zhang, S. Tao, and L. M. Yu. 2017. A DLMS/COSEM protocol-based data acquisition system for smart sensors. International Agricultural Engineering Journal, 26(4): 293–299.

1 Introduction

Data communication systems such as data acquisition, device control and data analysis have been studied for decades, and computer and electronic technology and agricultural technology integrations have produced thousands of new applications that collectively contain nearly all informatization processes in the chain of agricultural production (Dan et al., 2016; Romanov et al., 2016; Sun et al., 2015; Gao et al., 2014). Therefore, the application of agricultural information technology in China has made great achievements in the past two decades, greatly promoting the process of agricultural modernization. While compared with the developed countries, China's agricultural informatization started late with poor foundation, the overall level is relatively backward, and there are still a host of problems. Furthermore, the formation of these applications is not fully unified and standardized, and development of new applications relies primarily on exploratory specification. One of the most paramount problems needs to address is

Received date: 2017-07-05 **Accepted date:** 2017-08-23

* **Corresponding author: Gao Wanlin,** PhD, Professor, Research interests: agricultural informatization and application specific chip. Address: College of Information and Electrical Engineering, China Agricultural University, Beijing 100083 P.R. China. Tel: +86-010-62736755, Email:cau_szmtyjs@163.com.

how to design a set of standard communication protocol and implementation methods for smart sensors (Adamo et al., 2015; Jameel et al., 2015; Rodrigues et al., 2015; Chi et al., 2014). Especially, for smart sensor, which plays a crucial role in the process of agricultural informatization as it needs to be standardized.

The approaches of DLMS/COSEM model and its application in the field of power energy metering provide an alternative to experimental trial-and-error (Leo et al., 2016; Leo et al., 2015; Dantas et al., 2014; Limphapayom et al., 2014; Kheaksong et al., 2014; Otani et al., 2013; Feuerhahn et al., 2011; Štruklec et al., 2011). DLMS/COSEM model, as the key part of IEC62056 standard protocol, mainly includes four elements: an object model, to view the functionality of the meter as it is seen at its interface(s); an identification system for all metering data; a messaging method to communicate with the model and to turn the data to a series of bytes; and a transporting method to carry the information between the metering equipment and the data collection system. In fact, the DLMS/COSEM model, as an object model and identification secure system for all metering data, has been applied for AMI and AMR system in the field of smart metering (electricity, water, gas, etc.) for more than one decade (Sun et al., 2015; Gonzalez-Sotres et al., 2016). Traditionally, when constructing Advanced Metering Infrastructures (AMI), the existed problems include inefficient integration of Automatic Meter Reading (AMR); arduous maintenance of energy meters; not easy to change communication channel and not sufficient service and management (Mohammadali et al., 2014). For the same reason, in the process of agricultural informatization, it is also lack of this type of interaction protocol to solve the problems. The applications of using DLMS/COSEM protocol, as an international standard for electricity, heat/cooling, gas and water metering have been reaped huge fruits and brought individuals a multitude of conveniences for smart grid and electricity management (Leo et al., 2016; Leo et al., 2015; Dantas et al., 2014; Limphapayom et al., 2014; Kheaksong et al., 2014; Otani et al., 2013; Feuerhahn et al., 2011; Štruklec et al., 2011). Previous studies of meters and data center interactions emphasized potential advantages to unified organization, such as minimizing maintenance tasks, saving cost, and increasing the interconnectivity and interoperability of the system services. In order to make full use of these advantages, this paper presented a prototype system based upon DLMS/COSEM and was used to define the data model of smart sensors, namely COSEM object model, format the message content in a standardized way. The acquisition side gets sensor data in the same format, decoupling of manufacturers, device types, and types of communication channel.

2 Materials and methods

2.1 DLMS/COSEM model/protocol

DLMS/COSEM model has been developed for almost two decades, and its mission is to develop open standards for meter data exchange, ensuring interoperability in order to optimize business processes, increase efficiency and secure investment. The specification specifies a data model and communication protocol for data exchange with metering device. Figure 1 shows the 3-layer approach of DLMS Applications-Model-Protocol. Modelling layer specifies the object identification system (OBIS), the COSEM interface classes, and the interface object model for various functions of metering device. Application layer and protocol layer are communication profiles for COSEM architecture and various communication channels. The COSEM application layer provides services to establish a logical connection between client and server, and DLMS messaging services to access (Set/Get) attributes and specific methods of the COSEM interface objects.

DLMS as a common concept for abstract modelling of communication entities, and COSEM as setting the rules, based on existing standards, for data exchange with energy meters, and the main objectives of the model are to implement pre-standardization for meter data exchange, market relevance and identify possible applications. Under this model, there are also three main books: the Blue book describes the COSEM meter object model and the object identification system; the Green book describes the architecture and protocols to transport the model; the Yellow book describes the conformance testing process.

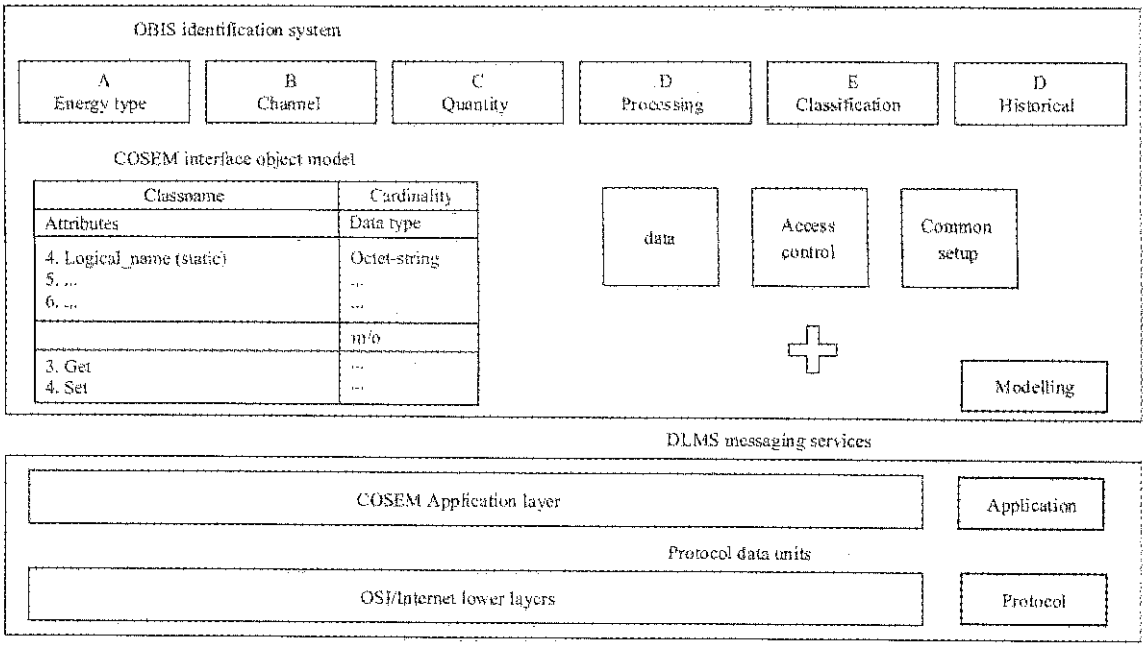

Figure 1 DLMS Application-Model-Protocol

The physical device is meter, it supports one or more communication profiles. Nowadays, the standard specifies two profiles: the 3-layer, connection oriented HDLC (High-Level Data Link Control)-based profile, and the TCP/IP based profile. A device uses the HDLC-based profile, it also has a physical address. A physical device hosts one or several logical devices. A logical device models a specific functionality of the physical device. For example, in a multi-energy meter, one logical device could be an electricity meter, a gas-meter etc. Each logical device has an address, called the logical device address. So, in this paper, logical devices include all kinds of smart sensors such as soil temperature, air temperature and humidity, soil moisture sensor, CO_2 etc.

To be concluded, DLMS/COSEM allows to build simple or complex meters, and provides a lot of flexibility and interoperability on the model level and on the protocol level. Based upon this thinking method, we will design a data acquisition system to serve for smart sensors of agricultural areas.

2.2 Data acquisition system

The core of smart sensor is a microprocessor and network communication technology, with automatic sensing, data processing, bi-directional data communication and function expansion, which can realize intelligent remote communication, real-time data interaction, user interaction and other functions. Without the smart sensors such as soil temperature, air temperature and humidity, soil moisture sensor, CO_2, NH_3, light, and other nutrient elements, and even a variety of sensors integrated into a device, nothing could ever be brought to the development process of agricultural informatization. The sensor data transmission protocol is not uniform will result in the process of replacement cumbersome. The standardization of agricultural informatization is the basis and guarantee for the rapid and healthy development of agricultural informatization. So, in the process of agriculture information technology, smart sensor data acquisition needs the unified process and standard protocol. At present, because of lacking these standards, the construction of agricultural informatization standard confused and supported poorly, resulting in smart sensors integrated other divided protocols in the communication process, and the sensor device replacement task becomes a single choice once damaged.

The requirements for the data acquisition system are to automatically manage all kinds of smart sensors applied in agricultural areas, and to resolve interactive problems. A data acquisition without changing is also required to improve system generalization ability. To satisfy these requirements, in this paper, designed a new system of sensor data getting and parameter setting

based on the above-mentioned protocol model is needed. The system is divided into three parts, smart sensor for sensing data and communicating with collector; collector for interacting with smart sensor and data center server; data center server for managing all smart sensors and collectors. Every part will work independently without interference from each other, only through DLMS/COSEM standard model to interact. Figure 2 shows a schematic view of the data acquisition system.

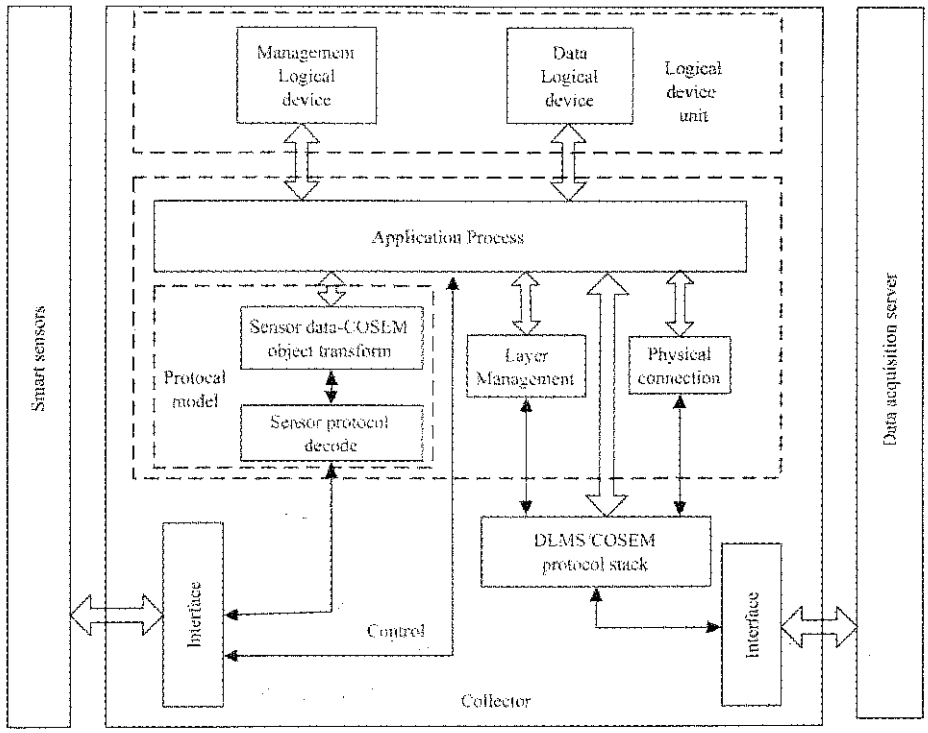

Figure 2 System architecture

For every logical device in the collector, that is to say, all the data in smart sensors are represented by means of mapping them to appropriate classes and related attribute values defined in the standard and the methods, as well as the operations defined to be executed on the attributes. The first attribute for every object is logical name, also gives OBIS code that identifies the object, and defined a class_id for every instantiation of an interface class. The collector provides two interfaces, one is for smart sensor and another supports data center server, both of them are compatible with DLMS/COSEM protocol.

2.3 Process of information exchange

The protocol concludes 3 layers: physical layer, link layer and application layer. Communication between layers is made using the specified service. Both sides of the communication use Client/Server structure, data request end (collector) is Client, data supply end (sensor) is Server. Communication process description is shown in Figure 3 as follows:

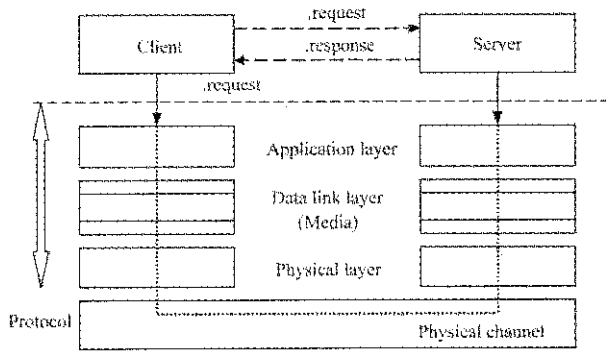

Figure 3 Process of information exchange

(1) Establish a physical layer connection: The physical layer is at the bottom of the communication model. DLMS protocol can be built on a variety of physical layers, the physical layer is used mainly for the underlying communication hardware operation (such as the initialization of PSTN, MODEM, TCP/IP open, close).

(2) Establish link layer connection: When the physical layer connection established, the first step is to establish the link between data communication. Link layers are mainly responsible for the reliability of data transmission,

including address verification, check of data frame length, CRC check and unpacking package for long data frames, and at the same time, provide service for the application layer by link transmission.

(3) Establish application layer connection: After the link layer connection established, the application layer connection is set up in the DLMS protocol to communicate with the data. The application layer connection creation process called Negotioation, and it is to provide configuration parameters for data communication. The request of application layer connection is initiated by the Client side, the Client end sends the AARQ frame, and the Server side responds to the AARE frame.

(4) Data communication: If the connection established, data communications can be set up. The Client side transmits the data request frame to the Server side in response to the data. When requesting different data, Client uses unique class_id, and OBIS specific data to identify different types of data.

(5) Release link and close connection: After the data communication finished, the end of the communication frame is sent and the communication process is ended. After that, the end of a communication process can be finished by sending a link end frame. Also, you can end the communication process without sending any data frames and rely on the timeout mechanism on the server side. Conventionally, the former should be used in general.

(6) Remove physical layer connection: Close the physical port (for example, hang up Modem) and end communication physically.

3 System testing

3.1 System implementation

The data acquisition system has the following general functions: data acquisition for following set of data (for example, soil moisture, air temperature, CO_2, etc.): Monthly values, Daily values, Profile data, Status data, Events and so on; data exchange; alarm handling; basic configuration.

Based on this platform shown in Figure 4, a number of functions were specifically implemented for the handling of devices in residential measurement and will be discussed in more detail in the following section. The system user interface enables the user to display, edit and manage all relevant functions and definitions within the system. The administrator can define automatic tasks and schedules according to needs of the daily operation. Spontaneous tasks, functions and actions can be executed manually.

The system supports direct communication to smart sensors connected over RS232 serial port using the standardized DLMS protocol or to the sensors connected to collectors over serial port. The communication to collectors was done over GPRS/GSM based TCP/IP.

Just shown in Figure 4, we have tested and got a wanted result.

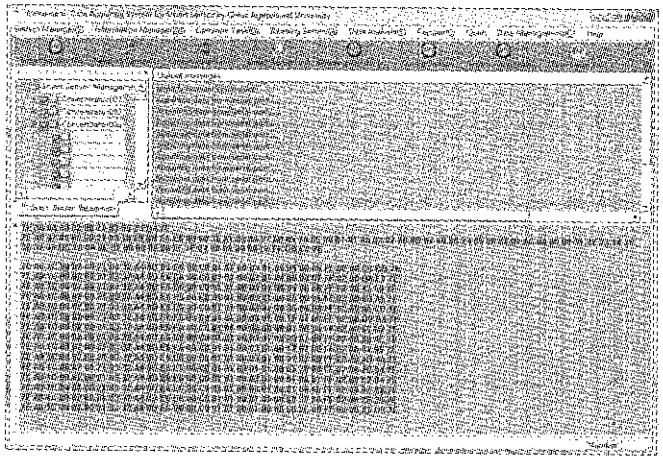

Figure 4 System user interface

3.2 Parameters configuration

The purpose of the conformance test is to verify that the device implementation conforms to the standard, and, if not, to show which parts of the standard are not correctly finished to test the COSEM objects implemented in sensors. Manufacturers ID, each COSEM object is identified by its logical name given by OBIS, class identifier and version. The interface class definitions also specify the data types to be used for each attribute. In some cases, a choice between data types is allowed. Figure 5 and Figure 6 are shown the parameters configuration GUI.

As part of testing the COSEM objects, the system reads the list of COSEM objects available from the sensor devices and checks the validity of the logical name of each object against the list of OBIS codes. In this system

only provides self-testing, for the practical application, we need apply for testing through the DLMS UA.

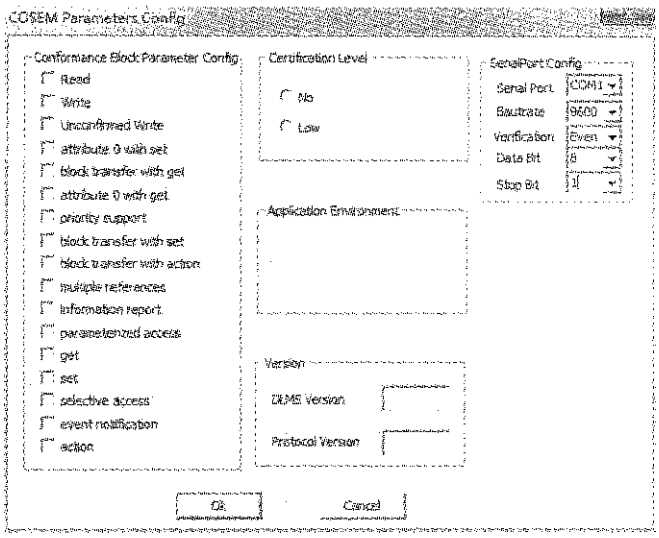

Figure 5 COSEM parameters configuration

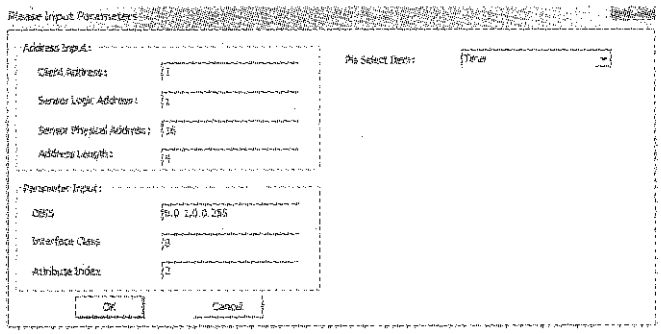

Figure 6 Communication parameter selection

4 Conclusions

In conclusion, agricultural informatization standardization in China is the supporter of the construction of information platform, and the starting point and end point of informatization are to reach the sharing mechanism of information resources and to form efficient automated management, both of which are indispensable. Only the work of agricultural informatization standardization has been done, with unified standards and norms as the foundation, can effectively reduce the cost of agricultural information resource development, greatly enhance the development of agricultural informatization and application efficiency, realize information exchange and resource sharing. In this paper we demonstrated an alternative approach that used DLMS/COSEM model on data acquisition system to get data from smart sensors applied in agricultural areas that are reliable and easy to maintain. This offered an opportunity to integrate a platform to explore a pathway to provide service for agricultural informatization standardization. Recently, more and more opportunities are available, especially for China agricultural informatization, to take advantage of these mature and new technologies. Even though these technologies present great challenges, they would be the most effective strategy for improving agricultural informatization standardization, which will create great opportunity for the future development of agricultural modernization.

Acknowledgements

The authors would like to thank their colleagues for their support of this work. The detailed comments from the anonymous reviewers were gratefully acknowledged. This work was supported by the National Spark Program Key Project (Grant#: 2015GA600002) and Shenzhen Peacock Plan (Grant#: KQTD20150917164531118).

[References]

[1] Adamo, F., F. Attivissimo, C. G. C. Carducci, and A. M. L. Lanzolla. 2015. A smart sensor network for sea water quality monitoring. *IEEE Sensors Journal*, 15(5): 2514–2522.

[2] Chi, Q., H. Yan, C. Zhang, Z. Pang, and L. D. Xu. 2014. A reconfigurable smart sensor interface for industrial wsn in iot environment. *IEEE Transactions on Industrial Informatics*, 10(2): 1417–1425.

[3] Dan, L., C. Xin, C. Huang, and L. Ji. 2016. Intelligent agriculture greenhouse environment monitoring system based on IOT technology. *International Conference on Intelligent Transportation, Big Data and Smart City*, 487-490. Halong Bay, Vietnam, Dec. 19-20.

[4] Dantas, H., Z. Erkin, C. Doerr, R. Hallie, and G. V. D. Bij. 2014. eFuzz: A fuzzer for DLMS/COSEM electricity meters. *SEGS '14 Proceedings of the 2nd Workshop on Smart Energy Grid Security*, 31-38. Scottsdale, Arizona, USA, November 07-07.

[5] DLMS UA 1000. 2nd Ed. 7.0. 2013. DLMS/COSEM Architecture and Protocols. *The Green Book DLMS User Association*.

[6] DLMS UA 1000. 2nd Ed. 8.0. 2014. DLMS/COSEM Architecture and Protocols. *The Green Book DLMS User Association*.

[7] Feuerhahn, S., M. Zillgith, C. Wittwer, and C. Wietfeld. 2011. Comparison of the communication protocols DLMS/COSEM, SML and IEC 61850 for smart metering applications. *IEEE International Conference on Smart Grid Communications*,

34(17): 410–415. Brussels, Belgium, Oct. 17-20.

[8] Gao, H. M., and Y. C. Liu. 2014. Conceptual design of mobile data collection system for traceability in agriculture. *Applied Mechanics & Materials*, 513-517(10): 1131–1134.

[9] Gonzalez-Sotres, L., C. Mateo, P. Frias, C. Rodriguez-Morcillo, and J. Matanza. 2016. Replicability analysis of plc prime networks for smart metering applications. *IEEE Transactions on Smart Grid*, PP(99): 1–1.

[10] Jameel, S., and Z. Farooqui. 2015. Energy efficient smart sensor network routing protocol using node scheduling. *International Journal of Computer Applications*, 126(5B): 188–91.

[11] Kheaksong, A., and W. Lee. 2014. Packet transfer of dlms/cosem standards for smart grid. *Proceedings of the 20th Asia-Pacific Conference on Communication*, 391–396. Pattaya, Thailand, Oct. 1-3.

[12] Leo, G. D., C. Liguori, V. Paciello, A. Pietrosanto, and P. Sommella. 2015. Towards visual smart metering exploiting wM-Bus and DLMS/COSEM. *IEEE International Conference on Computational Intelligence and Virtual Environments for Measurement Systems and Applications*, 1-6. Shenzhen, China, June 12-14.

[13] Leo, G. D., C. Liguori, V. Paciello, A. Pietrosanto, and P. Sommella, 2016. Smart meters in smart cities: an application of dlms-cosem on 169 mhz wm-bus. *Advanced Computer and Communication Engineering Technology*, 362: 735–746.

[14] Limphapayom, S., D. H. Le, and W. Pora. 2014. A simulation of a communication between a smart meter and a data concentrator unit conformed to DLMS/COSEM upon an HDLC profile. *International Conference on Electronics, Information and Communications*, 1-2. Kota Kinabalu, Malaysia, Jan. 15-18.

[15] Mohammadali, A., M. H. Tadayon, and M. Asadian. 2014. A new key management for AMI systems based on DLMS/COSEM standard. *International Symposium on Telecommunications*, 849–856. Tehran, Iran, Sept. 9-11.

[16] Otani, T., and M. Miyashita. 2013. Characteristics of AMI using DLMS/COSEM and IEEE 802.15.4g multi-hop wireless communication. *IEEE International Conference on Smart Grid Communications*, 143(6): 324–329. Vancouver, BC, Canada, Oct. 21-24.

[17] Rodrigues, D., R. M. Pires, and K. R. L. J. C. Branco. 2015. Validating knowledge-based framework through mission-oriented sensors array and smart sensor protocol. *Journal of Physics Conference Series*, 633: 012081.

[18] Romanov, V., I. Galelyuka, and Y. Sarakhan. 2015. Wireless sensor networks in agriculture. *IEEE Seventh International Conference on Intelligent Computing and Information Systems*, 77-80. Cairo, Egypt, Dec. 12-14.

[19] Štruklec, G., and J. Maršić. 2011. Implementing DLMS/COSEM in smart meters. *Energy Market*, 747–752.

[20] Sun, N., H. E. Yong-Sheng, J. X. Liu, N. T. Co, and S. Z. Elecco. 2015. Communication security protective technology of concentrator using dlms/cosem. *Electric Power Information & Communication Technology*, 13(9): 120–127. (In Chinese with English abstract)

[21] Sun, X., Y. Yang, C. Liu, and H. Guo. 2015. Design and development of near field communication intelligent data acquisition terminal system in fresh agricultural product supply chain. *Transactions of the Chinese Society of Agricultural Engineering*, 31(8): 200–206. (In Chinese with English abstract)

Microphone array speech enhancement method based on Wavelet Packet Threshold De-noising

Song Yue[1,2], Yang Bangjie[2,3], Gao Wanlin[1,2*], Yu Lina[4,5]

(1. *Key Laboratory of Agricultural Informatization Standardization, Ministry of Agriculture, Beijing 100083, China;*
2. *College of Information and Electrical Engineering, China Agricultural University,Beijing, 100083, China;*
3. *Center for Agricultural Resources Monitoring, Chinese Academy of Agricultural Engineering, Beijing, China;*
4. *Institute of Semiconductor, Chinese Academy of Sciences, Beijing, 100083, China;*
5. *School of Microelectronics, University of Chinese Academy of Sciences, Beijing, 100049, China*)

Abstract: Current microphone array speech enhancement methods, the delay-sum beamforming algorithm has only a certain noise cancellation capability for incoherent or weak coherent noise, if there is a strong coherent noise in the speech, this traditional method does not totally eliminate the noise. In view of the limitation and problems of the traditional wavelet and wavelet packet analysis, this paper proposed a wavelet packet de-noising method based on adaptive environment. It is effectively combined with the traditional delay-sum beamforming algorithm, which also has a good de-noising ability of coherent noise. Meanwhile, the time delay estimation error caused by noise was reduced, improved the accuracy of time delay estimation, made the final sum better. Through theoretical analysis and practical application, the results showed that this method could effectively remove noise in different environments, the de-noising ability is better than the traditional wavelet, wavelet packet, and other de-noising methods. This improved method can improve the final speech effect, improve speech intelligibility, and enable people to better accept.

Keywords: microphone array, de-noising, wavelet packet threshold

Citation: Song, Y., B. J. Yang, W. L. Gao, and L. N. Yu. 2017. Microphone array speech enhancement method based on Wavelet Packet Threshold De-noising. International Agricultural Engineering Journal, 26(4): 300–306.

1 Introduction

Noise exists in life. The intelligibility of the speech is being affected, which results in the human hearing fatigue, and seriously affects the living of the human beings. Therefore, it is an important research object in the speech signal processing to remove the background noise in the speech signal and improve the SNR. At present, single channel speech enhancement and multi-channel speech enhancement are the main technologies. Single channel methods include spectral subtraction, minimum mean square error method and Wiener filter method, but these methods can't meet the requirements of listening. In recent years the channel speech enhancement algorithm has become the focus of research. The microphone array is arranged in a certain spatial domain and way, and also has the characteristics of spatial selection, providing high-quality voice signals from the required source direction by means of electronic aiming. There are mainly three kinds of microphone array algorithms: the delay and the fixed beamforming algorithm, the adaptive beam forming algorithm and the adaptive algorithm. The fixed beamforming algorithm compensates time delay of each received signal of microphone array. In order to synchronize the speech signals of each channel and weight sum of the signals in each channel which is taken as the average processing. The incoherent noise can be eliminated, but the coherent noise in the speech is difficult to be eliminated.

Because of its good time-frequency characteristics, wavelet analysis has been widely used in deformation analysis, and has achieved good results (Ghanbari and Karami-Mollaei, 2006). However, the wavelet analysis is mainly used to extract the low-frequency signals, which

Received date: 2017-09-22 **Accepted date:** 2017-11-22

*** Corresponding author: Gao Wanlin,** PhD, Professor, Research interests: agricultural Informatization and application specific chip. College of Information and Electrical Engineering, China Agricultural University, Beijing 100083 P.R. China. Email: cau_szmtyjs@163.com, Tel: +86-010-62738536.

is easy to ignore intermediate frequency and high frequency useful information, and has negative impact on the analysis results. It will have a bad effect on the analysis result of high accuracy GPS deformation monitoring. When the sampling frequency is low, the traditional wavelet analysis is prone to the phenomenon of over de-noising, which can't extract the valuable information accurately. Wavelet packet analysis is a new method and has better de-noising ability. It does not only decompose the low-frequency part of observation data like wavelet analysis, but also the high frequency part of observation data, and can extract useful information of each frequency band effectively (Biswas et al., 2015). Nowadays, there are some methods such as improved single threshold processing and ordinary multi threshold processing, which can improve the de-noising effect better than the traditional wavelet packet. But these methods do not give full consideration to the distribution of signals and their noises, and the de-noising accuracy needs to be further improved (Berouti et al., 2003). Based on these problems, this paper presented a wavelet packet de-noising method based on the distribution of different signals and their noises, the wavelet packet selection of appropriate threshold criteria and threshold processing.

Based on the time delay estimation before the "way signal wavelet packet adaptive threshold de-noising, such treatment after a time delay estimation can enhance its accuracy and eliminate coherent noise (Allen, 1993). The make up for the delay-sum beamforming method can eliminate the defects of the incoherent noise. The simulation experiment showed compared with the traditional delay sum fixed beamforming algorithm, the method in this paper had better effect, and could improve speech perception test. The algorithm enhanced the signal naturalness and improved clarity.

2 Delay-sum beamforming algorithm based on wavelet packet adaptive threshold de-noising

The traditional delay sum beamforming algorithm firstly estimates the time delay of the received signals. Then the delay compensation is often affected by the presence of noise, and the accuracy of time delay estimation is affected. So, the wavelet packet adaptive threshold de-noising method is used for each signal, and then the time delay estimation is carried out, which can increase the accuracy of time delay estimation (Ayat et al., 2006). First, the coherent noise in the background noise is eliminated, then the weighted sum of each signal is transformed into a whole signal, and some incoherent noises or weak coherent noises are eliminated

The algorithm flow is as follows:

(1) The signal received by the microphone is firstly de-noised by wavelet packet threshold, and the coherent noise is removed;

(2) Each delay is calculated by each of the two signals after wavelet packet processing, the first road/bit as the reference signal, the other way with the N-1 signals through the autocorrelation method for time delay estimation and time delay compensation;

(3) The weighted sum of the signal which is compensated by the time delay forms a signal;

2.1 Principle of traditional delay-sum beamforming algorithm

The traditional delay-sum beamforming algorithm includes time delay estimation, time delay compensation and the weighted sum of three parts, selection of multiple microphone for receiving signals, in order to reduce the complexity of the algorithm, four linear microphone array models are used.

The input signal of the microphone array is $x_i(t)$, and the expression for the uniform linear array can be expressed as follows:

$$x_i(t) = s_i(t-\tau_{oi}) + n_i(t) \quad i=0,1,2,3 \tag{1}$$

$$y(t) = \sum_{i=1}^{N} wi(t)xi(t-\tau 0i) \tag{2}$$

The type transforms to the frequency domain:

$$Y(\omega) = \sum_{i=1}^{N} wi(\omega)Xi(\omega)e^{-jw\tau oi} \tag{3}$$

Among all, $s_i(t)$ is a pure/original speech signal; n_i is the i road microphone to receive the noise signal; W =[w1, w2, …, wN] T, T is a weighted vector of microphone array; $\tau 0i$ is a sound source to delay the i Road (by the microphone signal and the first signal autocorrelation calculated). The delay sum beamforming algorithm first signal of each microphone receives the time compensation, the synchronizes each channel speech signal, and then calculates the weighted sum of each

channel, usually takes 1/N weight wi. The advantage of the fixed beamforming method is simple and easy to implement, but usually reduces the effect of noise. In order to make the de-noising effect more ideal, the wavelet threshold de-noising method is added.

2.2 Wavelet Packet Threshold de-noising

Scaling relations between an orthonormal scaling function and a wavelet function:

$$\begin{cases} \phi(t) = \sqrt{2\sum_k h_{0k}\phi(2t-k)} \\ \psi(t) = \sqrt{2\sum_k h_{1k}\phi(2t-k)} \end{cases} \quad (4)$$

h_{0k}, h_{1k} are the filter coefficients in the multi-resolution analysis.

In order to further generalize the scale equation, the following recurrence relations are defined:

$$\begin{cases} w_{2n}(t) = \sqrt{2}\sum_{k\in Z} h_{0k} w_n(2t-k) \\ w_{2n+1}(t) = \sqrt{2}\sum_{k\in Z} h_{1k} w_n(2t-k) \end{cases} \quad (5)$$

When $n=0$, $w_0(t)=\phi(t)$, $w_1(t)=\psi(t)$

The above definition function combined with $\{w_n(t)\}_{n\in Z}$ to $w_0(t)=\phi(t)$ to determine the wavelet packet.

$$\begin{cases} d_j^{2n}[t] = \sum_{k\in Z} h_{1-2k} d_{j+1}[l] \\ d_j^{2n+1}[t] = \sum_{k\in Z} g_{1-2k} d_{j+1}[l] \end{cases} \quad (6)$$

Wavelet packet reconstruction formula:

$$d_{j+1}^n = \sum_{k\in Z} h_{1-2k} d_{j+1}[l] + \sum_{k\in Z} g_{1-2k} d_{j+1}[l] \quad (7)$$

According to the theory of wavelet packet transform, it can be in the low and high-frequency information, the characteristic signal is extracted, select the scale is 3, the signal decomposition is shown in Figure 1 by the wavelet packet, S representation of the original signal, said AD the low frequency, high frequency, number represents the number of decomposition (Zhang et al., 2014).

S=A1+D1=AAA3+ADA3+DDA3+AAD3+DAD3+ADD3+DDD3

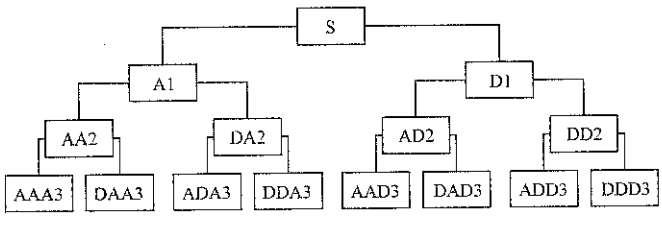

Figure 1 Wavelet packet decomposition

A model of a one-dimensional signal containing noise can be expressed as follows:

$$f(t)=s(t)+n(t)$$

where, $s(t)$ is the actual value of the signal; $n(t)$ noise, in order to remove n(t), making $f(t)$ as close as possible to the $s(t)$, the wavelet packet transform signal processing is applied. When the noise is reduced, the wavelet packet decomposition is performed, then the wavelet packet coefficients are processed in the form of threshold, and then the signal is reconstructed. The steps are as follows:

(1) Wavelet packet decomposition of signal detection. An appropriate wavelet function is chosen according to the noisy signal function, and the decomposition scale is determined (Zhuo and Ellis, 2014).

(2) Determining the best wavelet packet basis. Given an entropy criterion, compute the optimal tree.

(3) Threshold selection of wavelet packet decomposition coefficients. After the wavelet packet decomposition, the wavelet packet coefficient of each node is selected, and then a threshold is quantized.

(4) Wavelet packet reconstruction.

In the above process, the key lies in the choice of threshold and the quantization of the threshold, to a certain extent, it directly affects the quality of signal noise reduction (Tufekci, 2000).

There are 4 principles of threshold selection. The principles of these four thresholds are as follows:

(1) Unbiased likelihood estimation principle. Set a signal function $X(t)$ is a discrete time series, the length of n. Let $y(k)$ for the ascending sequence, $y_1(k)=y(k)^2$, then the unbiased likelihood threshold thr1 principle the calculation formula is as follows:

$$y_2(k) = \sum_{i=1}^{k} y_1(i) \quad (8)$$

$$r(k) = \frac{n-2k+y_2(k)+(n-k)y_1(k)}{n} \quad (9)$$

$$thr1 = \sqrt{\min(r)} \quad (10)$$

(2) Fixed threshold principle. The threshold value of thr2 is calculated as follows:

$$thr2 = \sqrt{2\log(n)} \quad (11)$$

(3) Heuristic threshold principle. The heuristic threshold principle is one of the methods between the

unbiased likelihood estimation principle and the fixed threshold principle:

$$eta = \frac{\|x\|^2 - n}{n} \tag{12}$$

$$crit = \frac{[\log(n)/\log 2]^{1.5}}{\sqrt{n}} \tag{13}$$

$$thr3 = \begin{cases} thr2 & eta < crit \\ \min(thr1, thr2) & eta \geq crit \end{cases} \tag{14}$$

(4) Extreme threshold principle. The principle of the extreme threshold value can be known by the maximum or minimum principle to select the threshold to produce a minimum mean square error of the extreme value, the threshold value of the formula is as follows:

$$thr4 = \begin{cases} 0 & n \leq 32 \\ 0.3936 + \dfrac{0.1892\log(n)}{\log 2} & n > 32 \end{cases} \tag{15}$$

Unbiased likelihood estimation threshold criterion and extreme threshold rule is a part of the coefficients, and is a more eclectic approach, so it can prevent excessive noise, de-noising is not obvious and the corresponding to (Pavez, 2012). Compared with the fixed threshold criterion and heuristic threshold rule, two methods are treated alike, all the wavelet packet coefficient method, it is better to remove the noise correspondingly, prone to excessive noise, suitable for high-frequency signal processing part (Biswas et al., 2015). To sum up, the signal noise reduction, after the N wavelet packet transform, the signal is decomposed into 2^n from the low to high-frequency segment, according to the different frequency range can choose different threshold principle.

When the threshold is determined, then the hard threshold method or soft thresholding method will be used to do the threshold processing for all the wavelet coefficients (Hu and Loizou, 2004). The hard threshold only retains the function which is greater than the threshold value, and the other wavelet coefficients are set to zero. The soft threshold method is used to set the wavelet coefficients less than the critical threshold to zero, and then the wavelet coefficients greater than the threshold are used to zero.

Hard threshold function:

$$\hat{W}_{j,k} = \begin{cases} W_{j,k}, |W_{j,k}| \geq \lambda \\ 0, |W_{j,k}| < \lambda \end{cases} \tag{16}$$

Soft threshold function:

$$\hat{W}_{j,k} = \begin{cases} sign(|W_{j,k}| - \lambda), |W_{j,k}| \geq \lambda \\ 0, |W_{j,k}| < \lambda \end{cases} \tag{17}$$

$sign(x)$ is a symbolic function, $\lambda = \sqrt{2\log(N)}$. Figure 2 is the effect diagram.

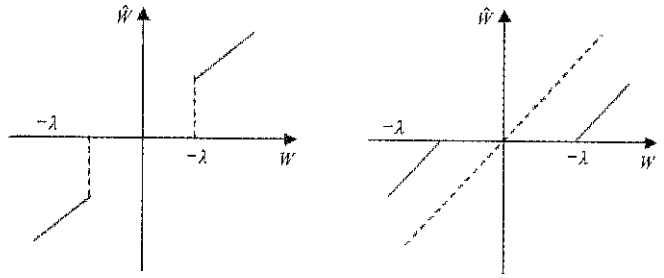

Hard thresholding method Soft thresholding method

Figure 2 Method of hard and soft threshold wavelet coefficients

As can be seen from Figure 2, the hard thresholding and soft thresholding methods have some issues (Tabibian et al., 2015). In the hard threshold method, the break point of the wavelet coefficient is obtained. Although the wavelet coefficients obtained by the soft thresholding method is continuous, it is not accurate enough to the actual signal. Therefore, we hope to obtain a continuous and a small deviation from the actual signal function, that is, the hard threshold and soft threshold function compromise a function.

The application of mathematical knowledge, an arbitrary integer value for smooth $f(x)$, using $\frac{f(cx)}{c}$ and the discrete convolution function, can get a smooth function, when C approaches 0, the smooth function approximation of the original function.

Applying this principle, the problem of hard threshold function is not continuous, and the hard threshold function is transformed into a new continuous function. The new function is to maintain the authenticity of the original hard threshold function and has the continuity of soft threshold function. The hard threshold function was improved due to $\frac{e^{(-x)^2}}{\sqrt{\pi}}$ the integral PI value of 1 V and it can be unlimited derivative, is a smooth function $f(\frac{x}{c}$

and $f(x)$ integral values are equal, so $f(x)=\frac{e^{-(\frac{x}{c})^2}}{c\sqrt{\pi}}$ the integral value is 1, $f(x)=\frac{e^{-(\frac{x}{c})^2}}{c\sqrt{\pi}}$ and hard threshold function $g(x)$ convolution:

$$(f_c * g)(x) = \int_{|R} f_c(y)g(x-y)dy = x+\frac{1}{2}\frac{\left(-e^{\left(-\frac{(x+\lambda)^2}{c^2}\right)}+e^{\left(-\frac{(x+\lambda)^2}{c^2}\right)}\right)}{\sqrt{\pi}} \quad (18)$$

The integral value of $\lambda=\sqrt{2\log(N)}$ is 1, Figure 3 is the schematic diagram of the effect.

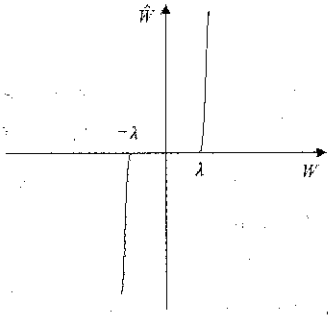

Figure 3 New threshold method

2.3 Time delay estimation and compensation

In this paper, the autocorrelation method is used to estimate the time delay, and the relative delay of two signals is the position of the maximum value of the generalized cross-correlation function of the two signals. By means of the Formula (1), the cross-correlation of two signals can be obtained:

$$\begin{aligned} R_{ij}(\tau) &= E[x_i(t)x_i(t+\tau) \\ &= R_{ii}(\tau-\tau_{ij})+R_{sn}(\tau-\tau_{ij})+R_{sn}(\tau)+R_{nn}(\tau) \end{aligned} \quad (19)$$

It is assumed that the signal is not correlated with noise, then:

$$R_{sn}(\tau-\tau_{ij})=R_{sn}(\tau)=R_{nn}(\tau)=0 \quad (20)$$

So (19) can be turned into $R_{ij}(\tau)=R_{ii}(\tau-\tau_{ij})$ (21)

Formula (21) shows that when $\tau=\tau_{ij}$, autocorrelation function is maximum. According to the above analysis, τ_{ij} is the relative delay two signal estimation. But usually because of various noises, signal and noise, noise and noise are not completely unrelated, it will cause delay estimation error. So, the first of four signals of wavelet threshold do de-noising, then make time delay compensation.

3 Simulation experiment

In the experiment, a pure speech signal in speech database was used, the sampling frequency is 16 kHz, each sample with 16-bit binary encoding, and SNR is white noise 3 dB the formation of noisy speech. The linear microphone array model was adopted, and the 4 microphones were used to receive the speech signal, and the first path was used as the reference signal, and the other 3 paths did the relative delay processing. In order to prove the correctness of the algorithm, we used MATLAB to do the simulation research, and then added the Gauss white noise Surf signal as shown in Figure 4. Figure 4 is a new algorithm of wavelet packet threshold de-noising results; these three methods were using DB4 wavelet function for the decomposition of the 3.

In order to evaluate the noise reduction effects of the noise reduction method, the signal-to-noise ratio (R_{sn}) and the mean square error (R_{mse}) of the denoised signal are used to evaluate the quality of noise reduction

$$R_{sn}=10\lg\left\{\frac{\sum_N s^2(n)}{\sum_N[s(n)-\hat{s}(n)]^2}\right\} \quad (22)$$

$$R_{mse}=\frac{1}{N}\sqrt{\sum_N[s(n)-\hat{s}(n)]^2} \quad (23)$$

Type $s(n)$ is the original signal; $\hat{s}(n)$ the signal is after the noise reduction; N is sampling points. The greater the signal noise ratio is, the mean square error will be, the better effect of noise reduction is. Table 1 is the comparison of noise reduction effect of noise Sref signal

Table 1 Noise reduction effect

Threshold quantization processing method	R_{sn}	R_{mse}
Hard threshold quantization	15.41	1.25
Soft threshold quantization	16.22	1.21
New threshold quantization	35.60	0.76

Wavelet hard threshold is 15.41, the mean square error is 1.25, the soft threshold of wavelet packet noise reduction ratio is 16.22, the mean square error is 1.21, the new algorithm of wavelet packet threshold ratio is 35.60, the mean square error is 0.76. It can be seen from the results that the new thresholding algorithm will greatly improve the signal-to-noise ratio, noise reduction effect good.

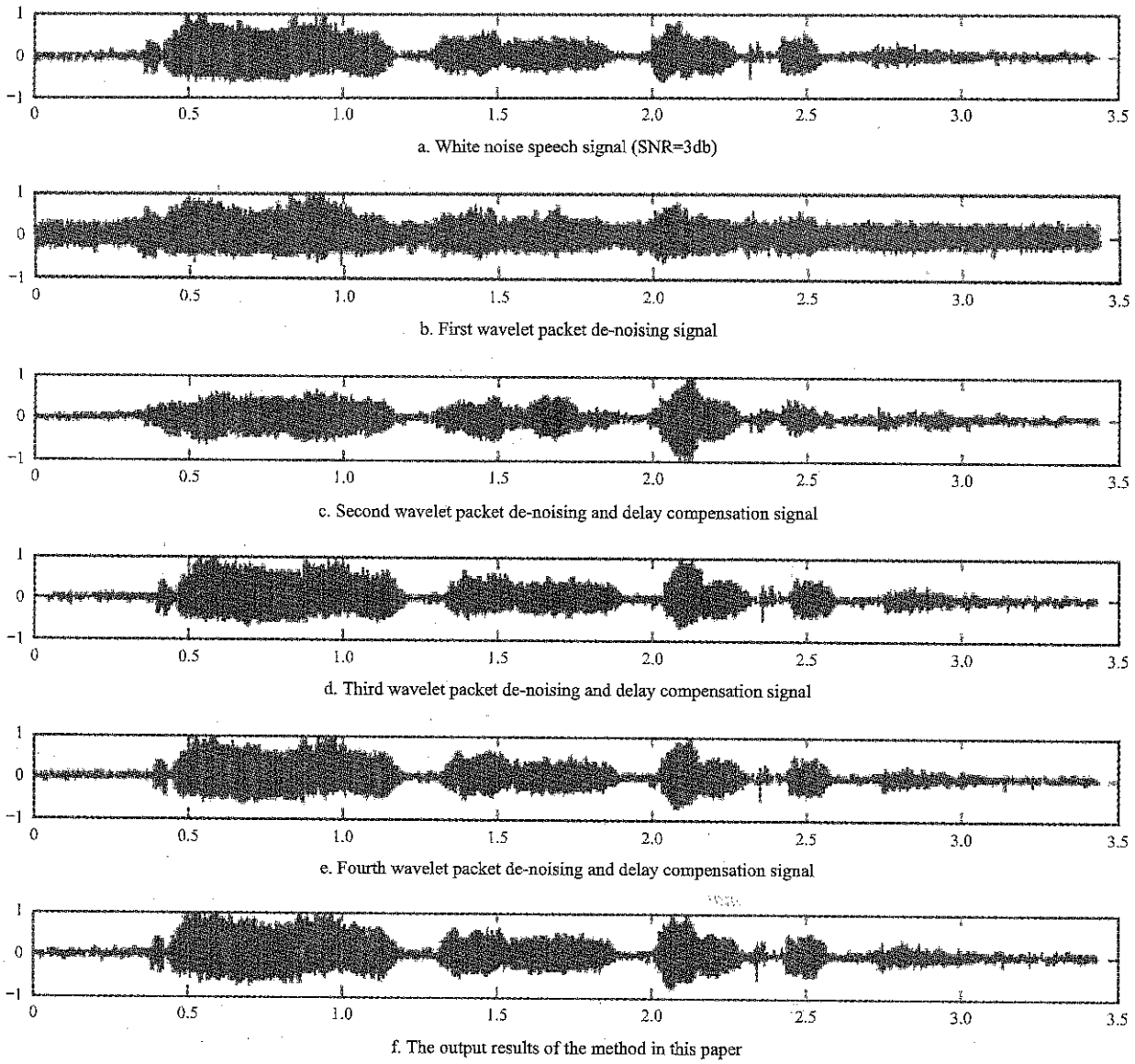

Figure 4 Wavelet packet de-noising effect diagrams

4 Conclusion

Threshold selection and threshold quantization. Choose the correct threshold principle to prevent the unobvious noise as well as the occurrence of excessive noise. The authenticity of soft threshold is continuous and deviates from the signal, and hard threshold discontinuous without losing the authenticity, so the hard threshold Fourier transform, it becomes a continuous function, thus, a new threshold de-noising method was put forward. The new method has an obvious improvement in noise reduction.

This paper presented a method combining wavelet threshold de-noising and microphone array speech enhancement, could improve the performance of traditional delay-sum beamforming method. It can not only eliminate the extraneous noise but also coherent noise. The simulation and experimental results showed that the noise will be eliminated and the signal to noise ratio is increased by the processing of the speech signal.

Acknowledgments

The authors would like to thank their colleagues for their support of this work. The detailed comments from the anonymous reviewers were gratefully acknowledged. This work was supported by the National Spark Program Key Project (Grant#:2015GA600002).

[References]

[1] Allen, J. B. 1993. How do humans process and recognize speech? *IEEE Transactions on Speech & Audio Processing*, 2(4): 567–577.

[2] Ayat, S., M. Manzuri-Shalmani, and R. Dianat. 2006. An improved wavelet-based speech enhancement by using speech signal features. *Comput Electr Eng*, 32(6): 411–25.

[3] Berouti, M., R. Schwartz, and J. Makhoul. 2003. Enhancement of speech corrupted by acoustic noise. *Acoustics, Speech, and Signal Processing, IEEE International Conference on ICASSP. IEEE*, 208-211. Washington, DC, USA, April 2-4, 1979.

[4] Biswas, A., P. Sahu, and M. Chandra. 2014. Admissible wavelet packet features based on human inner ear frequency response for Hindi consonant recognition. *Comput Electr Eng*, 40(4): 1111–1122.

[5] Biswas, A., P. K. Sahu, A. Bhowmick, and M. Chandra. 2015. Admissible wavelet packet sub-band-based harmonic energy features for Hindi phoneme recognition. *IET Sig Proc*, 9(6): 511–519.

[6] Ghanbari, Y., and M. R. Karami-Mollaei. 2006. A new approach for speech enhancement based on the adaptive thresholding of the wavelet packets. *Speech Communication*, 48(8): 927–940.

[7] Hu, Y., and P. C. Loizou. 2004. Speech enhancement based on wavelet thresholding the multitaper spectrum. *IEEE Transactions on Speech & Audio Processing*, 12(1): 59–67.

[8] Mohammadiha, N., T. Gerkmann, and A. Leijon. 2011. A new approach for speech enhancement based on a constrained Nonnegative Matrix Factorization. *International Symposium on Intelligent Signal Processing and Communications Systems*. 1-5. Chiang Mai, Thailand, Dec. 7-9.

[9] Pavez, E., and J. F. Silva. 2012. Analysis and design of wavelet-Packet cepstral coefficients for automatic speech recognition. *Speech Communication*, 54(6): 814–835.

[10] Sun, C., Q. Zhang, J. Wang, and J. Xie. 2014. Noise reduction based on robust principal component analysis. 2014. *Journal of Computational Information Systems*, 10(10): 4403–4410.

[11] Tabibian, S., A. Akbari, and B. Nasersharif. 2015. Speech enhancement using a wavelet thresholding method based on symmetric Kullback–Leibler divergence. *Signal Processing*, 106(C): 184–197.

[12] Tufekci, Z., and J. N. Gowdy. 2000. Feature extraction using discrete wavelet transform for speech recognition. In *Southeastcon 2000. Proceedings of the IEEE*. 116-123. Nashville, TN, USA, April 9.

[13] Vaidyanathan, P. P. 1993. *Multirate Systems and Filter Banks*. 3385–3388.

[14] Wilson, K. W., B. Raj, P. Smaragdis, and A. Divakaran. 2008. Speech denoising using nonnegative matrix factorization with priors. *IEEE International Conference on Acoustics, Speech and Signal Processing. IEEE*, 4029–4032. Las Vegas, NV, USA, March 31 - April 4.

[15] Yilmaz, E., H. V. Hamme, and J. F. Gemmeke. 2015. Adaptive noise dictionary design for noise robust exemplar matching of speech. *Signal Processing Conference*. IEEE. Nice, France, Aug. 31 - Sept. 4.

[16] Zhang, X., J. Huang, Y. Zhang, X. Zou, and L. Zeng. 2014. Speech denoising via low-rank and sparse matrix decomposition. *Etri Journal*, 36(1): 167–170.

[17] Zhuo, C., and D. P. W. Ellis. 2014. Speech enhancement by sparse, low-rank, and dictionary spectrogram decomposition. *2013 IEEE Workshop on Applications of Signal Processing to Audio and Acoustics*, 1–4. New Paltz, NY, USA, Oct. 20-23, 2013.

Visual analysis of wheat grain based on laser confocal micro-Raman mapping technology

Li Hui, Wu Jingzhu*, Liu Qian, Liu Cuiling, Sun Xiaorong, Zhang Liheng

(Beijing Key Laboratory of Big Data Technology for Food Safety, Beijing Technology and Business University, Beijing 100048, China)

Abstract: In this paper, Laser Confocal Micro-Raman (LCM-Raman) mapping technology was applied to realize the visual analysis of wheat grain including the epiderm thickness measurement and the internal chemical composition distribution. Raman analysis was carried out with the Thermo Scientific DXR Raman microscope spectrometer system. For mapping measurements, the whole area of kernel waist slice was chosen with the step size of 120 um. The wheat epiderm's chemical composition was quite different from the internal kernel, which resulted in great differences of Raman spectra. Combining Raman spectrum unfolding method with image processing technology, a new epederm thickness measurement method was established. Following, the chemical composition distribution visualization of starch, cellulose and protein was achieved by using the spectrum stripping method based on the full spectrum band or characteristic band. It could be found that the starch was mainly distributed in the endosperm, the cellulose and protein were mainly distributed in the paralysis layer, which were in accordance with the actual situation. Thus, the confocal Raman mapping technology was shown to be a powerful tool to realize fine analysis of wheat grain at molecular level.

Keywords: Raman mapping, wheat grain, epiderm thickness, chemical composition, distribution visualization

Citation: Li, H., J. Z. Wu, Q. Liu, C. L. Liu, X. R. Sun, and L. H. Zhang. 2017. Visual analysis of wheat grain based on laser confocal micro-Raman mapping technology. International Agricultural Engineering Journal, 26(4): 307–313.

1 Introduction

The content and distribution of chemical composition of seed are closely related to the physiological state, storage resistance, nutritional value, utilization value and quality breeding of seed (Cheng, 2009). Sun et al. (2012) indicated that the differences in the quality traits of wheat were mainly due to the different content and spatial distribution of the seeds (Sun et al., 2012; Tadesse et al., 2015). Therefore, it is of great practical significance to the fine analysis of the internal components of wheat seeds (Delwiche et al., 2010; Qi et al., 2012).

Du et al. (2013) introduced that Raman spectral imaging technology is an advanced detection method to obtain a detailed chemical image of the sample by collecting the Raman signal in a certain sample region, which is a new generation of fast, high precision, surface scanning laser Raman technology. It combines confocal microscopy technology introduced by Ma et al. (2016) and laser Raman spectroscopy technology introduced by Kay and Heinz-Detlef (2012), Zhou et al., (2015) perfectly, with high-speed, high-resolution imaging, and perfect combination with image and spectrum (Zhou et al., 2013). By integrating Raman spectra of large-scale, multi-collected points, Raman imaging is no longer just a simple spectrum, but rather a statistical description of a selected area as a whole. The pseudo-color image presented can directly reflect the distribution and concentration of the target in the sample, and can realize the real-time monitoring of the target (Zhai et al., 2017; He, 2010). Therefore, the study of the use of Raman imaging technology to achieve fine grain analysis of wheat grain, including two parts of the content that the thickness of the seed coat explained by Chen (2012) and the analysis of the internal distribution explained by

Received date: 2017-06-27 **Accepted date:** 2017-08-02

* **Corresponding author: Wu Jingzhu,** Beijing Key Laboratory of Big Data Technology for Food Safety, Beijing Technology and Business University, Beijing 100048, China. Email: pubwu@163.com, Tel: 010-68985506, Fax: 01068985285.

Huan (2014).

2 Materials and methods

2.1 Experimental materials

The two wheat varieties with different germination rates were selected as horizontal comparison samples. At the same time, the longitudinal comparison samples of different aging stages of the same cultivars were obtained by artificial accelerated aging test. The sample set information is shown in Table 1. The artificial aging test was carried out using the LH-80 seed aging tank of Hangzhou ShuoLian Instrument Co., Ltd., and the test temperature was set at 40°C and maintained in high humidity state. Different germination stages of the sample according to the national standard germination rate test (GB/T 3543.4-1995) measured the germination rate. Selected the fuller of wheat particles in each sample, and cut the lumbar slices (about 2 mm in thickness) with the blade to spare. The slices placed around 4°C refrigerators.

Table 1 Statistic information of samples

Variety	Origin	Sample number	Aging days, d	Germination Rate, %
Fengshou919	Henan	B4	0	95.5
		B4-1	2	82.75
		B4-2	4	46.75
Shannong17	Shandong	B6	0	70.5
		B6-1	2	49.5
		B6-2	4	15.25

2.2 Raman image collection

We chose the DXR laser confocal microscopic Raman spectrometer by Thermo Fisher Scientific as the Raman microscopic image acquisition system, as shown in Figure 1. The sections were fixed on a slide to perform a 10x magnification, and the sample area to be collected was selected for imaging. Instrument parameters: Laser power: 24 mw, grating: 50 um plit, exposure time: 3 s, acquisition times: 3 times, step size: 120 um×120 um, acquisition time: about 3.4 h.

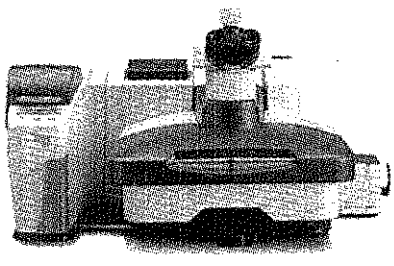

Figure 1 DXR laser confocal Raman spectrometer

3 Results and analysis

3.1 Measure the thickness of the seed coat

The seed coat has some influence on the seed germination because of its mechanical restraint and the permeability and other properties. Approximately 75% of the wheat seed coat is cellulose, the rest mostly minerals. The seeds internal are mainly composed of starch, protein, lipids and other substances. The difference between the seed coat and the internal chemical composition will cause a difference in the spectrum, thus providing a basis for the measurement of the thickness of the seed coat using the Raman imaging.

Taking the B4 sample as an example, first select the internal spectrum of the slice as the basis spectrum from the acquired Raman microscopic image. Then do the relevant image analysis of the Raman image, and get the distribution shown in Figure 2, it can be seen that the green ring area in the figure is the seed coat. Next save the map as BMP format for next image processing.

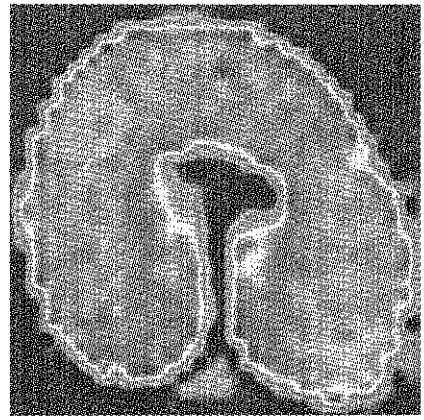

Figure 2 Raman image of wheat slice

3.1.1 Extract the seed coat target

The key to achieving the seed coat thickness measurement is to divide the green band region from the entire color image in Figure 3. In the image segmentation, according to different goals, there is often an optimal threshold. The methods of determining the optimal threshold are generally the experimental method, the histogram method and the adaptive threshold method. According to the characteristics of Figure 2, the histogram distribution of the three components of R, G and B is obtained first, as shown in Figure 3. It can be seen that the histogram of R and B has a significant bimodal and the difference is far, so choose R (i, t)>0.5 |

B (i, t)>0.6 as the threshold condition to divide the seed coat area, as shown in Figure 4. To verify the marked seed coat area (Figure 2) connecting components superimposed on the original color map, as shown in Figure 5. It can be seen that the segmentation effect is satisfactory.

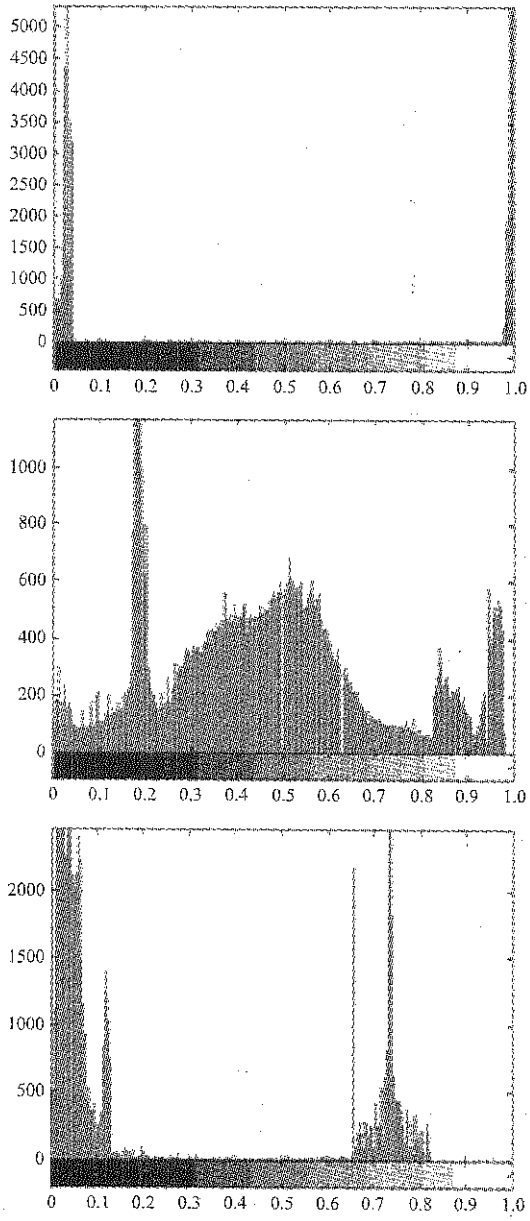

Figure 3 The histogram of R, G, B

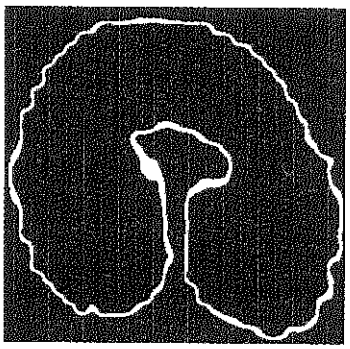

Figure 4 Seed coat area image

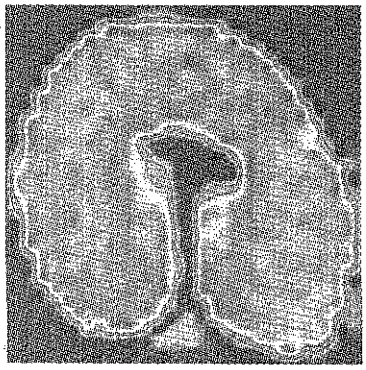

Figure 5 Mark the seed coat edge to the color image

3.1.2 Calculate the seed coat thickness Pixels number

The area of the seed coat is a thin band with uneven width, and the width of the band is the thickness of the seed coat. If the width of the annulus is much smaller than the length of the annulus, the annulus may be approximated as an elongated rectangle. It is possible to approximate the ratio of the area occupied by the endless belt to the loop length as the width of the endless belt, i.e., the thickness of the seed coat. The area and perimeter of the seed coat target can be extracted by the function region props.

3.1.3 Calibrate image scale

The image scale is the actual length value represented by each pixel in the image. It can be based on the number of pixels in the image to get the actual size of the object. The image scale of the seed Raman micrograph is calculated from the ratio of the actual measured value of the seed diameter to the number of pixels in the seed diameter of the image. The algorithm for the number of pixels in the seed diameter is the maximum value for the array containing the number of pixels per seed.

3.1.4 Calculate the seed coat thickness

The digital image is composed of pixels. The true length of the object can be calculated by calculating the number of pixels in the object region under the known of the real length represented by each pixel in the known image. The thickness of seed coat is the product of the number of pixels in the image and the scale of the image. Finally, the thickness of wheat seed coat can be calculated.

The accuracy of wheat seed coat thickness measured by Raman imaging technique should be compared with the actual thickness of wheat seed coat. But the wheat seeds are caryopsis, seed coat and fruit closely, without

special grinding method is extremely difficult to separate. Because our current research has not found the method of separating the seed coat, it is difficult to measure the accuracy of the method, but at least for the relevant research to provide a reference.

The group also tried to use this method to measure the changes of wheat seed coat thickness at different stages of aging. The results are shown in Table 2. Because there are only three different aging samples of the same variety and each sample only measured a seed coat thickness of one seed. At present, no statistical changes have been found, and further research is needed, such as increasing the number of aging samples, taking the same sample and taking the average number of measurements, etc.

Table 2 Thickness of wheat seed coat at different aging stages

Sample number	Image scale. um	Seed coat thickness pixels	Seed coat thickness, um
B4	11.6129	3.5029	40.6787
B4-1	12.4567	3.7609	46.8436
B4-2	11.4970	3.1053	35.7019
B6	10.4046	4.1367	43.0408
B6-1	12.7575	3.8213	48.7505
B6-2	11.6129	3.4074	39.5694

3.2 Seeds internal components distribution analysis

The Raman micrograph of wheat is a composite image of multiple components, which is a superposition of multiple functional groups. It is resulted that the specific compounds cannot be imaged, and there is no way to know the distribution of the compounds in the sample. It is necessary to extract and separate the spectral characteristic information of the single component from the composite information of the plurality of functional groups to obtain the image of the single component. And the feature information can be imaged to decompose the image of the single component from the composite image of various components. The image is stripped by spectroscopy to obtain a purely distributed image. The main methods are: single-wavelength image method, peak area image method, peak ratio image method and related image method.

The single-wavelength image pattern is characterized by the infrared absorption intensity at a particular wavelength, showing the corresponding distribution of the chemical functional groups. The selected characteristic wavelengths are characteristic and unique, and this pattern is suitable for analyzing simple components.

The method of peak area image is characterized by the peak area (peak area representing the corresponding chemical functional group) of the specific absorption peak of the infrared spectrum, showing the distribution information of the corresponding chemical functional group in the image analysis region.

The method of peak ratio image is characterized by the peak rate (peak ratio represents the corresponding chemical functional group) of the different absorption peaks of the infrared spectrum, showing the distribution information of the corresponding chemical functional group in the image analysis region.

The method of correlation image is characterized by a known Raman spectroscopy, and the correlation coefficient of each point is used to display the distribution information of the known chemical group in the image analysis region.

That is, to a Raman spectrum as the standard, calculated the correlation coefficient between the spectrum of each pixel on the Raman micrograph and the standard spectrum, and then imaged by correlation coefficient. It is applicable for the sample of complex internal components such as wheat.

3.2.1 Collect the Raman spectra of starch, cellulose and protein

First collect pure substances derived from wheat, starch, cellulose and protein, the starch and cellulose were purchased from SGS. Since there is no standard material site to purchase pure protein, replaced by gluten. Gluten is extracted from wheat (flour) in the natural protein, protein content was up to 75% to 85%. The wheat flour used in the experiment was from the ancient ship flour mill.

In order to make the representative of Raman spectrum of pure substance, the multi-point scanning is carried out by the surface scanning method. The averaged Raman spectra of starch, cellulose, and gluten are shown in Figure 6.

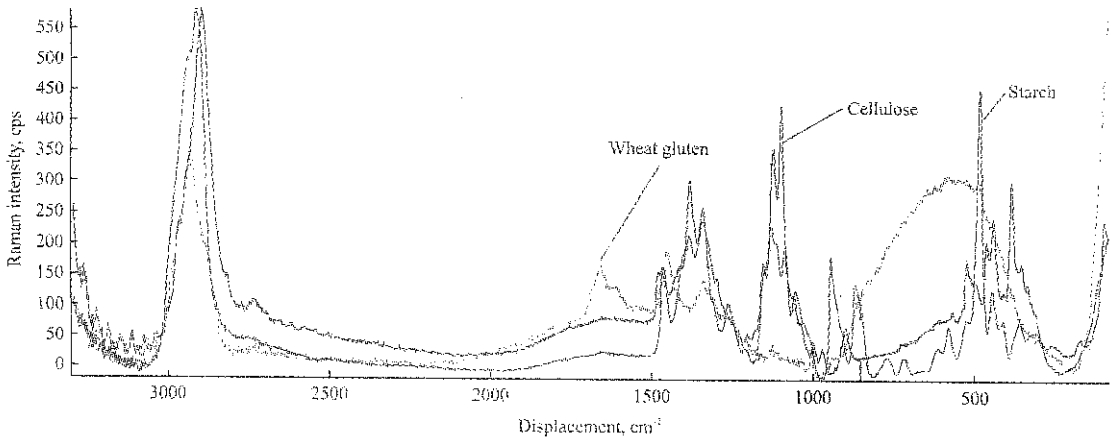

Figure 6 Raman spectroscopy of starch (red), cellulose (blue) and wheat gluten (green)

3.2.2 Distribution detection of starch, cellulose

The microscopic stripping of wheat Raman micrographs was carried out by correlation image method to obtain a single component distribution image. The Raman spectra of wheat slices were characterized by Raman spectra of starch and cellulose, and the images were analysed by correlation coefficient. The images were shown in Figure 7 and Figure 8. Red represented a high correlation coefficient; blue represented a low correlation coefficient.

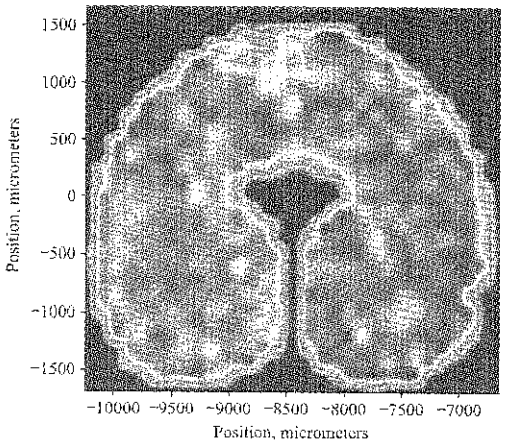

Figure 7 Distribution of starch

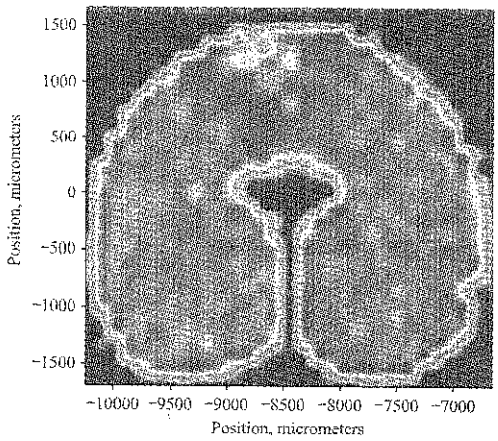

Figure 8 Distribution of cellulose

It can be seen from Figure 7 that the correlation coefficient of wheat endosperm is high in the starch distribution obtained by the correlation image analysis. In practice, the content of starch in wheat endosperm accounted for 100% of the total amount of wheat starch (in dry matter), but the correlation coefficient in the aleuronic layer is also high, while the aleuronic layer does not contain starch ingredients, which does not match the actual condition. It can be seen from Figure 8 that the cellulose distribution map is very similar to the starch distribution map, whose correlation coefficient is high in wheat endosperm and partial aleuronic layer. But the content of cellulose in wheat seed coat accounted for 75% of the content of cellulose in wheat, endosperm content of 5%, which does not meet the actual situation.

Starch and cellulose both belong to the polysaccharide, the chemical structures of little difference. The correlation image analysis method based on full band cannot distinguish starch and cellulose. Comparing the Raman spectra of starch and cellulose, it was found that the band with different spectral range was 1500-100 cm^{-1}, and the correlation image was analysed for the difference bands. The results were shown in Figure 9 and Figure 10. It can be seen that the starch is mainly distributed in the endosperm, and the cellulose is mainly distributed in the paralysis layer, which is more in line with the actual situation.

3.2.3 Detection of protein distribution

It can be seen from Figure 6 that the Raman spectra of wheat gluten have a large noise in the range of 1000-100 cm^{-1}, so the Raman images in the range of 3299-1000 cm^{-1} are taken for correlation image analysis to

obtain the protein distribution as shown in Figure 11. Red represents a high correlation coefficient; blue represents a low correlation coefficient. It can be seen that the correlation coefficient of wheat flour in the protein distribution is the highest, and the correlation coefficient of other regions is relatively low, which is in line with the actual situation.

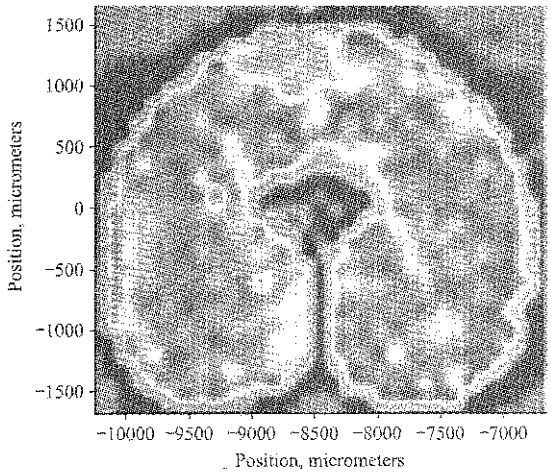

Figure 9 Distribution of starch

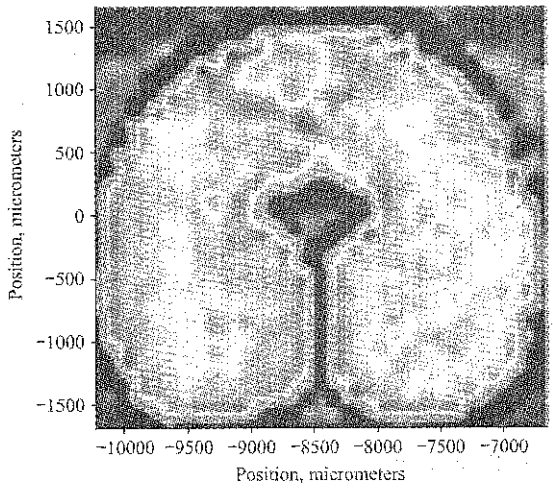

Figure 10 Distribution of cellulose

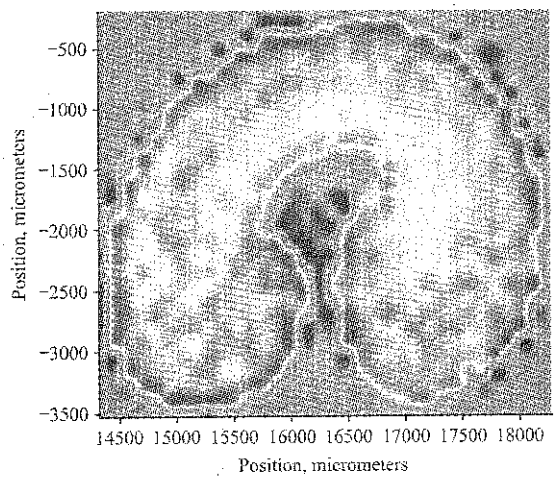

Figure 11 Distribution of protein

4 Conclusion

In this study, Raman microscopy was used to obtain the Raman images of the waist sections of wheat seeds. Raman images were obtained with the correlation image method. The distribution of three main nutrient components of starch, cellulose and protein was obtained, which was consistent with the actual situation. However, the experimental process still had the following problems:

(1) Manual slices are not smooth, affecting the focus, thus affecting the image quality and follow-up analysis. So, we contacted the Chinese Academy of Forestry for wheat slices, designed slice thickness of 50 um.

(2) In order to ensure that the imaging time is within the acceptable range, the scanning surface length of the experiment is 120 um × 120 um. Step size larger may miss some of the chemical composition of information to affect the analysis results. Follow-up need to balance the scanning step and the imaging time of the relationship between the two to seek the appropriate test conditions.

Acknowledgements

This work was supported by the State Key Laboratory Program of Soil Plant Machinery System Technology (2014-SKL-05) and International S&T Cooperation Program of China (2014DFA31660).

[References]

[1] Chen, L. L. 2012. Detection of wheat seed characters based on infrared microscopic imaging. M.S. thesis, Xi'an University of Electronic Science and Technology, Shanxi, Xi'an.

[2] Cheng, G. L. 2009. The comparative study of seed science and industry development at home ang abroad. Ph.D. dissertation, Shandong Agricultural University, Shandong, Taian.

[3] Delwiche, S. R., M. S. Kim. 2010. Damage and quality assessment in wheat by NIR hyperspectral imaging. *Proceedings of SPIE - The International Society for Optical Engineering*, 7676(1): 148–152.

[4] Du, Z. X. 2013. Raman spectroscopy imaging technology and application. *Weifang Higher Vocational Education*, 2: 44–45.

[5] He, X. H. 2010. Application of Raman spectroscopy imaging

in food safety. In *Proc. 3rd International Food Safety Summit*, 74–76. Bingjing, China, April 15, 2010.

[6] Huan, K. W. 2014. Study on nondestructive detection technique of wheat internal quality by near-infrared spectroscopy. Ph.D. dissertation, Changchun University of Science and Technology, Jilin, Changchun.

[7] Ma, K., Q. F. Zhou, C. X. Shi, D. L. Pei, and Y. F. Yan. 2016. The progress of confocal laser scanning microscope. *Journal of Agriculture*, 6: 30–35.

[8] Qi, L. J., X. X. Hu, G. Y. Zhou, S. Wang, J. M. Li, W. Lu, L. N. Wu, M. B. Lu, L. J. Sun, X. L. Yang, J. K. Song, and B. J. Wang. 2012. Analysis of wheat protein quality in main wheat producing areas of China from 2004 to 2011. *Scientia Agricultura Sinica*, 20: 4242–4251.

[9] Sowoidnich, K., and H. D. Kronfeldt. 2012. Shifted excitation Raman difference spectroscopy at multiple wavelengths for in-situ meat species differentiation. *Applied Physics B*, 108(4): 975–982.

[10] Sun, H., C. H. Yin, and R. Y. Zhao. 2010. Present situation of wheat quality evaluation and inspection technology in China. *Cereal and Food Industry*, 5: 14–18.

[11] Sun, Q., Q. Wang, and W. Q. Xue. 2012. Advances in nondestructive of seed quality. *Journal of China Agricultural University*, 17(3): 1–6.

[12] Tadesse, W., F. C. Ogbonnaya, A. Jighly, M. Sanchez-Garcia, Q. Sohail, S. Rajaram, and M. Baum. 2015. Genome-wide Association mapping of yield and grain quality traits in winter wheat genotypes. *Plos One*, 10(10): e0141339.

[13] Zhai, C., Y. K. Peng, Y. Y. Li, and J. Zhao. 2017. Detection of chemical additives in food using Raman chemical imaging system. *Chemical Journal of Chinese Universities*, 38(3): 369–375.

[14] Zhou, M. H., C. Y. Liao, Z. Y. Ren, H. M. Fan, and J. T. Bai. 2013. Bioimaging technologies based on surface-enhanced Raman spectroscopy and their applications. *Chinese Optics*, 6(5): 633–642.

[15] Zhou, Q., H. Q. Wang, and T. F. Lin. 2015. Research progress of laser Raman spectroscopy for the analysis and detection of specific substances in food. *Light Industry Science and Technology*, 2: 13–16.

Quick classification of agricultural science video in retrieval scenario

Li Jiaxuan[1,3], Yu Lina[2,4], Gao Wanlin[1,3*], Zhang Li[1,3], Feng Hui[1,3], Zhang Ganghong[1,3]

(1. *Key Laboratory of Agricultural Informatization Standardization, Ministry of Agriculture, Beijing 100083, China*;
2. *Institute of Semiconductor, Chinese Academy of Sciences, Beijing, 100083, China*;
3. *College of Information and Electrical Engineering, China Agricultural University, Beijing 100083, China*;
4. *School of Microelectronics, University of Chinese Academy of Sciences, Beijing, 100049, China*)

Abstract: Classification of audio plays an important role in a variety of multimedia applications, including audio retrieval, speech recognition, emotion analysis, etc. Therefore, many scholars have studied this area, but for different applications, classification should also focus on their differences. From the audio search perspective, we analyzed the differences between conventional and search-oriented classification, put emphasis on the speed. Then, pointed at the agricultural popular science video sound, we studied the structure and characteristic, and presented a fast filter algorithm FFA based on the rules. At last, we combined this algorithm with SVM so as to design a fast classification process, extract short-time energy, zero-crossing rate, spectral center of mass and other robust audio features, filter pure speech through silence feature and finish the rest classification by SVMs. By this two-step process experiments, we found that it could improve audio classification speed and be applied to the classification of the retrieval scene better. Although it is aimed at the agricultural knowledge audio, it can be used for the classification of not only speech-based audio, but also other kinds of audio with appropriate threshold changes.

Keywords: agricultural science video, retrieval scenario, audio classification, FFA, SVM

Citation: Li, J. X., L. N. Yu, W. L. Gao, L. Zhang, H. Feng, and G. H. Zhang. 2017. Quick classification of agricultural science video in retrieval scenario. International Agricultural Engineering Journal, 26(4): 314–322.

1 Introduction

Audio, as an extremely common data carrier, is an important part of multimedia. With the rapid development of the internet era, the popularization of agricultural popular knowledge has also undergone a great change. Agricultural Popular Knowledge Video (APKV) has been greatly welcomed by farmers. Compared with books, it is more intuitive and easy to understand, and has played a major role in the promotion of agricultural knowledge because of the lower requirements. Considering the large number of APKV, simple keyword retrieval is not enough, and there is a certain degree of cultural restrictions in this method, multi-mode video retrieval applications can greatly facilitate APKV retrieval. However, the multi-mode processing has high requirements for computer, which has a certain difficulty in the rural areas. Audio, as a one-dimensional data file which processes faster and requires less, is more suitable for APKV retrieval. There is now a video retrieval framework based on audio content, which uses the audio content to search for its video data (Jim, 2009.).

In audio retrieval, the classification of audio has always been an important step, the use of classification technology can reduce the total matching in the retrieval, as well as effectively improve the retrieval speed (Han et al., 2011). Many researchers in this area has done a lot of work, proposed different audio features and classification methods.

However, most of the researches on audio classification are independent, while the use of audio classification is various, including retrieval, speech recognition, speaker recognition, emotional analysis and other directions, audio classification and retrieval requirements are not combined

Received date: 2017-09-22 **Accepted date:** 2017-11-22
* **Corresponding author: Gao Wanlin,** PhD, Professor, Research interests: agricultural Informatization and application specific chip. College of Information and Electrical Engineering, China Agricultural University, Beijing 100083 P.R. China. Email: cau_szmtyjs@163.com, Tel: +86-010-62738536.

very well, the classification under retrieval scenario needs to consider the following aspects: First, the category of audio classification. The purpose of the audio classification is to divide the audio into a variety of fine and precise types, but in the retrieval scenario, classification also needs to ensure that the calculation time of audio classification is less than the directly similarity matching, if the categories are too many or the characteristics are too complex, classification will contrarily reduce the efficiency of the retrieval. Wold et al. (1996) classified the audio into 16 specific categories, but in audio retrieval of some particular type, it is difficult to find all categories, we only need to identify the main categories, and classify the remaining few categories as a broad category, as long as the collection can be reasonable divided. Second, the evaluation of audio classification. Most of the audio classification focused on the accuracy, so methods are often designed to be able to accurately identify the type of audio, but retrieval-oriented classification is different, the classification in retrieval is used to fragment the whole data into small sets, greatly reduce the retrieval matching and improve efficiency compared with the direct matching. Even if the recognition type is wrong, the retrieval is not affected if same audio contents of different files are identified in the same wrong set. Considering this extreme case: if the audio sample is a complete audio, then only a very short fragment of the same position of all the audio in the database can perfectly handle the retrieval, since all fragments of that location are in the same data set. Thus, the efficiency requirements for retrieval-oriented audio classification are higher than accuracy.

Based on this situation, this paper analyzed the characteristics of audio of APKV from the perspective of retrieval, and optimized, validated audio classification method. The specific structure is as follows: The first part introduced the APKV retrieval methods and discussed the difference between conventional and retrieval-oriented classification in audio retrieval. Detail research status in audio retrieval was presented in second part. In the third part, the characteristics of audio of APKV were analyzed, and the audio features with high distinction and high robustness were selected as the classification basis. The fourth part studied mute feature and put forward FFA based on it. In the fifth part, the FFA proposed ahead and SVM were merged into a fast classification process. The sixth part summarized the research and made some prospects of our work.

2 Research status

Audio classification is essentially a pattern recognition issue. It selects and models many extracted audio features and identifies audios with effective algorithms.

There are three main classify ideas: Based on single audio feature, which is seldom used now; Based on the feature vector, such as Audio Retrieval System(ARS) (Li and Li, 2000). There is also a method based on statistic features of audio features, which is the main direction of current and future research. This method uses some statistical learning algorithm, including Minimum Distance, Support Vector Machines, Neural Networks, Decision Tree, Hidden Markov Model and so on, to identify the audio type, provide an effective way for the realization of automatic and autonomous learning classification.

Foreign audio classification research carried out earlier. Wold et al. (1996) of the Muscle Fish company analyzed the audio loudness, pitch, brightness, harmonics and other distinguishing features of 409 sample data of ring tones, telephone sound, human voice and other 16 kinds, and designed audio classifier according to the nearest neighbor and Mahalanobis distance (Zhou et al., 2014). The 16 kinds of voice are often used as a later researcher's test data, such as Zhang (2015). Saunders (1996) used zero-crossing and short-term energy to classify voice and music in broadcast signals; Scheirer and Slaney (1997) used the 4Hz energy, zero-crossing rate, spectral center of mass and LPC cepstrum to divide the audio data into speech and music, Zhang et al. (2011) divided the audio signals in the television into three types: mute, signals containing music components and signals without music components, by means of short-term energy, zero-crossing rate, pitch frequency and spectral peak trajectory. And then the signals containing music components was been further divided into pure music, singing and music with background voice, the signals without music components

were been further divided into speech and noise.

The domestic research started relatively late, but also made some important progresses, one highlight is a system using HMM and semantic networks to detect critical audio events and reason the auditory context designed by Liu of the Microsoft Asian Research Institute (Liu et al., 2010). In addition, Lu et al. (2003) used MFCC, zero-crossing rate, short-time energy, spectral center of mass and spectrum width to propose three characteristics: spectral difference amplitude, sub-band period and noise frame ratio. The audio signal was divided into pure speech, non-speech, music, ambient sound and quiet. Zheng et al. (2006) proposed a large-scale quadratic fragmentation classification method, selected ten common audio features and used BP neural network for classification. In view of the agricultural field, Zhang et al. (2014) analyzed vegetable disease video, put forward "audio-based, video-supplemented" and made annotation for the speech part to get a good effect.

In the audio classification, the audio feature extraction is basic step. The extracted algorithm is divided into time domain analysis and frequency domain analysis. Among them, FFT (Fast Fourier transform) can convert the time signal to the frequency domain for analysis. In recent years, due to both shortcomings, people have been exploring the time-frequency domain analysis methods, Gabor and Haar wavelet transform are commonly used. Wu and Yan (2009) applied computer vision technology to the data stream process, generated audio fingerprints through Haar and Min Hash technology. Philips fingerprint features (Haitsma et al., 2002), as a classic high compression rate, high robust fingerprint extraction algorithm, also drew many researcher's attention, Zhao (2015) constructed an audio fingerprint based on Philips audio fingerprint extraction combined with ABV compression, designed filtering and retrieval classification algorithm. Jiang et al. (2005) of the Asian Institute of Asian Studies proposed new audio features such as noise rate and credit cycle to improve the recognition accuracy of ambient sound (Zhou et al., 2014). Zhang (2012) directly selected a part of the characteristics and indirectly expand the set of features through experiment to achieve a satisfactory classification accuracy of SVM.

As mentioned in the introduction, although the study of audio classification has been in-depth, most of researchers are focus on the accuracy, whether constructing new features, or the use of new methods, their purpose is to get high accuracy, but accuracy of classification is not the only decisive factor of retrieval efficiency. Meanwhile, there are not many targeted researches on audio classification, and there are few researches on AKPV's audio. For different audio scenes, the content of audio has the corresponding self-characteristics.

3 Materials and method

3.1 Structure analysis

APKV is voice-based, speech, speech with background music, speech with noisy, such as interviews all have a certain probability (Wold et al., 1996). Meanwhile, music and the environmental sound, as a supplement for the voice content, will not occupy too much proportion, so the probability of been retrieved is also lower than the voice part. Therefore, from the perspective of retrieval, the agricultural knowledge video audio is divided into mute, speech, non-speech (with music voice, noisy voice) and non-voice (music, noise). Music and noise are no longer further distinguished, mainly considering the following aspects:

- Compared with the voice type, the number of music and noise accounted for less, even as one set will not cause two much time loss.
- The distinction between music and noise also requires the addition of an SVM classifier, as well as the extraction of more features, so the time spent by the classification maybe more than the direct matching.
- Music and noise have one similarity, that is, they do not contain any voice signals.

Through this classification structure, we can ensure that sizes of sets of each type are average as much as possible, so there will not be too different for audio retrieval efficiency of different types.

There are many kinds of classification algorithms, the most traditional one is based on the rules to identify the type, fast but easy to produce "snowball effect", mostly used for mute recognition now. In the field of data mining,

a variety of classification algorithms are proposed. SVM is used as classifier in this paper to classify audio, which has been widely used in audio classification. Considering the requirements of the retrieval scenario, the classification speed is more important than the classification accuracy. We will focus on the mute, first analyze and identify the mute feature, and then quickly filter a part of the speech fragment through it, thus reduce the job of follow-up classification to achieve the purpose of speeding up. The specific algorithm will be described in detail later.

3.2 Feature extraction

In the process of audio classification, many scholars have proposed a large number of audio features, different audio features for different audio types have different effects (Li and Li , 2000), so it is necessary to consider the type of the research object while selecting audio features.

In the light of the previous study, we selected the following audio features as the basis for classification:

- Time domain

1) Short Time Energy (STE) and Lower STE Ratio (LSTER)

The energy of the audio signal changes significantly over time, and STE can reflect this change well. It is a time domain frame feature that represents the average energy of the signal points collected in an audio frame. The formula for calculating $STE(i)$ of the i-th frame is:

$$STE(i)=\sum_{n=0}^{L-1} x_i(n)^2,\ \ 1\le i\le M \tag{1}$$

where, x_i is the sequence of sample points in one frame after the original data has been framed; M is the total number of frames, and L is length of one frame.

LSTER is a time-domain feature based on STE: the proportion of frames with STE less than 0.5 times the average STE in one fragment. LSTER can well reflect STE fluctuations of an audio. Compared to voice, music's STE variance is not large, and the LSTER is lower.

2) Zero Cross Ratio (ZCR) and high ZCR Ratio (HZCRR)

ZCR is the fastest feature in the audio feature, which represents the number of times the signal waveform passes through the zero point in a window. It is a time-domain frame feature that reflects the signal's zero crossing speed and frequency. ZCR (i) of the i-th frame is expressed by Equation (2):

$$ZCR(i)=\frac{1}{2}\sum_{n=0}^{L-1}|sgn[x_i(n)]-sgn[x_i(n-1)]|,\ 1\le i\le M \tag{2}$$

where, $sgn(x)$ is a sign function, in the specific programming often through the adjacent sampling point product to produce positive and negative to represent.

HZCRR is a time domain fragment feature based on ZCR: In one audio fragment, the proportion of frames with ZCR 1.5 times higher than the average ZCR, which reflects ZCR fluctuations.

In practical applications, the detection of mute frame often finished through STE and ZCR, when the background sound is small, STE is more accurate, while ZCR is better under large background sound (Han et al., 2011).

- Frequency domain

After the Fast Fourier Transform, the spectrum of the signal can be obtained. On this basis, the following commonly used spectral characteristics are extracted:

1) Spectral Centroid (SC)

SC is a relatively common frequency domain frame feature, also known as audio brightness, refers to the center of gravity in the spectrum of all the frequencies contained in a frame, with the formula said as follows:

$$SC(i)=\int_0^{\omega_0}\frac{\omega|F_i(w)|^2\,d\omega}{|F_i(w)|^2\,d\omega} \tag{3}$$

SC reflects the spectral energy characteristics of the frame, the spectrum energy of the music is higher than that of the speech, so SC is also higher. Besides, voice, as a set of phonemes with different spectral energy, has more SC changes, while music's and noise's SC is more stable in a period. In this paper, we used the variance of SC in one audio fragment to distinguish voice and non-voice.

2) Sub-band Energy Distribution (SED)

In this paper, the frequency domain is devided into four sub-bands: $\left[0,\frac{\omega_0}{8}\right]$, $\left[\frac{\omega_0}{8},\frac{\omega_0}{4}\right]$, $\left[\frac{\omega_0}{4},\frac{\omega_0}{2}\right]$, $\left[\frac{\omega_0}{8},\omega_0\right]$, and then calculate the energy ratio of each sub-band:

$$SED(i)=\frac{1}{E}\int_{L_j}^{H_j}|F_i(\omega)|^2\,d\omega \tag{4}$$

where, E is the spectral energy of frame:

$$E(i) = \int_0^{\omega_0} |F_i(w)|^2 \, d\omega \quad (5)$$

and H_j, L_j is the upper and lower frequency boundaries of the sub-band.

SED reflects the distribution of frequency energy in each sub-band, and the sub-band energy distribution of music and speech is different. The frequency domain energy of music is evenly distributed in each sub-band.

3.3 Normalization

Because of the large difference between the value of different features, all the eigenvalues are normalized to eliminate the difference:

$$x_i' = \frac{x_i - \mu_i}{\sigma_i} \quad (6)$$

where, x_i is the i-th original value; μ_i is the mean; σ_i is the variance.

For the frequency domain frame feature in the above, this paper unified the average and standard deviation of all frame features in a fragment as the frequency domain fragment feature, and the audio fragment is the smallest processing unit of classification. The main purpose of this paper is to verify the effectiveness of fast filter, therefore we did not extract too many features.

3.4 Audio classification

SVM is a two-class algorithm. For multi-type classification of audio, it is common practice to construct multiple SVMs to determine the type in turn by tree structure (Lu et al., 2003; Jiang et al., 2005; Bai et al., 2005). Considering the rules-based approach can be better and faster to identify the mute, many literatures set the threshold to identify the mute section first, and then use SVM to finish follow-up identification for non-mute fragments.

In the classification, the handling of the mute section is generally direct discard after identified, because the mute does not contain any useful information. But in the retrieval scene, the length of the mute, the distribution of its length, etc. are also useful. In the current circumstances, mute recognition has been able to be fast and accurate, the direct discarding of mute is a lot of waste. In this scenario, that is, APKV audio retrieval or voice-based audio retrieval like it, mute to a certain extent means the emergence of speech, reasonable use of mute information can effectively reduce the number of fragments required for the classifier to be processed, thereby increasing the speed of classification.

Mute is divided into two types according to the scene: one is used to transition different audio types or theme paragraphs, be classified as mute section, this mute type time generally will not be more than 2 s (Wold et al., 1996); the other one is the pause when the speaker stops during reading, be classified as mute pause. Compared with the mute section, this type of mute is generally shorter, ranges from dozens of frames to hundreds of frames, and basically appears in pure speech fragments, a few will appear in music. However, on one hand, in the APKV audio, pure music is generally classical, gentle music, which is basically continuous and will not appear mute pause; on the other hand, pure music is generally used as background of the display part of the pictures, the time will not be too long, even if there is a small system of low frequency, therefore, we believe that high frequency continuous mute pause will only appear in the speech fragment.

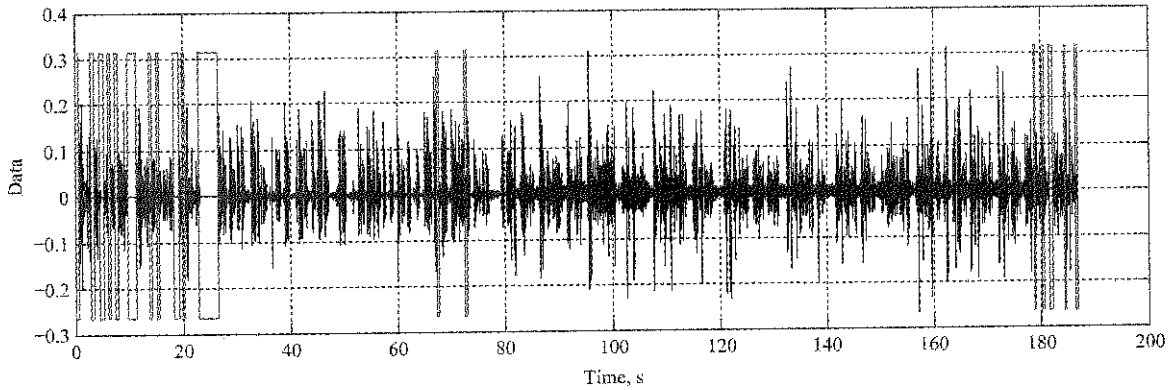

Figure 1 Continuous mute pause detection

In addition to speech, APKV voice also includes voice with background and with music, we selected a paragraph contains three types of audio clips for continuous mute pause detection, of which only 25 before and 175 after were speech fragments. Fragments inside red rectangles were recognized as a mute pause, you can find that most of mute pauses located in the speech fragment, and their interval was very short.

Based on this, this paper proposed Fast Filter Algorithm to quickly filter out part of pure speech fragments through the mute pause structure, thus reducing the number of fragments that SVM needed to identify. FFA was described as follows:

- Loaded audio file, extracted STE;
- Used STE dynamic threshold (Zhang et al., 2012) to identify a single mute frame, a continuous mute that accumulates more than 20 frames was defined as a mute pause, recorded start frame number sequence "Start" and end frame number sequence "End" of mute pause;
- Calculated the first order difference sequence of Start, named "Gap";
- Iterated through Gap, found points over 500 and saved their locations as sequence "NonPure";
- Defined pure speech fragment position matrix Pure n*2, each line of which could determine a speech fragment, and initialized it:

$$Pure = [1, NonPure(1)-1];$$

- Iterated through NonPure, if the number of mute pause between two jump points was more than three times, filtered the non-jump area as pure speech fragments:

$$Pure = [Pure; NonPure(i), NonPure(i+1)-1];$$

- If the last jump point was not the last mute pause, then made it complete:

$$Pure = [Pure; NonPure(end), length(Start)];$$

- According to the Start and End positions of each row in the pure sequence, the pure speech is extracted from the corresponding place;

We used the FFA to screen pure speech fragments of the audio file as we had used before, the result is shown in Figure 2, while flow chart of the FFA is shown in Figure 3.

The main time-consuming method of this algorithm is to extract STE, which can be used directly in the later classification, the rest of the algorithms are mainly simple logic judgment, so the overall process will not cause too much time. The traditional method of classification also needs to identify the quiet section, so this method can be well integrated into the traditional one.

Since the dynamic threshold parameter is set according to the experiment and can't be adapted to the whole case, there is still a partial recognition error, but this error is predictable. As long as the same threshold parameter is used at the time of retrieval, the same error can be generated, the retrieval results will not be affected. This paper does not discuss the retrieval method.

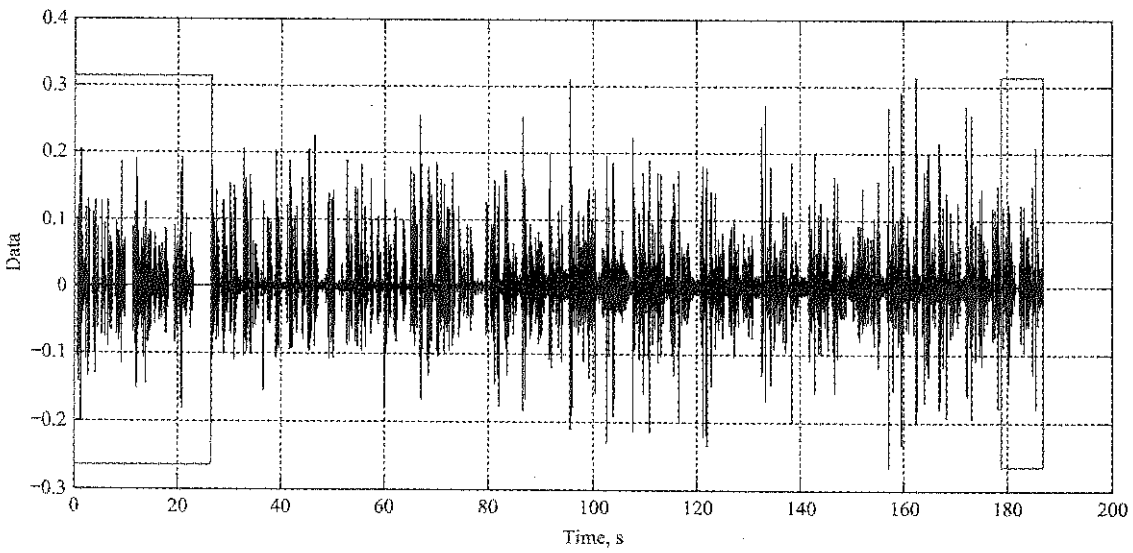

Figure 2 Pure speech filter

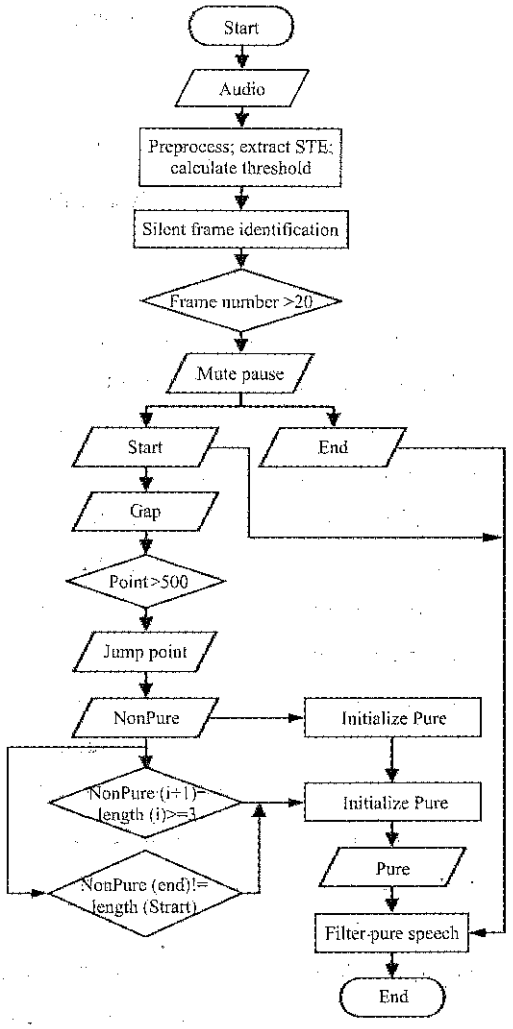

Figure 3 Fast filter algorithm

Considering that FFA may miss some of the speech, it is necessary to train two SVM classifiers. SVM1 is used to judge whether the voice component is included. SVM2 is used to judge whether it is a speech. First through the SVM1 to identify the non-voice type, and then through SVM2 to determine whether the remain is a speech.

It is generally to use the same length of the audio sub-fragment as the SVM object, the longer the fragment is, the better but slower the classification will be, and the classifier has nothing to do with it (Zheng et al., 2006). In addition, as the length of the retrieval target increases, the retrieval rate decreases linearly (Bai et al., 2005), considering the commonly used audio fragment length is 1 s. In the literature (Lu et al., 2003), and through experiments, the authors showed that although in general cases the longer the better effect, while there is a special case, for speech and non-speech recognition 0.3 s is the best. Based on this, this paper proposesd a variable fragmentation method, which used 1.2 s audio fragment in SVM1 processing. After distinguishing the fragment containing the speech, the audio fragment of 0.3 s was selected as the SVM2 object. There is no need to reread the data to extract features, only need to recalculate the standard deviation, mean and other statistical features of those fragments through the SVM2. In addition, the speed of 0.3 s audio fragment classification would be higher than 1.2 s, so this would not consume too much time.

Before the audio classification, the original audio data needed pre-processing, the experimental audio data used in this sample sampling rate of 44.1 KHZ, format wav, length of 30 minutes. First, the original data were extracted mono, and then down to 8 KHZ, pre-emphasis, plus Han Ming window frame, frame length 25 ms (200 sampling points), the frame shift 50% (100 sampling points). In the use of SVM, audio also needed to be divided into 1.2 s (95 frames), 0.3 s (23 frames) of the smallest classification unit, the audio fragment did not overlap.

Finally, this paper combined FFA and general classification method to design a classification process which is suitable for APKV audio retrieval. As shown in Figure 4, silence fragments and speech fragment identified in the above steps were eliminated, the remaining fragments were divided into sub-fragments, through the pre-trained SVM classifier to identify, and ultimately divided into four categories: mute, speech, non-speech, non-voice.

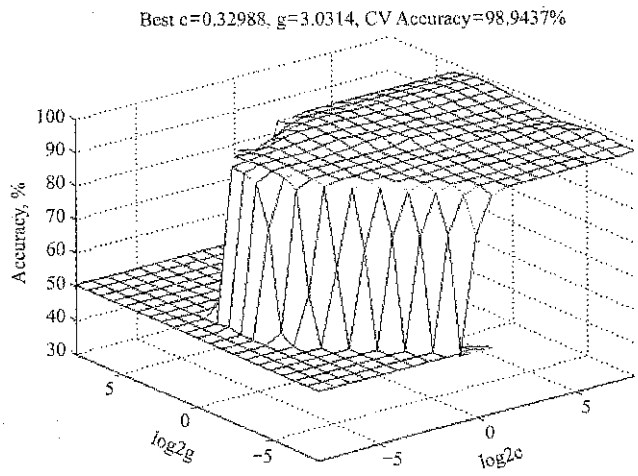

Figure 4 Parameter Cross Validation

4 Results and discussion

FFA improved the efficiency of classification mainly by reducing the subsequent SVM sample number need

recognition, so the impact on SVM1 was relatively large, and the impact of SVM2 was very small, we only concerned about its impact on the SVM1, so categories were only refined to pure-voice, non-voice, and segments contain voice identified by SVM1.

The experimental audio sources were extracted using Cool Edit software, mainly from seed industry, animal husbandry, aquaculture and other areas of agricultural science video data. The original data was dual channel, 44.1 KHZ, .wav format, totally about 30 minutes, and basically type of it was pure voice, meanwhile there was few non-voice and non-pure, which was agricultural science video' s common structure. Before the audio classification, the original audio data needed pre-processing, first, the original data were extracted mono, and then down to 8KHZ, pre-emphasis, plus Han Ming window frame, frame length 25 ms (200 sampling points), the frame shift 50% (100 sampling points). In the use of SVM1, audio also needed to be divided into 1.2 s (95 frames), the smallest classification unit, the audio segment did not overlap. Finally, we got about 1800 segments, the type of each audio segment was determined by the most significant type.

In order to investigate the effect of FFA, this paper designed three experiments. Experiment A only used FFA to filter pure voice; Experiment B only used SVM1 to identify whether the test data contains voice; Experiment C used FFA to filter pure voice segments of the original data, and then the subsequent identification of the remaining part was finished by SVM1.

We used the RBF radial basis function as the kernel function of SVM1, the training data were extracted from several videos and divided into two parts, one part of the manual segmentation of different types was as training data and the other part was as test set. In training, the kernel function parameter was determined by random grouping cross validation, and the 21-dimension feature vector discussed before used as the input of classifier.

The first experiment showed the filter effect of FFA, which is displayed in Table 1.

Where accuracy is calculated by Equation (7):

$$\text{Accuracy} = \frac{\text{Correct Results}}{\text{Correct Results} + \text{Wrong Results}} \quad (7)$$

Table 1 Result of experiment A

Type \ Result	Correct (frame)	Wrong (frame)	Accuracy
Pure voice	128196	176	99.9%
Non-pure	11706	1796	87.3%

The correct accuracy of FFA is almost 100%, which shows that our method to filter pure voice is effective, meanwhile, the non-pure accuracy is relatively low, but still reached 87%. This result means that FFA can perfectly filter pure voice, but there is probability that some pure voice segment is undetected, which needs further classified by SVM.

Experiments B and C are compared by the accuracy and the numbers of segments SVM1 needs processing:

Table 2 Comparison of experiments B and C

Type \ Value	Accuracy	SVM1 process number
B	91.95%	1788
C	97.88%	157

The most significant improvement of C is that SVM1 only needs to handle quite few segments, which can improve the classification speed especially when the original number is huge. However, after the FFA, the SVM accuracy may be reduced a little, around 80%, which means the pure speech FFA missed is also hard to be recognized correctly by SVM, but if we consider the correct segments FFA already recognized, the total accuracy of classification can reach about 98%, which is a marked improvement.

5 Conclusion

In this paper, we focused on the problem that the current audio classification research relevance is not obvious and practical value is not high, analyzed the emphasis of audio classification under retrieval scenario, that is, the speed is more important than the accurate. Then, according to the characteristics of agricultural science video audio, divided it into four types of mute, pure voice, non-pure voice and non-voice. Then, considering its pure voice-based feature, we proposed a fast filter algorithm FFA based on the mute feature, accelerated the follow-up classification speed by reducing the number of classification fragments, and designed a rapid classification process by combining this algorithm with SVM, using variable length audio segmentation to

improve the recognition accuracy, so as to ensure good accuracy on the basis of efficiency, made the audio classification be better applied to agricultural science video retrieval. Verified by experiments, FFA can achieve good filter effect, as well as improve SVM classification capacity.

In the future research work, we can try to use machine learning method to replace this enlightenment algorithm FFA, analyze pure voice quiet pause pattern to make more accurate filtering. Secondly, we can optimize the experiment for the rapid screening algorithm and design the audio and video retrieval method objectively, so as to further improve the accuracy of video retrieval when the rate is guaranteed.

Acknowledgments

The authors would like to thank their colleagues for their support of this work. The detailed comments from the anonymous reviewers were gratefully acknowledged. This work was supported by the National Spark Program Key Project (Grant#:2015GA600002).

[References]

[1] Bai, L., S. Y. Lao, J. Y. Chen. 2005. Audio classification and fragmentation based on support vector machines. *Computer Knowledge,* 32(4): 87–90.

[2] Fu, Z. T., Y. Su, L. Zhang, and X. Li. 2013. Method of video fragmentation for vegetable disease based on self-adaptive dual thresholds. *Transactions of the Chinese Society of Agricultural Engineering,* 29(9): 148–155.

[3] Haitsma, J., T. Kalker, and J. Oostveen. 2002. An efficient database retrieval strategy for audio fingerprinting. *2002 IEEE Workshop on Multimedia Signal Processing. IEEE,* 2002: 178–181. St. Thomas, VI, USA, Dec. 9-11.

[4] Han, J. Q., Y. R. Zheng, and G. B. Zheng. 2011. *Theory and Technology of Audio Information Retrieval.* Beijing: Science Press.

[5] Li, G. H., and H. F. Li. 2000. Audio retrieval based on content: concept and approaches. *Mini-micro System,* 11: 1173–1177.

[6] Li, H. F., and G. H. Li. 2000. Content-based audio retrieval classification. *Computer Engineering and Applications,* 36(7): 54–56.

[7] Jiang, H. C., W. Liang., S. W. Zhang, B. Xu. 2005. Audio feature extraction and analysis for audio scene classification. *National Conference on Man-Machine Speech Communication,* Beijing.

[8] Jim, Z. S. 2009. Video content retrieval based on audio. M.S. thesis. Shanghai Jiao Tong University, Shanghai.

[9] Li, X. X., C. D. Liu, H. Wen, Y. Su, Z. Fu, and L. Zhang. 2015. Video semantic annotation and fragmentation method of vegetable disease knowledge based on voice recognition. *Transactions of the Chinese Society for Agricultural Machinery,* 46(9): 308–313.

[10] Liu, Z., Y. Wang, and T. Chen. 2010. Audio feature extraction and analysis for scene fragmentation and classification. *Journal of VLSI Signal Processing,* 20(1): 61–79.

[11] Lu, L., H. J. Zhang, and S. Z. Li. 2003. Content-based audio classification and fragmentation by using support vector machines. *Multimedia Systems,* 8(6): 482–492.

[12] Saunders, J. 1996. Real-time discrimination of broadcast speech/music. *IEEE International Conference on Acoustics, Speech, and Signal Processing,* 1996. Icassp-96. *Conference Proceedings.* IEEE, 2: 993–996, May 07-10.

[13] Scheirer, E., and M. Slaney. 1997. Construction and evaluation of a robust multi-feature speech/music discriminator. *IEEE International Conference on Acoustics, Speech, and Signal Processing.* 2: 1331–1334. Munich, Germany, Apr. 21-24.

[14] Wold, E., T. Blum, D. Keislar, and J. Wheaten. 1996. Content-based classification, retrieval, and retrieval of audio. *IEEE Multimedia,* 3(3): 27–36.

[15] Wu, X. T., and D. Q. Yan. 2009. Analysis and research on method of data dimensionality reduction. *Application Research of Computers,* 26(8): 2832–2835.

[16] Zhang, L. X., Y. Y. Chen, D. L. Li, Z. T. Fu, and X. X. Li. 2014. Video fragmentation method for agricultural knowledge video call center. *Transactions of the Chinese Society of Agricultural Engineering,* 30(11): 188–194. (In Chinese with English abstract).

[17] Zhang, Q. 2012. The construction of a network audio data classification label marking and reprocessing system. M.S. thesis. Haerbin Institute of Technology, Heilongjiang.

[18] Zhang, T., and C. J. Kuo. 2001. Audio content analysis for online audiovisual data fragmentation and classification. *IEEE Transactions on Speech & Audio Processing,* 9(4): 441–457.

[19] Zhang, X. Y. 2015. Research on acoustic feature analysis in audio retrieval. Ph.D. diss. South China University of Technology, Guangzhou.

[20] Zhang, X. Y., Q. H. He, Y. X. Li, and W. L. Ye. 2012. An inverted index based audio retrieval method. *Journal of Electronics & Information Technology,* 34(11): 2561–2567.

[21] Zhao, J. 2015. Content-based intelligent retrieval repetitive detection of mass audio. M.S. thesis. Taiyuan University of Technology, Shanxi.

[22] Zheng, G. B., J. Q. Han, H. F. Li. 2005. Fragmentation-based audio retrieval algorithm. *Computer Knowledge,* 32(3): 73–75.

[23] Zheng, Y. B., J. Zhou, Z. Q. Bian, and D. Zhang. 2006. A two-stage content-based audio fragmentation algorithm. *Chinese Journal of Computers,* 29(3): 457–465.

[24] Zhou, M. Q., G. H. Geng, X. F. Wang. 2014. *Audio Retrieval Based on Content.* Beijing: Science Press.

Intelligent ammonia nitrogen online monitoring system

Wei Yaoguang[1,2*], Zhang Fan[1,2], Zhang Xu[1,2], Li Daoliang[1,2]

(1. *College of Information and Electrical Engineering, China Agricultural University, Beijing, China*;
2. *Beijing Engineering Technology Research Center of Internet of things in Agriculture, Beijing, China*)

Abstract: For aquaculture, ammonia nitrogen is one of the important water quality parameters, which has a significant impact on the growth and reproduction of aquatic organisms. Because the content of the ammonia nitrogen changed dynamically, it needs monitoring the content of ammonia nitrogen in aquaculture ponds on-line. However, the traditional ammonia detection methods are complex and difficult to realize on-line monitoring. An intelligent ammonia nitrogen online monitoring system has been proposed in this paper. The system is composed of sampling module, detection module, signal transmission module, calibration module and control module. The sampling module can automatically take water samples. The detection module includes the probe of pH and ammonia and detection reagents. It converts the ammonia nitrogen ion into free ammonia and detects the content of ammonia, which can reflect the concentration of ammonia nitrogen in water. The signal transmission module transmits the output of the ammonia probe into digital signal. The calibration module realized the intelligent calibration of temperature. The control module can automatic control the sampling and detection process. Compared with the traditional systems, the system can realize self-cleaning, self-calibration, field-testing and intelligent compensation. Furthermore, it can realize real-time measurement, avoid sample pretreatment, perform automatic compensation correction, and possess an anti-interference capability. The experimental results have shown that it has high stability, reliability and low error.

Keywords: aquaculture, ammonia nitrogen, on-line monitoring, intelligent compensation

Citation: Wei, Y. G., F. Zhang, X. Zhang, and D. L. Li. 2017. Intelligent ammonia nitrogen online monitoring system. International Agricultural Engineering Journal, 26(4): 323–331.

1 Introduction

Ammonia nitrogen is produced by the accumulation and decomposition of aquatic animal bodies and waste baits (Higgins, 2013). Free ammonia in water is harmful to the health of aquatic (Zhang et al., 2010). Free ammonia can cause breathing difficulties and other health problems among aquatic organisms, resulting in reduction in fish yield and considerable losses to fish cultivators. Existing test methods are mainly laboratory tests whose procedures are complex, laborious, time consuming, and expensive. Most importantly, the requirements of online monitoring and controlling in aquaculture are difficult to meet by laboratory-based methods, which can hardly realize rapid, precise, and real-time monitoring in situ. Fish farmers are in need of equipment for real-time monitoring of water quality. Therefore, the content of ammonia nitrogen in water has aroused significant interest among experts (Li, 2011).

In early of 1980s, USA, Canada, and other countries that are advanced in aquaculture, employed online water quality monitoring and automatic control technologies for the monitoring of ammonia nitrogen, realized the goals of high yield and high quality of aquaculture (Ruan et al., 2016). The common online methods include spectrophotometry and the electrode method. Spectrophotometry is commonly used in ammonia nitrogen determination. It mainly includes Nessler's reagent photometry, salicylic acid–hypochlorite colorimetric method, and indophenol blue method. However, spectrophotometry methods are easily influenced by turbidity and the presence of calcium, magnesium, and other metal ions. Thus, the accuracy and reliability of this type of detection method still need to be improved. Furthermore, the operating procedures of

Received date: 2017-09-22 **Accepted date:** 2017-11-22

* **Corresponding author: Wei Yaoguang,** Associated Professor, Research interest: Internet of things in Agriculture. Address: China Agricultural University, Beijing, 100083, China. Email: wyg@cau.edu.cn.

spectrophotometric methods and the structure of light source in these methods are also complex. SERES 1000 (France) and Bran+Luebbe M020 (Germany) are both detection instruments based on spectrophotometry. SERES 2000 (France), WTW TresCon (Germany), and YSI 6820 (USA) are detection instruments based on the electrode method. In recent years, the ammonia-sensitive electrodes, instead of ion-selective electrodes, detect ammonia nitrogen by the electrode method. The ammonia-sensitive electrode method improves the precision of ammonia detection (Jia et al., 2011). In addition, the electrode method can realize continuous and automatic detection of ammonia nitrogen content and demonstrate strong anti-interference capability, simple operation, wide measurement range, and automatic calibration (Wang et al., 2015; Qing et al., 2015).

Although the concentration of ammonia nitrogen in water influenced by pH, temperature, and ion concentration, the existed measurement methods do not take into account of the automatic compensation and correction of the effects of these factors. In addition, detection must be conducted when the pH value of a solution is higher than 11. However, the pH value of aquaculture water should be maintained between 6.5 and 8.5 for the health fish. Therefore, the monitoring system requires an automatic sampling device. Moreover, the system also needs an automatic cleaning device to allow for repeated detection.

The existing online ammonia nitrogen monitoring systems cannot meet these requirements. Accordingly, such a system with an ammonia-sensitive electrode was designed in this study to realize high-precision detection, real-time monitoring, multiparameter composite detection, and automatic compensation. Achievements in the online monitoring of the aquaculture environment are the basis for the standardization and intellectualization of monitoring; thus, these achievements can contribute to the sustainable development of the aquaculture industry (Xie et al., 2016).

2 Design of online ammonia nitrogen monitoring system

2.1 Overall framework

The framework of online ammonia nitrogen monitoring system designed in this paper is shown in Figure 1. The system is composed of a sampling module, calibration module, detection module, signal transmission module, control module and liquid waste processing module. The sampling module is to obtain aquaculture water sample for detection. The calibration module is to calibrate the ammonia-sensitive electrode and acquire the electrode potential slope. The detection module is to mix the sample being detected with sodium hydroxide solution (NaOH) and detect the ammonia nitrogen concentration in the sample by the compound sensor, as well as the temperature and pH of the mixed liquid. The signal transmission module is for processing signals, including voltage regulation, signal filtering, amplification, and zero adjustment. The control module is to calculate the concentration of ammonia nitrogen with the use of the voltage signal which gets from the signal transmission module, control the valve set switch according to the signals of liquid-level sensor in the reagent bottles, and manage the working process of the system. The liquid waste processing module handles the liquid waste after measurement to reduce environmental pollution and the emission of toxic substances.

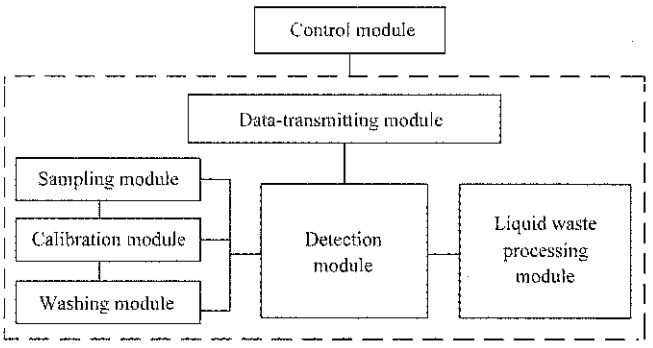

Figure 1 Structural framework of the online ammonia nitrogen monitoring system

The detection work cycle of the system includes cleaning, calibration of the ammonia-sensitive electrode, field sampling, detection of the concentration of ammonia nitrogen, liquid waste treatment and cleaning. Figure 2 showed the schematic diagram of the proposed system.

First, the monitoring system and cleaning system are turned on to ensure the accuracy of subsequent measurements. Second, the controller activates peristaltic pump 1 and opens port B of electromagnetic valve 2, port A of electromagnetic valve 3, and port A of

electromagnetic valve 4. Third, the lotion is used to clean the pipe and detection device and then discharged from the lower channel of the detection device after cleaning is completed.

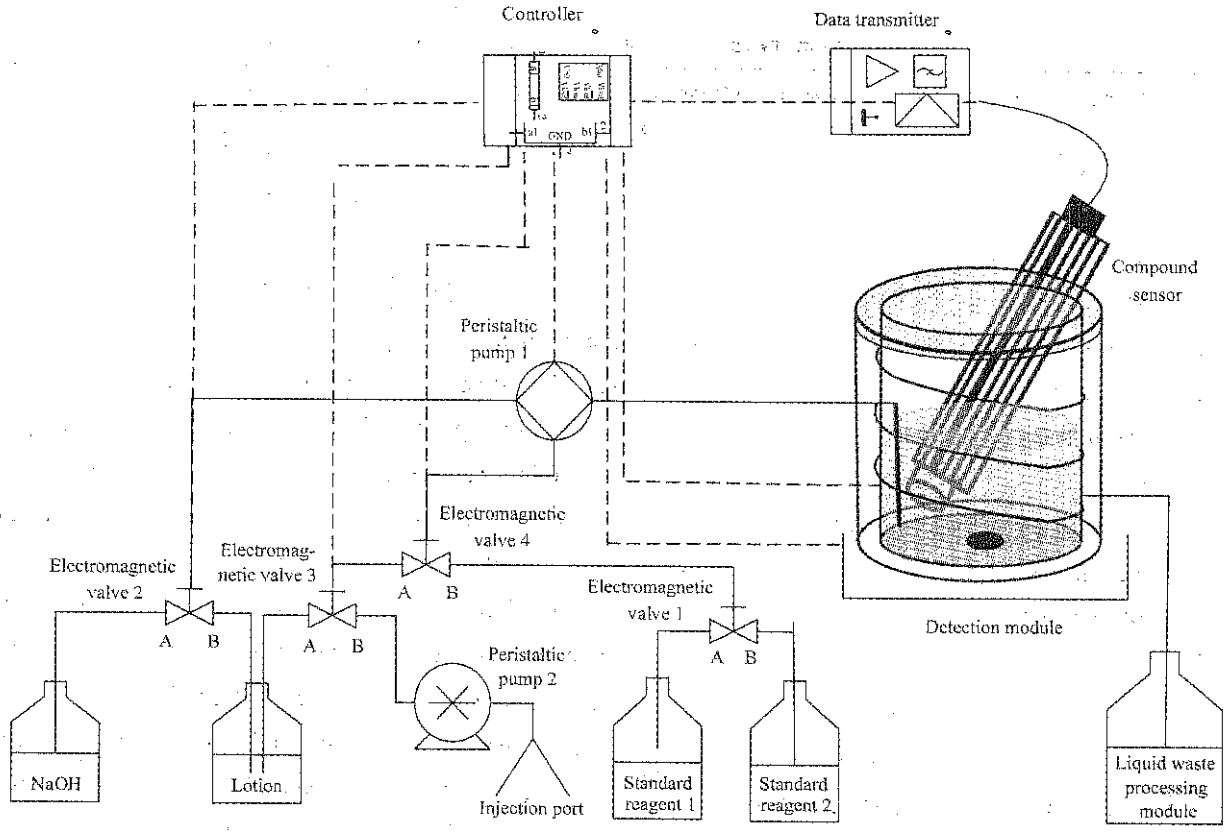

Figure 2 Schematic diagram of the online ammonia nitrogen monitoring system

The calibration of the ammonia-sensitive electrode starts after the initial completion of cleaning. First, peristaltic pump 1, port A of electromagnetic valve 1, and port B of electromagnetic valve 4 are opened, and 10 mL of a standard reagent is extracted by the liquid-level sensor. Second, electromagnetic valve 1 is shut off, port A of electromagnetic valve 2 is opened, and then the reagent is extracted and placed into the detection device. When the pH of the solution in the detection device is higher than 12, as measured by the pH electrode, electromagnetic valve 2 is shut off. Third, the thermostat is opened to maintain the temperature at 25°C, and the stirring device is activated. The reagent (NaOH) completely reacts with standard reagent 1 to transform all the ammonia nitrogen into free ammonia (NH3). Fourth, the signal for ammonia concentration, which is measured by the ammonia-sensitive electrode, is sent to the controller after being processed by the signal transmission module. The controller then records the voltage. After the completion of the detection, the wastewater is exported to the wastewater tank. Finally, the cleaning process is repeated. The calibration process of standard reagent 2 is similar to that of standard reagent 1. The calibration curve of the voltage and concentration of ammonia nitrogen are generated according to the voltage values of standard reagents 1 and 2, as measured by the ammonia-sensitive electrode.

After the second round of calibration and cleaning, the system initiates in situ sampling and the measurement of ammonia nitrogen concentration in the sample. The controller activates peristaltic pumps 1 and 2, turns on port B of electromagnetic valve 3 and port A of electromagnetic valve 4. After 10 mL samples are extracted from the fishpond into the detection device, the controller closes peristaltic pump 2 and electromagnetic valve 4 to complete the sampling process. The subsequent processes are similar to the calibration of standard reagent 1. A calibration curve is generated to reveal the ammonia nitrogen concentration of the sample. The electromagnetic valves are immediately shut off as soon as all of the aforementioned processes have been completed to prevent the reaction-induced NH3 from flowing back to the reagent containers and causing an inaccurate measurement.

Table 1 showed the on–off states of the electromagnetic valves and peristaltic pumps in each step.

The electromagnetic valves undergo three states, A: open port A of electromagnetic valve; B: open port A of electromagnetic valve; C: close the electromagnetic valves. Peristaltic pumps have two states: √: on; ×: off.

Table 1 On–off states of the controlled devices in the system

	Electromagnetic valve 1	Electromagnetic valve 2	Electromagnetic valve 3	Electromagnetic valve 4	Peristaltic pump 1	Peristaltic pump 2
Cleaning	O	B	A	A	√	×
Calibration	A	A	O	B	√	×
	B	A	O	B	√	×
Measurement	O	A	B	A	√	√

2.2 Design of detection module

The concentration of ammonia nitrogen in water can be measured by calculating the potential difference between the indicator electrode (glass electrode) and the reference electrode (silver–silver chloride electrode). As shown in Equation (1), the potential difference between two electrodes and the measured molar concentration of the ammonia solution has a logarithmic relationship (Chang, 2004).

$$E = E_0 - S * \lg[NH_3]_s \quad (1)$$

where, E_0 is the standard potential difference.

However, the ammonia nitrogen content in water is in the form of free ammonia NH3 and ammonium ion NH_4^+ chemical combination with a certain amount of nitrogen (Zhang et al., 2016; Temple-Boyer et al., 2009). Therefore, it added a sodium hydroxide solution (NaOH) to the aqueous sample to increase the pH to 11 or higher to convert the ammonium salts into free ammonia (NH_3) (Xing et al., 2013; Liu et al., 2007). The relative contents of free ammonia and ammonium ions in water depend on the temperature and pH value of the test sample, the relative contents of free ammonia and ammonium ions can be determined theoretically according to Equation (2). The ionization equilibrium constant of ammonia in water, *pKs*, is affected by temperature.

$$\frac{[NH_4^+]_s}{[NH_3]_s} = 10^{pKs-pH} \quad (2)$$

Ks is the ionization equilibrium constant of ammonia in sample, that $pKs = -\lg Ks = 9.3$ (when the temperature is 25°C and the ionic strength is 0.1); $[NH_3]$ S and $[NH_4^+]$ S are the concentrations of NH_3 and NH_4^+ in sample, respectively.

From Equation (2), we can conclude that nearly all the ammonium ions are converted into free ammonia when the temperature is 25°C, and the pH value is higher than 11 in the sample.

2.3 Design of signal transmission module

In this paper, the ammonia-sensitive composite electrode was selected to detect ammonia. Because the output of the ammonia-sensitive electrode is weak and has high output impedance characteristics, thus, the signal transmission module initially performs impedance matching. Meanwhile, the power of the transmission circuit produced a 50 Hz signal and influenced the output signal of the electrode. Then, a low-pass filter circuit was designed, which is composed of a second-order low-pass filter and a voltage follower to filter the jamming signal after impedance matching (Yang et al, 2010). Moreover, because the differential amplifier circuit is not completely symmetrical, the severe offset voltage and offset current can induce the zero-drift phenomenon. A zeroing circuit was designed to suppress the zero-drift phenomenon. In theory, the starting point of the output voltage of the ammonia-sensitive electrode is zero. As shown in Figure 3, the impedance-matching circuit is composed of an LMC7111 voltage follower, and the low-pass filter circuit and zeroing circuit are composed of low-power operational amplifier TLC27L4.

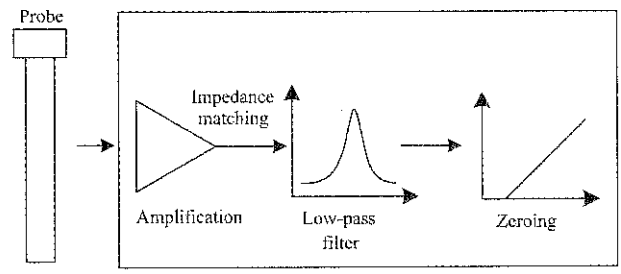

Figure 3 Overall structure of the signal transmission module

2.4 Design of control module

The output of the sensing probe was processed (amplification, filtering, and zeroing) and transformed into

a range of output voltages. After A/D conversion, the control module calculates the corresponding ammonia nitrogen concentration by using the output voltage (Geng, 2002; Hou et al, 2009). In addition, the A/D ports of the control chip also receive the signals from the temperature sensors and liquid-level sensor. The control module also controls the switch states of the electromagnetic valves, peristaltic pumps, magnetic stirrer, and the drive circuits of these components (Liu, 2010). In this paper, the control function of the system is realized by using microprocessor STM8L152C8. The overall structural diagram of the control module is shown in Figure 4.

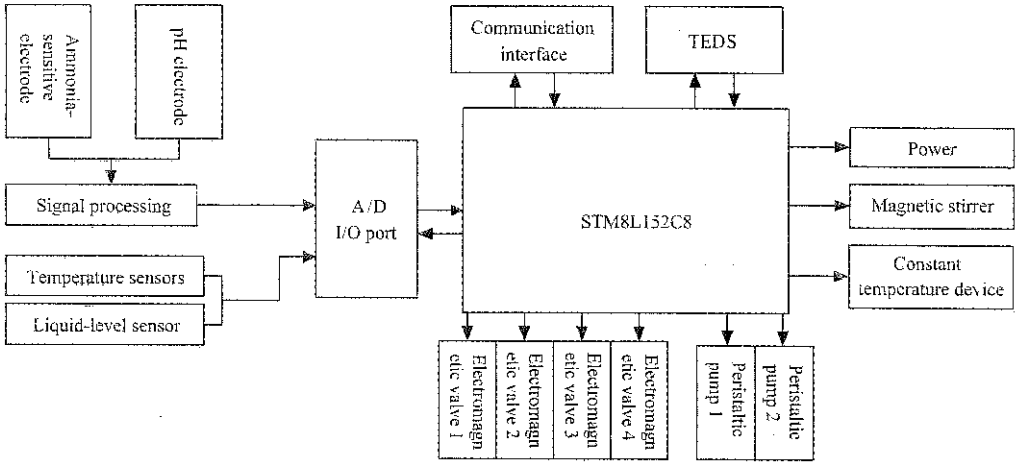

Figure 4 Overall structure of the control module

To realize the standardization and intellectualization of the online ammonia nitrogen monitoring system, it adapted the transducer electronic data sheet (TEDS) compensation correction model to achieve the calibration and compensation of the ammonia-sensitive electrode. The TEDS provides the definition of the sensor, calibration and compensation information. It stores the information of the sensors by the TEDS read/write operation. In this paper, the basic TEDS, which has three types (i.e., general TEDS, channel TEDS, and calibration TEDS), was used. The general TEDS and channel TEDS describe the channel numbers of the sensors, channel grouping, physical unit of the channel, data model, measurement range, and measurement accuracy. The calibration TEDS stores the calibration parameters of the sensors.

3 Results and discussion

3.1 Compensation and correction of ammonia-sensitive electrode

Equation (2) indicated that the proportion of free ammonia in the total ammonia nitrogen content in water was related to the pH content and the ionization equilibrium constant of ammonia, *pKs*. In addition, the ionization equilibrium constant of water was related to the temperature of and the solute in water. For example, the ionization degree of water can be increased by elevate the temperature, whereas the ionization degree of water can be reduced by lower temperature. Notably, the acidity and alkalinity of the solution remain unchanged. In addition, the ionization equilibrium constant of ammonia in water also changes with temperature changes. The fitting curve of the relationship between *pKs* and temperature is shown in Figure 5.

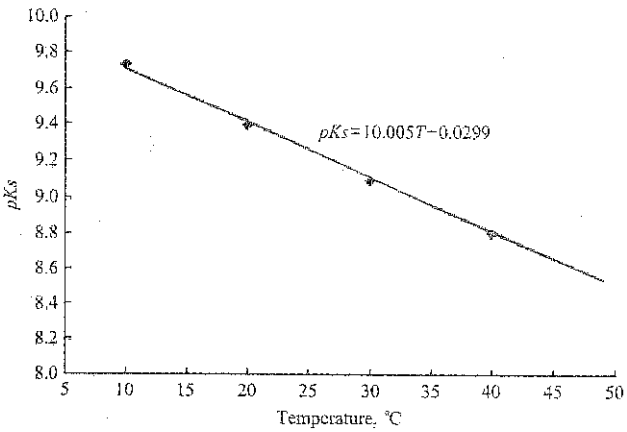

Figure 5 Fitting curve of the relationship between *pKs* and temperature

According to the fitting curve in Figure 5, the linear relationship between *pKs* and temperature can be expressed by Equation (3):

$$pKs = 10.005 - 0.0299T \quad (3)$$

By substituting Equation (3) into Equation (2), the

relationship between the percentage of free ammonia in the total ammonia nitrogen content and the temperature of water can be calculated by Equation (4).

$$\frac{[NH_4^+]_s}{[NH_3]_s} = 10^{10.005-0.0299T-pH} \quad (4)$$

The ratio of ammonia ions to free ammonia at different pH values and temperatures can be calculated by Equation (4). According to this ratio, we can calculate the percentage of free ammonia in the total ammonia nitrogen content, which changes with pH at different temperatures, as shown in Figure 6.

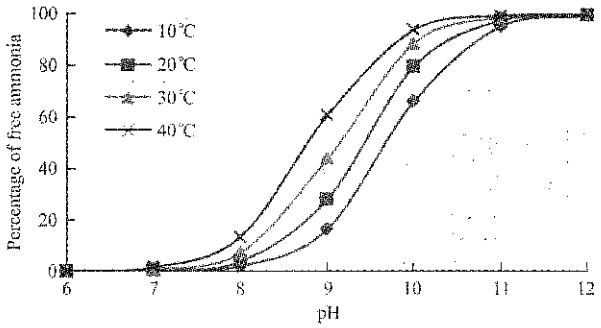

Figure 6 Fitting curves of the relationship of free ammonia with pH at different temperatures

As shown in Figure 6, the proportion of free ammonia can be divided into three stages. When the pH value is lower than 9, the proportion of free ammonia increases as the pH value increases, but the increase is slow. When the pH value is higher than 11, nearly the entire amount of ammonia nitrogen in water convert into free state, and the proportion remains unchanged as the pH value and temperature change. However, when the pH value is lower than 11 and remains unchanged, the proportion of free ammonia increases with temperature increasing.

We placed 50 mL of 10 mg/L solution of ammonia nitrogen into a beaker and adjusted the pH value to 7, 8, 9, 10, 11, and 12 with 1 mol/L NaOH solution. Subsequently, we placed the solution into a constant-temperature water bath, increasing the temperature from 10°C to 40°C, and then recorded the output of the ammonia-sensitive electrode every 10°C. Using these recorded output, we illustrated a cartesian coordinate system, in which the horizontal axis was the pH value and the longitudinal axis was the output voltage of the ammonia-sensitive electrode transmitter. The curves are shown in Figure 7.

As shown in Figure 7, the output voltage of the ammonia-sensitive electrode increases with an increase in pH at the same temperature. However, the effect of temperature changes on the output voltage is not apparent (Ling, 2015). Therefore, in this study, the influence of temperature was not considered, and the experiment was conducted at room temperature (25°C) to simplify the process.

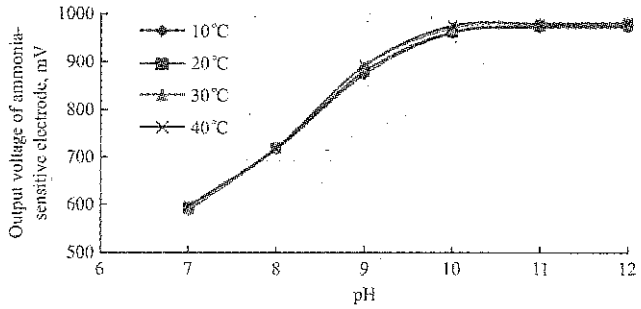

Figure 7 Variations in the output voltage of the ammonia-sensitive electrode transmitter with respect to pH values at different temperatures

3.2 Calibration of ammonia-sensitive electrode

We used standard ammonia solution to configure the sample solutions with 0.01 mg/L, 0.1 mg/L, 1 mg/L, and 10 mg/L concentrations. Subsequently, we placed them in water, immersed them at 25°C water bath, and adjusted their pH values to 7, 8, 9, 10, and 11 with 1 mol/L NaOH solution. The output voltages of the ammonia-sensitive electrode transmitter at different pH values and different concentrations of ammonia nitrogen were recorded. According to the experimental data, the curves of the output voltage of the ammonia-sensitive electrode transmitter versus pH for different pH values were generated and are presented in Figure 8.

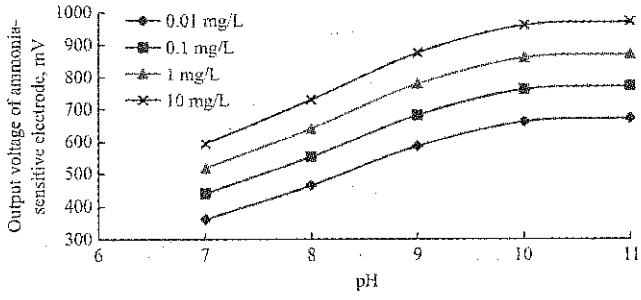

Figure 8 Variations of the ammonia-sensitive electrode transmitter output voltage with different pH concentrations

Using the obtained data, we illustrated a Cartesian coordinate system, which is shown in Figure 9, in which the horizontal axis is the logarithm of the ammonia nitrogen concentration and the longitudinal axis is the

output voltage of the ammonia-sensitive electrode transmitter. In this Cartesian coordinate system, each point indicates a unique concentration at different pH values. Under the same pH value, the logarithm of the concentration of ammonia nitrogen exhibited a good linear relationship with the output voltage of the ammonia-sensitive electrode transmitter. The fitting curves based on Equation (5) created using MATLAB and they are shown in Figure 9.

$$U = A * \lg[NH_3]_s + B \tag{5}$$

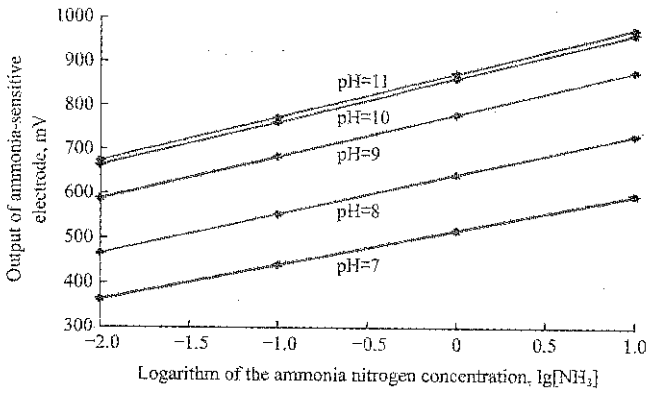

Figure 9 Relationship between concentration of ammonia nitrogen and output of ammonia-sensitive electrode

The A and B values at each pH value could be obtained from the fitting curve fitted using MATLAB. Consequently, we obtained Equation (6):

$$\begin{aligned} U_{pH7} &= 77.77\lg[NH_3]_s + 517.61 \\ U_{pH8} &= 88.96\lg[NH_3]_s + 642.43 \\ U_{pH9} &= 96.80\lg[NH_3]_s + 780.30 \\ U_{pH10} &= 99.32\lg[NH_3]_s + 862.41 \\ U_{pH11} &= 99.43\lg[NH_3]_s + 873.29 \end{aligned} \tag{6}$$

In the process of detecting ammonia nitrogen in water, we added NaOH solution in the test samples to adjust their pH values to 11 or higher in order to convert the ammonia nitrogen into free ammonia, then it escaped from water and was detected by the hydrophobic microporous breathable membrane of the ammonia-sensitive electrode.

Therefore, the calibration of the ammonia-sensitive electrode in this study adopted the calibration curve when the pH value is equal to 11 or higher. Therefore, the calibration algorithm is represented by Equation (7):

$$U_{pH11} = 99.43\lg[NH_3]_s + 873.29 \tag{7}$$

3.3 Analysis and test of ammonia-sensitive electrode

3.3.1 Standard reagent test

According to the general requirements by the National Environmental Protection Agency for the water quality of fisheries, the ammonia nitrogen content should not be higher than 0.02 mg/L[20]. Therefore, in this study, the sensor was tested using 0.01 mg/L, 0.1 mg/L, 1 mg/L, and 10 mg/L ammonia nitrogen standard solutions at room temperature (25°C). The specific method is as follows: first, the probes were placed into the 0.01 mg/L, 0.1 mg/L, 1 mg/L, and 10 mg/L 50 mL standard solutions. Second, the pH values of the solutions were adjusted to higher than 11 by adding NaOH solution of 1 mol/L. Third, for each standard reagent, 18 test experiments were conducted, and the average was calculated and recorded. Finally, with the use of the calibration algorithm in Equation (7). The actual measured concentrations and their corresponding absolute errors are presented in Table 2.

Table 2 Performance test and analysis results of the ammonia-sensitive electrode

The standard concentration, mg/L	Measured the voltage value, mV						Measured average, mV	Measured concentration, mg/L	Relative error
0.01	674.8	663.2	675.9	668.6	683.4	683.1	672.74	0.0096	4.16%
	668.9	671.0	679.3	640.9	669.2	652.9			
	673.5	680.2	675.1	684.5	667.8	697.1			
0.1	765.9	759.9	762.0	780.6	753.3	790.2	769.0	0.0965	3.5%
	768.5	769.3	751.2	781.6	779.8	794.8			
	756.9	773.9	774.5	757.6	771.2	752.1			
1.0	859.6	873.3	872.9	865.8	854.6	880.5	871.73	0.972	2.8%
	886.7	869.3	879.3	856.9	887.4	873.2			
	890.0	864.3	865.1	870.5	872.6	869.1			
10	972.5	980.3	965.6	991.2	957.8	968.6	976.13	10.413	4.13%
	982.6	992.5	994.7	987.1	975.6	955.2			
	968.9	980.7	965.2	976.6	982.4	972.8			

From the results in Table 2, we can conclude that the ammonia-sensitive electrode is suitable for the determination of ammonia nitrogen content in the water when the ammonia nitrogen concentration is high (Wang, 2014). However, the stability and the reproducibility of the test results are poor when the ammonia nitrogen concentration of the water sample is low under the same conditions. Some researchers believe that this phenomenon is caused by the long response time and the dissipation of ammonia gas (Zhang, 2015). Therefore, ammonia nitrogen testing should be performed in an airtight environment to avoid free ammonia (NH_3) dissipation, which results in a significant error.

3.3.2 Random sample test

To verify the accuracy of the ammonia-sensitive electrode, we selected domestic water from nine sampling locations as test samples and compared two different ammonia nitrogen detection systems. The first detection system is TresCon, and the other system is the one that designed in this study. Both systems adapted an ammonia-sensitive electrode for measurement. The calculation results are shown in Table 3, and they showed that the difference between the two detection systems is not significant. Therefore, the ammonia nitrogen detection system proposed in this paper is feasible (Nong, 2012).

Table 3 Consistency check on the determination results by two testing methods

Sampling locations		Average value of ammonia nitrogen content, mg/L		Difference value, d
		Detected by TresCon ammonia nitrogen detection	Detected by ammonia nitrogen detection	
Wastewater	Sewage plant 1	9.255	8.882	0.373
	Sewage plant 2	7.890	7.660	0.230
	Sewage plant 3	5.888	6.022	0.134
Domestic water	Reservoir 1	1.263	1.230	0.033
	Reservoir 2	0.884	0.859	0.025
	Reservoir 3	0.649	0.630	0.019
Aquaculture water	Fish pond 1	0.013	0.014	0.001
	Fish pond 2	0.010	0.011	0.001
	Fish pond 3	0.008	0.009	0.001
Σ				0.0817

4 Conclusions and future work

According to the actual need for water quality monitoring of the aquaculture industry, we studied the ammonia detection procedure and designed an online ammonia nitrogen monitoring system using an ammonia-sensitive electrode. The system has sampling, cleaning, calibration, field-testing, and liquid waste processing functions. It integrated different modules, including the sampling module, calibration module, detection module, signal transmission module, control module, and liquid waste processing module. In view of the weak output signal and high output impedance of the ammonia-sensitive electrode, an analog circuit for the ammonia-sensitive electrode was used to render the voltage signal of ammonia nitrogen concentration precise and stable. Finally, we tested the performance of the sensor, generated the calibration curve of the ammonia-sensitive electrode according to the test results, and corrected the ammonia-sensitive electrode. The experimental results showed that the error of the detection with an ammonia-sensitive electrode is within 5% and the system has a high accuracy and stability and can meet the requirements for the online monitoring of ammonia nitrogen in water.

Compared with the traditional systems, the online ammonia nitrogen monitoring system avoided complex sample pretreatment, automatically extracted the sample, and converted ammonia nitrogen in water into free ammonia. It can detect the content of free ammonia to reflect the concentration of ammonia nitrogen in water. In addition, this online monitoring system automatically controlled pH values and presented a self-cleaning function, thereby effectively improved the precision of test results. Moreover, its liquid waste processing module minimized the hazards of the detection procedure to the environment. Most importantly, it allows for real-time measurement, performs automatic compensation correction, and demonstrates anti-interference capability; thus, the monitoring system is intelligent and automatic.

Acknowledgements

This study was supported by the International Technology Cooperation of China. No.2015DFA00090. National Key Research & Design Program 2017YFD0701702. Independent Innovation and Transformation of Science& Technology Achievements Project of Shandong Province. No. 2014ZZCX07102.

Academician Workstation Project of Guangdong Province. No. 2012B090500008.

[References]

[1] Chang, S. 2004. Feeding technology of cloudy fish pellet feed. *Freshwater Fish*, 6: 47–48.

[2] Ding, Q. S., H. J. Tai, and X. Y. Wang. 2013. The intelligent sensor of water ammonia nitrogen in situ rapid detection. *Internet of Things Technologies*, 3: 35–39.

[3] Geng, Y. W. 2002. High resistance signal processing of water quality on-line monitoring. *China Instrumentation*, 6: 19–21.

[4] Higgins, P. 2013. Understanding ammonia in aquaculture ponds. *International Aquafeed*, 16(5): 22–24.

[5] Hou, H. L., and Y. Z. Wang. 2009. Measurement system of sodium ion concentration based on MSC1210. *Instrument technology*, 4: 12–16.

[6] Jia, T., and W. Zhang. 2011. Comparison research in two kinds of detection method of ammonia nitrogen in the water environment. *Science and Technology and Life*, 7: 176–177.

[7] Li, M. 2011. Interaction analysis of agricultural produce quality management and the development of agricultural industrialization cooperation mode. *Productivity Research*, 1: 43–45.

[8] Li, Y. N., Y. P. Jiang, and Z. D. Li. 2007. Intelligent flow integrating instrument based on MSP430 MCU. *Journal of Instrument and Meter*, 28: 510–513.

[9] Ling, C. F. 2015. The study of ammonia gas sensitive electrode rapid determination of ammonia nitrogen content in refining wastewater. *Guangdong Chemical*, 42: 172–173.

[10] Liu, K., and J. Sun. 2007. Water environmental quality comprehensive evaluation based on support vector machine (SVM). *Journal of Environmental Monitoring in China*, 23: 81–84.

[11] Liu, S. 2010. Design intelligent ammonia nitrogen measurement based on electrode method. *Computer and applied Chemistry*, 27: 587–590.

[12] Nong, Y. G. 2012. The research progress of ammonia nitrogen determination by ammonia gas sensitive electrode method. *The Wind of Science and Technology*, 7: 112–113.

[13] Qing, G., S. S. Yang, and Y. H. Liu. 2015. The design and implement of automatic ammonia nitrogen on-line detection system. *Electronic Design Engineering*, 23: 72–78.

[14] Ruan, Y., C. Lu, X. Guo, Y. Deng, and S. Zhu. 2016. Electrochemical treatment of recirculating aquaculture wastewater using a Ti/Ruo2-Iro2 Anode for synergetic total ammonia nitrogen and nitrite removal and disinfection. *T Asabe*, 59(6): 1831–40.

[15] Temple-Boyer, P., B. Hajji, J. L. Alay, J. R. Morante, A. Martinez. 2009. Properties of SiOxNy films deposited by LPCVD from SiH4/N2O/NH3 raseous mixture. *Sensors and Actuators A: Physical*, 74: 48–49.

[16] Wang, B. G., and J. Wu. 2008. Research of water quality on-line automatic monitor technology of total ammonia. *Journal of Environmental Science and Technology*, 31: 61–63.

[17] Wang, C., S. Jiang, and T. Wang. 2015. Research progress of ammonia nitrogen monitoring analysis method. *Resource Conservation and Environmental Protection*, 10: 50–51.

[18] Wang, H. C. 2014. Design of ammonia-nitrogen measuring instrument used for aquaculture. *Measurement and Testing Technology*, 41: 1–2.

[19] Xie, Y. K., Z. Y. Wen, Z. H. Mo, Z. Q. Yu, and K. L. Wei. 2016. Implementation of an automatic and miniature on-line multi-parameter water quality monitoring system and experimental determination of chemical oxygen demand and ammonia-nitrogen. *Water Sci Technol*, 73(3): 697–706.

[20] Xing, K. Z., Y. J. Guo, and C. X. Cheng. 2013. Aquaculture advanced sensing and intelligent processing key technology and products. *Tianjin Science and Technology*, 2: 46–47.

[21] Yang, Y. Z., T. Yu, and W. P. Ma. 2010. Hazards and the analysis method of ammonia nitrogen in water environmental and the commonly used process. *Shanxi Building*, 20: 356–357.

[22] Zhang, J. 2015. Discussion and optimization on existing problems in determining total nitrogen in water by different methods. *Environmental Science and Management*, 40: 99–102.

[23] Zhang, S., J. Li, and J. Z. Xue. 2016. The application of relationship between ammonia sensitive electrode measured value and the Nernst equation. *Guangzhou Chemical Industry*, 44: 134–135.

Development and evaluation of a traceability system for broiler/chicken in China incorporating RFID and 2D barcode technology

Chen Xuerui[1], Jia Jingdun[2], Gao Wanlin[1*], Ren Yanzhao[1]

(1. *College of Information and Electrical Engineering, China Agriculture University, No.17 Tsinghua East Road, Beijing 100083, China*;

2. *China Rural Technology Development Center, No.54 Sanlihe Road Xicheng District, Beijing 100045, China*)

Abstract: Chicken are considered as a necessity of daily life and popular with the public for their characteristics of rich in protein, low in calories and fat. With outbreaks of avian influenza and other diseases and increasing safety awareness of consumers, traceability for broiler supply chain is becoming an imperative tool to meet the requirements of all aspects in China. This study aims to design and complete a traceability system for broiler/chicken in China incorporating RFID and 2D barcode technology. Based on identification of traceability units and comparative analysis of identification technologies, a model was proposed for transmission of data in the supply chain. To verify the application effect of the system, a system evaluation was conducted. The results showed that the system was successfully applied in a sampled enterprise in broiler/chicken supply chain in China. Compared with the previously used system, vital information, which is useful for statistics data and analyzing the cost benefits of the enterprise, could be collected more easily by the BCTS, as well as problems could be quickly located and focused. The evaluation result also showed that the application of the BCTS is quite efficacious for improving the efficiency of management and tracing.

Keywords: traceability system, broiler/chicken, evaluation, RFID, 2D barcode

Citation: Chen, X. R., J. D. Jia, W. L. Gao, and Y. Z. Ren. 2017. Development and evaluation of a traceability system for broiler/chicken in China incorporating RFID and 2D barcode technology. International Agricultural Engineering Journal, 26(4): 332–340.

1 Introduction

Chicken are considered as necessities of daily life and popular with the public for their characteristics of rich in protein, low in calories and fat. According to the detailed reported by United States Department of Agriculture (USDA) (2017), the broiler meat production of China is 12.30 million metric tons in 2016, second only to the United States. So, the broiler/chicken quality safety does not only affect the health of the public but also would shock the poultry breeding industry in China.

The event of "fast-grown chicken" woke up the communal consciousness of food safety, and the bird flu threating to human and animal caught the public attention. In the past decades, similar food safety incidents have also brought great challenges to poultry farming. To maintain the healthy development of the poultry industry, the relevant provisions were introduced to restrain and regulate the production behavior (Ministry of Agriculture of the People's Republic of China, 2006; 2012). Therefore, the essential issue poultry industry faced is how to insure the safety and quality of broiler/chicken product and gain the trust of the public.

There are several definitions of traceability defined by the various agencies from diverse aspects and for disparate goals (Li, 1995; QR-008, 2006; FAO/WHO,

Received date: 2017-09-20 **Accepted date:** 2017-11-22

* **Corresponding author: Gao Wanlin,** Key Laboratory of Modern Precision Agriculture System Integration Research, Ministry of Education, China Agriculture University, No.17 Tsinghua East Road, Beijing 100083, China. Email: gaowlin@cau.edu.cn.

Development and evaluation of a traceability system for broiler/chicken in China incorporating RFID and 2D barcode technology

Chen Xuerui[1], Jia Jingdun[2], Gao Wanlin[1*], Ren Yanzhao[1]

(1. *College of Information and Electrical Engineering, China Agriculture University, No.17 Tsinghua East Road, Beijing 100083, China*;

2. *China Rural Technology Development Center, No.54 Sanlihe Road Xicheng District, Beijing 100045, China*)

Abstract: Chicken are considered as a necessity of daily life and popular with the public for their characteristics of rich in protein, low in calories and fat. With outbreaks of avian influenza and other diseases and increasing safety awareness of consumers, traceability for broiler supply chain is becoming an imperative tool to meet the requirements of all aspects in China. This study aims to design and complete a traceability system for broiler/chicken in China incorporating RFID and 2D barcode technology. Based on identification of traceability units and comparative analysis of identification technologies, a model was proposed for transmission of data in the supply chain. To verify the application effect of the system, a system evaluation was conducted. The results showed that the system was successfully applied in a sampled enterprise in broiler/chicken supply chain in China. Compared with the previously used system, vital information, which is useful for statistics data and analyzing the cost benefits of the enterprise, could be collected more easily by the BCTS, as well as problems could be quickly located and focused. The evaluation result also showed that the application of the BCTS is quite efficacious for improving the efficiency of management and tracing.

Keywords: traceability system, broiler/chicken, evaluation, RFID, 2D barcode

Citation: Chen, X. R., J. D. Jia, W. L. Gao, and Y. Z. Ren. 2017. Development and evaluation of a traceability system for broiler/chicken in China incorporating RFID and 2D barcode technology. International Agricultural Engineering Journal, 26(4): 332–340.

1 Introduction

Chicken are considered as necessities of daily life and popular with the public for their characteristics of rich in protein, low in calories and fat. According to the detailed reported by United States Department of Agriculture (USDA) (2017), the broiler meat production of China is 12.30 million metric tons in 2016, second only to the United States. So, the broiler/chicken quality safety does not only affect the health of the public but also would shock the poultry breeding industry in China.

The event of "fast-grown chicken" woke up the communal consciousness of food safety, and the bird flu threating to human and animal caught the public attention. In the past decades, similar food safety incidents have also brought great challenges to poultry farming. To maintain the healthy development of the poultry industry, the relevant provisions were introduced to restrain and regulate the production behavior (Ministry of Agriculture of the People's Republic of China, 2006; 2012). Therefore, the essential issue poultry industry faced is how to insure the safety and quality of broiler/chicken product and gain the trust of the public.

There are several definitions of traceability defined by the various agencies from diverse aspects and for disparate goals (Li, 1995; QR-008, 2006; FAO/WHO,

Received date: 2017-09-20 **Accepted date:** 2017-11-22

* **Corresponding author: Gao Wanlin,** Key Laboratory of Modern Precision Agriculture System Integration Research, Ministry of Education, China Agriculture University, No.17 Tsinghua East Road, Beijing 100083, China. Email: gaowlin@cau.edu.cn.

1997). All of the definitions of traceability have special importance, while similar with other research papers, this paper is tending to cite the definition of traceability that from European General Food Law (EGFL) as it is quite detailed with respect to what should be traced and followed (Petter and Melanie, 2013). And this definition of traceability is: "The ability to trace and follow a food, feed, food producing animal or substance intended to be, or expected to be incorporated into a food or feed, through all stages of production, processing and distribution" (Regulation (EC) No 178-2002).

Traceability system is primarily viewed as an effective tool for the food safety and quality by providing the recorded production information, but it is also related to improve consumer trust in products when a need of consumers for transparent information on the quality of the entire food chain is increasing (Qian et al., 2012; Myo and Yoon, 2014; Mattia and Jeffrey, 2016). Therefore, laws and decrees were promulgated by governments to propel the construction and development of traceability system, for the sake of food safety (Food and Drug Administration, 2005).

Consequently, large quantities of researches focused on traceability system were carried out by scholars around the world. In terms of object, the target object of existing researches includes pig (Jae-Don et al., 2014), beef (Lee et al., 2011; Feng et al., 2013), sheep (Heaton et al., 2014; Spanu et al., 2015), and so on (Qian et al., 2017; Zhao et al., 2014; Morcia et al., 2013). Whereas few studies aimed at the supply chain of broiler/chicken.

On the other hand, the highlights of these researches can be classified in the following aspects: framework of traceability system (Storoy et al., 2013), construction of the traceability system and studies on the relevant technical in the designed process (Wang et al., 2016; Parenreng et al., 2016), application of the system (Xiao et al., 2015). Performance of the traceability system attracts few attentions while performance indicators, such as accuracy of information transmission and coordination between links in the supply chain, are essential for a traceability system (Fabrizio and Paolo, 2011).

This paper aims to establish a RFID and 2D barcode based broiler/chicken traceability system (BCTS) and evaluate the performance of the BCTS. This system combined redesigned hardware devices with software system to assure the accuracy of traceability information and to simplify the manipulation in data collection and transmission. Moreover, a performance evaluation index system and performance evaluation model would be established to examine the validity of the BCTS.

2 System analysis

2.1 Survey design

As a common meat product, chicken's consumption in China is second only to that of pork. There are two main product forms: first, whole chicken is the complete body of broiler which were slaughtered and cleaned up; second, parts of chicken, such as whole leg, inner fillet and wing tip mid-joint-wing, which need to segment the whole chicken. Compared with the other farming animals, there are more technical specifications and standards to restrict the process of broiler breeding, slaughtering and processing. And the chick becoming chicken products required the participation of many different kinds of workers. So, the following 4 methods adopted to analyze broiler breeding, slaughter processing and obtain system requirements.

(1) Collection of literature and production data

The literature includes a variety of regulations and standards, which were published by nation, industry and regions, to restrict the process of broiler breeding, slaughtering and processing. Meanwhile logs and records of Hazard Analysis and Critical Control Point (HACCP) were collected. All of these collections determined the key parameters and vital functions of the BCTS.

(2) Observation

This method focused on the daily manipulation and management during a broiler life cycles. A half-a-month investigation were spent in different scale enterprises in Beijing, aiming to observe the feeding, immunizations, disinfection and the slaughtering process.

(3) Interview

During the interview, 15 managers, 20 workers and 30 feeders were selected from five enterprises in Beijing. The interviewees were asked to answer questions which were proposed in advance covering manipulate tasks,

business flow and traceability matters.

(4) Expert consultations

The construction of the BCTS is a process in which biological knowledge, animal medical technology and information technology were used comprehensively. So, it is necessary to consult professional experts in different fields.

2.2 Analysis of workflow in the broiler/chicken supply chain

As Figure 1 illustrated that the broiler/chicken supply chain workflow was composed of dozens of working nodes occurring in the fowlery and the slaughterhouse.

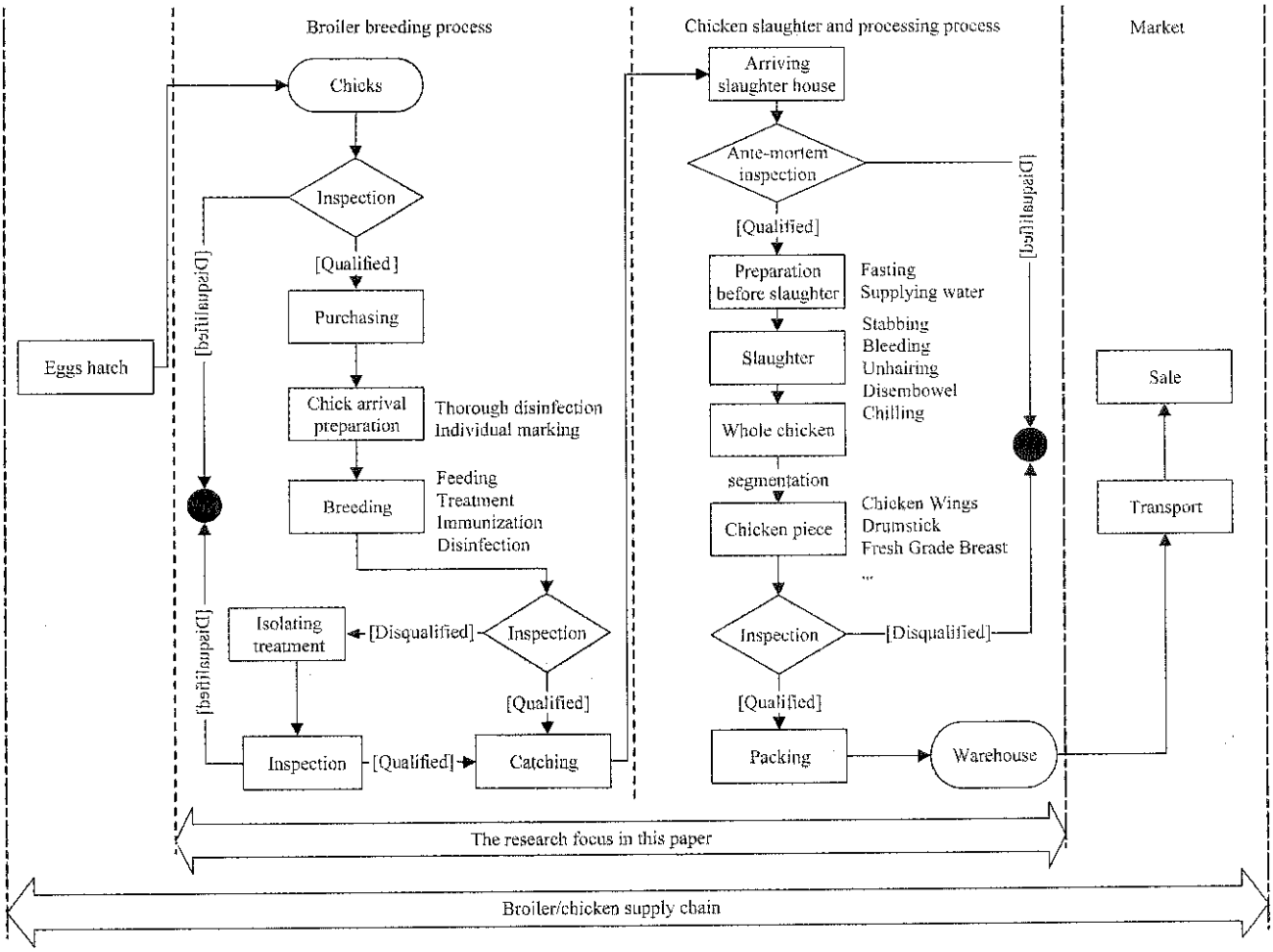

Figure 1 Broiler/chicken supply chain in China

After being certificated qualified, strong and without any diseases, chicks were purchased from breeding enterprise. Houses, the surrounding areas, and all equipment must be thoroughly cleaned and disinfected before the arrival of the bedding and chicks. Furthermore, before entering the building, vehicles, equipment and people should be disinfected to prevent pathogens entry. In the growth period of the body, individual marked broilers were fed scientifically, and accepted regular disinfection and immunization. Before catching, we must inspect the broiler body and guarantee that the broiler without any disease and any injury. Qualified broilers should be transferred to slaughterhouse, while the sick broiler would be isolated and treated, until completing its rehabilitation.

Once pass the ante-mortem inspection, the broilers stepped into the stage of waiting for slaughtering meanwhile the broilers were fasting and supplied by enough water. The broilers, after the slaughtering, became whole chicken some of which would be segmented according to the different requirements. At last, all of the broiler/chicken product could be transported to the market for sale.

In this research, we focused on the workflow, beginning with purchasing chicks and ending with packaged the broiler/chicken products entering warehouse, which happened in the fowlery and slaughterhouse.

2.3 Requirements analysis of the BCTS

The function requirements and performance requirements were exacted from collection of literature and production data, observation and interview, as shown in Table 1.

Table 1 Function requirements and performance requirements

Function requirements	Description	Performance requirements	Description
Broilers information	Assign a unique ID to each broiler and record all the information of the broiler.	Automaticity	The system can automatically acquire and transmit all kinds of broiler/chicken data.
Information acquisition and transmission	Obtain all the data generated in the process timely and transmit it accurately.	Flexibility	Once mode of operation, running environment, or software interfaces changes, the system has the ability to adapt.
Data storage and query	Store all the data and provide retrieving based on the keywords.	Precision	The system can meet the needs of all kinds of precision in the process of data input and output.
Information tracking and tracing	Provide the service for tracking and tracing to control the safety and quality of broiler/chicken product.	Secrecy	In order to ensure information security, the system automatically sets permissions for each account, and the information is encrypted.
Management and strategic decision support	The system has the ability to manage daily routine and provide data support for decision making.	User-friendliness	The use of the system must be easy to learn, and the relevant equipment must be easy to manipulate.

2.4 Critical traceability information of the BCTS

In terms of broiler breeding, slaughtering and processing, the Standardization Administration of the People's Republic of China combined with the General Administration of Quality Supervision, Inspection and Quarantine of the People's Republic of China published standards of GB/T 19478-2004 (operating procedure of chicken slaughtering) and GB/T 19664-2005 (production technique criterion for commercial broiler) to instruct operation. Subsequently, the Decree No.67 issued by the Ministry of Agriculture of the People's Republic of China pointed out the critical information should be record. According to the previous, we identified the significant traceability information for the BCTS which should be acquired.

3 Traceability information acquisition and transmission for the BCTS

3.1 Identification of traceability units

Figure 2 illustrated traceability units of the BCTS which were extracted from the workflow showed in Figure 1, and the corresponding operation procedure. At the beginning of feeding process, a purchased chick is the first traceability unit in this paper which is expressed as U1. The breeding process ending up with catching and be moved to slaughter. At this point, the broiler waiting for slaughter is the traceability unit and be represented by U2. Traceability unit transforms into whole chicken (U3) after the slaughtering process. And then traceability unit transforms into segments of chicken (U4) after the segmentation. At last, chicken product became to the traceability unit (U5) which would be transported to the warehouse.

3.2 Identification technologies

There are several types of information identification technologies for food quality traceability system, such as one-dimensional bar code (1D barcode) and two-dimensional bar code (2D barcode), radio frequency identification (RFID), and so on.

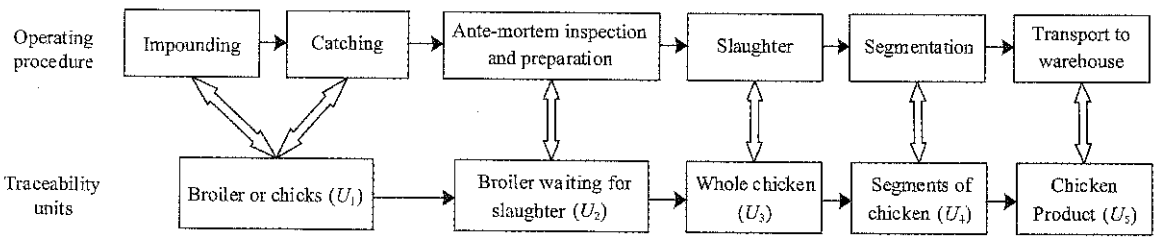

Figure 2 Traceable unit during the broiler/chicken workflow

Barcode technology is a technology that through coding, printing, optical sensing technology, the data carried by barcode were read and then translated into meaningful information. 2D barcode, by contrast, has larger storage spaces and is able to meet the needs of the expressing text. The RFID technology uses the special transmission characteristics of radio frequency signal to implement the automatic identification of object and to obtain relevant information. According to the principles of these technologies, barcode technology and RFID are

fit for the BCTS. There are 4 types of RFID tags classified by operating frequency that are low frequency, high frequency, ultra high frequency and microwave. Considering read range, price and security, high frequency RFID tags were selected to responsible for traceability units. And better than other 2D barcode in identifying speed and application scope, QR codes is more appropriate to show traceability information.

3.3 Traceability information model

Along the supply chain, tracing unit is changing and trace data constantly need to transfer, during that the delivery and recording of the key traceability information is crucial for enterprise's external and internal retrospect. Li et al., (2010) thought tracking information should include the data of unique identification, attribution, time, place, unit, operator etc., and proposed a traceability information model. Feng et al., (2013) made a further explanation on this method then used it to study the beef product traceability. On the basis of these studies, we put forward a broiler traceability information model to complete traceability, and the model was formulized as:

$$P(U)=\{Inf(U_1), Inf(U_2), Inf(U_3), Inf(U_4), Inf(U_5)\} \quad (U=\{U_1, U_1U_1U_1U_1\}) \quad (1)$$

$$Inf(U_i)=\{Id(U_i), Uni(U_i), Loc(U_i), Attri(U_i), Oper(U_i), Tim(U_i)\} \quad (i=1,2,3,4,5) \quad (2)$$

where, $P(U)$ is the aggregation of the traceability information in the supply chain; U is a set of traceability units; $Inf(U_i)$ is the aggregation of the traceability information of traceability units U_i; $Id(U_i)$ is the unique identification which is the key word for reading and updating in the information transmission. For instance, according to the Decree No. 67 mentioned above, a 15 digits code 411022800000001 is one initial value of $Id(U_i)$, and as the decree clearly pointed out that the species code of pigs, cattle, sheep is respectively 1, 2, 3 without state out the code of broiler, so 4 was chosen to represent the tracing object is broiler. 110118 denote the codes for the administrative divisions of the People's Republic of China, and 00000001 is broiler number. $Uni(U_i)$ describes the specific form of trace unit therefore $Uni(U_1)$ is broiler and $Uni(U_5)$ is chicken product. The location information of traceable unit is represented by $Loc(U_i)$, meanwhile, the information of breeding, inspection, anti-mortem inspection, segmentation etc. is expressed by $Attri(U_i)$. The participant is a factor not to be ignored and formulated by $Oper(U_i)$. In order to ensure the continuity of the data, the operation time $Tim(U_i)$ is recorded.

3.4 Information acquisition and transmission of U1-U5

The two kinds of data identification methods are Ultra High Frequency (UHF) RFID tag and QR code that has been applied in the BCTS. The use of RFID tag during the data transfer process from the traceability unit U_1 to U_5. At last, QR code was used to show all the tracing information of the product. The reading and writing of the traceability information need the support of devices, furthermore some equipment would be redesigned for the sake of convenient operation and elevating the work efficiency. The PDA (Personal Digital Assistant) P130 was selected to read/write UHF RFID tags, which was redesigned for the workers to manipulate easily. Moreover, the UHF RFID tag reader is indispensable equipment for tracing, and the QR printer is crucial device to switch the information carrier form RFID tag to 2D barcode label.

Once be impounded, the broiler will be assigned a foot ring to store all the traceability information produced in the breeding process which was written in by PDA. After catching and before slaughter, the data of ante-mortem inspection and preparation are written into the foot ring by PDA. When the traceability unit turn into U_3, all the information stored in foot ring are copied into a RFID tag which is adhered on the whole chicken. When the parts are separated from the whole chicken, the operator needs to copy a RFID tag for each segment employing UHF RFID tag reader. Then, the new information about the chicken product is added into the RFID tag by the UHF RFID tag reader. Finally, the worker will use QR printer to print 2D barcode label as the new information carrier.

4 System design and implementation

Based on the analysis of the breeding, slaughtering and processing, the BCTS was designed using the existing tracing technology to gain the goal of external trace and internal accountability. The BCTS is an

integrated management system which includes the data acquisition, storage, processing and query functions. Some of the software and hardware equipment are related to the BCTS, such as PDA, PC and industrial printer. As a RFID reader, the PDA (personal digital assistant) P130 embedded with a RFID reader module, whose operating system is Linux operating system and the processor is 32-bit. The BCTS was designed and it includes three subsystems: broiler breeding subsystem, slaughter-processing system and traceability query subsystem, shown in Figure 3.

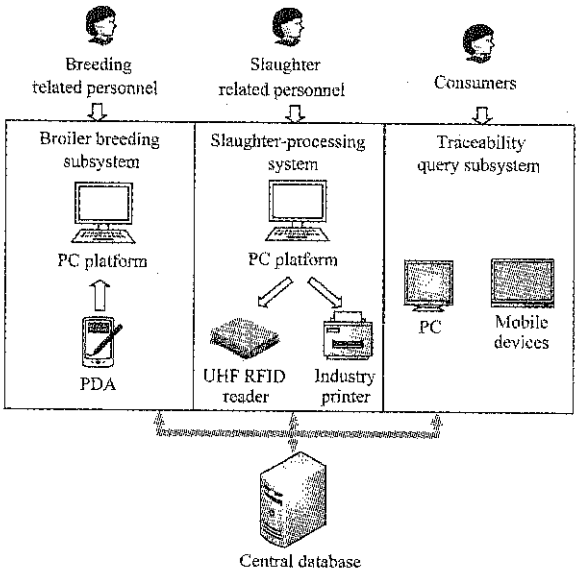

Figure 3 System architecture of BCTS

4.1 Breeding management subsystem

This subsystem includes two function modules: information acquisition and transmission module, information management module. The information acquisition and transmission module is a PDA-based module which is designed to obtain data over the broiler breeding process. The fowlery worker reads the identification code in broiler foot ring and temporarily stores the new records via the redesigned PDA combined with RFID reader, and then all information will be transferred to PC through USB interface. Not only data storage, daily affairs of the farm also are manipulated by the information management module on the PC platform. Furthermore, the system could conduct statistical analysis on the production situation of farms, such as automatically calculating the death rate, cost-benefit and so on.

4.2 Slaughter-processing management subsystem

In addition to records and management information, this broiler slaughter processing management subsystem could fulfill the task of the data transfer and exchange with the hardware support, such as barcode printer and PDA. The worker reads the identification information and writes the information produced in the slaughter-processing process into the tag so each part of the poultry products is inherited all the information of the chicken. Finally, the information about the broiler is transferred to a QR code (shown as Figure 4) which would be pasted on the surface of product.

Figure 4 An amplificatory QR code example

4.3 Traceability query subsystem

Lodging into the traceability query system, customers input the traceability code or scanner barcode and then the system retrieves the details of the product information. Figure 5 illustrates the retrieved information received by consumers, which details the broiler basic information and the information acquired at each stage in the workflow. The querier could find the information such as broiler breed, place of production, product name and product classification to help them understand products preliminarily. Furthermore, breeding information (impounding time, catching time, feeding records, treatment, immunization and disinfection), slaughter-processing information (slaughter house, data, preparation before slaughter and inspection) is also shown in the system.

5 Evaluation and results analysis

The purposes of establishing the BCTS is not only to guarantee the quality and safety of chicken products, at the same time also to improve the management of the producers and operators. To test if the system application result can reach the expectation, the affectivity of the BCTS was analyzed in this section.

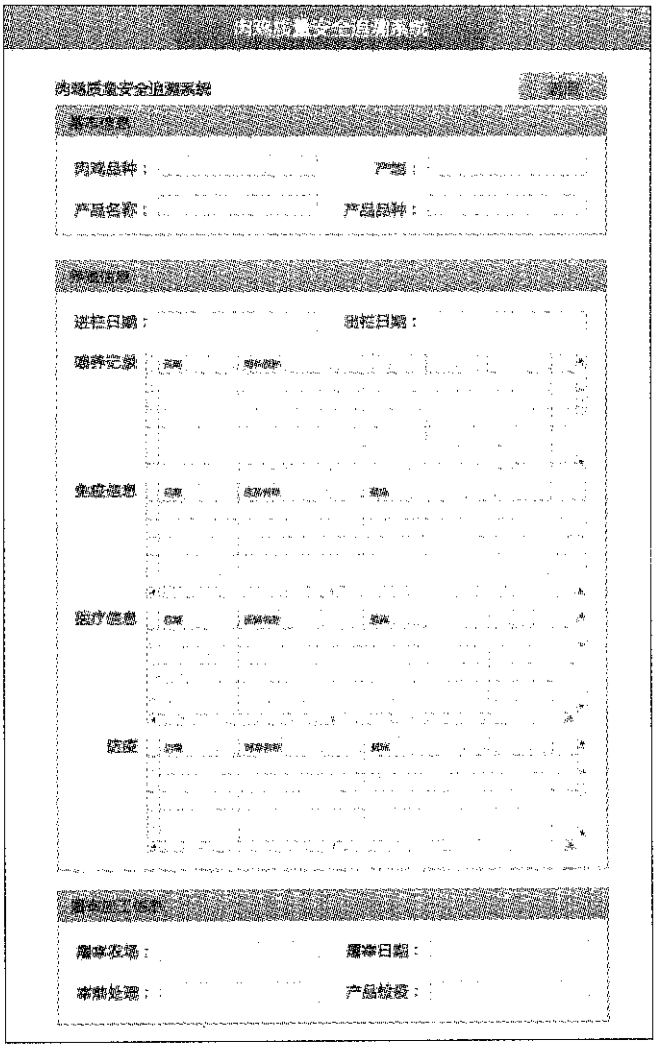

Figure 5 Interface of query subsystem

5.1 Construction of evaluation model

5.1.1 Construction of index system

Evaluation index is the basis and foundation for the performance evaluation and its quality directly affects the reliability and validity of evaluation results. Through theoretical analysis and interviews with managers, we found out that the performance of the BCTS is mainly manifested in the several aspects such as the ascension of the traceability ability, the improvement of product quality safety, the improvement of the efficiency of enterprise management, enhancing the product competitiveness and economic growth. Based on the relevant regulations in the Decree No. 67 issued by the Ministry of Agriculture of the People's Republic of China and the analysis of the above, a two-level index system to evaluate performance was built, complying with principles of systematisms, conciseness, scientificalness, comparability and operationality shown in the following Table 2.

Table 2 Framework of index system for performance evaluation of the BCTS

Evaluation goal	First level index	Second level index
Performance evaluation of the BCTS (U)	Traceability ability (p_1)	The integrity of traceability system (p_{11})
		Archived information situation of key production nodes (p_{12})
		The recall speed of defective product (p_{13})
		Pursue responsibility (p_{14})
		Positioning problem node (p_{15})
	Management level (p2)	The acquisition of the information on the quality and safety (p_{21})
		The speed of information exchange between nodes in the supply chain (p_{22})
		Personnel management efficiency (p_{23})
		Production information management efficiency (p_{24})
		Production and processing efficiency (p_{25})
	Product quality safety (p_3)	Hazard prevention (p_{31})
		The possibility of product quality and safety accidents (p_{32})
		Staff awareness of product quality and safety (p_{33})
		The degree of production specification (p_{34})
	Product competitiveness (p_4)	Consumer purchase intention (p_{41})
		Brand perception (p_{42})
		Market occupancy rate (p_{43})
	Economic growth (p_5)	Gross sales (p_{51})
		Cost of product recall (p_{52})
		Labor expense (p_{53})
		The investment of fixed assets (p_{54})

5.1.2 Performance evaluation model

Table 3 showed the difference in the two aspects of theoretical basis and applicable scope between diverse kinds of methods. Due to the indicators of performance has a certain degree of fuzziness, the fuzzy comprehensive evaluation method was selected to evaluate the performance of the BCTS.

Table 3 The comparison of different kinds of methods

Category	Methods	Theoretical basis	Applicable scope
Economic analysis	Index method, input-output method, etc.	Economics theory	The Researches focus on benefit
Mathematical statistics	Expectancy method, decision tree, regression analysis, etc.	Probability theory and mathematical statistics	Finding out the regularity phenomena from the numerous data
Fuzzy mathematics	Fuzzy comprehensive evaluation, fuzzy clustering, fuzzy distance model, etc.	Fuzzy mathematics	The object with the characteristics of "explicit connotation, fuzzy extension"
Operations research	Multi-objective decision, data envelopment analysis (DEA), etc.	Operations research theory	Used to determine the effectiveness of decision making units

5.2 Data acquisition scenario

According to the methods described above, 10 experts were invited to estimate the relative significance of

indicators. And 30 senior executives were sampled from different enterprises which have deployed and used the BCTS to mark the score of indicators. All the participants were asked and agreed to use the trace system and provide the score of indicators sincerely.

5.3 Results

5.3.1 Weight determination of indicators

On the basis of the fuzzy judgment matrix illustrated before, evaluation factor set are (p_1, p_2, p_3, p_4, p_5), (p_{11}, p_{12}, p_{13}), (p_{21}, p_{22}, p_{23}, p_{24}, p_{25}), (p_{31}, p_{32}, p_{33}, p_{34}), (p_{41}, p_{42}, p_{43}), (p_{51}, p_{52}, p_{53}, p_{54}). The comparison of relative importance between each two indicators in indicator groups belong to different levels was conducted by experts, following the regulation of Table 4.

Table 4 Rating scales of relative importance of index

Importance rank	Definition
r_{ij}=1	The importance of the two indicators i and j is equal
r_{ij}=3	The importance of the indicators *i* exceeds that of *j*
r_{ij}=5	The importance of the indicators *i* is inferior to that of *j*
r_{ij}=2, 4	The median of the adjacent rank descripted in previous

Not: $r_{ij}=1/r_{ji}$.

In accordance with the regulation scale, the comparisons were quantized by 10 experts and there are 10 weight vectors for each evaluation factor set. The weights of indicators were obtained by calculating the average of 10 weight vector, shown in Table 5.

Table 5 Weight of indicators for performance evaluation

Evaluation goal	First level index	Weight	Second level index	Weight
U	p_1	0.21	p_{11}	0.17
			p_{12}	0.23
			p_{13}	0.19
			p_{14}	0.20
			p_{15}	0.21
	p_2	0.18	p_{21}	0.17
			p_{22}	0.16
			p_{23}	0.23
			p_{24}	0.21
			p_{25}	0.23
	p_3	0.21	p_{31}	0.24
			p_{32}	0.23
			p_{33}	0.24
			p_{34}	0.29
	p_4	0.17	p_{41}	0.35
			p_{42}	0.39
			p_{43}	0.26
	p_5	0.23	p_{51}	0.33
			p_{52}	0.21
			p_{53}	0.27
			p_{54}	0.19

5.3.2 Results analysis

In this paper, 30 senior executives were requested to grade for indicators using 10-point system. Indicators' scores indicate the performance in this aspect of supply chain after using the system's, such as the score is 0 meaning that there is no change before and after used the BCTS, and an indicator score is 10 indicating that the indicator achieved the ideal state after using the system.

Finally, the mathematical expressions for the comprehensive fuzzy evaluation results is A= [0.25 0.41 0.18 0.07 0.09], so the performance of BCTS is good in line with the principle probabilistic priority.

6 Conclusion and discussion

Broiler/chicken traceability with integrated utilization of RFID and 2D barcode technologies provided an effective way to a certain extent to ensure the safety and quality of broiler/ chicken product.

This paper developed a broiler/chicken traceability system for the implementation of real-time traceability information management along broiler/chicken supply chain workflow. Considering key nodes and related regulations, relevant information was exacted as the significant data for guarantee the product quality and safety.

The system was successfully applied in a sampled enterprise in broiler/chicken supply chain in China. Compared with the system used before, vital information, which is useful for statistics data and analyzing the cost benefits of the enterprise, could be collected more easily by the BCTS, as well as the problems could be quickly located and focused. Furthermore, the traceability system would cause the enterprise to gain more trust from consumers. The evaluation result also showed that the application of the BCTS is quite efficacious for improving the efficiency of management and tracing.

A broiler/chicken traceability system was developed in this paper. Although the survey of relevant users indicated that the system is responsible for ensuring product quality and safety, there still existed some research points that have not been covered yet here, such as how to optimize the systematic, and what's the impact of system application on the chicken industry.

Acknowledgements

This research was funded by "The extension and the application of video device of complete sets of mobile portable agricultural practical technology" (2015GA600002). It is one of the projects of the "China Spark Program".

[References]

[1] Aung, M. M., and Y. S. Chang. 2014. Traceability in a food supply chain: safety and quality perspectives. *Food Control*, 39(1): 172–184.

[2] Dabbene, F., and P. Gay. 2011. Food traceability systems: Performance evaluation and optimization. *Computers and Electronics in Agriculture*, 75(1): 139–146.

[3] FAO/WHO, Joint FAO/WHO Food Standards Program. 1997. Rome: Codex Alimentarius Commission. Codex Alimentarius.

[4] Feng, J., Z. Fu, Z. Wang, M. Xu, and X. Zhang. 2013. Development and evaluation on a RFID-based traceability system for cattle/beef quality safety in China. *Food Control*, 31(2): 314–325.

[5] Food and Drug Administration. Food Safety Ordinance. 2005.

[6] Heaton, M. P., K. A. Leymaster, T. S. Kalbfleisch, J. W. Kijas, S. M. Clarke, J. McEwan, J. F. Maddox, V. Basnayake, D. T. Petrik, B. Simpson, T. P. Smith, G. G. Chitko-McKown, and the International Sheep Genomics Consortium. 2014. SNPs for parentage testing and traceability in globally diverse breeds of sheep. *Plos One*, 9(4): e94851.

[7] Joint Technical Committee QR-008. 2006. ISO 9000: 2006 Quality management systems—Fundamentals and vocabulary.

[8] Lee, J., D. Han, M. Rodolfo, J. Nayga, and S. Lim. 2011. Valuing traceability of imported beef in Korea: an experimental auction approach. *Australian Journal of Agricultural and Resource Economics*, 55(3): 360–373.

[9] Li, M. B., Z. X. Jin, and C. Chen. 2010. Application of RFID on products tracking and tracing system. *Computer Integrated Manufacturing Systems*, 16(1): 202–208.

[10] Li, T. 1995. ISO 8402-1994 Quality management and quality assurance vocabulary. *Construction Quality*, 2: 37–39.

[11] Mattevi, M., and J. A. Jones. 2016. Traceability in the food supply chain: awareness and attitudes of UK small and medium-sized enterprises. *Food Control*, 64: 120–127.

[12] Ministry of Agriculture of the People's Republic of China. 2006. Regulation on administration of livestock and poultry identification and the breeding files: No.67. *China Poultry*, 28(15): 57–58.

[13] Ministry of Agriculture of the People's Republic of China. 2012. Pilot scheme for animal electronic ear tags. *Hunan Journal of Animal Science & Veterinary Medicine*, 1: 44–45.

[14] Morcia, C., E. Rattotti, A. Stanca, G. Tumino, V. Rossi, S. Ravaglia, C. Germeier, M. Herrmann, I. Polisenska, and V. Terzi. 2013. Fusarium genetic traceability: Role for mycotoxin control in small grain cereals agro-food chains. *Journal of Cereal Science*, 57(2): 175–182.

[15] Oh, J., K. Song, J. Seo, D. Kim, S. Kim, K. Seo, H. Lim, J. Lee, H. Park, Y. Ryu, M. Kang, S. Cho, E. Kim, H. Choe, H. Kong, and H. Lee. 2014. Genetic traceability of black pig meats using microsatellite markers. *Asian-Australasian Journal of Animal Sciences*, 27(7): 926–931.

[16] Parenreng, S., N. Pujawan, D. Karningsih, and P. Engelseth. 2016. Mitigating risk in the Tuna supply through traceability system development. *International Food and Agribusiness Management Review*, 19(1): 59–82.

[17] Petter, O., and B. Melanie 2013. How to define traceability. *Trends in Food Science &Technology*, 29: 142–150.

[18] Qian, J., B. Fan, X. Wu, S. Han, S. Liu, and X. Yang. 2017. Comprehensive and quantifiable granularity: A novel model to measure agro-food traceability. *Food Control*, 74: 98–106.

[19] Qian, J., X. Yang, X. Wu, L. Zhao, B. Fan, and B. Xing. 2012. A traceability system incorporating 2D barcode and RFID technology for wheat flour mills. *Computer and Electronics in Agriculture*, 89(3): 76–85.

[20] Regulation (EC) No 178/2002. 2002. Available at: http://www.worldlii.org.

[21] Spanu, C., C. Scarano, M. Ibba, V. Spanu, and E. P. L. D. Santis. 2015. Occurrence and traceability of Listeria monocytogenes strains isolated from sheep's milk cheese-making plants environment. *Food Control*, 47: 318–325.

[22] Storoy, J., M. Thakur, and P. Olsen. 2013. The tracefood framework - principles and guidelines for implementing traceability in food value chains. *Journal of Food Engineering*, 115(1): 41–48.

[23] United States Department of Agriculture. 2017. Livestock and poultry: world markets and trade. Available at: http://usda.mannlib.cornell.edu/usda/fas/livestock-poultry-ma //2010s/2013/ livestock- poultry-ma-04-17-2013.pdf.

[24] Wang, X., Q. He, M. Maaja, J. Tomislav, and X. Zhang. 2016. Development and evaluation on a wireless multi-gas-sensors system for improving traceability and transparency of table grape cold chain. *Computer and Electronics in Agriculture*, 135: 195–207.

[25] Xiao, X., Z. Fu, L. Qi, T. Mira, and X. Zhang. 2015. Development and evaluation of an intelligent traceability system for frozen tilapia fillet processing. *Journal of the Science of Food and Agriculture*, 95(13): 2693–2703.

[26] Zhao, Y., B. Zhang, G. Chen, A. Chen, S. Yang, and Z. Ye. 2014. Recent developments in application of stable isotope analysis on agro-product authenticity and traceability. *Food Chemistry*, 145(7): 300–305.

Construction and thoughts regarding national agricultural big data infrastructure

Yu Limin[1,2&], Zhang Xiaojian[1&], Gao Wanlin[1*], Li Hui[1], Tao Sha[1], Wang Minjuan[1&], Zhang Guofeng[1]

(1. *College of Information and Electrical Engineering, China Agricultural University, Beijing 100083, China*;
2. *Shandong Agriculture and Engineering University, Shandong 250100, China*)

Abstract: This paper started with the current state of agricultural big data development in China, the adoption technology of a large agricultural data infrastructure was introduced, the construction content of a large national agricultural data infrastructure was analyzed, and the construction of Zhuozhou was proposed as the center and sub-model for China's agricultural data infrastructure and a reference and basis was provided.

Keywords: agriculture big data, infrastructure, construction content

Citation: Yu, L. M., W. L. Gao, H. Li, S. Tao, X. J, Zhang, M. J. Wang, and G. F. Zhang. 2017. Construction and thoughts regarding national agricultural big data infrastructure. International Agricultural Engineering Journal, 26(4): 341–348.

1 Introduction

Driven by the technological changes such as cloud computing, the Internet of Things, and mobile Internet, China has entered into the era of "big data". Big data has been used in such fields as e-commerce, marketing, clinical diagnosis, remote monitoring, drug research and development, and finance (Wang and Guo, 2016). The advent of big data technology has had a significant reshaping role in traditional production and life. The big-data thinking mode resulting from the big data era has affected all aspects of people's life.

Current economic development in China is now entering a "new normal" and is advancing the restructuring of the industrial structure and shifting in the mode of development. Within this backdrop, big data is rapidly gaining popularity and touching all fields of agriculture. Agricultural big data refers to the large data based on data analysis and use of big data concepts, techniques and methods to deal with agricultural production and sales of the entire chain generated by a large amount of data. Useful information got from the data processing guide agricultural production and management, circulation and consumption of agricultural products. The realization process of agricultural big data is an important part of agricultural informationization. The application of agricultural big data can provide new methods and ideas for agricultural research, government decision making, and the development of agriculture-related enterprises (Zhang et al., 2014). Wen (2013), president of Shandong Agricultural University, stated that agricultural big data involved all aspects of agricultural production and sales and was a cross-disciplinary data processing function. Wang (2013) also mentioned in the literature that establishing a national big data center for agricultural informatization and undertaking efforts to develop technologies such as cloud computing and big data mining are important means to solve the bottleneck in the development of China's agricultural informatization. We acknowledge the urgency and importance of agricultural big data construction.

An infrastructure is a material engineering facility

Received date: 2017-10-15 **Accepted date:** 2017-12-02

* **Corresponding author: Gao Wanlin,** Ph.D., College of Information and Electrical Engineering, China Agricultural University, Beijing 100083 P. R China. Email: 18615177887@163.com. &These authors contributed equally to this work and should be considered co-first authors.

that provides public services to social production and residents' livelihood. It is a public service system used to ensure the normal social and economic activities of a country or region. Infrastructure includes social infrastructure and is characterized by pioneering basic, non-tradable, indivisible, and quasi-public goods. It is generally led by the government and is the basis for the development of different undertakings of the national economy (Li et al., 2015). Chen (1999), an academician of the Chinese Academy of Sciences, stated that if the infrastructure in the industrial age was roads, railways, and bridges, a data information system is an important infrastructure in the era of knowledge-based economies. At this stage, government, research institutes, and companies are undertaking increasingly more researches and applying agricultural big data. According to the "Experimental Program of Big Data in Agricultural and Rural Areas" issued by the Ministry of Agriculture in 2016, during the 13th five-year plan, agricultural big data center construction and application would be focused on the following four tasks: data sharing, single product big data and market-oriented and big data application. Therefore, at the government level, agricultural big data infrastructure is the construction of agricultural big data foundation and it is an urgent solution to the problem.

2 Major agricultural big data infrastructure construction technology

2.1 Data acquisition technology

The data of agricultural information perception is the basis of agricultural big data construction and application. Agricultural information sensing technology is the basis of smart agriculture. As the nerve end of smart agriculture, it is the largest and the most basic link of demand in the entire smart agriculture chain and involves agricultural sensor technology including Radio Frequency Identification (RFID), Global Positioning System (GPS), and RS technologies (Li, 2012). Agricultural sensor technology is the core of both the agricultural Internet of Things and smart agriculture. Agricultural sensors can sense different information regarding production links such as farmland, facility agriculture, livestock husbandry, and aquaculture, as well as crop information, farmland environment information, and farm machinery operation information, providing rich real-time information for wisdom agriculture (Zhang et al., 2017); it is the source data for agricultural informatization. RFID technology is a non-contact automatic identification technology that automatically identifies a target object through radio frequency signals and obtains relevant data. The technology has a wide range of applications in the traceability of agricultural products providing insight into the collection of agricultural products circulation data.

GPS is a new generation of satellite navigation and positioning systems developed by the United States in the 1970's and completed in 1994. It has the capability of all-round real-time three-dimensional navigation and positioning at sea, on land, and in the air. It has all-weather functionality, high accuracy, automation, high efficiency, and some other salient features. In smart agriculture, with GPS technology, real-time three-dimensional positioning and precise timing capabilities, real-time farmland water, fertility, weeds, pests and diseases, crop seedling, and yield are described and tracked to obtain the production process with point-in-time location information (Yang et al., 2002). RS technology uses high-resolution sensors in smart agriculture to collect surface reflectance or radiation information of terrestrial spatial distributions. During different crops growth periods, RS monitoring is implemented and a large number of spatio-temporal changes of crop information are collected (Li, 2012).

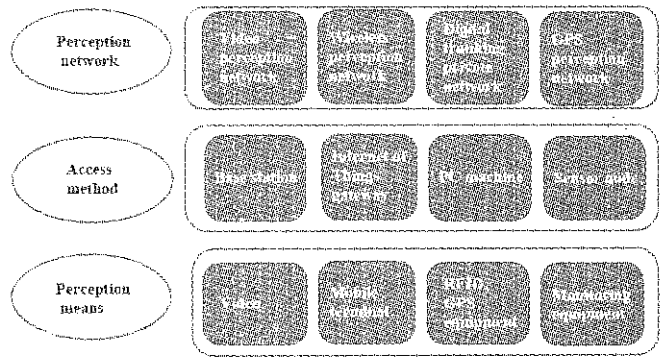

Figure 1 Data awareness infrastructure diagram

2.2 Data transmission technology

In smart agriculture, the most widely used agricultural information transmission technology is wireless sensor networks (WSNs). A WSN is a self-organizing multi-hop network system formed by wireless communication. It

consists of a large number of sensor nodes deployed in the monitoring area. A node has the functions of sensing acquisition, computing, wireless communication, automatic networking, and the ability to cooperate with other nodes to complete the monitoring mission (Peng et al., 2011). In agricultural informatization, this system completes the timely and accurate transmission of the collected data.

2.3 Data storage technology

Cloud storage is a new concept extended and developed in the concept of cloud computing. It is an emerging network storage technology that refers to network storage technology through cluster applications, network technology or distributed file systems and other functions. A large number of different types of storage devices work together through the application software to jointly provide the external data storage and business access functions of a system. This is a big data storage technology.

In the process of information collection, a large number of different formats of data are generated by sensors and other technologies. The agricultural big data center collects the different production data, processes, and circulates this to cloud storage devices to form the storage and management core of agricultural big data.

3 Goals of agricultural big data infrastructure construction

The national agricultural big data infrastructure is based on a government network and assumes the national agricultural remote sensing map as the data foundation. With the support of big data technology, the construction serves the goal of agricultural data management, information sharing, agricultural monitoring and early warning, and decision support visualization important agricultural information infrastructure. The goal of the project is to build an agricultural big data center at the ministerial and provincial levels and consolidate agricultural information from governments, research institutes, enterprises, and agricultural workers in different manners to integrate, share, and analyze agricultural big data. Further, an objective is to avoid the construction of duplicate infrastructures, eliminate excessive data management, and improve the comprehensive utilization of agricultural data resources and economies of scale.

4 Content of agricultural big data infrastructure construction

The main steps of the agricultural big data infrastructure platform construction are to build an agricultural big data center at the national and provincial levels, including the application of a set of data acquisition platform software; establish two basic supporting hardware and software environments; construct an agricultural remote sensing geography database, agricultural production link database, and agricultural products processing and circulation database; provide network access to agriculture-related databases based on in-depth data mining analysis; and develop a number of applications.

4.1 Data acquisition platform construction

In support of the process of agricultural production including arable land, sowing, fertilizing, plant protection, harvesting, storage and transportation, processing and sales of agricultural products, and circulation of agricultural products, relying on big data collection technology, an extensive large-scale agricultural data collection network was established. This was implemented at the provincial level to develop common content standards using personalized data sharing-compatible data acquisition software to ensure the maximum consistency of data, the establishment of data collection, and the updating and maintenance of the long-term mechanism.

4.2 Hardware and software support environment

The acquisition of the necessary hardware and system software and the implementation of an operating environment for agricultural big data is required. The related equipment must have sufficient scalability to address the requirements of application development.

4.3 Four databases construction

Based on different front-end data collection methods, we can build an agricultural remote sensing geographic database, agricultural production database, agricultural product processing and circulation database, and network

access agriculture-related database.

4.4 Application platform construction

4.4.1 Big data processing platform

The big data processing platform is mainly used for the processing of large amounts of agricultural data; the different data models can be divided into batch data processing, real-time data processing and relational data processing (Wang and Guo, 2016).

4.4.2 Big data storage platform

In the area of big data storage, a unified and efficient agriculture big data management platform was implemented and a massive unstructured data storage system based on distributed technology was established to manage data resources such as pictures, documents and videos. A large-scale structured data storage system must provide efficient retrieval of data services, research data resource integration, sharing, integration, and other key technologies to promote the open sharing of agricultural big data (Wang and Guo, 2016).

4.4.3 Big data analysis platform

According to the characteristics of agriculture, existing data mining and machine learning algorithms are improved to facilitate the data analysis of agricultural information. The construction of an agricultural big data analysis and mining platform includes the development of new data mining technologies such as data network mining, special group mining and graph mining. It also breaks through the data fusion and similarity connection based on objects in the agricultural field such as big data fusion technology, consumer demand and agricultural production management analysis.

5 Mode of agricultural big data infrastructure construction

In accordance with the unified planning, unified standards, unified construction, unified management, the strategic deployment of the provincial hierarchical design ideas, the construction of data resources as the core, big data technology as a support to business needs-oriented services in agriculture, and the whole industry chain to build a big data center. The center includes visualization of agricultural data collection, processing, analysis, sharing and management. The Beijing-Tianjin-Hebei region established a national agricultural data center in Zhuozhou to collect and compile different types of data for all regions in the country and provide a unified data

Figure 2 Construction of agricultural big data center

storage, data collection, data processing and analysis, and data visualization comprehensive service center to build a national network. The central blueprint included addressing the key areas of the agricultural industry data collection (a network), based on an agricultural remote sensing map for the entire agricultural industry chain big data display (a map), to address the requirements of the agricultural areas of big data product development (a Platform), using big data to promote modern agricultural science and technology innovation. The construction of sub-data centers in all provinces to complete the national data collection, data preprocessing and pre-analysis of the display process, and then to transmiss the information to the data center in Zhuozhou to complete the data collection. The analysis of the mining work is displayed in the agricultural data center. Infrastructure distribution diagram is as the following.

6 Agricultural big data infrastructure central structure

The central structure of the national agricultural big data infrastructure consists of a large platform with a two-tiered system at the national and provincial levels, providing data sharing services, functional services, and application support shared by all levels of the agricultural sectors. Through the distributed deployment of a big data platform, data front-end acquisition and data cleaning are

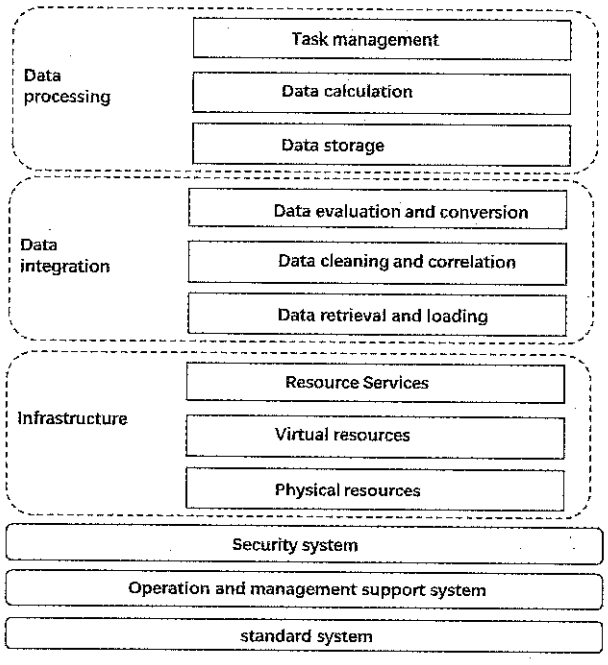

Figure 3 Big data computing center architecture diagram

facilitated to achieve vertical and horizontal integration and interconnection of data applications at all levels across the provinces. Drawing on the construction mode of the national big data center and relying on the existing infrastructure and agricultural data resources of the Pizhou Experimental Station of China Agricultural University, Beijing-Tianjin-Hebei region established a national agricultural data center in Danzhou and provincial data sub-centers in all provinces.

6.1 National center construction (Zhuozhou)

6.1.1 Basic service cloud platform construction

Based on cloud computing technology to build a flexible, shared and intensive basic service cloud platform, taking into account the overall agricultural data centers and the regional agricultural sub-data centers distance and diversification of network transmission issues, taking into account the unified planning, unified management, unified design of the building, build a unified cloud management platform in the overall agricultural data center (Zhuozhou) to uniformly dispatch and manage the cloud resources of the overall agricultural data center and the agricultural sub-datacenters (provinces) in various provinces in the whole country to realize the global management and maintenance, and the cloud service host will be deployed near each data center to achieve optimal resource allocation and distribution.

A unified cloud service management center will be established to centrally manage the local resource management of agricultural data centers and the cloud resources of the provincial agricultural sub-regions across geographic regions to unify the management processes and management models. Through the establishment of a basic service cloud platform, the instant delivery of cloud services ,such as cloud hosts, cloud desktops, cloud storage, and cloud sharing space enhances business continuity, effectively reduces the total cost of ownership, and builds a comprehensive agricultural infrastructure.

6.1.2 Big data integration and analysis service platform construction

The provincial data sub-center obtained the true and unique data based on the data integration and sharing. Big data centers within the vertical and horizontal to realize data sharing. That will break the barriers to business and

allow the data generated during all stages of agricultural production to converge. Actively contact and coordinate with other departments to open up the interoperability of data channels to achieve the exchange of environmental data sharing. Use big data technology to complete the platform for collecting, processing, managing and analyzing internet related information of concerned industry. Internet data collected by multi-source and multi-channel is stored in high quality form. National agricultural data center establishes a unified management, efficient operation, distributed storage, resource sharing platform. The national agricultural data center completes the work of collecting, analyzing, and displaying the data uploaded by the agricultural sub-data centers in the different regions.

The integration of data resources refers to the preprocessing of the collected data by the agricultural sub-data centers in each region and then uploading the data to the national agricultural data center for data integration. The data integration mainly uses the configured authorized data sources for data extraction using the collection tools according to the rules established for in-depth cleaning and conversion of data, while the task of data integration process can achieve dynamic monitoring to meet the requirements of big data analysis. At the same time, ensure the process can be maintained, supervised, controlled and manageable.

6.1.3 Data synchronization and cleaning

By configuring data synchronization tools, data replication between databases and automatic synchronization can be established. For data resources with considerable amounts of data and difficult data changes, data synchronization is performed by analyzing database logs. For data resources with small amounts of data and definite data changes, ETL tools are used to time-align data resources and obtain change data to extract data.

According to the conversion rules, the data in the exchange information base is transformed according to the information model in the basic relational library. The conversion of the data involves hundreds or thousands of operations, therefore, how to make them efficient, scalable, and maintainable is extremely important. The conversion of data is based on the conversion rule set. The rule set design must be managed in an open manner. That is, users can add conversion algorithms according to their requirements. If users require complicated data conversion, this can be achieved through a series of conversion combinations.

6.1.4 Data quality monitoring

Build data quality detection and configuration function module, support the custom configuration of data quality monitoring model, use technology monitoring and business logic verification, and carry out data source acquisition, transmit and apply the whole process of standardization, consistency and accuracy check to achieve the result which based on logical verification and monitoring management of data from different sources.

6.2 Regional sub-center construction (provinces)

6.2.1 Basic services cloud platform construction

Based on the virtualization technology to build a basic service cloud platform, the virtual machine can be quickly released through a template-based and process-based workflow for performing daily work, study, and scientific research. Through a unified cloud computing management platform, the resources within the regional and national agricultural data centers are centrally dispatched and managed, significantly improve the utilization efficiency of the information technology infrastructure resources.

6.2.2 Basic data processing and analysis platform construction

The core tasks of a provincial agricultural sub-data center are data collection, data standardization, and preliminary analysis, and then uploading data to the national agricultural big data center for deeper data mining, analysis, and visualization work. The main task in the regional agricultural sub-center is to complete the data collection and data preprocessing.

6.2.2.1 Data collection

Data acquisition is a preparatory work for big data analysis. The data acquisition system must collect data from multiple data sources and unify the logical model of different data to standardize the storage and integration of the data in all fields and stages of agriculture. For

structured databases, such as Oracle, SQL Server, the use of database content derived achieve data collection. Using JDBC and other sophisticated database access technology to achieve data acquisition. Establishing a complete set of data acquisition interface achieve efficient data collection process. The core of an agricultural big data center construction is data, hence, the authenticity, accuracy, uniqueness, and authority of the data are crucial. If the data is not accurate, any result can become meaningless. At present, the issue of "multiple sources of data" is more prominent. Many departments are producing data. Because of the different standards and methods of data collection, the sources of data are different and there can be a situation that the data conflict. If the data are different, the results of the analysis will be different. Therefore, establishing a scientifically efficient and standard compatible data collection platform at the provincial sub-center is the basis for subsequent work.

6.2.2.2 Data preprocessing

The collected data processing and streamlining, delete useless, duplicate, wrong data to achieve format conversion, data cleaning and data verification, etc., involve the following four stages: 1) Format conversion: in accordance with the unified data standards and the established format conversion rules, the structured data follow format conversion processing. Transcoding: the data from different sources in the data represented by the code, a unified conversion into the platform used in the format of the code. Data truncation: exceeded the length of the data field, from the back to the front part of the truncated (to deal with half a character case), the need to cut the entire contents of the field (and add the field description), save the file, the same record multiple truncation field merge for a document, mergers need to develop a format to distinguish. 2) Data cleaning: Based on the predetermined strategy, structured and unstructured data are de-duplicated, and the type of data is checked and filtered. Garbage filtering: Garbage filtering is performed on all types of garbage data accessed by each data source. Sample Based Filter: The user provides a filtered sample, the system filters the data according to the sample. Data Deduplication: Support for deduplication of structured data and unstructured data. 3) Data verification standard: During data exchange, the data exchange layer calculates the verification value of the transmitted data. After the data is received by the receiver, the correctness and completeness of the data are verified through the verification value. 4) Generate floor and floor data storage data sharing platform. After data preprocessing, the data is stored in a parallel file system and then uploaded to the national agricultural data center for further analysis.

6.2.2.3 Preliminary analysis and visualization of data

After the data preprocessing, invalid data is removed and the existing data can be analyzed preliminarily through the established rules (models). The analysis structure can be visualized to display, to a certain extent, the performance of a specific area, field, process big data analysis of scientific research.

7 Conclusion

It is necessary to coordinate the construction of an agricultural big data infrastructure from the national and regional levels. The global planning and construction of a standardized agricultural big data center by the state can not only avoid the misuse of resources caused by repeated acquisition of basic geographic information but also facilitate the sharing of basic data and form an effective information updating mechanism. In the process of construction, we must not only attach importance to the policy of organization and coordination, equipment configuration, data standardization, and information sharing but also the requirement to strengthen personnel training, especially the training of agricultural big data application talents (Zhou et al., 2000; Hua and Wang, 2016).

[References]

[1] Chen, Y. Y. 1999. Strengthening the construction of the national spatial data infrastructure. *Leading Decision Information*, (43): 21. (In Chinese)

[2] Hu, B. F., and Y. F. Wang. 2016. The United States and Britain government big data construction application research and enlightenment. *Frontier*, (07): 78–83. (In Chinese)

[3] Li, D. L. 2012. Internet of things and wisdom agriculture. *Agricultural Engineering*, 02(1): 1–7. (In Chinese)

[4] Li, T. Z. and J. L. Lu, and X. L. Hou, and J. Ma. 2015.

Internet big data innovative infrastructure and its construction ideas. *Technology Economics*, (07): 33–40, 50. (In Chinese)

[5] Peng, X. D., and T. M. Zhang, and Y. Chen, and J. Y. Li. 2011. Application of wireless sensor networks in agriculture. *Agricultural Mechanization Research*, (08): 245–248. (In Chinese)

[6] Wang, R. J. 2013. Bottleneck of China's agricultural informatization development and countermeasures. *Chinese Academy of Sciences,* (03): 337–343. (In Chinese)

[7] Wang, W. S., and L. F. Guo. 2016. On China's agricultural big data center construction. *Big Data,* (01): 28–34. (In Chinese)

[8] Wen, F. J. 2013. Strategic significance and synergetic mechanism of agricultural big data research. *Higher Agricultural Education*, (11): 3–6. (In Chinese)

[9] Yang, M., and C. S. Zhao, and T. Zhang, and X. C. Yan, and H. W. Yao. 2002. 3S technology in the development of fine agriculture. *Journal of Agricultural University of Hebei*, (04): 241–243. (In Chinese)

[10] Zhang, H. R., and Z. L. Li, and T. F. Zou, and X. Y. Wei, and G. C. Yang. 2014. Agricultural big data review. *Computer Science*, 2014(S2): 387–392. (In Chinese)

[11] Zhang, J. H., J. H. Zhang, and J. Z. Wu, and S. Q. Han, and M. S. Zhu, and H. Shi, and F. F. Li, and F. T. Kong. 2017. Advances and performance analysis of agricultural sensor technology. *Agricultural Outlook*, 13(1): 38–48. (In Chinese)

[12] Zhou, X., W. Z. Wu, and L. Zhang. 2000. Several issues of national spatial data infrastructure construction. *Bulletin of Surveying and Mapping*, (10): 22–23. (In Chinese)

Agricultural informatization: research and design on the rural tourism recommendation system

Zhang Xiaojian[1], Yu Limin[2], Gao Wanlin[1*]

(1. *College of Information and Electrical Engineering, China Agricultural University, Beijing 100083, China*;
2. *Shandong Agriculture and Engineering University, Shandong 250100, China*)

Abstract: In recent years, the application of recommended technology in the field of tourism has been favored by many researchers. The recommendation system can recommend visitors to the potential preferences and help visitors to choose. China's rural tourism has become a trend, but the recommended technology in rural tourism applications is less research. In this paper, firstly, we aimed at the characteristics of rural tourism in season, tourists, geography spatial distribution and re-voyage rate and made the analysis. In term of in season, it means with seasonal characteristics. In term of tourists, most of them are urban people. In term of geography spatial, tour trip threshold is 20 km from the city, which means the distance from the city within 20-100 km within the scope of the rural tourism is the frequent occurrence of the zone. Secondly, according to the characteristics of seasonal and geo-spatial distribution, a collaborative filtering algorithm combined time and geographical context was proposed. Thirdly, based on the established rural tourism project in Hebei province, the rural tourism recommendation system was established. The system includes information display interaction, log collection and processing, recommendation engine, four main modules of data storage, and each module's function and business processes were introduced. Finally, the application of Hebei rural tourism system is possible and it can provide the users with personalized tourism information and help users make quick and accurate choice.

Keywords: rural tourism, recommendation system, personalized tourism, collaborative filtering, context

Citation: Zhang, X. J., W. L. Gao, and L. M. Yu. 2017. Agricultural informatization: A rural tourism recommendation system research and design. International Agricultural Engineering Journal, 26(4): 349–355.

1 Introduction

Rural tourism is a new type of business, which uses the rural natural environment, pastoral landscape, production and management form, folk culture, farming culture, farmhouse and some other resources to provide the city tourists with tourism, leisure, experience, fitness, entertainment, shopping and vacation (Guo and Han, 2010; Zhang, 2014). In recent years, rural tourism in China has been developed rapidly. According to the information that Chinese industry research network released in *2017--2020 Research of Chinese Leisure Agriculture and Rural Tourism Market Analysis and Development Forecast Report* (China Industry Research, 2016), at the end of April 2015, there were 95,000 villages in China has carried out the activities of leisure agriculture and rural tourism, the units engaged in leisure agriculture and rural tourism business reached 1.93 million, of which more than 2.2 million are farm music, more than 41,000 are scale parks, received nearly 840 million tourists, and the annual operating income is more than 320 billion RMB. At the same time, Dr. Huang (2015) through questionnaire survey and use of logistic model analysis showed that China's domestic tourism is a major trend from town to rural areas. So how to help visitors quickly and accurately find their attractions of interest, improve users to find their needed information efficiency so as to promote the development of rural tourism is very worthy of study.

Recommendation system is defined as an information

Received date: 2017-09-22 **Accepted date:** 2017-12-02

* **Corresponding author: Gao Wanlin,** Professor of College of Information and Electrical Engineering, China Agricultural University, 100083, China. Email: xjzhang0504@163.com. Tel: +8613161975123. &These authors contributed equally to this work and should be considered co-first authors.

filtering system, for predicting a user's article "score" or "preference" (Grossman, 2010; Lu et al., 2015). At present the recommended system in the application of tourism, unlike the widely used and matured online business sites such as Amazon (Linden et al., 2003; Smith et al., 2017), DVD rental website Netflix (Gomez-Uribe et al., 2016; Hallinan and Striphas, 2016), Taobao (Grossman, 2010), is on the research and developing stage. There are specific applications, such as Triplehop's TripMatcher (used by www.ski-europe.com) and VacationCoach's expert advice platform (used by www.travelcity.com). They simulate the consultation process between tourists and travel agencies according to the user's current needs, preferences and propose constraints, to provide users with tourism programs. Quna recommended tourist attractions or travel packages to users based on information such as destination, departure date, and number of tour days. Werthner et al (2015) found that with the development of information and communication technology, travelers are reducing their reliance on tourism agencies, and focusing on the network for tourism information. But at the same time, the development of the internet has made the tourism information produced an overload phenomenon. Park and Jang (2013) proved that when the choices of travel are too much, the effect is often the opposite. Coupled with the time people fragmented, so the tourism platform needs to recommend technology to help visitors find fast and accurate travel advice, thus saving tourists time and improving platform efficiency. Although China's rural tourism has become a trend, while according to the research that recommended technology in rural tourism has not been studied and applied. Because rural tourism has its own characteristics compared with the urban tourism in aspects of season, tourists, geography spatial distribution and revisit rate, it can't directly use the recommended technology and system of urban tourism. Therefore, it is of great significance to study the recommendation system of rural tourism with the characteristics of rural tourism itself.

Recommendation system algorithm generates a recommendation list, and it is mainly divided into four kinds: collaboration filtering recommendation, knowledge-based recommendation, content-based recommendation, and hybrid recommendation. Collaboration filtering recommendation technology is proposed first, and is the most researched, the most widely used and the most recommended technology. In the tourism recommendation, it has also been widely studied and applied (Nilashi et al., 2015; Ortega et al., 2016; Koohi et al., 2017). Collaboration filtering recommendation algorithm can be divided into two types of methods, neighborhood-based and model-based (Koren et al., 2015; Shi et al., 2014; Hernando et al., 2016). The model-based approach used the users' past behavior to learn and establish the prediction model. It needs to go through a large number of real historical data for model training. If the amount of data is not enough or model selection is not good, the effect will be much lower than the neighborhood-based method.

Neighborhood-based method can be divided into user-based CF and item-based CF. User-based CF recommend some items to the users, which are from the third party sharing the same hobbies and interests with them. The recommended results focus on small groups of users with similar interests and hot spots. It is an older algorithm, had already been applied in the e-mail personalized recommendation system Tapestry in 1992. Item-based CF recommended users with the items which are similar with their previous likes. Recommendation will be focusing on maintaining the user's historical interest, and it is a relatively new algorithm. In the famous e-commerce site Amazon (Smith and Linden, 2017) and DVD rental website, Netflix (Gomez-Uribe and Hunt, 2016) have been widely used. Since item-based CF is suitable for long tail items, and can provide compelling recommendations, therefore, the system uses item-based CF as the basic algorithm. Lamsfus et al. (2015) pointed out that context played an important role in tourism choice, which was also a hot topic in tourism research. Therefore, this paper presented a rural tourism recommendation algorithm based on the characteristics of rural tourism in Hebei Province, the use of object-based collaborative filtering algorithm, and the integration of user time and geographic context information, and the design of rural tourism recommendation system in Hebei Province.

1.1 Characteristics of rural tourism

The study of rural tourism recommendation system must be based on the characteristics of rural tourism itself to design the recommended system. According to the previous studies on rural tourism, it is concluded that rural tourism has distinctive characteristics in terms of seasonality, tourists, geography spatial distribution and re-visited rate. Specifically, it has the following four points:

1) Seasonal strong (Zhang, 2017). Although other forms of tourism are seasonal, the seasonal nature of rural tourism is particularly evident. Hebei Province is located in the north of China, with spring, summer, autumn and winter seasons. Rural tourism mainly has natural scenery, folk customs and agricultural characteristics, so, the features and themes of different seasons tourism will be different, and there are obvious off-season and peak season phenomena. For example: For tourists like picking, while picking will be varies at different seasons. For tourists who love nature scenery, while scenery in different seasons will be very different.

2) Tourists are mostly urban people. City's fast-paced life has led to an increasing number of urban diseases, which have prompted urban residents and workers to drive to the countryside away from the city, be close to nature and look for cleanliness. This demand has greatly contributed to the development of rural tourism, so rural tourism is mainly for urban people holiday leisure.

3) In the geographical distribution. As the rural transport is under developed, accommodation and other facilities are not perfect, so most of the rural tourists will choose self-driving travelling. This limited the rural tourism in the geographical distribution of space. Those tourism attractions that are far away from the urban area will be rarely chosen. Lu (2014) and others made hot research analysis on domestic and foreign rural tourism in recent 20 years, they concluded that the rural tourism travel threshold was 20 km away from the city, 20-100 km from the city within the scope of the rural tourism is the frequent occurrence of the zone.

4) High re-visited rate. This is also a major feature which is different from the other tourism. Rural tourism is mostly used as a leisure and entertainment, for ease the pressure, and be close to nature, the relative re-visited rate is very high.

2 Main algorithms and techniques

2.1 Item-CF

The core idea of the collaborative filtering algorithm based on items is to calculate the similarity between items by analyzing the user's behavior records. There are two main steps: The first step is to calculate the similarity between items, the second step is based on the similarity between items and the user's historical behavior to generate a recommended list.

In this paper, the similarity between items was calculated by cosine, assuming that the number of users in the system is n and the number of items is m, the user's score matrix for the item is a matrix of $n \times m$. Remember $r_{p,q}$ that the user u_p the item i_q score, then each item can be expressed as all users of its rating vector, which is $i_q = <r_{1,q}, r_{2,q}, \ldots\ldots r_{n,q}>$, the similarity between items can be calculated by the following formula:

$$sim(i_p, i_q) = \frac{\vec{i_p} \cdot \vec{i_q}}{\| \vec{i_p} \| \| \vec{i_q} \|} = \frac{\sum_{u \in U} r_{u,p} r_{u,q}}{\sqrt{\sum r_{u,p}^2} \sqrt{\sum r_{u,q}^2}}$$

Calculate the similarity between items, the next step is to combine the user's historical behavior, that is, the user's rating of historical items, to the user to generate an initial recommendation list. This article is based on the predicted user's score on the items, thus inferring the user's favorite degree of the item. The item-based CF algorithm predicts the item's rating based on the rating of the neighbor of the item. The formula is as follows:

$$\hat{r}_{u,p} = \frac{\sum_{i_q \in N^k(i_p)} sim(i_p, i_q) r_{u,i_q}}{\sum_{i_q \in N^k(i_p)} sim(i_p, i_q)}$$

where, $N^k(i_p)$ represents the set of neighbors of the item, that is, the k items that are most similar to the item i_p, K takes 25.

2.2 Fusion context technology

Context, also known as the situation in the recommended system, the situation generally in the recommended system plays a filtering role. There are three ways to apply, including the situation pre-filtering, post-filtering and situational modeling (Adomavicius and Tuzhilin, 2011). In recent years, the application of

context in tourism recommendation system has been paid more and more attention by researchers. Such as Trattner et al. (2016) used the weather conditions as the context for the impact of POIs, the results showed a significant increase in the Rank-GeoFM algorithm. Kaya and Bridge (2016) proposed a way to recommend the location of the shot to improve the existing algorithm. Vakeel and Ray (2017) defined the motivation as a recommended contextual factor that could be used to explain the delivery to the user. They distinguished the seven motivations of different POI check-in users as a basis for post-filtering methods. This paper will use context filtering to filter out unrelated recommendations and adjust the ranking in the list based on location and time contexts.

Location context, according to the characteristics of the rural tourism mentioned earlier, within 20-100 km from the city within the scope of the rural tourism is the frequent occurrence of the zone. So, when the user is located in the town, the priority recommended place for him (or her) will be 20-100 km away from the town. When the user has been in the rural tourism process, the system will recommend the nearby attractions. Time context, according to the characteristics of the rural tourism mentioned earlier, is seasonal strong, this paper will first get to the user's system time, and then generalize the season to the recommended list to filter.

3 Design of country tourism recommendation system

3.1 Introduction of rural tourism platform in Hebei Province

Hebei Province rural tourism platform is mainly based on the status quo and characteristics of rural tourism development in Hebei Province. It provides tourist information for rural tourism. Based on data mining and recommendation technology, it provides users with personalized service. The goal is to expand the rural tourism service channels, thus driving the development of rural tourism industry in Hebei Province. Platform architecture design is shown as follows.

Programming language: Java, development tools: eclipse, server: tomcat 7.0, database: MySQL, Using SpringMVC + hibernate technology architecture development.

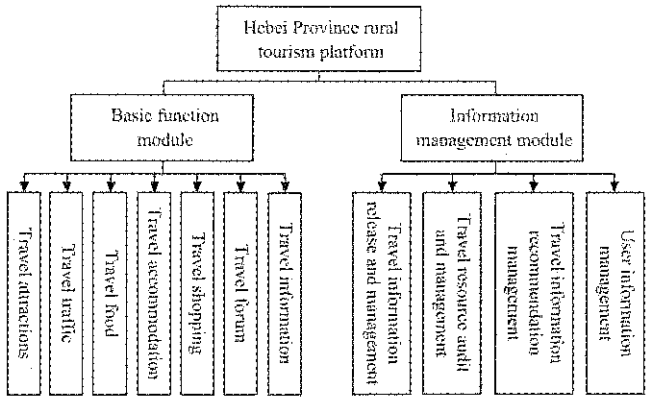

Figure 1 Structure of rural tourism platform in Hebei Province

Rural tourism recommendation system is based on Hebei rural tourism platform for the design and development. Using Java language, the user's behavior log collection, analysis and storage, and the design of the recommended algorithm were written into the rural tourism platform in Hebei Province, and the recommended system functions were embedded in the rural tourism platform. The design of the recommended system is described in detail in the next section.

3.2 Design of rural tourism recommendation system

The rural tourism recommendation system analyzed the travel information of the user in the past, gave users choices to help them to overcome the information overload and the selective problems. Figure 1 depicted the framework of a rural tourism recommendation system. The system consists of information display interactive module, log collection and processing module, recommended engine module, data storage module which composed of four major components. Figure 2 described the main functions of each section and the system business process description.

3.2.1 Information display interactive module

The information display interaction module is mainly used to complete the interaction and data transfer between the system and the user in the form of a graphical interface. The main way of interaction is system automatic push and user feedback search.

System automatic push includes two cases, one is user login automatically after the recommendation of the list recommended to the user, this is the user without any operation in the case. The other is the user login in the

browsing process for some of the recommended information generated behavior, such as: click, browse, collection. This assumes that the user clicks, views, and collects the behavior that represents the user's interest in the object. These behaviors generate a behavior log, which is collected and processed by the log acquisition module and used as a basis for the next recommendation list.

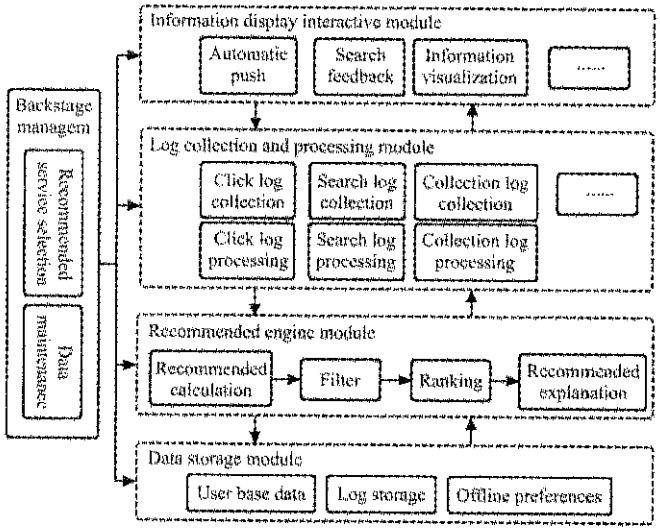

Figure 2 Architecture diagram of rural tourism recommendation system

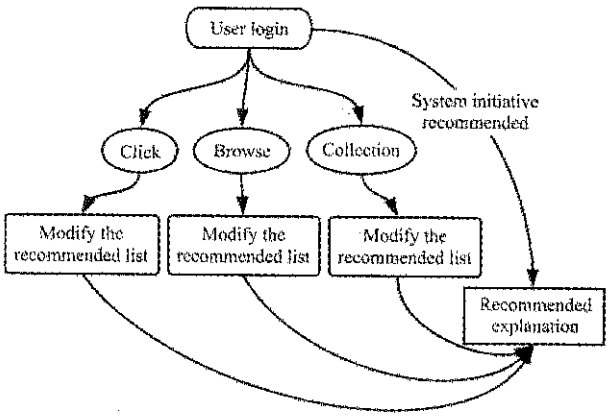

Figure 3 System actively pushes the flow chart

User active search feedback refers to the user with the purpose of the search. The system gives the user feedback on the basis of search keywords and the recommended list.

The visualization of the recommended information. The system uses two forms, the first is the traditional list of forms of display, which is directly based on the recommended list of sorting order. The second is displayed on the map, call the Baidu map API, where the distance will also calculate the distance to the user's current location, and finally the attractions and attractions to the user's current location of the path will display on the map.

3.2.2 Log collection and processing module

User records have a large part of the log information, so log information collection and processing play an important role. This function is mainly on the user click log, search log, collection and purchase log collection. The log collection and processing module adopt flume framework, which is divided into three layers: agent layer, collector layer and store layer. Where the agent layer is responsible for log collection. the collector layer is deployed on the central server to receive the log data sent by the agent layer and is written to the corresponding store layer after a simple process. The store layer is responsible for providing permanent or temporary log storage services and sending the log to the recommendation engine module as a basis for recommendation.

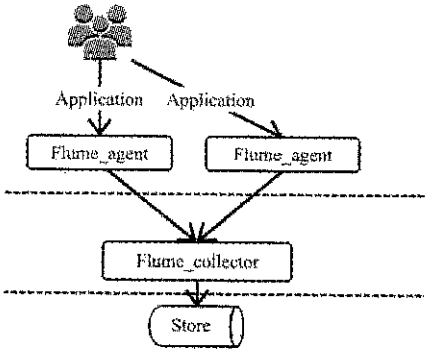

Figure 4 Information collection principle flow chart

3.2.3 Recommended engine module

The engine is the core of the system, and is responsible for the calculating, filtering and sorting of recommended information. According to Xiang (2012), the recommendation engine architecture is shown in Figure 5.

Part 1 is responsible for getting user behavior data from the database and cache, and generating the eigenvectors of the current user by analyzing the different behaviors. The module finally outputs the user's eigenvector. Part 2 is responsible for translating the user's feature vector into a list of initial recommended items. Part 3 is responsible for filtering the initial recommendation list, ranking processing, and giving a recommended explanation to generate a final recommendation list.

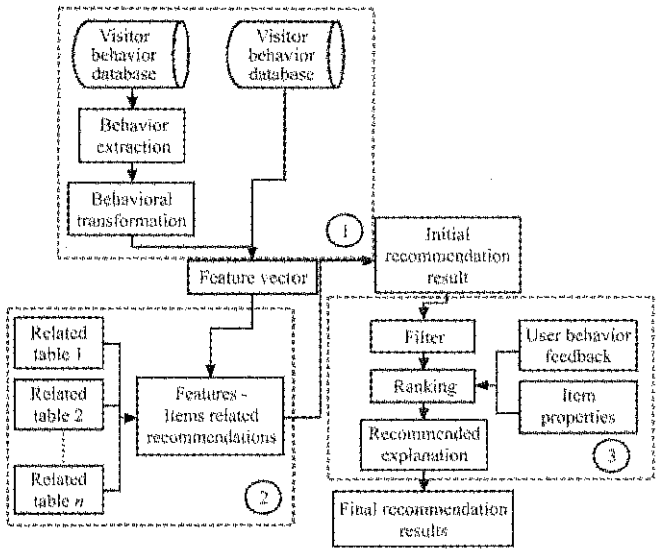

Figure 5 Recommended engine architecture

3.2.4 Data storage module

Data storage includes not only basic user data and item data storage, but also the list of offline recommended storage, log storage, etc., This recommended system uses the MySQL database for data storage. MySQL database, using the standard SQL data language form, with small size, fast, supporting Java language, multi-threaded, supporting GIS spatial expansion, can meet the needs of the system.

4 Conclusion

The idea of applying the recommended technology in rural tourism in combination with the characteristics of the rural tourism itself was put forward. It is based on the application of the recommended technology in the tourism industry, and it mainly included the followings:

1) The characteristics of rural tourism were studied, they are seasonal strong, tourists are mostly urban people, the distribution of geographical space, the characteristics of high re-visited rate .The seasonal and geographical distribution are used as a context to improve the recommended accuracy.

2) Designed rural tourism recommendation system is mainly composed of four modules: information display interactive module, log acquisition and processing module, recommended engine module and data storage module, and the functions of the modules were explained.

3) The recommended techniques - the collaborative filtering technology and fusion context technology, as well as the technical principles were introduced.

This is the preliminary study of rural tourism recommendation technology and system, and there are two shortcomings. First, this study mainly took into account the user travel time and the user's current geographical location, in fact, there are many factors that affect the user's choice of tourism, such as the user age, weather and etc. We will do more research later. Second, the design of this system is mainly for the characteristics of rural tourism in Hebei Province. If you want to promote the rural tourism in whole country, for different regions, we need to consider the actual and local factors. We plan to study the different characteristics of rural tourism in different regions in future in order to apply the rural tourism recommendation system to the national rural tourism platform.

[References]

[1] Adomavicius, G., and A. Tuzhilin. 2011. Context-aware recommender systems. *Recommender Systems Handbook*, 217–253. Springer US.

[2] China Industry Research. 2016. 2017–2020 Research of Chinese leisure agriculture and rural tourism market analysis and development forecast report. Available at: www.wenku.baidu.com.

[3] Gomez-Uribe, C. A., and N. Hunt. 2016. The Netflix recommender system: Algorithms, business value, and innovation. *ACM Transactions on Management Information Systems (TMIS)*, 6(4): 1–19.

[4] Grossman, L. 2010. How computers know what we want—before we do. *TIME*, (2010): 2–7.

[5] Guo, H. C., and F. Han. 2010. Review on the development of rural tourism in China. *Progress in Geography*, 29(12): 1597–1605.

[6] Hallinan, B., and T. Striphas. 2016. Recommended for you: The Netflix Prize and the production of algorithmic culture. *New Media & Society*, 18(1): 117–137.

[7] Hernando, A., J. Bobadilla, and F. Ortega. 2016. A non-negative matrix factorization for collaborative filtering recommender systems based on a Bayesian probabilistic model. *Knowledge-Based Systems*, 97(C): 188–202.

[8] Huang, R. 2015. Study on the domestic tourism demand of urban residents in China. Ph.D. diss. Huazhong University of Science and Technology, WuHan.

[9] Kaya, M., and D. Bridge. 2016. Improved recommendation of photo-taking locations using virtual ratings. *Proceedings of the Workshop on Recommenders in Tourism co-located with 10th ACM Conference on Recommender Systems (RecSys*

2016), Boston, MA, USA, Sep. 5.

[10] Koohi, H., and K. Kiani. 2017. A new method to find neighbor users that improves the performance of Collaborative Filtering. *Expert Systems with Applications: An International Journal*, 83(C): 30–39.

[11] Lamsfus, C., D. Wang, A. Alzua-Sorzabal, and Z. Xiang. 2015. Going mobile: Defining context for on-the-go travelers. *Journal of Travel Research*, 54(6): 691–701.

[12] Linden, G., B. Smith, and J. York. 2003. Amazon. com recommendations: Item-to-item collaborative filtering. *IEEE Internet Computing*, 7(1): 76–80.

[13] Lu, J., D. Wu, M. Mao, W. Wang, and G. Zhang. 2015. Recommender system application developments: a survey. *Decision Support Systems*, 74(C): 12–32.

[14] Lu, X. L., Y. H. Cheng, and L. W. Wang. 2014. 20 Years of rural tourism. *Resources Science*, 36(1): 0200–0205.

[15] Nilashi, M., O. B. Ibrahim, N. Ithnin, and N. H. Sarmin. 2015. A multi-criteria collaborative filtering recommender system for the tourism domain using Expectation Maximization (EM) and PCA–ANFIS. *Electronic Commerce Research and Applications*, 14(6): 542–562.

[16] Ortega, F., A. Hernando, J. Bobadilla, and J. H. Kang. 2016. Recommending items to group of users using Matrix Factorization based Collaborative Filtering. *Information Sciences*, 345(C): 313–324.

[17] Park, J. Y., and S. S. Jang. 2013. Confused by too many choices? Choice overload in tourism. *Tourism Management*, 35(4): 1–12.

[18] Shi, Y., M. Larson, and A. Hanjalic. 2014. Collaborative filtering beyond the user-item matrix: A survey of the state of the art and future challenges. *ACM Computing Surveys (CSUR)*, 47(1): 3.

[19] Smith, B., and G. Linden. 2017. Two decades of recommender systems at Amazon. com. *IEEE Internet Computing*, 21(3): 12–18.

[20] Trattner, C., A. Oberegger, L. Eberhard, D. Parra, and L. B. Marinho. 2016, Understanding the impact of weather for POI recommendations. *RecTour@ RecSys,* 2016: 16–23.

[21] Vakeel, K., and S. Ray. 2016. A motivation-aware approach for point of interest recommendations. *RecTour@ RecSys*, 2016: 24–29.

[22] Werthner, H., A. Alzua-Sorzabal, L. Cantoni, A. Dickinger, U. Gretzel, D. Jannach, and B. Stangl. 2015. Future research issues in IT and tourism. *Information Technology & Tourism*, 15(1): 1–15.

[23] Xiang, L. 2012. *Recommended system practice.* Beijing: Post & Telecom Press.

[24] Yehuda, K., and R. Bell. 2015. Advances in Collaborative Filtering. *Recommender Systems Handbook.* Springer US, 77–118.

[25] Zhang, X. R. 2017. A study on the countermeasures to solve the seasonal dilemma of rural tourism. *Agricultural Economy*, (02): 58–59.

[26] Zhang, Z. Q. 2014. A review on the current development of rural tourism at home and abroad. *Chinese Agricultural Science Bulletin*, 30(08): 307–314.

Image registration method of visible and thermal infrared images based on phase congruency for water stress monitoring

Li Han[1], Zhang Man[1*], Li Bin[2], Zheng Wengang[2], Li Minzan[1]

(1. *Key Laboratory for Modern Precision Agriculture System Integration Research, Ministry of Education, China Agricultural University, Beijing 100083, China*;

2. *Beijing Research Center for Information Technology in Agriculture, Beijing Academy of Agriculture and Forestry Sciences, Beijing 100097, China*)

Abstract: In order to realize image fusion for the development of an automatic water stress monitoring system, this paper presented a phase congruency and speeded-up robust feature detection method (SURF) based on image registration algorithm. The proposed method combined the advantages of phase congruency model and SURF. The advantage of phase congruency based on edge detection method is that it is invariant to illumination, and contrast variation, which makes it more suitable for edge detection for images from different types of sensors, and easier to set threshold for wide classes of images. The advantage of SURF is its speed and robustness. The proposed algorithm firstly performed edge detection based on phase congruency for visible and thermal infrared images, then conducted feature point detection and matching for the feature points on edge images. Next, affine transform method and linear interpolation method were used for visible and thermal infrared images. The proposed algorithm was applied to 15 pairs of visible and thermal infrared images. More than three pairs of feature points were obtained for all those 15 pairs of images after false match filtering using RANSAC method. The time used is within 5 seconds, and the RMSE is within 10 pixels. The experimental results showed that both the efficiency and accuracy of the registration method could meet the practical requirement.

Keywords: thermal infrared image, phase congruency, edge image, SURF

Citation: Li, H., M. Zhang, B. Li, W. G. Zheng, and M. Z. Li. 2017. Image registration method for water stress monitoring based on phase congruency for visible and thermal infrared images. International Agricultural Engineering Journal, 26(4): 356–363.

1 Introduction

The increasing shortage of water and increasing costs of irrigation worldwide have led to extensive explorations on developing irrigation scheduling methods that maximize the water efficiency. As the development of precision irrigation systems, the need for real time irrigation scheduling method is more and more intense to maintain the soil moisture within fine bands. Jones has divided the irrigation scheduling approaches into three main categories: soil water content measurement, soil water balance based on calculations, and plant 'stress' sensing (Jones, 2004). He then analyzed the advantages and disadvantages of each class. Because of the non-contact and non-destructive characteristics of imaging method, both visible imaging and thermal imaging have presented potential of being developed into real time automated irrigation scheduling systems, respectively.

Many studies have been reported to use visible imaging for visible wilting detection. A method for non-contact, and quantitative detection of plant water stress through machine vision techniques was presented when the water stress symptoms showed in the early period (Kacira and Ling, 2001; Kacira et al., 2002). The feasibility of features extracted from the projected canopy area of plants for plant water stress detection was proved. Mizuno et al. (2007) developed a farmer support system using features extracted from image data acquired by the

Received date: 2017-10-31 **Accepted date:** 2017-12-23

* **Corresponding author: Zhang Man**, Professor, Doctor. Key Laboratory for Modern Precision Agriculture System Integration Research, Ministry of Education, China Agricultural University, Beijing 100083, China. Email: cauzm@cau.edu.cn.

Field Server for irrigation scheduling purpose. The proposed system was proved to be effective for plant wilting detection. However, the potential yield of the crops may already have been lost when wilting symptom is shown. Some studies also utilized color images to determine the crop coefficient to estimate water requirements through water balance method (Fernández-Pacheco et al., 2014; Escarabajal-Henarejos et al., 2015).

There has been a great amount of studies exploited water stress analysis using thermal sensing information of the plants. The development of thermal imagers allows thermal information in one thermal image to be obtained simultaneously, based on which, a number of studies have developed applications of thermal imaging for the detection of plant 'stress' and irrigation scheduling. Jonesn (1999) proposed a new approach of using physical dry and wet reference surfaces of known conductance to calibrate absolute temperature measurements. The calculated conductance and the obtained estimates using a diffusion porometer were proved to be well correlated. Some other papers have proven the reliability using this method for water stress monitoring of crops (Kaukoranta et al., 2005; O'Shaughnessy and Evett, 2010; Padhi et al., 2012). The thermography method makes the automated analysis of large areas of canopy possible compared with the porometer measurements. However, during the plant water stress analysis using thermal images, the region of interest usually requires manual cropping. And because of the low resolution of the IR image, usually a visible image is required for reference to identify the area of interest to be cropped.

Researchers have performed experiments to validate the potential of information fusion by combining visible and thermal infrared images to provide better estimation of water stress status (Leinonen and Jones, 2004; Möller et al., 2007; Raza et al., 2014). Based on these researches, to accomplish the information fusion, the registration between visible and thermal infrared images is a necessary step. Moreover, in order to build an automated irrigation scheduling system based on thermal imaging, a fast and automatic registration method of visible and IR images is needed instead of using a manual method.

Compared with registration between images from the same type of sensors, the registration between visible and thermal images mainly has three challenges: (1) major image intensity diversities because visible image and thermal image were formed based on different principles; (2) translation, rotation and scale difference are all presented resulted from the different fields of view (FOV), focus, and resolution difference of the two cameras; (3) edge and feature points of the two images are not consistent.

Speeded-up robust feature detection method (SURF) has shown great robustness for image registration between visible images (Bay et al., 2008; Sengupta and Lee, 2014) as the feature points detected by it are invariant to location, scale and rotation. However, if we use SURF directly to visible and thermal images, the registration ratio is very low according to those three challenges mentioned above. Therefore, we need to develop an intensity invariant method for registration between visible image and thermal image. The edges detected using phase congruency were reported to be invariant to image contrast compared with Harris operator (Harris, 1988; Kovesi, 2003).

Therefore, the general objective for this study was to develop a fast registration method between visible and thermal images based on phase congruency. Specific objectives of this paper were:

(1) to evaluate if the edge feature could be used for registration between images from different types of sensors (i.e. thermal and visible sensors);

(2) to develop an efficient and practical algorithm for image registration between thermal image and visible image based on both phase congruency and SURF method.

2 Materials and methods

2.1 Materials

Fifteen eggplant (variety: Jingqie1#) seeds were sown on December 10th, 2014 into (34 cm*24 cm) pots in an experimental greenhouse of Beijing Academy of Agriculture and Forestry, Beijing, China. The potting material was peat and chicken manure mixed with the proportion of 1:5. Thermal images and visible images were taken for each plant separately after two days of drought treatment (May 11th and 12th) with thermal and

digital CCD cameras mounted on two tripods simultaneously. The two cameras were aligned and adjusted in order to obtain images with less translation and rotation. The thermal camera (TauTM 336, FLIR systems, Inc., USA) operated in the region of 7.5-13.5 μm with 0.05°C thermal resolution, and the spatial resolution of the thermal camera was 336 (vertical)×256 (horizontal) pixels. The visible images obtained using the digital camera (J1, Nikon Inc., Japan) were saved as a JPG format with 3872×2592 pixels. All measurements were taken between 13:00 and 15:00 hours on May 13th. To verify the robustness of the proposed algorithm against illumination and environment change, this study also collected 10 pairs of thermal infrared and visible images in corn field between 10:00 and 17:00 hours on June 21st. The proposed algorithm was realized using Matlab (Ver. R2010a, Mathworks, Natick, Ma, USA).

2.2 Algorithm description

Figure 1 showed the flowchart of the proposed method. Firstly, edge images of the input thermal infrared image and visible image were detected by calculating phase congruency (Morrone et al., 1986; Lowe, 2004; Mikolajczyk et al., 2005), respectively. Then, SURF was applied to both edge images to detect feature points, and 64-dimension descriptor was also calculated. The detected feature points on the edge images were then matched based on Euclidean distance. The false matched pairs were then filtered out through random sampling consensus method (RANSAC) (Fischler, 1981). The thermal infrared image was transformed utilizing affine parameter matrix calculated using the left matched pairs of feature points. Finally, the transformed thermal infrared image was merged with the original visible image.

2.3 Phase congruency model

Morrone et al. (1986) developed the local energy model and the measure of phase congruency. The phase congruency is defined to be the ratio of local energy, which is not dependent on the magnitude of the signal. This feature makes it robust when there are changes of image illumination and/or contrast. Thus, feature significance over multiple images captured under different illuminations can be calculated using fixed threshold values.

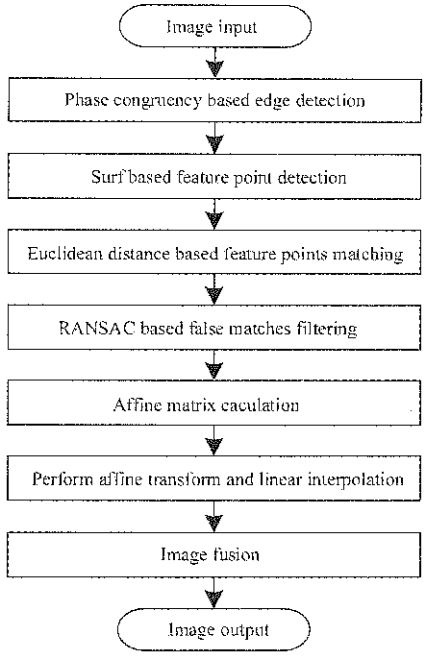

Figure 1 Flow chart of image automatic registration algorithm between thermal image and visible image

The phase congruency of one-dimension signal is defined by Equation (1) (Morrone et al., 1986).

$$PC(x)=\frac{\sum_n A_n \cos(\phi(x)-\bar{\phi}(x))}{\sum_n A_n(x)} \quad (1)$$

where, A_n represents the amplitude of the Fourier components; $\phi(x)$ represents the phase angle at a location x in the signal, and $\bar{\phi}(x)$ is the mean of phase angle of the Fourier components.

To provide better localization accuracy and improve the noise sensitiveness of phase congruency, Kovesi developed a modified version of phase congruency, which is defined by Equation (2) (Kovesi, 2003).

$$PC(x)=\frac{\sum_n W(x)\lfloor A_n(x)(\cos(\phi(x)-\bar{\phi}(x))-|\sin(\phi(x)-\bar{\phi}(x))|-T\rfloor}{\sum_n A_n(x)+\varepsilon} \quad (2)$$

where, $W(x)$ is a weight factor for frequency spread; ε is a constant, which is used to avoid the numerator to be divided by zero. The valid values are obtained through energy values minus the estimated noise influence, which is T in Equation (2). The symbol $\lfloor\ \rfloor$ denotes that the enclosed quantity is zero when its value is negative, and equal to itself is positive.

In practice, $A_n(x)$ is obtained through calculating the convolution of the input signal and log-Gabor wavelets as

shown in Equation (3).

$$A_n(x)=\sqrt{[I(x)]*M_n^o]^2+[I(x)]*M_n^e]^2} \quad (3)$$

where, $I(x)$ is the input signal; M_n^o and M_n^e refer to the odd and even log-Gabor wavelet on n scale, respectively.

Equations (1) to (3) all applied to one-dimension signal for phase congruency feature calculation. Phase congruency of one dimension was firstly calculated in different orientations uniformly divided, usually six partitions. Then the phased congruency of two-dimension images was calculated using data from oriented log-Gabor wavelets. To combine phase congruency information over six orientations, Equation (3) was modified. The numerator of the new equation was the modified local energy, in which Equation (3) was weighted, and conducted a noise compensation. Then the modified local energy was summed over all orientations. The sum of filter response amplitudes over all orientations and scales was the denominator. The result of this approach is an edge image of the image, which is invariant to image illumination and contrast.

2.4 Edge image based feature points detection and matching

2.4.1 Feature points detection and descriptor calculation

Lowe (2004) developed an efficient local feature detection and description method named scale invariant feature transform (SIFT). The detected local features and their descriptor obtained through SIFT method are robust to variations in image translation, scaling, rotation, and also invariant to illumination, noise to some extent. Because of its advantages, SIFT has been used in numerous vision applications, such as object recognition, image registration and so on. Inspired by SIFT, SURF was developed (Bay et al., 2008). SURF has achieved dramatically speed improvement and better performance compared with SIFT according to the author. The framework of SURF is different with SIFT mainly in the following aspects: (1) It uses a blob detector based on the Hessian matrix to find points of interest instead of using Gaussian filter; (2) Integral image is used to quickly evaluate the determinant of the Hessian matrix; (3) Descriptor and its orientation assignment are based on the sum of Haar wavelet responses. The detailed SURF method can be found in the paper (Bay et al., 2008).

2.4.2 Feature point pair matching

After the feature points from thermal infrared image and visible image were detected using SURF, the next step was to match the pairs by comparing the descriptors of the points. The matching process was divided into two steps: coarse matching using Euclidean distance measure, and false matched pair filtering using RANSAC method.

2.4.3 Image fusion of thermal infrared image and visible image

The difference between one infrared image and one visible image, which were obtained at the same time and similar position, was scale, rotation, shear, and position difference. When affine transformation was applied, one visible image was used as reference image, and the other thermal infrared image was used to be transformed to match the reference image. The affine transformation model can be defined as Equation (4).

$$\begin{bmatrix}x'\\y'\end{bmatrix}=\sigma\begin{bmatrix}\cos(\theta), & \sin(\theta)\\-\sin(\theta), & \cos(\theta)\end{bmatrix}\begin{bmatrix}x\\y\end{bmatrix}+\begin{bmatrix}t_x\\t_y\end{bmatrix} \quad (4)$$

where, (x,y) represents one-point position on the thermal infrared image; (x',y') represents the corresponding point position after transformation, which is also the related point position on the reference image; σ is the scaling factor which modifies the scale difference; θ is the rotation angle which modifies the rotation difference, $[t_x\ t_y]'$ modifies the translation difference.

When the number of obtained matching feature point pair between thermal infrared image and visible image is larger than 3, the affine transformation parameters σ, θ, and $[t_x\ t_y]'$ can be calculated. Hence, the thermal infrared image can be transformed to match the reference image. Cubic interpolation method was chosen during the transformation process and the transformed points outside input image were assumed to be zero. The image fusion between the transformed thermal infrared image and visible image was completed using a wavelet based method.

2.4.4 Performance evaluation method of the proposed registration method

The developed algorithm was evaluated with 15 pairs of images. RMSE was used as an accuracy measure for the registration, which was calculated using Equation (5).

$$RMSE = \frac{1}{m}\sqrt{\sum_{i=1}^{m}((x_i' - x_{ri})^2 + (y_i' - y_{ri})^2)} \quad (5)$$

where, m was the number of pairs of the matched feature points after RANSAC was applied; (x_i, y_i) and (x_{ri}, y_{ri}) were the coordinates of one matched point pair on thermal infrared image and visible image, respectively. (x_i', y_i') was the corresponding coordinate after applying affine transformation to (x_i, y_i).

3 Results and discussion

The results were exhibited as following in this section after the proposed algorithm was applied to the image pair shown in Figure 2, which was randomly chosen from the 15 image pairs of thermal infrared images and visible images.

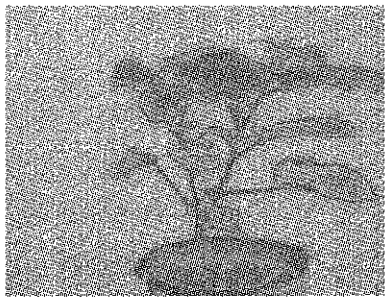

a. Thermal infrared image

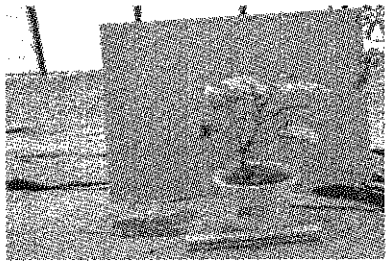

b. Visible image

Figure 2 Example images of thermal image and visible image to be registered

LoG (Laplacian of Gaussian Method) operator and Canny operator are two popularly used edge detection methods. Figure 3 showed the edge images detected based on phase congruency model, LoG operator and Canny operator. Figure 3a, Figure 3b and Figure 3c were edge images of thermal infrared image detected using phase congruency model, LoG operator, and Canny operator, respectively. Figutr 3d, Figure 3e and Figure 3-f were edge images of visible image detected using phase congruency model, LoG operator and Canny operator, respectively. The marked areas on the images were zoomed in to show the differences of these two methods. The results indicated that edges detected using LoG operator and Canny operator were binary value, while edges detected base on phase congruency model include phase congruency information, and were more consistent. The edge detected by phase congruency model for thermal infrared image and visible image were more consistent, which was due to its robustness to image illumination and contrast change.

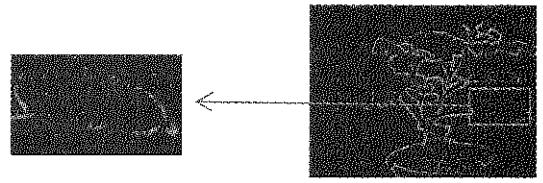

a. Edge image of thermal infrared image based on phase congruency model

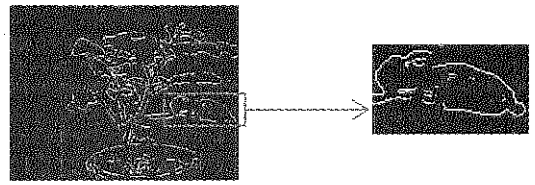

b. Edge image of thermal infrared image based on LoG operator

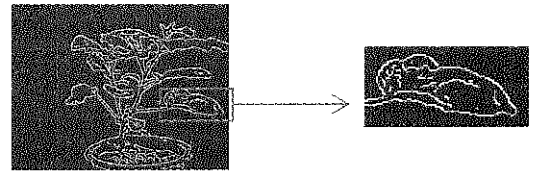

c. Edge image of thermal infrared image based on Canny operator

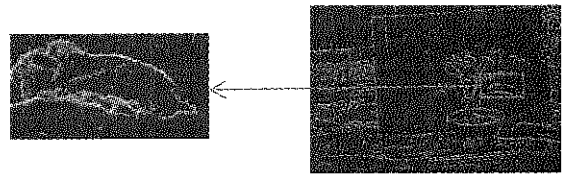

d. Edge image of visible image based on phase congruency model

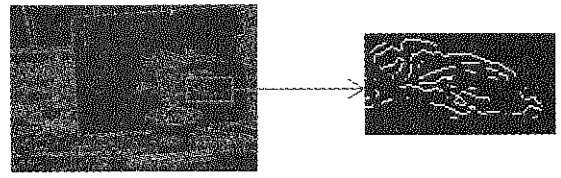

e. Edge image of visible image based on LoG operator

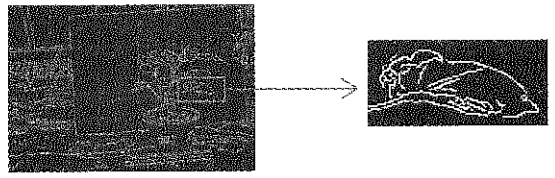

f. Edge image of visible image based on Canny operator

Figure 3 Edge images detected using different methods

Figure 4 showed the feature points detected by SURF method, and the matching result of the feature points from thermal infrared and visible edge images. The feature points were marked in circles, and the matched pairs of points were connected using lines of different

colors. Figure 4a showed the matched result based on Euclidean distance. Therefore, RANSAC was used to filter out the false matches, the result of which was given in Figure 4b.

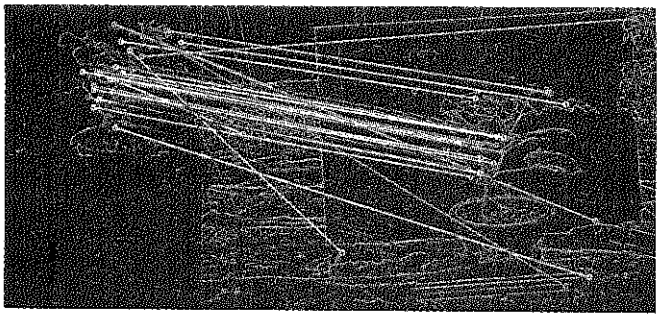

a. Euclidean distance based feature points matching

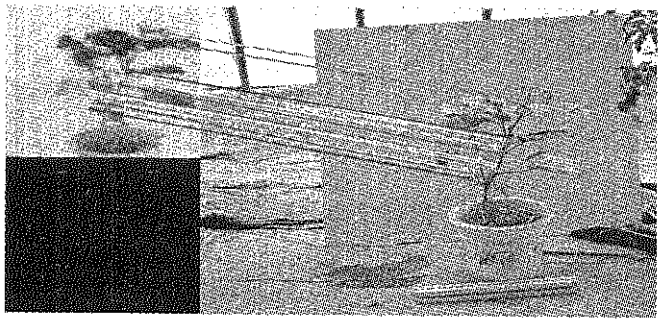

b. RANSAC based false matches filtering

Figure 4 Feature points and the matching results of them

After false match filtering using RANSAC, the affine transformation parameter can be calculated using Equation (4). The thermal infrared image was transformed to match the reference image, the result of which was shown in Figure 5a. Figure 5b is the fusion result of the transformed infrared image and the reference visible image in gray scale, and Figure 5c is the fusion result in RGB space. As shown in Figure 5a-c, the transformed thermal infrared image and visible image were aligned well by visual examination.

The test results were given in Figure 6 and Table 1, which illustrated the performance of the developed algorithm. More than three pairs of feature points were obtained for all those 15 pairs of images after false match filtering using RANSAC method. The time used is within 5 seconds, and the RMSE is within 10 pixels, which could meet the practical requirement when developing an automatic water stress monitoring system. When applying this algorithm in different environment, the situation that less than 3 matching pairs were found might happen. When this happened, the algorithm would let the user choose, either jumping this pair or invoking a control point choosing function, which allowed the user to manually choose the feature point pairs to help with the registration. Next step, a user-friendly application will be developed based on the proposed algorithm.

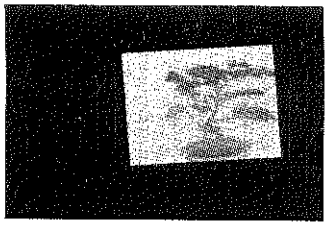

a. Thermal infrared image after performing affine transform

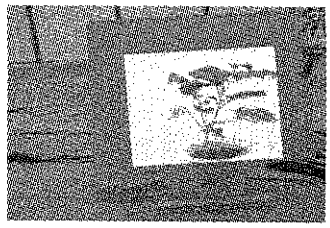

b. Fusion gray image of affine transformed thermal infrared image and original visible image

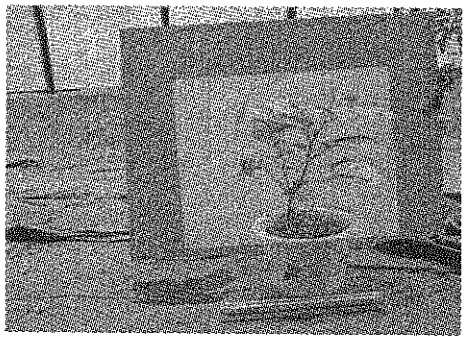

c. Fusion RGB image of affine transformed thermal infrared image and original visible image

Figure 5 Affine transformation of IF image and fusion image result

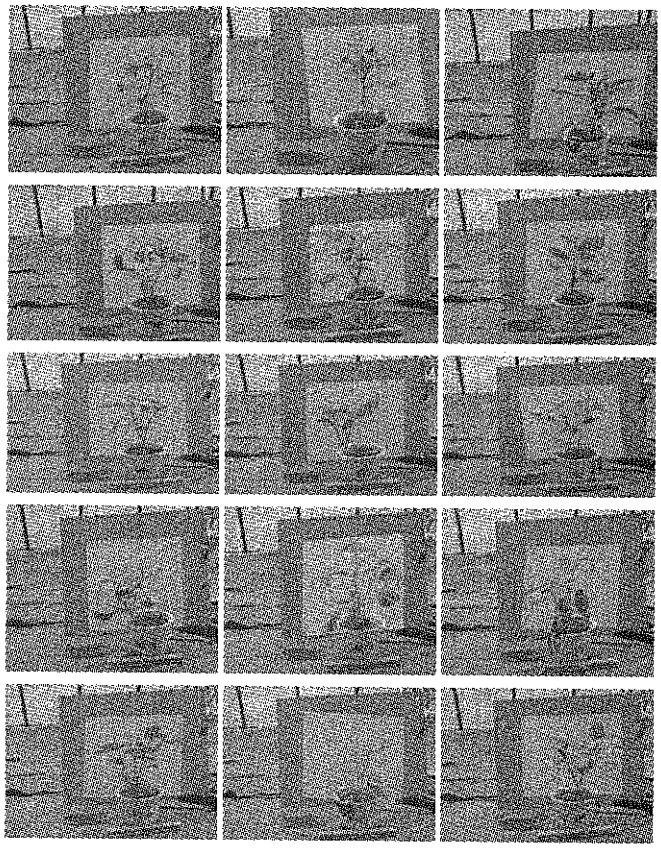

Figure 6 Image registration results for 15 pairs of visible image and thermal infrared image

Table 1 Time used and matching accuracy using the proposed algorithm

Image pair number	Time, s	Number of matched pairs	RMSE
1	3.8	19	6.5
2	4.1	14	6.6
3	3.8	11	7.2
4	3.7	6	4.8
5	4.0	8	5.4
6	3.9	13	5.4
7	3.6	22	5.8
8	3.6	19	6.4
9	3.6	30	6.9
10	3.6	18	8.5
11	4.0	13	8.0
12	3.8	18	5.3
13	3.7	8	6.5
14	3.6	27	5.8
15	3.6	21	6.5

4 Conclusions

The automatic fusion of thermal infrared image and visible image is necessary for developing a thermal infrared image based on automatic water stress monitoring system. Fast and accurate registration between thermal infrared image and visible image is a key step before image fusion. However, the registration between images from different types of image sensors has several challenges, including illumination difference, contrast difference, translation, rotation and sale difference. A phase congruency and SURF based registration method was proposed in this paper to deal with the challenges mentioned above. The highlight of the proposed method is that it combined the advantages of phase congruency model and SURF. The advantage of phase congruency based edge detection method is that it is robust to illumination, and contrast, which makes it more suitable for edge detection for images from different types of sensors, and easier to set threshold for wide classes of images. The advantage of SURF is its speed and robustness. The experimental result for 15 pairs of thermal and visible images obtained in the green house demonstrated that the proposed method is both fast and accurate, which met the requirement of an automatic water stress monitoring system.

Acknowledgments

This research was supported by the project supported by National Natural Science Foundation of China (31701319), the National Key Research and Development Program (Grant No. 2016YFD0300606 & 2016YFD0200602), Beijing outstanding talent training funds (2015000020060G129), CAU Special Funds for Basic Research Projects (2017QC020), and Beijing Natural Science Foundation (4131002).

[References]

[1] Bay, H., T. Tuytelaars, and L. V. Gool. 2006. Surf: speeded up robust features. *Computer Vision and Image Understanding,* 110(3): 404–417.

[2] Escarabajal-Henarejos, D., J. M. Molina-Martínez, D. G. Fernández-Pacheco, F. Cavas-Martínez, and G. García-Mateos. 2015. Digital photography applied to irrigation management of little gem lettuce. *Agricultural Water Management,* 151: 148–157.

[3] Fernández-Pacheco, D. G., D. Escarabajal-Henarejos, A. Ruiz-Canales, J. Conesa, and J. M. Molina-Martínez. 2014. A digital image-processing-based method for determining the crop coefficient of lettuce crops in the southeast of Spain. *Biosystems Engineering,* 117(1): 23–34.

[4] Fischler, M. A., and R. C. Bolles. 1987. Random sample consensus: a paradigm for model fitting with applications to image analysis and automated cartography. *Readings in Computer Vision*, 726–740.

[5] Harris, C. 1988. A combined corner and edge detector. *Proc 4th Alvey Vision Conf,* 1988(3): 147–151.

[6] Jones, H. G. 1999. Use of thermography for quantitative studies of spatial and temporal variation of stomatal conductance over leaf surfaces. *Plant Cell and Environment,* 22(9): 1043–1055.

[7] Jones, H. G. 2004. Irrigation scheduling: advantages and pitfalls of plant-based methods. *Journal of Experimental Botany,* 55(407): 2427.

[8] Kacira, M., and P. P. Ling. 2001. Design and development of an automated and non-contact sensing system for continuous monitoring of plant health and growth. *Transactions of the ASAE American Society of Agricultural Engineers,* 44(4): 989.

[9] Kacira, M., P. P. Ling, and T. H. Short. 2002. Machine vision extracted plant movement for early detection of plant water stress. *Transactions of the ASAE American Society of Agricultural Engineers,* 45(4): 1147.

[10] Kaukoranta, T., J. Murto, J. Takala, and R. Tahvonen. 2005. Detection of water deficit in greenhouse cucumber by infrared thermography and reference surfaces. *Scientia Horticulturae,* 106(4): 447–463.

[11] Kovesi, P. 2003. Phase congruency detects corners and edges. *DICTA,* 309–318.

[12] Leinonen, I., and H. G. Jones. 2004. Combining thermal and visible imagery for estimating canopy temperature and identifying plant stress. *Journal of Experimental Botany*, 55(401): 1423.

[13] Lowe, D. G. 2004. Distinctive image features from scale-invariant key points. *International Journal of Computer Vision,* 60(2): 91–110.

[14] Mikolajczyk, K., T. Tuytelaars, C. Schmid, A. Zisserman, J. Matas, F. Schaffalitzky, T. Kadir, and L. Van Gool. 2005. A comparison of affine region detectors. *International Journal of Computer Vision,* 65(1-2): 43–72.

[15] Mizuno, S., K. Noda, N. Ezaki, H. Takizawa, and S. Yamamoto. 2007. Detection of wilt by analyzing color and stereo vision data of plant. *International Conference on Computer Vision / Computer Graphics Collaboration Techniques and Applications*, (400-411): 400–411. Springer, Berlin, Heidelberg, Germany.

[16] Möller, M., V. Alchanatis, Y. Cohen, M. Meron, J. Tsipris, A. Naor, V. Ostrovsky, M. Sprintsin, and S. Cohen. 2007. Use of thermal and visible imagery for estimating crop water status of irrigated grapevine. *Journal of Experimental Botany,* 58(4): 827.

[17] Morrone, M. C., J. Ross, D. C. Burr, and R. Owens. 1986. Mach bands are phase dependent. *Nature,* 324(6094): 250–253.

[18] O'Shaughnessy, S. A., and S. R. Evett. 2010. Canopy temperature based system effectively schedules and controls center pivot irrigation of cotton. *Agricultural Water Management,* 97(9): 1310–1316.

[19] Padhi, J., R. K. Misra, and J. O. Payero. 2012. Estimation of soil water deficit in an irrigated cotton field with infrared thermography. *Field Crops Research,* 126(1): 45–55.

[20] Raza, S. E., H. K. Smith, G. J. Clarkson, G. Taylor, A. J. Thompson, J. Clarkson, and N. M. Rajpoot. 2014. Automatic detection of regions in spinach canopies responding to soil moisture deficit using combined visible and thermal imagery. *Plos One*, 9(6): e97612.

[21] Sengupta, S., and W. S. Lee. 2014. Identification and determination of the number of immature green citrus fruit in a canopy under different ambient light conditions. *Biosystems Engineering,* 117(1): 51–61.

Approach to online management for document format information resources

Wang Yan[1,2], Lin Kequan[1,2], Zhao Long[1,2], Gao Wanlin[1,2*], Huang Liangji[1,2], Xu Min[1,2], Wang Jie[1,2]

(*1. Key Laboratory of Agricultural Informatization Standardization, Ministry of Agriculture, Beijing 100083, China;*
2. College of Information and Electrical Engineering, China Agricultural University, Beijing 100083, China)

Abstract: The office business could be efficacious significantly being adept in using modern IT trends such as online documentation while implementing the web OA (Office Automation). In this study, we modeled an approach for online document-formatted information management and design. This is a web-based document-formatted information management system which is capable of producing reporting documents management module in real project. A kind of middleware named WebOffice is used which integrates document editor on client computer with the system's webpage for online editing, downloading and uploading documents. This system uses different utilities such as SWF (Shock Wave Flash) tools for creating and manipulating document format, FlexPaper is web-based multi-formatter document viewer and freemarker template for inserting data and Jacob (a JAVA-COM bridge) is for extracting data from documents, which makes necessary conversion of information between the document format and digital format. The system has a friendly and stable user interface design, which gives decoupling between modules and is easier for module rewriting and adding. With this system, people could manage office documentation online and will be accessible automatically. It will simplify the work flow and collaboration among departments and also improve the productivity of government office routine work.

Keywords: EDMS, document-formatted information, online management, JAVA-COM bridge, WebOffice

Citation: Wang, Y., K. Q. Lin, L. Zhao, W. L. Gao, L. J. Huang, M. Xu, and J. Wang. 2017. Approach to online management for document format information resources. International Agricultural Engineering Journal, 26(4): 364–369.

1 Introduction

The transformation of government management system to intensive model put forward new requirements to government document management. In particular, the effectiveness of documents for government decision making and business communication has been improved after a number of policies have been adopted by the state to streamline documents as well as to enhance the standardization. Electronic document management system (EDMS) can provide multi-dimensional benefits, especially portability, propagation speed, performance, stability (Jamieson et al., 2017, Hung et al., 2009, Jr, 1995) and the availability of information for management and organization (Alshibly et al., 2016). Grudin (2017) considered the issue on office automation into Computer-Supported Cooperative Work (CSCW). Although it is a long process and will comsume much time (Sutton and Lemay, 1999), one of the major concern about boosting up efficiency of the personal may be how to implement a document information resource management online. With the combination of office component and browser, users can manage document-format information without threshold. Therefore, combining office management and internet is a significant practice to be done. Xie (2011) has evaluated most important functions of the electronic document and record management program for government

Received date: 2017-07-05 **Accepted date:** 2017-08-23

* **Corresponding author: Gao Wanlin,** Ph.D., Professor. Research interests: agricultural Informatization and application specific chip. Address: College of Information and Electrical Engineering, China Agricultural University, Beijing 100083 P.R. China. Tel: +86-010-62736755, Email: cau_szmtyjs@163.com.

management. What is more, the critical issues for web development technology have been solved, so a few management behaviors of documents resources can be shifted online.

Yin-Ho et al. (2003) researched some XML-based examples with document creation, document change, document control and document access compatible with ISO9000 and expanded the capabilities of XML and Internet technologies applied in electronic document management systems. Castillo-Barrera et al. (2013) proposed a method to implement an ontology-based EDMS which makes it easy to develop an EDMS. Boh (2012) integrated a business information system and an electronic document management system demonstrated that connecting different types of information together is significant and important. Burtylev et al. (2003) developed an EDMS and explored its advantage and efficiency. Hang and Tembo (2014) integrated workflow-based electronic document management into management systems and make the systems reliably.

But all these existing systems only study document management work online, while disconnection problem between business processes and document management still exists which can be fixed by adding data extraction and recognition modules. The use of computing facility to process simple operations automatically will help government to downsize on large scale. Only integrated role permissions could not meet the requirements fully. Therefore, this study combines the factual needs of the project and the operative management of documents status which makes the operation of online document that can reasonably promote the project process. While meeting the requirements of online document operation, the online document management should be taken into account of the security issues (Boh, 2012) of document contents and embodiment of the management intelligence.

This system used Apache POI (Poor Obfuscation Implementation) technology to extract the document contents, achieved statement analysis, replication checking and other intelligent features which maximize labor and resources savings on the basis of realization of scientific document management. This paper designed and implemented a web-based document-format resource management system. By implementing standardized business document main pages, online editing and previewing documents, the automatic archiving and report generation features combined document management and business process effectively and enhanced the efficiency of government offices.

2 Materials and method

2.1 Online document management strategy

Taking the need for online document-formatted management and programming into conditions, we divided document processing related operations into different modules and designed corresponding interface between modules. The design of interface is shown in Figure 1.

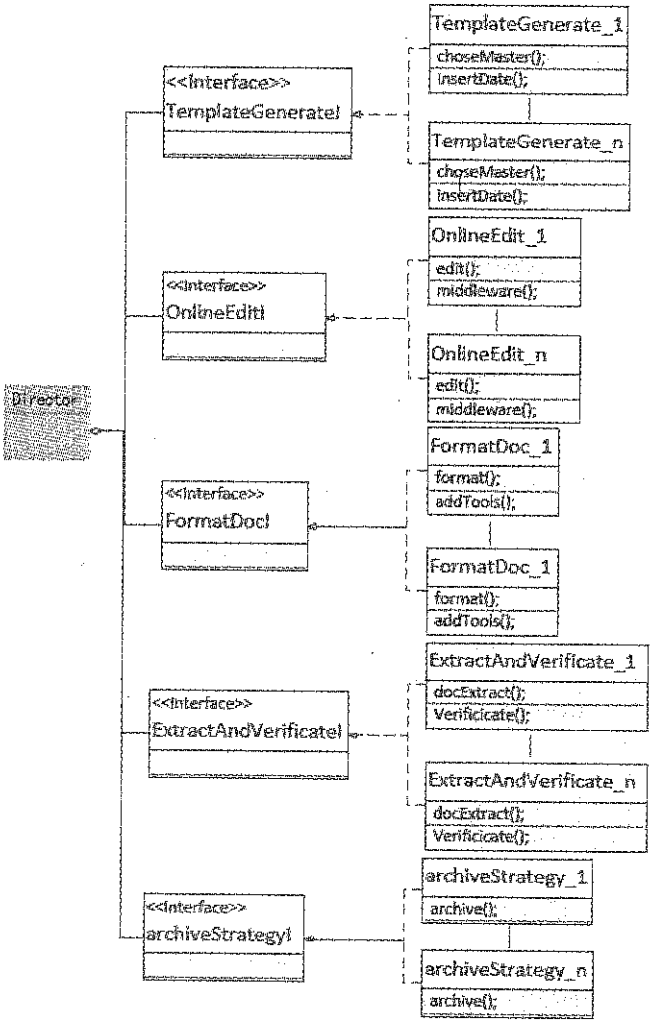

Figure 1 Interface design

The design is based on the idea of builder pattern to facilitate code reconstruction and improve the development efficiency and reliability. Through the

design, program can choose the method to realize functions by way of configuration, such as different documents online editors. In this paper, we selected one method for each step of operation. The selection is based on the consideration of the experimental requirements and method performance.

2.2 Online document management

Users can insert all kinds of primary information and complete a number of verification steps through an HTML form. The system automatically extracts the information entered by the user, inserts them into user concerned master document and finally generates editable template document. This feature uses FreeMarker to markup positions in documents and inserts collected user information into the corresponding position. It is realized by calling ftl2word method in the Docutils class using the FreeMarker template technology to put collected data into a data set which will be inserted into templates marked by FreeMarker. The core code is as follows:

```
Template t = null;
Try {
        configuration.setDirectoryForTemplateLoading
        (new File (direcotry));
        t = configuration.getTemplate (inputFile);
        BufferedWriter out =
        new BufferedWriter (new OutputStreamWriter(
        new FileOutputStream (tofile), "utf-8"));
        t.process (dataMap, out);
}
```

Where, the dataMap used above is the data set we used to transport data.

The module calls WebOffice components directly in the browser side and opens the prepared template document responded by server side, or an empty document if template yet not generated for users with the most familiar document-editing mode and a more comfortable working environment. The module technology architecture is shown in Figure 2.

This module calls default document editor of the client system, such as Microsoft Office, Kingsoft WPS and so on, which makes the online document editing environment like a native one. Users can edit document online and also do other operations, e.g. save, upload, download, etc.

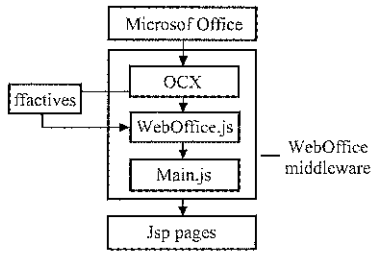

Figure 2 Online editing technology framework

While provided users document online previewing function, this module needs to ensure that the content of the document will not be modified. Thus, the module will transform document from doc-format to swf-format, then use flash technology to play the documentation online.

First, we call doc2swf method in the DocUtils class, and create a new process to run SwfTools program then perform given instructions to convert document from doc-format to swf-format. The core code is as follows:

```
String command = PDF2SWF_PATH +" "+inputFile+"
-o "+toFileName+" -T 9 -f";
Try {
        Process process = Runtime.getRuntime ().exec
                (command);
        BufferedReader bufferedReader =
        new BufferedReader ( new
        InputStreamReader(process.getInputStream()));
        While (bufferedReader.readLine ()! = null);
        Try {
                process.waitFor ();
            } catch (InterruptedException e) {
                e.printStackTrace ();
            }
         System.out.println("convert into SWF files
         Successfully!");
    }
```

Where, command is the instruction that SwfTools program will perform; PDF2SWF_PATH is the path of the executable file of SwfTools program; inputFile is the name of the file need to convert; toFileName is the name of the converted file.

FlexPaper plugin is used to preview documents online. When users click the link of the document needed to be previewed, the program posts a request to the database, queries the network path of converted document and provides the position to FlexPaper plugin at last. Figure 3 shows how it works.

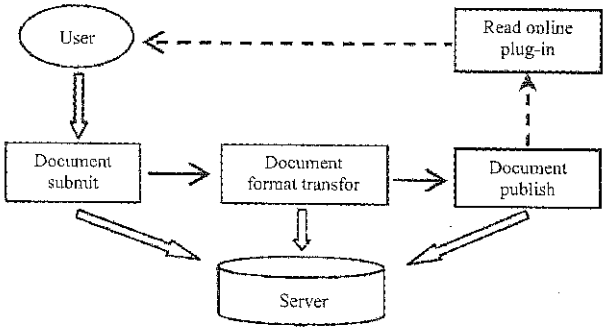

Figure 3 Online preview operating principle

The critical information which filled by users into the document is needed to be extracted for storing in a database and for further analyzing and querying. This module uses the POI interface to read a document and convert it into the HWPF Document object. The programs primarily read tables and bookmarks in the object to locate the critical information and then store them into appropriate fields in the database. The main code will extract the contents by location, the table is as follows:

```
HWPFDocument document =
new HWPFDocument (new FileInputStream (file));
Range range = document.getRange ();
TableIterator iterator = new TableIterator (range);
Iterator = docUtils.readWord (targetFile);
if (iterator.hasNext()){
    Table = iterator.next ();
    Row = table.getRow (9);
    Content = row.getCell (0).text ();
    Int len = content.length ();
    documentVo.setProjname (content);
    documentService.edit (documentVo);
    }
```

Certain document editors have bookmarking facility in order to expedite editing. If a user removes the bookmarks of any critical information, the program will not be able to locate the said information. Therefore, we set the macro attribute in the template to restrict users to delete existing bookmarks and add new bookmarks. New bookmarks can be same as the earlier ones; it will not affect the positioning function of the program.

Considering that at the end of the entire workflow, the documents involved in the evaluation will need to be archived and classified according to the valuation results. Thus, the module is designed to permit users to choose different filters themselves, then automatically classify documents and store them in different folders. We classified documents through comparing some special properties such as whether award winning, project reporting date etc. Taking awarding a prize or not as an example, users select the "award" option to find all the projects won the awards and then assign a name to the folder, such as "award-winning projects". You can access to all the books that won the China Agricultural Science and Technology Project Award, which have been stored into the folder named "award-winning projects". Primarily, the program queries all the documents that meet the conditions according to the user selected filters; then create a folder with a specified name and copy appropriate documents to the folder using JAVA file interface.

2.3 Online document management

Based on the actual work processes and platform requirements of China Agricultural Science and Technology Award project, this paper designed to integrate document operations into the business processes of reporting and evaluating applicants. To introduce online document management to traditional government office work, the document operation is marked as a key node in the workflow. The specific design process is shown in Figure 4.

In this solution, the project of report China Agricultural Science and Technology Award is presented as project recommendation, which is document-format. The document managing function in the business process is to put the content of these documents into management. Major document management operations are: document template generation and inserting formatting information, online documents editing and amendment, document critical information extraction, document format conversion, online previewing and automatic archiving.

Considering users often require to submit varieties of documents, while the basic information of users is the same, this paper designed a function to import formatted information into document templates. Thus, we adopted a method of collecting user information in the format of html-form and then automatically imported them into different master documents by the program which is in

fact separately filling basic information of users. Documents editing can avoid user's duplication fillings and provide well-organized authentication and management of user information.

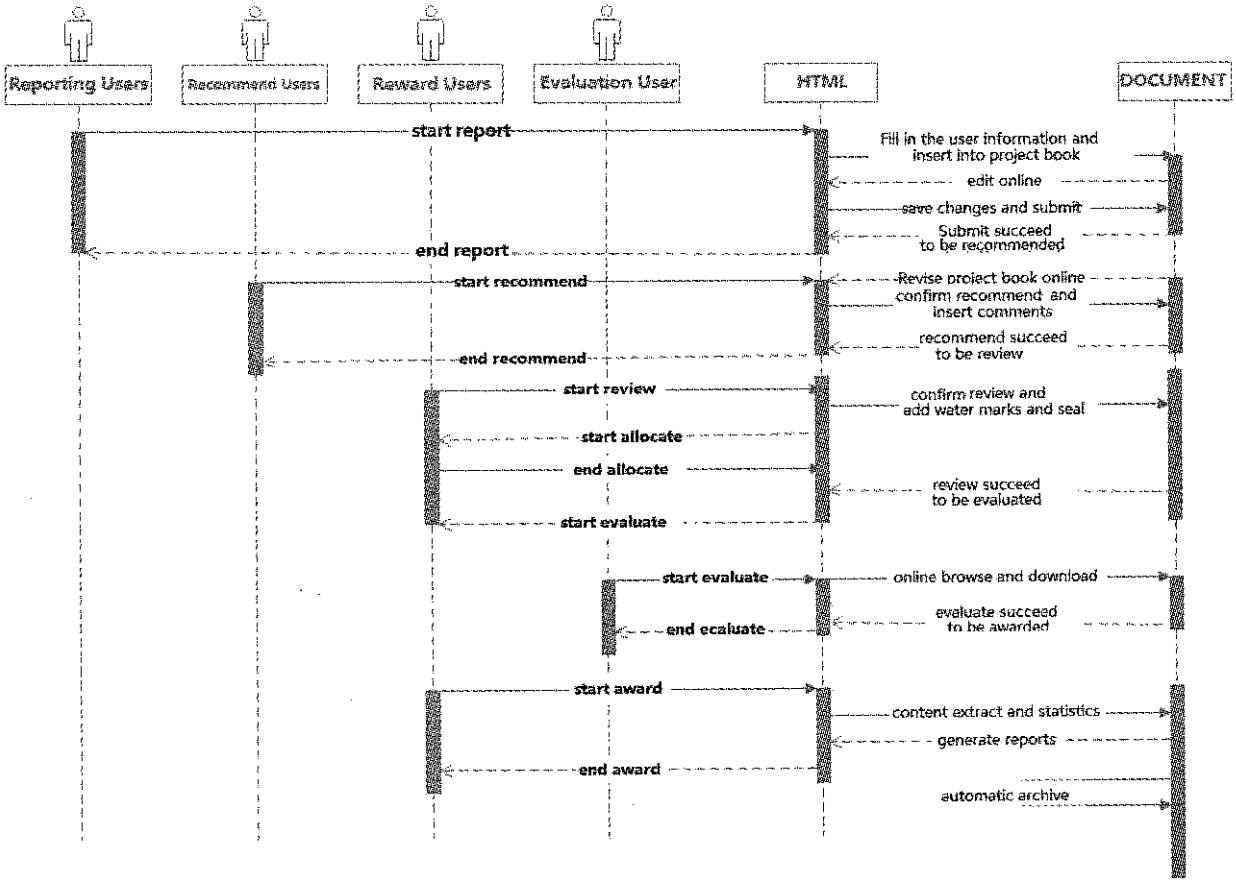

Figure 4 Business process and document management state

Our purpose is to provide online reviewing functions as well as online editing to facilitate different users to confer document content in detail, and to make online document editing process more convenient and complete. After the formation of the final draft of the documents, proof materials will be inserted, such as watermarks and seal into documents and provide a certain degree of protection. Here the document is converted to protect pdf-format for users to print and swf-format for users online previewing.

Using this method, users can effectively avoid secondary editing of official documents, and they only need to install browser plugin, flash player to preview swf-file with compatibility.

In the evaluation phase of project, the system provides document critical information extraction for the evaluating-user to finish jobs such as duplicating checks, statistics analyzing, through the system logically. After the evaluation phase, users can also archive documents individually through configuring archiving path.

3 Results and discussion

Based on the actual work processes and platform requirements of China Agricultural Science and Technology Award System, this paper designed and implemented the platform for online reporting and evaluating China Agricultural Science and Technology Award. By combining and improving existing online documents operations related to technologies, we successfully combined the document review procedure and document operation, solved the contradiction between online business and offline document management, effectively promoted the efficient and transparency of government office.

After the above analysis and proven, the realized system in this paper integrated online document operation into the reporting and evaluating of Chinese Agricultural Science and Technology Award effectively and promoted the progress of reporting and evaluating through performing appropriate operates on documents online.

This method achieved the document-based online information resources management, and improved efficiency of government office. Meanwhile, it facilitated system users to operate and reduced user workload through the features like automatically inserting, user information into template, archiving documents and produce statistical reports automatically.

However, online editing module in this solution is based on WebOffice platform and uses ActiveX plugins, which will bring a few disadvantages in terms of cross-platform services. We need to open the system with the IE browser to install WebOffice plugin at the first time. For some special browser, support is not perfect, and further improvement is required. In order to overcome above-mentioned problems, the system provided a template through which a user can download documents and fill offline and then upload, which will block the reporting process, occurred while installing WebOffice plugin, to enhance the robustness and reliability.

4 Conclusions

Information from online document processing techniques has confirmed many of the effective implementations regarding constructing the online resource management system, but it still has many problems to solve. In this paper, by using WebOffice platfom and combing Jacob and flexpaper with swf tool, the office file was converted to PDF, and then it was turned to SWF and displayed on the page, the methods employed have been worked stably for more than two years. In the future, we will continue to seek and improve the system with ever increasing power of new technologies.

Acknowledgements

The authors would like to thank their colleagues for their support to this work. The detailed comments from the anonymous reviewers were gratefully acknowledged. This work was supported by the National Spark Program Key Project (Grant #: 2015GA600002) and Chinese Universities Scientific Fund (Grant #: 2017XD003).

[References]

[1] Alshibly, H., R. Chiong, Y. Bao. 2016. Investigating the critical success factors for implementing electronic document management systems in governments: Evidence from Jordan. *Journal of Information Systems Management*, 33(4): 287–301.

[2] Boh, M. 2012. Planning of integration for a business information system and an electronic document management system. *Plos One*, 7(6), e39647.

[3] Burtylev, I. N., K. V. Mokhun, Y. V. Bodnya, and D. N. Yukhnevich. 2013. Development of electronic document management systems: advantage and efficiency. *Science & Technology*, 3(2A): 1–9.

[4] Castillo-Barrera, F. E., H. A. Durán-Limón, C. Médina-Ramírez, and B. Rodriguez-Rocha. 2013. A method for building ontology-based electronic document management systems for quality standards-the case study of the iso/ts 16949:2002 automotive standard. *Applied Intelligence*, 38(1): 99–113.

[5] Grudin, J. 2017. Computer-supported cooperative work: History and focus. *Computer*, 27(5): 19–26.

[6] Hang, T. P., and T. Tambo. 2014. Integrated management systems and workflow-based electronic document management: an empirical study. *Journal of Industrial Engineering & Management*, 7(1): 194–217.

[7] Hung, S. Y., K. Z. Tang, C. M. Chang, C. D. Ke. 2009. User acceptance of intergovernmental services: An example of electronic document management system. *Government Information Quarterly*, 26(2): 387–397.

[8] Jamieson, T., J. Ailon, V. Chien, O. Mourad. 2017. An electronic documentation system improves the quality of admission notes: a randomized trial. *Journal of the American Medical Informatics Association*, 24(1): 123–129.

[9] Jr, R. H. S. 1995. Electronic document management: Challenges and opportunities for information systems managers. *Mis Quarterly*, 19(1): 29–49.

[10] Sutton, M. D., P. Lemay. 1999. Terms of reference: The foundation for implementing document management systems. *Journal of Information Systems Management*, 16(1): 78–83.

[11] Xie, S. L. 2011. Evaluation of the electronic document and record management program in a Canadian municipality. M.S. thesis, The University of British Columbia, Vancouver, Canada.

[12] Yao, Y. H., A. J. C. Trappey, P. S. Ho. 2003. XML-based ISO9000 electronic document management system. *Robotics & Computer Integrated Manufacturing*, 19(4): 355–370.

Automated and low-cost reconstruction method for cactus 3D phenotyping

Yang Zhaolu[1,2], Yue Jun[1*], Li Zhenbo[2], Zhang Zhiwang[1]

(1. *College of Information and Electrical Engineering, Ludong University, Yantai, 264025, China*;
2. *College of Information and Electrical Engineering, China Agricultural University, Beijing 100083, China*)

Abstract: The plant 3D modeling is the extremely crucial part of analysis of phenotypic characteristics of plants and agricultural visualization. The limitations of 3D modeling algorithms make the cost of restoring plant structures very high. This paper presented a new image-based automated plant 3D reconstruction system with lower cost. In order to obtain faster and more robust 3D information and reconstruction effect, our method used feature points extracted by the SURF, not merely because the SURF feature points could be detected quickly but also is better than other approach on overall performance. The proposed algorithm first detected the feature points and matching points to estimate the camera pose, but there were many mismatching points in brute force matching method, so we leveraged GMS to eliminate mismatching and it was able to obtain more accurate matching and more detailed information. In addition, in the final stage we adopted bundle adjustment to optimize the reconstruction results of all views. Experiments have been conducted to validate the proposed method.

Keywords: lower cost, plant 3D reconstruction, SURF, GMS, bundle adjustment

Citation: Yang, Z. L., J. Yue, Z. B. Li, and Z. W. Zhang. 2017. Automated and low-cost reconstruction method for cactus 3D phenotyping. International Agricultural Engineering Journal, 26(4): 370–379.

1 Introduction

3D reconstruction is a classical and vital puzzler in the field of computer vision. The 3D reconstruction of plants and its application on agricultural development has received considerable attention in the last decade (Edelsbrunner et al., 2011; Paproki et al., 2012; Clark et al., 2011). With the rapid development of information and agricultural technology, people have more and more needs for 3D model whether in agriculture or in industry. "Virtual plant" is a potential and effective means for observing the growth of plants, simulating the plants morphology and describing the three-dimensional information of plants in space (Vos et al., 2010). On one hand, we can explore the growth rules of plants by observing the growth information, which can be able to guide the agricultural production and facilitate the development of biological research (Tang et al., 2015). On the other hand, we can study the distribution of branches and leaves and obtain the space information of object, which can be applied into the robot picking (Min et al., 2016), target detection and location technology (Xiong et al., 2017).

In the early stage, people who studied the 3D model based on multiple images all first tried to calibrate the camera, get the intrinsic and extrinsic parameters of the camera, then through counter-projecting the matching points from two images to the 3D space and a 3D reconstruction could be achieved. But it was a cumbersome process of the traditional camera calibration, each capture needed a new calibration. So, in some circumstances that the camera parameters needed real time changes or could not use calibration object, this method was less practical and was very difficult to achieve. Reconstruction based on uncalibrated image sequences does not need to determine the camera parameters in advance, it just captures a group of image sequences through a freely moving ordinary camera then the 3D coordinates of the object and the object can be obtained after the intrinsic and extrinsic parameters have

Received date: 2017-09-24 **Accepted date:** 2017-11-12
* **Corresponding author: Jun Yue,** Ph.D, Professor, College of Information and Electrical Engineering, Ludong University, China. Email: yuejuncn@126.com.

been calculated. This method has been a hot issue for years because it has the advantages of convenient, real time and low cost.

Flowers are essential agricultural products, which research process and virtual reality technology increasingly close contact. The flowers, as a wide variety of plants in nature, its morphological structures are ever-changing. On one hand, it is of great significance to study the three-dimensional model of flowers on the classification and identification. On the other hand, it is of great importance to acquire and reconstruct the three-dimensional structure of flowers quickly, accurately and simply for robot automation.

2 Related work

Current state-of-the-art 3D reconstruction system includes hardware following the needs and the budget. In general, the hardware includes sensors and computation units. There are various kind of sensors composed by cameras and scanners, such as, LIDAR (Light Detection and Ranging), lasers, Time-of-Flight cameras, and Microsoft RGB-D cameras. Image-based 3D modeling contains a stereo-vision system, space carving system, and a light field camera system, which all require more than one camera (Liu et al., 2017). Kaminuma et al. (2004) applied a laser range finder to reconstruct 3D models which represented the leaves and petioles as polygonal meshes, and then quantified the morphological traits from these models. Lee and Ehsani (2009) developed a laser scanner-based system to measure citrus geometric characteristics. Laser scanners are useful tools for the acquisition of high-precision 3D point clouds of plants, but provide no information on volumetric and surface area, while having a poor resolution (Paulus et al., 2013). A combination of binocular stereo-vision and structure-from-motion techniques for the reconstruction of small plants from multiple viewpoints also showed good results (Ni et al., 2014; Wu, 2013). While the stereo-vision system is insensitive to movement and has color information, it has a poor depth resolution and is susceptible to sunlight.

There is a great deal of work that utilizes consumer-grade range camera technology (Kinect) for scene reconstruction (Zhang, 2012). Chene et al. (2012) applied Kinect on 3D phenotyping of plants. Azzari et al. (2013) used Kinect to characterize vegetation structure. And there are many similar works. Wang and Zhang (2013) used two Kinect devices to make a 3D reconstruction of a dormant cherry tree that was moved into a laboratory environment.

Reconstruction based on two images is the foundation of reconstruction from multiple images (Zhao et al., 2012; Segundo et al., 2013; Wei et al., 2015), this paper carried out the reconstruction based on two images with invariable intrinsic parameters of the camera. How to stably extract and accurately match the feature points is a crucial step for 3D reconstruction. On the current terms, the feature point detection algorithms which are effective and widely used should be the SIFT (Scale Invariant Feature Transform) feature extraction algorithm, but SURF (Bay et al., 2008; Zhong et al., 2016) is an upgraded version of SIFT (Zhang Z, and Tang Q., 2016), and the overall performance is better than SIFT. For this paper, the basic idea of the proposed algorithm is: through feature points detected by the SURF (Zhang et al., 2015) to achieve the first step of a 3D reconstruction, and leverage GMS (Grid-based Motion Statistics) (Bian et al., 2017) to eliminate mismatching, then to calculate the fundamental matrix by refined matching and enhance the robustness of the fundamental matrix by RANSAC (Random Sample Consensus) (Vourvoulakis et al., 2016) iterative algorithm; finally, we adopt bundle adjustment to optimize the reconstruction results of all views.

3 Multi-view 3D reconstruction method

Based on two images reconstruction is the foundation of reconstruction from multiple images. With the captured images of the plant objects from different perspectives, we need to find the relationship between each of the two. Firstly, we used a chessboard to estimate the camera intrinsic parameters, including the image dimension in pixels, the focal length. Then, we need to compute the feature points and its matching pairs among different view images. Projective reconstruction and robust estimation techniques were employed to define the relative position between images, i.e., the position of the camera at each image acquisition. Once each camera pose is defined, a sparse 3D point cloud for the plant surface is

produced based on feature matching. The flow chart of this method is shown in Figure 1.

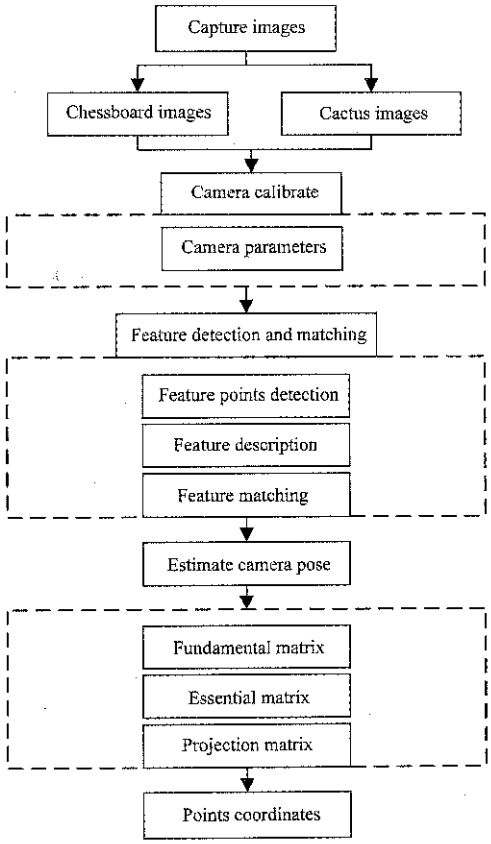

Figure 1 Method flow chart

We followed the Bay's method SURF, which is an excellent algorithm. We transformed an image into a large collection of feature vectors, each of which was invariant to image translation, scaling, and rotation, partially invariant to the illumination changes and robust to local geometric distortion.

Here's an outline of what happened in our reconstruction process.

1) Enter the cactus image to be reconstructed in pairs, examine and read the corresponding matching pair.

2) The fundamental matrix was estimated from the matching points for each pair of views (I_i, I_{i+1}), and then combined with the intrinsic parameters to obtain the essential matrix E, the corresponding rotation matrix R and the translation vector T.

3) The 3D coordinates of the point were calculated according to the camera parameters obtained from the corresponding matching point and projection matrix.

4) Projection matrix was used to reproject the 3D point and minimize the projection error between the reconstruction point and the measurement image point.

5) All images require cluster optimization to optimize the error, keep the 3D point with the error less than the set threshold, on the contrary, remove the larger error point.

3.1 Extraction and matching of SIFT feature points

The SURF approach extracts and describes interest points of an image in a fast, robust and reliable way. The SURF descriptor is both scale and rotation-invariant, and can be used to find corresponding points in a pair of images. This approach has been successfully applied to the image registration problem considering images taken from very different points of view, which is the ideal for solving both encountered problems in the 3D reconstruction pipeline. It is also faster than other similar approaches such as SIFT, allowing the pre-alignment stage to be performed in real-time and identification of un-scanned regions during the acquisition stage.

3.1.1 Extract cactus feature points

The extraction of the SURF feature points on cactus images includes the following steps: the detection of the extreme point in scale space, accurate localization of key point, assigning the main orientation of key point and creating the key point descriptor.

Constructing a scale space on cactus images by Gaussian filter: this is the initial preparation. We created internal representations of the original image to ensure scale invariance. For the two-dimensional image $I(x, y)$, the scale space representation $L(x, y, \sigma)$ at different scales can be obtained by convolution of the image $I(x, y)$ and the Gaussian kernel $G(x, y, \sigma)$.

SURF detector based on the Hessian matrix has better performance in terms of calculation time and accuracy. However, rather than using a different measure for selecting the location and the scale, we rely on the determinant of the Hessian for both. Given a point $x=(x, y)$ in an image I, the Hessian Matrix $H(x, \sigma)$ in x at scale σ is defined as follows:

$$H(x,\ \sigma)=\begin{bmatrix} L_{xx}(x,\ \sigma),\ L_{xy}(x,\ \sigma) \\ L_{xy}(x,\ \sigma),\ L_{yy}(x,\ \sigma) \end{bmatrix} \quad (1)$$

where, $L_{xx}(x, \sigma)$ is the convolution of the Gaussian second order derivative $\frac{\partial^2}{\partial x^2}g(\sigma)$ with the image I in point x, and similarly for $L_{xy}(x, \sigma)$ and $L_{yy}(x, \sigma)$.

SURF improved the original Hessian and proposed a

fast detector and refined the original Hessian Matrix as:

$$H(x, \sigma) = \begin{bmatrix} D_{xx}, D_{xy} \\ D_{xy}, D_{yy} \end{bmatrix} \quad (2)$$

where, D_{xx}, D_{xy}, D_{yy} represent the convolution of the box filter and the cactus image, and the Hessian matrix determinant (3) can be approximated:

$$Det(H_{apprax}) = D_{xx}D_{yy} - (0.9D_{xy})^2 \quad (3)$$

Compare a pixel with its 26 neighbors in 3×3 regions at the current and adjacent scales, if a point is the maximum or minimum in the 26 neighbors among the current scale and the upper and lower scales of the DOG scale space, then we consider the point as a feature point in the scale.

3.1.2 Feature description

Assigning the orientation for each key point, so that the detector has a character of rotation invariance.

$$m_w = \sum_w dx + \sum_w dy \quad (4)$$

$$\theta_w = \arctan\left[\sum_w dx \Big/ \sum_w dy\right] \quad (5)$$

Equations (4) and (5) are the gradient magnitude and the orientation of pixel (x, y) at its scale $L(x, y)$. In actual calculation, a gradient histogram is formed from the gradient orientations of sample points within a region around the key point. The scope of the gradient histogram ranges from 0 to 3600, each 100 represents a direction, so there are 36 directions in all. The highest peak in the histogram is detected as the dominant direction of the key point.

The wavelet responses dx and dy is summed up over each sub-region and formed a first set of entries to the feature vector. In order to introduce in information about the polarity of the intensity changes, we also extracted the sum of the absolute values of the responses, $|dx|$ and $|dy|$. The feature vector of cactus is denoted as $V = \{\sum dx, \sum |dx|, \sum dy, \sum |dy|\}$, and each feature point forms a vector of 16×4 = 64 dimensions. Finally, the normalization of the feature vector is made to have a certain robustness to the change of brightness. Compared with the SIFT dimension, it is reduced by half and the matching speed is greatly accelerated during feature matching.

We extracted SURF key points from the cactus images, for visualization, a circle is used to indicate the location of the SURF feature point, the center of the circle is its characteristic point, the size of the circle radius (line segment) corresponds to different scales, and the orientation corresponds to the main direction. Compare (a) and (b) in Figure 2, the same feature points in both figures are in the same direction, and the most of the small circles whose feature points are located in the target crop area.

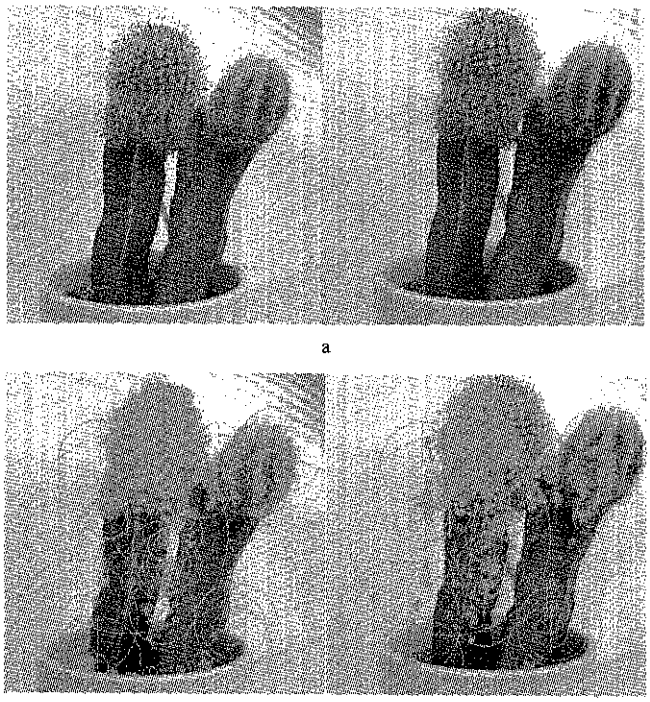

a

b

Figure 2 Cactus images and images SURF feature point

3.1.3 GMS feature matching

GMS (Grid-based Motion) feature matching algorithm outperforms the traditional rate detection algorithm in terms of recall, accuracy and F measurement, and has high matching performance in SLAM and pose estimation. S_{ij} is used to represent the degree of matching of two images in different regions, and its calculation as shown in Equation (6):

$$S_{ij} = \sum_{k=1}^{K=9} |\mathcal{X}_{i^k j^k}| \quad (6)$$

$$cells\{i, j\} \in \begin{cases} T, & if\ S_{ij} > \mathcal{T}_i \approx \alpha\sqrt{n_i} \\ F, & otherwise \end{cases} \quad (7)$$

Among them, $|\mathcal{X}_{i^k j^k}|$ is the number of matches between the cells $\{i^k, j^k\}$, through the experiment

conclusion that the proposed G = 20×20 cells. The α of the threshold $\mathcal{T}_i \approx \alpha\sqrt{n_i}$ is determined experimentally and α=6, n_i is the number of all the features in a single cell, as shown in Figure 3. And then determine whether the region matches according to the threshold.

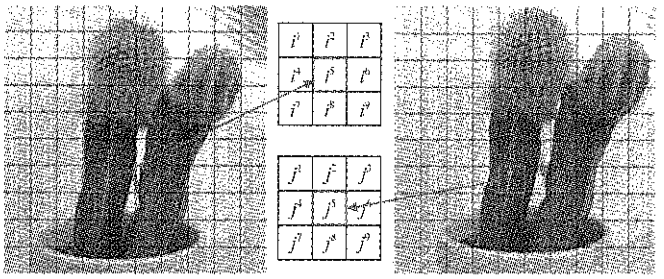

Figure 3 Cells $\{i, j\}$ surrounding area matching degree

For the two images (I_a, I_b), the feature points and are first detected and described by SURF, and then the GMS feature matching algorithm is used. The specific steps are as follows:

1) In each cell i of I_a, find the cells j that has highest number of matching in I_b;

2) According to (4) (5) to calculate S_{ij} and $\mathcal{T}_i$, if $S_{ij} > \mathcal{T}_i$, Inliers = Inliers $\cup \mathcal{X}_{ij}$;

3) Repeat step 2, with gird patterns shifted by half cell-width in the x, y and both x and y directions.

Output matching inliers.

3.2 Cactus imaging model

According to the matching feature points in the cactus image and the calibrated camera parameters, the coordinates of the feature points in the world coordinate system are obtained. According to the image model, it is assumed that the spatial coordinates $X(X_W, Y_W, Z_W)$ of the feature points and the pixel coordinates $x(u, v)$ are used for convenience, and the homogeneous coordinates are compared with the matrix. The above relationship is expressed by Equation (8):

$$S\begin{bmatrix} u \\ v \\ 1 \end{bmatrix} = \begin{bmatrix} \frac{1}{dx} & 0 & u_0 \\ 0 & \frac{1}{dx} & v_0 \\ 0 & 0 & 1 \end{bmatrix} \begin{bmatrix} f & 0 & 0 & 0 \\ 0 & f & 0 & 0 \\ 0 & 0 & 1 & 0 \end{bmatrix} \begin{bmatrix} R & t \\ 0^T & 1 \end{bmatrix} \begin{bmatrix} X_w \\ Y_w \\ Z_w \\ 1 \end{bmatrix}$$
$$= \begin{bmatrix} \alpha_x & 0 & u_0 & 0 \\ 0 & \alpha_y & v_0 & 0 \\ 0 & 0 & 1 & 0 \end{bmatrix} \begin{bmatrix} R & t \\ 0^T & 1 \end{bmatrix} \begin{bmatrix} X_w \\ Y_w \\ Z_w \\ 1 \end{bmatrix} = M_1 M_2 X = PX \tag{8}$$

where, S is the scale factor; R is the 3D rotation matrix, and t is the 3D translation vectora. M_1 is an intrinsic parameter matrix of 3×4, M_2 is a 4×4 external matrix, and P is a projection matrix.

In this paper, we assuming that the first image taken by the camera is not rotated and translated, the rotation and translation of the second image are referenced to the first image, and the projection matrices P_1 and P_2 of the two images are represented by Equation (9)

$$\begin{cases} P_1 = K(I, 0) \\ P_2 = K(R, t) \end{cases} \tag{9}$$

where, K is the internal parameter; I is the unit matrix of 3×3; R and t are the external parameters calculated in the above Equation (9).

3.3 Calculate 3D point

According to the projection matrix under the two cactus images, the three - dimensional coordinates of a feature point on the cactus are calculated by using the triangulation principle.

$$\begin{aligned} S[u, v, 1] &= P_1[X, Y, Z, 1]^T \\ S'[u', v', 1] &= P_2[X, Y, Z, 1]^T \end{aligned} \tag{10}$$

We can eliminate S and S' then obtain a linear system of equations for space X, as shown in Equation (9).

$$AX = 0 \tag{11}$$

We set P_{11}, P_{12}, P_{13} as the row vector corresponding to P_1, which is the projection matrix of the first view, $[u_i, v_i, 1]^T$ is the homogeneous coordinate of the ith matching point on the corresponding image of P_1, X_i is the 3D coordinate of the corresponding matching point, there are: (where no variable parameter description)

$$S\begin{bmatrix} u_i \\ v_i \\ 1 \end{bmatrix} = \begin{bmatrix} P_{11} \\ P_{12} \\ P_{13} \end{bmatrix} X_i \Rightarrow \begin{cases} su_i = P_{11}X_i \\ sv_i = P_{12}X_i \\ s = P_{13}X_i \end{cases} \Rightarrow \begin{cases} P_{13}X_i u_i = P_{11}X_i \\ P_{13}X_i v_i = P_{12}X_i \end{cases}$$
$$\Rightarrow \begin{cases} P_{13}X_i u_i - P_{11}X_i = 0 \\ P_{13}X_i v_i - P_{12}X_i = 0 \end{cases} \Rightarrow \begin{bmatrix} P_{13}u_i - P_{11} \\ P_{13}v_i - P_{12} \end{bmatrix} X_i = 0 \tag{12}$$

Similarly, the projection matrix P_2 of the second view, the homogeneous coordinates of the corresponding feature points are similarly obtained.

$$\begin{bmatrix} P_{23}u_i' - P_{21} \\ P_{23}v_i' - P_{22} \end{bmatrix} X_i = 0 \tag{13}$$

We have Equation (14) by Equations (12) and (13):

$$\begin{bmatrix} P_{13}u_i - P_{11} \\ P_{13}v_i - P_{12} \\ P_{23}u_i' - P_{21} \\ P_{23}v_i' - P_{22} \end{bmatrix} X_i = 0 \quad (14)$$

Then let $A = \begin{bmatrix} P_{13}u_i - P_{11} \\ P_{13}v_i - P_{12} \\ P_{23}u_i' - P_{21} \\ P_{23}v_i' - P_{22} \end{bmatrix}$, using the least squares method and singular value decomposition (SVD) to obtain the spatial coordinates of the cactus feature point X_i.

4 Experimental results and analysis

Our experimental images consist of two parts, which are checkerboard grid calibration images and the flower reconstruction images.

The checkerboard grid calibration images as shown in Figure 4, the size of checkerboard is 6×9 and the square grid size is 30 mm. Table 1 below shows the calibration parameters of the camera parameters. As shown in Figure 5, the images here are the cactus images for modeling, from left to right and from top to bottom, followed by 1, 2, ... 8.

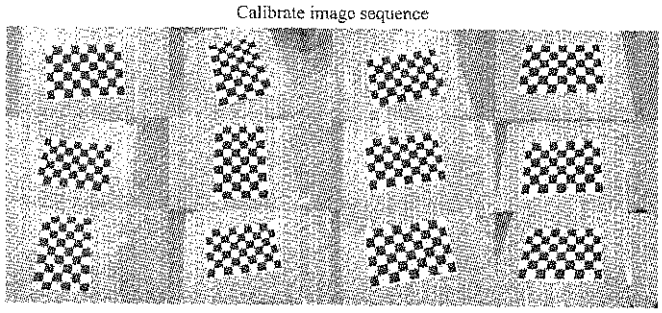

Figure 4 Calibration the board images

Table 1 Camera calibration results

α_x	α_y	u_0	v_0
2732.770013	2826.76907	1605.28042	707.01711

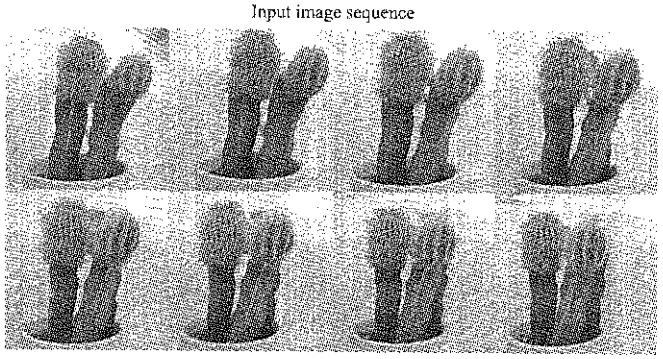

Figure 5 Flower images

Compared the experimental results of SURF algorithm with SIFT, BRISK in terms of detecting the cactus image features, including the detection time, matching time, and the results are indicated in Table 3 and Figure 6. The results of Table 3 show SURF are superior to the SIFT algorithm in the feature detection time and are slower than the BRISK algorithm with fewer detection points. From Figure 6 we can see the difference between different algorithms more intuitively. The SURF algorithm has better feature detection time and matching time (MT1 and MT2) than the SIFT algorithm. Although the binary description BRISK algorithm sub-feature detection time is shorter, the number of features is less than the first two algorithms, not up to the reconstruction requirements.

The result of SURF feature detection as shown in Figure 2, while the left image in (b) of Figure 2 shows more feature points. After the right image in Figure 2 of (b) is transformed through a small angle view, a part of the feature points detected in the left image cannot be detected, resulting in a mismatch. Table 2 shows the statistical results of features which are extracted by SURF and matched by GMS, the first image is matched with other images respectively, which 'Ratio 0.8' corresponds to the results when the test ratio of 0.8, 'Ratio 0.6' corresponds the test ratio of 0.6, and the 'GMS matching' is the result of the improvement under the same ratio. As can be drawn from Table 2, GMS matching can be used to get more accurate matching points, and the relative ratio detection can eliminate some mismatches.

Figure 7 represents the matching results with different ratio and GMS, when ratio increases, the matching rate will be reduced, that is more stringent constraints. After GMS rejecting, a more accurate matching effect can be obtained. The experimental data are shown by the dotted lines in GMS 0.8 and GMS 0.6.

Compared (a) and (b) from Figure 8, we can see that there are many intersections and a large number of mismatching feature points in (a), and (b) is the result after eliminating false matches by GMS algorithm, the matching effect has been significantly improved, although the loss of some of the characteristics of the points, the matching effect is satisfactory.

Table 2 SURF feature extraction and matching statistics

No.	SURF Feature points	Ratio 0.8	GMS matching	Rejected	Ratio 0.6	GMS matching	Rejected
1	3604	—	—	—	—	—	—
2	4031	938	865	73	801	767	34
3	3346	413	357	56	330	293	37
4	4129	467	409	58	362	333	29
5	3516	774	683	91	649	602	47
6	4101	851	781	70	733	687	46
7	3885	938	850	88	797	751	46
8	3164	501	429	72	412	374	38

Table 3 SURF, SIFT algorithms feature detection time and matching results

No.	SURF	SIFT	BRISK	SURF-time	SIFT-time	BRISK-time	MT1	MT2
1	3604	6413	500	2.12092	7.42036	0.266826	—	—
2	4031	7159	500	2.22658	7.59101	0.261633	4.31987	6.15177
3	3346	5554	500	2.09494	7.37978	0.237669	3.79879	6.25809
4	4129	7548	500	1.78397	7.57924	0.255044	4.23271	6.49967
5	3516	6765	500	2.16111	7.51676	0.245189	4.23754	5.82961
6	4101	5422	500	2.28378	7.39009	0.217273	3.89011	6.28724
7	3885	5153	500	1.78775	7.40541	0.220348	3.88077	6.29944
8	3164	5945	500	2.10788	7.60861	0.235914	3.82521	6.16743

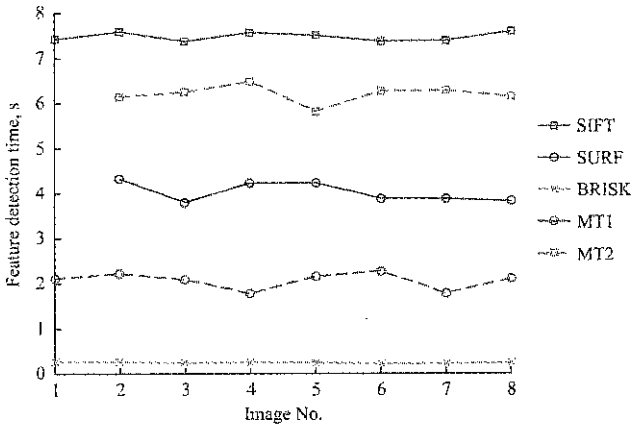

Figure 6 Different algorithm for feature detection, matching time

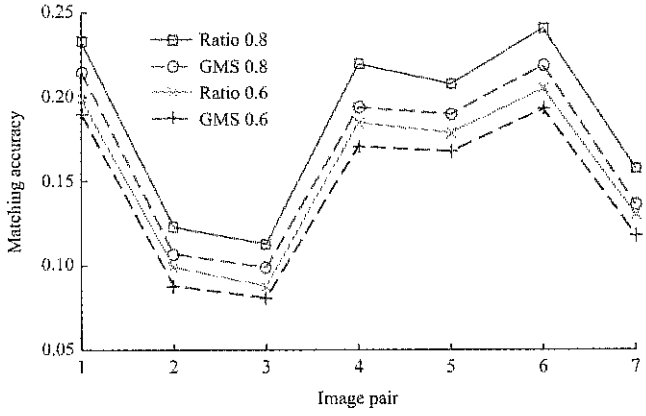

Figure 7 Different Ratio and GMS matching effect

a. Unchecked mismatching b. GMS reject mismatching

Figure 8 Feature matching renderings

After the feature matching is completed, the position of the camera is estimated according to the corresponding matching points, and then the coordinates of the 3D point are calculated by using the triangulation method. Finally, the bundle adjustment algorithm is used to optimize the position. Reconstruction point cloud results are shown in Figure 9, the red box represents the camera, the red number indicates the camera's position.

This experiment collected eight images. We observed the input image and the position of the camera in the

point cloud. The collected images covered only the front part of the object. The information of the back side was not processed. Compared (b) front point cloud, (d) back point cloud, the color of the back point cloud is slightly lighter than the color of the front point cloud, indicating that the number of space points acquired on the back side is less. Reconstruction of the frontal reconstruction works well, more than 20,000-point cloud data were obtained, and we can see cactus general outline from the reconstruction point cloud map.

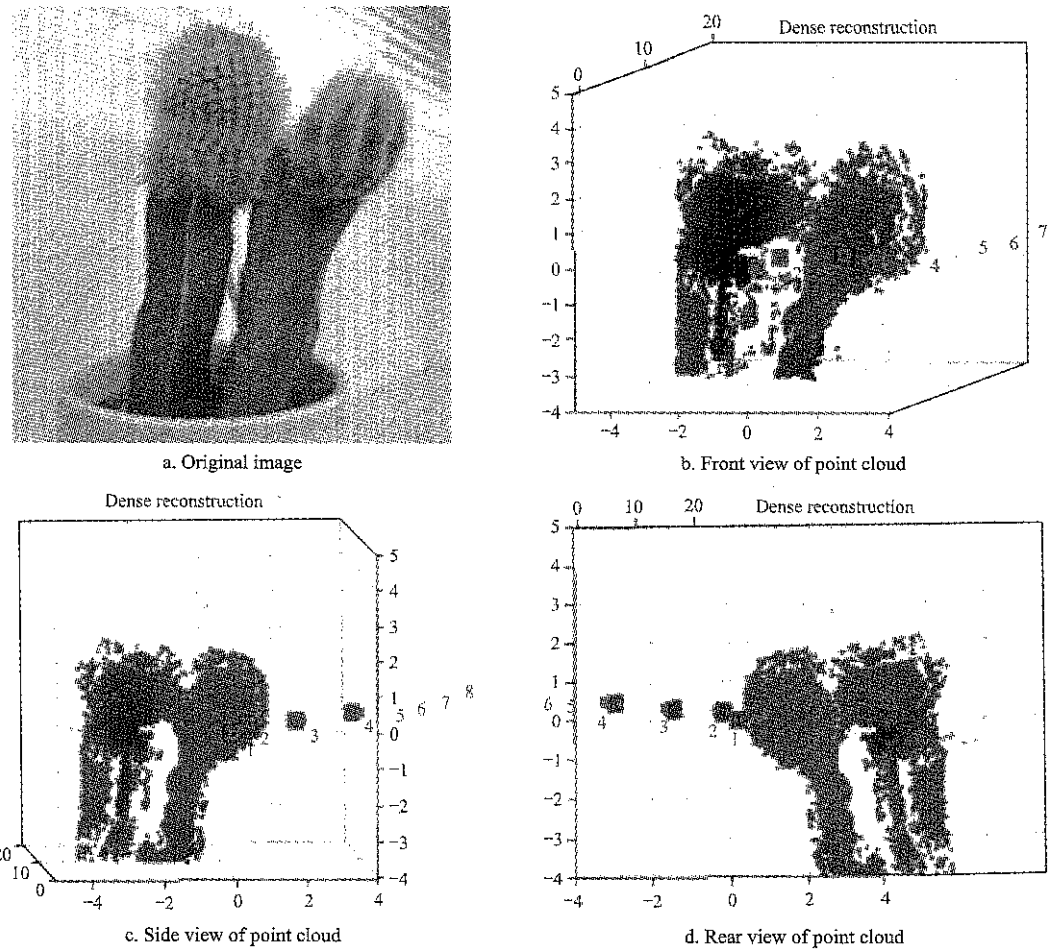

a. Original image b. Front view of point cloud c. Side view of point cloud d. Rear view of point cloud

Figure 9 Reconstruction point cloud

In order to reproduce the cactus prototype and obtain better visual effects, we further processed the point cloud and imported the resulting point cloud into the MeshLab software. After performing the surface reconstruction and texture mapping operations, the reconstruction map was obtained and it is shown in Figure 10. The reconstruction of the top obtained by our method and the bottom reconstruction is the result of SIFT and ratio method. (a), (b) and (e), (f) are front and side views reconstructed using different methods respectively, with a few noise points; (c), (g) and (d), (h) is the result of de-noising. It can be easily seen from Figure 10 that the reconstruction effect has been remarkably improved after de-noising, and the surrounding noise points were basically eliminated. The cactus reconstruction model obtained by this method is more complete, and the reconstruction results of other methods are large-scale empty and missing more data. Therefore, the method in this paper can get better reconstruction results.

5 Conclusion

In this paper, we proposed an automated and low-cost cactus morphological reconstruction method based on SURF features from multi-view. The three-dimensional model of the reconstructed object was obtained from a group of cactus images information taken at different angles. SURF was used to detect and characterize the feature points. The GMS matching algorithm was used to eliminate the mismatch. Then the pose of the camera was automatic estimated based on the calibrated camera

parameters to obtain the point cloud data. Finally, the texture objects were restored. Experimental results showed that this method proposed effectively improved the matching accuracy and achieved a better matching effect.

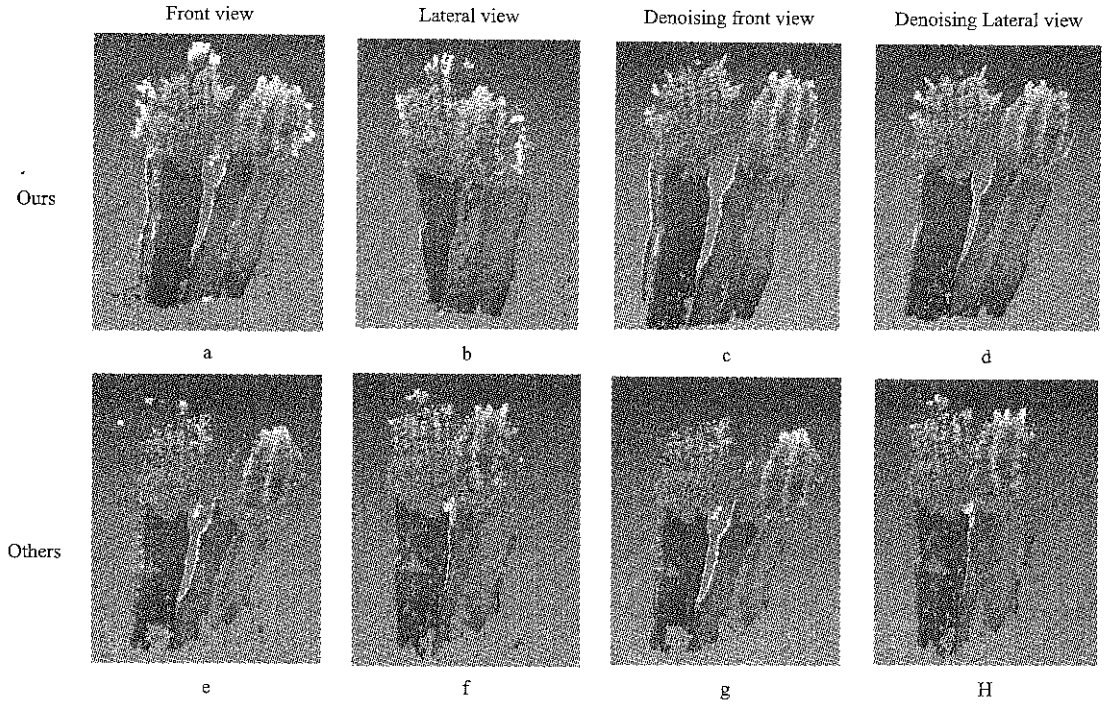

Figure 10 Different methods to reconstruct

6 Future work

Although this paper has completed the reconstruction of the simple cactus model, there are still many imperfections and problems to be solved. In addition, plant architecture is usually complex, including large amounts of self-occlusion (leaves obscuring one another), and many smaller surfaces that appear similar. Therefore, how to measure plants in 3D in a non-destructive manner remains a serious challenge in plant phenotyping.

In the future work, we need to improve the following aspects:

(1) Simplify the operational steps of cactus rebuilding, make the operation intelligent and combine with the developmental heat of artificial intelligence today, to establish a sound mechanism for human-computer interaction as the goal.

(2) Achieve a complete flower reconstruction. In this paper, the reconstruction of flower plants is only the surface reconstruction of the organs of flower plants. If the complete plant model needs to be rebuilt, multiple modeling and model additions are needed to obtain the complete flower model.

(3) Improve the universal applicability of the reconstruction system. The reconstruction in this paper can only be carried out on the relatively simple structure of flowers. If the topological structure of flowers and other plants is too complicated, the reconstruction result will be distorted.

Acknowledgements

The authors would like to acknowledge the contribution to this research provided by the sponsors of National Natural Science Foundation of China (61472172, 61673200) and Provincial Natural Science Foundation Project (ZR2016FM15).

[References]

[1] Azzari, G., M. L. Goulden, and R. B. Rusu. 2013. Rapid characterization of vegetation structure with a Microsoft Kinect sensor. *Sensors*, 13(2): 2384–2398.

[2] Bay, H., A. Ess, T. Tuytelaars, and L. V. Gool. 2008. Speeded-up robust features (SURF). *Computer Vision and Image Understanding*, 110(3): 346–359.

[3] Bian, J. W., W. Y. Lin, W. Y. Lin, Y. Matsushita, S. K. Yeung, T. D. Nguyen, and M. M. Cheng. 2017. "GMS: Grid-Based Motion Statistics for Fast, Ultra-Robust Feature Correspondence," *2017 IEEE Conference on Computer Vision and Pattern Recognition (CVPR)*, Honolulu, Hawaii, USA, 2017, pp. 2828–2837.

[4] Chene, Y., D. Rousseau, P. Lucidarme, J. Bertheloot, V. Caffier, P. Morel, E. Belin, and F. Chapeau-Blondeau. 2012. On the use of depth camera for 3D phenotyping of entire plants. *Computers & Electronics in Agriculture*, 82(1): 122–127.

[5] Clark, R. T., R. B. Maccurdy, J. K. Jung, J. E. Shaff, and S. R. Mccouch. 2011. Three-dimensional root phenotyping with a novel imaging and software platform. *Plant Physiology*, 156(2): 455–465.

[6] Edelsbrunner, H., C. Tomasi, and P. Benfey. 2011. Detailed reconstruction of 3D plant root shape. *IEEE International Conference on Computer Vision*, 24(4): 2026–2033.

[7] Kaminuma, E., N. Heida, Y. Tsumoto, N. Yamamoto, N. Goto, N. Okamoto, A. Konagaya, M. Matsui, and T. Toyoda. 2004. Automatic quantification of morphological traits via three-dimensional measurement of Arabidopsis. *Plant Journal for Cell & Molecular Biology*, 38(2): 358–365.

[8] Lee, K. H., and R. Ehsani. 2009. A laser scanner based measurement system for quantification of citrus tree geometric characteristics. *Applied Engineering in Agriculture*, 25(5): 777–788.

[9] Liu S, L. M. Acosta-Gamboa, X. Huang, A. Lorence. 2017. Novel low-cost 3D surface model reconstruction system for plant phenotyping. *Journal of Imaging*, 3(3): 39.

[10] Min, Y., X. J. Zou, L. F. Luo, N. A. Liu, Y. D. Mo, M. Y. Chen, and C. L. Wang. 2016. Error analysis of dynamic localization tests based on binocular stereo vision on litchi harvesting manipulator. *Transactions of the Chinese Society of Agricultural Engineering*, 32(5): 50–56. (In Chinese with English abstract)

[11] Ni, Z., T. F. Burks, and W. S. Lee. 2014. 3D reconstruction of small plant from multiple views. In Proceedings of *the ASABE and CSBE/SCGAB Annual International Meeting*, Montreal, QC, Canada, 13–16 July.

[12] Paproki, A., X. Sirault, S. Berry, R. Furbank, and J. Fripp. 2012. A novel mesh processing based technique for 3D plant analysis. *Bmc Plant Biology*, 12(1): 1–13.

[13] Paulus, S., J. Dupuis, A. K. Mahlein, and H. Kuhlmann. 2013. Surface feature based classification of plant organs from 3D laser scanned point clouds for plant phenotyping. *BMC Bioinformatics*, 14(1): 238.

[14] Segundo, M. P., M. P. Segundo, L. Gomes, O. R. P. Bellon, and L. Silva. 2013. Automating 3D reconstruction pipeline by surf-based alignment. *IEEE International Conference on Image Processing. IEEE*, 2013: 1761–1764.

[15] Tang, L. Y., C. Hou, H. Y. Huang, C. C. Chen, J. Zou, and D. Lin. 2015. Light interception efficiency analysis based on three-dimensional peach canopy models. *Ecological Informatics*, 30: 60–67.

[16] Vos, J., J. B. Evers, G. H. Buck-Sorlin, B. Andrieu, M. Chelle, P. H. B. de Visser. 2010. Functional-structural plant modelling: a new versatile tool in crop science. *Journal of Experimental Botany*, 61(8): 2101.

[17] Vourvoulakis, J., J. Kalomiros, and J. Lygouras. 2016. FPGA accelerator for real-time SIFT matching with RANSAC support. *Microprocessors & Microsystems*, 49: 105–116.

[18] Wang, Q., and Q. Zhang. 2013. Three-dimensional reconstruction of a Dormant Tree using RGB-D cameras. 2013 Kansas City, Missouri, July 21 - July 24.

[19] Wei, Q., Z. Xu, and J. Wang. 2015. Research and implementation of 3D reconstruction technique based on images. *International Conference on Information Science and Control Engineering. IEEE*, 2015: 408–411.

[20] Wu, C. 2013. Towards linear-time incremental structure from motion. In Proceedings of the *2013 International Conference on 3D Vision*, 127–134. Seattle, WA, USA, 29 June–1 July.

[21] Xiong, J. T., Z. L. He, L. Y. Tang, R. Lin, and Z. Liu. 2017. Visual localization of disturbed grape picking point in non-structural environment. *Transactions of the Chinese Society for Agricultural Machinery*, 48(4): 29–33, 81.

[22] Zhang, Z. 2012. Microsoft Kinect sensor and its effect. *IEEE Computer Society Press*, 19(2): 4–10.

[23] Zhang, Z. B., S. L. Zhao, X. W. Luo, and F. Q. Wei. 2015. Matching method of green crops based on SURF feature extraction. *Transactions of the Chinese Society of Agricultural Engineering*, 31(14): 172–178. (In Chinese with English abstract)

[24] Zhang, Z., and Q. Tang. 2016. Camera self-calibration based on multiple view images. *Nicograph International. IEEE*, 2016: 88–91.

[25] Zhao, L. L., G. H. Geng, X. F. Wang, and Q. Liu. 2012. Three dimensional reconstruction algorithm based on uncalibrated multiple images. *Journal of Computer Applications*, 32(10): 2802–2805.

[26] Zhong, S. S., Y. F. Chen, M. Zhang, Z. Xie, and C. Liu. 2016. MSURF: A new image matching algorithm which combines homography and SURF algorithm. *International Conference on Geoinformatics. IEEE*, 2016: 1–7.

MEMBERSHIP APPLICATION FORM

Affix Photo here

ASIAN ASSOCIATION FOR AGRICULTURAL ENGINEERING (AAAE)

I wish to become a member of the AAAE
Membership Categories: (Mark the appropriate box)

☐ LIFE MEMBER	As per the age of a member (minimum US$ 400)
☐ REGULAR MEMBER	US$ 50 per calendar year, and US$ 150 minimum for 3 years*
☐ CORPORATE MEMBER	US$ 400 minimum for 2 years (for industries only)

PERSONAL DETAILS

NAME (Prof./Dr./Mr./Ms.) .....

DATE OF BIRTH: .....

TITLE/POSITION: .....

ORGANIZATION: .....

Mailing Address: .....

.....

Phone: ..... E-mail: .....

Fax: .....

QUALIFICATIONS ATTAINED:

.....

.....

Number of years of professional experience: .....

.....

Special field(s) of interest: .....

Affiliation with other society or association: .....

.....

Please make payment either by bank draft/cheque in favor of "**SINOMACH Academy of Science and Technology Co., Ltd**" and mail to the address below, or ask the AAAE Secretariat for bank information.

AAAE Secretariat
Room 306, College of Food Science and Nutritional Engineering, China Agricultural University
Tel: +86-10-62737401
Fax:+86-10-62737401
Email: aaaese@aliyun.com; iaejeditor@aliyun.com

For Office Use Only Date received: .....

Secretariat Acknowledged ..... Verification of National Affiliation .....
Membership Grade Approved ..... Membership Number .....
Membership Plaque/Certificate/Card issued .....

*Inclusive of US$ 10 for air mailing of journal and other material

JOURNAL SUBSCRIPTION INFORMATION

INTERNATIONAL AGRICULTURAL ENGINEERING JOURNAL (IAEJ)

The *International Agricultural Engineering Journal* (IAEJ) is an International Journal focusing on Research and Development in Agricultural Engineering and is published by the Asian Association for Agricultural Engineering (AAAE). It is a peer-reviewed international journal published only in printed form with 4 issues per year. The official ISSN registration number is 0858-2114. IAEJ is one of the most prestigious international journals in the field of agricultural engineering and has been indexed and abstracted in EI Compendex (Core), Scopus, Elsevier Bibliographic Databases, etc.

Subscriptions to the International Agricultural Engineering Journal (IAEJ) are invited which will enable researchers to get access to the valuable scientific and technological findings of the scientists, engineers, research scholars and professors worldwide working in a diverse range of fields in agricultural engineering.
Subscription rates are as follows:

US$ 280* per annum (four issues)

* Including postage, excluding any bank charges

Please make payment either by bank draft or by cheque:

(1) Payment by check in favor of "**SINOMACH Academy of Science and Technology Co., Ltd**" to the address below:

AAAE Secretariat
Room 306, College of Food Science and Nutritional Engineering, China Agricultural University
Tel: +86-10-62737401
Fax:+86-10-62737401
Email: aaaese@aliyun.com; iaejeditor@aliyun.com

Bank information:

For bank transfer of RMB (人民币转账):
单位名称：国机集团科学技术研究院有限公司
单位地址：北京市海淀区丹棱街 3 号
开户银行：交通银行股份有限公司北京海淀支行
银行账号：110060576018150140601
开户银行代码：301100000099

For bank transfer of US dollars:
Beneficiary Bank: BANK OF COMMUNICATIONS CO. LTD., BEIJING MUNICIPAL BRANCH
SWIFT Code: COMMCNSHBJG
Bank Address:
Beneficiary: SINOMACH Academy of Science and Technology Co., Ltd
Beneficiary A/C No.: 110060576146600001678
Address: No.3 Danling Street, Haidian District,Beijing, P.R.China
Phone No.: +86 10 82606751

Please indicate the volume you intend to subscribe, your shipping address, contact details by email. If you have any other inquiries, please contact AAAE Secretariat by aaaese@aliyun.com.

Call for papers for the International Agricultural Engineering Journal (IAEJ)

Dear All:

The **International Agricultural Engineering Journal (IAEJ)** is an international journal focusing on research and development in agricultural engineering published by the **Asian Association for Agricultural Engineering (AAAE)**.

IAEJ is a peer-reviewed international journal, publishing in four issues per year. The official ISSN registration is 0858-2114. **The scope of *IAEJ* include: soil and water engineering, farm machinery, farm structures, post-harvest technology, biotechnology, food processing and emerging technologies and any other topic related to agricultural engineering.** International Editorial Board was comprises of outstanding scientists and professionals from all other world involved in various agricultural engineering disciplines. *IAEJ* is one of the most prestigious international journals in agricultural engineering and has been indexed and abstracted in *EI Compendex (Core), Scopus, Elsevier Bibliographic Databases*, etc.

IAEJ welcomes high quality research articles from scientists, engineers and academicians worldwide working in a diverse range of fields in agricultural engineering. Authors are solicited to share their valuable scientific and technological findings with this journal by submitting manuscripts on research, projects, survey works, innovative developments and agro-industrial experiences etc.

Manuscripts for review and possible publications should be submitted via e-mails to iaejeditor@aliyun.com. Submission must be original and should not have been published previously or be under consideration for publication elsewhere.

For more information about submission format, please see the *Guidelines for Authors* in IAEJ.

Yours sincerely,

Prof. CHENG Yongqiang

Secretary General of AAAE
Executive Editor-in-Chief
International Agricultural Engineering Journal (IAEJ)

Chinese Society for Agricultural Machinery (CSAM)

SINOMACH | CAAMS

Chinese Academy of Agricultural Mechanization Sciences (CAAMS)

Bird's-eye View of the Campus of CAAMS

National and International Conferences Sponsored by CSAM

MOST-USDA Workshop on Agricultural Products Processing and Food Safety

Hanging Garden Between the Two Main Office Buildings of CAAMS

VIP Guest Room of CAAMS

Academic Conference Room of CAAMS

Conference Hall of CAAMS

Chinese Academy of Agricultural Mechanization Sciences (CAAMS) was established in 1956. It is a large-scale scientific and technological enterprise with the strongest R&D capabilities in modern agriculture machinery, agro-product processing and packaging industry. It also engages in the development of related high-tech industries such as electro-hydraulic system, information, and media, etc. There are over 8,000 staffs, two-thirds of whom are professional researchers and technicians.

CAAMS has remarkably strong R&D platforms and resources including 5 national key laboratories and testing centers, and administration offices of agricultural machinery committees, societies, associations and alliances. It has completed more than 3,000 scientific and technological projects at national and ministerial level, obtained 2,600 important technological achievements and provided over 3,000 new agricultural machines in 9 categories in the past 60 years.

CAAMS has established cooperative relationships with universities, associations, societies, research institutions and government agencies in over 80 countries around the world. The Editorial Office of International Commission of Agricultural and Biosystems Engineering (CIGR) Journal and the Secretariat of the Asian Association for Agricultural Engineering (AAAE) are both located in CAAMS.

While adhering to its enterprise culture of "Manufacture best agro-machinery to benefit agricultural production and processing", CAAMS will continue to focus on its major business and commit to lead China's agricultural equipment industry.

The Chinese Society for Agricultural Machinery (CSAM), whose administrative body is in CAAMS was established in 1963 with a total membership of over 12,500. To help executing China's strategies of sustainable development and vitalizing the country through science and education, CSAM aims at serving agricultural machinery technicians, promoting academic exchanges, increasing international cooperation, and promote agricultural mechanization for the betterment of farmers. It plays an important role in advancing the integration of science and technology with economy for the purpose of speeding up the realization of China's modernization.

The main publications of the CSAM are Transactions of the Chinese Society of Agricultural Machinery, Farm Machinery, and China Agricultural Mechanization. Together with the Chinese Society of Agricultural Engineering(CSAE), CSAM co-sponsors the CIGR Journal.

Address: No.1 Beishatan, Deshengmen Wai, Beijing, 100083, China
Website: http://www.caams.org.cn
http://www.agro-csam.org

International Agricultural Engineering Journal

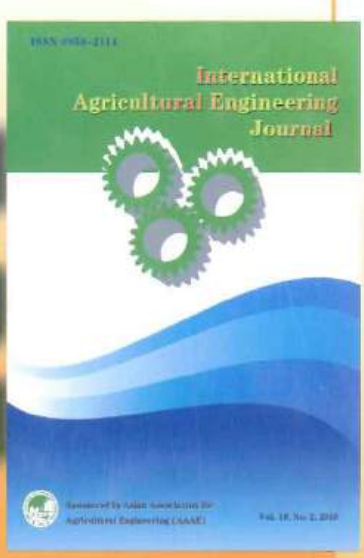

International Agricultural Engineering Journal (IAEJ) was launched at the Asian Institute of Technology (AIT), Bangkok, Thailand in 1992. Since 1992, IAEJ has been sponsored and published by the Asian Association for Agricultural Engineering (AAAE) with a frequency of four issues per year and it is the official journal of AAAE. It is published only in print copy and over 660 papers in 25 volumes have been published during past 25 years.

IAEJ is an international and multidisciplinary journal. The major goal of this journal is to communicate advances in agricultural engineering, with a particular preference to Asia, to researchers, practicing engineers and decision makers of developing countries. IAEJ publishes peer-reviewed research papers (both theoretical and applied) and state-of-the-art reviews related to agricultural and biosystems engineering. Its scope includes soil and water engineering, farm machinery, ergonomics, farm structures, renewable energy, postharvest technology, food process engineering, agricultural biotechnology, IT in agriculture, and emerging technologies. Subjects of basic engineering and science such as instrumentation, precision agriculture, protected cultivation, global warming, climate change, terramechanics, environment in agriculture, and new materials are also included in the scope of IAEJ.

IAEJ publishes original papers only and the submission of a manuscript will be taken to imply that the contributions are original and that no similar manuscript has been or is being submitted to other journals. Manuscripts are solicited from all areas of specialization in agricultural and biosystems engineering. It is a valuable service provided by AAAE to its members to publish papers in "International Agricultural Engineering Journal" regularly. IAEJ adopts Chicago Style and follows the flAEJ Guidelines for Authors' strictly.

Through the persistent efforts of the former Editors-in-Chief of IAEJ, Prof. David Gee-Clough, Prof. Vilas M. Salokhe, Prof. Rameshwar S. Kanwar and Dr. Wang Yingkuan and former Executive Editor-in-Chief, Prof.Zhang lanfang, the IAEJ has grown into one of the prestigious international journals in the field of agricultural engineering. We thank all the former Editors-in-Chief and editorial board members for their leadership and generous supports, and special thanks should also go to the current Editor- in-Chief, Prof. Li Shujun, Executive Editor-in-chief, Prof. Cheng yongqiang for their excellent services.

IAEJ is indexed and abstracted in: El Compendex (Core), Scopus, Elsevier Bibliographic Databases, Agricultural Engineering Abstract by CAB International, Global Health (GH), Chemical Abstracts (CA), Cambridge Scientific Abstracts-Natural Sciences (CSA-Nat Sci), Cambridge Scientific Abstracts-Technology (CSA-T), Pollution Abstracts, Ulriches Periodicals Directory (Ulrich PD), and Applied Mechanics Review.

IAEJ is a quarterly journal, publishing four issues per year. In order to accelerate and streamline the manuscript handling process, an online manuscript submission system, together with the website of IAEJ was set up in 2012. After the launch this journal has provided open access to its contents on the principle that making research findings freely available to the public supports a greater global exchange of knowledge, which in turn can enhance the usefulness and visibility of IAEJ.

Contact Information:
International Agricultural Engineering Journal Room 306, College of Food Science and Nutritional Engineering, China Agricultural University
Tel: +86-10-62737401 Fax:+86-10-62737401
Email: aaaese@aliyun.com iaejeditor@aliyun.com